Development of bimodal grain structures and their effect on toughness in HSLA steel

Chakrabarti, Debalay.

Thesis (PhD.)--University of Birmingham, Department of Metallurgy and Materials, School of Engineering.

2007

Contents

Short Abstract

To understand the formation of bimodal ferrite grain structures (i.e. mixed coarse + fine grain sizes) in TMCR HSLA steel plates, as-continuously cast HSLA steel slabs with varying microalloying additions (Ti, Nb and V) were reheated to temperatures in the range 1000-1300 °C and deformed at 1110 °C and 980 °C temperatures in Gleeble 3500. The interdendritic segregation during continuous casting and the consequent inhomogeneous microalloying precipitate distributions (with interdendritic regions being the precipitate-rich regions) has resulted in severely bimodal austenite grain structures under certain reheat conditions (due to the significantly higher pinning force in solute-rich regions compared to solute-poor regions). The segregation of microalloying elements can also promote bimodality during deformation by affecting the local recrystallisation kinetics. Notch-bend fracture tests were performed at –160 °C to investigate the effect of a bimodal grain size distribution on fracture toughness by comparing local fracture stress values for uniformly fine, uniformly coarse and bimodal ferrite grain structures. Analysis of local fracture stress values suggests that bimodality can raise the scatter in the fracture test results and therefore, it is undesirable. Current methods of measuring bimodality are not useful at consistently quantifying small differences in bimodality between microstructures of steel, and hence, two easy-to-measure parameters (peak height ratio, PHR and peak grain size range, PGSR) have been suggested in this study to quantify bimodality in HSLA steels.

Thesis Abstract

Three as-continuously cast HSLA steel slabs with varying microalloying additions (Ti, Nb and V) were quantified through thickness in terms of secondary dendritic arm spacing, second phase volume fraction and particle distributions using optical microscopy and high resolution SEM. Prior austenite and ferrite grain sizes and distributions (banding and bimodality, Footnote 1) have been determined following reheating of the as-cast slabs to temperatures in the range 1000-1300 °C and on a thermomechanical control rolled (TMCR) HSLA steel plate of similar composition. The as-cast slabs showed inhomogeneous microalloying precipitate distributions with the separation between precipitate rich and precipitate poor regions being consistent with interdendritic segregation and hence the secondary dendrite arm spacing. Grain size bimodality was not significant in the as-cast condition but reheating quarter-thickness samples in the temperature range 1000-1300 °C resulted in different levels of bimodality, with severely bimodal structures occurring under certain reheat conditions. The fine grain areas in the reheated microstructures were associated with high number densities of microalloying precipitates whereas the coarse grained areas were precipitate poor. The susceptibility of the slabs to the formation of bimodality, based on the steel chemical compositions and critical reheat temperature ranges, has been identified, both experimentally and theoretically using Thermo-Calc modelling of precipitate stability in the solute rich and the solute depleted regions formed during casting.

Bimodal ferrite grain sizes have been observed in TMCR HSLA steel plates hence, calculations based on existing models and deformation experiments were carried out to understand the effect of deformation on the formation of bimodality in steels with significant microalloy segregation. Results suggest that segregation of microalloying elements can promote bimodality during deformation by affecting the local recrystallisation kinetics. From the calculations the critical TMCR parameters (e.g. deformation temperature and hold time) to avoid the formation of bimodality for a given starting slab structure can be identified.

Notch-bend tests were performed at –160 °C to investigate the effect of a bimodal grain size distribution on fracture toughness by comparing local fracture

stress values for ‘ideal’ microstructure samples (developed by reheat + isothermal holding heat-treatment) with uniformly fine, uniformly coarse and bimodal grain structures. Analysis of fracture stress values suggests that bimodality can have a significant effect on the toughness by generating high scatter in the fracture test results. Local cleavage fracture stress (σ_f) values were linked to the grain size distributions to explain that in the case of bimodal grain size distribution the grains both from the fine grain population as well as from the coarse grain population can initiate cleavage and that is responsible for the high scatter in σ_f.

Current methods of measuring bimodality work well for distinguishing between structures with significantly different levels and / or types of bimodality, however, these are not as good at consistently quantifying small differences between microstructures, for example for steels processed under different conditions. A new method to construct the grain size distributions (in area-percent versus linear scale of equivalent circle diameter grain size) and to quantify bimodality in HSLA steels based on two parameters (peak height ratio, PHR and peak grain size range, PGSR) measured from such distributions is presented in the thesis. The parameters were found to be simple, easy to measure, less subjective and more consistent compared to the standard and non-standard parameters used in the literature.

[Footnote 1: Grain size bimodality refers to abnormally large grains, surrounded by small grains in the microstructure. Banding refers to alternate arrangement of two different microstructural regions (based on grain sizes (coarse and fine grain regions) / phase / compositions) almost in parallel fashion.]

Acknowledgement

I would like to gratefully acknowledge the following:

- Dr. C L Davis for her guidance, encouragement and friendship throughout my Ph.D. From the day I first applied to her back in 2002, till today, she has helped and supported me in many ways; not only academically but also financially and personally.

- Dr. Martin Strangwood for his valuable academic suggestions and friendly discussions, mainly on cricket.

- Prof. Paul Bowen (Head of the Dept.) and the Department of Metallurgy and Materials, The University of Birmingham, for the provision of research facilities.

- Prof. Ian Jones and Prof. J. F. Knott for being a source of constant encouragement.

- The Universities UK, and the Dept. of Metallurgy and Materials, The Univ. of B'ham, for funding my Ph.D. with the Oversees Research Scholarship, ORS, and the Departmental Scholarship, respectively. The Royal Academy of Engineering for the financial support to attend the Microalloying Conf. (2005) in San Sebastian, Spain.

- Corus Steel Plc. (formerly British Steel) not only for the provision of material but also for offering me a job in STC at the later stages of my Ph.D.

- Every individual from the Dept. of Metallurgy and Materials, The Univ. of B'ham. Among them Mick Cunningham, Pauline, Anne Cabezas, Derek Bully, John, Paul Stanley, Lesley Tomkins and Jasbinder Singh deserve special mention.

- All my friends and colleagues from N206 (our office), with whom I spent a glorious time for more than three long years. Tracey, Matty, Chris and Bilinda, Mizo, Heiko, James, Stu, Andy, Simon, Alex, Cat, Andrei, Dimitri, Edmond, Ahmed, Theo, Yunhui and Mr. Wu, I am grateful to you all.

- All my friends outside my workplace in B'ham, particularly from 75-Tenmouth Rd., 41-Exeter Rd. and 53-Bristol Rd. houses (among them Salar-bhi, Ravi, Raju-bhi, Bineet, Biswajit-da, Shantanu-da, Muttu, Pattavi, Anand and Kabil deserve special mention).

- All my childhood friends from India (especially from Midnapore and B.E. College), especially Papu (Sumit Pratihar) and Sanghamitra (Mrs. Pratihar), who have helped me in various ways. I had a great few days with BD (Dr. Buddhadeb Jana) and Rahul (and his friends) in Rotherham, during the last few days of my thesis-writing.

- Debashish-Da (Dr. Debashish Bhattacharjee) not only forwarded my resume to Claire, but also stood-beside me in difficult time. Prof. A. K. Chakrabarti, Prof. K. K. Ray, Dr. S. B. Singh (all from IIT Kharagpore), Prof. P. J. Roychowdhury and Prof. P. S. Banerjee (all from B. E. College) helped and inspired me throughout my career, besides giving lessons in Metallurgy.

- Regards to the elders of my family (Dadu-bhi, Thamma, Very-good, Mana, Mandal-dadu and Mamu) from whom I am always being blessed. I thank Piu for doing her level best to support ourselves and to make our stay in Birmingham a wonderful one. I wish 'rupu (Debaroop)' all my luck for a very enjoyable life.

- Finally, I would like to express my sincere gratitude to my parents (Baba and Ma), who have always been a 'back-bone' to me. They have brought me up with all the care, comfort and affection in the world, facing lots of difficulties and hardship by their own. I am immensely proud to be their child, and in that note I can never think of anybody else, but them, to dedicate my thesis.

Background

The project originates back to December 1996, when Corus Steel Plc. (formerly British Steel) experienced difficulties meeting an impact toughness of 27 Joule at -50 ºC on 40 mm thick high-strength low alloy (HSLA) steel (C-Mn-Nb-V chemistry) plate (thermo-mechanically controlled rolled, TMCR) for a bridge contract. The initial solution of the problem was to add nickel and increase the titanium level, but that increased the cost of production. Therefore, internal investigations were carried out to determine the cause of the failure, and to rectify the problem without incurring additional alloying cost. The initial investigation revealed that the ferrite grain structure in the TMCR plate was duplex (mixed coarse and fine grain sizes), where streaks of coarse ferrite grains could be seen in a predominantly fine ferrite and pearlite matrix (shown in the photograph below).

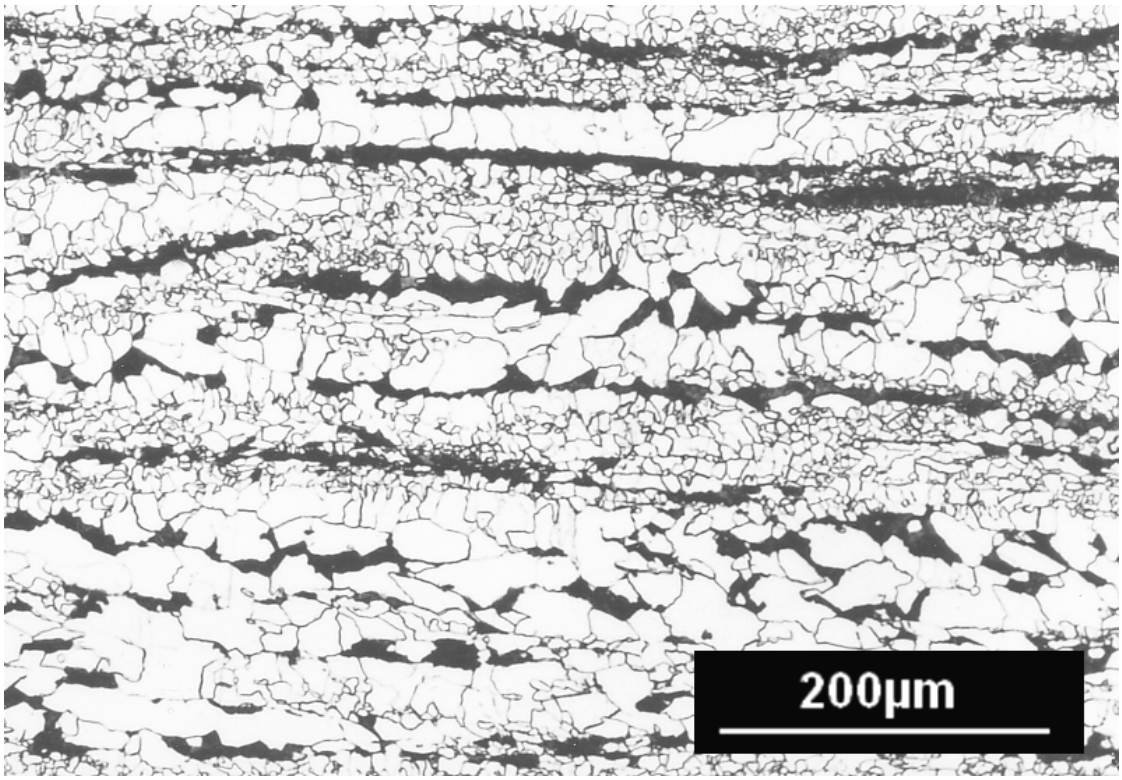

(** Photograph taken from the Corus R&D technical report no. STC/SMT LPC/CKR/07082/2003/R, written by G A Claxton, M J W Green and C Mawdsley)

As the initial part of the investigation Arline Couch in her Ph.D. thesis [Couch 2001] showed that the microalloying elements (especially Nb) can be distributed inhomogeneously in the continuously cast slab, due to interdendritic segregation, and that can generate grain size duplexity upon reheating (mixed coarse and fine austenite grain sizes). However, the spatial distribution of precipitates had not been studied in the as-cast slab. In the present thesis, the spatial distribution in microalloy-precipitate density, precipitate size, and local compositions have been related to the formation of grain size duplexity upon reheating. The current thesis also tries to understand how the spatial distribution in initial austenite grain size, composition and precipitate density can affect the grain refinement during commercial controlled rolling. Duplex (mixed coarse- and fine-grain sizes) grain structure should result in a ‘bimodal’ grain size distribution. In an additional aspect to the work, the current thesis attempts to represent and quantify the different extents of bimodality, commonly observed in reheated and TMCR-steel. To find out the reason behind the failure in achieving the desired impact toughness levels in the plates supplied by Corus for the bridge contract the current thesis investigates the role of grain size bimodality on low-temperature impact toughness.

Symbols and Abbreviations

Formation of bimodality

HSLA	:	High strength low alloy
TMCR	:	Thermomechanical controlled rolling
RLT	:	Recrystallisation limit temperature
RST	:	Recrystallisation stop temperature
T_{NR}	:	No recrystallisation temperature or recrystallisation stop temperature
$T_{95\%R}$	:	Temperature at which 95 % deformed austenite recrystallised
$T_{5\%R}$	:	Temperature at which 5 % deformed austenite recrystallised
CE	:	carbon equivalent
k_p	:	Equilibrium partition ratio
C_S	:	Solute concentration inside solid phase
C_L	:	Solute concentration inside liquid
f_S	:	Volume fraction of solid
C_0	:	Average composition of solute
SDAS	:	Secondary dendrite arm spacing
α	:	Ferrite
δ	:	Delta-ferrite
γ	:	Austenite
EDS	:	Energy dispersive X-ray spectroscopy
WDS	:	Wave-length dispersive X-ray spectroscopy
X_p	:	Volume fraction of precipitation
$\dot{N}$	:	Nucleation rate of precipitates
$\dot{G}$	:	Growth rate of precipitates
t	:	Time
t_{pin}	:	Critical time for precipitate pinning
t_d	:	Interpass delay time

T	:	Temperature
K_S	:	Solubility product
[M]	:	Concentration of microalloying element
[X]	:	Concentration of interstitial (C or N)
T_{DISS}	:	Temperature of dissolution
D_{diff}	:	Diffusion co-efficient or diffusivity
$(D_0)_{diff}$	:	Diffusion constant
Q_{diff}	:	Activation energy for diffusion
γ_s	:	Precipitate-matrix Interfacial energy
R	:	Radius of the grain
D	:	Grain diameter
D_0	:	Initial grain diameter
Rc	:	Critical grain radius
Z	:	Grain size heterogeneity factor
r	:	Precipitate radius
d	:	Precipitate diameter
f	:	Volume fraction of precipitate
r^*	:	Critical precipitate size for grain boundary pinning
ρ	:	Grain boundary curvature
T_{GC}	:	Grain coarsening temperature
Fp	:	Precipitate pinning force
ε	:	Applied strain
ε_c	:	Critical strain required for dynamic recrystallisation
$\dot{\varepsilon}$	:	Strain rate
Z	:	Zener Hollomon parameter
R	:	Universal gas constant
Q_{def}	:	Activation energy for deformation
T_{def}	:	Temperature of deformation
$t_{0.05P}$	:	Time for 5 % precipitation
$t_{0.05R}$	:	Time for 5 % recrystallisation
Q_{rex}	:	Activation energy for recrystallisation

σ_y	:	Uniaxial yield stress
σ_{GB}	:	Contribution to yield stress from Grain boundary strengthening.
σ_P	:	Contribution to yield stress from precipitation strengthening.
σ_{SS}	:	Contribution to yield stress from solid solution strengthening.
σ_i	:	Contribution to yield stress from internal frictional stress.
σ_{DIS}	:	Contribution to yield stress from dislocation strengthening.
k_y	:	Strengthening co-efficient in Hall-Petch equation.
b	:	Burger's vector.
μ	:	Shear modulus.
f_{sub}	:	Volume fraction of sub-grain in the microstructure.
D_{sub}	:	Average sub-grain size in the microstructure.
ITT	:	Impact transition temperature
27J-ITT	:	27 Joule Impact transition temperature
FATT	:	Fracture appearance transition temperature
DBTT	:	Ductile-brittle transition temperature
USE	:	Upper shelf energy
LSE	:	Lower shelf energy
σ_F	:	Principle fracture stress
σ_f	:	Local fracture stress
f	:	Precipitate volume fraction
D	:	Average grain diameter
d	:	Average particle diameter
a	:	Crack length
E	:	Young's modulus
ν	:	Poisons ration
γ_s	:	Surface energy
t'	:	Carbide thickness
γ_p	:	Effective surface energy for plastic deformation
γ_{mm}	:	Effective surface energy for matrix-matrix interface

γ_{pm}	:	Effective surface energy for particle-matrix interface.
K_{1C}	:	Plane strain fracture toughness
CVN	:	Charpy V-notch energy
δ_c	:	Critical crack tip opening displacement
3PB	:	Three-point bend loading
4PB	:	Four-point bend loading.
N_f	:	Free nitrogen content in steel.
σ_{np_ys}	:	Non-precipitation hardening yield strength.
L	:	Applied load in bend test
L_{GY}	:	General yield load in bend test
σ_1	:	Maximum principle stress
σ_{GY}	:	General yield load.
EBSD	:	Electron-backscattered diffraction
OIM	:	Orientation imaging microscopy

Measurement of bimodality

G	:	ASTM grain size number
N_A	:	Number of grains per unit area
$\overline{L_3}$	:	Mean lineal intercept
A	:	Individual grain area

1 Formation of bimodality in HSLA steel

1.1 Principles of microalloyed steel

Microalloyed steels are high strength low alloy steels (HSLA) that contain the microalloying elements, Ti, Nb and V. Microalloying elements are added singly or in combination, characterised by their low contents (less than 0.1 wt%) and by the formation of relatively small and stable carbide-nitride precipitates. The fine precipitates provide grain refinement and / or precipitation strengthening and improve the mechanical properties of the steel. Microalloying additions can increase the yield strength by a factor of two to three times compared to that of plain carbon-manganese steel [Gladman 1997, Tither 1992] at much lower carbon equivalent, CE $\left(CE = wt\%C + \frac{wt\%Mn}{6} \right)$ [Lincoln 1993]. Low steel carbon equivalents are useful for better toughness, formability and weldability [Gladman 1997].

For the last thirty years HSLA steels with microalloying elements have widely been used in pipeline, shipping, construction and automobile applications. The proportions of HSLA steel used for different products and applications in the mid-1980s (compared to carbon or other alloy steels) are summarised in **Table 1.1.1** [Tither 1992]. Microalloyed steels can be substituted for plain carbon steels because of their superior properties (strength, toughness and weldability), better weight reduction and lower cost [Bleck 2005, Korchynsky 2005]. Commercial thermomechanical controlled rolled (TMCR) and air-cooled HSLA steels generally have yield strengths in excess of 550 MPa with impact transition temperatures less

than - 30 °C in plate thicknesses up to ~ 60 mm. Properties can be improved further by controlled or accelerated cooling after TMCR [Gladman 1997, Tither 1992, Korchynsky 2005].

The pressure to reduce the weight of automobiles [ULSAB 1998] and the ever-present threat from lightweight materials such as aluminium- or magnesium-based alloys has led to continuous improvement in high strength steel (HSS). Mechanical properties of various improved steel grades are shown in **Fig. 1.1.1**. Even in the advanced high strength steels (AHSS) (such as dual phase, complex phase or TRIP steels) microalloying elements not only provide strengthening effects but also control the evolution of microstructures, from their effect on phase transformations (**Table 1.1.2**) [Bleck 2005]. Although, Al and some other elements (like B) are also added in steel at small quantities these are not generally termed as microalloying elements [Gladman 1997]. The combination of microalloying additions along with thermomechanical controlled rolling (TMCR) and controlled cooling is the most suitable commercial processing route for the mass production of high strength steels.

A duplex or bimodal (two modes in grain size distribution) ferrite grain structure, comprising of a population of large sized grains within a matrix of small sized grains, has often been reported in TMCR Nb-microalloyed HSLA steels [Wu 2004a, Bhattacharjee 2003, Cai 2005]. Bimodal grain size distributions have been reported to cause a variation in mechanical properties, and are particularly detrimental for impact fracture toughness (can cause significant scatter) of TMCR microalloyed steel plates [Shehata 1982, Wu 2005]. Therefore, bimodal grain structure is to be avoided and for that the formation of this grain structure, the principles behind microalloying additions and the steel processing (casting, reheating and rolling) details need to be studied.

1.1.1 Effects of microalloying elements:

The various effects of microalloying elements on microscopic features and macroscopic properties of steels are summarised in **Table 1.1.2** [Bleck 2005]. The most important actions of each microalloying element in steel are listed below [Heisterkamp 1971, Gladman 1997]:

V: The higher solubility of V compounds (carbide and nitride) ensures that there is complete dissolution of V during slab reheating to provide interphase precipitation during the austenite to ferrite transformation (~ 700-900 °C) or random precipitation in ferrite phase. Those precipitates are fine in size (< 5 nm) and provide precipitation strengthening in steel [Gladman 1971].

Ti: Precipitation of large TiN particles (that can affect the toughness [Balart 2000, Fairchild 2000 a] in liquid steel (due to the low solubility of TiN in austenite) can be avoided by a restricted Ti addition (< 0.02 wt% Ti) to give a fine (~ up to 400 nm) and extremely stable TiN distribution. Such precipitates limit grain growth during reheating and improve toughness, especially in the heat-affected zones of weldments [Gladman 1997, Tither 1992].

Nb: The most significant effect of Nb in HSLA steel is its ability to form strain-induced, fine Nb(C, N) precipitates upon deformation below ~ 1000 °C. A marked drop in the solubility of Nb in austenite between high (~ 1300 °C) and low (~ 900 °C) temperatures leads to such strain-induced precipitation. Strain-induced precipitates

retard the recovery and recrystallisation of the deformed austenite structure and that is used for grain refinement in thermomechanical controlled rolling [Gladman 1997, DeArdo 2003].

Apart from microalloying elements the specific effects in microalloyed steels can be influenced by the additions of aluminium (Al) or any other more conventional alloying elements [Gladman 1997]. Aluminium is commonly used as a deoxidant, but an excess of around 0.02 wt% or more residual Al remains in solution in Al treated steel. Residual Al combines with free nitrogen in solution to form AlN particles. TiN is the only microalloy precipitate that is more stable in austenite than AlN. Any un-dissolved AlN particles prevent grain coarsening during reheating.

1.1.2 Processing of microalloyed steel

A common processing route for HSLA steel plate is shown in **Fig. 1.1.2** [Gray 1983]. After steel making (in basic oxygen furnace or electric arc furnace) the molten metal is continuously cast. Continuous casting not only improves the casting yield (compared to ingot casting), but also a smaller section size can be cast (smaller billet or bloom sections instead of large ingots). This reduces the amount of hot working required to produce the semi-finished and finished products saving energy, time and cost [Gladman 1997]. The continuous cast slabs are reheated prior to rolling. Reheating reduces the inhomogeneity of the cast structure, makes the steel soft for subsequent deformation and dissolves the majority of microalloy precipitates to achieve the maximum benefit of microalloying. A three stage controlled rolling schedule with double hold is quite a common practice to achieve the maximum grain refinement. Any stage of processing (casting, reheating or rolling) may be responsible

for the observed grain size bimodality in some final rolled plate and therefore, the microstructural changes taking place at every processing stage need to be studied.

1.2 Continuous casting of slabs

The microstructure (grain size and dendritic arm spacing), precipitation and segregation developed during continuous casting of steel can have a direct effect on the structure and properties of the end product and therefore, should be studied.

1.2.1 Introduction to continuous casting process

The continuous casting process for steel is shown in **Figure 1.2.1 a** and the close-up of the upper mold region in **Figure 1.2.1 b**. In this process, molten steel flows from a ladle, through a tundish into the mold. The tundish holds enough metal to provide a continuous flow to the mold, even during an exchange of ladles, which are supplied periodically from the steelmaking process. The tundish can also serve as a refining vessel to float out detrimental inclusions into the slag layer. If solid inclusion particles are allowed to remain in the product, then surface defects such as "slivers" may form during subsequent rolling operations, or they may cause local internal stress concentration, which lowers the fatigue life. To produce higher quality product, the liquid steel must be protected from exposure to air by a slag cover over the liquid surface in each vessel and by using ceramic nozzles between vessels. If not, then oxygen in the air will react to form detrimental oxide inclusions in the steel. To withstand the temperature of hot molten metal (1500-1600 ^{o}C) highly basic MgO lining and ZrO_2 are used as refectories in Tundish and submerged entry nozzle, respectively (**Fig. 1.2.1 b**) [Irving 1993, Schrewe 1989].

Once in the mold, the molten steel freezes against the water-cooled walls of a bottomless copper mold to form a solid shell. The mold is oscillated vertically in order to discourage sticking of the shell to the mold walls. Drive rolls lower in the

machine continuously withdraw the shell from the mold at a rate or “casting speed” that matches the flow of incoming metal, so the process ideally runs in steady state. The liquid flow rate is controlled by restricting the opening in the nozzle according to the signal fed back from a level sensor in the mold [Irving 1993].

The most critical part of the process is the initial solidification at the meniscus, found at the junction where the top of the shell meets the mold, and the liquid surface. This is where the surface of the final product is created, and defects such as surface cracks can form, if problems such as level fluctuations occur. To avoid this, oil or mold slag is added to the steel meniscus, which flows into the gap between the mold and shell. In addition to lubricating the contact, a mold slag layer protects the steel from air, provides thermal insulation, and absorbs inclusions [Irving 1993.

Below mold exit, the thin solidified shell (6-20 mm thick) acts as a container to support the remaining liquid, which makes up the interior of the strand. Water or air mist sprays cool the surface of the strand between the support rolls. The spray flow rates are adjusted to control the strand surface temperature with minimal reheating until the molten core is solid. After the center is completely solid (at the “metallurgical length” of the caster, which is 10 – 40 m) the strand is cut with oxyacetylene torches into slabs or billets of any desired length.

A wide range of strand dimensions can be cast depending on final application: ‘slabs’ for flat products such as plate and strip, ‘blooms’ for sections such as beams, and ‘billets’ for long products such as wire. Techniques have also been developed to cast steel directly to thin strip (<3 mm thick) and cast strip is now available commercially. When casting large cross sections, such as slabs, a series of rolls must support the soft steel shell between mold exit and the metallurgical length, in order to minimize bulging due to the internal liquid pressure. Extra rolls are needed to force the strand to “unbend” through the transition from the curved to the straight portion of the path shown in **Fig. 1**. If the roll support and alignment are not sufficient, internal cracks and segregation may result. These defects will persist in the final product, even after many rolling and other operations, so it is important to control the casting process.

The process is started by plugging the bottom of the mold with a “dummy bar”. After enough metal has solidified like a conventional casting onto its head, the dummy bar is then slowly withdrawn down through the continuous casting machine and steady state conditions evolve. The process then operates continuously for a

period of one hour to several weeks, when the molten steel supply is stopped and the process must be restarted. The maximum casting speed of 1-8 m/min is governed by the allowable length of the liquid core, and to avoid quality problems, which are generally worse at higher speeds.

1.2.2 Grain size of continuous cast slab

The three morphological crystal zones (fine-grained ‘chill’ zone at the surface followed by columnar zone and central equiaxed zone), which are typically present in the transverse section of an as-cast ingot of an alloy are shown in **Fig. 1.2.2 a** [Bower 1967]. The similar crystal zones can also be seen in a continuously cast steel slab, **Fig. 1.2.2 b**. The surface ‘chill’ zone is produced by a high rate of nucleation of fine, randomly oriented, equiaxed crystals in the highly supercooled liquid adjacent to the mould wall. Further nucleation is stopped adjacent to the ‘chill’ zone (as the supercooling in the liquid is lost by the latent heat of fusion released by the ‘chill’ zone) and the growth of the favourable oriented grains, those with continues towards the preferred crystallographic direction (<100> in steel) more parallel to the temperature gradient, continues due to constitutional supercooling. These grains form the columnar crystals in the ‘columnar’ zone [Reed-Hill 1973]. The central zone (equiaxed zone) of the as-cast shape consists of large equiaxed crystals produced by nucleation in the highly constitutionally supercooled interior liquid, and by broken off parts of crystals in the columnar zone swept by convection in the liquid to the central zone [Reed-Hill 1973, Flemings 1974, Irving 1993]. Overall, an increase in as-cast grain size can be expected from the sub-surface ‘chill’ zone towards the slab centre due to the drop in cooling rate, giving a longer residence time in the mushy zone and hence greater growth, prior to impingement [Zhang 2000, He 2005].

Zhang et al. [Zhang 2000] reported a gradual increase in ferrite grain size from sub-surface (46-50 μm at 10 mm from top) to the quarter-thickness (76-93 μm) and to the mid-thickness (88-115 μm) position for three continuous cast steel slabs (composition, wt %: 0.09-0.10 C, 0.020-0.045 Nb, 0.001-0.009 Ti, 0-0.05 V, ~ 0.008 N; slab thickness: 290 mm), which showed bimodal (mixed fine and coarse grain size) ferrite grain structures after TMCR. The grain size distributions were also studied at those locations but the distributions did not show the presence of bimodality. Therefore, it was concluded that the bimodality developed during reheating / rolling schedules [Zhang 2000].

1.2.1 Dendritic solidification and segregation

The basic cause of segregation is that the liquid rejects many solute element atoms during freezing because they have lower solubility in the solid as compared to the liquid. Solidification of steel during continuous casting is predominantly ‘dendritic’ in the above mentioned columnar zone. Due to the constitutional supercooling and preferred crystallographic growth, the columnar zone grains contain branched, tree-like dendritic crystals. **Fig. 1.2.3** shows a schematic diagram that illustrates dendritic solidification [Flemings 1967]. In **Fig. 1.2.3** the darker shading in between the dendrites shows the increase in solute content in the liquid around the solidifying dendrites. Solute atom redistribution during dendritic solidification follows the liquidus and solidus curves of the equilibrium phase diagram. At any given temperature the solute concentration of the solid can be designated as C_S and that of the liquid as C_L, as defined by a tie-line at that temperature. The redistribution,

or partitioning, of the solute can then be defined as the equilibrium partition ratio, k_p, as [Reed-Hill 1973, Flemings 1974]:

$$k_p = \frac{C_S}{C_L} \qquad \text{eqn. 1.2.1}$$

with this parameter, solute redistribution in the liquid, C_L, as a function of the weight fraction of solid, f_S, in the solidifying volume element can be given by the Scheil equation as:

$$C_L = C_0(1 - f_S)^{k_p - 1} \qquad \text{eqn. 1.2.2}$$

where, C_0 is the initial alloy composition within the volume element [Flemings 1974]. Segregation ratio, r $\left(r = \frac{C_L}{C_0} \right)$, is the measure of solute segregation (i.e. enrichment) of the liquid with progressive solidification. The Scheil equation is based on a number of simplifying assumptions (such as negligible undercooling, complete diffusion of solute in the liquid in the volume element, negligible diffusion of solute in the solid, and constant 'k_p' throughout solidification), however, can accurately represent solute enrichment in the solid as solidification proceeds [Flemings 1974, Krauss 2003]. The first solid to solidify, or the first dendrites to grow in steel, have the lowest solute content but as solidification proceeds, the concentration of solute / solutes in the dendrites increases. However, the liquid adjacent to the growing dendrites also gets richer in solutes (dark shading in **Fig. 1.2.3**). After significant solidification secondary (or tertiary) arms of neighbouring primary dendrites impinge each other trapping the solute-rich liquid in the interdendritic regions. When the solute-rich, interdendritic liquid solidifies compositional variation exists between interdendritic and dendrite centre regions of the casting and that is termed as interdendritic segregation or microsegregation.

The tendency to microsegregation of a solute element depends on its equilibrium partition ratio, 'k_p' value (assumed to be independent of temperature) as a solute element with a low 'k_p' value has a high tendency to segregate. A list of 'k_p' values of some elements commonly found in HSLA steel is given in **Table 1.2.1** [Krauss 2003, Ghosh 2001, Priestner 1998]. The extent of microsegregation also depends on the dendrite size, particularly on the secondary dendritic arm spacing (SDAS). A larger SDAS may increase the size of the interdendritic areas and concentration of solute elements within the interdendritic liquid and hence, the microsegregation increases [Krauss 2003]. The secondary dendritic arm spacing increases with increasing distance from the chill surface; with decreasing cooling rate; and with increasing section size as shown in **Fig. 1.2.4 (a) and (b)** [Irving 1993, Flemings 1974, El-Bealy 1996]. An increase in SDAS have been reported by Zhang et al. [Zhang 2002] with the increase in distance from slab surface (80-86 μm at 10 mm from surface, 190-220 mm at quarter-thickness and 230-290 mm at mid-thickness) corresponding to a cooling rate decrease. However, the sub-surface and quarter-thickness positions from both sides of the slab have not been compared in terms of SDAS.

The size of the columnar zone and associated interdendritic segregation and shrinkage porosity can greatly be reduced by the use of in-strand or in-mould electromagnetic stirring [Haggart 1990]. Stirring fragments the columnar dendrites and increases the size of the equiaxed solidification zone reducing segregation levels. [Krauss 2003].

Apart from interdendritic or microsegregation, macrosegregation (compositional variation over distances much larger than the interdendritic spacing), is also a common phenomenon in continuously cast steel. Various types of

segregation, which are often encountered in the longitudinal section of continuously cast slabs, are shown in **Fig. 1.2.5** [Irving 1993, Lesoult 2005]. Centreline segregation (the most common form of macrosegregation) is a positive segregation (local composition higher than average composition) that takes place at the slab-centre, where the last (solute-rich) liquid solidifies. Composition variation due to centreline segregation results in higher local hardenability at the centreline and form greater amount of lower temperature transformation products (i.e. martensite or bainite in ferrite + pearlite steel) during casting after subsequent hot-rolling. Varying microstructure can cause non-uniformity in mechanical properties of the finished product [Ghosh 2001, Lesoult 2005]. Although there are several parameters governing centreline segregation, the tendency of macrosegregation also depends on the segregation ratio (r), which can be determined primarily by 'k_p' (as listed in **Table 1.2.1**) in the same way as microsegregation [Moore 1984, Krauss 2003]. For continuously cast slabs, the most successful corrective action for centreline segregation is called 'soft reduction' the principle of which is to mechanically reduce the total thickness of the slab during its cooling and solidification [Lesoult 2005].

Presslinger et al. [Presslinger 2006] analysed segregation levels by quantitative imaging of elemental distribution (concentration mapping, CM) on continuously cast slab (210 mm thick) of HSLA steel (0.1-0.15 C, 1.5 Mn, 0.15 Si, <0.02 P, <0.005 S, 0.015 Nb, 0.002 Ti, all wt %) using electron probe microanalyser (with wave length dispersive spectrometer, WDS). Concentration maps of C, Mn, Si and P, **Fig. 1.2.6 (a)**, show the spatial distribution in composition resulted from the macrosegregation and / or microsegregation. The intensity of Mn and Si segregation at solute-rich and solute-poor regions from slab-surface to slab-centre are shown in **Fig. 1.2.6 (b)**. The macrosegregation of microalloying elements to the last solidifying

liquid is also evident from the presence of the microalloy carbide/carbonitride network at the slab centre, **Fig. 1.2.6 (c)** [Presslinger 2006].

1.2.3 Solidification sequence of HSLA steel

In different grades of HSLA steels the carbon-content can vary between 0.05-0.2 wt % [Tither 1992]. Depending on the C-content of the steel, different solidification modes control the evolution of the cast structure, as shown in **Fig. 1.2.7**. These sequences are for equilibrium cooling, however, in actual steel solidification, the kinetic effects can modify the phases and sequences expected. As solidification proceeds the macrosegregation of elements such as C and Mn (**Fig. 1.2.6 b**) can increase the carbon equivalent gradually and that can alter the mode of solidification at certain depth below the surface. As discussed earlier, the extent of microsegregation depends on the secondary dendrite arm spacing (SDAS), which can be dependent on the solidification mode. Greater freezing range promotes dendrite coarsening and that results in higher SDAS, which increases the segregation at the interdendritic regions [Krauss 2003] [El-Bealy 1996]. Therefore, by influencing the SDAS, the solidification mode can affect the extent of microsegregation.

1.2.4 Examples of microalloy segregation in as-cast steel

A number of evidences available in the literature on the segregation of microalloying elements in HSLA steel and those are listed in **Table 1.2.2**. **Table 1.2.2**, **Fig. 1.2.8** and **Fig. 1.2.9** indicate to the stronger tendency of clustering and segregation of Nb, compared to Ti and V in HSLA steel.

1.2.5 Precipitation in continuous-cast HSLA steel

Several investigations have been carried out to study the precipitates in continuously cast HSLA steel slabs by using optical microscopy, scanning electron microscopy (directly on polished + etched sample) or transmission electron microscopy (using thin-foil or extraction-replica technique) fitted with X-ray analysis (EDS) facility. Compositions of the investigated steels, locations of the slab studied and the precipitates (or inclusions) observed in some of those studies are listed in **Table 1.2.3**, and some of the precipitates are shown in **Fig. 1.2.10**. Some important findings such as the nature, shape, size and distribution of the precipitates and the precipitation sequence discussed in those studies are summarised in **Table 1.2.4**. To understand the sequence of precipitation the thermodynamic stability of the precipitates needs to be studied [Zhang 2000, Jun 2003, Couch 2001].

1.3 Theories behind the precipitation during casting and precipitate dissolution during reheating

The overall formation and dissolution rate of precipitates depends on the nucleation rate, the growth rate and on the reaction time. Nucleation rate and the growth rate both depend on the solute supersaturation (amount of the solutes above the equilibrium composition). The level of solute supersaturation and hence, the stability of the precipitates, depends on the solubility in the matrix phase (liquid, austenite or ferrite).

1.3.1 Prediction of solubility and thermodynamic modelling

From the thermodynamic principle, the solubility product can be derived by relating the equilibrium concentration of solutes (in mole fraction or wt %) to the equilibrium constant (K_S) for the precipitation reaction, [M] + [X] $\leftrightarrow$ (MX), (where M is the microalloying element, X is the interstitial element (C or N) and MX is the precipitate) in the following form:

Solubility product, K_S = [M].[X] ……..eqn. 1.3.1

where, [M] and [X] are the concentrations in wt %. Thermodynamically, the solubility product can be related to the temperature (T in K) using the standard Gibbs free energy (ΔG^0), temperature (T) relation at equilibrium and that can give the usual form of the solubility product equation [Gladman 1997]:

$$\ln(K_S) = A - \frac{B}{T} \qquad \text{……..…eqn. 1.3.2}$$

where A and B are constants. There are three factors that can deviate the thermodynamically derived solubility product from the actual solubility [DeArdo 2003]: (i) it strictly applies to an equilibrium condition that rarely exists in practice (ii) it only applies to binary or ternary systems and so there will be lot of variability in commercial steels as other elements can alter the solubility product through their effect on the interaction coefficient [Wagner 1952] (iii) it will be altered by the Gibbs-Thompson or capillary effect that considers the role of particle curvature on solubility (the solubility of a particle varies inversely with its curvature [Porter 1992]). Solubility products can also be determined experimentally by different techniques [Gladman 1997, DeArdo 2003], which can pick up the non-equilibrium condition but

every technique has its own limitation. This leads to wide range of solubility product values and limits their use in predictive manner [Palmiere 1994].

But for a theoretical understanding of stability of microalloy precipitates in steel the solubility product is a useful concept. A comparison of solubility products for simple microalloy carbides and nitrides (such as TiN and NbC) at different temperatures is given in **Fig. 1.3.1 (a and b)** from which several conclusions can be drawn.

1. For each of the microalloy elements the nitride is less soluble than the carbides in austenite.
2. TiN is the most stable and VC is the most soluble microalloy precipitate in austenite. In terms of precipitate stability in microalloyed steel TiN > AlN >NbN≈NbC≈VN≈TiC>VC. Therefore, a similar precipitation sequence is followed in precipitation during casting and the reverse sequence is followed in precipitate dissolution during reheating.
3. The solubility of TiN in liquid steel is about 10-100 times larger than that in austenite and the solubilities of NbC and NbN in ferrite are about an order of magnitude less than the corresponding solubilities in austenite at the same temperature.

The microalloy-carbides and nitrides show extensive mutual solubility due to their similarity in crystal structure and lattice parameters to form simple carbonitrides (such as Nb(C,N)) or complex carbonitrides (such as (Ti,Nb)(C,N)) [Gladman 1997]. Several thermodynamic models (such as regular solution models [Hillert 1970, Strid 1985, Eckstein 1993, Zou 1991, Speer 1987, Adrian 1995] or ideal solution models [Okaguchi 1987, Akamatsu 1993, Verger 1985]) have been developed to predict the

precipitation sequence of simple and complex carbonitrides, and the composition of precipitate and matrix as a function of austenising temperature and chemistry.

The use of simple solubility products or thermodynamic models were valid when computing power was limited but has been superseded for more than 20 years by thermodynamic programs based on sub-regular models for ternary and higher interactions. Thermo-Calc, MT-DATA and ChemSage are some of the computer programmes used to predict the compositional changes and precipitation. Thermo-Calc software can handle single equilibria, property diagrams or phase diagrams with up to twenty elements in steel with a large number (~ 200) of possible phases [Jansson 1993]. A large number of thermodynamic models have been implemented for use with different database. To study the precipitation and compositional changes along with phase transformation during casting / reheating, 'property diagrams' are very useful. Using Thermo-Calc for a particular steel composition property diagrams can provide mole fraction, driving force, or composition of different phases / precipitates / inclusions at every temperature step (temperature is the single variable) during casting / reheating [Jansson 1993].

1.3.2 Limitations of thermodynamic modelling

The basic assumption behind the thermodynamic models (also the thermodynamic software that uses the models) that 'the precipitation takes place under thermodynamic equilibrium conditions' is a matter of concern as thermodynamic equilibrium is rare in practice and non-equilibrium heating / cooling of the steel takes place during commercial processing [Gladman 1997].

In the non-equilibrium situation the kinetics of precipitation and dissolution become more important than the thermodynamic stability of the precipitates. For example in Ti-Nb microalloyed steel NbC precipitates on existing TiN particles and the lack of homogenisation develops composition differences across the particle. There are several references to composition gradients within the particles [Gladman 1997, Jun 2003, Houghton 1993], resulting from the inability of precipitates to homogenise rapidly as temperature falls. Sometimes when the steel is rapidly reheated to a high temperature (Nb, Ti)(C, N) particles formed at the lower temperature dissolve partially or completely and new particles (such as Ti(C, N)), , which are more stable at high temperature, precipitate at a different location [Hong 2003]. Some models have tried to incorporate the changes during non-equilibrium processing (such as the formation of composition gradients within the precipitates [Akamatsu 1993, Rose 1997]) but it is not possible to predict all the changes / possibilities that arise during actual practice.

The validity of any thermodynamic model is also dependent on the quality of the data used, such as the solubility product and chemical analysis. Models do not consider the macro and micro-segregation of microalloy elements and the effects of vacancies and trace elements on the precipitation (for example P is known to retard the formation of Nb-precipitates [Cochrane 1978]). Moreover, the mechanism and rate at which precipitate dissolution occurs, is not considered in those models [Gladman 1997] and it becomes essential to gain a more complete understanding on the kinetics of precipitation and dissolution.

Despite the difficulties posed by non-equilibrium or segregation effects, knowledge of the particle and matrix equilibrium conditions developed during commercial reheating is advantageous.

1.3.3 Precipitate dissolution during reheating

On reheating, the size of the precipitates generally decreases and eventually disappears due to dissolution. Dissolution is the reverse of precipitation and follows the same thermodynamic principles of precipitate stability, as explained by the solubility product in **section 1.3.1**. From the solubility product-temperature relation in **eqn. 1.3.3** the equilibrium dissolution temperature (T_{DISS}) can be obtained:

$$T_{DISS} = \frac{B}{A - \ln(K_S)} \quad \text{.....eqn. 1.3.3}$$

Although the equilibrium dissolution temperature (T_{DISS}) is a good theoretical concept, its application is limited due to the limited applicability of solubility products (**section 1.3.1**) and, therefore, thermodynamic software is used in predicting the variation in precipitate volume fraction and driving forces for dissolution (as mentioned in section **1.3.1**).

Equilibrium dissolution temperature (T_{DISS}) indicates a particular temperature at which precipitates dissolve completely. However, during reheat gradual dissolution of complex precipitates is seen. For example, Hong et al. [Hong 2003] have observed a gradual dissolution of Nb-rich (Nb, Ti)(C, N) precipitates over 1100-1300 ºC in 0.06 %C, 0.56 %Nb steel. Thermodynamic software (based on subregular models) can predict this gradual dissolution and can also show the change in concentration of complex carbonitrides (e.g. more TiN in (Nb, Ti)(C, N)) as the temperature increases during reheating [Rose 1996].

However, the thermodynamic models cannot predict the exact temperature for the complete precipitate dissolution. For example, Davis and Strangwood [Davis

2002] and Palmiere et al. [Palmiere 1994] have observed that (Nb, Ti)(C, N) precipitates remain after reheating at temperatures 40-90 ºC above the complete dissolution temperatures that are predicted by using thermodynamic models or software for steels with 0.05-0.1 % C, 0.023-0.057 % Nb. Precipitates retained at such high temperature could be due to (i) increase in size and (ii) increase in solubility of Nb-precipitates formed at the interdendritic regions, where the local composition of Nb was higher than the average. Therefore, depending in the location on the as-cast slab, macro-segregation and micro-segregation of alloying elements need to be considered for better prediction of dissolution temperature.

1.3.4 Precipitate coarsening during reheating

Much experimental work has shown that, during heating, precipitates that remain undissolved in the matrix have a tendency to coarsen at the expense of smaller ones, whilst there is no substantial change in the solute content of the matrix during this coarsening process [Gladman 1997, Porter 1992]. The driving force for this process is provided by the consequent reduction in the total interfacial energy. Several conditions for precipitate coarsening have been studied in HSLA steel, which indicated that coarsening of microalloy precipitates (small volume fraction of particles) is a diffusion-controlled process [Ardell 1972, Lifshitz 1961]. In microalloyed steel it has been shown that the higher the temperature before the precipitates completely dissolve, the coarser the Nb(C, N) particles become, although the volume fraction of those precipitates present in the matrix was reduced [Gladman 1967, Coladas 1977, Cheng 2000, San 2005].

Particle coarsening not only depends on the diffusivity coefficient but on the total diffusion flux. Diffusion flux for any particular solute (say microalloying element M) is the product of the diffusion coefficient and the matrix concentration, D.[M], and thus the concentration of solute (in solution) is also important in determining coarsening [Gladman 1997]. For more stable precipitates (say TiN) or if the solute / interstitial ratio ([M]/[X]) in the matrix is close to stoichiometric, there is less [M] free in solution (most of the M will be combined with X as precipitate) and that will decrease the coarsening rate. Partial dissolution of precipitates can also increase the rate of coarsening by increasing the solute level (Nb in case of Nb(C, N)) in the matrix [Speer 1989, Gladman 1997]. Therefore, in presence of micro-segregation, the rate of coarsening is expected to be higher at that region, where dissolved solute level is higher, which depends on the initial segregation levels and on the stability of precipitates in solute-rich (segregated) and solute-poor (non-segregated) regions.

1.3.5 Diffusion in microalloyed steel

The rate of coarsening depends on diffusion (particularly on the slowest diffusing species). The diffusion constant $(D_0)_{diff}$ and activation energies (Q_{diff}) for the microalloying elements including Al and important interstitials (C and N) in the austenite and ferrite phase are listed in **Table 1.3.1** [Smithells 1983]. Diffusion of Nb and Ti within precipitates is much slower (~ 10^4 times less) than within the matrix [Sarian 1969, Shewmon 1963]. The variations of diffusion coefficients (D_{diff} in m^2/s) calculated from the given $(D_0)_{diff}$ and Q_{diff} values, $\left[D_{diff} = (D_o)_{diff} \exp\left(-\frac{Q_{diff}}{RT} \right) \right]$ with

temperature (T) are given in **Table 1.3.2** and shown in **Fig. 1.3.2**. The presence of vacancies can change the diffusion mechanism by making the diffusion faster [Faulkner 1996].

1.3.6 Summary of precipitation and segregation in steel

From the above-mentioned examples of Nb-microalloyed steel the following conclusions can be drawn.

- Cubic TiN, faceted AlN, spherical NbC / Nb(C, N), spherical, cubic or dendritic (Nb, Ti)(C, N), spherical or needle shape VC / V(C, N) or (Nb, V)(C, N) are the common precipitates observed in as-cast Nb-microalloyed steel.
- Formation of the precipitates follows a sequence based on the thermodynamic stability (i.e. TiN, AlN, NbC / Nb(C, N), VC / V(C, N)). Due to such a sequence Nb(C, N) can precipitate on pre-existing TiN or AlN. To understand and predict the precipitation sequence, the precipitate thermodynamic stability and solubility of precipitates in different phases (from concepts such as solubility product) needs to be studied.
- Formation of Nb-rich dendritic precipitates or eutectic Nb-rich (Nb,Ti,V)(C, N) particles at interdendritic boundaries indicates that segregation of microalloying elements (predominantly Nb) takes place during solidification.
- Microsegregation could lead to an inhomogeneous distribution of precipitates. Apart from that the segregation can have an effect on the rate of coarsening and dissolution of the precipitates. Therefore, on reheating the precipitate volume fraction and size can vary between solute-rich and solute-poor regions.

As precipitates pin the austenite grain boundaries such variation can effect the grain growth on reheating.

1.4 Grain growth during reheating

Grain growth occurs by the expansion of large grains at the expense of smaller grains such that the material volume remains constant. The driving force for grain growth is the minimisation of grain boundary energy. Grain growth can occur in two modes: normal grain growth and abnormal grain growth. For normal grain growth, the kinetic law is represented by [Gladman 1997]:

$$R \propto t^n \quad \text{.....eqn. 1.4.1}$$

where, R is the average grain size, t is the time and usually $n \leq 0.5$. Abnormal grain growth (also known as secondary recrystallisation) is characterised by the rapid increase in size of the large grains, at a rate much faster than eqn. 1.4.1 predicts. Microalloying elements produce fine precipitates in steel and those precipitates inhibit austenite grain growth (when undissolved) during reheating by grain boundary pinning, which results in a finer grain size. When the precipitates have dissolved then solute drag, by the microalloying elements, also reduces the rate of grain growth, but less effectively than precipitates.

1.4.1 Grain growth inhibition and the concept of limiting grain size

A number of theoretical and experimental studies have been carried out to understand grain growth in the presence of pinning particles considering either random or non-random particle distributions.

1.4.1.1 Random distribution of spherical particles

The intersection of an isolated grain of radius, R, by a spherical second-phase particle of radius, r, is shown in **Fig. 1.4.1.** The retardation of grain growth by second phase particles was first theoretically studied by Zener [Zener 1948a]. Zener's model [Zener 1948a] balances the driving force for grain growth against the pinning force (or Zener drag) exerted by the second phase particles retarding grain growth. Assuming a random distribution of particles (therefore, no segregation to boundaries or sweeping up of particles by boundaries) a limiting condition for grain growth is presented by Zener's model:

$$D = \xi.\frac{d}{f} \qquad \text{……..……eqn. 1.4.2}$$

where, grain diameter, D = 2R, particle diameter, d = 2r and in Zeners model, ξ = 4/3. Hillert [Hillert 1965] first introduced the concept of a critical grain radius, R_c, and considered the grain size variation in a structure. Extending Hillert's concept further Gladman [Gladman 1966] tried to explain both the observed normal and abnormal grain growth phenomena in Al-killed steel (in the presence of AlN and NbC particles). He assumed the grain shape to be tetrakaidekahedron (or cubo-octahedron) and introduced a heterogeneity factor, Z to represent the variation in grain structure during grain growth. Z is the size ratio (R/R_o in terms of radius) of the growing grain (R) to the neighbouring average sized, pinned grains (R_o). In the presence of particles Gladman [Gladman 1966] derived the critical particle radius, r*, above which particles are ineffective at pinning the grain boundary:

$$r^* = \frac{6R_0 f}{\pi}\left(\frac{3}{2} - \frac{2}{Z}\right)^{-1} \qquad \text{……..…eqn. 1.4.3}$$

or $R_0 = \frac{\pi}{6}\left(\frac{3}{2} - \frac{2}{Z}\right)\frac{r^*}{f}$ …….eqn. 1.4.4

Considering $D = \xi.\frac{d}{f}$ (eqn. 1.4.2), therefore, $\xi = \frac{\pi}{6}\left(\frac{3}{2} - \frac{2}{Z}\right)$ in Gladman's model. For the growth of austenite grains in the presence of AlN and NbC particles in steel, Gladman observed that Z ~ (1.41-2) and hence, ξ = (0.05-0.26).

According to Gladman [Gladman 1966] some particles can become ineffective in pinning the grain boundaries (particle size, r > r*) during reheating due to coarsening (increase in r) or even dissolution (decrease in f, and hence, decrease in r*). In such a situation, the growth of the large grains in the microstructure can offer the higher release in energy (due to higher Z value), and that can exceed the energy increase in unpinning. Therefore, the large grains become unpinned and grow in size. Small grains cannot grow as those are still pinned. This will create the situation of abnormal grain growth. Hence, precipitate coarsening or partial dissolution of precipitates leads to a situation where abnormal grain growth can occur. Upon complete dissolution of precipitates abnormal grain growth will stop and normal grain growth will resume (as in absence of particles) for the larger grains, Z > 4/3, consuming smaller grains, till the large grains impinge upon each other.

Hellman and Hillert [Hellman 1975] considered the unpinning of the grain boundary from particles and the effect of grain boundary curvature (ρ) on grain growth that Zener [Zener 1945] or Gladman [Gladman 1966] did not consider. Assuming that close to the pinning particle the grain boundary may take a catenoid shape, **Fig. 1.4.2**, Hellman and Hillert [Hellman 1975] introduced a correction factor 'β' (which is a function of ρ/r), in the limiting grain size [Hellman 1975]:

$D = \frac{4}{9}\beta\frac{d}{f}$ ……..eqn. 1.4.5

Hellman and Hillert [Hellman 1975] derived the curvature of the most critical element of the grain boundary that must be stabilised as ρ = 3D. Using such relation they derived the β value and finally came to another limiting condition [Hellman 1975]:

$$D = \frac{4}{9}\frac{d}{f^{0.93}} \qquad \text{……..eqn. 1.4.6}$$

Compared to eqn. 1.4.2, for Hellman and Hillert [Hellman 1975] the limiting condition is $\xi \approx 4/9$ for normal grain growth and $\xi < 4/3$ for abnormal grain growth.

To explain the grain growth in an Al-Al_2O_3 system, where there is no coarsening or dissolution of precipitates (and other models failed to predict the mean grain size [Tweed 1984]), Rios [Rios 1987] considered the energy dissipated during the motion of an interface through a random particle dispersion rather than Zener's opposing force approach. Rios [Rios 1987] proposed a limiting condition of

$$D = \frac{1}{6}\frac{d}{f} \qquad \text{…….eqn. 1.4.7}$$

The above condition was also found useful in explaining the austenite grain growth data reported by Coladas et al [Coladas 1977], where grains were growing in the presence of coarsening NbC precipitates.

1.4.1.2 Effect of non-random particle distribution

Several researchers (Doherty et al. [Doherty 1987], Anand et al. [Anand 1975], Srolovirtz et al. [Srolovitz 1984], Gladman [Gladman 1992], Nes et al. [Nes 1985]) have studied non-random particle distributions (in two-dimensions, 2D or three-dimensions, 3D), where unpinning is very difficult and therefore, the grain size is very small and most of the particles are in contact with grain boundaries. The

limiting condition of grain growth from such studies can be summarised in the following form:

$$D = \xi . \frac{d}{f^{0.5}} \qquad \text{……..……...……..……eqn. 1.4.8}$$

1.4.1.3 Complex grain growth models and grain growth mechanism map

Some studies have evaluated the limiting conditions for normal or abnormal grain growth experimentally or using grain growth models and presented the results in a combined form as a grain growth mechanism map [Flores 1997, Rios 1987, Andersen 1995 a and b]. In such maps the conditions suitable for normal and abnormal grain growth have their own characteristic fields either in time-temperature space, **Fig. 1.4.3 (a)** [Flores 1997, Andersen 1995a and Andersen 1995b], in grain size-grain size space, Fig. **1.4.3 (b)** [Rios 1987]. The grain growth mechanism maps indicate to a slow and normal grain growth at low temperatures (below ~ 900 °C in 0.03 C-0.036 Nb-0.015 V steel, (all wt %), **Fig. 1.4.3 (a)** [Flores 1997], and below ~ 1070 °C in 0.08 C, 0.07 Nb, 0.025 N steel (all wt %), **Fig. 1.4.4** [Andersen 1995 a, b]) as the Nb(C, N) and / or V(C, N) particles effectively hinder grain growth by pinning the grain boundaries. In the intermediate temperature range (900 - 1100 °C in **Fig. 1.4.3 (a)**, and 1070 - 1170 °C in **Fig. 1.44**) precipitates are prone to dissolve and abnormal grain growth dominates. Above that temperature range precipitates dissolve completely and grain growth becomes normal once again.

1.4.2 Experimental studies on abnormal grain growth in steel

Various researchers have studied the reheating response of C-Mn steels, microalloyed steels or Al containing steels in the range 900 to 1300 °C. Steel compositions and reheating parameters for some of the studies are listed in **Table 1.4.1**. In those experiments the microalloyed steels followed similar behaviour as predicted by the model of Andersen and Grong [Andersen 1995a and Andersen 1995b], i.e. restricted, normal grain growth at lower temperatures (~ 900-1100 °C), followed by abnormal grain growth at intermediate temperatures (~ 1100-1200 / 1250 °C), **Fig. 1.4.5**, and again normal grain growth at high temperatures (> ~ 1200 / 1250 °C). Discussions on some specific topics reported by those reheating studies are listed in **Table 1.4.2**.

1.4.3 Summary on bimodality upon reheating

Limiting conditions for grain growth in the presence of second phase particles suggested by different models can be generalised in the form:

$$D = \xi . \frac{d}{f^n} \qquad \text{……..…eqn. 1.4.9}$$

where, 'ξ' ranges from 0.05-4 and 'n' varies from 0.33-1. Conditions for normal and abnormal grain growth are represented by different values of ξ. Generally for the random distribution of particles n ≈ 1, and for grain boundary precipitation n ≈ 0.5. The studies on reheating of microalloyed steels suggest that there are three stages of austenite grain growth: restricted normal grain growth in the presence of pinning particles retaining the initial unimodal grain size distribution, coarsening / partial dissolution of precipitates making the pinning unstable and then large grains, which have a size advantage, grow abnormally producing a bimodal distribution, and upon

long holding times or an increase in reheat temperature precipitates dissolve completely and more grains grow rapidly (until they impinge upon each other), bringing back the unimodal distribution. Dogan et al. [Dogan 1992] considered the non-uniform distribution of pinning particles to explain the retention of fine grains upon long holding at high temperature. This indicates an important limitation of all the grain growth models, discussed earlier, that the models do not consider the effect of segregation on grain growth. Davis and Strangwood [Davis 2002] and Couch [Couch 2001] indicated that the interdendritic segregation can give rise to an inhomogeneous precipitate distribution and different precipitate solubility in different regions. Therefore, the local composition decides the grain structure rather than the overall composition and that may lead to a wide variation in grain size at different regions.

However, Davis and Strangwood [Davis 2002] or Couch [Couch 2001] did not conducted detailed quantification of the inhomogeneous precipitate distribution in the as-cast steel. The present investigation aims to do that and also tries to follow the changes taking place in the precipitates and grain structure upon reheating in the microsegregated regions. Results from the present study could be useful in incorporating the effect of segregation on grain growth of Nb-microalloyed steels in existing models.

1.5 Grain refinement during TMCR

As shown by the processing route in **Fig. 1.1.2**, following reheating the homogenised, red-hot, and softened steel slabs are subjected to thermo-mechanical

controlled rolling (TMCR). In this section the role of microalloying elements during TMCR on controlling the grain size is discussed in detail.

1.5.1 Thermo-mechanical controlled rolling (TMCR)

The steel chemistry alone does not guarantee high strength coupled with good toughness. TMCR is a superior process to conventional hot-rolling (HR) as TMCR improves both the strength and toughness of the steel through extensive grain refinement (final grain size ~ 5-8 μm), whilst the grain refinement is limited in HR (final grain size~10-25 μm) [Gladman 1997, Tanaka 1981, Teoh 1995]. This can be best understood by comparing the processing routes of both HR and TMCR, **Fig. 1.5.1** [Tanaka 1981, Teoh 1995].

HR processes have a high finish rolling temperature (~ 1050-1150 °C), **Fig. 1.5.1 (a)**. Complete deformation is given within the region (above T_R) where austenite grains recrystallise completely before austenite transforms to ferrite. Ferrite grains can nucleate only at austenite grain boundaries (low defect density in austenite only in the form of grain boundaries) and that results in a coarser ferrite grain size.

A typical TMCR schedule is characterised by reheating (or soaking) the steel at ~ 1150-1250 °C to ensure complete (or near complete) dissolution of micoalloying elements in austenite, followed by rolling deformations at different stages, with hold periods in between.

The concept of T_R in **Fig. 1.5.1 (b)** needs to be clear in order to understand the different stages of rolling in TMCR. Instead of a sharp temperature value, T_R actually represents a temperature range over which static-recrystallisation kinetics change gradually. Theoretically that temperature range can be defined by the upper

temperature limit (known as recrystallisation limit temperature, RLT) or lower temperature limit (known as recrystallisation stop temperature, RST or no recrystallisation temperature, T_{NR}). To describe RLT and RST Palmiere et al. [Palmiere 1996] have used $T_{95\%R}$ and $T_{5\%R}$, respectively, which depend on applied strain as shown in **Fig 1.5.2**. $T_{95\%R}$ and $T_{5\%R}$ represent the temperatures where 95 % and 5 % of the deformed structure recrystallise, respectively, within the interpass delay time (~10-20 sec) for commercial rolling. Deformation above $T_{95\%R}$ (RLT) results in a complete recrystallisation, below $T_{5\%R}$ results in no recrystallisation and deformation within the range of $T_{95\%R}$ and $T_{5\%R}$ results in partial recrystallisation during interpass times.

The deformation stages for TMCR are as follows:

1.5.1.1 Stage-I: Deformation in recrystallisation region above RLT (or $T_{95\%R}$)

The coarse austenite grains after reheating are refined in size by repeated deformation (several roughing passes) and complete recrystallisation. Presence of fine TiN particles prevents grain growth during interpass delay times and maintains fine recrystallised grain structure. After stage-I rolling a delay time is given during which the temperature drops below RST.

1.5.1.2 Stage-II: Deformation in non-recrystallisation region below RST (or TNR or T5%R)

Microalloying elements in steel, especially Nb, retard recrystallisation through stain-induced fine, Nb(C, N) precipitates and increases RST (discussed in detail in

section 1.5.2 and 1.5.3). Successive deformation passes below RST (~950-1050 °C in Nb steels [Gladman 1997, Tanaka 1981]) generates a heavily deformed austenite grain structure, with elongated and pancake-shaped austenite grains (austenite conditioning) containing a high density (S_v in mm^{-1}) of near-planar crystalline defects (such as, grain / sub-grain boundaries, deformation bands, and incoherent twin boundaries), which act as the nucleation sites for ferrite grains and provide fine ferrite structure (rapid rate of ferrite nucleation) after suitable cooling below A_3 (austenite to ferrite transformation temperature) and provides finer ferrite grain size than HR [Cuddy 1984].

The RST (or T_{NR}) value needs to be high so that a large extent of deformation can be given in the non-recrystallisation region to achieve maximum grain refinement from austenite conditioning. Cuddy's diagram (**Fig 1.5.3**) [Cuddy 1982] shows that Nb is the most effective element in retarding recrystallisation and increasing T_{NR}. The precipitation of Nb(C, N) both in deformed and undeformed austenite (much faster in deformed austenite, **Fig. 1.5.4**) follows C-curve kinetics with the nose of the curve appearing at ~ 900-950 °C in most cases, **Fig. 1.5.5** [le Bon 1975, Watanabe 1977, Ouchi 1982, Saito 1997, DeArdo 2003]. Faster precipitation in deformed austenite is due to the presence of defects (eg grain / sub-grain boundaries, deformation bands, stacking faults), which act as preferred nucleation sites for Nb(C, N) precipitation, resulting in heterogeneous precipitate distribution, **Fig. 1.5.6**.

1.5.1.3 Stage-III: Deformation within intercritical (austenite + ferrite) region

Intercritical rolling is applied only in cases where high strength (yield strength and ultimate tensile strength) is required. After stage-II rolling a delay time is given

so that the temperature of steel drops below A_3. In stage-III, deformation bands continue to form within untransformed austenite grains, which enhance ferrite nucleation resulting in a finer ferrite grain size. Also the recovery of deformed ferrite grains produces fine sub-grains within deformed ferrite grains. Smaller sub-grain sizes result in higher strength steels [Gladman 1997]. Lowering the finish rolling temperature within the intercritical region increases the strength of the steel but decreases the ductility and impact toughness due to higher retained strain within the microstructure [Gladman 1997, Bakkaloglu 2002].

During intercritical rolling V(C, N) (or even Nb(C, N)) can precipitate in fine scale either as random precipitates or at the ferrite-austenite boundary as inter-phase precipitates. Such precipitates are fine in size (usually < 10 nm) and offer precipitation strengthening [Gladman 1997, Ubhi 1989, Morales 2003, Gunduz 2005, Zajec 2005].

1.5.2 Examples of precipitation-recrystallisation interaction in Nb-steels

A list of some studies on the interaction between strain-induced Nb(C, N) precipitation and austenite recrystallisation, along with the investigated steel compositions, deformation schedules and isothermal holding times after deformation is given in **Table 1.5.1**. The recrystallisation kinetics are generally studied metallographically (by revealing austenite grains using hot picric acid etching) or from the softening curves (drop in flow stress measured from double-deformation tests with a hold in between). Precipitation kinetics are generally studied by observing Nb(C, N) precipitates in TEMs using extraction replicas. A summary of the findings from the above mentioned investigations are listed below.

Solute drag and precipitate pinning: Around 0.02 % Nb can retard recrystallisation by one order of magnitude when dissolved in austenite by the solute drag effect. Recrystallisation is further retarded by one to two orders of magnitude when 0.01 % Nb is freshly precipitated as fine Nb(C, N) [Hansen 1980, Kwon 1991]. The location of the precipitates is important in retarding recrystallisation. Freshly precipitated Nb(C, N) particles effectively retard recrystallisation due to their heterogeneous nucleation on sub-boundaries or other crystalline defects, whilst any undissolved precipitates, even of very small size (~10 nm), are ineffective in retarding recrystallisation due to their random distribution. Therefore, Nb should dissolve completely during reheating and precipitate freshly during rolling [Hansen 1980]. Some observations on the strain-induced precipitates in HSLA steel are listed in **Table 1.5.2**.

Effect of precipitate size (radius, r) and volume fraction (f) on recrystallisation: For the effective retardation of recrystallisation, the pinning force exerted by the heterogeneously distributed Nb(C, N) precipitates on the moving grain-boundaries or sub-boundaries (which is required for recrystallisation following strain-induced boundary migration [SIBM] mechanism) should be of same order (may be less in magnitude) as the driving force for recrystallisation (reduction of strain energy by reducing dislocation density, $\Delta\rho$, of the deformed matrix) [Hansen 1980, Speer 1989, Palmiere 1996, Kwon 1991]. Considering different models (rigid boundary model, flexible boundary model or sub-boundary model) and considering random or heterogeneous (precipitated on sub-boundaries [Hansen 1980]) precipitate distributions the pinning force, F_p, usually takes the form:

$$F_p \propto \frac{f}{r} \text{ or } F_p \propto \frac{f}{r^2} \qquad \text{.....eqn. 1.5.1}$$

Therefore, the smaller the precipitate size (radius, r) and the higher the precipitate volume fraction (f), the larger the pinning force and the greater the retardation of recrystallisation (F_p). That is the reason why precipitate coarsening allows recrystallisation (by increasing 'r') to take place, whilst an increase in Nb, C and N in steel retards it more effectively (by increasing f) [Speer 1989, Hansen 1980, Luton 1980].

Formation of a bimodal grain size distribution: Palmiere et al. [Palmiere 1996] have measured the $T_{5\%R}$ (i.e. T_{NR}) and $T_{95\%R}$ by studying the austenite grain aspect ratio and the softening behaviour of steel. With an increase in the Nb content in steel from 0.02 Nb to 0.09 Nb, the volume fraction of strain-induced Nb(C, N) increased and simultaneously $T_{5\%R}$ rose from ~ 900 °C to ~ 1030 °C because of a stronger retardation of recrystallisation. For the investigated steels the temperature range for partial recrystallisation (between $T_{95\%R}$ and $T_{5\%R}$) varied between ~ 30-70 °C. The partially recrystallised microstructure developed upon deformation within this range was termed as 'duplex' due to the presence of fine-recrystallised and coarse-unrecrystallised austenite grains. Therefore, a duplex or bimodal microstructure can form during rolling by partial recrystallisation, **Fig. 1.5.7**. No attempt, however, was made to link the areas of partial or unrecrystallised grains to specific precipitate distribution.

1.5.3 Dutta-Sellars model on precipitation-recrystallisation interactions

The model most frequently referred to for strain-induced precipitation, austenite recrystallisation and recrystallisation-precipitation interaction in Nb-microalloyed steels is the Dutta and Sellars model [Dutta 1987, 1992, 2001]. Using chemical supersaturation as the driving force and considering the bulk diffusion of Nb as the rate-controlling factor behind strain-induced Nb(C, N) precipitation Dutta and Sellars [Dutta 1987] derived the expression for 5 % strain-induced precipitation:

$$t_{0.05p} = A[Nb]^{-1}\varepsilon^{-1}Z^{-0.5} \times \exp\left(\frac{270{,}000}{RT}\right) \times \exp\left\langle \frac{B}{T^3(\ln K_S)^2} \right\rangle \quad \text{…….eqn. 1.5.2}$$

where, 3×10^{-6} is the value of the constant 'A' (dimensionless constant), 2.5×10^{10} K^3 is the value of the constant 'B', [Nb] is the amount of Nb in solution in austenite, ε is the applied strain, T is the isothermal holding temperature where precipitation is taking place, K_s is the supersaturation ratio following the solubility product equation given by Irvin et al. [Irvine 1967], Z is the Zener-Hollomon parameter, which is related to strain rate, $\dot{\varepsilon}$, and deformation temperature (T_{def}) by the following equation:

$$Z = \dot{\varepsilon}\exp\left(\frac{Q_{def}}{T_{def}}\right) \quad \text{……..…….eqn. 1.5.3}$$

where, Q_{def} is the activation energy for deformation (particularly for dislocation movement) and here it is taken as 400 kJ/mole. By convention, 5 % precipitation is considered as the minimum amount of detectable precipitation for Nb-microalloyed steels and many researchers have reported the experimentally obtained value of $t_{0.05p}$ [le Bon 1975, Watanabe 1977, Ouchi 1982, Janampa 1982].

The predictions of the Dutta and Sellars model were found to achieve satisfactory agreement with experimental values (for overall range in composition, wt %: 0.06-0.17 C, 0.005-0.015 N, 0.03-0.084 Nb; ε: 0.3-0.8; initial austenite grain size (D_0): 25-405 μm, T_{def}: 900-1100 °C; T: 800-1100 °C) but for a wide range of values of A ~ 3×10^{-6} to 2.5×10^{-5} and B ~ 1×10^{10} to 6×10^{10} K^3. Dutta and Sellars [Dutta 1987] have attributed this variation to the different methods used for the detection of Nb(C, N) precipitation.

Recently, the Dutta and Sellars model has been extended to predict the variation of Nb(C, N) precipitate radius and volume fraction with isothermal holding time, **Fig. 1.5.8**, by considering growth and coarsening (controlled by bulk and pipe diffusion of Nb) of the heterogeneously nucleated (on the nodes of dislocation sub-structures) strain induced precipitates. Prediction of precipitate size and volume fraction using the model agrees well with the experimental results of Hansen [Hansen 1980] and Janampa [Janampa 1982] except for Nb level more than 0.09 wt %.

Besides the Dutta and Sellars work on Nb(C, N) precipitation kinetics, Sellars with co-workers [Sellars 1979, 1980, 1985] have published several papers on recrystallisation kinetics in C-Mn steels and in Nb-microalloyed steels (0.03-0.04 Nb). Those studies suggest that the final recystallised grain size (D_{rex}) is directly proportional to the initial grain size (D_0) and inversely proportional to the applied strain (ε) as:

$$D_{rex} \propto D_0^m \varepsilon^{-n} \qquad \text{……..……..……eqn. 1.5.4}$$

where, constants m ≈ 0.67, n ≈ 1 for C-Mn steel; m ≈ 0.67, n ≈ 0.64 for (0.03-0.04) Nb steel. Considering the retardation effect of [Nb] in solution Sellars [Sellars 1985] derived the relation for the time for 5 % recrystallisation ($t_{0.05R}$):

$$t_{0.05R} = 6.75\times10^{-20} D_0^2 \varepsilon^{-4} \times \exp\left(\frac{300{,}000}{RT}\right) \times \exp\left(\frac{2.75\times10^5}{T-185}[Nb]\right) \quad \text{(for } \varepsilon$$

$< \varepsilon_c$, the strain required for dynamic recrystallisation)

……...…….eqn. 1.5.5

where, D_0 is in microns and the activation energy for recrystallisation (Q_{rex}) is considered as a constant of 300 kJ/mole for Nb-microalloyed steel. Using eqn 1.5.2 and eqn 1.5.5 in an Avrami analysis (with exponent ≈ 2, following Sellars [Sellars 1980]) the time for any fraction of precipitation and recrystallisation can be obtained for Nb-microalloyed steels. Dutta and Sellars [Dutta 1985] have plotted, **Fig. 1.5.9 (a),** the variation in times for precipitation start (for 5 % precipitation, $t_{0.05p}$), recrystallisation start (5% recrystallisation time, $t_{0.05R}$) and recrystallisation completion (85 % recrystallisation, $t_{0.85R}$,) in 0.07 C-0.004 N (wt %) steel for different Nb levels (studied by Cuddy [Cuddy 1981] at ε = 15 %, $\dot{\varepsilon}$ = 10 / s) against isothermal holding temperatures. Based on the findings in the literature on Nb(C, N) precipitation (le Bon [le Bon 1975] and Ouchi [Ouchi 1982]) Dutta and Sellars [Dutta 1987] assumed that the recrystallisation stop temperature (RST or T_{NR}) occurs when $t_{0.05p}$ equals $t_{0.05R}$. It was also assumed that recrystallisation limit temperature (RLT) arises when $t_{0.85R}$ (i.e. almost complete recrystallisation) equals $t_{0.05p}$. Thereby, using **Fig. 1.5.9 (a)** RST and RLT values are obtained (interval between RST and RLT ~ 60 °C) and the predicted values agreed well with the experimentally determined values by Cuddy [Cuddy 1981] for the same steel, **Fig. 1.5.9 (b)**.

Some other models for the precipitation-recrystallisation interaction in Nb-steels can be found in literature that consider some of the factors (such as the effect of non-equilibrium vacancy concentration on precipitation and recrystallisation [Arieta 1993], the precipitation-recrystallisation interaction under continuous cooling [Bai

1992, Sun 1993], the dependence of activation energy for recrystallisation (Q_{rex}) on the steel composition and temperature [Medina 1991, 1994, 1995, 1996], driving forces for precipitate and recrystallisation [Dutta 2003] and stronger effect of solute drag in retarding recrystallisation at higher temperature (above 950 °C) beside the precipitate pinning [Hodgson 1992]) not covered by Dutta and Sellars [Dutta 1987, 1992, 2001]. However, most of these models are either extensions or modifications of original Dutta and Sellars model [Dutta 1987], and the prediction of recrystallisation time (50 % recrystallisation time, $t_{0.5R}$) using those models are similar to that obtained from Dutta and Sellars prediction, for the similar conditions [Rose 1996, Dutta 2003].

1.5.4 Summary on the effect of precipitation and recrystallisation on bimodality

The most important conclusion that can be drawn from the discussion of the models is that none of the models have considered the effect of segregation of microalloying elements on precipitation or recrystallisation kinetics. If local composition determines the kinetics, then in a segregated structure $t_{0.05p}$, $t_{0.05R}$ or even TNR values will be different at solute-rich and solute-poor regions. Sellars et al. [Sellars 1979, 1980, 1985] predicted that the final grain size after recrystallisation to be proportional to the initial grain size (eqn 1.5.4). Therefore, it is expected that a bimodal microstructure after reheating will remain bimodal after rolling (and a uniform starting microstructure will remain uniform after rolling) only with an overall decrease in grain size. But the situation becomes more complicated in the presence of segregation as it can influence strain-induced precipitation and therefore, recrystallisation. As a result, different recrystallisation behaviour in the different

regions (solute-rich or solute-poor) might be expected to affect the bimodality level upon rolling.

1.5.5 Bimodality during intercritical rolling

Variation in ferrite grain size in the rolled plate and even bimodality in grain size distribution can originate during intercritical rolling within the two-phase (austenite + ferrite) field.

Bodin et al. [Bodin 2001] have observed a bimodal ferrite grain size distribution in C-Mn steel (0.1 C, 0.5 Mn, 0.0045 N) after intercritical rolling ~ 825 °C to 775 °C temperatures. Metallographic studies on the samples quenched from different processing stages revealed that bimodality was absent after reheating (1250 °C for 30 minutes) or initial rolling passes (four passes between 1050-950 °C) before intercritical deformation. Orientation imaging mapping (OIM) in electron backscatter diffraction (EBSD) studies showed that the fine grains surrounding the coarse grains in the microstructure were sub-grains, separated from each other by low angle boundaries. Based on that study Bodin et al. [Bodin 2001] have concluded that the ferrite grains, which are transformed from intercritically deformed austenite grow at a rapid rate due to the transformation-induced (TI) ferrite recrystallisation mechanism. The authors mentioned that the recrystallisation kinetics in TI mechanism are faster compared to SIBM (strain-induced boundary migration) and SGC (sub-grain coalescence) as phase transformation provides extra driving force apart from reduction in dislocation density. The fine grains (i.e. the sub-grains) come from extensive recovery of intercritically deformed ferrite.

Hong et al. [Hong 2002b] have reported similar bimodal ferrite grain structures after heavy deformation (~ 80 % reduction in a Gleeble 1500 simulator) and 10-minutes holding of a Nb-microalloyed steel (0.014 C, 0.052 Nb) within the 750-600 °C temperature range, **Fig. 1.5.10**. According to them, if heavy deformation is given within intercritical region, strain-free ferrite grains transformed from deformed austenite grow abnormally by consuming strained pre-existing ferrite grains by strain-induced boundary migration (SIBM) and even the strain-induced Nb(C, N) precipitates are unable to stop that. SIBM is induced by the difference in dislocation density across the grain boundary. Hong et al. [Hong 2002b] have recommended avoiding heavy deformation or slow cooling within the intercritical range during TMCR to reduce bimodality. Novikov [Novikov 1997] have also mentioned bimodality in ferrite structures arising from abnormal ferrite grain growth by SIBM.

1.6 Summary on the formation of bimodality

From the review of the literature the bimodal distribution in ferrite grain structure of the continuous cast controlled rolled (TMCR) thick plates of Nb-microalloyed steel can arise during various stage of processing.

1) Bimodality in cast structure due to the mixture of fine equiaxed and large columnar grains.
2) Bimodality of austenite grains during reheating
3) Bimodality during rolling within the austenite phase or within the intercritical (austenite+ferrite) region.

In a recent paper, to explain the formation of a banded, bimodal microstructure comprising of coarse bainite and fine acicular ferrite in alternate bands, **Fig. 1.6.1**, Cai and Boyd [Cai 2005] have considered the bimodality contributions coming from different processing stages in Nb-microalloyed steels (0.04-0.07 C, 0.05-0.08 Nb, 0.013-0.018 Ti, 0.003-0.009 N, 0.015-0.044 Al). They ignored any bimodality in the cast structure, but severe bimodality in austenite grain structure was found by reheating the steels to commercial reheating temperatures (1150-1250 °C). This bimodality has been attributed to the abnormal grain growth during reheating. Referring to the previous literature [Asahi 1998] it was suggested that the bimodality generated during reheating was aggravated by strain-induced boundary migration in the initial roughing deformations during TMCR. If low deformation strains are applied at high temperatures on an initial bimodal microstructure, larger grains will have lower strain energy than the smaller grains (due to lower internal strain), and the activation energy for growth of the larger grains will be lower than that required for the nucleation of recrystallisation. Therefore, instead of nucleation of new strain-free grains by recrystallisation, pre-existing large grains will grow further. Cai and Boyd [Cai 2005] have managed to reduce the microstructural banding / bimodality in rolled plates by increasing the applied strain (from, $\varepsilon \sim 0.11$ to $\varepsilon \sim 0.18$) for the initial roughing passes and decreasing the start deformation temperature (from ~ 1180 to 1140 °C). Although, Cai and Boyd [Cai 2005] have not considered the effect of microalloy segregation on bimodality and that is the major limitation of this study.

Previous literature has mentioned that microstructural banding usually originates with the pattern of alloy segregation in the as-cast slab [Krauss 2003], where segregated and non-segregated regions transform to solute-rich phase band (pearlite) and solute-lean phase band (ferrite), respectively, after rolling. Davis and

Strangwood [Davis 2002] and Couch [Couch 2001] have indicated that segregation can create bimodality during reheating (or rolling) by forming an inhomogeneous precipitate distribution. Therefore, segregation is an important factor on the formation of banding and bimodality, and the present study considers that. Although the previous studies have not conducted detailed characterisation of the inhomogeneous precipitate distribution (effect of segregation) in as-cast steel and that makes the first objective of the present work. The present investigation also aims to follow the precipitates and grain structure (grain size and spacing between fine and coarse grain size band) from the as-cast to reheated and rolled steels. That will help in understanding the stability and pinning effect of inhomogeneously distributed precipitates (due to segregation) on the formation of bimodality and banding in the final product. Also an effort has been made to understand the combined effect of deformation and segregation on bimodality.

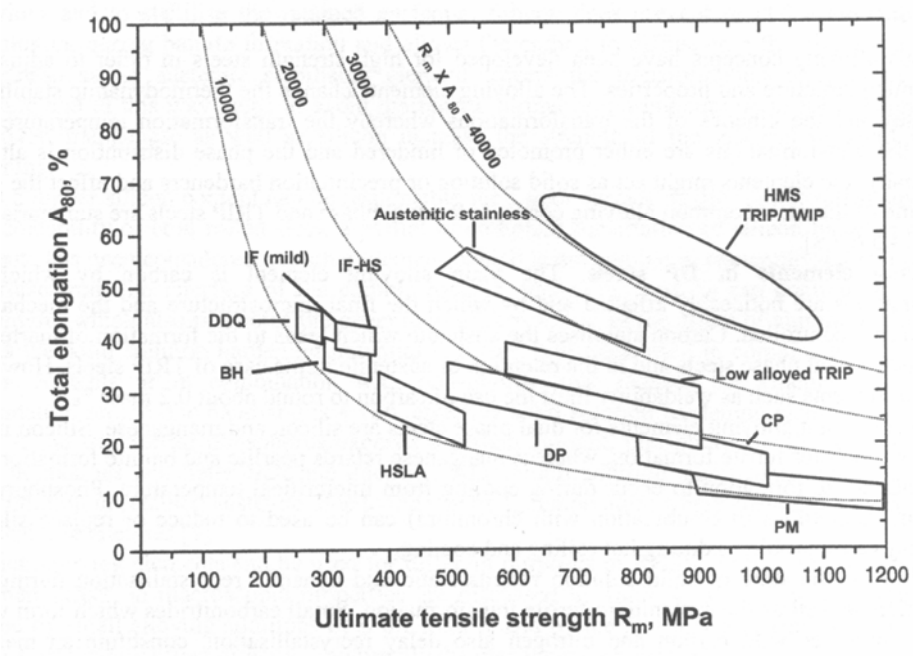

Fig. 1.1.1: Typical mechanical property ranges (ultimate tensile strength and elongation) of different grades of mild and high strength steels [Bleck 2005].

[**Note: The abbreviations used in the figure are as follows:

IF (mild): Interstitial free mild steel, microalloyed, single ferrite phase microstructure and deep-drawing grade.
IF-HS: Interstitial free steel, strengthened by Mn and P addition.
DDQ: Deep drawing grade mild steel.
BH: Bake hardening grade steel, additional strengthening occurs during paint baking.
HSLA: High strength low alloy steel, containing microalloying elements.
DP: Duel phase steel, with ferrite + 5-30 volume percent martensite islands.
Austenitic stainless: Complete austenite microstructure contains high amount of nickel (Ni) and chromium (Cr).
TRIP: Transformation induced plasticity steel (low alloyed or high alloyed) with ferrite + bainite + retained austenite microstructure.
CP: Complex phase steel with strengthened ferrite + bainite + martensite.
PM: Partly or fully martensitic steel.
HMS-TRIP: High Mn steel with the concept of strain-induced retained-austenite to martensite transformation.
HMS-TWIP: High Mn steel with the concept of strain-induced mechanical twinning.]

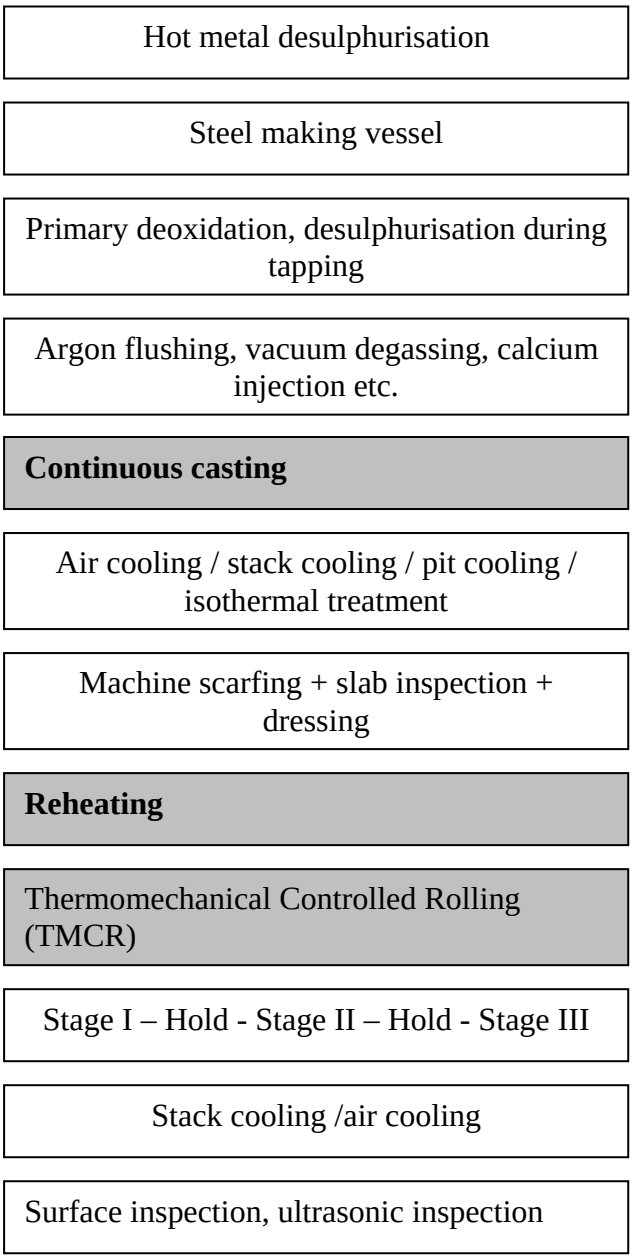

Fig. 1.1.2: Flow chart showing the typical processing route for TMCR-microalloyed-pipeline steels. The dark shaded stages are important from the point of view of grain structure and therefore, are studied in the present investigation to understand bimodality in grain size.

(a)

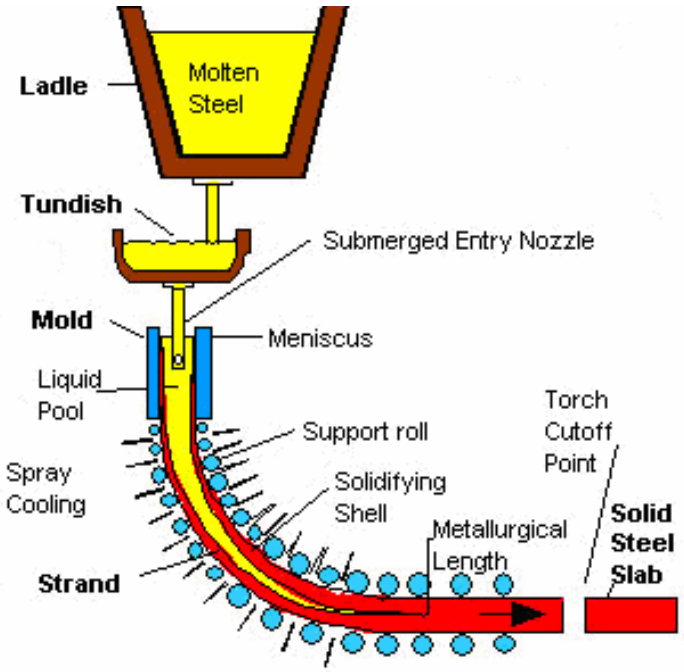

(b)

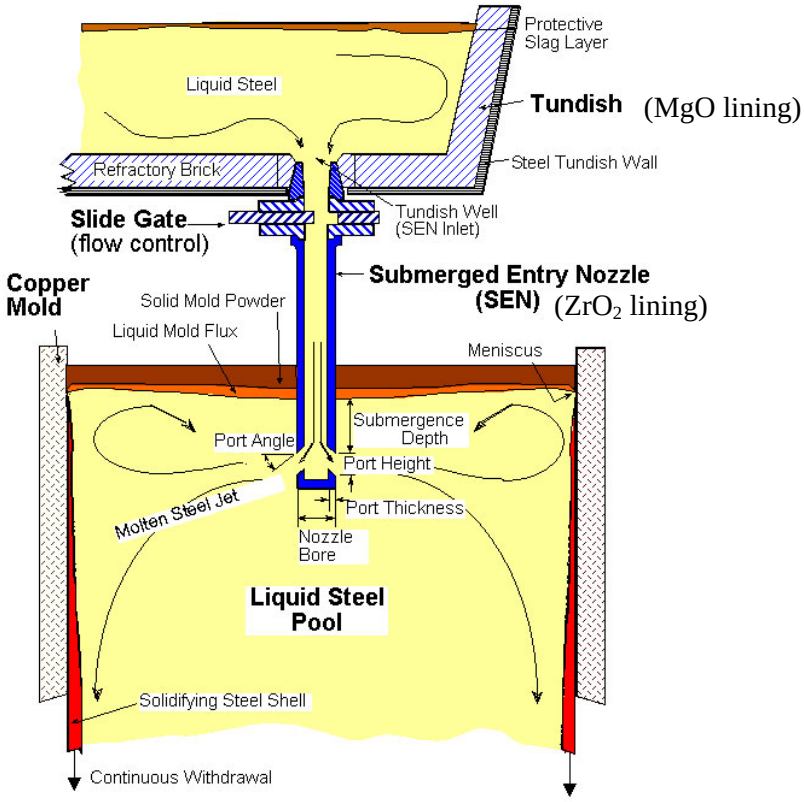

Fig. 1.2.1: (a) Schematic diagram of the continuous casting process for steel and (b) the close-up of the upper mold region showing the start of solidification in continuous casting.

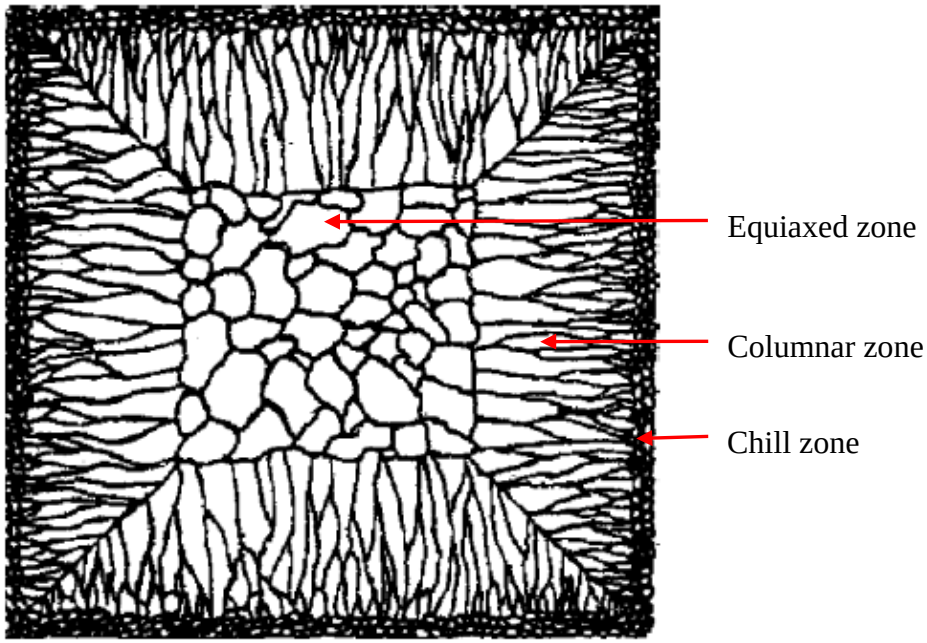
Equiaxed zone
Columnar zone
Chill zone

Fig. 1.2.2: (a) Sketch of cast structure of an ingot showing chill, columnar and equiaxed crystal zones [Bower 1967], and (b) the section of a continuous cast slab showing the same crystal zones.

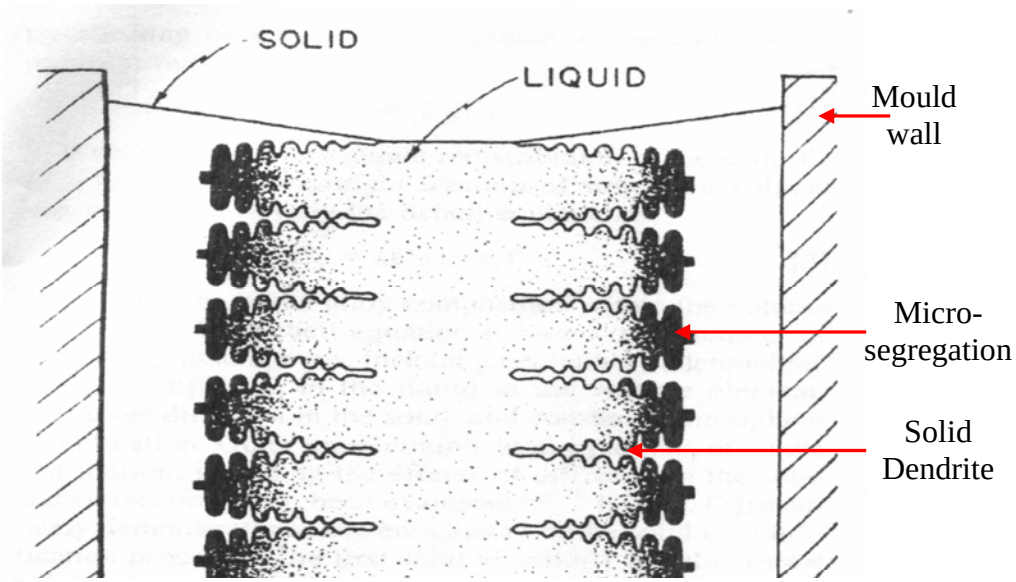

Fig. 1.2.3: Schematic of dendritic solidification during continuous casting [Flemings 1967]. The dark shading in the liquid adjacent to the dendrites represents microsegregation, i.e. higher concentration of solute atoms in the liquid at interdendritic regions due to the rejection of solute by the newly formed solid, which is lean in solute.

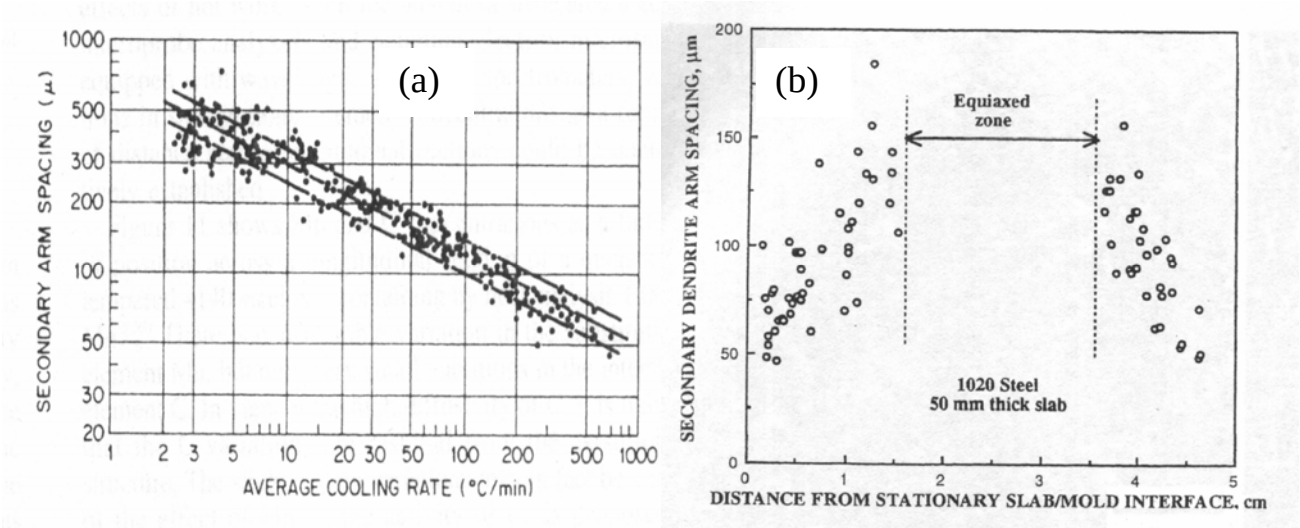

Fig 1.2.4: Secondary dendritic arm spacing as a function of (a) cooling rate (for commercial steels containing 0.1-0.9 wt. percent carbon) [Flemings 1974] and (b) distance across an as-cast 1020 steel slab [Flemings 1974, Krauss 2003].

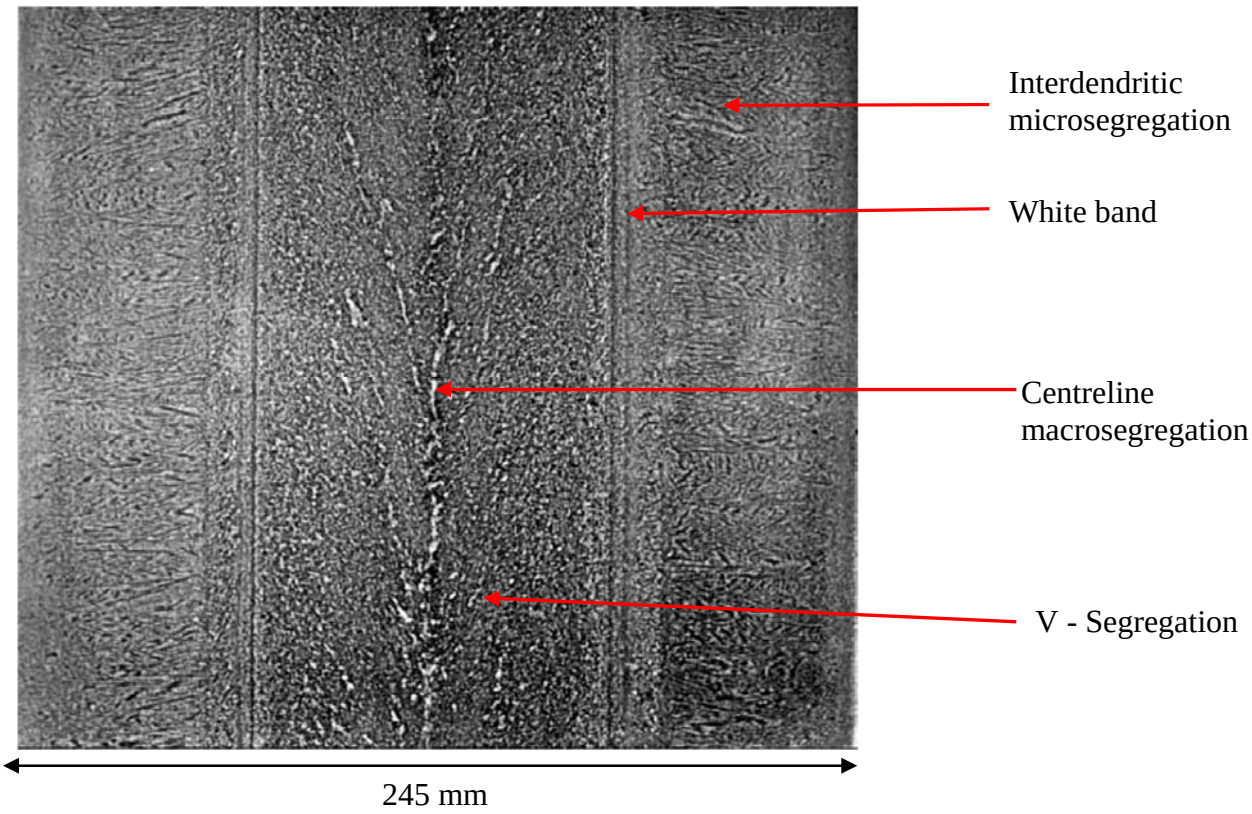

Fig. 1.2.5: Longitudinal section of a carbon steel continuous cast slab (245 mm thick), showing interdendritic microsegregation in the columnar zone close to the upper and lower surfaces, centreline macrosegregation and V-segregation around the central region. Also shown are the white bands at quarter-thickness position from top [Irving 1993, Lesoult 2005].

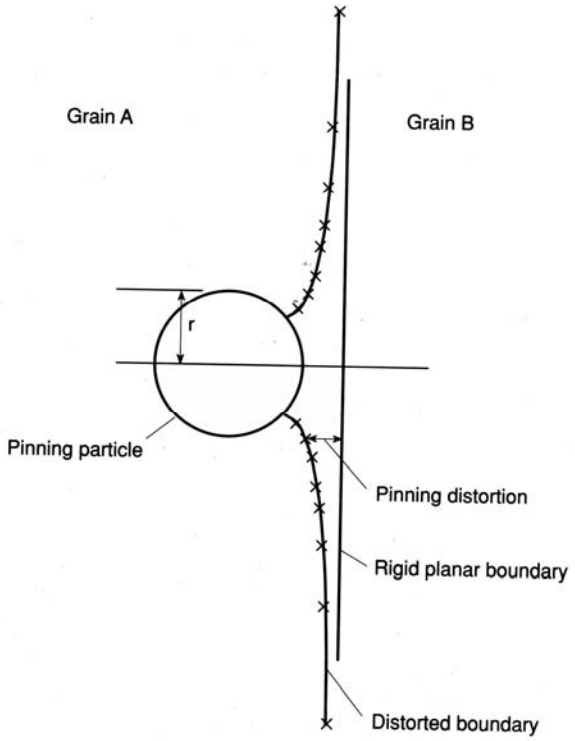

Fig. 1.4.1: Pinning of grain boundaries (between two grains, A and B) by a spherical second phase particle (particle radius, r) [Gladman 1997].

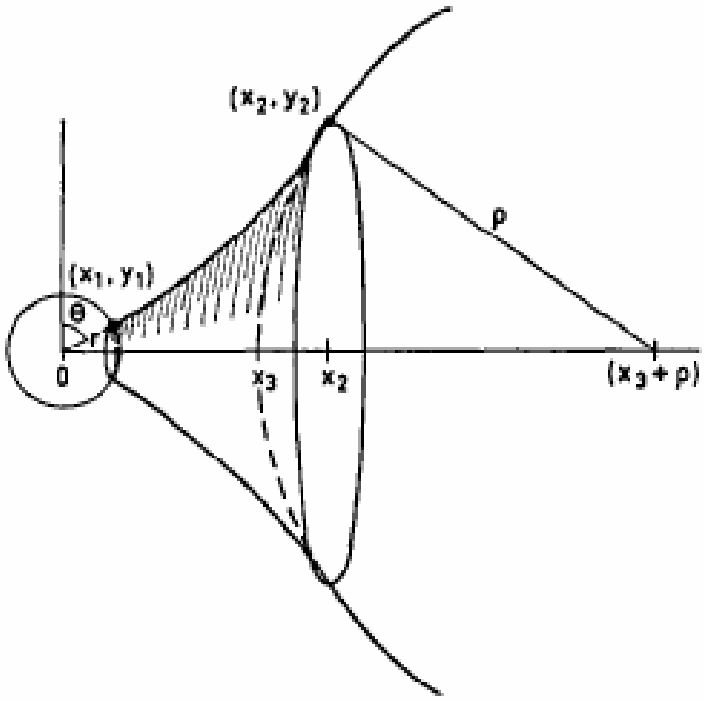

Fig. 1.4.2: Catenoid shape of the grain boundary with radius of curvature, ρ, close to the pinning particle (radius, r) as considered by Hellman and Hillert [Hellman 1975].

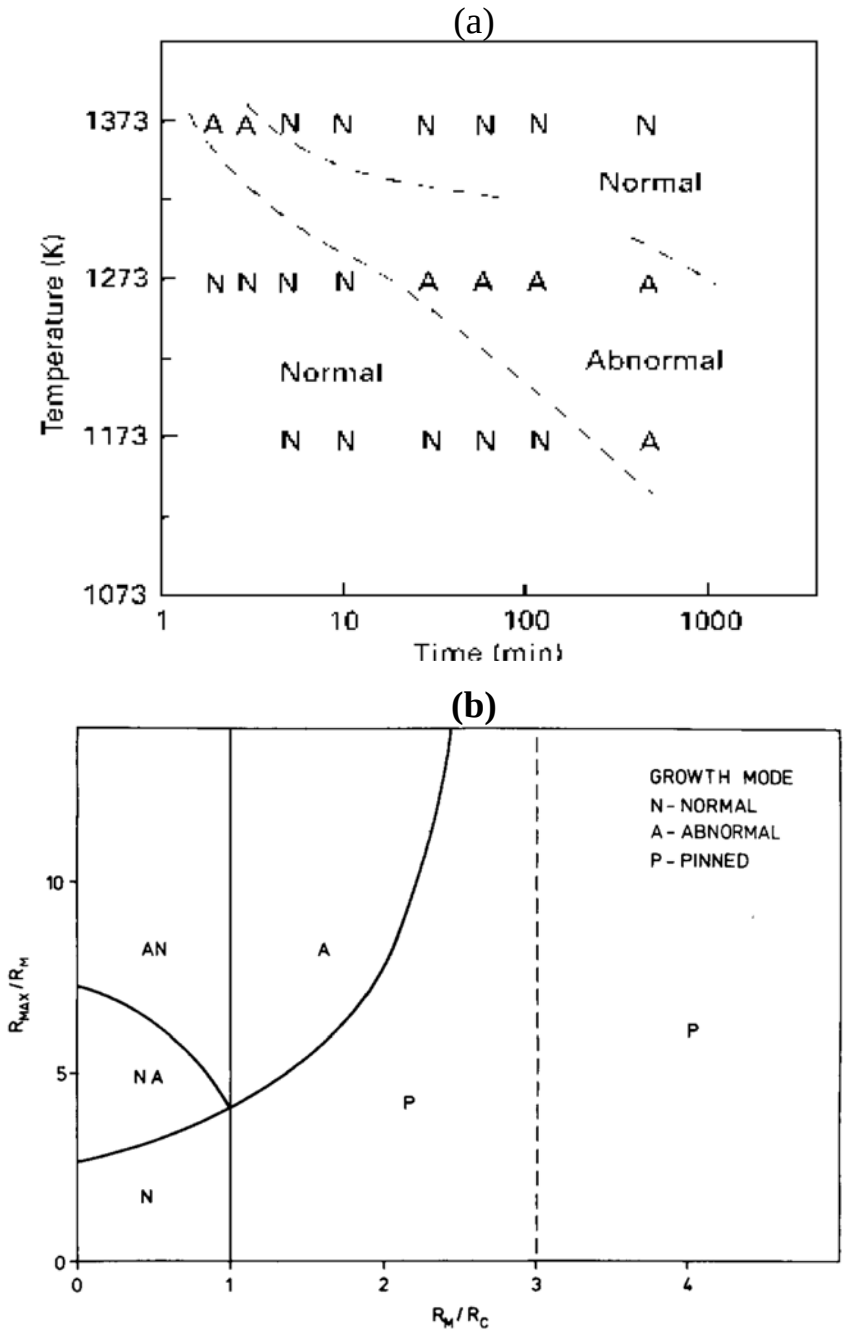

Fig. 1.4.3: Regions for normal and abnormal grain growth: (a) Temperature-time diagram for 0.3 C, 0.036 Nb, 0.15 V steel obtained from reheating studies and numerical calculations of grain growth rate [Flores 1997] and (b) numerically calculated grain growth mechanism map based on the heterogeneity in grain size distribution in any system in the presence of pinning particles. Here R_{max} is the maximum grain radius, R_M is the mean grain radius and R_C is critical grain radius for pinning [Rios 1987].

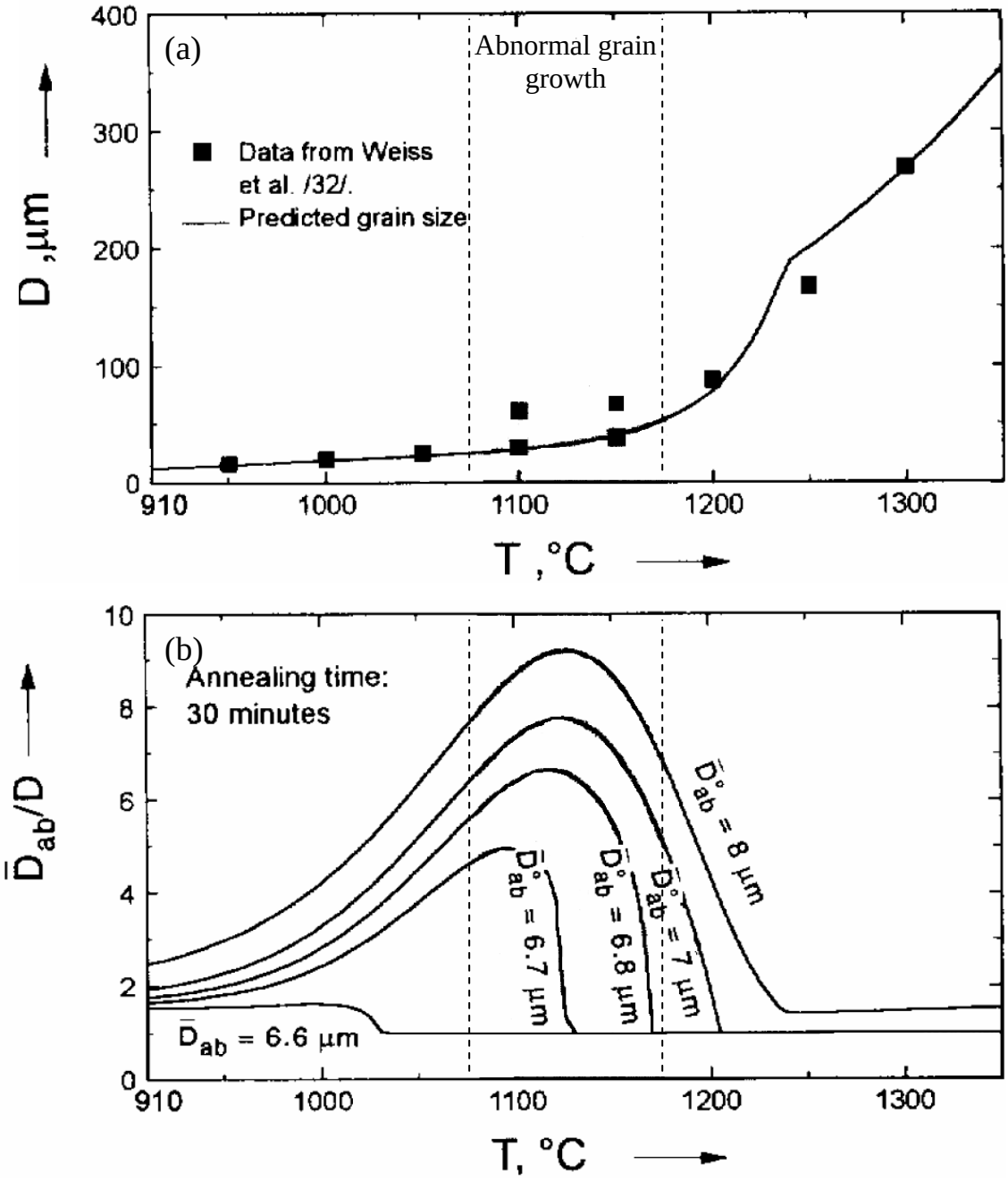

Fig. 1.4.4: Evolution of austenite grain structure during reheating of a Nb-N microalloyed steel: (a) comparison between predicted and measured austenite grain sizes (where, D is the average grain diameter after reheating in µm); (b) maximum variation in grain size heterogeneity with temperatures (where, D_{ab} is the largest grain diameter after reheating, D_{ab}^{0} is the largest initial grain diameter before reheating, 6.6-8.0 µm). The region in between two dotted lines represents the region for abnormal grain growth [Andersen 1995 a and b].

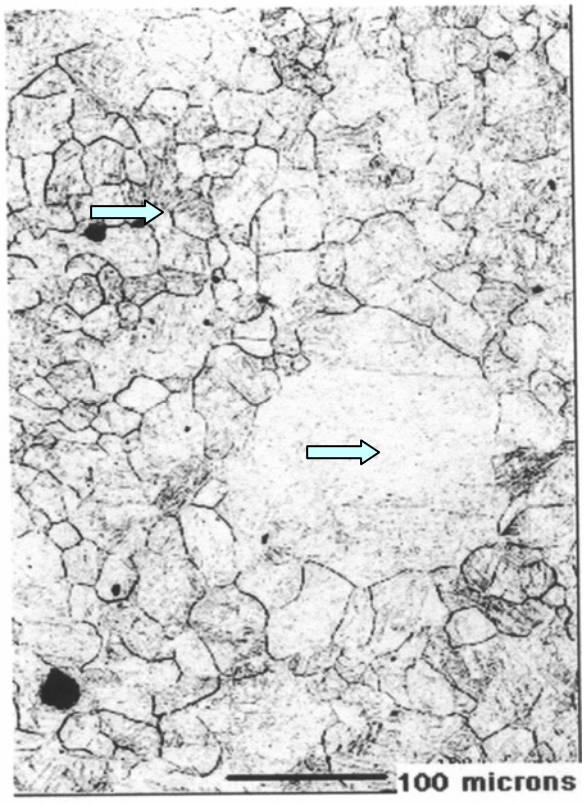

Fig. 1.4.5: Duplex or bimodal austenite grain structure with abnormally large grain present along with fine austenite grains after 1100 °C reheating (for 1 hr.) of 0.1 C-0.04 Nb microalloyed steel [Couch 2001]. Arrows indicate both large and small grains.

(a) (b)

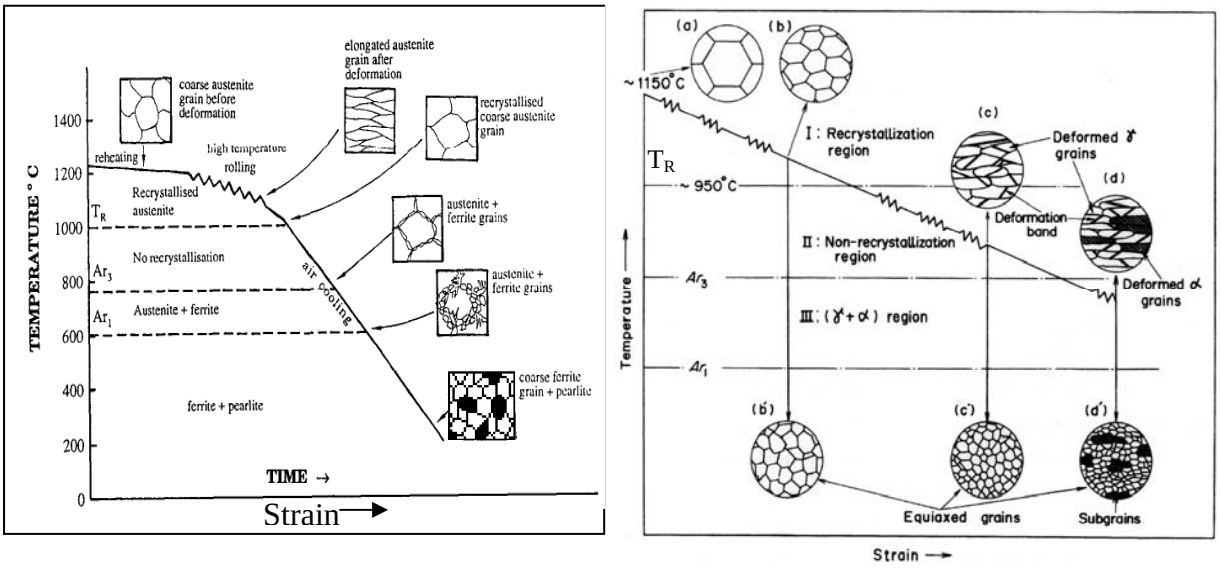

Fig. 1.5.1: Schematic showing the typical rolling schedule and the associated microstructural changes for (a) hot-rolling [Teoh 1995] and (b) thermomechanical controlled rolling (TMCR) [Tanaka 1981] of steels.

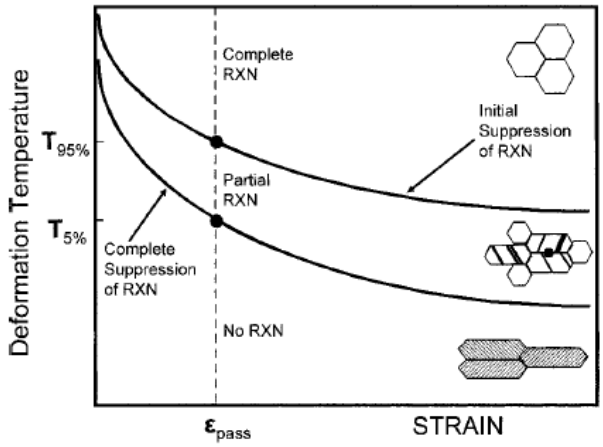

Fig. 1.5.2: Schematic illustration of austenite grain structure resulting from various deformation conditions (deformation temperature and strain) [Palmiere 1996]. Dashed line represents the effect of various deformation temperatures at a constant level of strain (ε_{pass}). $T_{95\%}$ and $T_{5\%}$ are the temperatures for 95 % and 5 % recrystallisation respectively.

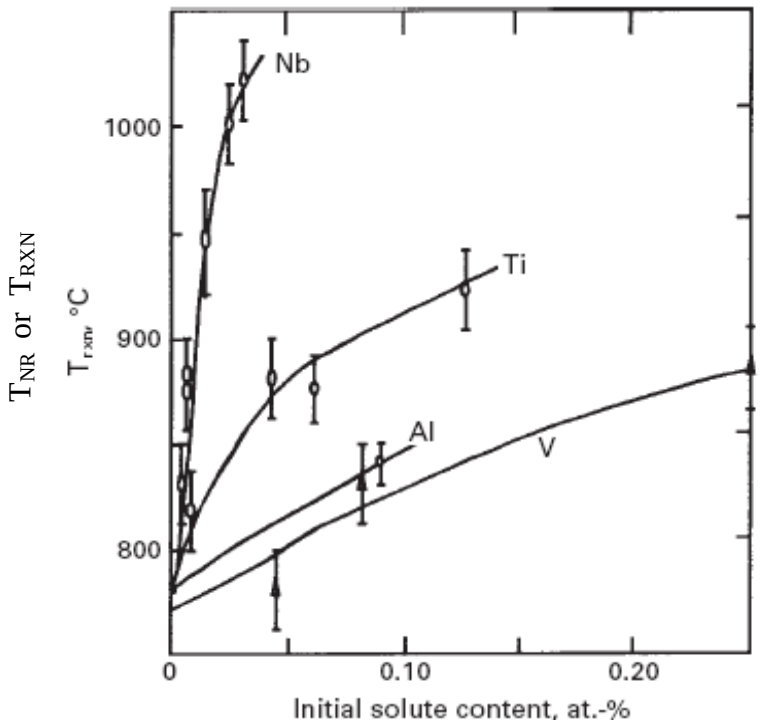

Fig. 1.5.3: Increase in recrystallisation stop temperature with the increase in microalloying element in 0.07 C-1.40 Mn-0.025 Si steel [Cuddy 1982].

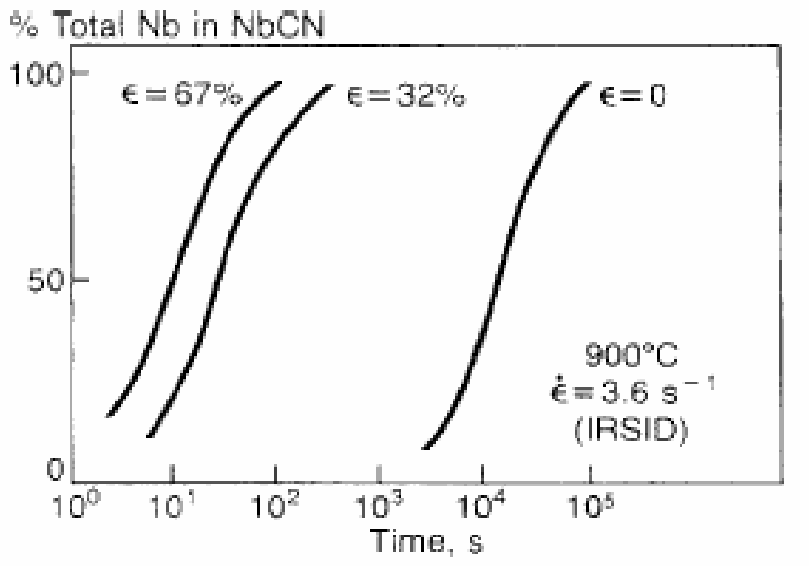

Fig. 1.5.4: Influence of strain level on kinetics of Nb(C, N) precipitation at 900 °C in 0.17 C, 0.04 Nb, 0.011 N steel [le Bon 1975]. Nb(C, N) precipitation becomes rapid as strain increases.

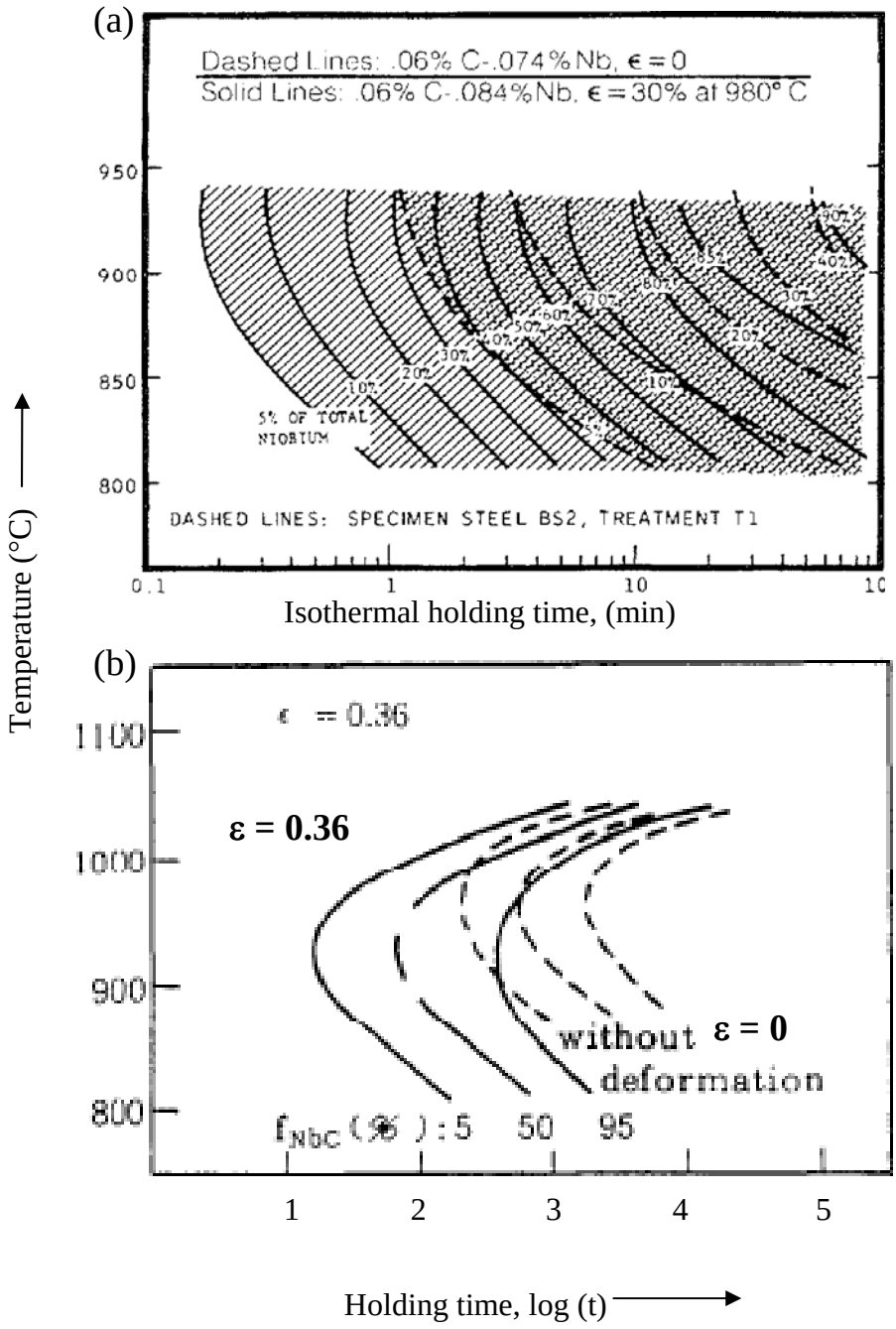

Fig. 1.5.5: C-curve kinetics of strain-induced Nb(C, N) precipitation in deformed austenite following (a) Watanabe (0.06 C-0.08 Nb steel) [Watanabe 1977 91] and (b) Saito (0.05 C, 0.041 Nb) [Saito 1997]. Also shown are the C-curves for precipitation in un-deformed austenite, which is very sluggish.

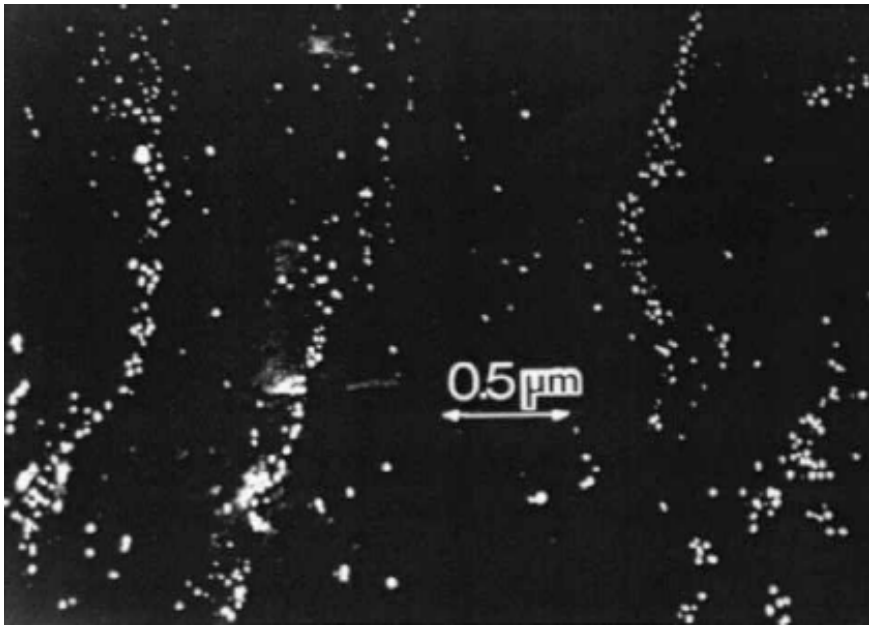

Fig. 1.5.6: Heterogeneous distribution of strain-induced Nb(C, N) precipitates in 0.09 C-0.07 Nb steel after 25 % rolling and holding at 950 °C [DeArdo 2003].

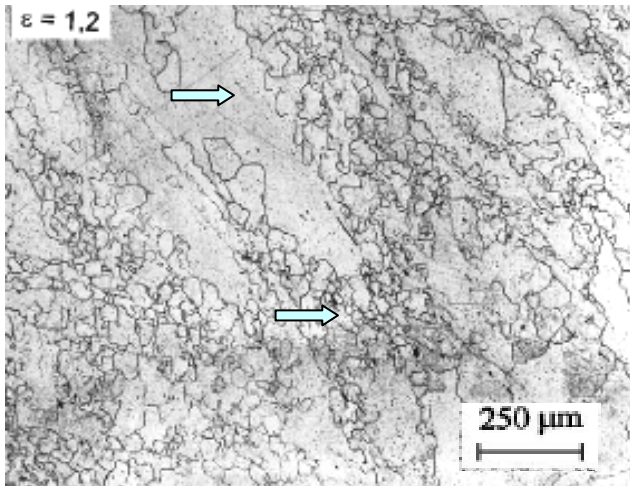

Fig. 1.5.7: Partially recrystallised microstructure containing coarse-unrecrystallised grains and fine-recrystallised grains (both indicated by arrows) [Fernandez 2003].

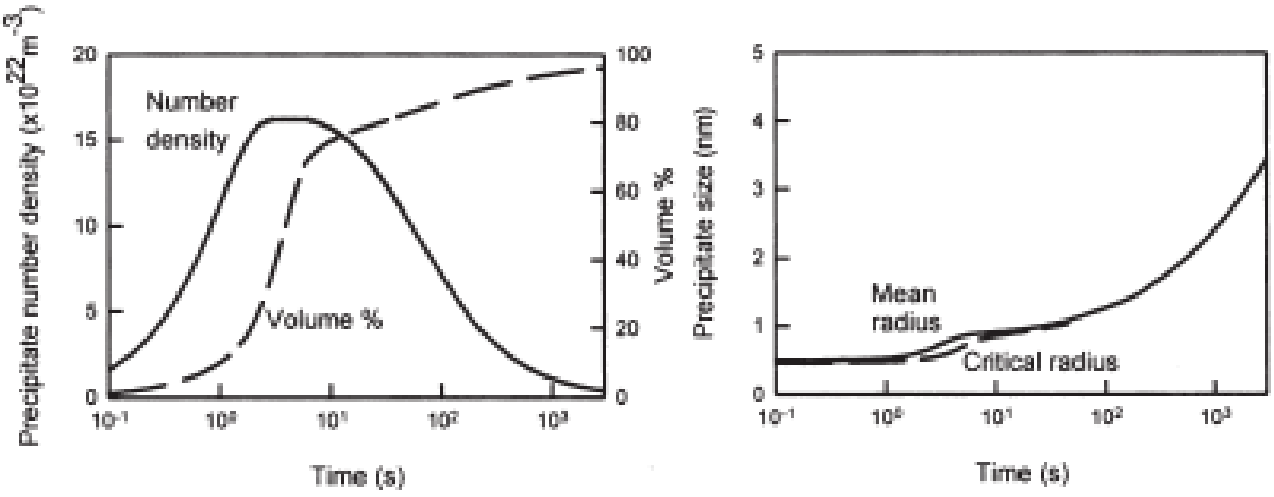

Fig. 1.5.8: Variation in number density, volume fraction and size of strain-induced Nb(C, N) precipitates in austenite in 0.084 C-0.015 N-0.06 Nb steel after 1300 °C reheating, deformation (at 0.33 true strain) and isothermal holding at 950 °C.

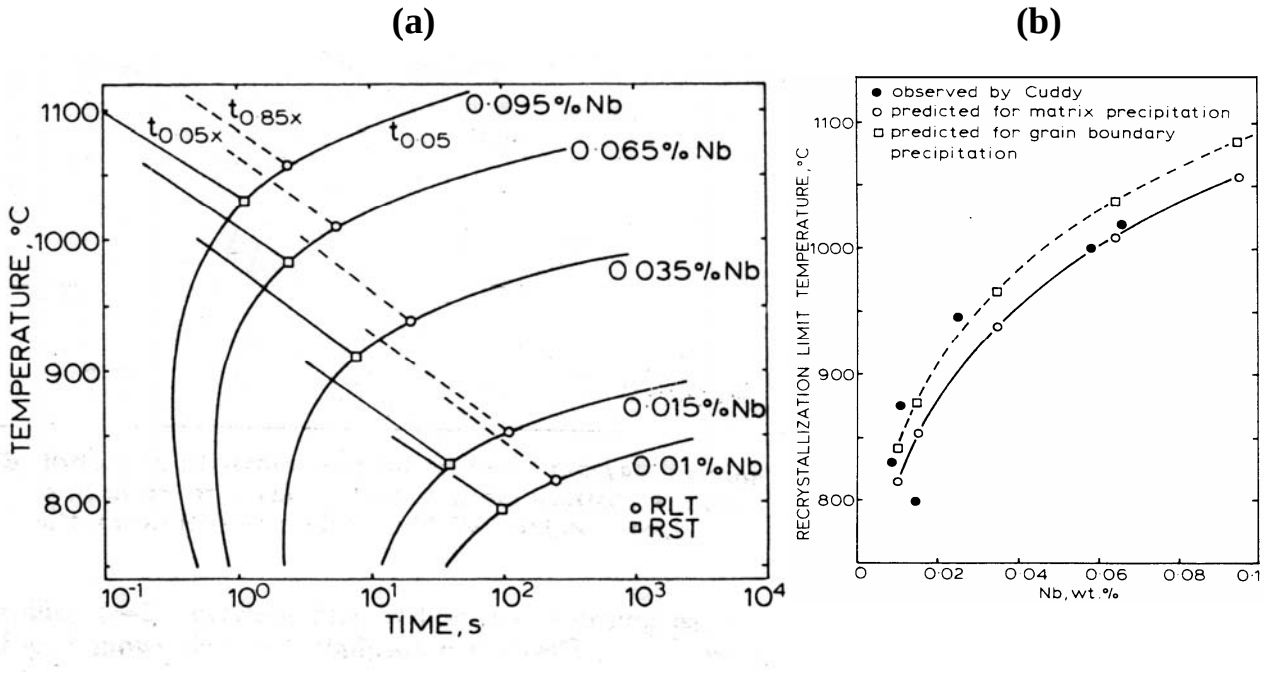

Fig.1.5.9: Interaction of recrystallisation and precipitation from the Dutta-Sellars model [Dutta 1987]:

(a) Determination of 'Recrystallisation limit temperature', RLT, (the lower temperature limit for 'full'-85% recrystallisation) and 'Recrystallisation stop temperature', RST, (the upper temperature limit for complete stoppage of recrystallisation) from the interaction between 5 % recrystallisation time ($t_{0.05X}$, solid straight lines) and 85 % recrystallisation time ($t_{0.85X}$, dotted straight lines) and the start time for strain induced matrix precipitation (5 % precipitation time, $t_{0.05}$ or basically $t_{0.05P}$, curved lines) for various Nb content in 0.07 C-0.004 N steel.

(b) Comparison of RLT predicted for strain induced matrix precipitation and strain induced grain boundary precipitation (from figures similar to 1.5.6 a) with experimental values reported by Cuddy [Cuddy 1981, Dutta 1987].

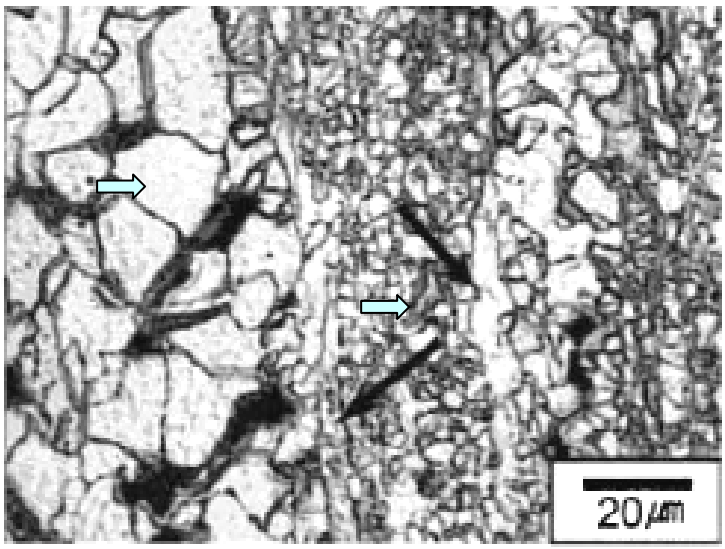

Fig. 1.5.10: Bimodal ferrite grain structure formed after heavy intercritical deformation at 645 °C and 10 minutes holding [Hong 2002b]. Coarse and fine grains are arrowed.

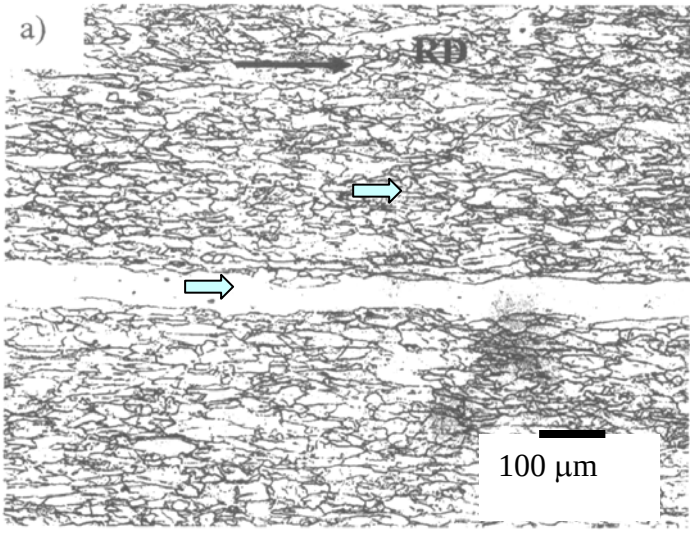

Fig. 1.6.1: Microstructural banding with coarse grain band in between the bands of fine grains (both arrowed) as observed by Cai and Boyd [Cai 2005].

Table 1.1.1: Proportion (in percentage) of HSLA steel used for different end products and applications relative to carbon and alloy steel [Tither 1992].

Application and End Use		Europe (%)	North America (%)	Japan (%)
Line Pipe		95	95	95
Ship-building		40	20	75
Offshore				
	Plates	90	30	70
	Sections	70	20	10
Pressure Vessels		30	25	85
Structural		30	20	10
	Section, Automotives	70	70	30
	Section, Ships	15-30	20	10
	Rebar	100	5	10
	Plates	25	20	10-30
Sheet and Coil (including galvanised sheet)				
	Automotive	20	10	10-30
	Building (not rebar)	95	80	70

Table 1.1.2: Effect of microalloying elements (including Al) on microscopic features and macroscopic properties of steels.

Element	Microscopic effect						Macroscopic effect					
	Coarse precipitates	Fine precipitates	Grain boundary segregation	Grain refinement	Cementite formation	C enrichment in γ_{Ret}	Kinetics of recrystallisation	Kinetics of γ/α transformation	Kinetics of γ/α_B transformation	Ms-temperature	Matrix strengthening	
Nb		+		++		+	--	- / +	-	-	++	
Ti	+	+		+			-	+				
V		+		+			-	+			+	
Al		+		+	-	+		+		+		

[**Note: here γ_{Ret} is retained austenite; γ is austenite; α is ferrite; α_B is bainite; Ms is martensite start temperature. Meaning of the symbols used in the table are as follows: +: positive effect of the microalloying element, i.e. the microalloying element promotes the effect; (-): negative effect of the element, i.e. the element opposes the

effect; ++: highly positive effect; --: highly negative effect; -/+: element can have either positive or negative effect depending on other factors].

Table 1.2.1: The equilibrium partition ratio ('k_p') of various alloying elements in steel [Krauss 2003, Ghosh 2001, Priestner 1998].

Element	Equilibrium partition ratio, 'k_p'
S	0.02
O	0.02
P	0.13
C	0.13
Nb	0.23
N	0.28
Ti	0.61
Si	0.66
Ni	0.80
Mn	0.84
V	0.90
Al	0.92

Table 1.3.1: The diffusion constant $(D_0)_{diff}$ and activation energies (Q_{diff}) for the microalloying elements (also for Al) and important interstitials (C and N) in austenite and ferrite phase.

Element	D_0 (m^2s^{-1}) in ferrite	Q (kJ per mol^{-1}) in ferrite	D_0 (m^2s^{-1}) in austenite	Q (kJ per mol^{-1}) in austenite
C	0.62×10^{-6}	80.4	0.10×10^{-4}	135.7
N	0.50×10^{-4}	77.0	0.91×10^{-4}	168.6
Ti	3.15×10^{-4}	248.0	0.15×10^{-4}	251.2
V	0.61×10^{-4}	267.1	0.25×10^{-4}	264.2
Nb	1.30×10^{-4}	240.0	5.30×10^{-4}	344.6
Al	0.30×10^{-2}	234.5	-	-

Table 1.3.2: Diffusivity $(D)_{diff}$ for the microalloying elements (and also Al) and important interstitials (C and N) within austenite phase at various temperature (T (C): Temperature in ºC and T(K): Temperature in K).

T (ºC)	T (K)	Nb diffusivity	Ti diffusivity	V diffusivity	C diffusivity	N diffusivity
900	1173	2.39004E-17	9.7622E-17	4.2902E-17	9.0563E-12	2.82407E-12
1000	1273	3.83613E-16	7.38418E-16	3.6034E-16	2.70184E-11	1.09819E-11
1050	1323	1.3131E-15	1.81077E-15	9.2561E-16	4.38636E-11	2.00513E-11
1100	1373	4.10944E-15	4.1596E-15	2.2198E-15	6.87417E-11	3.50399E-11
1150	1423	1.18699E-14	9.01276E-15	5.006E-15	1.04382E-10	5.88775E-11
1200	1473	3.19034E-14	1.85296E-14	1.0683E-14	1.54069E-10	9.55067E-11
1250	1523	8.03587E-14	3.63348E-14	2.1692E-14	2.21667E-10	1.5008E-10
1300	1573	1.90864E-13	6.82632E-14	4.2105E-14	3.11634E-10	2.29158E-10
1350	1623	4.29801E-13	1.23361E-13	7.8455E-14	4.29015E-10	3.40896E-10
1400	1673	9.22015E-13	2.15182E-13	1.4085E-13	5.79432E-10	4.9522E-10

Table 1.4.1: Some studies on abnormal grain growth of microalloyed steel during reheating along with the investigated steel composition and reheat schedule.

Reference	Composition (weight-percent)	Reheat temperature (°C)	Reheat time (minutes)
Cuddy 1983	C-Mn steel: 0.09 C, 0.007 N, 1.4 Mn, 0.01 P, 0.01 S, 0.025 Si Nb, Ti, V Microalloyed stel: 0.06-0.08 C, 0.003-0.018 N and either 0.035-0.10 Al, or 0.075-0.11 V, or 0.016-0.225 Ti, or 0.01-0.11 Nb	900-1300	30
Palmiere 1994	Nb-microalloyed steel: 0.08-0.09 C, 0.008-0.024 N, 0.020-0.090 Nb	950-1300	30
Dogan 1992	Al-steel: 0.01 C, 0.03 Al-0.01 N or 0.09 Al-0.04 N	1000-1200	Up to 180
Cabrara	Ti, V, Al- steel: ~ 0.03 C, ~ 0.12 N, ~ 0.09 V, 0.01-0.02 Al, 0.002-0.018 Ti	850-1250	Up to 180
Couch 2001	Nb, Ti, V microalloyed steel: 0.08-0.15 C, 0.2-0.31 Si, ~ 1.4 Mn, 0.027-0.046 Al, 0.027-0.045 Nb, 0.0004-0.0019 Ti, 0-0.132 V, 0.003-0.012 N	900-1300	Up to 180

Table 1.4.2: Topics related to the formation of the abnormal grain growth during reheating and discussion of those topics.

Topic	Discussion
Bimodality in grain structure	Cuddy and Raley [Cuddy 1983] observed a discontinuous austenite grain growth in Nb-microalloyed steels compared to continuous grain growth in C-Mn steel, and that produced a duplex grain structure comprising of abnormally coarse and fine austenite grains. However, the separation between the coarse and the fine grain regions or the specific location of such grain regions in terms of the dendrite structure on steel have not been reporteed. Palmiere et al. [Palmiere 1994] also measured the austenite grain size distribution upon reheating and found three regimes of behaviour in Nb-microalloyed steels, with an increase in temperature from 950 to 1300 °C: (a) unimodal distribution of initial grains exhibiting suppressed normal grain coarsening; (b) bimodal distribution of retained grains and abnormally coarsened grains; and (c) unimodal distribution of abnormally coarsened grains exhibiting accelerated normal grain coarsening. Couch [Couch 2001] has also reported such bimodal austenite grain structure upon reheating Nb-microalloyed steels (0.1 C, 0.04 Nb) to 1100-1150 °C for 60 minutes, **Fig. 1.4.5**.
Concept of T_{GC}	Cuddy and Raley [Cuddy 1983] and Palmiere et al. [Palmiere 1994] tried to measure a grain-coarsening temperature, T_{GC} (the temperature at which abnormal or discontinuous grain growth starts) from the point of discontinuity in the average grain diameter - vs. -reheat temperature plot. It was found that T_{GC} increases with an increase in the complete dissolution temperature, T_{DISS}, of the microalloy precipitates but was always lower than T_{DISS}. Based on an atom probe microscopic study of Nb(C, N) precipitate dissolution Palmiere et al. [Palmiere 1994] derived an empirical relation between T_{DISS} and T_{GC}: T_{GC} (°C) = T_{DISS} (°C) – 125 °C; which is valid for the compositions investigated by them (**Table 1.4.1**). Also T_{GC} has been found to vary with the type and concentration of microalloying element in the steel. According to Cuddy and Raley [Cuddy 1983] steels containing insoluble TiN coarsen at higher temperatures (~ 1200-1250 °C) than steels containing more soluble V(C, N) (980-1050 °C). T_{GC} for Nb-microalloyed steels increased with the increase in Nb-level (from ~ 1000 °C for 0.01 Nb to ~ 1200 °C for 0.11 Nb for Cuddy and Raley [Cuddy 1983]; and from ~ 1000 °C for 0.02 Nb, ~ 1100 °C for 0.049 Nb, ~ 1200 °C for 0.090 Nb for Palmiere et al. [Palmiere 1994]).

Role of AlN	Apart from microalloy precipitates AlN particles also play a vital role in controlling the grain growth behaviour of steel during reheating. Dogan et al. [Dogan 1992] have observed suppressed, abnormal and uniform grain growth conditions during reheating of two different Al-containing steels. AlN particles were also studied using TEM. Abnormal grain growth started at a higher temperature (T_{GC} ~ 1100 °C) for the higher Al- and N-containing steel (therefore, lower AlN solubility), compared to low Al, N steel (T_{GC} ~ 1000 °C). After abnormal grain growth started, the growing large grains did not consume all the small grains, even after long holding (3 hrs) at 1200 °C, and ~ 1 area-percent of small grains remained within the large grains as colonies. It has been explained by Dogan [Dogan 1992] that the distribution of AlN particles might not be perfectly random and the regions of higher AlN particles would be more resistant to grain growth and give rise to the fine grain regions. Cabrara et al. [Cabrara 1996] noticed the onset of abnormal grain growth during reheating only due to the dissolution of AlN particles even in presence of more stable TiN or (Ti, V)(C, N) particles in steels containing Ti, V and Al.

Table 1.5.1: Some studies on strain-induced Nb(C, N) precipitation and austenite recrystallisation in Nb-microalloyed steels, along with the steel compositions and the values of parameters used in deformation test (T_s: soaking temperature, t_s: soaking time, ε: strain, ε: strain rate, T_{def}: deformation temperature, T_{hold}: isothermal holding temperature, t_{hold}: isothermal holding time).

Reference	Composition (weight-percent)	T_S (°C) – t_s (minutes)	ε (Percentage or true strain)	ε (Per second)	T_{def} (°C)	T_{hold} (°C)	t_{hold} (seconds)
Hansen 1980	~ 0.1 C, ~ 0.01 N, 0.005-0.021 Nb	1250-60	50 %	2.6	950	800-950	Up to 10, 000
Kwon 1991	0.01 C, 0.008-0.025 N, 0-0.042 Nb	1300-30	0.03	0.1, 10	900-1100	900-100	Up to 1000
Speer 1989	0.008-0.025 C, 0.05-0.36 Nb, 0.008-0.08 N	1204-60	20%, 50 %	6, 10	954	899-1066	10, 100, 1000, 10000
Palmiere 1996	~0.09 C, 0.020-0.090 Nb, 0.008-0.024 N	1250-180	0.3	10	900-1100	900-1100	10
Luton 1980	0.001-0.055 C, 0.054 Nb, 0.001-0.005 N, 0-0.059 Al	1150-30	0.10, 0.025	0.013, 0.13	900-1000	900-1000	10, 100, 500, 1000
Rainforth 2002	30 Ni, 0.01 C, 1.61 Mn, 0.01 Nb	1250-15	0.025, 0.045		950	950	1 to 1000

Table 1.5.2: Some findings on the strain-induced Nb (C, N) precipitation in Nb-microalloyed steels.

Factors	Observations and usual values
Precipitate shape and size	Strain-induced Nb(C, N) precipitates are spherical in shape and very fine in size (average size less than ~ 7 nm, after $\varepsilon \approx 0.2$-0.4 deformation strain, and 1000 sec holding within 850-1100 °C) [Hansen 1980, Speer 1989, Kwon 1991, Luton 1980, Rainforth 2002].
Precipitation time	Precipitation is also very rapid, starting within 1 s of deformation (shown by Rainforth [Rainforth 2002] for $\varepsilon = 0.25$ at 950 °C) and being completed within 100-1000 s holding [Hansen 1980, Speer 1989, Kwon 1991].
Precipitate volume fraction	The equilibrium volume fraction (f) of precipitates lies between 4×10^{-4} and 9×10^{-4} [Hansen 1980, Speer 1989, Palmiere 1996]. With an increase in Nb, C and N level in the steels and also upon stoichiometric addition of Nb, C and N, 'f' increases [Hansen 1980, Kwon 1991].
Precipitate coarsening	Soon after precipitation completes precipitates start to coarsen and that can result in a drop in precipitate number density (~ 2.7×10^{14} / m^2 after 100 s to 1.5×10^{14} / m^2 after 1000 s holding [Kwon 1991] and increase in precipitate size (maximum precipitate size 10-15 nm after 1000 s holding to 20-30 nm after 10000 s holding [Hansen 1980]). But coarsening is limited as even after 10,000 s holding the average precipitate size remained within 10-15 nm [Hansen 1980, Kwon 1991]. Rate of coarsening increased with an increase in Nb content in the steel (as diffusion flux increases) [Hansen 1980, Speer 1989].

2 Effect of bimodality on properties

High strength low alloy (HSLA) steels with microalloying elements are sold to customers based on their superior combination of high strength and good toughness, distributed uniformly throughout the product. These mechanical properties come from a fine, uniform, predominantly ferrite grain structure with a dispersion of small strengthening precipitates. However, a bimodal ferrite grain size distribution (coarse grains present in the matrix of fine grains) has been seen in some Nb-V TMCR steel plates [Bhattacharjee 2004, Wu 2004 a, Shehata 1982]. To understand the effect of such a bimodal grain size distribution on mechanical properties it is necessary to study the effect of such microstructure on strength and fracture toughness of steels.

2.1 Strengthening mechanisms in microalloyed steels

The prime strengthening mechanisms that operate in microalloyed steels [Gladman 1975, Tsai 1997, Jian 1990, Talbot 200a] are as follows:

1) Grain boundary strengthening (σ_{GB}) coming from grain refinement (i.e. fine grain size)
2) Precipitation strengthening (σ_P) coming from the dispersion of fine microalloy precipitates, generally Nb(C, N) and V(C, N) in ferrite phase [Ashby 1958].
3) Solid solution strengthening (σ_{SS}) coming from the dissolved solute atoms (generally substitutional solutes such as Mn, Si, P, Si and Cu)

Apart from the above mentioned mechanisms some other mechanisms also contribute to the overall strength such as dislocation strengthening (σ_{DIS}), sub-grain hardening

(σ_{SB}), and texture strengthening (σ_T). Combining the separate contributions from the major strengthening mechanisms by linear addition (most commonly used, other form of additions such as root mean square have also been used [Kejian 1993]), the yield stress (σ_y) of microalloyed steel can be expressed as [Hall 1951]:

$$\sigma_y = \sigma_i + \sigma_P + \sigma_{SS} + k_y.D^{-\frac{1}{2}} \quad \text{.....eqn. 2.1.1}$$

where, σ_i is the internal frictional stress (or Pearl-Nabarrow, P-N, stress; $\sigma_i \approx 70$ MPa [Morrison 1966]) and k_y is the strengthening co-efficient that depends on the ability of the material to allow the dislocations to cross-slip across the boundary (reported values of k_y fall in the range of 15.1 – 22 N $mm^{-3/2}$ for HSLA steel [Gladman 1997, Morrison 1966, Knott 1982])

2.1.1 Grain size dependence of strength

The interest of the present investigation lies in the selection of grain diameter (D) in **eqn. 2.2.1**. In most studies calculating σ_y for the ferrite-pearlite microstructure, the value of 'D' used is the average ferrite grain diameter (in mm), which can be measured following standard techniques by optical microscopy ASTM 112 [ASTM 112 2005] or by image analysis ASTM 1382 [ASTM 1382 2005]. Also the effect of a mixed grain size structure, consisting of large polygonal ferrite grains (average size, D; strengthening co-efficient k_y) and small sub-grains (average size, D_{sub}; volume fraction, f_{sub}; strengthening co-efficient k_{sub}) on σ_y can be expressed as [Bramfitt 1973]:

$$\sigma_y = \sigma_0 + k_y.D^{-\frac{1}{2}}.(1 - f_{sub}) + k_{sub}.D_{sub}^{-\frac{1}{2}}.f_{sub} \quad \text{……..……..……eqn. 2.1.2}$$

however, this proportionality approach still needs to be verified in controlled rolled steels with bimodal ferrite grain structures (mixture of large and small grains).

2.2 Fracture of HSLA steels

Industrially the toughness of steel and its variation over temperature is determined by the Charpy impact test. The test results are presented in the form of impact transition curves (either in terms of fracture energy or fracture surface appearance, **Fig. 2.2.1**), which show the transition in fracture behaviour over temperature: low fracture energy (brittle fracture) at lower temperature (below T_l) by a cleavage mechanism and high fracture energy (ductile fracture) at higher temperature (above T_h) by a fibrous mechanism. Fracture transition behaviour of steel can be characterised by an impact transition temperature (ITT), which can be defined in various ways (such as 27J-ITT**,** DBTT and FATT), **Fig. 2.2.1**.

Fibrous mechanism can be characterised by the presence of microvoids on a generally slanting fracture surface, **Fig. 2.2.2 (a) and (b)**. Cleavage mechanism can be characterised by the presence of river lines (showing the crack paths) and cleavage facets (section of grains on the fracture surface) on the flat fracture surface, **Fig. 2.2.2 (c) and (d)**. Commercial TMCR-microalloyed steel grades show higher Charpy energy (usually more than 100 J at –40 °C) compared to plain-C-steels or normalised microalloyed steels (usually less than 30 J at –40 °C) [Tither 1992].

2.2.1 Mechanism of cleavage fracture

Considering the various models and the experimental studies on cleavage fracture [Griffith 1921, Orowan 1946, Low 1954, Stroh 1954, Zener 1948, Cottrell 1958, Smith 1966, Liu 1982, Hull 1960, McMahon 1965, Knott 1963, Lindley 1970, Curry 1976], and depending on the critical step for fracture: either the propagation of a grain-sized (D) microcrack to the neighbouring grain (changing its orientation) [Cottrell 1958, Chen 1992, Yan 1993, Groom 1975] or the propagation of a particle-sized (t') microcrack to the neighbouring matrix [Smith 1966, Curry 1978, Hahn 1984, Bowen 1987]; the fracture stress can be summarised in the following form:

$$\sigma_f \propto D^{-\frac{1}{2}} \text{ or } \sigma_f \propto t'^{-\frac{1}{2}} \qquad \text{.....eqn. 2.2.1}$$

The effect of carbide size on fracture can also be related indirectly to the grain size as Curry and Knott [Curry 1978] observed that the largest carbide size in the microstructure can be proportional to the ferrite grain size in annealed or normalised mild steels. Recent studies on microalloyed steels indicate that the presence of a large TiN particle in a large grain makes the steel more prone to fracture [Petch 1986, Echeverria 2003]. Therefore, the combination of large second phase particle along with large grain size (found especially in weld metals) is detrimental for fracture. All the above conditions can be represented by a normalised Griffith-Orowan type equation [Curry 1978, Echeverria 2003], that considers the plastic deformation at the crack-tip before crack propagation, in the following form:

$$\sigma_f = \left[\frac{4E\gamma_p}{\pi(1-\nu^2)x} \right]^{\frac{1}{2}} \qquad \text{.....eqn. 2.2.2}$$

where, x is the length of the microcrack that causes failure. For grain-sized microcrack: x = D and $\gamma_p = \gamma_{mm}$ i.e. the effective surface energy for matrix-martix interface). For particle-sized microcrack: x = t' and $\gamma_p = \gamma_{pm}$, i.e. the effective surface energy for particle-matrix interface.

2.2.2 Effect of ferrite grain size on fracture

The effect of ferrite grain size on fracture can be best understood from **Fig. 2.2.3**, which shows that σ_f lies in the range of ~ 500-1300 MPa for annealed or normalised mild steels (C ~ 0.03-0.07) for a wide range of grain sizes (~ 30-800 μm) [Ritchie 1974]. For TMCR-microalloyed steels (with ferrite + pearlite structure) it has been found that the average ferrite grain size lies within 5-10 μm, and σ_f values usually fall in the range ~ 1500-2400 MPa [Wu 2004a, Wu 2004b, Bhattacharjee 2004]. Mintz et al. [Mintz 1982] have reported that grain size has a more dominant effect on 27J-ITT then carbide particle size for low C (<0.06 C)-steels. For a constant range of carbide thickness (e.g. 0.5-1 μm) the 27J-ITT was found to drop ~ 160 °C, with a decrease in ferrite grain size from ~ 600 to 5 μm, **Fig. 2.2.4**. Microalloying along with TMCR not only improves strength but also improves fracture toughness of steel by decreasing ferrite grain size.

2.2.3 Effect of particles, inclusions and pearlites on fracture

Apart from the role of grain size on 27 J-ITT **Fig. 2.2.4** also shows that, for a constant ferrite grain size (~ 40 μm), the 27J-ITT dropped ~ 60 °C (from + 40 °C to -20 °C) as the grain boundary carbide thickness decreased from >1.5 μm to <0.5 μm. It

was found that there is a higher limit of grain boundary carbide thickness (~2 μm for 40 μm grain size) above which any further increase has no influence on the ITT [Mintz 1982]. Rosenfield and Shetty [Rosenfield 1986] have calculated a lower limit of particle size, ~ 0.7 μm, below which particles cannot trigger cleavage in steel for 4PB test specimens (blunt-notched specimens tested at -130 ºC, at 2 mm / min cross-head speed) of 0.1 wt % C-steel with a ferrite-pearlite microstructure (10-15 % pearlite). In TMCR-microalloyed steels Nb(C, N) or V(C, N) particles are of very fine size (generally < 100 nm), and therefore are not expected to nucleate cleavage in slow-notch bend tests with low-temperature blunt-notch-bend test specimens.

TiN particles (can be up to ~ 3 μm in size) and Al_2O_3 inclusions remain strongly bonded with the matrix and can nucleate cleavage crack by acting as stress-raisers [Echeverria 2003, Balart 2000, Fairchild 2000]. TiN particles (> 1 μm) were most effective in causing fracture in TMCR steels when located within suitable (low misorientation) coarse ferrite grains (~ 18-50 μm) [Echeverria 2003, Balart 2000]. MnS inclusions are much softer (compared to TiN or Al_2O_3) during hot rolling of steel, and elongate along the rolling direction. MnS inclusions severely affect ductile elongation and upper shelf impact energy (USE) by promoting void nucleation at the inclusion-matrix interface. MnS can also nucleate cleavage (by de-bonding) and particularly affect the fracture properties (fracture stress and ITT) of TMCR steels transverse to rolling direction [Tweed 1987, Baker 1972]. Complex inclusions can also form in steel by the formation of one kind of particle or inclusion on other (TiN-Al_2O_3-MnS) and such large inclusions can also be detrimental for cleavage [Balart 2000].

Beside large ferrite grains, particles or inclusions the large pearlite colonies have also been found to nucleate cleavage, especially in rolled linepipe steels with

strongly banded ferrite-pearlite distributions [Knott 1981]. Large (colony size) micro-cracks form preferentially in the pearlite and spread at higher stress levels into the ferrite. Depending on the location of crack nucleation, either in pearlite or in ferrite, a bimodal distribution in fracture toughness can be seen in banded ferrite-pearlite structures [Knott 1981, Knott 2007]. The fracture properties of pearlite are dependent on the thickness of the individual cementite plates. Studies on eutectoid steels showed that, whereas coarse pearlites crack easily, fine pearlites show higher resistance to cracking [Porter 1979]. Even in absence of pearlites, any carbon redistribution that leads to the formation of macro-phase or M-A (martensite-austenite) constituent can take part in cleavage crack initiation [Knott 1981].

2.2.4 Measurement of cleavage fracture stress

To determine σ_f most studies used three- or four-point bend tests (3PB or 4PB) on blunt notched specimens at temperatures lower than -100 °C. For the blunt notched specimen a larger volume fraction of material comes under the high stress field compared to sharp pre-cracked specimens and grains / particles within that zone (active zone) can contribute to fracture. Temperatures lower than -100 °C (approx) ensure complete cleavage fracture. The Richie, Knott and Rice (RKR) model [Richie 1973] suggested that cleavage fracture could occur only when the critical fracture stress is exceeded by the local tensile stress ahead of a sharp crack (or blunt notch) over a characteristic distance, X_c (which is close to twice the grain diameter for mild steel), ahead of the crack tip. Although the definition of X_c has been modified later on by other authors [Curry 1978], the RKR model first demonstrated the need for understanding the stress distribution ahead of the crack tip.

2.2.4.1 FEM analysis

The stress-strain distribution ahead of a crack tip can be calculated from finite element methods. The most established finite element analysis (widely used to determine fracture stress) is by Griffiths and Owen [Griffiths 1971], which illustrates the variation of maximum principal tensile stress (and strain) with distance ahead of the notch tip, **Fig. 2.2.5**, for a blunt notched four point bend (4PB) specimen, **Fig. 2.2.6,** for various applied load, L, (or applied nominal stress, σ_{nom}). Normalisation of applied loads or stress makes the analysis widely applicable as the general yield load (L_{GY}) or yield stress (σ_y) takes care of the effect of change in test temperature or composition of steel.

Fig. 2.2.5 shows that the maximum principal stress (σ_1) reaches the highest value within the plastic zone formed ahead of the crack tip. Assuming that the fracture initiates at the point where σ_1 reaches the highest value, the principal fracture stress (σ_F) can be obtained from **Fig. 2.2.5**. More accurate measurement of fracture stress is the local fracture stress (σ_f), which can be obtained by measuring the distance of cleavage origin from the notch root (characteristic distance) and using that distance in **Fig. 2.2.5**. For C-Mn and C-Mn-Ti steels (0.07-0.18 C, 1.24-1.6 Mn, 0-0.02 Ti, all wt %) Wang et al. [Wang 2002] have found that σ_f values (for blunt notched specimens tested at –196 °C) are close to σ_F; $\sigma_f \approx (0.8\text{-}1.0)\sigma_F$. In this study for ~ 85 % of all specimens the characteristic distance was within 200-500 μm in front of the notch, i.e. close to the point where σ_1 reaches a maximum value. For Ti-microalloyed forging steels (0.2-0.3 C, 0.015-0.064 Ti, all wt %) Linaza et al. [Linaza 1995] have also reported that for ~ 75 % of all the bend test samples tested, the difference between σ_F

and σ_f lies within 10 %. The above studies indicate that the cleavage origin lies around the highest σ_1 value, which helps the crack to grow. Large differences between σ_F and σ_f can be attributed to the fracture initiation being far from the point where σ_1 reaches the highest value, due to the presence of large grain size or particle size, for which a low value of local tensile stress is sufficient for cracking.

2.2.5 Effect of grain size distribution on the fracture stress

To understand the effect of grain size variation on cleavage fracture, the distinguishing parameter should be sufficiently stable and should be least affected by the changes in test temperature, specimen geometry, and loading type. Bowen et al. [Bowen 1986] have concluded (for ferrite, bainite or martensite microstructures in A533B pressure vessel steel) that the local cleavage fracture stress, σ_f, becomes almost independent of test temperature when tested below – 100 °C, whereas, K_{1C} (plane strain fracture toughness) varies significantly with temperature over the whole range of test temperatures (-20 to –196 °C). Chen and Wang [Chen 1998] have also reported minimum variation in σ_f (standard deviation, s.d/mean value ~ 3-10 %) compared to fracture toughness, K_{1C} (s.d / mean~100 %), crack tip opening displacement, δ_c (s.d / mean ~ 100 %) or Charpy V-notch energy, CVN (varying between 20-160 J) for different steel compositions (base metal and weld metal of C-Mn, or C-Mn-Ti steels), test temperatures (-70 °C to –196 °C), sample geometry (specimen width and thickness~12.7 to 20 mm, crack length~4.25-6.93 mm) and loading type (3PB or 4PB). Therefore, σ_f is the most stable parameter to measure the

fracture behaviour of steel and suitable to study the effect of grain size variation on fracture.

Zhang and Knott [Zhang 2000] have studied the effect of mixed microstructures (bainite + martensite) and grain size on fracture by analysing the fracture results (K_{IC} or σ_f) using a Weibull probability distribution plot. Lower scatter in K_{IC} has been found (± 6 $MPam^{1/2}$) for fine-grained (packet size ~ 6 μm, formed by reheating at 950 °C) mixed (bainite + martensite) microstructure compared to coarse-grained mixed (packet size ~ 40 μm, formed by reheating at 1250 °C) microstructure (± 20 $MPam^{1/2}$). It has been concluded that the fine-grained mixed structure acts like a single-phase material (quasi-homogeneous) due to the finer scale of heterogeneity (individual effects of bainite or martensite average out) and that results in lower scatter. In the coarse-grained mixed structure individual effects of bainite and martensite are distinct (either bainite or martensite is responsible for fracture) due to the larger scale of heterogeneity and that leads to higher scatter. Wu and Knott [Wu 2004b] have identified the range of possible experimental errors, **Table 2.2.1**, for the bend testing with sub-sized Griffith-Owen specimen of 0.1 % C weld metal and calculated the total error (± 80 MPa) at around 5 % of mean σ_f (1500-1570 MPa). Therefore, any deviation higher than that range could be due to the variation in microstructural features (such as grain size variation or particle size variation) taking part in cleavage.

From the presence of un-propagated ferrite-grain-sized cracks on the broken 4PB blunt-notched specimens (tested at –130 °C) of C-Mn steels (0.04-0.18 C) Chen et al. [Chen 1992] have concluded that ferrite grain size (D) determines σ_f for blunt notched specimens, whilst carbide size determines σ_f for sharp-cracked (COD) specimens. Echeverria and Rodriguez-Ibabe [Echeverria 2003] and Sun and Boyd

[Sun 2000] have observed large sized cleavage facets (top 30 % facets by size) at the origin of cleavage fracture for microalloyed steels (0.06-0.21 C, 0.007-0.016 Ti, 0-0.067 Nb, 0.002-0.019 V, all wt %). Sun and Boyd [Sun 2000] and Shehata and Boyd [Shehata 1981] have also reported better correlation between 'σ_f' and largest ferrite grain size of the microstructure, rather than the average grain size for Nb-microalloyed steels (0.06 wt % C, 0.06 wt % Nb). The above findings suggest that larger grains in the microstructure initiate cleavage fracture.

Chen et al. [Chen 1990] have extended this idea to analyse the scatter in σ_f (varying between 1280-2200 MPa) for base and weld metals of C-Mn and Ti-B steels (0.06-0.18 C, 1.24-1.60 Mn, 0-0.03 Ti, all wt %) with maximum ferrite grain size varying from 45-55 μm. From the study of σ_f values and the spacing between coarse and fine grain size regions within the microstructure, it was concluded that the scatter in σ_f is caused by the grain size distribution, and in particular by the distribution of the grains within 'most coarse grained groups', which cover less than 5 % of all grains. Assuming that the fracture has initiated within the largest grain for the lowest σ_f value, Chen et al. [Chen 1990] have determined the possible γ_p values (between 100-200 J/m^2) from **eqn. 2.2.2**, which are then used to predict the range of coarse grain sizes (30-55 μm) that can be responsible for the scatter in σ_f (again using **eqn 2.2.2**).

In a recent paper Wu and Davis [Wu 2004a] have used a similar concept as Chen et al. [Chen 1990], i.e. to predict the experimentally observed scatter in σ_f (varying between 1400-2100 MPa, **Fig. 2.2.7**) using **eqn 2.2.2** (for, γ_p = 52 J/m^2) from the distribution of ferrite grain sizes within the coarse grain size regions, for a duplex ferrite grain structure (maximum ferrite grain size ~ 30-40 μm) in two different TMCR-Nb-microalloyed steel plates (~ 0.11 C, 0.024 and 0.04 Nb steels, all wt %). σ_f

values were found to be independent of test temperature within the tested range (–160 °C to – 196 °C). Ferrite grain size distributions within the coarse grain regions were measured by setting a lower grain size threshold of 6 μm. Wu and Davis [Wu 2004a] have found good agreement between the predicted and the experimentally obtained distribution of σ_f values, **Fig. 2.2.8**. The lack of data towards the lower value side (from 1400 to 1100 MPa) in **Fig. 2.2.8** can be attributed to the low probability of sampling very large grains due to their rarity in the microstructure and the number of tests conducted may be insufficient to pick up their effect.

2.2.6 Effect of duplex grain structure and mesotexture on ITT

Impact transition temperature (ITT) is known to be proportional to the inverse square root of grain size ($D^{-1/2}$) following the Cottrell-Petch relation [Cottrell 1958]:

$$ITT = A - B.D^{-\frac{1}{2}} \qquad \text{……..……..eqn. 2.2.3}$$

where, ITT can be 27J-ITT, FATT or DBTT and A and B are constants.

Various researchers have developed quantitative relationships by linear (or other) regression analysis to predict different Charpy impact transition temperatures (ITT), such as 50%-ITT (FATT) and 27J-ITT for steels, **Table 2.2.2**.

The interest of the present investigation lies in the use of ferrite grain size (D). For a duplex grain structure comprising of coarse polygonal ferrite grains (~ 17-30 μm) and fine acicular ferrite grains (~ 0-16 μm) in TMCR-line pipe steel (0.5 C, 0.06 Nb, 0.011 S, all wt %) Shehata and Boyd [Shehata 1982] have reported that 27J-ITT correlates with a measure of the largest polygonal ferrite grain size, and not with the mean grain size. Average metallographic grain size also failed to predict the ITT for

steels with duplex ferrite grain structure and mesotexture, studied by Bhattacharjee et al. [Bhattacharjee 2003, 2004]. Bhattacharjee at el. [Bhattacharjee 2003] and Maehara et al. [Maehara 1984] have shown that the mean size of the cleavage facets on the impact fracture surface could be almost 2-3 times larger than the mean ferrite grain size for TMCR Nb-microalloyed steels (0.08-0.12 C, 0.026-0.04 Nb, all wt %). The optical measurement of grain size is a two-dimensional (2-D) section whereas the fracture surface is three-dimensional (3-D) and a crack will tend to sample the true 3-D grain diameter rather than the sectioned version. This would account for the facet size being larger by a factor of 1.61 (as suggested by Gladman and Underwood [Gladman 1997]). Therefore, the facet size being 2-3 times larger than the average 2-D grain size indicates that a single facet may sample more than one grain.

It has been shown by Bouyne et al. [Bouyne 1998] that the unit of fracture in a bainite microstructure is a packet, which has high angle boundaries, and not a lath with low-angle boundaries (<10°). Kim et al. [Kim 2003] have shown in a bainitic microstructure in Mn-Mo-Ni low alloy steels (~ 0.2 wt % C) that the grain size matches the facet size when groups of grains with low angle boundaries are considered to be a single grain, the effective grain, ignoring boundaries with angles less than a threshold value of 15-18°. Such groups of grains (with low-angle boundaries) can develop during TMCR by a local texture effect, known as ‘mesotexture’, and that can affect the fracture properties by influencing the effective unit of fracture.

Bhattacharjee et al. [Bhattacharjee 2003] selected a 12° misorientation angle as the threshold to calculate the ‘effective grain size’ in a TMCR microalloyed steel (0.1wt% C, 0.045wt% Nb), with bimodal ferrite grain structure **(Fig. 2.2.9)**, based on their observation (using OIM on the cleavage facet, **Fig. 2.2.10**), that a single

cleavage facet can comprise more than one grain with up to 12° misorientation (due to mesotexture). Consideration of the effective grain size and the grain boundary carbide thickness provided much better prediction of ITT (using Mintz's equations listed in **Table 2.2.2**) compared to average grain size, **Fig. 2.2.11** [Bhattacharjee 2003]. The presence of mesotexture results in an increase in the average 'effective' grain size as clusters of small grains can behave, with respect to crack initiation and propagation, as one large grain.

2.2.6.1 Measurement of mesotexture by EBSD

The fine ferrite grains that form within one large austenite grain (after $\gamma \rightarrow \alpha$ transformation) have low angle boundaries (less than approximately 15 degrees misorientation) between them and that constitutes a 'mesotexture'. A preliminary measure of mesotexture is the distribution of grain boundary misorientation angles (**Fig, 2.2.12**) by orientation imaging microscopy (OIM) using electron-backscattered diffraction (EBSD) in a scanning electron microscope (SEM) [Bouyne 1998, Wu 2004c, Bhattacharjee 2003]. Mesotexture levels in commercially produced TMCR plates are not widely reported, however, Wu et al. [Wu 2004 c] showed that the surface layer, up to 2mm depth, in a commercially TMCR produced 0.024 wt% Nb steel, had about 55% of grain boundaries with a misorientation angle below 12 degrees, much higher than in the central area (~30% of grain boundaries with a misorientation angle below 12 degrees). It was also found that the fine ferrite grains and not the coarse grains in a duplex ferrite grain structure are generally mesotextured. It was shown for a laboratory rolled steel of a single composition that

the extent of mesotexture might be dependent upon the processing schedule, particularly on the number of rolling passes and the reduction ratio [Wu 2004 c].

2.2.7 Summary on the effect of bimodality on fracture

The above discussion indicates that the large grains present in the microstructure influence cleavage fracture and the larger the grain size the lower will be the cleavage fracture stress. Therefore, in a duplex or bimodal grain structure the large grains or large grain regions present in the matrix of small grains can initiate cleavage fracture and therefore, the material may need to be downgraded. The presence of 'mesotexture' in rolled structure can further downgrade the steel by allowing the cleavage crack to propagate easily.

Based on the experimental observation that coarse grains usually nucleate cleavage, Chen et al. [Chen 1990] and Wu and Davis [Wu 2004 a] have basically assumed that the distribution of coarse grains decides the scatter in fracture stress. Shehata and Boyd [Shehata 1982], Bhattachejee et al. [Bhattacharjee 2003, 2004] and Wu and Davis [Wu 2004 a] have studied the effect of bimodal grain structures on fracture in TMCR steel, where mesotexture can also influence the fracture apart from bimodality (due to mesotexture number of small grains behave as a large grain and thereby, narrow the overall grain size variation). Even in the absence of mesotexture the grain size distribution in rolled steel is quite narrow (largest grain size, ECD ~ 30-40 μm, [Wu 2004a, 2004b, Shehata 1982]), and that can average out any effect of grain size variation on properties.

The above discussion inspired the present study to carry out notch-bend fracture tests on simulated microstructures with wider grain-size distributions of 'unimodal' or

‘bimodal’ nature and with random texture. The comparison of scatter in cleavage fracture stress between unimodal and bimodal microstructures along with the measurement of cleavage initiating facet size is expected to provide better understanding on the effect of bimodality on fracture. There could also be a possibility that bimodality, if not severe, may not be harmful for the toughness of steel and up to a certain (low) level of bimodality can be allowed in steel without downgrading it. That highlights the need for quantifying the level of bimodality as a quality control measure in steel.

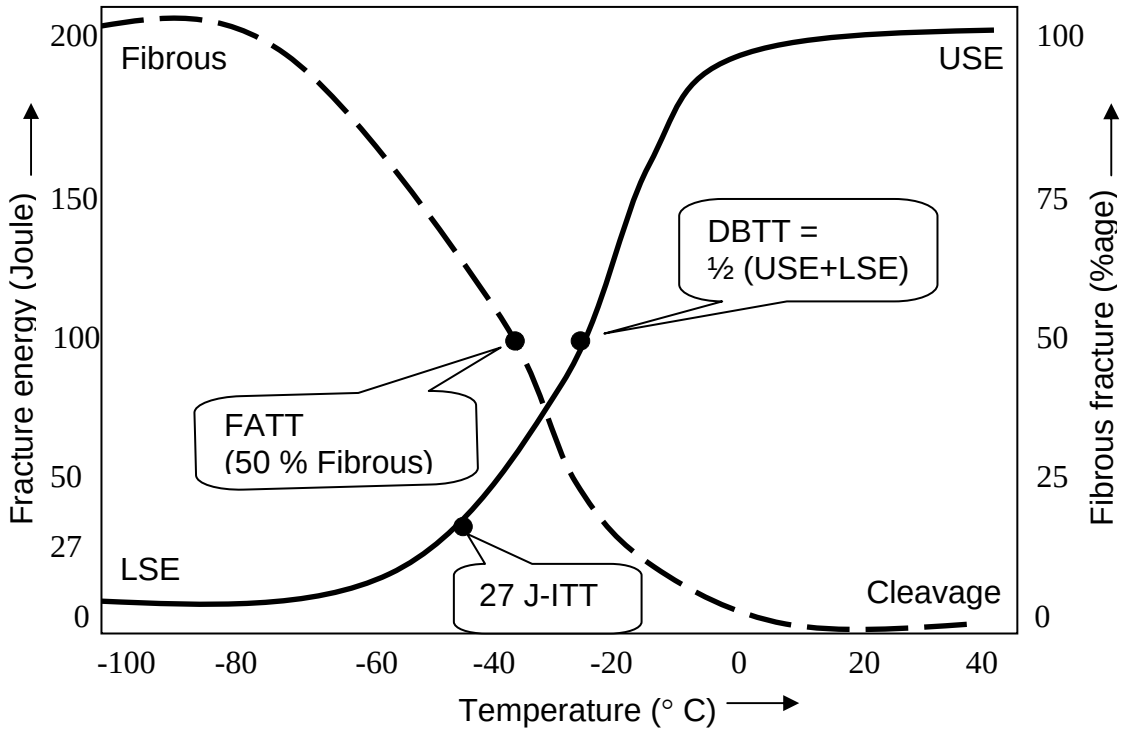

Fig. 2.2.1: Typical impact energy transition curve (solid line) and fracture appearance (fibrous-cleavage) transition curve (dashed line) for HSLA steel. USE represents ‘upper shelf energy’ and LSE represents ‘lower shelf energy’ for impact fracture. Various ductile brittle transition temperatures like 27 J-ITT, FATT and DBTT are indicated on the figure.

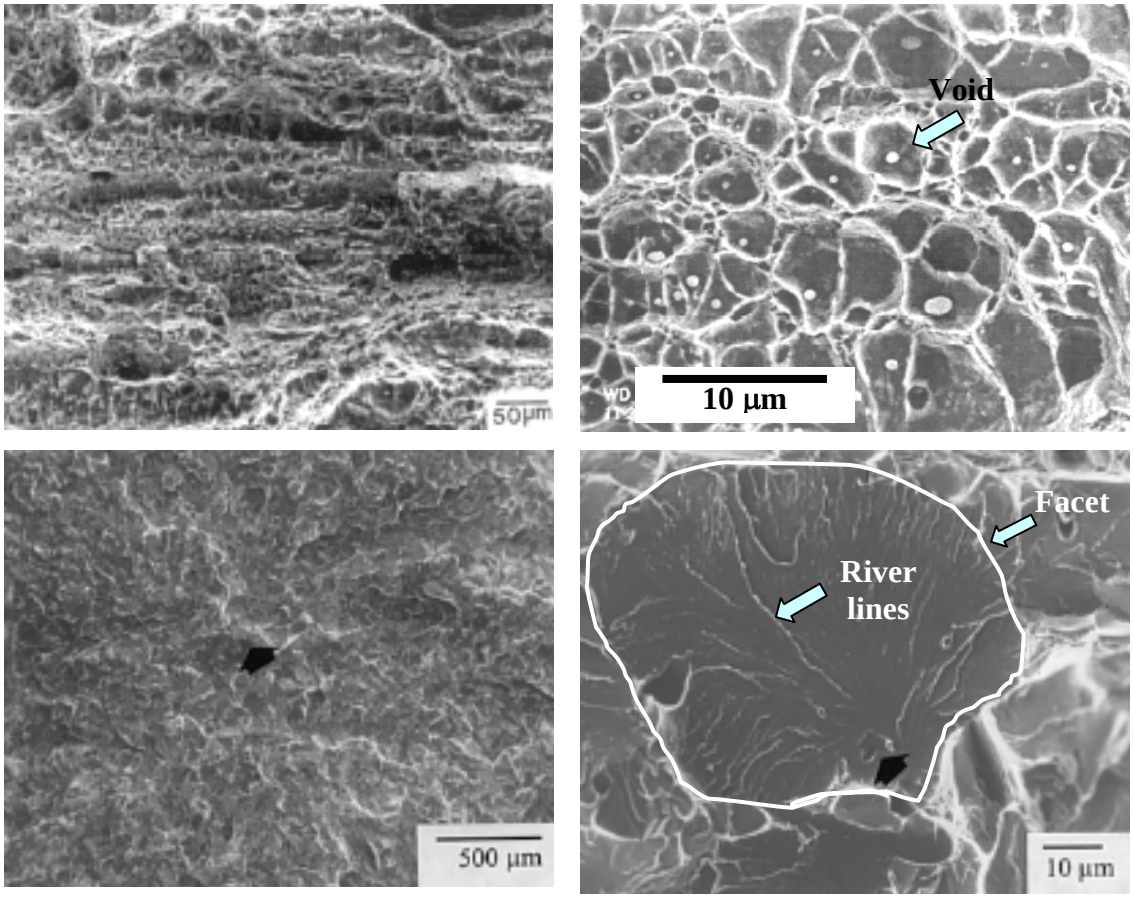

Fig. 2.2.2: Ductile fracture surface at (a) lower magnification and (b) higher magnification, showing micro-voids (arrowed) nucleated from spheroidal carbide particles. Brittle fracture surface at (c) lower magnification and (d) higher magnification, showing a cleavage facet (nucleated from TiN particle) and river lines (both arrowed).

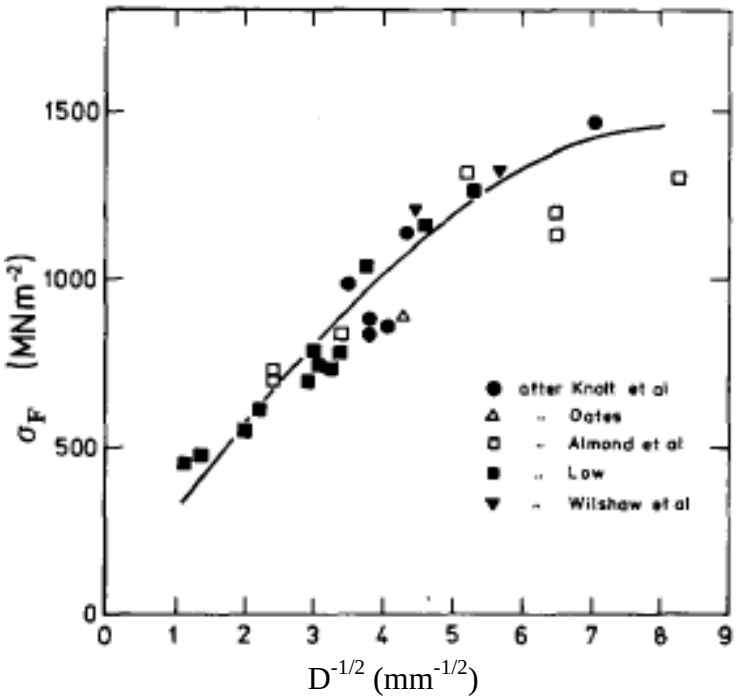

Fig. 2.2.3: Variation in cleavage fracture stress (σ_F, MPa) with $D^{-1/2}$ showing the increase in σ_F with the decrease in grain size (D, mm) [Ritchie 1974].

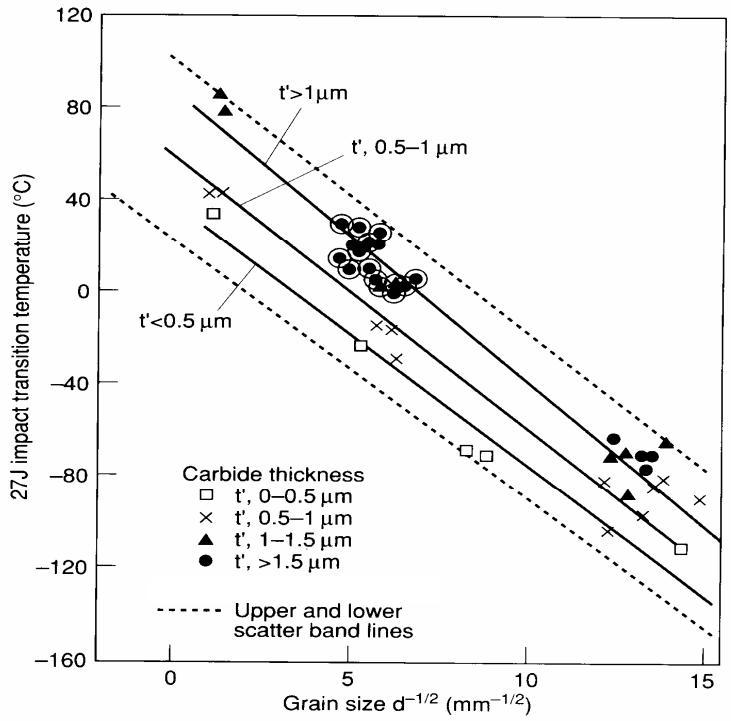

Fig. 2.2.4: Influence of grain size (mm) and carbide thickness (μm) on 27 J-ITT [Mintz 1982].

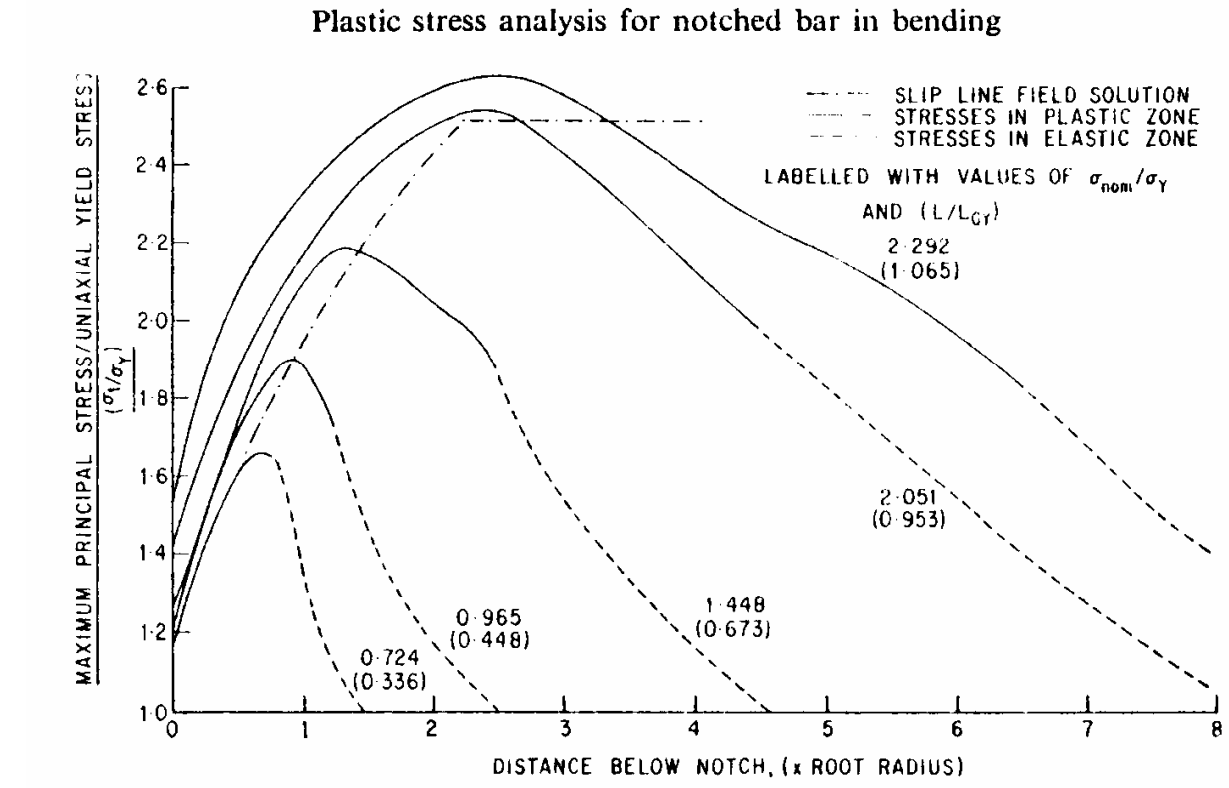

Fig. 2.2.5: The variation of maximum principal stress (σ_1) ahead of the notch root at various applied nominal stress (σ_{nom}) or applied loads (L), as determined by Griffiths and Owen. σ_Y and L_{GY} represents yield stress and general yield load, respectively [Griffiths 1971].

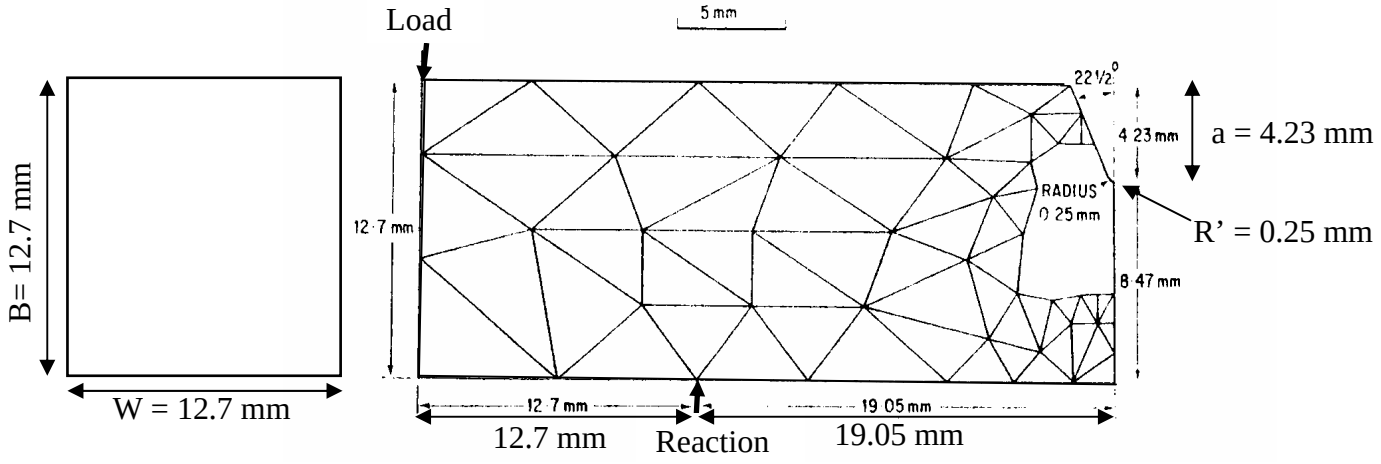

Fig. 2.2.6: Design of the specimen used by Griffiths and Owen [Griffiths 1971] for notch-bend test along with the triangular mesh used by them for FEM analysis. Specimen breathe, (B), and specimen width (W) are 12.7 mm; Notch length, (a) = 4.23 mm; Notch root radius, (R') = 0.25 mm; Total specimen length, (L) = 77 mm. Such specimen was first used by Knott and Cottrell [Knott 1963] and later on used in several investigations.

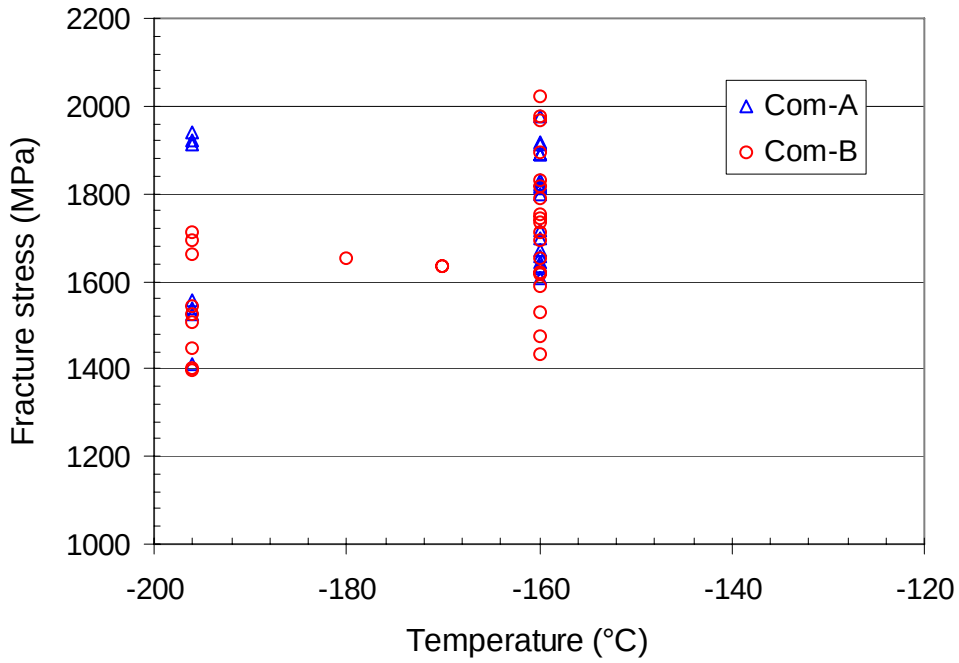

Fig. 2.2.7: Variation in local fracture stress (MPa) with test temperature for 0.011C - 0.024 Nb (Com A) and 0.011 C - 0.040 Nb (Com B) microalloyed TMCR steels [Wu 2004a].

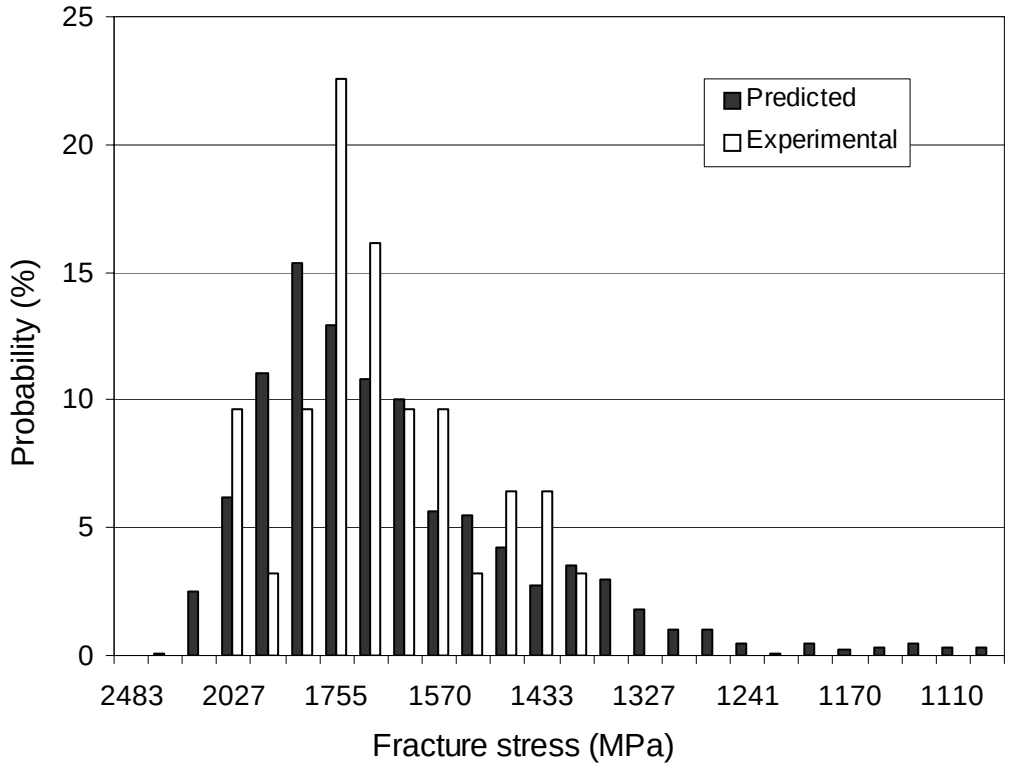

Fig. 2.2.8: Comparison of the local fracture stress (σ_f) distribution predicted from the grain size distribution (using eqn. 2.2.5) with the experimentally obtained σ_f distribution [Wu 2004 a].

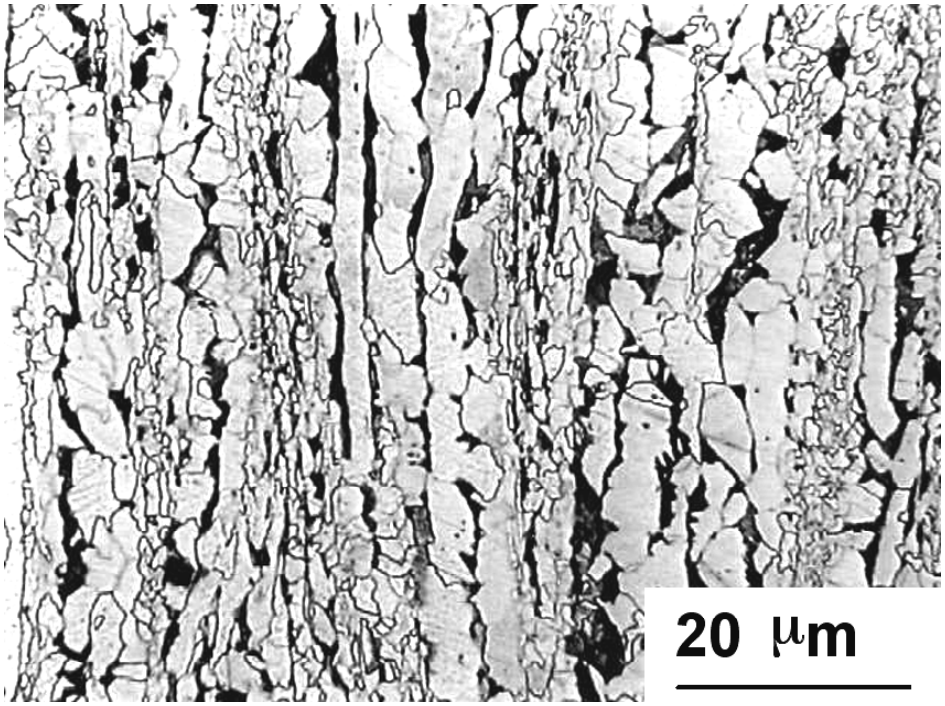

Fig. 2.2.9: Bimodal ferrite grain size distribution in 0.1 C-0.045 Nb thermomechanical rolled steel [Bhattacharjee 2003].

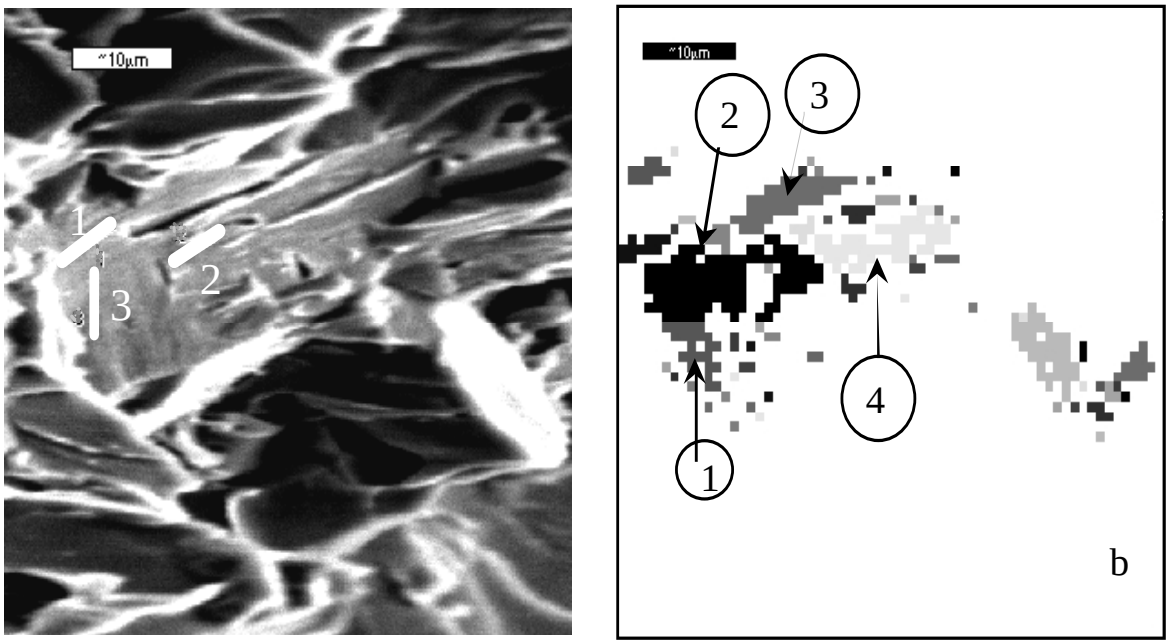

Fig. 2.2.10: Secondary electron image and corresponding OIM image of one cleavage facet from a 0.045wt % Nb steel processed by TMCR and containing significant mesotexture. Misorientation angles of 5.9°, 6.3°, and 11.8° were measured across lines 1, 2 and 3 respectively. Four different grains (determined from misorientation values) are marked on the OIM image [Bhattachajee 2004].

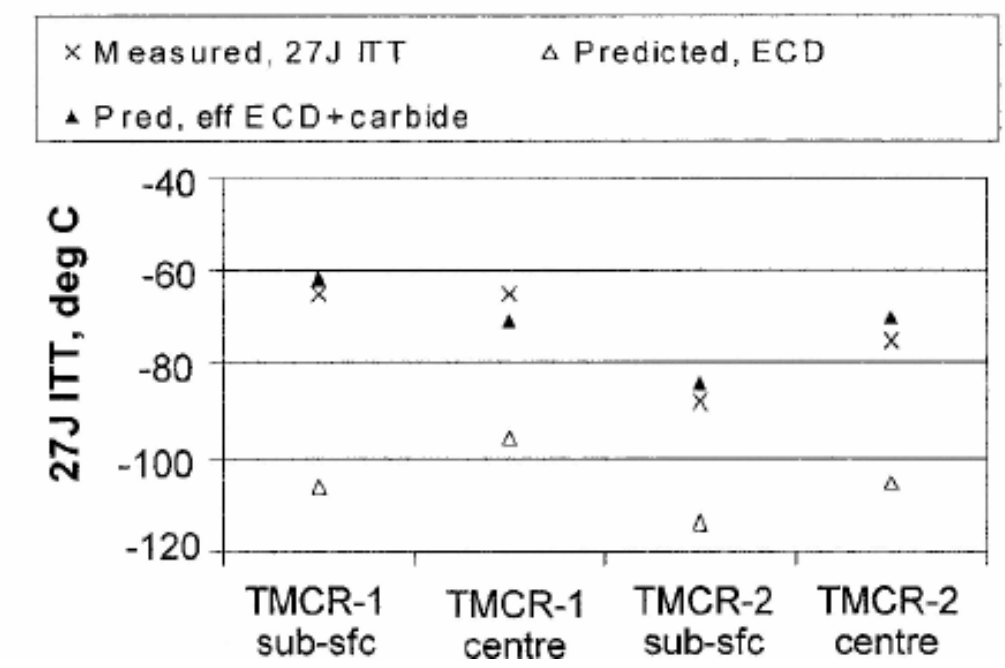

Fig. 2.2.11: Prediction of 27 J-ITT for the sub-surface and centre location of two TMCR steel plates (TMCR-1 and TMCR-2) with same steel composition (0.01 C-0.045 Nb) but different rolling schedule. Better prediction is achieved when effective grain size (equivalent circle diameter, ECD) is considered (taking mesotexture into account) along with the size of fine carbides (~ 0.085 μm) present in the microstructure [Bhattachajee 2003].

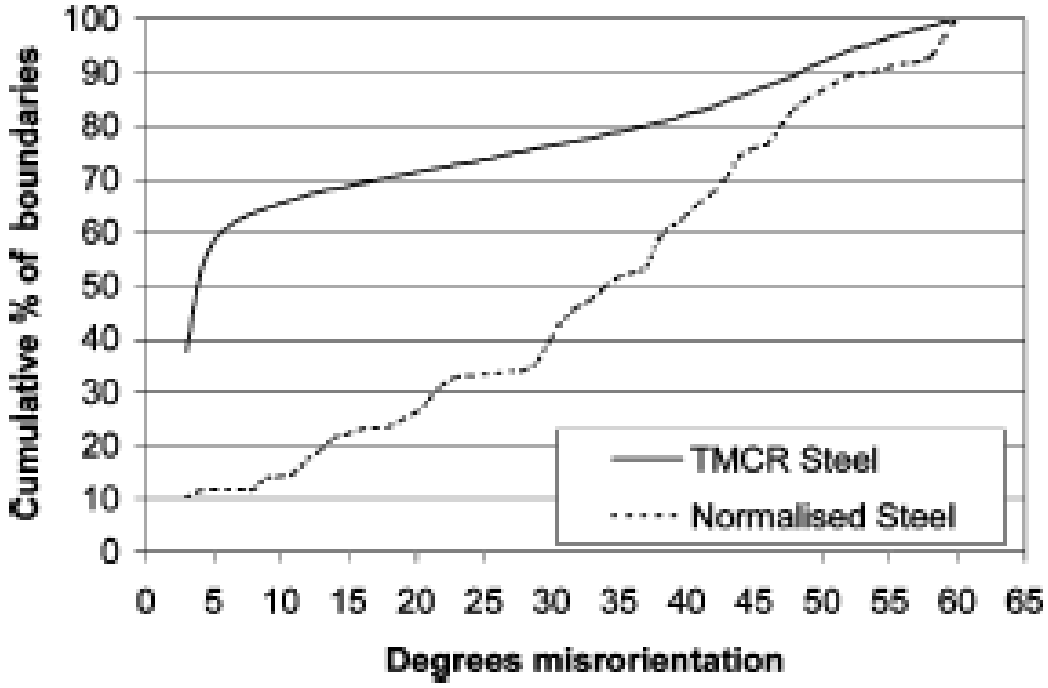

Fig. 2.2.12: Difference in the distribution of grain boundary misorientation angle between TMCR (0.01 C-0.045 Nb) steel and normalised steel (0.13 C-0.79 Mn). TMCR steel shows more number of grains at low misorientation angle (~ 65 % grains with misorientation angle < 10°), i.e. higher mesotexture compared to normalised steel (~ 15 % grains with misorientation angle < 10°) [Bhattachajee 2003].

Table 2.2.1: List of the ranges of error in basic measurements of σ_f [Wu 2004 b].

Error Source	Error range
Specimen breadth, B	± 0.01 mm
Depth below notch, W-a	± 0.02 mm
Moment arm, S	± 0.5 mm
Machine load cell calibration	± 0.02 kN
Chart recorder calibration	± 0.02 kN
Load reading from recorder	± 0.05 kN
Test temperature control	± 3 °C

Table 2.2.2: Equations to predict ITT (50 %-ITT or FATT and 27 J-ITT)

Reference	Equations	Symbol of parameters
Pickering 1963	$50\% - ITT = -19 + 44(wt\%Si) + 700(wt\%N_f)^{\frac{1}{2}} + 2.2(\%pearlite) - 11.5(D)^{-\frac{1}{2}}$	grain size (D), carbide thickness (t'), pearlite content (%-pearlite), free nitrogen level, wt % (N_f), carbide thickness t', Mn level in steel (%Mn), Si level in steel (%Si), precipitation hardening effects of alloying elements (ΔY),
Mintz 1979, 1982	$27J - ITT(^0C) = 173(t')^{\frac{1}{2}} - 8.3(D)^{\frac{1}{2}} + 0.37(\Delta Y) - 42$	
	$50\% - ITT(^0C) = 112(t')^{\frac{1}{2}} - 13.7(D)^{\frac{1}{2}} + 15(\%pearlite)^{0.33} + 0.43(\Delta Y) + 20$ Where, $\Delta Y = \sigma_{ys} - \sigma_{np\_ys}$; and $\sigma_{np\_ys} = 43.1(wt\%Mn) + 83(wt\%Si) + 15.4(D)^{-\frac{1}{2}} + 1540(wt\%N_f) + 105$	

3. Measurement of Bimodality

Grain size is a major factor influencing the mechanical, electrical and magnetic properties of materials. Measurement is required to allow manufacturers to meet customers' specifications and to monitor and control grain size during the material's processing. Grain size is typically measured on sections through the grains on a polished plane (i.e. planar grain size) cut from the material at appropriate locations and orientations. To understand the grain size variation the measured grain size values can be represented as either number frequency or area frequency histograms. 'Mode' is the most frequent value (or range of values) in the histogram. For most materials the grain size distributions conform to a single log-normal (Gaussian) distribution or similar unimodal (e.g. skewed Gaussian) distribution, **Fig. 3.1 (a)**. Grain structures with such unimodal distributions are commonly measured using the methods described in ASTM E112 [E 112], i.e. the chart comparison method, the Jeffries planimetric method and the Heyn-Hilliard-Abrams linear intercept method. These methods do not describe the distribution of grain sizes as observed on the plane of polish. Rather, they produce an arithmetic numerical average value, in terms of ASTM grain size number, G; the number of grains per unit area, N_A; or the mean lineal intercept, $\overline{L_3}$.

There are situations where grain structures do not exhibit a unimodal grain size distribution. Rather, deviations from unimodal distributions (e.g. duplex condition) have been observed. The standard test method, ASTM E 1181 [E 1181] defines various types of duplex grain sizes within two broad categories: randomly varying (includes, I. isolated coarse grains in a fine grain matrix; II. extremely wide distributions of grain sizes; and

III. bimodal distribution) and topologically varying (includes, I. variation in grain size across the product; II. necklace structures; and III. banded structures of alternate sizes). Within this classification, a 'bimodal distribution' is a type of duplex condition (randomly varying) with two distinctly separate distributions with two different 'mode' values, **Fig. 3.2 (b)**.

Within steels, the presence of large grains in the microstructure has been correlated with anomalous mechanical behaviour, for example low toughness [Chen 1992, Shehata 1982, Echeverria 2003]. ASTM E 930 [E 930] provides a method of measuring largest grain size (ALA grain) in a microstructure comprising of isolated coarse grains (covering 5 % or less of the specimen area) in a matrix of much finer grains (type-I in randomly varying duplex condition). According to ASTM E1181 [E 1181] a duplex grain structure can be characterised and represented by the nature of duplexity (a qualitative description), percentage of area occupied by 'coarse' and 'fine' grain populations in the microstructure and the corresponding average (or ALA) grain sizes of those populations measured according to ASTM E 112 [E 112] or ASTM E 930 [E 930]. For the statistical determination of the grain size distributions mentioned in ASTM E 1181 [E 1181], average grain intercept lengths are plotted against intercept length, either on linear or on logarithmic scales. To measure the standard parameters (area percent and average grain sizes corresponding to coarse and fine grain populations) from the bimodal grain size distribution, the distribution needs to be separated into coarse and fine grain populations, **Fig. 3.2 (b)**. In ASTM E 1181 [E 1181] an arbitrary division, based on a visual inspection of the distribution graphs is made to separate the populations. This measurement method works well for microstructures with reasonably distinct fine and coarse grain distributions; however for materials with small differences in bimodality

(that may still have a large effect on properties) the arbitrary division of graph populations may lead to inaccuracies.

As the grain structure may not be perfectly equiaxed, grain intercept lengths for each grain need to be measured at several orientations (at least three). Therefore, when intercept lengths are measured for a large number of grains, an enormous amount of data is generated. Also, the intercept length measurements are not as simple to perform with modern software-based image analysers, as was the case with older hardware-based systems. Image analysis software has developed more in measuring individual grain area, which requires fewer data to construct grain size distributions compared to grain intercept length. Peyroutou and Honnoral [Peyroutou 1991] and Van der Voort and Friel [Voort 1992] have used individual grain areas (A) instead of grain intercept lengths as the measure of grain size to calculate ASTM grain size numbers (G) using the following equation:

$$G = [-3.3223 \times LogA] - 2.955 \qquad \text{eqn. 3.1}$$

These studies selected various microstructures (from different materials) with severe duplexity and used number percent and area percent grain size distributions to represent and to measure the duplexity, **Fig. 3.2**. It was found that an area-weighted histogram gave a better representation of a duplex condition than a numerical frequency histogram (two modes are present in the area-percent distributions in **Fig. 3.2 (b) and (d),** whereas, number-percent distributions only show a single mode) [Voort 1992]. The uneven nature of the area-percent distribution in **Fig. 3.2 (f)** could be due to the low number of grain size measurements (only 291 grains measured) and it was concluded that more than 1000 grain measurements are needed for a better representation of duplexity [Voort 1992].

Different approaches have been adopted to separate the 'fine' and 'coarse' populations in area-percent distributions based on ASTM grain size numbers. Using the intersection point between the number-percent and area-percent distributions as the separation point (or 'breakpoint') was only suitable for a few microstructures (such as **Fig. 3.2 (f)**). For other microstructures the distribution data have to be inspected visually and the breakpoint decided from a 'gap' in the grain-area data, lying in between the two modes of the distribution (**Fig. 3.2 (b) and (d)**) [Voort 1992]. The 'gap' is not well defined and therefore, a degree of subjectivity is again introduced into the measurement. To quantify the grain size variations in the microstructures the area-percent and average grain sizes (in ASTM G) of 'fine' and 'coarse' populations were measured, based on the selected 'breakpoints'. As an example Van der Voort and Friel [Voort 1992] showed that, by changing the approach used to separate both populations in **Fig. 3.2 (d)** (i.e. intersection point or visual inspection of data set), the 'breakpoint' could change (ASTM 10 for the intersection point and ASTM 8 for the 'gap' in data). As the measurements of area-percent and average grain size values, for the 'coarse' and 'fine' grains, are dependent on the 'breakpoint' selected, any change in 'breakpoint' will result in differences in measured bimodality and hence inaccuracies in describing the microstructures.

Peyroutou suggested an alternate approach of using an arithmetic grain size scale, dividing the grain area range into 25 classes (equal weighting) to plot number-percent and area-percent distributions (personal communication referred to in Van der Voort and Friel [Voort 1992]), **Fig. 3.3**. The distributions in Fig. 2.3.3 show an uneven nature that make it difficult to separate a unimodal distribution from a bimodal one. The intersection of number-percent and area-percent distributions was used as the 'breakpoint' separating the populations. The arithmetic approach was found to be suitable only for distributions with

well-separated, non-overlapping populations [Voort 1992]. For the arithmetic method the number of classes chosen could influence the breakpoint and hence the results for bimodality (area-percent and average size of the populations as per the ASTM standard).

Apart from the ASTM standard measures other parameters have also been used to describe bimodal structures. For example 'average size ratio' (ratio of average-'coarse'-size to average-'fine'-size) has been used to represent a mixture of powders of two different sizes, where each size lies within a narrow range [Molina 2002, Petersson 2005]. This parameter looks to be useful only for the case of distinctly separate 'coarse' and 'fine' populations of grains, where both populations lie within a narrow size range and a clear 'gap' lies between them. In the case of overlapping-populations the 'average size ratio' is dependent on the measurement of average grain-size for each population and that again depends on the selection of 'breakpoints'. Therefore, 'average size ratio' is also a subjective parameter. Another parameter, 'ratio of largest to average grain size' was used to quantify duplexity in commercial microalloyed steels [Couch 2001]. This parameter represents the skew of the grain size distribution rather than bimodality and so does not uniquely identify bimodality, for example a unimodal distribution with a 'tail' toward coarse grain sizes without a second mode can also give a high value of the ratio.

3.1 Summary on the measurement of bimodality

The bimodal ferrite grain size distribution is reported to cause a variation in mechanical properties, and is particularly detrimental for impact fracture toughness (causing significant scatter), of TMCR microalloyed steel plates [Wu 2004 a, Chen 1990]. Hence this microstructure is undesirable. Bimodality has also been observed in austenite grain structures in these steels in their as-cast and reheated condition [Couch 2001, Palmiere 1997]. Such bimodality can develop during the various stages of processing

(cast slab, reheat, rolling), therefore, any measure of bimodality must be able to distinguish its extent in all three microstructure types.

To construct grain size distributions previous studies have been conducted on various microstructures but with extreme bimodality. In practice, varying extents of bimodality can be seen and a less severe bimodality may still be important as it may affect the material properties, and therefore, needs to be measured. The present study aims to represent and measure different extents of bimodality in microalloyed steels. Representation of bimodality based on the selection of 'breakpoint' (which is subjective) can lead to inaccuracies and therefore, the present study also aims at measuring bimodality by a less subjective method.

3.2 Objective of the present investigation

TMCR microalloyed steels with ferrite + pearlite structures are sold to customers based on their superior combination of strength and toughness that comes from the fine, uniform ferrite grain size. Previous studies indicate that bimodality in the ferrite grain size distribution can be detrimental to the fracture toughness of steels as coarse grains can cause premature cleavage failure [Shehata 1982, Bhattacharjee 2004, Wu 2004 a]. However, all those studies were carried out on rolled steels, where a narrow grain size distribution can average out any effect of grain size variation on properties. Moreover, mesotexture in rolled steel can influence fracture apart from the grain size distribution. Therefore, the present investigation aims to relate unimodal and bimodal ferrite grain size distributions with fracture stress (which is reported as the most stable fracture parameter [Bowen 1986, Chen 1998]) for ferrite + pearlite microstructures, with similar inclusion and pearlite contents, but with random texture and varying grain size range. Such experimental design is expected to distinguish clearly the fracture response of a bimodal

grain structure from a unimodal structure particularly in terms of variation in fracture stress.

To relate bimodality with steel properties and to control the bimodality in commercial steels there is a need to measure bimodality. Established methods of representation of bimodality from grain size distributions have only been checked on extremely bimodal microstructures. The present investigation aims to check those methods on reheated or TMCR HSLA steel microstructures with varying levels of bimodality. That makes an objective for the present study to identify the most suitable method for the representation of bimodality, particularly suitable for less sever bimodality conditions. Measurement of standard parameters for bimodality is currently based on the selection of a 'breakpoint' within the grain size distribution and that is subjective. The present study also aims to develop a less subjective, simple and easy to measure set of parameters that are useful from the fracture toughness point of view and can be a quality control measure.

Bimodality may downgrade the steel and therefore, there is a need to avoid it. That makes the main objective for the present investigation to identify the source and cause of bimodality during commercial processing, so that necessary measures can be taken to prevent it. To achieve this objective, the present study aims to carry out quantification of precipitate distribution and grain structure in continuously cast steel and to follow those features to reheat and to rolled steels. That can identify the role of precipitate stability and precipitate pinning on the formation of bimodality. The majority of previous studies regarding abnormal grain growth in HSLA steel ignored any effect that can arise from the segregation of microalloying elements and the present study considers that effect for better understanding of the sequential microstructural changes (regarding banding and bimodality) during commercial processing.

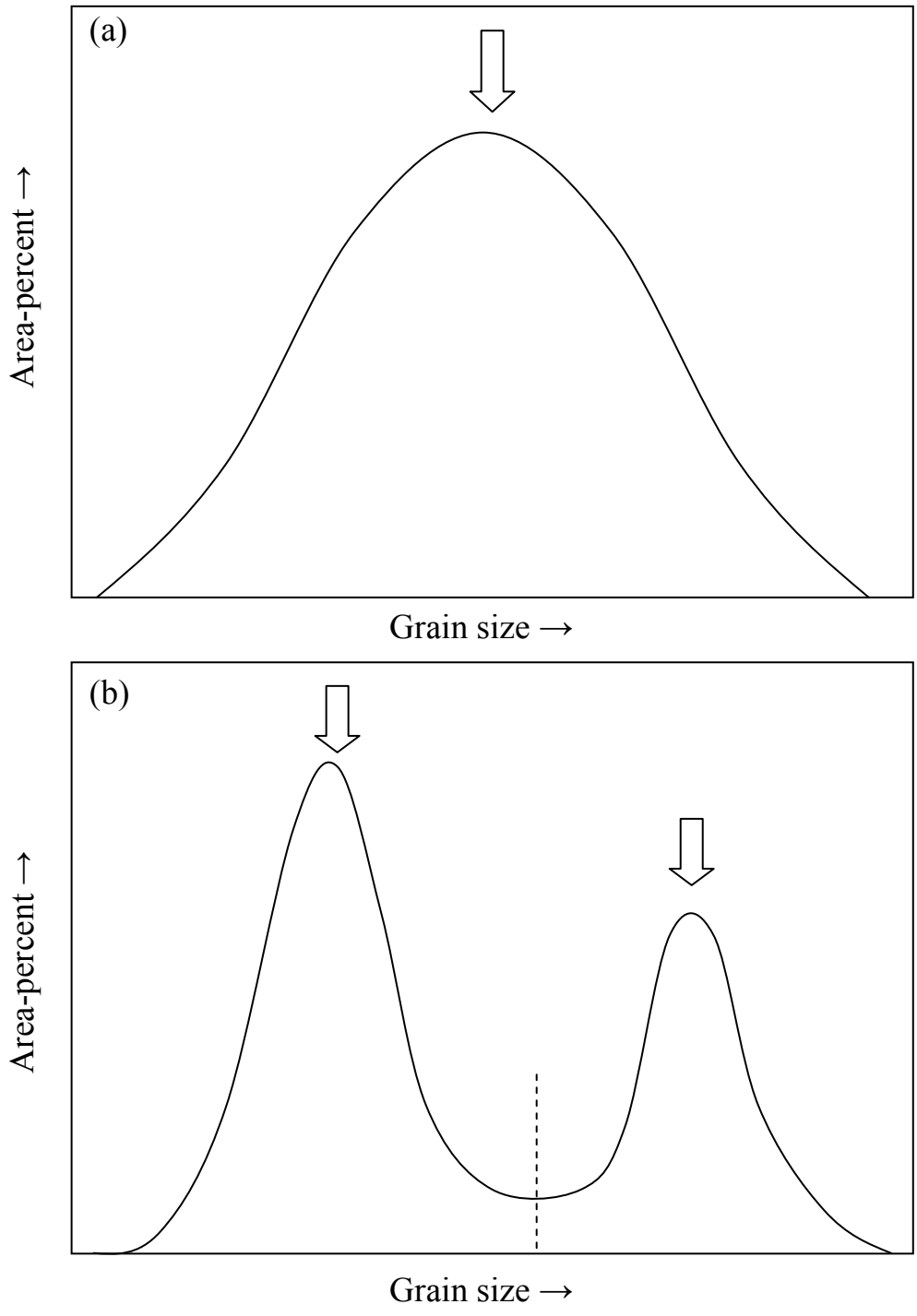

Fig. 3.1: Typical grain size distributions (frequency in area-percent-vs.-grain size either in linear or in log scale) showing, (a) unimodal and (b) bimodal nature with distribution modes indicated by arrows. To measure the standard parameters (area-percent and average size) the bimodal distribution need to be separated (dotted lines) into 'fine' and 'coarse' populations.

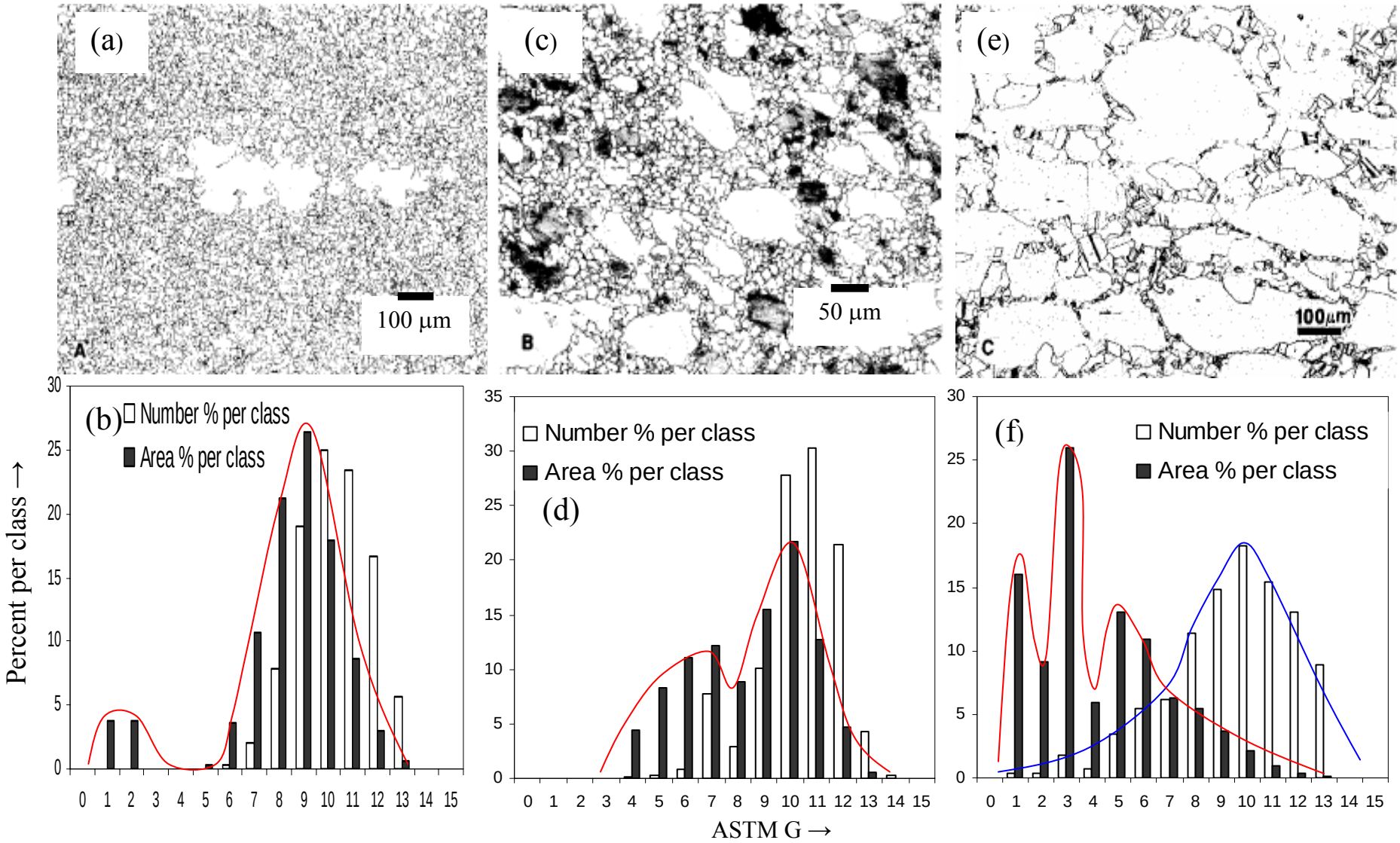
(a)
100 µm
A
(c)
50 µm
B
(e)
100µm
C
(b)
Number % per class
Area % per class
(d)
Number % per class
Area % per class
(f)
Number % per class
Area % per class
Percent per class →
ASTM G →

Fig. 3.2: Severe duplex microstructures for (a) C-steel (c) Inconel 718 alloy and (e) 625 alloy. Grain size distributions are plotted in number-percent and area-percent histograms based on ASTM G scale (ASTM number 0 to 15) in (b), (d) and (f) for the microstructures shown in (a), (c) and (e), respectively. To construct the distributions number of grain sizes measured are as follows: (b) 7180, (d) 915 and (f) 291.

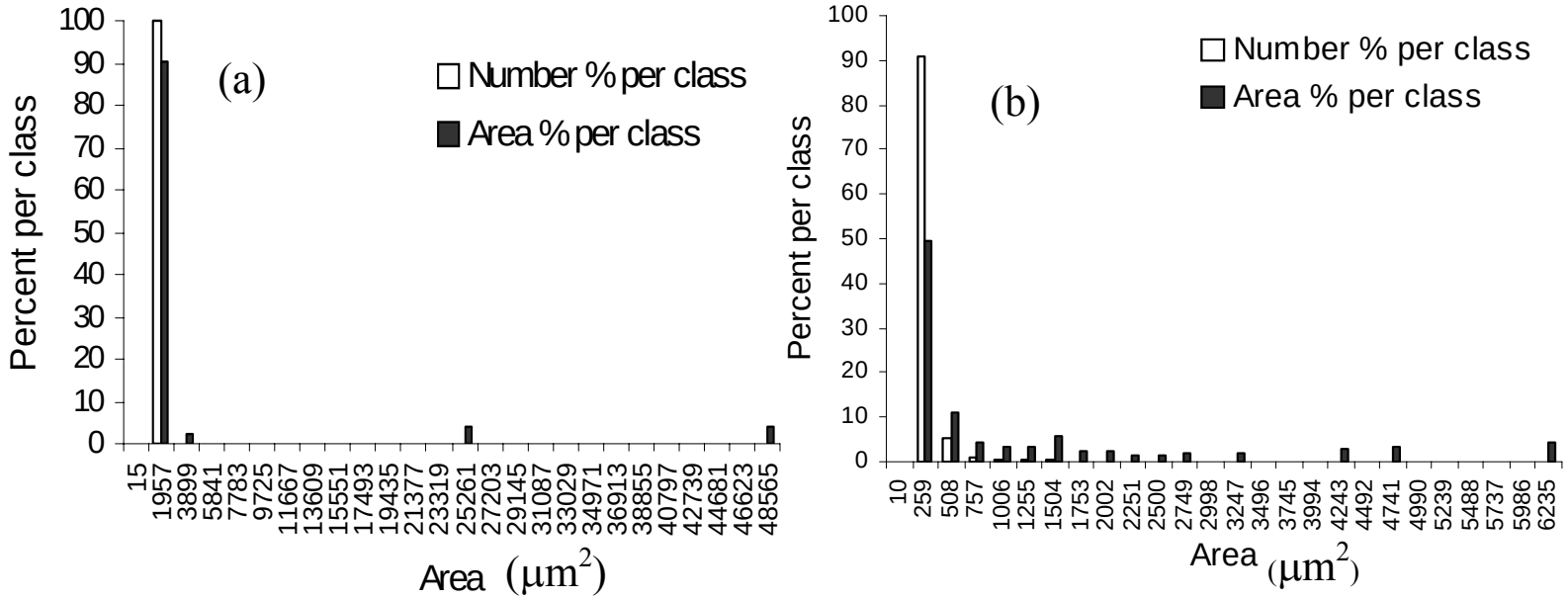

Fig. 3.3: Grain size distributions are plotted in number-percent and area-percent histograms based on 25-area class scale for (a) C-steel microstructure (shown in Fig. 3.2 a) and for (b) Inconel 718 alloy (shown in Fig. 3.2 c).

4 Experimental details

To achieve the objectives of the present investigation commercial continuous-cast slabs and thermomechanical controlled rolled (TMCR) HSLA steel plate were studied in terms of microstructure (especially grain size and precipitate distribution) and mechanical properties. As-cast steels were also heat-treated to determine the effect of reheating on the grain structure and properties. This chapter describes the experimental methods used for heat-treatment, microstructural characterisation, precipitate study, mechanical testing and fractography, as well as thermodynamic prediction and deformation simulation.

4.1 Material

Three as-continuously cast (290 mm thick and 1800 mm wide) low-carbon (~ 0.1 wt % C) microalloyed steel slabs, **Table 4.1**, produced with similar continuous casting process parameters were investigated. Such steel grades are commercially used in the controlled-rolled condition for pipeline applications. Nominal chemical compositions of the as-cast slabs in **Table 4.1** show that slab 1 contains the highest Nb, Al and V levels, whilst, slab 3 is V-free but contains the highest amount of Ti. The Nb level of slab 2 is intermediate between that of slab 1 and slab 3.

A rolled plate sample, TMCR-1, (44 mm thickness) from the ¼ width position of a single steel cast of composition similar to as-cast slab 1 (although, containing higher Ti) was also studied. The plate-rolling schedule was based on reheating to 1150-1200 °C and rolling to a 3:1 < 810 °C double hold TMCR schedule, **Fig. 4.1**, with the aim finish rolling temperature (FRT) being 700-720 °C. The total rolling reduction was ~ 5:1.

4.2 Heat-treatment of as-cast slabs

Two different heat-treatments were carried out on as-cast samples: (a) reheating treatment to establish conditions for the formation of bimodality and (b) reheat + hold treatment to determine the effect of bimodality on fracture properties.

4.2.1 Reheating treatment

10×10×10-mm samples were cut from the quarter-thickness position of the as-cast slabs, sealed in evacuated 19 mm internal diameter silica tubes to prevent oxidation and subjected to various re-heating treatments **Fig. 4.2** and **Table 4.2**.

4.2.2 Reheating + holding treatment

Reheating and isothermal holding heat-treatments, **Fig. 4.3** and **Table 4.3**, were carried out on three-sets of 12×12×60-mm samples (12 samples in each set), which were taken from the quarter-thickness position of the as-cast slab 1. Each set of samples was reheated to different temperatures, 940 °C, 1140 °C and 1210 °C (at a rate of 3 °C / minute), soaked for 1 hr., followed by quenching to 700 °C (by rapidly transferring from the reheating furnace to a holding furnace at 700 °C) and isothermal holding for 1 hr. and finally slow furnace-cooling to room temperature. Calculated bainite start (Bs) and martensite start (Ms) temperatures for the slab 1 composition following different models fall within a range of 650-670 °C [Steven 1956, Bodner 1989] and 400-450 °C [Andrews, Steven 1956, Rowland, Nehrenberg, Payson], respectively. Holding at 700 °C and slow cooling was applied in order to transform the austenite, formed after reheating, into a mixture of ferrite + pearlite in each set of samples, avoiding the formation of any bainite or martensite.

4.3 Microstructural characterisation

4.3.1 Sample preparation

Heat-treated samples and longitudinal sections (generally taken from sub-surface, ¼-thickness and ½-thickness positions) of as-cast and rolled steels were prepared for optical examination and image analysis by mounting in bakelite, grinding and polishing to a 0.05 μm Al_2O_3 finish. To reveal the ferrite-pearlite microstructure the samples were etched in 2%-nital (2 ml HNO_3 in 100 ml ethanol). The prior-austenite grain structures of quenched and tempered samples were revealed by etching the polished surface in a saturated aqueous picric acid solution at 70 °C.

4.3.2 Microstructural study

The as-cast, heat-treated and TMCR specimens were examined on a Leica DMRX or a Zeiss Axioskop 2 microscope equipped with KS400 image analysis software to quantify the microstructures in terms of secondary dendrite arm spacing (SDAS), coarse (> 1 μm) inclusion distribution, ferrite and austenite grain size - equivalent circle diameter (ECD) – and grain aspect ratio distributions, and fraction of second phase (pearlite or bainite). SDAS was derived from the average of 500 measurements of the centre-to-centre distance between two consecutive secondary dendrite arms, in the direction perpendicular to the arms, within the field of view at 100×. Inclusions finer than 1 μm were observed using a Jeol 6300 scanning electron microscope (SEM) and, by combining optical microscope and SEM, a minimum of 1000 inclusions were measured in terms of equivalent circle diameter (ECD) for each

sample and used to plot the inclusion size distribution, in terms of number-frequency histograms. Coarse and fine grain regions within the microstructures were also identified and the centre-to-centre spacing between coarse-to-coarse and fine-to-fine grain regions (or bands) was also measured.

4.4 Grain size distribution and the measurement of bimodality

About 1000 grains were measured in terms of individual grain area and equivalent circle diameter (ECD) grain size (obtained directly from KS-software) on the as-cast and reheated samples and about 2000 grains were measured for the rolled structures to construct each grain size distribution. The average aspect ratio of the grains tended to fall in the range of 0.8 - 0.9 for the as-cast and reheated samples and 0.6-0.7 for the rolled samples, indicating that grains were predominantly equiaxed and therefore, ECD was an appropriate measure of grain size.

The microstructures were assigned a bimodality severity index (0 to 4) based on visual inspection and basic quantification (area percent of coarse grained regions determined by manually selecting areas for analysis, and equivalent circle diameter (ECD) values for the observed largest and smallest ferrite grains), **Table 4.4**. The most bimodal microstructure and a non-bimodal structure were used to define the extremes of the arbitrary scale (4 and 0 respectively). The rating was subjective in nature but used to distinguish different microstructures in terms of severity in bimodality, so that a non-subjective method could be developed to measure the range of bimodalities observed in the steels examined.

The grain size distributions (number-percent and area-percent) were plotted in terms of ASTM grain size number (following Peyroutou and Honnoral [Peyroutou 1986] and Van der Voort and Friel [Voort 1992]), individual grain area (following

Peyroutou's 25-area-class approach [Voort 1992]) and ECD-grain size. Both ASTM grain size number (ASTM G) and ECD-grain size can be related to the individual grain area by the following equations [Voort 1992]:

$$G = [-3.3223 \times Log\,\overline{A}] - 2.955 \qquad \text{.....eqn. 4.1}$$

$$ECD = \sqrt{\frac{4 \times \overline{A}}{\pi}} \qquad \text{..... eqn. 4.2}$$

Table 4.5 relates the range of grain areas (μm^2) and the range of ECD-grain sizes (μm) with the ASTM G grain size classification (commonly used for steels).

To construct distributions based on ASTM G, grain areas were grouped into a histogram fashion following the relationships in **Table 4.5**. For the area-percent histograms the actual areas of each grain in each class were summed and used to calculate the area-percent per class. The number-percent histograms were drawn based on the total number of grains within each ASTM G class. An arithmetic grain size scale dividing the overall grain area range into 25-classes (equal-weighting) was used to construct number-percent and area-percent distributions following Peyroutou's 25-area-class approach [Voort 1992]. A new method, using an arithmetic (linear) scale of ECD-grain size and dividing the entire ECD-grain size range into 15 classes (equal-weighting), was also applied to plot grain size distributions.

Both the 'modes' (peaks, G_1 and G_2 in **Fig. 4.4 (a)**) were identified from the bimodal area-percent distributions based on an ECD-scale and the grain size (ECD) class corresponding to the minimum area-percent in between the 'modes' was also chosen as the 'breakpoint'. Based on the 'breakpoints' selected (following the

different approaches discussed in **Chapter 3**), standard parameters (area-percent and average-size corresponding to 'coarse' and 'fine' populations) were determined.

Each peak (or mode) in a bimodal area-percent grain size distribution can be characterised by its peak height (area-percent) and the corresponding grain size (ECD) value. Based on an area-percent distribution with a linear-ECD-scale, to quantify the extent of bimodality two parameters, peak grain size range (PGSR) and the peak height ratio (PHR), **Fig. 4.4 (a)**, were determined. For a typical normal (i.e. unimodal) distribution both parameters, PGSR and PHR, are equal to zero, **Fig. 4.4 (b)**. For a bimodal situation a distinct 'coarse' distribution appears with a separate peak. As the size and the area-fraction of coarse grains increases further in the matrix of fine grains, both parameters increase and a severely bimodal structure can be identified by a 'high' value of PGSR and PHR approaching ~ 1 (i.e. the area fractions of coarse and fine grains are almost the same), **Fig. 4.4 (c)**. As the coarse grain fraction increases further PHR becomes greater than 1, and the structure becomes less bimodal (and coarser) once again.

The grain size distributions and the corresponding PHR and PGSR values for the present study were checked with the visual observation of bimodality and compared to the standard methods of representation of bimodality (area-percent and average size) to find the validity and usefulness of the suggested parameters.

4.5 SEM study of the microstructure and precipitates

High-resolution electron microscopy is essential in studying the microalloy precipitates, which are generally sub-micron size, in HSLA steel. Compared to optical and scanning electron microscopy (SEM), higher magnification and better resolution can be achieved in transmission electron microscopy (TEM), although, rigorous

specimen preparation is required for TEM. Moreover, TEM specimens are very small in size and, therefore, representative of a very small volume of the bulk material. Considering the location of micro-segregated and macro-segregated regions in steel casting a larger microstructural area may need to be studied to distinguish any changes in precipitate density or local composition. Therefore, the present investigation decided to use high-resolution SEM (equipped with energy dispersive X-ray spectroscopy, EDS, and wave-length dispersive X-ray spectroscopy, WDS, analysis), on the polished + lightly - etched specimen surface to identify any effect of segregation and inhomogeneous precipitate distribution on the microstructure during processing.

4.5.1 SEM

Inclusions finer than 1 μm and precipitates in the as-cast, reheated and TMCR-steels were characterised using a Jeol 6300 SEM, fitted with ThermoNoran Vantage EDS (energy dispersive X-ray spectroscopy) facility and by Jeol 6060, Jeol 7000 or by Philips XL-30 environmental SEM all equipped with Oxford Inca EDS systems. All the SEMs used in the present investigation, along with the facilities available in those SEMs are listed in **Table 4.6**. Jeol 7000 and Philips XL-30 are fitted with a field-emission gun (FEG) to achieve higher resolution than the Jeol 6300 and 6060, where a tungsten-filament is used. Secondary-electron (SE), and back-scattered electron (BSE) imaging specimens were mounted in conducting bakelite to observe under SEM. SE (for surface topography), and BSE (for compositional contrast), were used in all the SEMs to identify the elements present within precipitates / inclusions / segregated regions. Accelerating voltages from 5 to 20 kV were used in the present study. Larger kV values (15-20 kV) were used for microstructural observation, whilst,

lower kV values (5 – 10 kV) were used for EDS analysis of fine microalloy precipitates to maintain a small enough interaction volume (which is the region in the matrix beneath or around the particle excited by the incident electron beam) for the minimum response from the matrix and therefore, to achieve greater precision in analysis. Number and area-density of the precipitates at interdendritic (pearlite) or dendrite-centre (ferrite) regions was measured over 30-fields of view (each field of view covers ~ 16 μm^2 area with 1-12 particles per field) from each region.

Apart from EDS analysis, Oxford Inca WDS (wave-length dispersive X-ray spectroscopy) was also used in the Jeol 7000 SEM (at 15 kV voltage) to identify precipitates, segregated regions, or to study local compositions. A working distance of 10 mm was maintained constant for each analysis (EDS or WDS) based on the design of the SEM (considering distance of detector from specimen, take-off angle and detector area). Point-analysis was generally used to study the elements present in the precipitates / inclusions. A dead time of ~ 20 % at an acquisition rate > 2 kcps (over 100 s acquisition time) was aimed for in each EDS analysis. For elemental analysis of precipitates the EDS spectrum (or a number of spectra) collected from the precipitate was (were) compared against the EDS spectrum (or spectra) collected from the matrix surrounding the precipitate. A direct estimation of the interaction volume around the point of analysis could be obtained from the Inca software, and caution was taken so that the interaction volume for one analysis (from a precipitate or from a point on the matrix) did not interact with any other precipitate. From the EDS spectrum characteristic peaks were identified (both manually using 'confirm element' option and automatically using 'Auto ID' option) and the elemental concentrations were directly obtained from 'quantify-spectra' option, given in Inca-software. Generally K_α analytical lines of the elements (such as Fe, Mn, Al, Si, S, Ti, Nb and V) were used

for identification. Sometimes the existence of the K_β line was also checked to ensure the existence of an element (such as Nb).

Local compositions (particularly Nb-level) at interdendritic (pearlite) and at dendrite-centre (ferrite) regions were studied over 1 mm^2 area on the specimen surface by analyzing 30 fields of view (each field of view covers ~ 840 μm^2 area) at 5000× from each region (within the selected 1 mm^2 area), and performing EDS-area-analysis over the same area. EDS results were reconfirmed by analyzing the same regions by WDS. A number of point-analyses were carried out under WDS mode on the same regions to measure the average Nb-level (which is obtained by standardising the WDS system with a pure Nb-sample) within the interdendritic and dendrite-centre regions.

4.6 Hardness test and determination of yield strength

Vickers macrohardness testing was carried out to determine hardness based on the average of 5 indents, under a load of 20 kg according to BS427: 1990 standard. Room temperature hardness tests were performed from surface to centre along the thickness direction of the TMCR-1 rolled plate, at an interval of 2 mm. 10×10×10 mm sections were cut from one sample of each sample set (slab 1-940-700-hold, slab 1-1140-700-hold and slab 1-1210-700-hold) that were reheated and isothermally held at 700 °C. To determine the difference in yield stress, depending on the temperature of reheat, between those samples at –160 °C, hardness tests were carried out at that temperature using a mixture of methanol and liquid nitrogen. To minimise the heat-exchange (i.e. to avoid temperature rise) the sample was tested within a chamber, insulated by refractory, cotton and thermo col. Although, immersion of the diamond indenter from room temperature into the cooling liquid can change its size or shape,

that change can be negligible due to the isobaric expansion and contraction behaviour and the low coefficient (~ 0.8×10^{-4}) of thermal expansion and contraction of diamond [Prelas 1998, Zhang 1999]. Therefore, the effect of temperature on the diamond indenter was not considered in the hardness tests and no correction was made. These measured hardness values were used to calculate the yield strength of the reheat + hold samples at – 160 °C, in order to determine the cleavage fracture stress values from notch-bend tests carried out at the same temperature. Yield strength (σ_y) and Vickers hardness (H_V) are reported to be proportional (σ_y = K. H_V) and temperature has little effect on the proportionality constant (K), which has a value ~ 3 [Shu 1986 a and b]. Zhang [Zhang 1999] has determined the proportionality constant from a series of hardness and tensile tests for rolled steels with similar compositions (C: 0.08-0.1, Si: 0.21-0.36, Mn: 1.4-1.5, P: 0.010, S: 0.002-0.003, Ni: 0.02-0.50, Nb: 0.023-0.053, Al: 0.026-0.041, Ti: 0.006-0.10, N: 0.004-0.007) as slab 1, and suggested a value 3.13 for K. Therefore, this value was used to convert H_V to σ_y.

4.7 Impact test

Charpy impact test specimens (10×10×55 mm), with a standard V-notch (2 mm deep notch, 45° angle, 0.25 mm root radius) centred on one face, were machined in the T-L orientation from the sub-surface (centre of the notch front approximately 5.5 mm below the rolling surface) and quarter-thickness (centre of the notch front approximately 11 mm below the rolling surface) positions of the TMCR-1 rolled plate, **Fig. 4.5**. The impact tests were carried out following BS EN ISO 14556:2000 using an Instron PW30 300J pendulum impact-testing machine over the temperature range -40°C to -100° C, controlled using a mixture of liquid nitrogen and methanol. The specimens were soaked for 5 minutes at the test temperatures before being tested

and a thermocouple was attached to the specimens close to the notch to record the temperature. The impact fracture energy (Joule) for each specimen were recorded and the broken halves of each specimen was collected for fractographic analysis to study the impact transition behaviour in terms of fracture energy and fracture surface appearance.

4.8 Three-point bend test (3PB)

Three point bend fracture tests were carried out on sub-sized (10×10×55 mm) Griffith-Owen blunt-notch specimens (**Fig. 4.6**) made from reheated (940 °C, 1140 °C and 1210 °C) + isothermally held (700 °C) heat-treated blocks to determine the effect of ferrite-grain size distribution on cleavage fracture. Specimens were machined in such a way that the notch front lies along the original casting direction of the as-cast slab and the fracture propagates along the direction perpendicular to it (same as T-L orientation in rolled steel), **Fig. 4.6 (a)**. Tests were carried out at –160 °C, to ensure brittle fracture, at a loading rate 0.5 mm / min (stroke controlled test) using DMG (Denison Mayes Group) single screw driven mechanical testing machine with 50 kN load cell (100 kN frame) mounted axially on the upper cross-head. The samples were tested in the presence of liquid nitrogen vapour within a closed chamber (specimen chamber), which was insulated from all sides by refractory, cotton and thermo col. The test temperature of – 160 °C was achieved and maintained within ± 2 °C by continuously pouring liquid nitrogen inside the specimen chamber and soaking for long time before each test to cool down the system sufficiently, so that heat-transfer was minimised. The specimen temperature was continuously monitored during the test by inserting a thermocouple wire within the specimen through a small hole (15 mm long hole with the thermocouple wire exactly fitting within it) drilled at one end

of the specimen. The machine load and displacement data for the test were digitally recorded by a Rubicon control system at 12-bit resolution. Philips X-Y data recorder was also used to backup digital data with an analogue plot. The load-displacement results were interpreted using the Griffith-Owen finite element analysis [Griffith 1971], **Fig. 4.7**. Although Griffith-Owen's analysis is calculated for 4PB specimens, however, its use for 3PB specimens is reasonable, as the 4PB stress distributions are not expected to differ much in 3PB.

4.8.1 Determination of the principal fracture stress, σ_F

Fig. 4.8 gives the distribution of maximum principal stress ahead of the notch root (distance, x / notch root radius, ρ) for various normalised stress (nominal principal stress, σ_{nom} / uniaxial yield stress, σ_y) or normalised load (fracture load, L_F / general yield load, L_{GY}). In the present study the general yield load, L_{GY}, of the 3PB specimen was calculated using the following formula [Knott 1973]:

$$L_{GY} = 1.155\ C_f\ B\ (W\text{-}a)^2\ (\sigma_y/3S) \quad \text{.....eqn. 4.3}$$

where, 1.155 is the von-Mises parameter; $C_f = 1.22$, is the constraint factor; B = 10 mm, is the thickness of the specimen; W = 10 mm, is the specimen height; 'a' = 3.33 mm, the notch-depth; S = 20 mm, the bending span; and σ_y is the uniaxial yield strength (MPa) at the test temperature (which is calculated from H_V at - 160 °C). Largest maximum principal stress ($\sigma_{1\ max}$) corresponding to the fracture load (L_F) is termed as the 'principal fracture stress', σ_F ($\sigma_{1\ max} = \sigma_F$). Joining the maximum points of the stress distribution curves (**Fig. 4.7**) the variation of largest maximum principal

stress (σ_F / σ_y) can be obtained for various normalised fracture load (L_F / L_{GY}), **Fig. 4.8**. **Fig. 4.8** was used to calculate σ_F values using corresponding fracture load (L_F) values.

4.8.2 Determination of the local fracture stress, σ_f

From the fractographic study on the fracture surface, the cleavage initiation site was identified for each notch-bend specimen and the minimum distance (along the perpendicular direction to the notch-front) of the cleavage initiation site (X_f) from the tip of the blunted notch was measured (**section 4.9**). Using that distance (X_f) along with the fracture load (L_F) and uniaxial yield stress (σ_y) for the same sample in **Fig. 4.7**, the local fracture stress (σ_f) was calculated.

4.9 Fractography

For fractographic study, sections were cut from the broken test pieces ~ 1 cm below the fracture surfaces, cleaned ultrasonically, and mounted on a metallic stub using adhesive carbon-tape. The entire fracture surface of each Charpy impact specimen was viewed under a Jeol-6300 SEM at low magnification (25×) and long working distance (40 mm), to estimate the fraction (area-percent) of crystalline fracture. Average cleavage facet sizes were also determined from Jeol 6300 SE-micrographs taken from the impact fracture surfaces (Charpy specimens) at ~ 4000×. The facet size was calculated from the average between the maximum chord length of a facet, and the chord length perpendicular to the maximum chord, passing through the facet centre point. Only those facets, which were parallel to the microscopic plane

of fracture, were measured to minimise parallax error. More than 100 facets were measured on Charpy impact specimens to determine the average facet size.

Fracture surfaces of notch-bend samples were also investigated under various magnifications in a Jeol 6300 to identify the cleavage initiation site by tracing the river lines back to their origin. The first facet size (cleavage originating facet size) was measured and the perpendicular distance of the cleavage origin from the root of the notch was also measured. In case the first facet was not clear, all the facets surrounding the cleavage origin were measured and the average size was considered as the first facet size.

4.10 Measurement of gross texture and 'mesotexture'

Longitudinal samples from TMCR-1 rolled steel at 0.1 mm, 0.5 mm, 1 mm, 2 mm, 3mm, 5 mm and 20 mm (mid-thickness) below the plate-rolling surface, were prepared by normal polishing to a 0.05 μm Al_2O_3 finish, followed by electropolishing in a solution containing 89% glacial acetic acid, 8% perchloric acid and 3% H_2O for mesotexture study. EBSD (electron backscattered diffraction) in a Jeol 840 SEM was used to determine the grain boundary misorientation distribution.

An HB-30 (Hiltonbrooks Ltd., Cheshire) texture goniometer stage was used to measure gross crystallographic texture of reheat + hold bend test samples in terms of pole figures. The machine measures grain orientation from X-ray diffraction (XRD) based on Schulz's back reflection method. Co-K_α type X-ray radiation was set at 40 kV and 30 mA. The set up of texture goniometer is shown in **Fig. 4.9** [Ahmad 2005]. Two 10×25×3 mm slices were taken out from one sample of each set of reheat + hold samples (slab 1-940-700-hold, slab 1-1140-700-hold, slab 1-1210-700-hold), **Fig. 4.10**. Both slices were placed side by side to make a larger area (20×25 mm) for X-ray

analysis on lightly ground surfaces. At first a diffraction scan was carried out between 2θ (incident angle of radiation relative to the sample surface) values from 30° to 120°. Three intensity peaks were found at 2θ angles corresponding to ideal Bragg reflections from three sets of planes ({110}: ~ 52.4 °; {200}: ~ 77.2 °; {220}: ~ 99.7 °). Using these 2θ angular positions {110}, {200} and {220} pole figures were constructed with the help of HBTex dada collection software (Hiltonbrooks Ltd., Cheshire) installed in a digital computer. Background intensities at 2° above and below each 2θ Bragg condition were measured to correct the intensity readings for pole figures from background radiation.

4.11 Thermodynamic prediction from Thermo-Calc

Thermo-Calc software (versions M and N) from the Royal Institute of Technology, Stockholm, Sweden, was used both in DOS- and Windows-mode to predict the phase-fraction (including precipitates) and the composition within the phases under equilibrium condition. All the alloying elements shown in **Table 4.1** were considered for the prediction. Predictions were made over the temperature range 1600 °C to 600 °C. Temperature, atmospheric pressure, and steel compositions were the input parameters for the prediction. In the present study Thermo-Calc software was used to predict various metallurgical phenomena, such as, solidification sequence during casting, partitioning of elements within solid and liquid phases during solidification, precipitation sequence and the stability of precipitates. Predicted compositions of first-formed δ-ferrite, last solidifying liquid, and ferrite associated with last liquid or experimentally determined compositions from segregated and non-segregated regions were fed into the Thermo-Calc software to understand the role of segregation on the stability of microalloy-precipitates.

4.12 Deformation simulation in Gleeble 3500 thermomechanical simulator

A Gleeble ®3500 (Dynamic Systems, Inc**,** Poestenkill NY, US) thermomechanical simulator was used for plane-strain compression testing at 980 °C and 1110 °C to study the effect of deformation on the grain size variation. 10×15×20 mm specimens were cut from the ¼-thickness position of as-cast slab 1 (**Fig. 4.11**), encapsulated inside silica tube for reheating treatment to 1150 °C or 1225 °C (~ 1 hr. soaking) and water-quenched. Within the Gleeble 3500, the specimens were rapidly reheated (heating rate: 20 °C / s) back to their original reheat temperatures (1150 or 1225 °C), soaked for 5 minutes and cooled down to the deformation temperatures at a rate of 8 °C / s. Using plane-strain anvils (tungsten-carbide) the specimens were compressed at a high strain-rate, $\dot{\varepsilon} = 10$ / s, up to a true strain, $\varepsilon = 0.3$ and held for 10 s before quenching in water (using water-spray on the samples from spraying nozzles). The values of heating rate, cooling rate, strain, strain rate and hold period used for the present investigation are usual in commercial plate rolling [Kwon 1991, Dutta 2003]. Between the anvil and specimen 0.25 μm tantalum foil was used to avoid sticking of the anvil to the specimen surface. Quicksim software was used to run the thermo-mechanical programming in Gleeble 3500. The cooling rate, deformation parameters (strain and strain rate) and hold time (10 s) used in the present study were usual for commercial TMCR practice and were selected from previous literature.

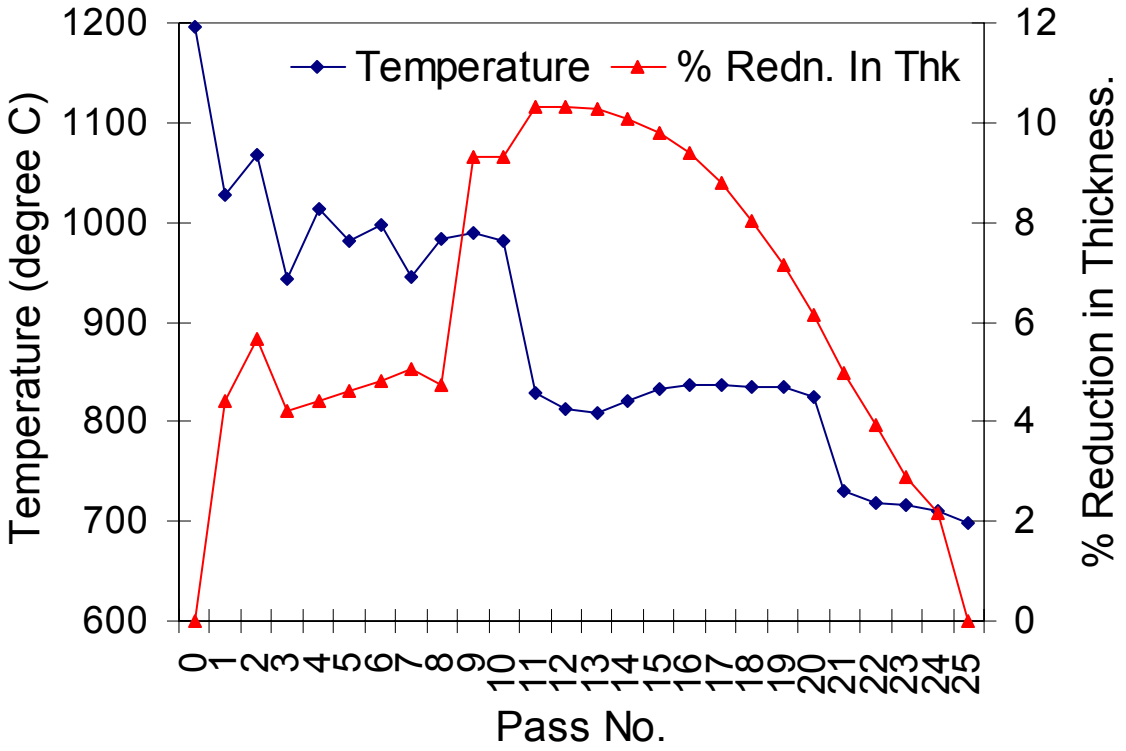

Fig. 4.1: Double hold TMCR schedule for the TMCR-1 rolled plate (44 mm final thickness) where temperature variation (°C) and percent-reduction in thickness during rolling are plotted against deformation pass number.

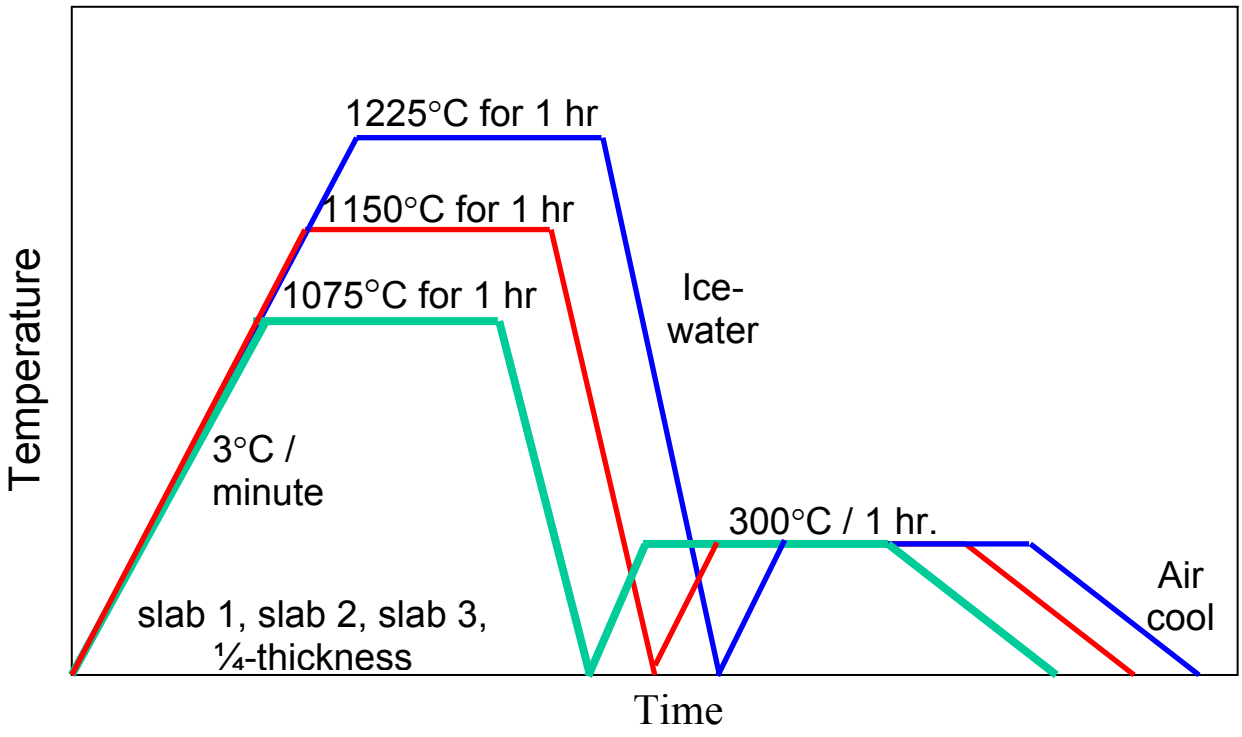

Fig. 4.2: Reheating schedule of slab 1, slab 2 and slab 3, ¼-thickness specimens.

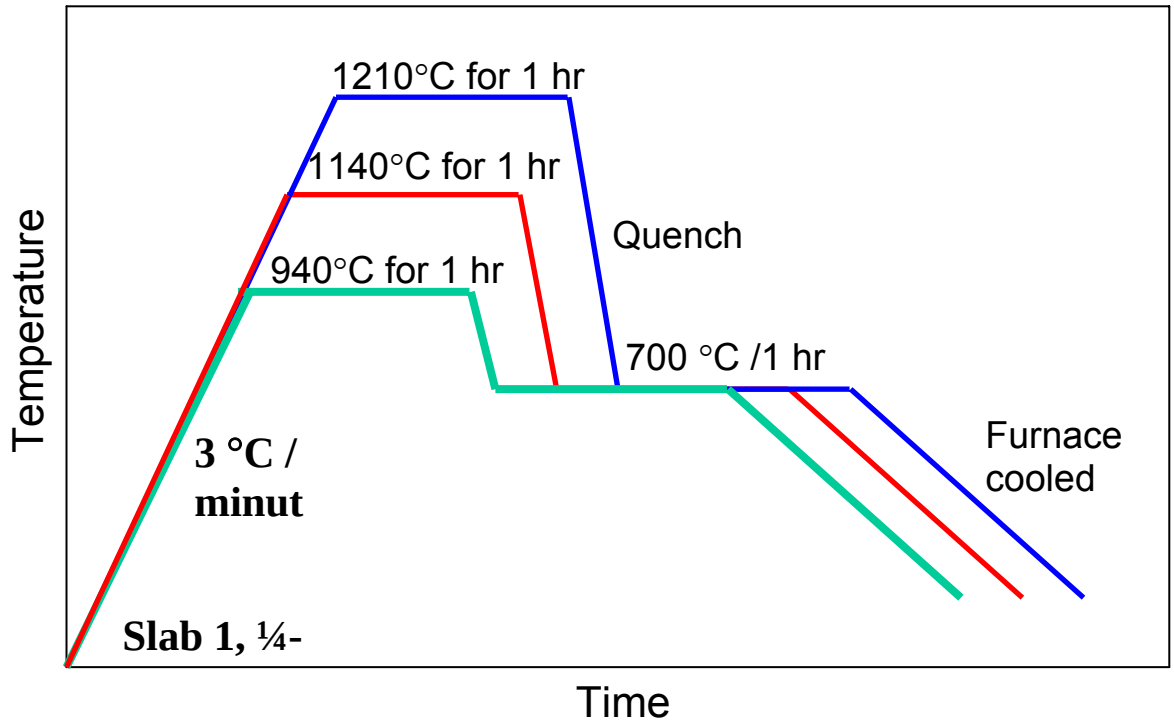

Fig. 4.3: Reheating and isothermal holding schedule for slab 1, ¼-thickness specimens.

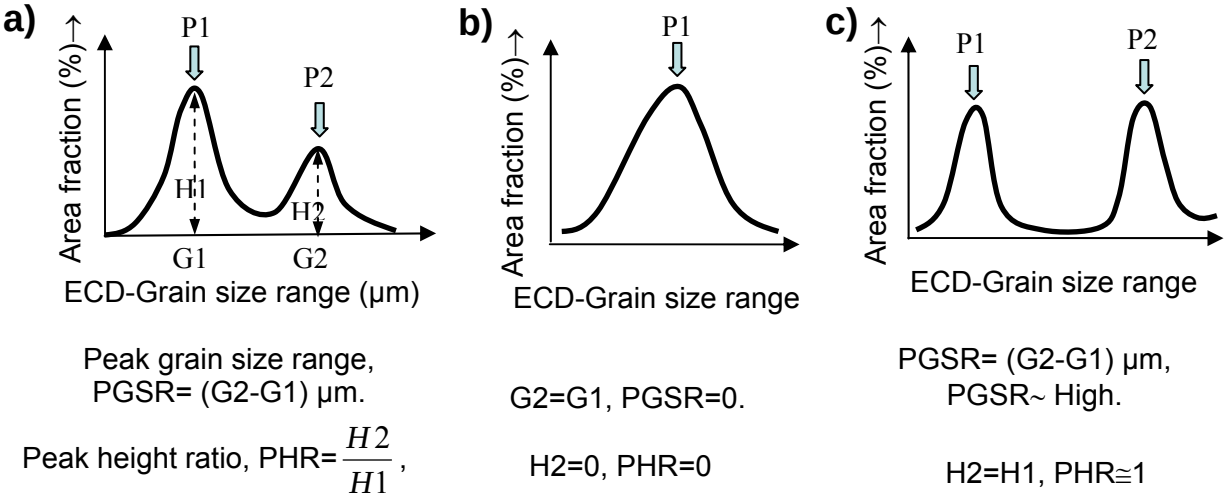

Fig. 4.4: Quantification of the extent of bimodality; (a) definition of PGSR and PHR; (b) schematic example of PGSR and PHR for a uniform

distribution; and (c) schematic example of PGSR and PHR for a highly bimodal distribution.

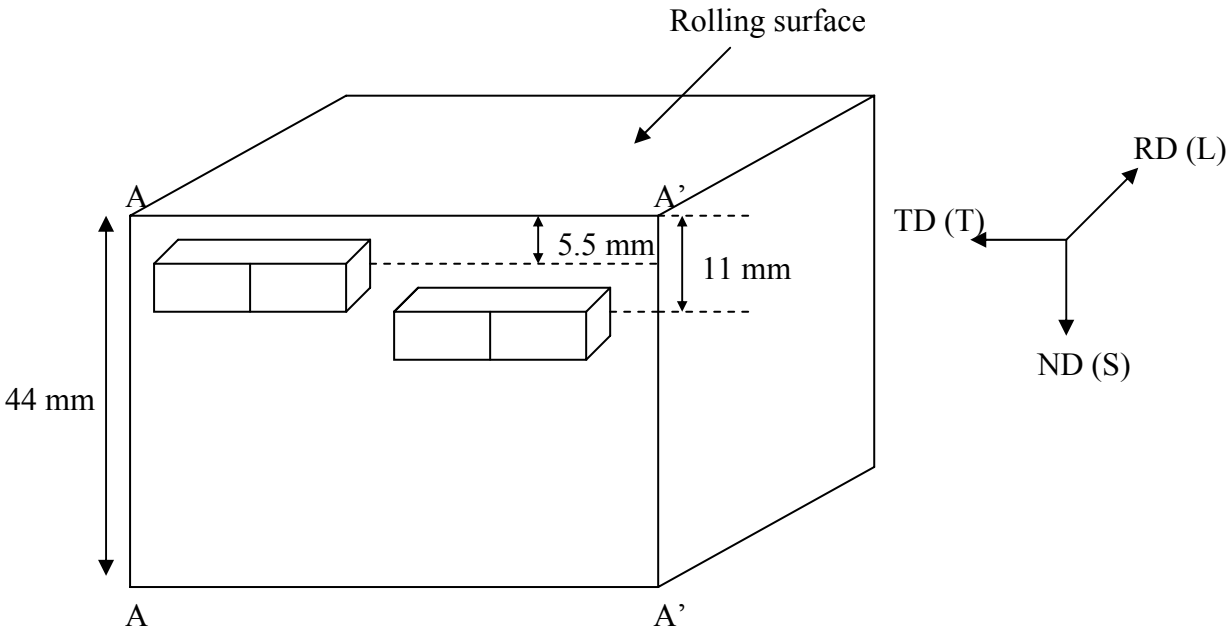

Fig. 4.5: Charpy impact test specimens taken from the sub-surface (centre of the notch front ~5.5 mm from rolling surface) and quarter-thickness (centre of the notch front ~11 mm from rolling surface) position of TMCR-1 steel plate (T-L orientation).

(a)

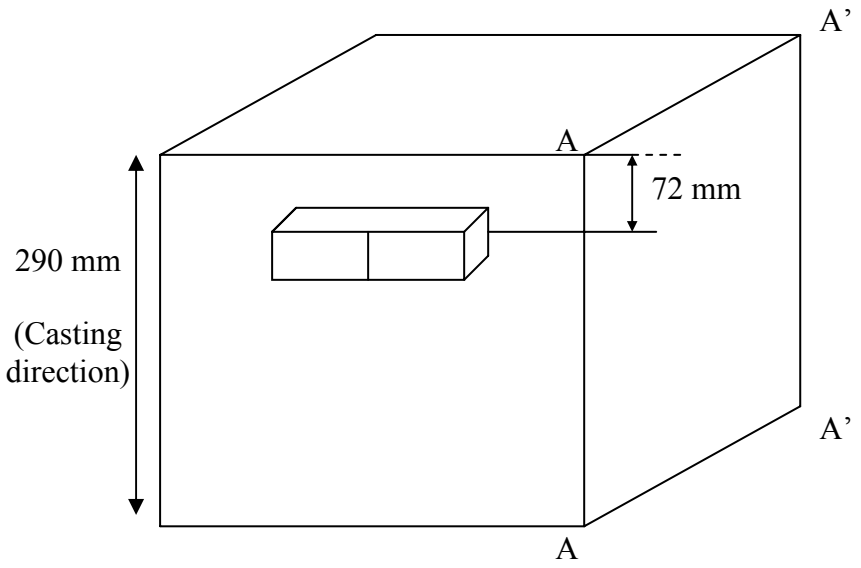

(b)

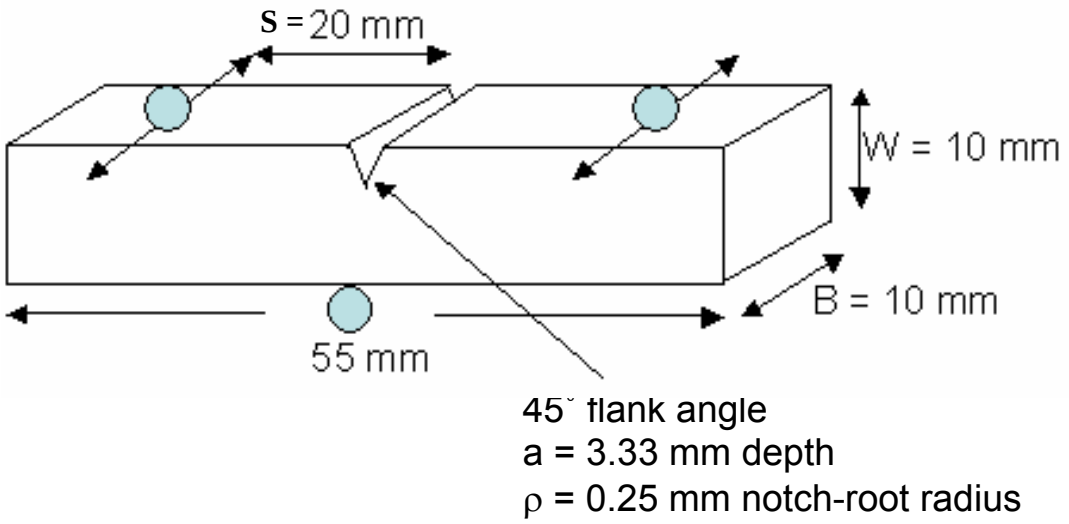

Fig.4.6: (a) Location (¼-thickness position of the as-cast slab 1) and (b) design of the samples used for three-point bend test.

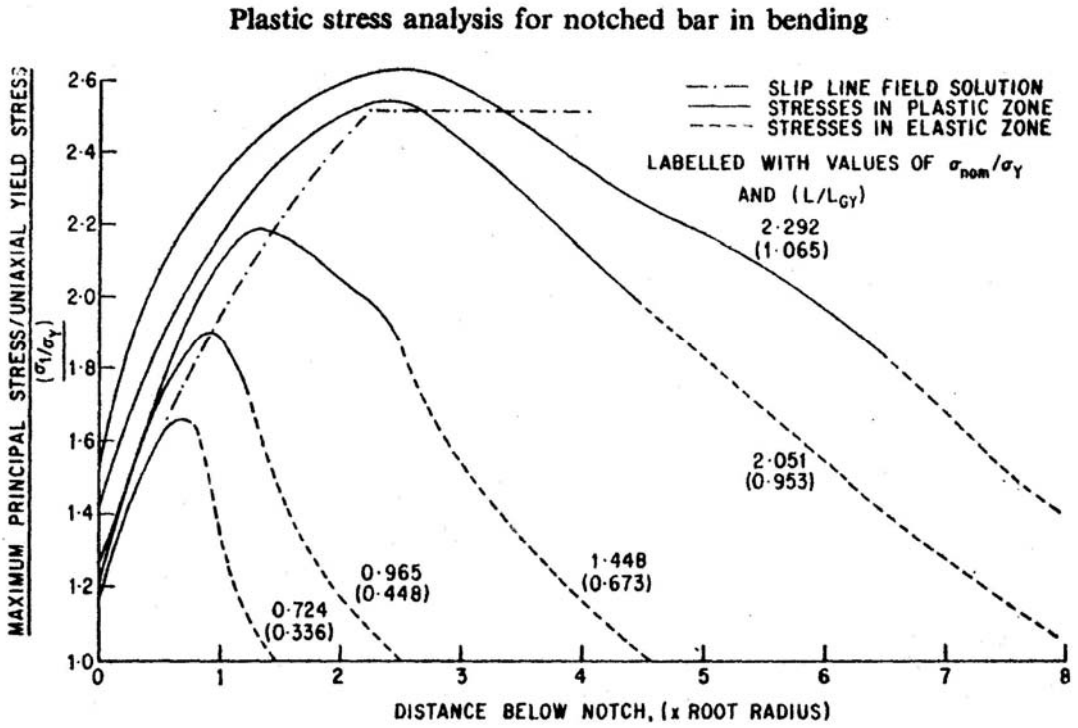

Fig. 4.7: The variation of maximum principal stress below the notch root at various loads (J R Griffith and D R J Owen, J. mech. Phys. Solids, 1971, Vol. 19, pp. 419-431)

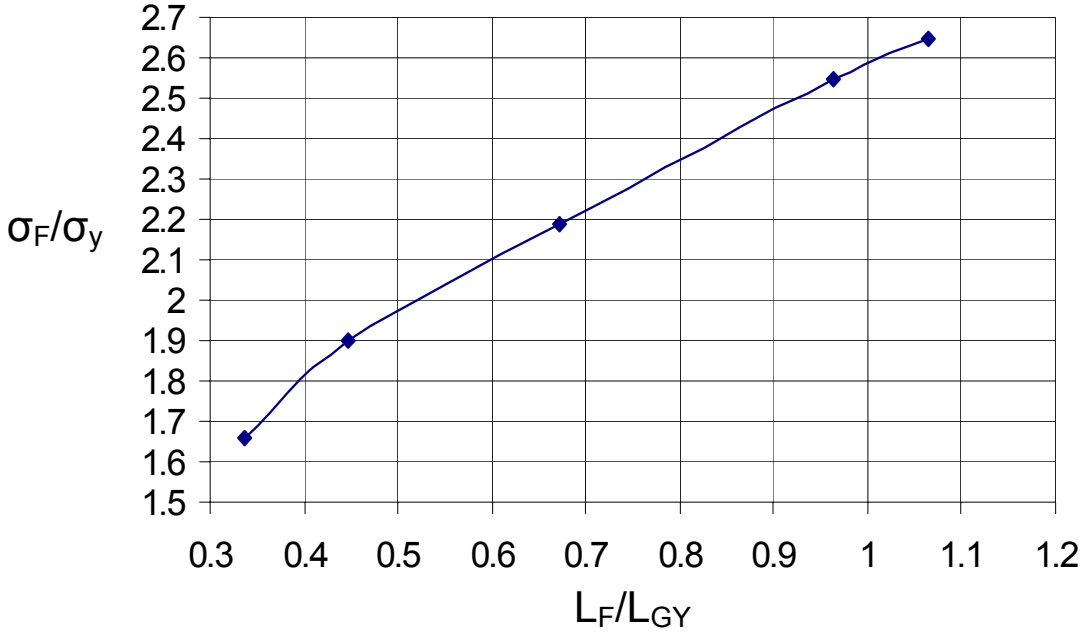

Fig. 4.8: The variation of the largest maximum principal stress with applied load obtained from Griffith-Owen stress distribution plot. Principal fracture stress (σ_F) is calculated from the ratio of L_F / L_{GY} (L_F and L_{GY} Loads are sometime represented as P_F and P_{GY}, respectively).

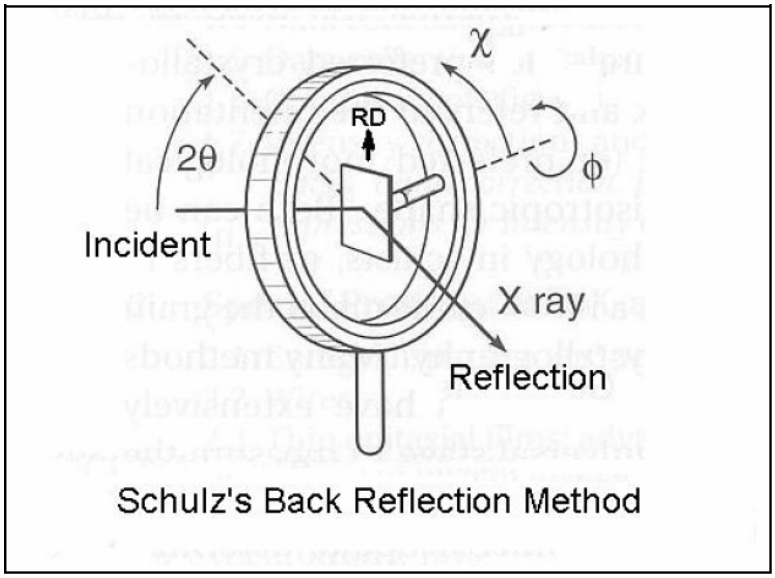

Fig. 4.9: Schematic diagram showing the texture goniometer that measures crystallographic texture from Schulz's back reflection method.

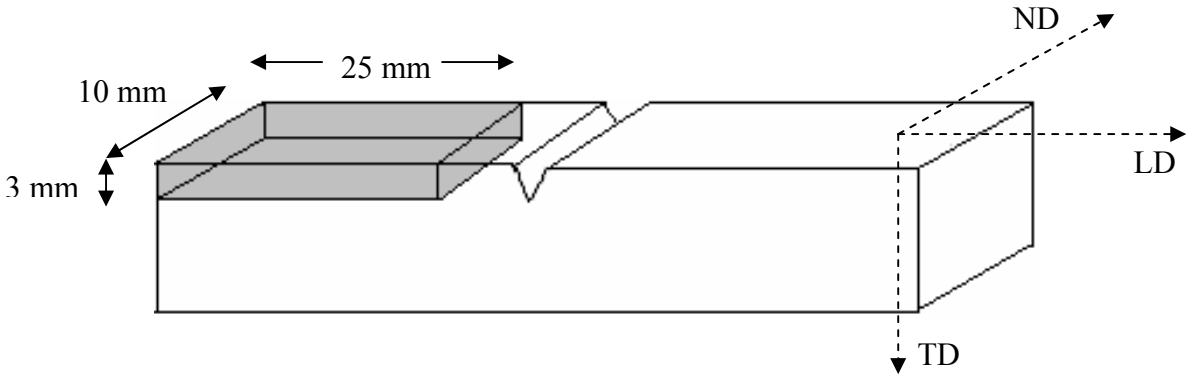

Fig. 4.10: Samples for gross texture measurement were taken from the reheat + hold blocks (used for thre-point bend tests). Two samples cut from the same specimen were joined side by side so that the X-ray beam strikes over larger area of ND-LD plane to measure the texture components on ND-TD plane, which is the plane of interest (fracture plane) for the present study.

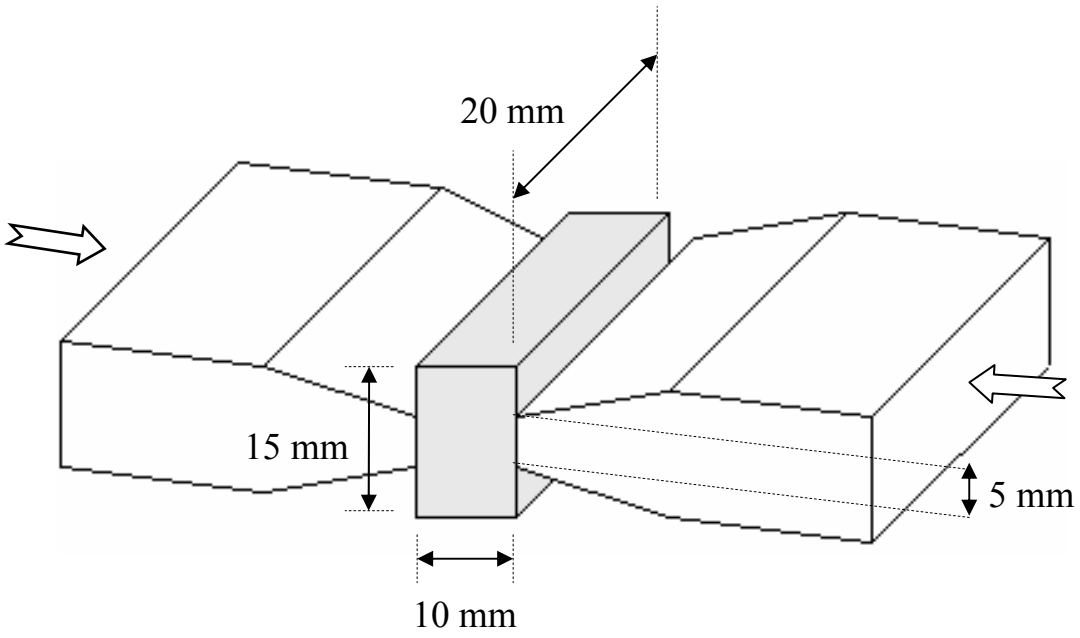

Fig. 4.11: Compression of plane strain specimen (10×15×20 mm) under plane strain anvil, with 5×20 mm contact area.

Table 4.1: Chemical compositions (wt %) of the as-cast slabs and rolled plate.

Sample	C	Si	Mn	P	S	Ni	Al	Nb	Ti	N	V
As-cast Slab 1	0.10	0.31	1.42	0.017	0.005	0.32	0.046	0.045	0.002	0.008	0.052
As-cast Slab 2	0.10	0.28	1.41	0.013	0.001	0.30	0.029	0.027	0.001	0.008	0.050
As-cast Slab 3	0.09	0.38	1.52	0.011	0.002	0.51	0.036	0.020	0.009	0.007	-
TMCR-1	0.09	0.34	1.53	0.014	0.003	0.28	0.046	0.041	0.004	0.007	0.05

Table 4.2: Re-heating heat treatment schedules for quarter thickness samples of as-cast slabs

Sample	Reheating temperature and time	Cooling	Holding / Tempering
Slab1 / Slab 2 / Slab 3-1075-WQ-T	1075 °C / 1 hr.	Ice-water quench to room temperature (RT)	Tempering at 300 °C / 1 hr. Air cooled to RT
Slab1 / Slab 2 / Slab 3-1150-WQ-T	1150 °C / 1 hr.		
Slab1 / Slab 2 / Slab 3-1225-WQ-T	1225 °C / 1 hr		

***A**ll heating rates 3 °C/min to reheating temperature.

Table 4.3: Re-heating+isothermal holding heat treatment schedules for quarter thickness samples of as-cast slab 1

Sample	Reheating temperature and time	Cooling	Holding / Tempering
Slab 1-940-700-hold	940 °C / 1 hr.	Quench to 700 °C	Holding at 700°C / 1 hr. Furnace cooled to room temperature
Slab 1-1140-700-hold	1140 °C / 1 hr.	Quench to 700 °C	
Slab 1-1210-700-hold	1210 °C / 1 hr.	Quench to 700 °C	

***A**ll heating rates 3 °C/min to reheating temperature.

Table 4.4: Bimodality severity scale, based on the visual observation in terms of area-percent 'coarse' grain regions and the size difference (ECD) between the largest and smallest grains.

Visual observation	Not Bimodal	Low Bimodal	Average Bimodal	Quite Bimodal	Heavily Bimodal
Bimodality level	0	1	2	3	4
Area-percent coarse-grain regions in microstructure	0	~ 0-10 %	~ 10-25 %		~ 25-40 %
Difference in size (ECD) between largest and smallest grains (approx)	0	~ 60 μm (reheated slabs) ~ 20 μm (TMCR)	~ 70 μm (reheated slabs) ~ 25 μm (TMCR)	~ 190 μm (reheated slabs) ~ 30 μm (TMCR)	~ 270 μm (reheated slabs) ~ 35 μm (TMCR)

Table 4.5: Classifying individual grain areas (μm^2) and ECD-grain size (μm) in terms of ASTM grain size number (G).

ASTM G	Range of Grain Areas (μm^2)		Mean grain area (μm^2)	Range of ECD (μm)	
15	2.8	5.6	3.9	1.9	2.7
14	5.6	11.1	7.9	2.7	3.8
13	11.1	22.3	15.8	3.8	5.3
12	22.3	44.6	31.5	5.3	7.5
11	44.6	89.1	63	7.5	10.6
10	89.1	178	126	10.6	15.1
9	178	356	252	15.1	21.3
8	356	713	504	21.3	30.1
7	713	1430	1010	30.1	42.7
6	1430	2850	2020	42.7	60.2
5	2850	5700	4030	60.2	85.2
4	5700	11400	8060	85.2	120.5
3	11400	22800	16100	120.5	170.3
2	22800	45600	32300	170.3	240.9
1	45600	91200	64500	240.9	340.7
0	91200	182400	129000	340.7	481.8
00	182400	364800	258100	481.8	681.4

5 Measurement of bimodality

The current methods of measuring bimodality tend to characterise the different types of duplexity rather than the extent. As discussed in **chapter 3** the standard methods for measuring bimodality were developed and verified on microstructures with relatively extreme levels of bimodality. The bimodal grain size distribution is reported to be undesirable as it can cause a variation in mechanical properties, and is particularly detrimental for impact fracture toughness (causing significant scatter), of TMCR microalloyed steel plates [Wu 2004 a, Chen 1990]. This effect may vary with the difference in the severity of bimodality within the microstructure. Hence, steel microstructures need to be distinguished in terms of this extent of bimodality. Various microstructures of reheated-water quenched slab and TMCR-rolled samples examined in the present investigation were classified (**Fig. 5.1** and **Fig. 5.2**) according to a visual bimodality severity scale discussed previously, **Table 4.4**, for ease of subsequent analysis. As discussed in **chapter 3** the established methods for plotting grain size distributions is either based on the ASTM G scale or based on the 25-area class scale [Voort 1992]. ASTM E 1181 standard quantifies bimodality in terms of average size and area-percent of grains corresponding to coarse and fine populations [E 1181]. The classification of microstructures in terms of bimodality scale is a subjective qualitative assessment of the degree of bimodality. However, it has been used as a first approximation of separating the structures in order to assess the ability of the different representation and quantification methods (of bimodality) in distinguishing small changes in microstructure (in terms of bimodality) and to pick up less severe bimodality.

5.1 Grain size distributions based on ASTM G scale

ASTM G is related to the individual grain area on a logarithmic scale, and so, as the grain size increases, the ASTM G number decreases, but the range of individual grain areas (or ECD-grain sizes) within an ASTM G class increases, **Table 4.5**. Using the ASTM G scale revealed that for the reheated slab microstructures the heavily bimodal (visual scale level-4) structure was clearly distinguished, **Fig. 5.3(a)**, for the area percent distribution only but not for the number percent distribution. For bimodal area percent distributions the separate peaks (modes) of the distributions can be clearly identified. The greater sensitivity of the area percent, compared to the number percent distribution, to bimodality agrees with previous findings [Voort 1992]. The quite bimodal (level-3) reheated slab structure also showed separate coarse and fine grain peaks for the area percent distribution, **Fig. 5.3(b)**. However, the average (level-2), low (level-1) and not bimodal (level-0) structures did not show separate peaks, **Fig. 5.3(c)** and **(d)**, with the distributions showing a smooth (no uneveness or breaks in between) unimodal nature. For the TMCR structures ASTM G scale can distinguish level-4 bimodality, **Fig. 5.3(e)** but cannot distinguish level-1, level-2 and even level-3 bimodality, **Fig. 5.3(f)**.

Use of grain areas in teams of ASTM grain size number (G) scale (logarithmic scale on a linear plot) is useful in revealing the nature of the distributions [Voort 1992]. As the grain areas exhibit an approximately log-normal distribution, use of ASTM G scale produces a smooth, Gaussian curve for area percent distribution for a uniform grain structure. Non-Gaussian distributions for heavily bimodal microstructures are relatively easy to pick up as, for such distributions, both peaks (modes) are distinctly separate and both parts of the distribution are smooth. For the microstructure of INCONEL 625 alloy as an example (which showed a necklace type of duplex structure) Van der Voort et al. [Voort 1992] showed that a limited number of grain measurements or the type of

duplexity (more complex than bimodal) could result in unevenness and more complex distributions, than unimodal or bimodal (based on ASTM G scale) and that could create difficulty in identifying the nature of the distribution. Van der Voort et al. [Voort 1992] suggested that the measurement of 1000 grains or more would be needed to produce a smooth unimodal or bimodal distribution curve following this method (irrespective of material and the type of duplexity) and therefore, more than 1000 grains are measured in the present investigation.

As noted above, the distributions plotted by ASTM G scale are only sensitive to above average bimodality. Although the distributions can be presented over 0-15 ASTM number class (16-classes) actually the distributions extend over a smaller number of classes, e.g. only 8 to 12 ASTM G classes in **Fig. 5.3**. The number of classes for a particular distribution depends on the grain area values measured and especially, on the overall spread (difference between largest and smallest grain area) in the grain area data set. As an example, the level-2 reheated slab, **Fig. 5.3(c)**, distribution extends over ASTM 5 to ASTM 12 (8-classes), whereas, level-4 reheated slab, **Fig. 5.3(a)**, extends over ASTM 1 to ASTM 12 (12-classes). That is due to the difference in overall spread in grain-area data between level-4 reheated slab (smallest grain area: 20 μm^2; largest grain area: 61730 μm^2) and level-2 reheated slab sample (smallest grain area: 18 μm^2; largest grain area: 4028 μm^2), **Table 4.5**. The overall spread in grain area for level-2 reheated slab sample (smallest grain area: 18 μm^2; largest grain area: 4028 μm^2) is higher than that for level-4 TMCR sample (smallest grain area: 3 μm^2; largest grain area: 1064 μm^2). But level-4 TMCR distribution, **Fig. 5.3(e)**, extends over a greater number of classes (9-classes) than level-2 slab, **Fig. 5.3(c)**, distribution (8-classes), **Table 4.5**. Therefore, depending on the measured grain size values and overall spread in data set, the sensitivity of the area-percent distributions to distinguish bimodality will be different for different

samples (as the class number changes). That makes the ASTM G scale (using every ASTM number class interval) less sensitive to determining bimodality for lower bimodality conditions (level-1 and 2), when a greater number of classes could be required.

The reason that distributions plotted by ASTM G scale do not describe the level-3 bimodality in a TMCR sample, **Fig. 5.3(f)**, is again related to an insufficient number of classes dividing the distribution. For level-3 TMCR microstructure the areas of the grains in the coarse grained regions were found to lie between ~ 360 μm^2 and 720 μm^2. Therefore, almost the entire coarse grain size population comes within a single ASTM G class (ASTM 8), **Table 4.5**. ASTM 9 class covers ~ 178 to 356 μm^2, and the measured grain area data suggest that, within that range, the area percent of grains in the fine population drops (from ~ 15 percent to 0 percent), but as the level-3 TMCR microstructure is not 'heavily bimodal', the area-percent corresponding to ASTM 9 class is still higher than that for ASTM 8 class and that is the reason why area-percent distribution for the same sample in **Fig. 5.3(f)** does not show any bimodality. Use of a greater number of classes could again be helpful in determining this bimodality.

To quantify the bimodal distributions, using the ASTM E 1181 [E 1181] approach of measuring the area percentage of 'coarse' and 'fine' populations and corresponding average grain sizes, the 'breakpoint' between the distributions, (to separate 'coarse' and 'fine' populations) needs to be determined. The breakpoint was determined according to the intersection between the number and area percent distributions [Voort 1992] and by the 'gap' in data set method [E 1181, Voort 1992]. Finding the 'gap' by analysing the data set to separate both populations was not well defined in previous studies regarding duplex grain size distributions. It was mentioned that this separation requires some judgement on the part of the metallographer [Voort 1967]. To plot the grain size

distributions all the measured individual grain area or grain size (ECD) values need to be arranged in ascending order. In the present study the 'gap' is measured from the largest difference between two consecutive individual grain size values. Judgement is required to ensure that the 'gap' lies between the mode values corresponding to coarse and fine populations and due to that the selection of breakpoint by this approach is subjective. The area percent and average grain size values for the 'coarse' and 'fine' populations, measured following different approaches are shown in **Table 5.1**. As can be seen in **Table 5.1** the choice of breakpoint significantly affects the area-percent and average size of coarse and fine grain populations, which are also the standard measure of bimodality. The intercept method (selecting intersection point between number percent and area percent distributions as breakpoint) does not give a reliable method as the area percent of coarse populations (49-57 % for level-3 and level-4 microstructures) in **Table 5.1** according to this method, are higher than the estimated area percent range of coarse populations (10-40 %) for the same samples, **Table 4.4**. For level-4 reheated slab number- and area-percent distributions intersect at ASTM 6 class, **Fig. 5.3(a)**. Hence, the end of ASTM 6 class (i.e. ASTM 5.5; Area~2850 μm^2) should be considered as the 'breakpoint'. This selection is not satisfactory as the 'coarse' population appears to start at ~ ASTM 3 and peaks at ~ ASTM 2, **Fig. 5.3(a)**. Similarly, for the other bimodal distributions the intersection points do not appear to be the breakpoints from the visual observations.

Using the largest 'gap' in the data set appears satisfactory from visual observations in separating the populations, **Fig. 5.3**, and the calculated coarse-area-percent values (19-34 % for level-3 and level-4 microstructures), **Table 5.1**, come within the estimated range (10-40 % for level-3 and -4), **Table 4.4**. Still this approach is subjective in nature as the definition of 'gap' is not very specific and depends on the

user's interpretation about the 'gap' in data. Also finding out the 'gap' requires further data analysis after plotting the grain size distributions. Selection of breakpoint is a drawback of the ASTM 1181 standard [E 1181] and Van der Voort et al. [Voort 1992] methods of quantifying the bimodality.

In spite of these drawbacks the use of ASTM G scale is helpful considering the following points:

- With the measurement of more than 1000 grains for each microstructure, area-percent distributions based on ASTM G scale are smooth and clearly picked up 'not-bimodal' (i.e. unimodal) and 'heavily bimodal' conditions.
- The distributions are helpful in visually comparing different microstructures in terms of the grain size as all the distributions are based on the same scale.

5.2 Grain size distributions based on individual grain area (25-class) scale

As the distributions based on ASTM G number were not sensitive to average and low bimodality (level-2 and 1) microstructures the data were replotted using the 25-class separations as suggested by Peyroutou [Voort 1992]. **Fig. 5.4** shows the representative distributions for the reheated slab and TMCR samples studied based on the 25-class method. Sensitivity of the distributions has increased by using 25-area classes to divide the data. The area-percent distributions for level-2 reheated slab (**Fig. 5.4(b)** and level-3 TMCR (**Fig. 5.4(e)**) samples indicate bimodality, which starts at ~ 2145 μm^2 for level-2 slab sample (**Fig. 5.4(b)**) and ~360 μm^2 for level-3 TMCR sample (**Fig. 5.4(e)**). This bimodality was not detected for the 16 ASTM G classes, **Fig. 5.3 (c & f)**. The 25-area class method could pick up slight variations in area-percent grain size, over the entire grain area range in the microstructure.

On the other hand the area-percent distributions using 25-area-classes are quite uneven in nature, **Fig. 5.4**. That can make identification of grain structure (whether unimodal or bimodal) in these distributions more difficult. As an example, for not-bimodal, level-0 TMCR sample, **Fig. 5.4(d)**, unevenness around 187.5 μm^2 to 237.5 μm^2 area classes makes the distribution appear as if a 'fine' population (peaking ~ 87.5 μm^2) exists along with a separate 'coarse' population, which peaks around 200 or 237.5 μm. Moreover, in case of heavily bimodal distributions, the uneven nature within the 'coarse' population creates difficulty in identifying the 'mode' for the 'coarse'-population. For example, in level-4 slab distribution, **Fig. 5.4(a)**, the mode corresponding to 'coarse' population could be ~ 30,000 / 37,500 / 40,000 or 47,500 μm^2. As Van der Voort et al. [Voort 1992] have mentioned the number of grain measurements could cause unevenness in the distribution, therefore, a greater number of grain size measurements (than around 1000 to 2000 grains measured in present study) for each sample may be required to make the 25-area-class distributions more smooth.

In **Fig. 5.4** for all the bimodal samples, the area percent and number percent distributions intersect within the second or third grain area class from the origin of the plot (out of 25 classes). Using the intersection point between number percent and area percent distributions as a 'breakpoint' (as suggested by Peyroutou [Voort 1992]) the coarse and fine populations are separated at the upper limit of the class where the intersection has taken place (e.g. at ~ 5000 μm^2 for **Fig. 5.4(a)** and at ~ 495 μm^2 for **Fig. 5.4(b)**). However, the populations appear to separate at ~ 20000 μm^2 in **Fig. 5.4(a)** and at ~ 1815 μm^2 in **Fig. 5.4(b)**. Therefore, from the visual observation of the distributions based on 25-area classes the intersection point approach does not appear satisfactory. It might be useful for distributions where 'coarse' and 'fine' populations are distinctly separate from each other and the 'fine' population is restricted within a sufficiently

narrow range so that it finishes within the second or third grain area-class from the origin of the plot (as in the case of the C-steel microstructure studied in Van der Voort et al. [Voort 1992]). It will also be helpful for the duplex condition where isolated coarse grains (ALA grains) lie within uniformly fine grains. In the present study, the distributions (even for the heavily bimodal condition) are flatter with greater overlap (each population occurs over a wide range) and the 'intersection point' approach yields area-percent values of coarse grains (40-66 % considering all the microstructures from level-1 to level-4) that are consistently larger than the estimated range (0-40 % for the same microstructures), **Table 4.4**.

Therefore, the advantage and limitations of using 25-area-classes are as follows:

Advantage:

- As 25 classes and an 'arithmetic scale' are used the distributions are very sensitive and could pick up lower bimodality microstructures (level 1 or 2 bimodality).

Limitations:

- Distributions are uneven in nature and therefore it is difficult to pick up unimodal or bimodal grain structures (or mode values for bimodal distributions) from such distributions.
- Intersection points between number- and area-percent distributions are not useful in separating 'fine' and 'coarse' populations.

5.3 Grain size distributions based on ECD-grain size (15-class) scale

Considering the advantages and limitations of the existing methods for plotting grain size distributions a new procedure has been used in the present study. An arithmetic scale is used (as in the 25-area class method) but the plots were based on ECD-grain size

with 15-numbers of classes dividing the data set for all the microstructures (irrespective of the spread in data).

Previous literature suggests that the bimodal-grain structure can be best identified from the 'area' covered by grains of different size. ECD-grain size is also a function of grain area and can be used in an arithmetic scale plot. ECD-grain sizes can also be converted to ASTM G using **eqn. 4.1** and **4.2**.

Elementary statistical methods [Wetherill 1967, Weiss 1981] mention that the choice of class number and the class interval to plot histograms is basically a matter of judgement, which depends on the number and the range of observations. They also suggest not using 'too small' or 'too large' a number of classes (depending on the number of measurements) [Wetherill 1967, Weiss 1981] and recommend using 5-15 number of classes. For the microstructures in the present study, ASTM G scale divides the histograms into 8 to 12 classes (varying between microstructures) and could not pick up bimodality in certain conditions (level 1 and 2). Using 25-area classes the histograms are discontinuous with the present number of grain size measurements. The ECD-scale method selected 15-number of classes as the highest value of the statistically recommended range. The number '15' is also chosen as a compromise between two previous methods (ASTM G and 25-area-class), to achieve smoother histograms as well as to pick up 'lower bimodality conditions' (level-1 and -2). Varying the number of classes for the arithmetic method could influence the 'breakpoint' and hence the measure of bimodality [Voort 1992] and therefore, specifying a particular number '15' is always useful and makes the method less subjective.

The grain size distributions in **Fig. 5.5**, based on the ECD-scale, are quite smooth in nature and the area-percent histograms clearly represent unimodal and bimodal conditions. For the bimodal area-percent distributions both modes can be easily identified

(marked by arrows in **Fig. 5.5**). Use of the ECD-scale with 15-classes makes the distributions suitable to pick up level-1 or level-2 bimodality. However, area-percent distributions corresponding to 'coarse' and 'fine' populations are more distinct for level-3 or level-4 microstructures (due to higher bimodality) compared to level-1 and level-2. Overall, this method of plotting grain size distributions improves the visual representation of bimodality for the microstructures investigated in this study.

For the bimodal distributions based on ECD-scale the area percent of the coarse population calculated (38 – 65 % considering all the microstructures from level-1 to level-4) based on the 'intersection point' (between number- and area-percent distributions) as the 'breakpoint' was found to be more than the visually estimated range (0-40 % in **Table 4.4**). Therefore, the breakpoint based on any 'gap' in data (in terms of largest difference between the two consecutive individual grain sizes, ECD, as discussed earlier) was determined. The area-percent and average-size (both in ECD and ASTM G) for 'coarse' and 'fine' populations, calculated based on the 'gap' are listed in **Table 5.2**. The bimodal area-percent distributions (**Fig. 5.5**) reach a minimum value in between both the 'modes', and the 'coarse' and 'fine' populations appear to separate at those 'minima'. The 'gap' in the data set falls around or within the class where area-percent reaches the 'minimum', **Fig. 5.5**. Hence, the grain-size class, where area-percent reaches a minimum value, can also be considered for separating the populations. In the present study, lowest grain-size value (ECD) corresponding to that class, was selected as the 'breakpoint'. By doing this, the 'breakpoint' can be directly obtained from the distributions and additional data analysis, required to identify the 'breakpoint' (after plotting grain size distributions) can be avoided. Standard parameter values (area-percent and average-size of the populations) obtained by considering the 'minima' as the 'breakpoint' are close to the values measured from the 'gap' in data set and also lie within the visually estimated

range, **Table 5.2**. Therefore, this 'minimum area-percent class' approach of separating the populations can be useful as it is quick and easy. However, some bimodal distributions do not show a single minimum, e.g. **Fig. 5.5(c)**, where two different classes (~40 μm and ~ 50 μm) correspond to minimum area percent (~ 3.3 %). In this situation the 'gap' in data set was considered and as the largest 'gap' in data set lies around the 50 μm-class, 50 μm was selected as the 'breakpoint' instead of 40 μm. Hence, a degree of subjectivity in measuring bimodality with this approach remained.

The 'standard' parameter used to measure bimodality (area % coarse grained region) was compared to the visual bimodality severity scale, **Fig. 5.6**. It can be seen that the area percent coarse distribution, when the value is calculated using the breakpoint determined by the 'gap' in any data set (which is also the standard way of separating 'coarse' and 'fine' populations [E 1181]) gives a good measure of bimodality. **Fig. 5.6** indicates that the 'average bimodal' (level-2) condition arises when the coarse-area percent exceeds ~ 12 %. Similarly 'heavily bimodal' condition (level-4) appears as coarse area-percent exceeds ~ 25 %. However, as discussed above, there is a degree of subjectivity in determining the breakpoint, which may make the analysis operator-dependent. Hence comparison of bimodality between different groups of researchers becomes inaccurate. In order to remove any subjectivity from the measure of bimodality and to reduce the level of analysis (determination of breakpoint) two new parameters were used in this study.

5.4 PHR and PGSR parameters to quantify bimodal distributions

Peak height ratio (PHR) and peak grain size range (PGSR) are two parameters, **Fig. 4.4**, that are independent of any 'breakpoint' in the grain size distribution curves.

From the area-percent distributions based on an ECD scale the PGSR values can be obtained directly as the difference in lowest ECD values (for each class) corresponding to the mode values for the coarse and fine grain sizes, **Table 5.3**. PHR values can be calculated easily from the area-percent values (area-percent per class) used to plot the distributions, **Table 5.3**. PHR and PGSR values thus obtained are related to the bimodality level for the corresponding microstructures, **Fig. 5.7**. As expected, PHR and PGSR increase with increased bimodality level. PGSR values can also be presented in a normalised form (divided by corresponding average ECD-grain size for all the grains measured), **Fig. 5.7(c)**. This was done to allow the PGSR values for the reheated slab and TMCR samples to be plotted on the same graph but also to magnify the difference in PGSR between TMCR samples at different bimodality levels. PHR and normalised PGSR appear to rise almost linearly (fit lines are shown in **Fig. 5.7**) as the bimodality level increases. To verify such relationships more studies are required. However, such an empirical relationship would be useful from the view point that the bimodality in different microstructures can be compared based on PHR and PGSR values. Also from the visual appearance of severity in bimodality, PHR and PGSR values for the area-percent grain size distributions can be predicted.

Fig. 5.7 indicates that 'average bimodality' (level-2) appears as PHR exceeds ~ 0.2 and PGSR exceeds ~ 50 μm for reheated slabs and ~ 10 μm for TMCR steels. The 'highly bimodal' condition (level-4) arises as PHR exceeds ~ 0.4 and PGSR exceeds ~ 150 μm for reheated and ~ 20 μm for rolled steels.

5.5 Conclusions

HSLA steel samples with microstructures showing a range in severity of bimodality were quantified using the ASTM 1181 method and using two new parameters proposed in this study. The main conclusions are as follows:

- Grain size distributions (plotted as number percent or area percent) based on ASTM grain size number (G) scale were unable to distinguish the microstructures with less severe bimodality.
- The arithmetic approach of using individual grain area with 25-area-class could pick up less severe bimodality conditions but the distributions were uneven, and therefore, it was difficult to clearly identify the unimodal or bimodal nature.
- The area-weighted histograms are far superior compared to the number-frequency histograms in representing bimodality (also indicated by a previous study [Voort 1992]).
- The selection of breakpoint based on the intersection between number-frequency and area-frequency distributions didn't appear satisfactory from visual inspection and the quantification of bimodality following this approach fell outside the visually estimated limits.
- The distributions proposed in this work, based on ECD-scale (15-class) appear to be a good practical choice to represent and to quantify the bimodality (considering the minimum-area percent class in between both the modes as 'breakpoint') for the steel microstructures studied here.
- Standard parameters (area-percent and average-size corresponding to 'coarse' and 'fine' populations) provide useful microstructural details but are subjective in nature.

- PHR and PGSR are easy to measure and less subjective (as they are independent of 'breakpoint' selection) parameters and therefore, can be used to quantify and classify different microstructures in terms of bimodality.

5.6 Future work

The present study has demonstrated the need for future work. More microstructures need to be studied from different steel compositions to verify the usefulness of the ECD-scale to plot grain size distributions and PHR, PGSR parameters for the quantification of bimodality during steel processing. The applicability of ECD-scale and the suggested parameters could also be checked on the bimodal microstructures of the other materials. It is necessary to study the effect of different bimodality regimes on mechanical properties (especially on cleavage fracture) and based on that study, to suggest values of bimodality required during processing to control the quality of steel.

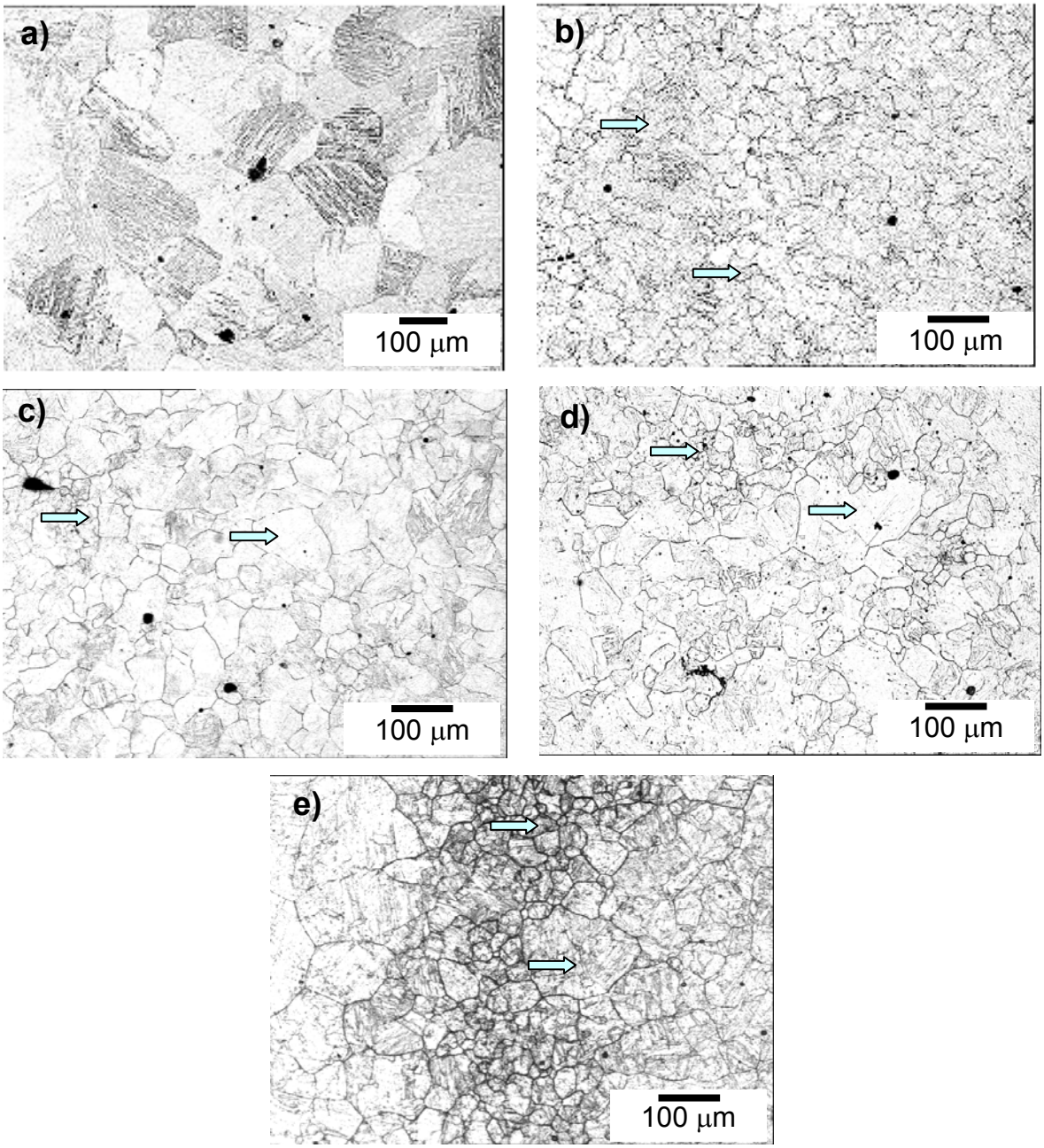

Fig. 5.1: Micrographs from the reheated slab samples showing varying levels of bimodality: (a) level-0 (not bimodal), (b) level-1 (low bimodal), (c) level-2 (average bimodal), (d) level-3 (quite bimodal) and Level-4 (heavily bimodal), where the coarse and fine grains are arrowed for the bimodal microstructures.

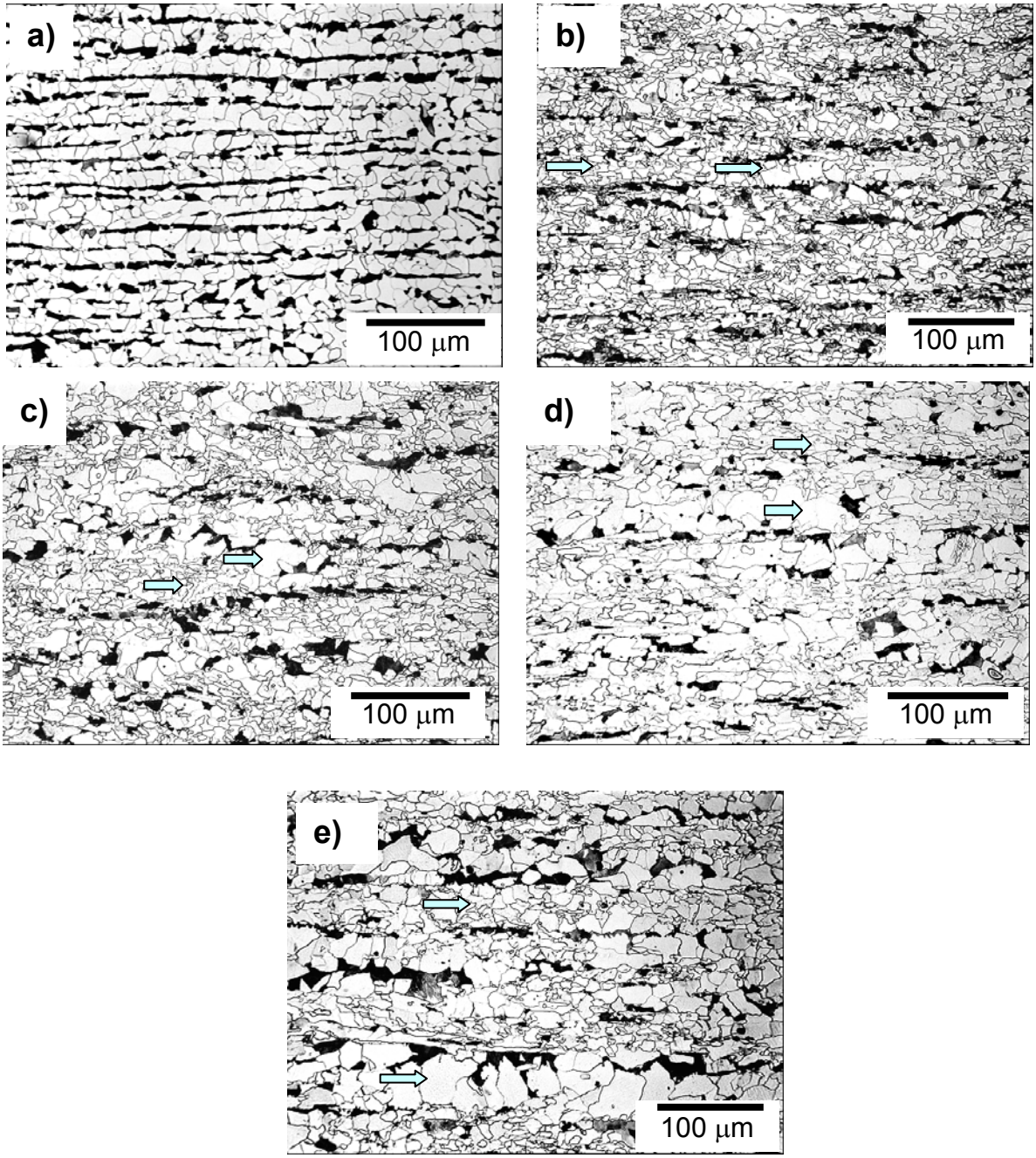

Fig. 5.2: Micrographs from the thermomechnical rolled (TMCR) plate samples showing varying levels of bimodality: (a) level-0 (not bimodal), (b) level-1 (low bimodal) (c) level-2 (average bimodal), (d) level-3 (quite bimodal) and (e) level-4 (heavily bimodal), where the coarse and fine grains are arrowed for the bimodal microstructures.

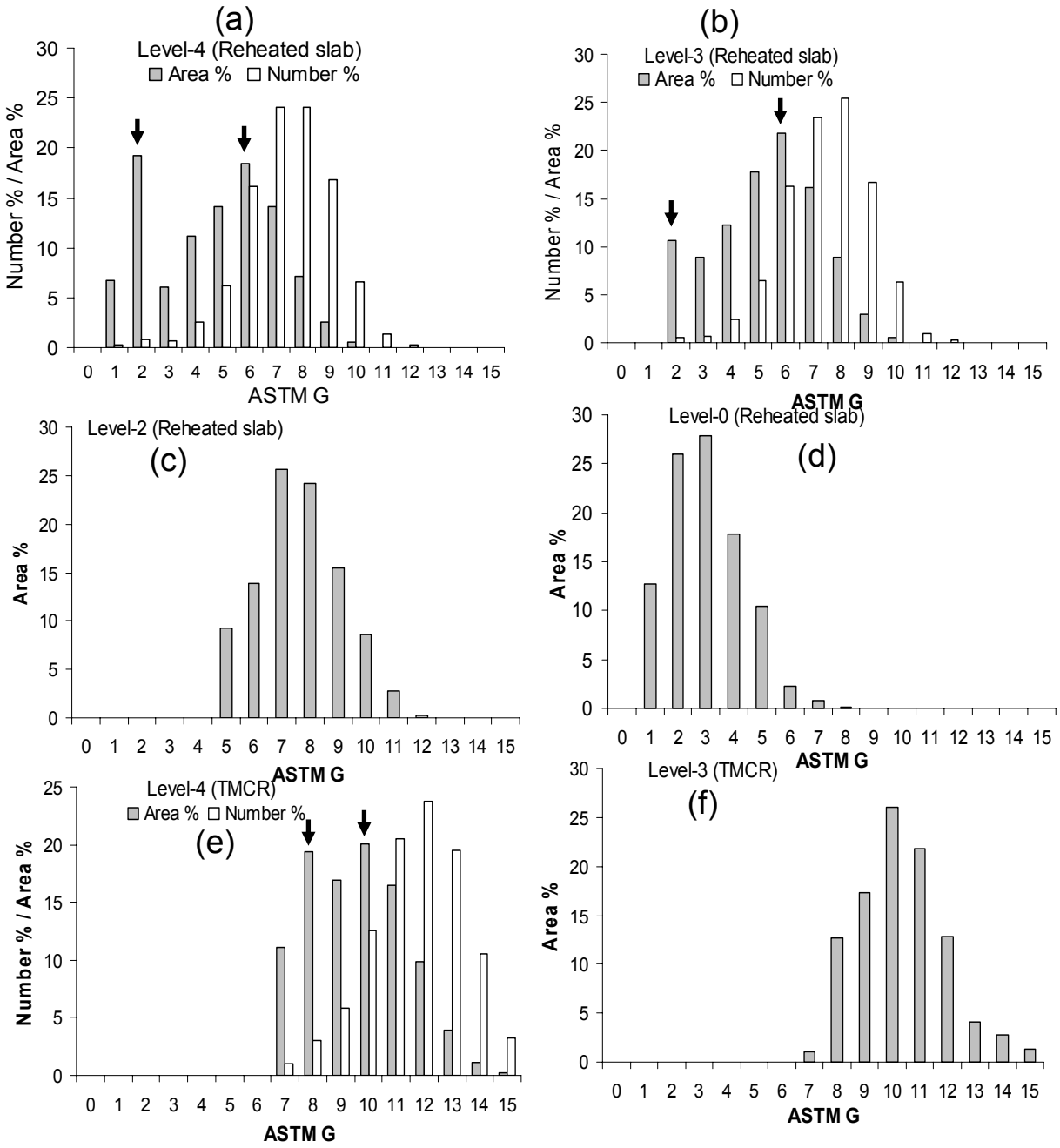

Fig. 5.3: Grain size distributions based on ASTM G scale for the reheated slabs (a) heavily bimodal (level-4), (b) quite bimodal (level-3), (c) average bimodal (level-2) and (d) not bimodal (level-0). Also shown are the distributions for (e) heavily bimodal (level-2) and (f) quite bimodal (level-3) samples of TMCR plates. For bimodal area percent distributions both peaks are arrowed and corresponding number percent distributions are also shown, so that the intersection point between both the distributions can be selected as the 'breakpoint'.

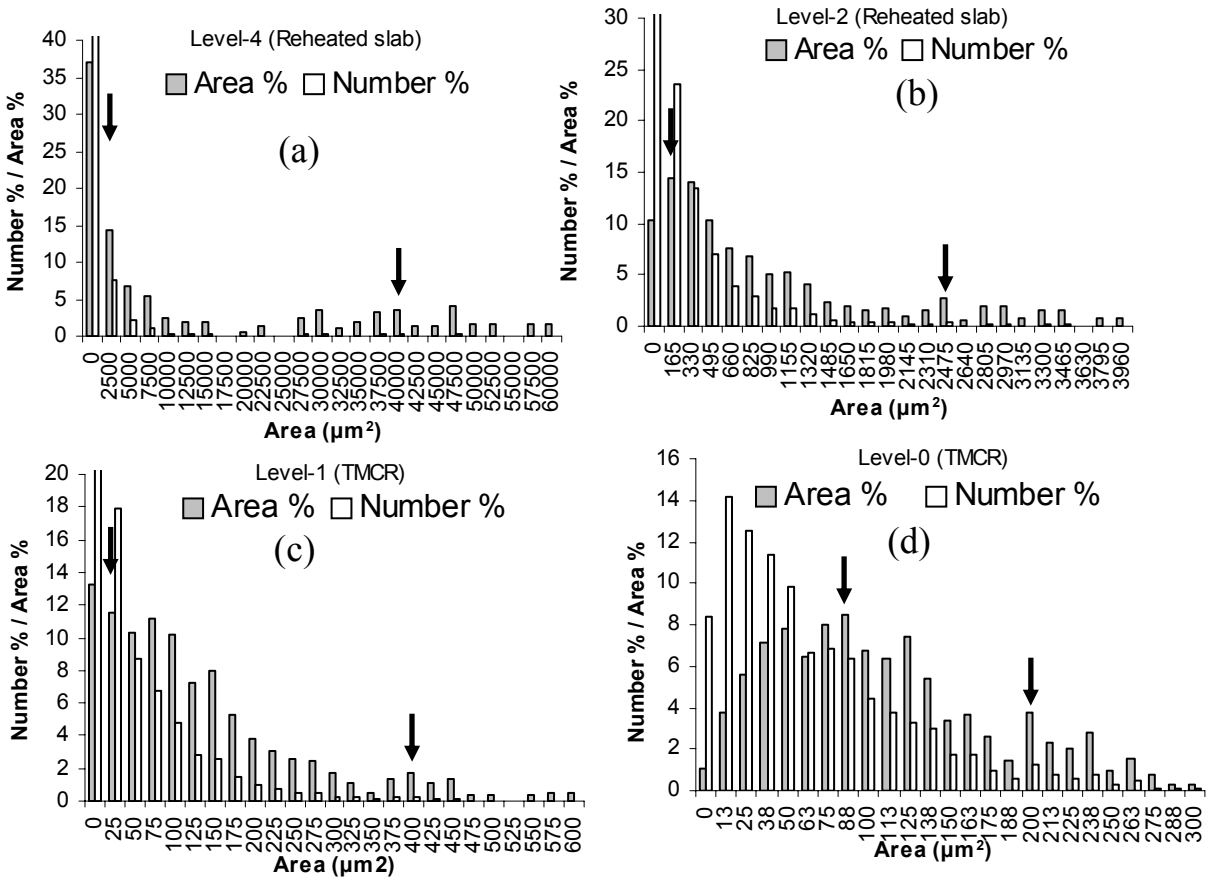

Fig. 5.4: Grain size distributions (number % and area %) on individual grain area scale (25-class) for (a) heavily bimodal (level-4) and (b) average bimodal (Level-2) reheated slab samples. Same distributions for (c) low bimodal (level-1) and (d) not bimodal (level-0). Possible 'modes' for the bimodal area-percent distributions are arrowed.

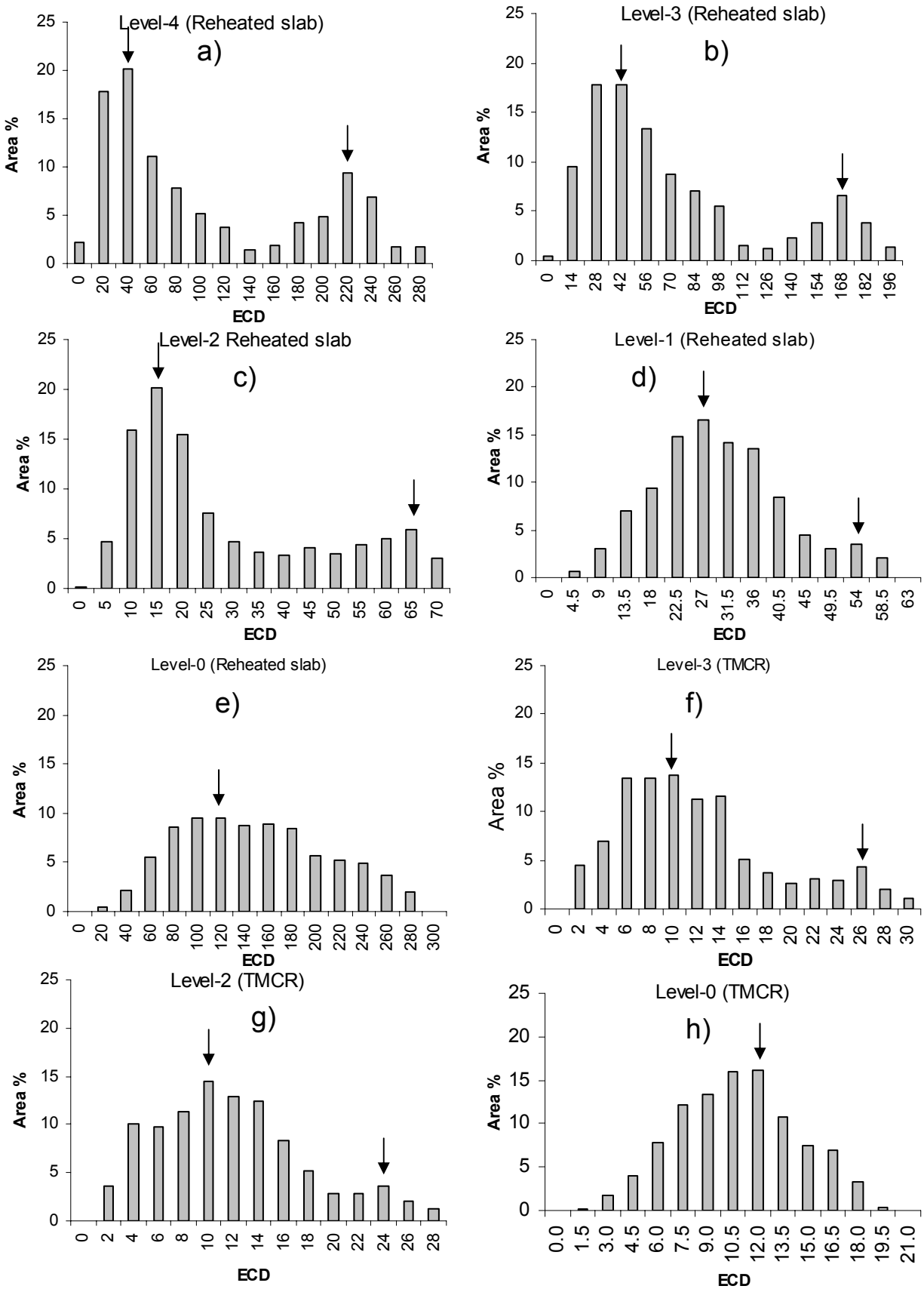

Fig. 5.5: Grain size distributions in area percent based on ECD grain size range scale (15-class) for (a) level-4 (b) level-3 (c) level-2 (d) level-1 and (e) level-0 reheated slab samples and for (f) level-3 (g) level-2 and (h) level-0 TMCR samples. Peaks for the grain size distributions are arrowed. For

each sample same data set were used to plot the distributions based on ASTM G scale, 25-area class scale and ECD-scale.

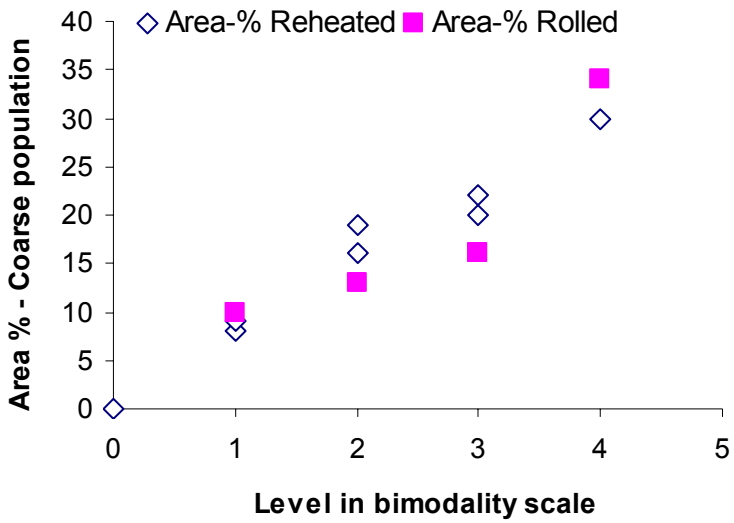

Fig. 5.6: Area-percent of the microstructures (for all samples) covered by 'coarse' population plotted against the corresponding bimodality levels.

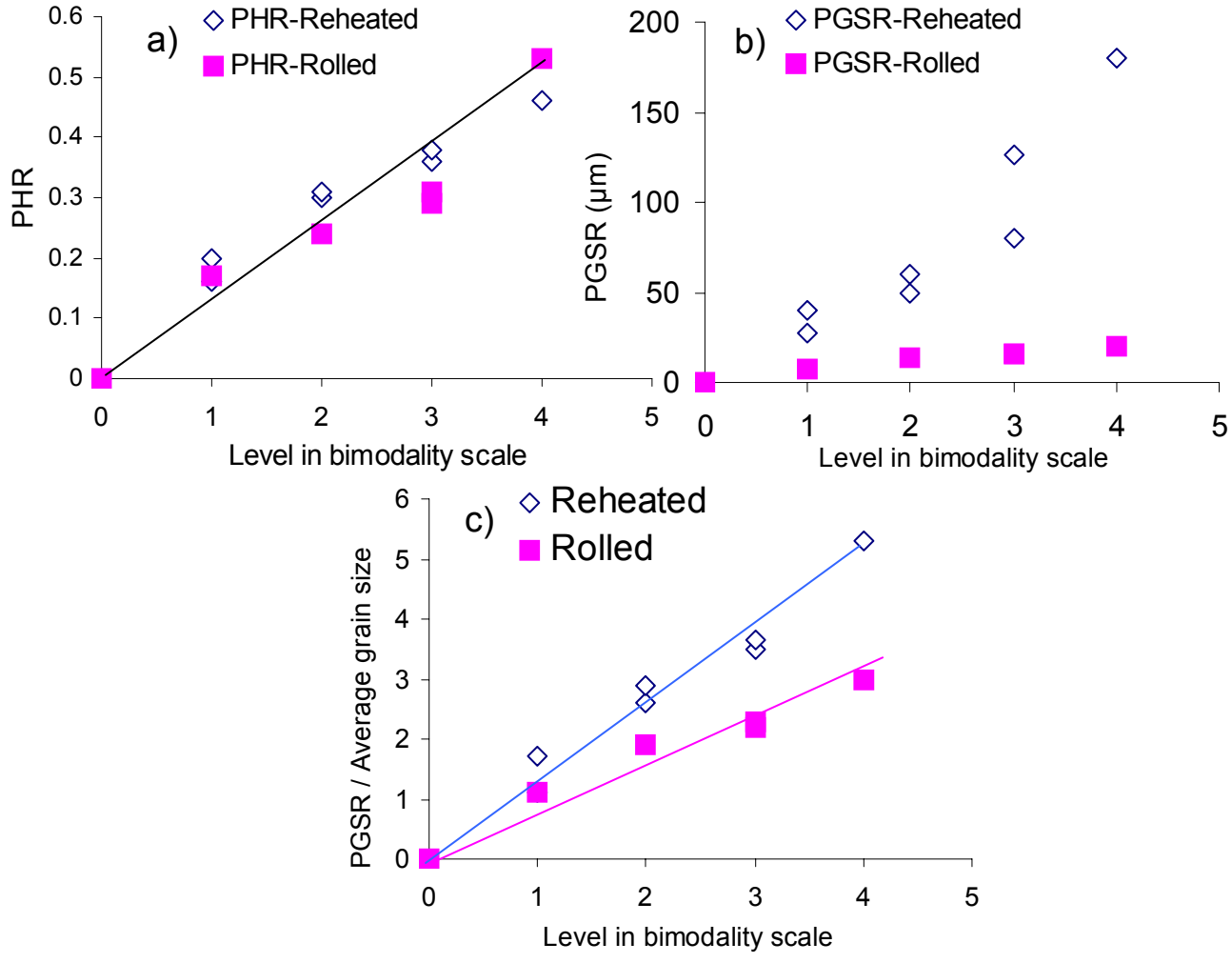

Fig. 5.7: (a) PHR and (b) PGSR (μm) values plotted against the corresponding bimodality levels. (c) Normalised PGSR (PGSR / average ECD-grain size for the corresponding microstructures plotted against bimodality levels. Best-fit lines are shown on (a) and (c).

Table 5.1: Measurement of standard parameters (area–percent of 'coarse' and 'fine' grain populations and corresponding average grain sizes) considering 'intercept method' and 'gap in data' to select the 'breakpoint' from the area-percent grain-size distributions, based on ASTM G scale.

		'Fine' population			'Coarse' population		
Bimodality level	Breakpoint method	Area-%	Average grain size (ASTM G)	Average grain size (ECD)	Area-%	Average grain size (ASTM G)	Average grain size (ECD)
Level – 4 (Reheated slab)	Intercept	43	7.3	32.7	57	3.8	110.0
	Gap in data	71	6.7	40.7	29	1.7	222
Level-3 (Reheated slab)	Intercept	51	7.3	32.7	49	4.2	95.5
	Gap in data	81	6.7	39.7	19	2.5	171.4
Level-4 (TMCR)	Intercept	49	11.5	7.6	51	8.3	23.2
	Gap in data	66	11.2	8.5	34	7.7	27.9

Table 5.2: Comparison of standard parameters (area–percent of 'coarse' and 'fine' grain populations and corresponding average grain sizes) based on the selection of breakpoint following 'gap in data' approach (obtained by analysing the data set and followed in standard and established work) and 'minimum area percent class' approach (obtained from the area-percent grain-size distributions on ECD-scale).

Specimen	Selection of Breakpoint	'Fine' population			'Coarse' population		
		Area-%	Average grain size (ASTM G)	Average grain size (ECD)	Area-%	Average grain size (ASTM G)	Average grain size (ECD)
Level – 1 (Reheated slab)	Gap in data	93	8.1	24.6	7	5.7	57.0
	Minimum area class	91	8.1	24.3	9	5.8	55.0
Level – 2 (Reheated slab)	Gap in data	85	8.6	20.7	15	5.4	61.6
	Minimum area class	84	8.6	20.4	16	5.5	59.5
Level - 3 (Reheated slab)	Gap in data	81	6.7	39.7	19	2.5	171.4
	Minimum area class	82	6.7	39.3	20	2.6	167.6
Level - 4 (Reheated slab)	Gap in data	71	6.7	40.7	29	1.7	222
	Minimum area class	70	6.7	40.3	30	1.8	218.8
Level – 1 (TMCR)	Gap in data	91	11.8	6.8	9	9.2	16.6
	Minimum area class	90	11.8	6.8	10	9.2	16.8
Level- 2 (TMCR)	Gap in data	89	11.4	7.9	11	8.2	23.7
	Minimum area class	87	11.4	7.8	13	8.3	22.9
Level- 3 (TMCR)	Gap in data	85	11.5	7.6	15	7.9	26.1
	Minimum area class	84	11.5	7.5	16	8.0	25.0
Level-4 (TMCR)	Gap in data	66	11.2	8.5	34	7.7	27.9
	Minimum area class	66	11.2	8.5	34	7.7	27.9

Table 5.3: PHR and PGSR values for the all the reheated slab samples and the TMCR plate samples studied with different levels of bimodality.

	Bimodality Level	PHR	PGSR (μm)
Reheated slabs	0	0	0
	1	0.20, 0.16	27, 35
	2	0.30, 0.31	50, 55
	3	0.37, 0.38	126, 80
	4	0.46	180
TMCR plates	0	0	0
	1	0.17	7.5
	2	0.24	14
	3	0.29, 0.31	16, 16
	4	0.53	22

6 Effect of bimodality on toughness

As discussed in **section 2.2** the literature indicates that the presence of a bimodal ferrite grain size distribution can affect the cleavage fracture toughness of commercial HSLA steels [Shehata 1982, Wu 2004a], as the large grain regions within the microstructure facilitate cleavage crack nucleation and growth. However, no data linking the ferrite grain size bimodality and Charpy impact toughness has been reported, although cellular automata finite element (CAFE) modeling results have suggested that the presence of large grains can increase the amount of scatter in the transition regime [Wu 2005]. To gain more understanding about this aspect three-point bend (3PB) tests and Charpy impact tests were carried out, at sub-zero temperatures, in the present study, on heat-treated slab steel (reheat + isothermal hold) and on TMCR steel both comprising bimodal ferrite grain structures. The parameters (PHR and PGSR) suggested for the quantification of bimodality (**chapter 5**) from the grain size distributions have also been related to the fracture toughness (particularly to the scatter in fracture stress) of the steel.

6.1 Low-temperature slow notch-bend tests on idealised microstructures

Chen et al. [Chen 1990] and Wu and Davis [Wu 2004 a] assumed that the distribution of coarse grain sizes in a microstructure (both for uniform and duplex grain structure) determine the scatter in fracture stress, **section 2.2.6**. A duplex or bimodal grain structure can be comprised of coarse- and fine-grain regions arranged in alternate bands. The effect of such duplex ferrite grain structures on fracture has been studied so far for steels [Shehata 1982,

Bhattacharjee 2003, 2004, Wu 2004a], where the narrow grain size distribution (largest grain size, ECD ~ 30-40 μm, [Wu 2004a, 2004b, Shehata 1982]) and the presence of mesotexture [Bhattacharjee 2003] will have reduced the effect of grain size bimodality on the variation in the mechanical properties (**section 2.2.8**). Hence, there is still a need to understand the effect of a bimodal grain size distribution on the scatter in the fracture parameters.

The above discussion inspired the present study to carry out notch-bend fracture tests on simulated (idealised) microstructures with a large grain-size range (larger than the TMCR steel), with 'unimodal' or 'bimodal' distributions and with random texture (i.e. no mesotexture). The comparison of scatter in cleavage fracture stress between unimodal and bimodal microstructures, along with the measurement of cleavage initiating facet size, is expected to provide better understanding on the effect of bimodality, and grain size on fracture. For example it may be possible that a low level of bimodality only has a minimal effect on toughness (level or scatter) thereby enabling a lower acceptable limit of bimodality to be identified.

To understand the effect of grain size variation on cleavage fracture, the measured parameter should be preferably be unaffected by changes in test temperature, specimen geometry, loading type etc. Previous literature indicates that the local cleavage fracture stress (σ_f), which is measured by three-point bend (3PB) or four-point bend (4PB) tests on notched (or pre-cracked) specimens, is the most stable parameter to measure the fracture behaviour of steel [Bowen 1986, Chen 1998, Wu 2004 a] and therefore, is most suitable for studying the effect of grain size variation on fracture.

Chen et al. [Chen 1992] have concluded that in the case of blunt-notched specimens the transfer of a grain sized crack across the grain boundary is the critical step for fracture

and therefore, blunt-notch specimens are a better choice to study the role of grain size on fracture. Hence, the present investigation used blunt-notched three-point bend tests at a sufficiently low temperature (– 160 °C) to ensure complete cleavage fracture.

6.1.1 Microstructure, texture and precipitates of notch-bend samples

Three sets of samples with different idealised microstructures, **Fig. 6.1**, were prepared using simulated (reheat + isothermally hold) heat-treatment. Slab 1-940-700-hold samples (reheated to 940 °C) show a fine-uniform grain structure, **Fig. 6.1 a**, with unimodal (PHR=0, PGSR=0) and narrow grain size distribution (maximum grain size ~ 31 μm), **Fig. 6.1 b**. The distribution is also quite symmetrical with a skew of ~ 1.05. Slab 1-1140-700-hold samples (reheated to 1140 °C) show a duplex grain structure, **Fig. 6.1 c**, where coarse ferrite grain regions are present in between fine-grain regions. The grain size distribution, **Fig. 6.1 d**, indicates the quite bimodal, level 3, structure (PHR=0.33, PGSR=40). The distribution is more skewed (skew ~ 1.99) and wider (maximum grain size ~ 72 μm) than the distributions of TMCR-steels (**Fig. 5.2**), and the difference in grain size between the peaks (or modes) corresponding to the coarse and fine-grain populations (PGSR ~ 40 μm) is also higher than that for TMCR-steels (PGSR ~ 7-22 μm), **Table 5.3**. The separations between two neighbouring coarse grain regions (or fine grain regions) in the bimodal grain structure in the TMCR steel examined lie between ~ 20-50 μm, **Fig. 2.2.9** and **Fig. 5.2,** whilst the separation in slab 1-1140-700 sample is ~ 250-300 μm. The larger difference between coarse and fine grain sizes (due to the wider grain size distribution) and larger separation between coarse and fine grain regions in slab 1-1150-700-hold sample, compared to TMCR samples, means that the notch is more likely to fully sample either the coarse or the fine grain regions in slab 1-

1150-700-hold sample (than in a TMCR sample) which should enhance any effect of bimodality on the fracture properties. Slab 1-1210-700-hold samples show a coarse-ferrite grain structure, **Fig. 6.1 e**, with a wide grain size distribution (maximum grain size ~ 108 μm), which is unimodal (PHR=0, PGSR=0) and less skewed (skew ~ 1.2), although, there is a slightly extended tail towards the right-hand side (coarse-grain sizes).

Optical microscopy as well as SEM confirmed that pearlite was the only second phase present and had a similar range of area-percent (ranging between 12-14 %) in all the samples. This is because all the samples were held at 700 °C (above the bainite transformation temperature) followed by slow furnace-cooling. The size distribution of the inclusions (identified as MnS and Al_2O_3 by EDS analysis), **Fig. 6.2**, was found to be similar in all the samples. This is expected as all the samples were collected from the same location (¼-thickness) of the same as-cast slab (slab 1) and the inclusions were expected to remain unaffected upon reheating to the temperatures used. The measurement of {110}, {100} and {211} gross texture in the bend-test samples revealed that there were no preferred texture components dominating in any of the three sets of samples and the grains within the samples were oriented in a random fashion, **Fig. 6.3**. Therefore, the effect of texture on the fracture stress of notch-bend samples used in the present study is expected to be negligible. Hence, the present study used three sets of samples with uniformly fine, bimodal and uniformly coarse ferrite grain structures, with similar pearlite content, inclusion distribution and random texture.

Microalloy precipitates were studied on the polished + etched surface, **Fig. 6.4**, of each set of bend test samples using high-resolution SEM (both secondary electron imaging, SE, and backscatter electron imaging, BSE) and the size distribution (**Fig. 6.5)**, average size,

number-density (number / mm^2) and composition (using EDS analysis) of such precipitates were measured, **Table 6.1**. Precipitates smaller than ~10 nm could not be viewed clearly under SEM, and therefore, such precipitates could not be studied. The average size of the detectable precipitates (80-122 nm) as well as the largest precipitate size (450-580 nm) for the three sets of samples were within a close range of values, however, they increased with the increase in reheating temperature (from 940° C to 1210 °C), **Table 6.1 and Fig. 6.5**. Conversely the number density of the precipitates decreased (45×10^4 / mm^2 to 10×10^4 / mm^2), as reheating temperature increased, **Table 6.1**.

Thermo-Calc software can be used to predict the stability of precipitates during reheating of slab 1 steel, **Fig. 6.6**. The prediction shows that AlN and complex microalloy carbonitride precipitates gradually dissolve with the increase in reheating temperature above 800 ºC and completely dissolve at ~ 1150-1160 ºC. Palmiere [Palmiere 1994] and Davis and Stangwood [Davis 2002] reported (Nb, Ti)(C, N) precipitates in HSLA steel to remain undissolved (which may be due to micro-alloy segregation resulting in local regions of high microalloying element content and therefore higher precipitate stability) at temperatures 40-70 ºC higher than the equilibrium dissolution temperature for the same precipitates. As-cast precipitates can therefore remain in slab 1-1140-700-hold or even in slab 1-1210-700-hold samples, however, at a lower fraction compared to slab 1-940-700-hold sample. The increase in size and the decrease in number density of precipitates, **Table 6.1**, is due to the dissolution of some of the as-cast precipitates and coarsening of others, at the higher reheating temperatures (1140 and 1210 °C). Within the 1140 °C and 1210 °C reheated samples, the dissolved solutes are expected to be re-precipitated during isothermal holding (700 °C) and slow cooling. The literature suggests the re-precipitation takes place at 700 ºC or below

(along with the austenite to ferrite transformation) as small Nb-rich or V-rich particles (precipitate size < 10 nm), either, in the form of interphase precipitation or random precipitates within transforming austenite [Gladman 1997, Ubhi 1989, Morales 2003, Gunduz 2005]. The number density of such fine-precipitates could not be measured due to their small size, however, these precipitates affect the hardness of the reheated + hold samples (discussed later).

EDS analysis of the precipitates in reheated + hold samples revealed that the majority contain Nb, either individually or combined with Ti, V or Al, **Table 6.1**. Therefore, such precipitates are Nb-rich simple or complex carbonitrides, as expected from Thermo-Calc prediction, **Fig. 6.6**. Apart from Nb-rich precipitates, AlN particles were also found. The fraction of Ti-rich (Nb, Ti)(C, N) increased with the increase in reheating temperature, which also increased the Ti content within the precipitates [(Ti/Nb+Ti)~0.15-0.55], **Table 6.1**. This also indicates dissolution of Nb-rich precipitates as the reheating temperature increased. Coarse cuboidal TiN particles (≥ 1 μm size) are known for their role in initiating cleavage [Balart 2000, Fairchild 2000a, Echeverria 2003] but such precipitates were not found in any of the samples. The largest sized precipitates were (Nb, Ti)(C, N) up to 580 nm in size and such particles were not cuboidal but more rounded (sharp edges were absent). Average size of grain boundary carbides (Fe-C) for all three samples were within 100-200 nm. As mentioned in **section 2.2.4**, Rosenfield and Shetty [Rosenfield 1986] have used the same steel composition (0.1 wt % C-steel with ferrite + ~10-15 % pearlite microstructure) and test conditions (Griffith-Owen specimens, 4PB tested at -130 ºC and 2 mm / min cross-head speed for the measurement of σ_f) as studied by Curry and Knott [Curry 1978] to calculate a lower limit in particle (carbide) size, ~ 0.7 μm (700 nm), below which particles are unlikely

to initiate and control cleavage. This lower limit value can depend on the test temperature and strain–rate. In case of Charpy impact tests, where strain-rate is much higher than slow 3PB or 4PB notch-bend tests, carbide particles can play a vital role in initiating cleavage fracture beside the ferrite grain size, and hence to predict the impact transition temperatures Mintz equations carbide sizes ranging between 200-800 nm have been considered. The steel composition, pearlite level and test conditions used in the present study (3PB specimens tested at -160 ºC at 1 mm / min cross-head speed) are similar to that considered by Rosenfield and Shetty [Rosenfield 1986] and Chen et al. [Chen 1992] (**refer section 2.1.2**) and therefore, the precipitates and grain-boundary carbides within the existing size range are unlikely to play a dominant role in cleavage in the present samples. It has been discussed in **section 2.2.3** that pearlite colonies can also nucleate cleavage fracture, beside the ferrite grains / grain boundary carbides / large precipitates [Knott 1981]. However, the propagation of the crack through the ferrite grains can still be important. Presence of coarse ferrite grains at the neighbourhood of the cracked pearlite can help the crack to grow and the fracture stress can be low. Presence of fine ferrite grains around the cracked pearlite can offer higher resistance to the crack propagation and will result in higher fracture stress. Hence, the variation in cleavage fracture stress for the present samples can be directly related to the ferrite grain size variation within the microstructures.

The present investigation aims to compare the scatter in fracture stress for the bimodal grain size distribution to that for the uniformly fine and uniformly coarse grain size distributions, so that the effect of bimodality on fracture can be identified.

6.1.2 Variation in principal fracture stress (σ_F)

To predict the yield strength for the three-sets of samples at –160 °C, hardness measurements were taken at that temperature by keeping the specimens within a specially insulated chamber and maintaining the specimen temperature by liquid nitrogen (temperature variation: ± 2 °C). The measured hardness values (H_v), along with the predicted yield strength (σ_y) (using, $\sigma_y = 3.13 \times H_v$ [Zhang 2000a]) for each set of samples, are listed in **Table 6.2**. The small increase in hardness with the increase in reheat temperature from 940 °C to 1140 °C (for slab 1-940-700-hold and slab 1-1140-700-hold sample), **Table 6.2**, in spite of the grain growth, could be due to the dissolution of some of the as-cast precipitates (Nb- and V-precipitates from the as-cast steel), **Fig. 6.6**, and subsequent re-precipitation in a finer form (less than 10 nm size precipitates that contribute to precipitation hardening) [Gladman 1997, Ubhi 1989, Morales 2003, Gunduz 2005] during isothermal holding and slow cooling. The small drop in hardness with the further increase in reheat temperature from 1140 °C to 1210 °C (for slab 1-1140-700-hold and slab 1-1210-700-hold sample) could be due to the fact that the decrease in hardness due to the increase in grain size has a more dominant effect than the increase in hardness due to the fine precipitate formation.

The general yield load, P_{GY}, **Table 6.2**, calculated from the σ_y was used in **Fig. 4.8** to determine the principal fracture stress, σ_F, **Table 6.3**. The fracture load values were obtained from the digitally recorded (also checked by analog chart) load- vs. -displacement values, Appendix-I. **Table 6.3** shows that the scatter (in standard deviation, s.d.) in σ_F values is highest for slab 1-1140-700-hold samples (s.d. = ± 132 MPa, i.e. ~ 7 % of the mean σ_F of 1767 MPa), followed by slab 1-1210-700-hold (s.d. = ± 104 MPa, i.e. ~ 5.5 % of the mean σ_F of 1756 MPa) and slab 1-940-700-hold (s.d. = ± 58 MPa, i.e. ~ 3.3 % of the mean σ_F of 1860 MPa) samples. The possible experimental errors in the present investigation are similar to

that reported by Wu and Knott [Wu 2004 b], **Table 2.2.1**. From **Table 2.2.1** the possible total experimental error was calculated to be ± 80 MPa, with the s.d. ~ 2.5 % of the mean fracture stress value (~1500 MPa). Therefore, the scatter in σ_F for slab 1-940-700-hold samples is close to the experimental limit, whereas, for the other samples the scatter is much higher than that limit. σ_F values in **Table 6.3** and **Fig. 6.7** for the slab 1-1140-700-hold samples may be due to the bimodal grain size distribution since the narrower and more uniform grain size distribution in slab 1-940-700-hold samples leads to a minimum variation in fracture stress values and, whilst the slab 1-1210-700-hold samples have the largest range of grain size values the distribution is unimodal and the variation in fracture stress is less than that of the slab 1-1140-700-hold samples. However, the measurement of σ_F is based on the assumption that cleavage originates at the point ahead of the notch-root where the maximum principal tensile stress reaches the highest value, and that is not always true. The local fracture stress, σ_f, considers the actual distance of the cleavage initiation site from the notch-root and represents the local tensile stress, required for the propagation of a crack across the grain boundary (critical step for fracture) to cause fracture. Therefore, σ_f is a more accurate measure of the effect of microstructure on the fracture behaviour and needs to be studied.

6.1.3 Variation in local fracture stress (σ_f)

To determine the cleavage initiation site in the bend test samples, the fracture surfaces of all the samples were studied under SEM. For each sample, tracing the river lines back to the cleavage origin identified the fracture initiation site, **Fig. 6.8**. The minimum distance of the initiation site from the notch root and the facet size at the cleavage origin was measured. The perpendicular distance (in μm) of the initiation sites (I.S) from the notch root are listed

in **Table 6.4**. The local fracture stress (σ_f) values measured using that distance from the Griffith-Owen stress distribution, **Fig. 2.2.5**, are also given in **Table 6.4**. **Fig. 6.9** shows the σ_f values for the three-sets of samples against the corresponding distance of cleavage initiation sites from the notch-root. The cleavage initiation sites in most of the samples (~ 82 %) are within 200-500 μm distance, which is considered as the active zone [Wang 2002], as within that distance the maximum principle stress (σ_1) reaches the highest value. For a couple of samples of slab 1-1210-700-hold steel, the fracture stress values are low (1246 and 1424 MPa) and for those two samples the initiation sites are also far from the active zone (100 μm and 1214 μm, respectively). At the initiation site for those two samples ~ 4 μm sized MnS inclusions have been found, **Fig. 6.10**. For all other samples inclusions were not present at the cleavage origin. As inclusions played a dominant role in the fracture for those two samples, the samples can be discounted from the consideration of grain size distribution on fracture. That makes the characteristic distances within 200-500 μm for ~ 85 % of all the specimens tested, which is the same have as observed by Wang et al. [Wang 2002] for C-Mn and C-Mn-Ti steels (0.07-0.18 C, 1.24-1.6 Mn, 0-0.02 Ti).

From 3PB tests (at –196 °C) on a heat-treated (homogenized at 900 °C for 2 hr. and air-cooled) C-Mn steel (0.18 C, 1.49 Mn, 0.36 Si) with ferrite + pearlite structure Wang et al. [Wang 2002] have found that σ_f (local fracture stress) values usually lie within the range $(0.8\text{-}1.0)\times\sigma_F$ (where, σ_F is principle fracture stress). This was found to be true in the present study for all the samples listed in **Table 6.5**. Average σ_f values are within the range (0.90-0.95)×(average σ_F), **Table 6.5**, which is also close to the range, [average σ_f = (0.90-0.94)×(average σ_F)], reported by Wang et al. [Wang 2002]. Therefore, the principle and local

fracture stress values measured in the present investigation follow a similar trend to that reported earlier, and that verifies the validity of the experimental results.

From 4PB tests at –130 °C on blunt-notched C-Mn steel (heat-treated specimens with ferrite + pearlite microstructures) specimens, Chen et al. [Chen 2004] have concluded that notch-toughness ($Q = \sigma_f/\sigma_0$) increases with the decrease in grain size and is independent of the carbide particle size. Similarly, in the present investigation the notch-toughness (Q) increased (slab 1-1210-700-hold < slab 1-1140-700-hold < slab 1-940-700-hold), with the decrease in average grain size, **Fig. 6.11 a**. The individual notch toughness values of the samples, **Table 6.4**, also fall within the range of values (~ 1.5-3.0) reported by Chen et al. [Chen 2004]. This shows that in the present investigation ferrite grain size plays a vital role in controlling the fracture toughness. As mentioned by many previous investigations the average fracture stress increases with the decrease in average grain size (D) in the microstructure [Knott 1973, Ritchie 1974, Curry 1979] (**Fig. 2.2.3**), and such a relationship also holds for the samples tested here, **Fig. 6.11 b**. However, the interest of the present investigation lies in the variation in σ_f, **Fig. 6.12**, rather than the average values.

Discounting the samples where inclusions initiated cleavage, the effective scatter (in standard deviation, s.d.) in σ_f values for slab 1-1210-700-hold samples (s.d. = ± 56 MPa, i.e. 3.6 % of the mean σ_f value of 1594 MPa) becomes similar to that for slab 1-940-700-hold samples (s.d. = ± 64 MPa, i.e. 3.5 % of the mean σ_f value of 1743 MPa), **Fig. 6.12**, and both fall close to the range of possible experimental error (s.d ~ 2.5 % of the mean fracture stress value). These values of scatter are much lower than that for slab 1-1140-700-hold samples (s.d. = ± 131 MPa, i.e. 7.8 % of the mean σ_F value of 1767 MPa) which exceeds the experimental error by a long way. Therefore, the local fracture stress (σ_f) values show a

greater degree of scatter for the bimodal grain structure (slab 1-1140-700-hold) compared to the unimodal grain structures (slab 1-940-700-hold and slab 1-1210-700-hold). The σ_f values for slab 1-940-700-hold samples lie within a narrow range, whereas, the values for slab 1-1140-700-hold can be divided into two groups separated by ~ 250 MPa (between average values for the two groups, 1746 MPa and 1496 MPa), **Fig. 6.12**. To understand the effect of grain size variation on the variation in $\sigma_{f,}$ and whether there is any significance to the 'two groups' of σ_f data for the bimodal grain structured samples, the cleavage originating facet size values were determined from fractographic study.

6.1.4 Role of grain size on the variation in fracture stress

The size of the cleavage facets at the fracture origin (i.e. the first facet size) for all the samples, along with the corresponding σ_f values, are listed in **Table 6.5**, and are related in **Fig. 6.13a**. **Fig. 6.13a** shows that the first facet size becomes larger as σ_f decreases. Such a relationship is expected as: (i) grain size is controlling the cleavage fracture, and therefore, σ_f varies proportionally against $D^{-1/2}$ (where, D is the 2Dim grain size) and (ii) facet size is proportional to the grain size. In the absence of any texture component (as is the case for the reheat + hold samples) it is unlikely that the small grains will join together to form large effective grains and result in large facet sizes, as has been seen for a TMCR sample with high mesotexture [Bhattacharjee 2003]. Hence, facet size values can be taken as the 3Dim grain size. The propagating cleavage crack samples the 3Dim grain size. Also the shape of the grains is mostly polygonal (aspect ratio: 0.8-0.9) in the reheat + hold samples. Therefore, the grains can be assumed to have a tetrakaidecahedral shape and a factor 1.61 can be used to calculate 2Dim grain size [Gladman1997] as: (2Dim grain size) = (3Dim grain size / 1.61).

Fig. 6.13b shows the increase in σ_f with $(D_F)^{-1/2}$, where, D_F is the cleavage initiating grain size calculated from the first facet size. The predicted cleavage initiating grain size (D_F) values are also superimposed on the corresponding grain size distribution for all three sets of samples in **Fig. 6.14**.

Chen et al. [**Chen 1990**] have concluded that the scatter in σ_f is caused by the distribution of grains within the most coarse grain group in the microstructure, and that covers around the top 5 % of all grain sizes (by number) (refer **section 2.2.6**). The present results indicate that top 10-15 % of grains (by number) in terms of grain size take part in initiating cleavage fracture. In TMCR steels with duplex ferrite grain structure Wu and Davis [Wu 2004a] have related the σ_f values to the large ferrite grains within the coarse grain patches in the microstructures and used the coarse ferrite grain size distribution to predict the variation in σ_f, **Fig. 2.2.8** (refer **section 2.2.5**). **Fig. 2.2.8** shows that the higher the frequency of occurrence of a particular 'coarse grain size' within the microstructure (i.e. higher the frequency in grain size distribution), the higher its probability to initiate cleavage fracture.

Wu and Davis [Wu 2004a] have constructed the coarse-grain size distribution by setting a lower threshold limit of 6 μm for the measurement of grain size within the coarse grain patches. The selection of coarse grain patches within the microstructure is subjective and the selection of a lower threshold limit (the 6 μm value) appears rather arbitrary. Even within the fine grain region there can be a grain greater than 6 μm in size that could take part in nucleating cleavage. The relations between coarse grain size in the microstructure and fracture parameters (fracture stress or ITT) are widely discussed in the literature. Not only Wu and Davis [Wu 2004a] but also several other studies [From 1999, Shehata 1982] have considered a lower grain size threshold to establish such relations. For example, in the case

of controlled rolled HSLA steels with mixed (coarse + fine) ferrite grain structure From and Sandstrom [From 1999] considered a 10 μm grain size as the threshold; and Shehata and Boyd [Shehata 1982] set the threshold as the grain size ≥ 75 % of the largest grain size. However, these threshold values will depend on the number of grains measured and on the number of tests conducted. Hence, the selection of threshold grain size (as the lower cut-off) is also subjective. In the present investigation a less subjective method to explain the variation in fracture parameter is considered using the overall grain size distribution constructed by the measurement of a large number of grains (> 1000 grains) over a region comprised of both the coarse- and the fine-grain patches.

6.1.5 Relation between the cleavage originating grain sizes and the grain size distribution

The position of the cleavage initiating-grain sizes (D_F) on the grain size distributions, **Fig. 6.14**, needs to be explained to identify the grain sizes, or part of the grain size distribution that usually initiates and controls cleavage. This can then be used to understand the scatter in fracture stress for the bend test samples, **Fig. 6.12**.

6.1.5.1 Slab 1-940-700-hold

For the case of the fine uniform grain structure of slab 1-940-700-hold samples, the cleavage originating grain sizes (D_F) fall within the range ~ 17-26 μm, which is higher than the grain size range (14-16 μm) corresponding to the mode of the grain size distribution, **Fig. 6.14a**. The smallest grain size that initiates cleavage (i.e. $D_F \approx 17$ μm) is still larger than ~ 85 % of grains (by number) present within the microstructure and ~ 55 % of the total grain area.

Therefore, large grains are responsible for cleavage, which is supported by the study of Echeverria and Rodiguez-Ibabe [Echeverria 2003], who have observed that on the cleavage fracture surface ~ 70 % of the facets are smaller than those responsible for brittle fracture initiation. The area-percent columns within 17-26 μm grain size vary from ~ 9.9 % to 5.0 %, **Fig. 6.1 b & Fig. 6.14 a**. The grain size distribution in **Fig. 6.1 b**, shows that there are grains of larger size (> 28 μm), however, at much lower frequency. These large grains do not take part in nucleating cleavage, within the limited number of samples (11 samples) tested due to the low probability of their being in the 'active zone' during 3PB testing. Around 38 % of all the grains (by area) are sized between 17-26 μm in the microstructure, and hence, those grains are responsible for the variation in fracture stress. Therefore, it appears that the grains which are sufficiently large in size (larger than the mode value) and cover sufficient area-percent within the microstructure (i.e. high probability of sampling within the active zone) usually control cleavage. The same concept was suggested by Chen et al. [Chen 1990] and Wu and Davis [Wu 2004a] that the probability of a grain size (or grain size range) controlling cleavage fracture depends on two factors: (a) the grain size has to be sufficiently large, and (b) a sufficiently large number of grains within the microstructure should belong of that particular grain size (i.e. sufficiently high probability of occurrence). High probability of occurrence increases the chance of sampling a particular grain size at the notch-root.

6.1.5.2 Slab 1-1210-700-hold

In the slab 1-1210-700-hold samples, with uniformly-coarse ferrite grain structure, all D_F values lie towards the coarser half of the ferrite grain size distribution (i.e. grain sizes larger than the mode-size range, 49-56 μm), **Fig. 6.14 c**. The smallest D_F value ($D_F \approx 53$ μm)

is still larger than ~ 85 % of all the grain sizes (by number) and ~ 67 % of grain area. Cleavage initiating grain sizes (D_F) for most of the samples (except for the discounted samples) fall within the range 53-77 μm, which is higher than the grain size range corresponding to the mode value. Around 31 % of all the grains (by area) fall within the 53-77 μm size range and take part in cleavage initiation.

Therefore, in the case of the coarse uniform grain structure it can be concluded that usually the large grains (larger than the mode grain size), which are sufficiently available (high area-percent, > 4%) within the microstructure, control cleavage fracture. However, in case of the discounted samples (samples with 1424 MPa and 1246 MPa local fracture stress) very large grains (grain size ~ 102 μm and ~ 111 μm, respectively), which were present with a very low area-percent within the grain size distribution, **Fig. 6.1**, have been found at the cleavage origin with large MnS inclusions also present within those grains, **Fig. 6.10**. Therefore, the presence of large inclusions within large grains created a suitable combination for failure that cleavage was initiated far away from the active zone, at a much lower value of local fracture stress, σ_f, by the mechanism of inclusion initiated cleavage [Echeverria 2003, Zhang 2000a].

Theoretically, the largest grain size in the microstructure if present at the cleavage origin could result in lowest value of fracture stress, σ_f. **Fig. 6.13** and **Fig. 6.14** (**a and b)** indicate that the highest value of σ_f can be obtained when cleavage is initiated by a grain size slightly greater than the 'mode' of the grain size distribution. Ignoring the sulphide initiated cleavage, the fracture at lowest σ_f can be initiated by the largest grain size that occupies ≥ (4-5) % microstructural area, **Fig. 6.14 a** and **b**. Hence, there may be a possibility to predict the scatter (highest and lowest values) in σ_f, for similar number (~10) of tests conducted, using

these two grain sizes. There is a need to check this possibility for other microstructures and for larger number of tests to see if this is still valid, or lower σ_f can be found than the lowest expected due to the participation of very large grains (close to largest size in distribution) in cleavage.

6.1.5.3 Slab 1-1140-700-hold

For the slab 1-1140-700-hold samples the principle (σ_F) and local fracture stress (σ_f) values can be separated into two clusters or two groups: (i) high-stress group and (ii) low-stress group, indicated by dotted ovals in **Fig. 6.7** and **Fig. 6.12**, and this may be explained from **Fig. 6.14 b**. **Fig. 6.14 b** indicates that the existence of two fracture stress groups may be due to the involvement of grain sizes belong to two separate populations, fine-population and coarse-population, of the overall grain size distribution. Cleavage fracture within the high-stress group of samples (σ_f values 1666-1864 MPa), was initiated by grain sizes ranging between 29-42 μm. That grain size range falls within the fine-population of the grain size distribution, being larger than the grain size corresponding to the mode (20-25 μm) of the fine population, **Fig. 6.1d**. Within the microstructure 29 % of all the grains belong to the size range between 29-42 μm and are taking part in cleavage. Overall, the smallest D_F value ($D_F \approx$ 29 μm) is still larger than ~ 89 % of all the grain sizes (by number) and ~ 68 % of grain area, and therefore, even in the bimodal distribution larger grains nucleate cleavage.

Conversely, cleavage within the lower-stress group (comprised of three samples showing lower σ_f values, 1462-1520 MPa) was initiated by 55-64 μm grain sizes, **Fig. 6.14 b**. That grain size range belongs to the coarse population (coarse population mode ~ 60 μm) of the distribution and covers 13 % of the all the grains (by area), **Fig. 6.1d**. Grain sizes

between 43-54 μm are not taking part in nucleating cleavage probably due to their low frequency of occurrence (only ~ 6 % or less by area within the microstructure).

The presence of the coarse-population (with a second distribution mode, at higher grain sizes than the first mode) in a bimodal grain size distribution, therefore, increases the availability (area-percent frequency) of large grain sizes within the microstructure, and that increases the probability of sampling those large grains at the notch root. Those large grains are taking part in initiating cleavage fracture and result in low fracture stress values. Hence, it appears that the presence of the coarse-population within the bimodal grain size distribution is responsible for the few low fracture stress values (due to larger grain sizes within the coarse populations initiating fracture) and that increases the overall scatter in fracture stress (with the scatter far exceeding the range of possible experimental error). The above discussion suggests that not only the large grains from the fine population take part in initiating cleavage but also the grains belonging to the coarse population take part in cleavage. This means the Wu and Davis approach [Wu 2004a] of only considering the 'coarse grain' patches to predict the scatter in σ_f is not appropriate for a very bimodal grain structure and will predict lower scatter than observed.

Previous researchers indicated that in commercially rolled HSLA steels a single cleavage facet can be made of more than one ferrite grains, or bainitic laths, with low misorientation between them [Shehata 1982, Bhattacharjee 2003, Kim 2003]. Such a situation is not considered in the present study, for the idealised microstructures, due to the random orientation of the grains. However, OIM studies need to be carried out in future on the cleavage facets of fractured samples to be sure about that.

6.1.6 Conclusions derived from notch-bend test results

The following conclusions, with respect to the role of grain size distribution and bimodality on fracture stress values, can be drawn from the results of the notch-bend tests:

1) In the samples tested the smallest grain size that initiates cleavage (D_F) is larger than ~ 85-90 % of grains (by number) present within the microstructure. Therefore, top 10-15 % of grains (number-percent) in terms of grain size initiate cleavage.

2) The grain sizes that initiate cleavage fracture cover sufficient area-percent (≥ 5 %) within the microstructure, and therefore, can be frequently sampled at the active zone.

3) For the case of the bimodal grain structure not only the large grains of the fine population but also the grains belonging to the coarse population take part in cleavage. That resulted in a separation of σ_f values into two groups, leading to a higher scatter in σ_f values compared to the uniform grain structures.

6.1.7 Indications from the bend test results for the measurement of bimodality

One of the purposes behind the fracture study in the current work is to identify what aspects of the bimodal grain size distribution affect the fracture toughness. Following the discussion on the effect of grain size on notch-bend test results in **section 6.1.5**, the unimodal grain size distribution is unlikely to generate high scatter in fracture stress results. The presence of the coarse population in the grain size distribution of slab 1-1140-700-hold steel has been shown to result in low fracture stress values in a few samples (3 out of 11) and that may increase the overall scatter (in terms of standard deviation, s.d, or s.d / mean value in percentage) in fracture stress. Besides increasing the scatter the low fracture stress values can also drop the average fracture stress of the steel. The increase in scatter or the drop in average

fracture stress may become more / less severe with an increase / decrease in the severity of bimodality. The need for measurement of bimodality has been discussed earlier in **section 2.2.8** and two parameters (PHR and PGSR) have been suggested to measure the severity of bimodality in **Chapter 5**.

It also appears from the above discussion that most of the grains that initiate cleavage are not only large in size (larger than the mode-grain size) but also belong to the grain size range that covers sufficient area-percent in the microstructure (> 5 %). Keeping that in mind the possibility of scatter in fracture stress for various imaginary grain size distributions, **Fig. 6.15**, can be identified. The scatter can be represented in various ways, the range between highest and lowest values, the s.d or the s.d/mean value in percent. Due to the presence of separate coarse population the bimodal grain size distribution, **Fig. 6.15 b** (as in slab 1-1140-700-hold**),** is expected to generate higher scatter (s.d. or s.d./mean) compared to the unimodal distribution, **Fig. 6.15 a** (as in slab 1-940-700-hold**)**. Increase in PHR and PGSR (i.e. the increase in bimodality level) basically represent the increase in the area-fraction (**Fig. 6.15 c)** and size (**Fig. 6.15 d)** of the coarse-grain population, respectively, compared to the fine-grain population. If PGSR remains the same, an increase in PHR (**Fig. 6.15 c**), can increase the chance of getting low fracture stress (σ_f) values further (by increasing the probability of sampling larger grains) and therefore, can increase s.d. (or s.d. / mean), although, the range of σ_f values remains the same. An increase in PGSR (**Fig. 6.15 d**) can increase the s.d. (or s.d. / mean) as well as the range of values. Considering the above discussion measurement of PHR (peak height ratio) and PGSR (peak grain size range) parameters may be useful not only for the quantification of bimodality but also for the prediction of scatter in fracture toughness. The area-percent of grains within the coarse population (compared to the area-percent of

grains within the fine population) is a factor of importance in this context; however, the measurement of area-percent occupied by the coarse population is not as simple (refer to **Chapter 5** for details) as the measurement of PHR.

In **Chapter 5** the initial visual classification of bimodality into levels 0-4, whilst subjective and operator dependent, has been shown to be related to PHR and PGSR values, which are independent and can be used to rank the severity of grain size bimodality in steels (**chapter 5**). Using the notch-bend test results from the present study (for reheat + hold microstructures) as well as the results reported by Wu and Davis [Wu 2004a] (for TMCR steel) the scatter (standard deviation values) in fracture stress can be related to the bimodality level (visual classification and PHR) of the corresponding microstructures, **Fig. 6.16**. Whilst care must be taken when making recommendations based on limited data sets, **Fig. 6.16** indicates that the scatter in fracture stress increases with an increase in bimodality level. PHR and PGSR quantify bimodality levels, and therefore, can be related directly to the scatter in fracture stress. Further studies are necessary to fully quantify the effect of different levels of bimodality on fracture toughness (and Charpy impact toughness) and hence, to specify the levels of PHR and PGSR for the manufacturers to control to ensure consistent product properties.

6.2 Effect of bimodality on the properties of TMCR steel

Notch-bend tests on idealised microstructures indicate that larger grains that are present at sufficiently high area-percent within the microstructure promote cleavage fracture and the bimodal grain size distribution shows higher scatter in fracture stress, compared to the unimodal distribution. However, the final product is the rolled (TMCR) plate and the

effect of bimodality on the properties of TMCR steel matters the most. Toughness can be measured using various parameters, such as local fracture stress (σ_f), plane-strain fracture toughness (K_{IC}), Charpy impact toughness (Impact energy and fracture appearance), crack tip opening displacement (δc) etc. Out of these the Charpy impact test is the most common and industrial measure of fracture toughness for TMCR steel. However, to understand the effect of bimodality on the Charpy toughness of TMCR steel, the possible effect of bimodality on the σ_f and K_{IC} of the same steel need to be discussed.

6.2.1 Possible effect of bimodality on σ_f of TMCR steel

The notch-bend test results on simulated (reheat + hold) samples indicated that grain size bimodality can affect the toughness of steel negatively by generating higher scatter in fracture results. For those notch-bend test samples the plastic zone sizes can be determined from the Griffith-Owen stress distribution (using the elastic-plastic boundary), **Fig. 4.7**. The plastic zone sizes ahead of the notch root for the slab 1-1150-700-hold samples vary between ~ 500-1200 μm (average ~ 900 μm). Therefore, the plastic zone covers ~ 4-6 grain size (coarse and fine grain) regions, as each grain size (coarse or fine) region in slab 1-1150-700-hold is ~ 150-200 μm wide. The cleavage initiation sites for all the tested samples fall within the plastic zone. However, within the plastic zone lies the active zone, which can be defined by two different ways. First, the stress criterion, which says that the active zone is the region ahead of the notch-root, where the maximum principle stress (σ_1) exceeds the local fracture stress (σ_f) and second, the active zone can be defined by the stress-strain dual criterion [Mendiratta 1996, Wang 1998, Zhang 2001, Wang 2004], which requires a critical plastic strain ($\varepsilon_p \geq \varepsilon_{pc}$) for initiating a cleavage crack (crack nucleated by the movement of

dislocations or twins around a second phase particle or at the phase boundary) and a critical tensile stress ($\sigma_{yy} \geq \sigma_f$) for its propagation (initially through the particle-ferrite boundary and then the ferrite grain boundary), **Fig. 6.17**. Whatever is the definition of active zone, the low temperature (-196 ºC) notch-bend (3PB) test results (on C-Mn steel with ferrite-pearlite structure) indicated that it spreads over ~ 200 μm to 500 μm ahead of the notch-root [Wang 2002].

The active zone width, (500-200) μm ≈ 300 μm [Wang 2002], therefore, is similar to the separation (200-300 μm) between two neighboring coarse-grain regions (or fine-grain regions) in slab 1-1150-700-hold sample and therefore, along the notch length at each location only one or two grain size regions (coarse and / or fine-grain region) can lie within the active zone. Depending on the location of those regions either a grain (or group of grains) from coarse-grain region or a sufficiently large grain (or grains) from the fine grain region (that is still smaller than the grains from coarse grain regions) can act as the weakest link for cleavage crack propagation. The cleavage crack propagating grains also occupy sufficiently higher area fraction in the microstructures so that those grains are sampled within the narrow active zone. Combination of all the above factors result in a higher scatter in fracture stress for notch-bend test samples with bimodal grain structure compared to unimodal grain structure.

The bimodal microstructures of TMCR steel, **Fig. 5.2**, show that the separation between two neighbouring coarse (or fine) grain regions was between 30-50 μm, approximately. Therefore, each grain size band is ~ 15-30 μm in width. Hence, for the notch-bend tests the active zone (~ 300 μm) is much wider in size than an individual grain size band. The active zone can, therefore, sample a large number of coarse grain bands in the

bimodal TMCR structure and will include a large sized grain at the cleavage origin (from any of the coarse grain region), even if the volume fraction of that grain size is low. As a result, the notch-bend test on TMCR steel with bimodal ferrite grain sizes can produce lower fracture stress values, than that expected from the average grain size of the microstructure (as usually the very large grain sizes will initiate cleavage). The overall scatter, however, will also be lower than the notch-bend results on idealised microstructure. Slow notch-bend test at low-temperature (say, less than -100 ºC) is not a commercial (quality-control) practice for TMCR plates and hence, hasn't been carried out in the present study. Due to the same reason plane-strain fracture toughness (K_{IC}) hasn't been studied here however, the possible effect of a bimodal TMCR structure on K_{IC} is worth discussing.

6.2.2 Possible effect of bimodality on K_{IC} of TMCR steel

Ritchie et al. [Ritchie 1974] postulated that for plane-strain fracture toughness tests the cleavage fracture stress of steel had to be exceeded over some microstructurally significant characteristic distance ahead of the notch-tip before fracture could occur. Detailed crack tip stress analysis was carried out to examine the relationship between toughness, yield stress, fracture stress, and the characteristic distance. The temperature dependence of K_{IC} of mild steel was accurately predicted by assuming this distance to be equal to two grain diameters. If the same holds true for TMCR steel, then depending on whether the coarse or fine grain band is sampled at the notch-tip in a bimodal microstructure (with alternate coarse and fine bands), K_{IC} may vary. If the fine grain band is sampled at the notch-tip within the characteristic distance, then the fine grains will offer higher resistance to fracture, requiring higher local stress for the crack to propagate across the grain boundary and resulting in

higher K_{IC}, compared to a coarse grain band at notch-tip. In a recent publication Knott [Knott 2007] summarized the possible effect of spatial variations in microstructure on the fracture toughness results. He suggested that no engineering material is truly homogeneous and spatial heterogeneity must be present in different forms, such as inhomogeneous distribution of non-metallic inclusions, spatial distribution of pearlite and ferrite, or of fine and coarse grain sizes (and crystallographic texture) arising from a combination of inhomogeneous plastic deformation (during working) and inhomogeneous distribution of carbide pinning particles. Spatial distribution of major alloying elements can influence phase transformation and the toughness of transformed microstructures, through their effect on hardenability. Knott [Knott 2007] concluded that spatial heterogeneity can lead to wider than normal scatter in fracture toughness results (both local fracture stress values obtained from low temperature-slow notch bend test and K_{IC} values obtained from plane-strain fracture toughness test) depending on the local microstructure sampled at the 'critical distance' ahead of the notch root. Cumulative probability distribution of σ_f and K_{IC} values can even show a bimodal distribution in the case of spatially heterogeneous structures [Knott 2007] (as found in mixed bainite + martensite microstructure with a systematic variation of proportion of bainite, from 15 % to 45 %, over a wavelength of 250-500 μm [Zhang 1999]). Following this discussion a bimodal ferrite grain size distribution in TMCR steel is expected to cause higher scatter in K_{IC} compared to uniform grain structure, however, the extent of this scatter would need to be studied in the future.

6.2.3 Possible effect of bimodality on Charpy toughness of TMCR steel

The variation of Charpy impact energy (CVN-energy) with temperature (**Fig. 2.2.1**) can be divided into three regions: (i) upper shelf energy (USE) region (ii) impact transition (IT) region and (iii) lower shelf energy (LSE) region.

6.2.3.1 Effect of bimodality on USE region

In the upper shelf energy (USE) region for the TMCR steels fracture occurs completely in a ductile mode, i.e. the fracture appearance shows ~ 100 % ductile fracture. Vodopivec [Vodopivec 2003] calculated the plastic zone size ahead of the Charpy notch-tip (root radius, ρ = 0.2 mm) at room temperature (+20 ºC, where, 100 % ductile fracture have been found) for 0.17 wt % C steel (other elements, 0.32 Si, 1.28 Mn, 0.02 P, 0.01 S, 0.045 Al, all in wt %), with ferrite + pearlite microstructure, to be in the order of 1.48-1.76 mm (1480-1760 μm). The plastic zone in TMCR steel (expected to be similar to that calculated by Vodopivec [Vodopivec 2003]), therefore, will sample a large number of coarse and fine grain bands (say, ~ 50-80) but the stress within that zone, however, will remain insufficient to initiate cleavage fracture. As a result, the failure will occur in a ductile mode (similar to the room temperature tensile test of TMCR steel) by the slow and stable propagation of the notch due to the nucleation, growth and coalescence of micro-voids resulting from the plastic deformation of the entire cross-section of material sampled. Qiu et al. [Qiu 2006] compared the Charpy impact energy transition in 0.10 C-1.43 Mn-0.31 Si (all wt %) steel (as-rolled and rolled + reheated + annealed samples) over + 40 to - 40 ºC temperature ranges for unimodal and bimodal ferrite grain structures, with different average grain sizes (4-10 μm), similar to the TMCR steel. In the bimodal ferrite grain structure [Qiu 2006] the separation between two neighboring coarse (or fine) grain size regions (~30-35 μm) is also in the similar range (~ 30-

50 μm) as observed in the commercial TMCR steel. Qiu et al. [Qiu 2006] found that the numerical-average grain size controlled the USE and the effect of bimodal grain structure on USE was insignificant. The same has been found true for the room temperature strength of the steels. Hence, complete ductile failure depends on the average grain size, and the bimodality in grain size distribution is unlikely to generate scatter in USE values (possibly due to the large plastic zone size, which is the sampling volume in USE region).

The effect of sampling volume in each specimen on the properties of a bimodal grain structure can be best understood by comparing the through thickness Vickers macro-hardness (20 kg) profile measured on (bimodal) TMCR-1 steel plate (5 hardness readings taken at each location), in the present study, **Fig. 6.18**, and through thickness micro-hardness values separately measured within the coarse-grain and the fine-grain bands of two TMCR steels (Com-A and Com-B) by Wu and Davis [Wu 2004a], **Fig. 6.19**. Both the Com-A and Com-B plates are similar to TMCR-1 in terms of composition, processing and bimodality. The smaller micro-hardness indent size, 13-15 μm (which is the sampling size in this case), compared to the width of a single grain size band (~20-30 μm) ensures that each indent falls entirely within a single grain-size (coarse or fine) band and that could pick up a larger difference in hardness (~ 15-20 %) between those two regions, **Fig. 6.19**. Each macro-hardness indent, 450-460 μm in size (which is the sampling size), covered several grain-size bands (each 20-30 μm thick) and that resulted in much smaller difference between minimum and maximum values (5 % in average) at each measurement location (averaging out the local resistance to hardness indentation), which remained reasonably consistent throughout the depth, **Fig. 6.18**. Therefore, the effect of bimodality on hardness is more prominent in micro-hardness readings than macro-hardness readings due to the smaller sampling size (or

sampling volume) in micro-hardness test. The same logic can be applied to understand the effect of bimodality on toughness. Large sampling size (i.e. the plastic zone size), compared to a single grain size band, in the USE region will not depend on any local effect and will show the effect of average microstructure (average grain size, average inclusion size and volume fraction).

On other hand, Qiu et al. [Qiu 2006] also reported that the impact transition temperature (50 %-ITT based on fracture appearance transition) could not be related to the numerical average grain size, however, could be related to the weighted average grain size (measured considering the area-fraction of grain sizes in the microstructure) [Qiu 2006]. As bimodality increases the area-fraction of larger grains, the effect of bimodality on impact transition region is worth studying.

6.2.3.2 Effect of bimodality on IT region

In the impact transition (IT) region for HSLA steels failure is comprised of both ductile (i.e. fibrous or dimpled fracture) and brittle (or cleavage fracture) fracture, **Fig. 6.20**. As the test temperature drops from the USE region (100 % ductile fracture mode) to the IT region (mixed, ductile + brittle fracture mode) the plastic zone size in ferrite + pearlite steel drops as well (from ~ 1.5 mm at + 20 ºC to ~ 0.87 mm at -60 ºC as calculated by Vodopivec et al. [Vodopivec 2003]), however, the maximum stress ahead of the notch-root still remains insufficient to propagate a cleavage fracture. Therefore, the crack propagation starts in ductile mode and the initial plastic deformation consumes a large part of the energy (CVN energy, Joule) required for fracture. Higher the temperature, larger is the fraction of ductile

fracture (larger ductile region) and higher is the CVN energy [Hertzberg 1995, Tanguy 2005].

As the ductile crack grows, the length of the crack becomes higher towards the mid-width (or mid-section) of the specimen compared to the edges, **Fig. 6.20** and **Fig. 6.21**, which is known as the tunneling effect. Due to the tunneling effect the maximum principle stress is usually located towards the mid-width of the specimen, where the ductile crack length is also highest [Tanguy 2005, Haufild 2005]. The root-radius (ρ) and the plastic zone size (r) at the ductile crack tip are much smaller than that at the tip of the initial Charpy-notch, and reduces further as the crack propagates (i.e. with the increase in tunneling effect). As a result the maximum principle stress ahead of the ductile crack tip raises compared to the stress ahead the notch-root, with crack propagation. The brittle fracture mode starts when the plastic zone size and crack tip radius have decreased to a critical value [Vodopivec 2003], so that, the principle stress ahead of the crack tip reaches a 'high-enough' value, which is required to initiate and propagate a cleavage crack. For a ferrite + pearlite steel this critical plastic zone size ($r \approx 22$ μm) and crack tip radius ($\rho \approx 0.062$ μm) have been calculated [Vodopivec 2001]. Hence, the critical plastic zone size (i.e. the sampling volume) in TMCR steel can be in the same order as the width of a coarse- or a fine-grain size band (20-30 μm), and the plastic zone can sample a single grain size band. Now, the 'large enough' stress required for cleavage can depend on which grain sized band is present at the crack tip plastic zone, and hence, the local effect becomes significant (not the effect of average grain size).

The presence of large cleavage facets at the cleavage origin over the entire impact transition (IT) region (both higher and lower temperature side) for commercial steels shows that the grain size (or grain size distribution) should have a significant effect on the impact

transition temperature [Hausild 2005, Tanguy 2005]. After propagating a distance 'x' from the notch-root of the ductile crack finds a very coarse-grain sized band at its tip, **Fig, 6.21 a**, then the local stress may be 'large enough' to start cleavage from the coarse grains, as coarse grains will require lower principle stress compared to fine-grains. However, if the ductile crack finds a fine-grain band at its tip after propagating the same distance 'x', **Fig, 6.21 b**, the local stress may not be sufficiently high to initiate cleavage from there (as finer grains require larger principle stress to fail). Hence, the ductile crack may propagate further (> 'x' distance), absorbing more Charpy energy (i.e. higher toughness), until it finds a sufficiently coarse-grain band to start cleavage (or the stress ahead of crack-tip reaches 'large enough' value so that cleavage can be initiated and propagated even from a fine grain region). For a uniformly fine grain structure, cleavage will initiate only when the maximum principle stress exceeds the local fracture stress, which is similar everywhere due to the similarity in grain sizes.

The literature indicates that a large scatter in CVN energy can be expected in the impact transition region due to various reasons including temperature control during testing, accuracy in notch design, splitting at the interface of ferrite and pearlite bands in TMCR steel and, most importantly, on the local situation ahead on the ductile crack tip [Reed-Hill 1973, Shanmugam 1996]. From the above discussion a bimodal grain structure might be expected to result in higher scatter (depending on whether coarse- or fine-grain regions are encountered at the ductile crack tip), compared to a unimodal grain structure. The effect of bimodality on the scatter in impact energy values can be studied experimentally by comparing the CVN energies for a bimodal grain structure and for a unimodal grain

structure, over the transition region. Using a unimodal grain structure material as a reference allows scatter due to temperature control and notch variability to be accounted for.

6.2.3.3 Effect of bimodality on LSE region

The CVN energy at upper shelf energy (USE) region or at impact transition (IT) region includes crack initiation energy + crack propagation energy. Due to the increase in yield stress with the decrease in temperature, at sufficiently low temperature (usually, < -40 ºC for commercial TMCR steels [Tither 1992]) the principle stress ahead of the machined-notch root become so large that almost anything at the notch-root (a large grain, an inclusion, a precipitate [Hausild 2005]) become active to initiate and propagate cleavage. Hence, the failure occurs entirely by cleavage and fracture energy (includes only the crack initiation energy term and no propagation energy term) values are very low (typically 2-10 Joule). Therefore, the location of cleavage initiation (either coarse grain band or fine grain band) will not affect the scatter in CVN-energy.

6.2.4 Microstructural characterisation of TMCR-1 plate

The microstructures of commercial TMCR-1 plate were studied along the thickness direction from the sub-surface (0 mm from top rolling surface), towards mid-thickness (22 mm from top rolling surface) and are presented in **Fig. 6.22**. The images in **Fig. 6.22** show a bimodal ferrite grain structure with patches of coarse ferrite grains in a banded fine ferrite and pearlite matrix. The area-percent grain size distributions, based on equivalent circle diameter (ECD) grain size scale, are also presented in **Fig. 6.22**. The TMCR-1 plate exhibits

a bimodal distribution of ferrite grains and both the modes (or peaks) of each distribution are arrowed, **Fig. 6.22**.

From the measurement of PHR and PGSR parameters for the bimodal grain size distributions, **Table 6.6**, the bimodality increases with an increase in depth below the rolling surface. The measurements are supported by the microstructures in **Fig. 6.22**, which show fewer coarse grain patches and a smaller size of the abnormally large grains at the sub-surface location (2 mm) compared to the ½-thickness (22 mm) location. The separation between two neighboring coarse (or fine) grain regions was between 30-50 μm.

Wu and Davis [Wu 2004a] have previously observed distinct coarse-grain patches at the sub-surface location in two TMCR Nb-microalloyed steels (termed as Com-A and Com-B steels; refer **section 2.2.6** for details), however, the coarse-grain regions in the sub-surface layer were apparently fewer than those near the centre of the plates, **Fig. 6.23**.

The skew of the grain size distributions and the average (ECD) ferrite grain size corresponding to the sub-surface (2 mm from top), quarter-thickness and mid-thickness positions of TMCR-1 plate are listed in **Table 6.7**. The 'skew' is a characterization of the degree of asymmetry of the distribution around its mean value. For a symmetrical distribution skew ~ 1, however, as a distribution inclines towards the larger value side (usually the right-hand side) the skew becomes greater than 1. The increase in skew towards the centre of the TMCR-1 plate indicates an increase in size and area of large grains in the bimodal microstructure, and the same is expected from PHR and PGSR parameters given in **Table 6.6**. The average grain size (in ECD) also increases with the depth below the rolling surface. An increase in average ferrite grain size from sub-surface towards mid-thickness has also been reported by Wu and Davis [Wu 2004 a] (7-8 μm at sub-surface, 10-12 μm at

centre) and Bhattacharjee et al. [Bhattacharjee 2003] (5-6 μm at sub-surface and 6-7 μm at centre) in different TMCR-Nb microalloyed steels with duplex ferrite grain structures.

Approximately 12-13 area-percent second phase (pearlite + bainite) was measured in the TMCR plate, with the bainite being ~ 1 % at sub-surface and quarter-thickness locations, however, increasing to ~ 3 % at the mid-thickness location, possibly due to macro-segregation.

Bhattacharjee et al. [Bhattachrjee 2003] observed that a number of grains with up to 12º misorientation between them could be present within a single cleavage facet (refer **section 2.2.7**). They concluded that the cleavage crack ignores grain boundaries with less than ~12º (misorientation threshold) orientation difference and hence, mesotexture (measure of closely oriented group of grains) can influence the ITT (impact transition temperature). To study the mesotexture in TMCR-1 plate the distribution of grain boundary misorientation angles (a measure of mesotexture) has been measured by EBSD analysis at seven different locations, from the sub-surface towards mid-thickness position, **Fig. 6.24**. The mesotexture is higher near the surface of the plate and drops towards the centre. Within 2 mm from the rolling surface 25 to 40% of grains show misorientation less than 12°, whereas, after 2 mm depth only 10 to 20% grains show misorientation below 12°. The difference in mesotexture between the centre and surface may be due to the difference in temperature (surface chilling from the rolls) and / or difference in strain level due to the different material flow resistance.

The mesotexture of TMCR-1 steel (used in present study) can be compared to the TMCR steels studied by Wu and Davis [Wu 2004c] and Bhattacharjee et al. [Bhattacharjee 2003]. TMCR-1 steel shows much weaker measotexture (~ 28 % grain boundaries at 2 mm depth and ~ 16-17 % grain boundaries from 5 mm depth to the plate centre location, with

misorientation angle < 12°) than that reported by Wu and Davis [Wu 2004c] (~ 35-55 % grain boundaries with misorientation angle < 12° at 2 mm depth) and Bhattacharjee et al. [Bhattacharjee 2003] (~ 40-60 % grain boundaries with misorientation angle < 12° at plate centre location). However, the mesotexture in TMCR-1 steel is similar to that in hot-rolled and normalized C-Mn steel (0.13 % C, 0.079 % Mn, 0.12 % Si), which show only ~ 15 % grain boundaries with misorientation angle less than 12° at plate-centre [Bhattacharjee 2003]. Low mesotexture in hot-rolled and normalized steel showed negligible effect on ITT prediction made using optically measured grain sizes [Bhattacharjee 2003] and therefore, the same is expected for TMCR-1 steel.

6.2.5 Measuring the scatter in Charpy test results

To draw the impact transition curves from the scattered impact energy values (or percentage brittle fracture values) over the testing temperature range researchers have adopted various approaches: (i) following the points corresponding to the minimum impact energy values (representing the worst situation) at each temperatures (or maximum percentage cleavage fracture values) [Bhattacharjee 2003], (ii) following the average impact energy values (or average percentage cleavage) at each temperatures [Petch 1986] or (iii) drawing the best fit line following an equation (using tanh or exponential functions fitted by least square fit) that considers all scattered points [Wallin 1991, Todinov 2001].

However, the aim of the present investigation is to quantify the scatter in measured values. As a simple measure of the scatter at each testing temperature, the ratio of the standard deviation to the mean (i.e. average) value (in percentage) can be used [Ratchev 2006]. Scattering in CVN energy is usually approximated industrially from the use of two

separate curves (upper and lower limits), **Fig. 6.25a**, which can show the possible error (in terms of the difference in temperatures, DBTT(U): upper bound ITT at 50% energy, and DBTT(L): Lower bound ITT at 50% energy) at a given impact energy (say, 50 % energy or 27 Joule) [Steel University Website]. The lower limit curve follows the points corresponding to the minimum (i.e. lowest) energy values and represents the worst situation (ITT corresponding to DBTT(U)). The upper limit curve follows the maximum energy points (i.e. highest energy values) and represents the best situation (ITT corresponding to DBTT(L)). Similar curves can also be drawn for the fracture appearance transition, **Fig. 6.25b**, however, the upper limit curve there represents the worst situation (ITT corresponding to FATT(U)), i.e. maximum cleavage fracture and the opposite for the lower limit curve (ITT corresponding to FATT(L)). Corresponding to ½×(USE + LSE) or 50 % crystalline fracture the higher and lower impact transition temperatures (DBTT and FATT) can be obtained using the upper and lower limit curves, as shown in **Fig. 6.25**. To understand the effect of grain size bimodality on the scatter in CVN energy for the commercial rolled plates, the scatter in CVN energy values reported in the literature [Shanmugam 1996, Talbot 2002] for rolled steel with unimodal ferrite grain structures have been compared against the scatter in CVN energy values obtained from CVN tests carried out in the present study on TMCR-1 steel, with bimodal ferrite grain structure.

6.2.6 Scatter in Charpy energy for unimodal grain structure

Shanmugam and Pathak [Shanmugam 1996] carried out Charpy impact tests (21 samples machined from the T-L orientation and tested over the impact transition region) on hot-rolled microalloyed steel plate (0.2 C, 1.26 Mn, 0.068 V, and 0.015 Ti, all wt %), with

uniform ferrite grain size distribution in ferrite-pearlite banded microstructure (average ferrite grain size ~ 14 μm), **Fig. 6.26a** and **Fig. 6.26b**. In terms of the ratio of standard deviation / mean impact energy value (in percentage) the unimodal grain structure showed 14-15 % scatter, **Fig. 6.26c.** The range of error in ITT values was ~5 ºC (best and worst DBTT values are 0 ºC and +5 ºC, respectively) for the unimodal structure, **Fig. 6.26c**. The higher scatter towards the USE region in **Fig. 6.26c** has been attributed to the occurrence of splitting on the fracture surface [Shanmugam 1996].

Talbot [Talbot 2002] also reported the scatter in impact energy and percentage crystalline fracture values over the impact transition regions for two Nb-microalloyed laboratory rolled steels (0.05-0.09 % C, 0.023-0.057 % Nb), with unimodal grain structures (average grain size at mid-thickness position ~ 6-7 μm), **Fig. 6.27 (a** and **b)**. Two different controlled rolling schedules have been used to roll each steel composition. In between 11-15 samples (machined from T-L orientation) have been tested from each steel plate. The impact transition values showed a steep nature in transition behaviour with FATT and DBTT values lying between -90 ºC to -110 ºC, **Fig. 6.27 (c** and **d)**. However, the range of error in DBTT and FATT values remained within ~ 12 ºC, **Fig. 6.27 (c** and **d)**. The ITT values for the steels investigated by Shanmugam and Pathak [Shanmugam 1996], ~ 0 ºC, and Talbot [Talbot 1996], ~ 100 ºC, are very different, however, the range of ITT values, considering the scatter does not exceed 12 ºC in either case. Splits have been found on the fracture surfaces of the broken Charpy specimens in both studies [Shanmugam 1996, Talbot 2002] and that could come from the separation along the ferrite-pearlite interface in the banded microstructure [Shanmugam 1996]. Literature suggests splitting can cause scatter in Charpy results beside the microstructural variation (grain size, phase fraction, precipitate and inclusion size),

experimental variation (mainly the specimen temperature control) and the variation in specimen dimension (mainly notch-design) [Sterjovski 2004, Shanmugam 1996, Bramfitt 1997]. The above discussion indicates that the combined contribution from all the factors may cause a scatter of ~ 12 ºC or less in ITT, for the unimodal ferrite grain structures, where ~10-20 was the number of samples tested from each steel plate.

6.2.7 Scatter in Charpy energy for bimodal grain structure

In the present study, to understand the effect of bimodality on the impact toughness, Charpy specimens were prepared from the sub-surface and ¼-thickness locations of TMCR-1 steel (18 samples tested from each location), **Fig. 4.5**. The centre of the notch in the sub-surface and the ¼-thickness samples lies at ~ 6 mm depth (spans over 1 mm depth to 11 mm) and ~ 12 mm depth (spans over 7 mm depth to 17 mm), respectively, below the rolling surface. The microstructure and grain size distribution at 6 mm and 12 mm depth showed bimodal ferrite grain structures, **Fig. 6.22**, with slightly lower bimodality and average grain size at 6 mm depth; however that difference is very small. The notch of the sub-surface specimens also samples part of the region just below the rolling surface (say 1-2 mm depth), where the bimodality as well as the average grain size was the least, **Table 6.6** and **Table 6.7**. Large sulphide-inclusions, usually present at the plate-centre location (due to segregation) can reduce the impact toughness values and, therefore, that location was avoided.

The transition in impact energy and fracture appearance (percent-crystalline fracture) over the temperature range of - 40 ºC to -100 ºC are listed in **Table 6.8** and shown in **Fig. 6.28**. Within the impact transition region (-60 ºC to -90 ºC) the standard deviation, with

respect to the mean value, varies ~ 21-100 % (50 % average) for the sub-surface samples and 18-56 % (42 % average) for the quarter-thickness samples in terms of the impact energy at each testing temperature (therefore, the sub-surface samples show higher scatter in impact energy). In terms of the percent-crystalline fracture the same ratio is 56 % in sub-surface samples and 63 % in quarter-thickness samples (hence, quarter-thickness samples show higher scatter in fracture appearance). Therefore, in terms of scatter in measuring parameters sub-surface samples can not be distinguished from quarter-thickness samples, as may be expected from their similar levels of bimodality and average grain size, **Table 6.6** and **Table 6.7**. The difference between higher and lower DBTT and FATT values shows the range of ITT (or the error in ITT) resulting from the scatter in experimental data. That range is ~ 20 ºC to 30 ºC (~25 ºC average) for the TMCR-1 steel with bimodal grain structure, **Fig. 6.28** (best and worst DBTT and FATT values lying between -63 ºC to -95 ºC), which is higher than that for the unimodal structure (less than ~12 ºC) for the same number of samples tested (between 11 to 21 samples). Therefore, the samples from TMCR 1 plate with bimodal ferrite grain structure showed higher scatter in impact energy (and fracture appearance) values compared to the hot-rolled and TMCR steels with unimodal ferrite grain structure.

Splits have been found on the fracture surfaces of the broken Charpy samples of TMCR 1 steel basically towards the high impact energy (USE) region as observed by Shanmugam and Pathak [Shanmugam 1996] and Talbot [Talbot 2002]. As mentioned earlier, splitting and all the other factors responsible for generating scatter in Charpy results can result in a variation of ~12 ºC for the unimodal structures. In terms of steel composition, processing schedule, average grain size (5-7 μm), pearlite-fraction (~ 10-12 %), and the nature and sizes of inclusions and precipitates the steels studied by Talbot [Talbot 2002] are

very similar to the TMCR-1 steel tested here. Still the higher scatter in Charpy results (range of ITT ~ 25 ºC) in TMCR-1 steel, compared to the steels investigated by Talbot [Talbot 2002] and Shanmugam and Pathak [Shanmugam 1996] (for 11-21 number of samples tested from each steel) indicates that the grain size bimodality in TMCR-1 steel may be an important factor in generating scatter (following the mechanism discussed in **section 6.2.3.3**).

6.2.8 Conclusions derived from impact test results and the future studies needed

The present study analysed the effect of grain size bimodality on Charpy impact toughness of TMCR steel, basically, from the theoretical point of view. Bimodality in grain size may not have a significant effect on upper shelf energy, USE, regions (due to the plastic deformation of almost entire cross section) and lower shelf energy, LSE, regions of Charpy impact transition curves, however, can generate higher scatter (in impact energy or fracture appearance) within the impact transition region (where grain size plays a vital part in initiating cleavage) depending on which grain size band (coarse / fine) is sampled at the notch root. Charpy tests carried out on unimodal (lower scatter, difference between best and worst DBTT ~ -12 ºC) and bimodal ferrite grain structures (higher scatter, difference between best and worst DBTT ~ -25 ºC) also indicate the same possibility, for the small number of samples tested (~11-21 samples tested on each steel plate).

In actual practice, the Charpy toughness requirements for commercial TMCR plates are not based on the transition temperature, but on the impact energy. For a specific test temperature (say, -40 ºC) the standard requires the mean CVN energy value of three Charpy tests to be higher than a particular energy value (say, 27 J), which is pre-decided between the customer and the producer (mentioned in the order), based on the steel grade and plate

thickness, [ASTM A 20]. Beside that, the minimum CVN energy out of those three results should not be lower than another specified value (say, 21 J) [ASTM A 20], which could even be 70 % of the mean value [BSEN 10045]. If bimodality increases the scatter in CVN energy, then the chance of finding one or two very low values out of the three test results increases, and thereby, increases the chance of failure from standard requirement. It has been discussed in **section 6.2.3.2** that in the impact transition region of a sample with bimodal grain structure the advancing ductile crack may or may not travel an extra distance 'x', depending on the availability of a large grain size band at the crack tip. In future, detailed studies are required to calculate the extra energy (in Joule) a specimen can absorb at the standard testing temperature if the ductile crack travels over an excess distance 'x', which will depend on the actual grain sizes and the spacing between the grain size bands, before fracture. That can help us to understand how far a grain size bimodality can affect the requirement of standard specification.

However, the Charpy impact test results presented in this study is incomplete and shows the need of various future studies. As mentioned earlier, the Charpy impact test results are usually associated with high degree of scatter and that depends on various microstructural factors (grain size variation, sizes and distributions of carbides and inclusions, size and fraction of pearlite or bainite, microstructural banding and associated splitting, or segregation of impurities etc.) and experimental factors (experimental set up, specimen temperature control, specimen design etc.). Hence, it will always be difficult to understand the individual contribution from 'grain size bimodality' on toughness. Curry and Knott [Curry 1976] made the carbides solely responsible for the cleavage fracture (both cleavage initiation and propagation) in mild steel, however, the grain size (D) is still important as the carbide size is

proportion to the grain size [Curry 1978], and hence, DBTT $\propto D^{-1/2}$. Beside the ferrite grains and grain boundary carbides large pearlite colonies have also been found to nucleate cleavage fracture in the banded ferrite-pearlite microstructure of linepipe steels. The effect of pearlite size on fracture and its variation on the scatter of the fracture toughness parameters need to be studied in detail. The scatter due to the experimental variation needs to be represented mathematically, following the approach used by Wu and Knott [Wu 2004b] to measure the scatter in σ_f. After that large number of impact tests needs to be carried out on severely bimodal and perfectly unimodal grain structures from similar TMCR steels (similar composition, pearlite fraction, shape, size and distributions of carbides and inclusions, ferrite-pearlite band spacing etc.) and test results need to be compared and analysed statistically. Fracture surfaces of the broken samples should also be studied in detail to identify the locations of the cleavage origin (distance of the cleavage origin from the notch-root and the size of the cleavage originating facet / facets). Combining all those details can be conclusive to understand the effect of bimodality on the scatter in impact test results. Later on similar studies can also be carried out on microstructures with different levels of bimodality (using the measurement of bimodality as discussed in section 5), to find the effect of severity in bimodality on impact toughness.

The effect of processing parameters, particularly the rolling reduction ratio, on the scatter in Charpy toughness also needs to be studied. Reduction ratio in rolling can influence the spacing between fine and coarse grain bands, a higher reduction ratio leads to a shorter inter-band spacing and hence reduces the width of an individual grain size band [Wu 2004c]. Shorter band width means more number of grain size bands can fall within the plastic zone ahead of an advancing ductile crack tip. Hence, the chance of sampling a sufficiently larger

sized grain increases and the scatter may reduce. Reduction ratio may also influence the texture ('meso-texture') in steel [Wu 2004c]. Significant mesotexture can mean the fine grains to appear as a single coarse grain, and thereby, may reduce the scatter once again.

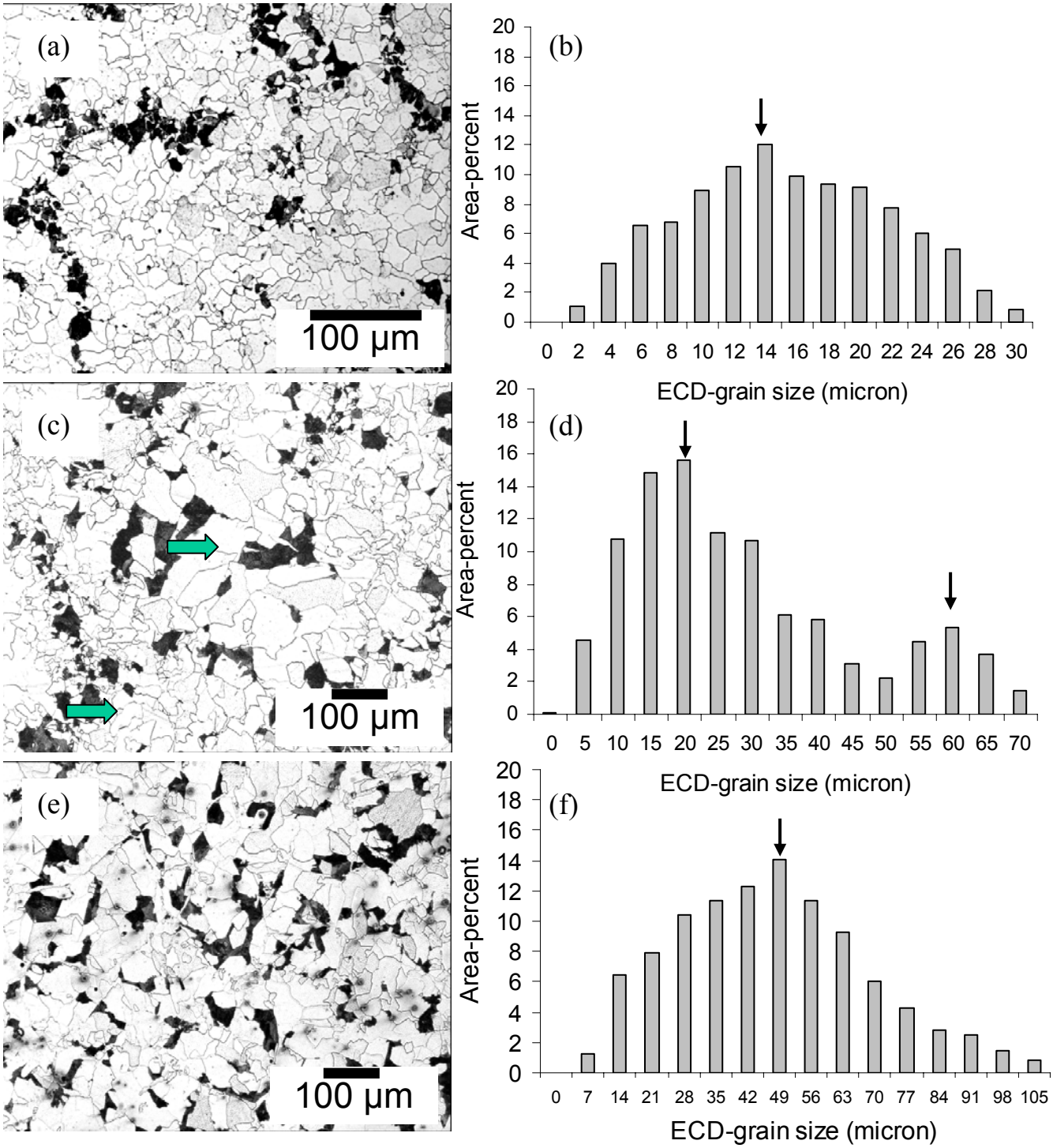

Fig. 6.1: Idealised microstructures in the notch-bend test samples showing, (a) uniformly-fine grain structure in slab 1-940-700-hold sample, (c) duplex structure in slab 1-1140-700-hold sample, and (e) uniformly-coarse grain structure in slab 1-1210-700-hold sample. (b), (d) and (f) are the corresponding area-percent ferrite grain size distributions

(based on 15-class ECD-scale) for the microstructures shown in (a), (c) and (e), respectively. Peaks for the grain size distributions are arrowed.

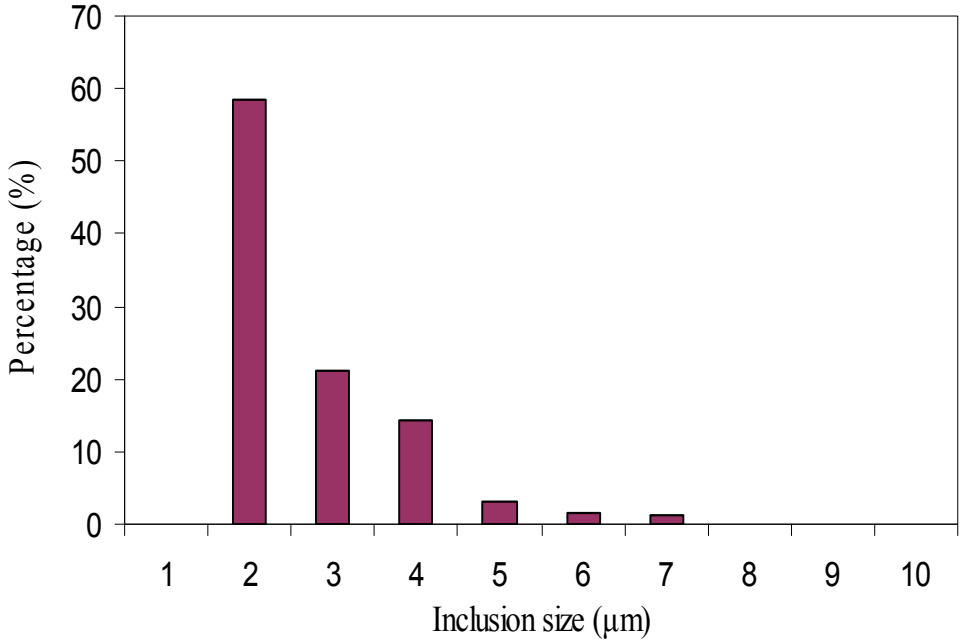

Fig. 6.2: Distribution of the inclusion size in the as-cast slab 1 (quarter-thickness) steel. Mean inclusion size: 2.15 μm and average area percent of inclusions: 0.08%.

(a) slab 1-940-700-hold (110)	(b) slab 1-1140-700-hold (110)	(c) slab 1-1210-700-hold (110)
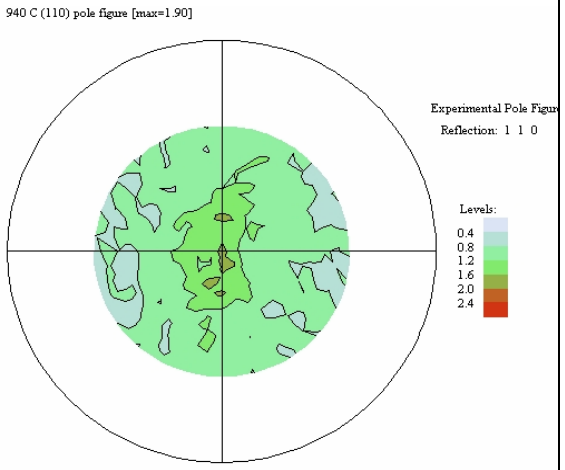	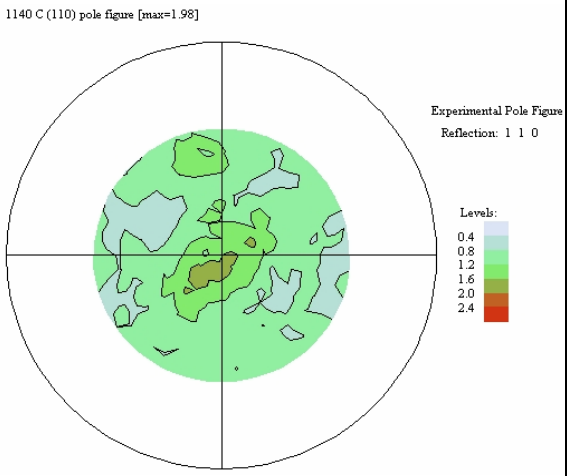	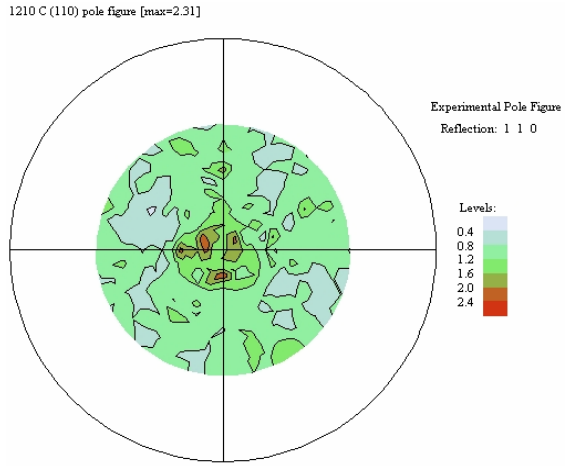
(d) slab 1-940-700-hold (200)	(e) slab 1-1140-700-hold (200)	(f) slab 1-1210-700-hold (200)
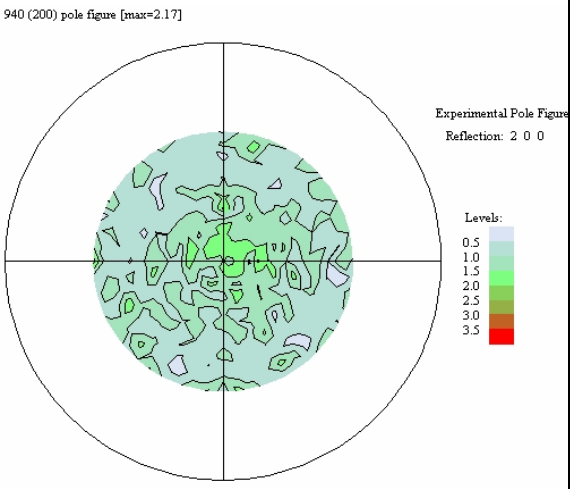	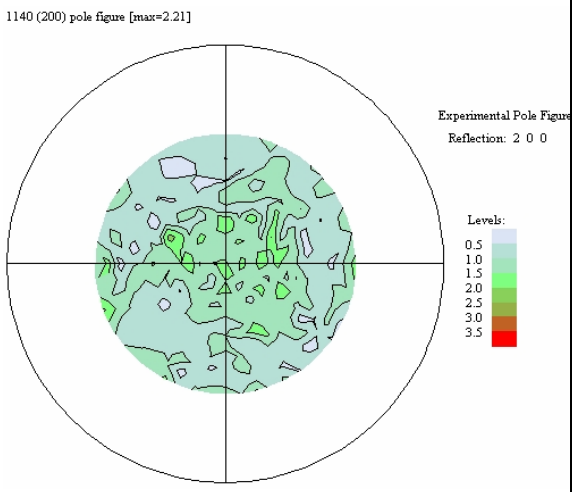	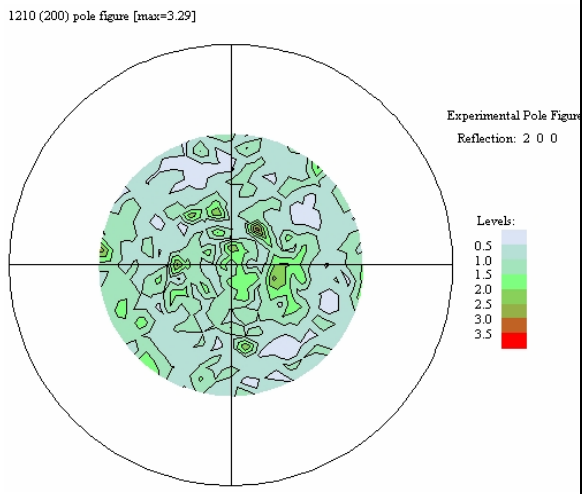

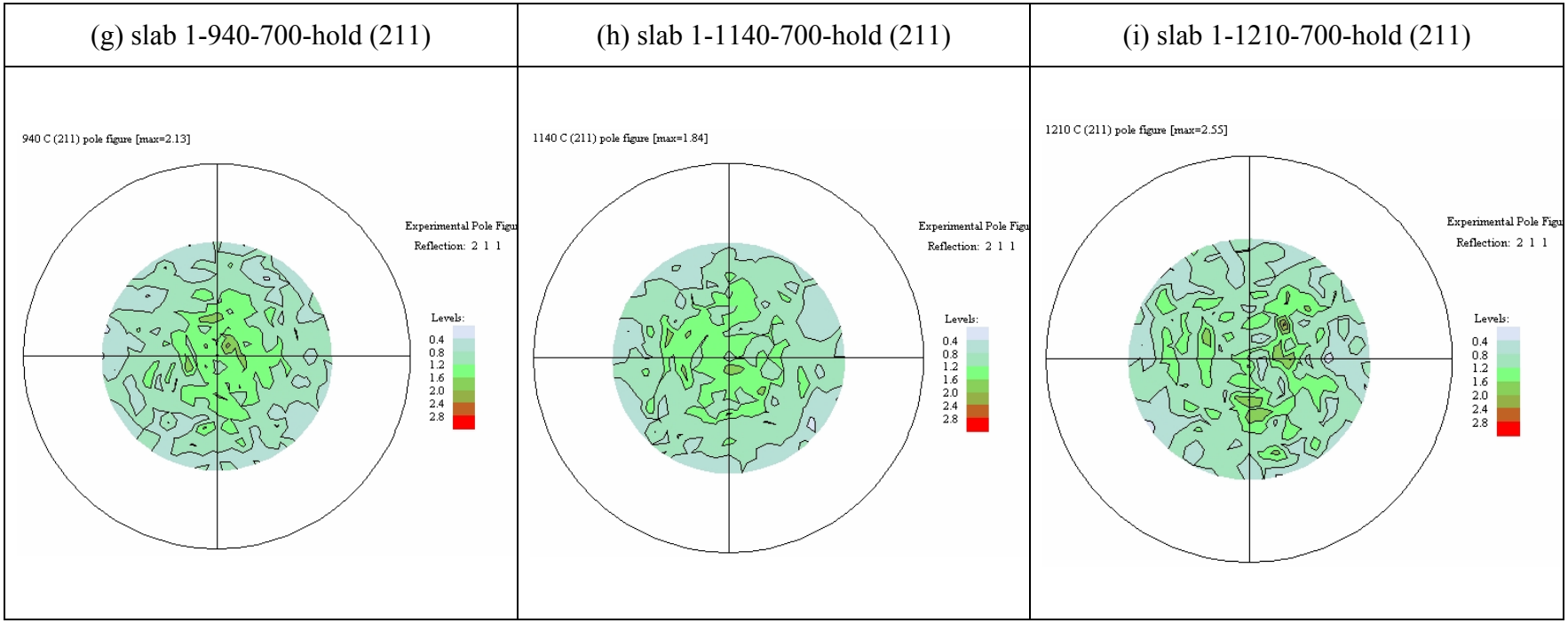

Fig. 6.3: Pole figures for slab 1-940-700-hold, slab 1-1140-700-hold and slab 1-1210-700-hold notch-bend test samples: (a), (b) and (c) show the (110) pole figures, (d), (e) and (f) show the (200) pole figures and (g), (h) and (i) show the (211) pole figures. The reheating temperature of the sample as well as the texture component studied is listed above each pole figure. For each texture component the pole figures are presented with the same scale.

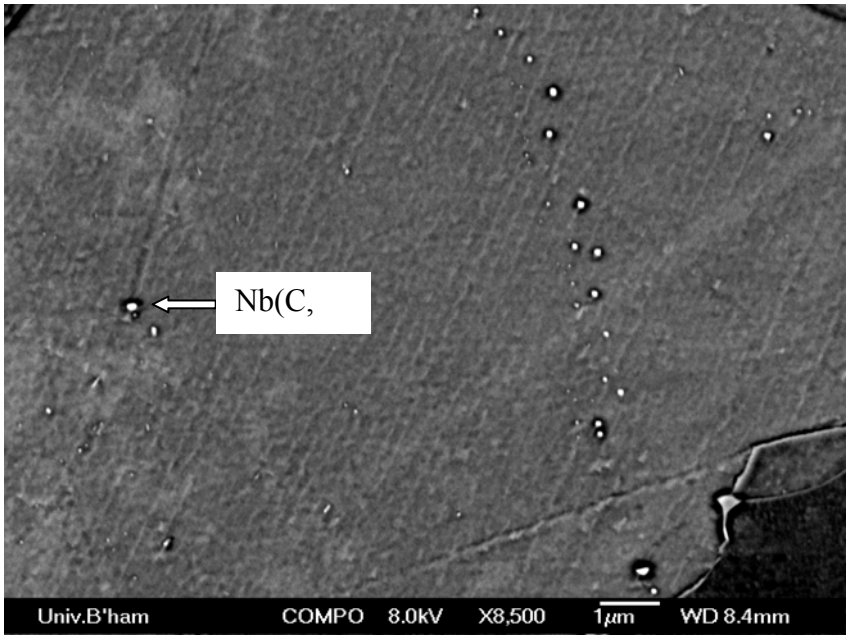

Fig. 6.4: Nb(C, N) precipitates on the surface of slab 1-1140-700-hold sample (Back-scattered electron, BSE, image).

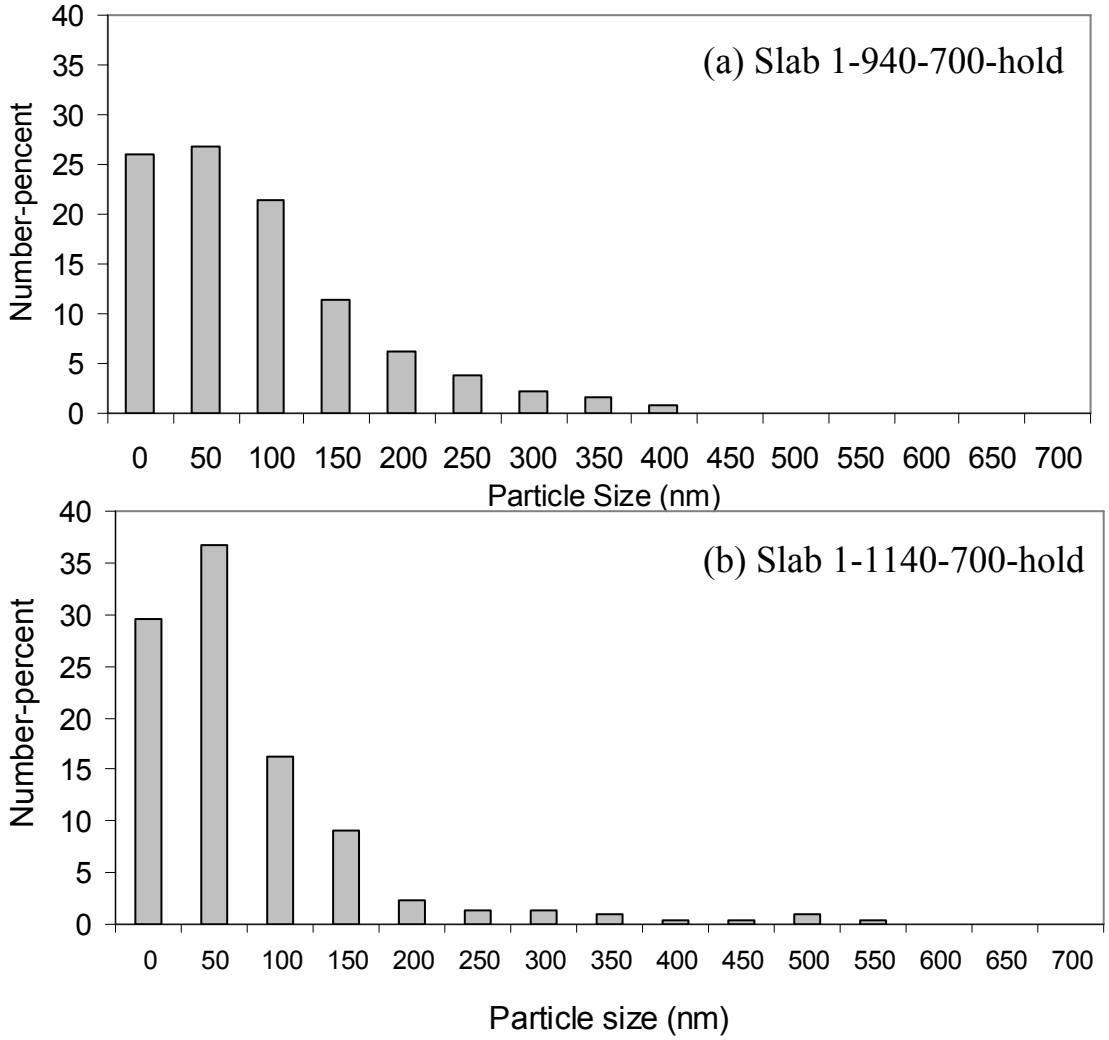

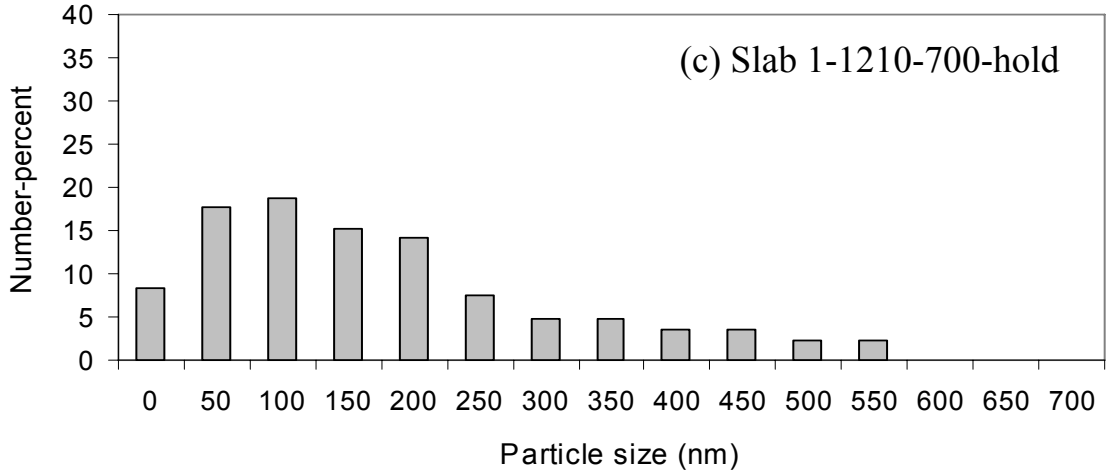

Fig. 6.5: Particle size distribution in (a) slab 1-940-700-hold, (b) slab 1-1140-700-hold and (c) slab 1-1210-700-hold samples.

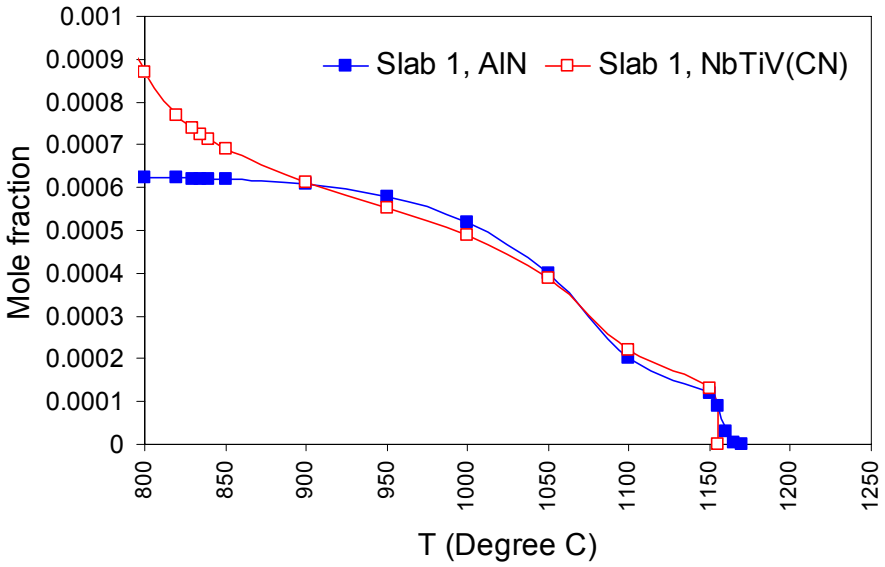

Fig. 6.6: Thermo-Calc prediction showing the drop in mole fraction of precipitates in slab 1 steel with the increase in reheating temperature.

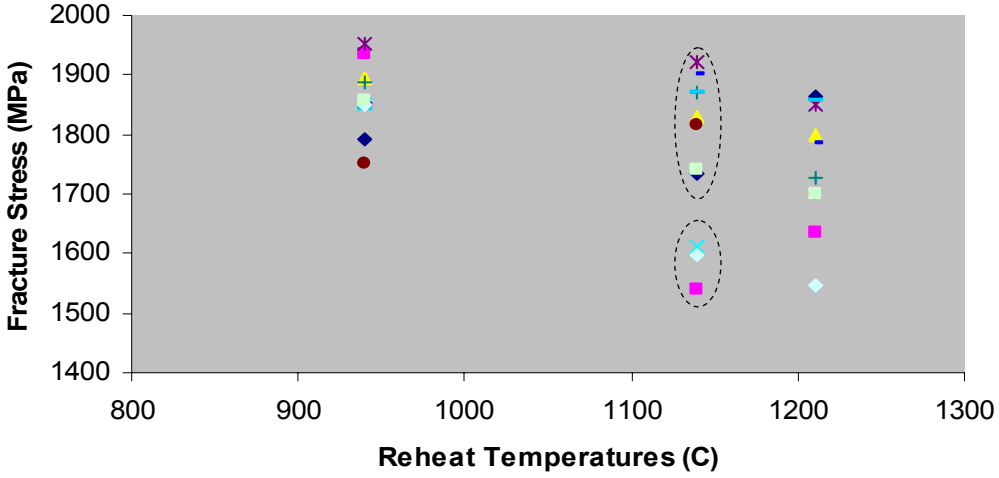

Fig. 6.7 Scatter of the principle fracture stress (σ_F) for notch-bend test specimens reheated to different temperatures (data given in **Table 6.3**).

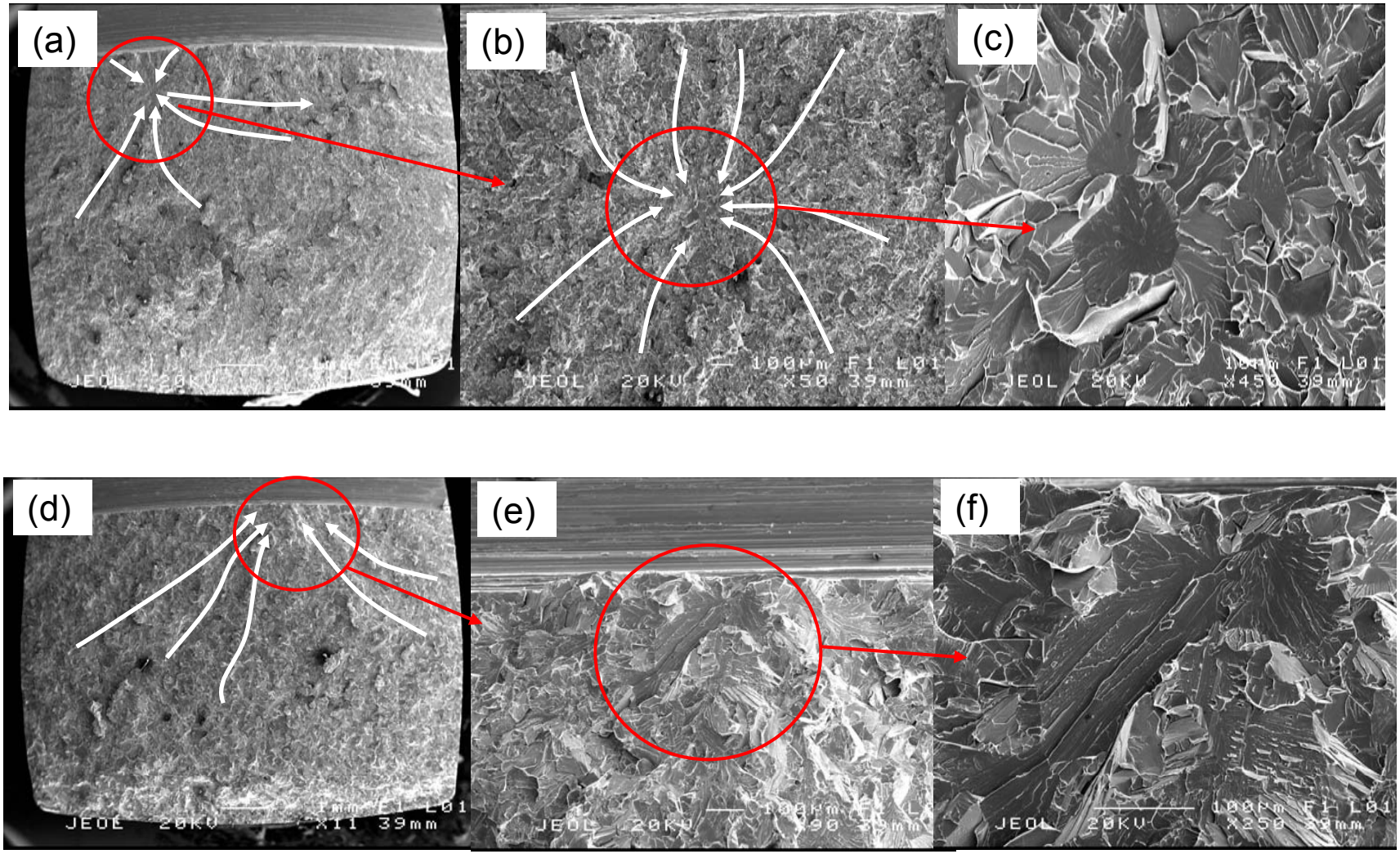

Fig. 6.8: Identification of the cleavage initiation sites by tracing the river lines back to the origin for the fractured three-point bend test specimens reheated to 940 °C (a, b and c) and 1210 °C (d, e and f). Distance of cleavage initiation site (I.S) from the notch tip and the size of the initial facet / facets (first facet) around the cleavage origin were measured.

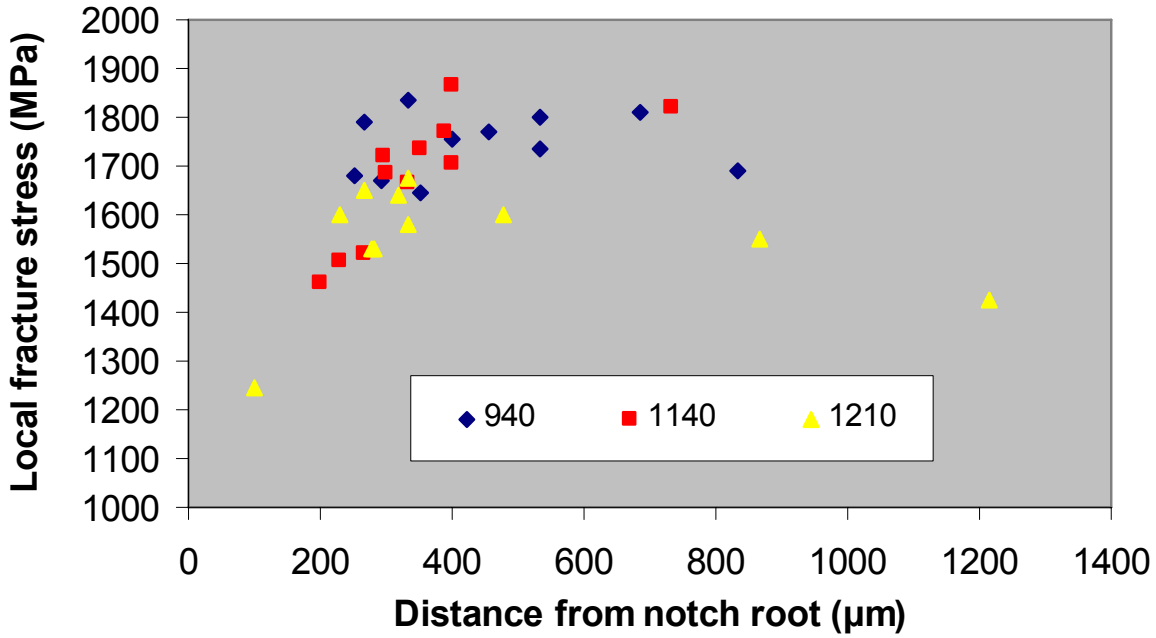

Fig. 6.9: Variation of the local fracture stress, σ_f (MPa) values for bend test samples plotted against the corresponding distance of cleavage initiation site, I.S (measured from the notch tip) showing that the cleavage initiation site in most of the samples (~ 82 %) are within the active zone (200-500 µm) where maximum principle stress reaches the highest value. 940, 1140 and 1210 represents the three-sets of samples based on their reheating temperatures (°C).

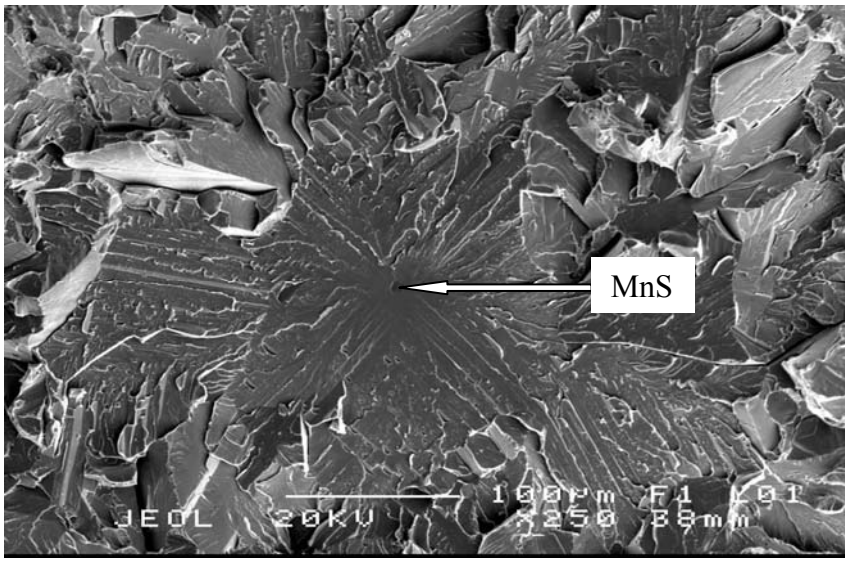

Fig. 6.10: Large MnS inclusion (~4 µm) initiating cleavage within a large size facet in slab 1-1210-700-hold sample showing local fracture stress, 1246 MPa.

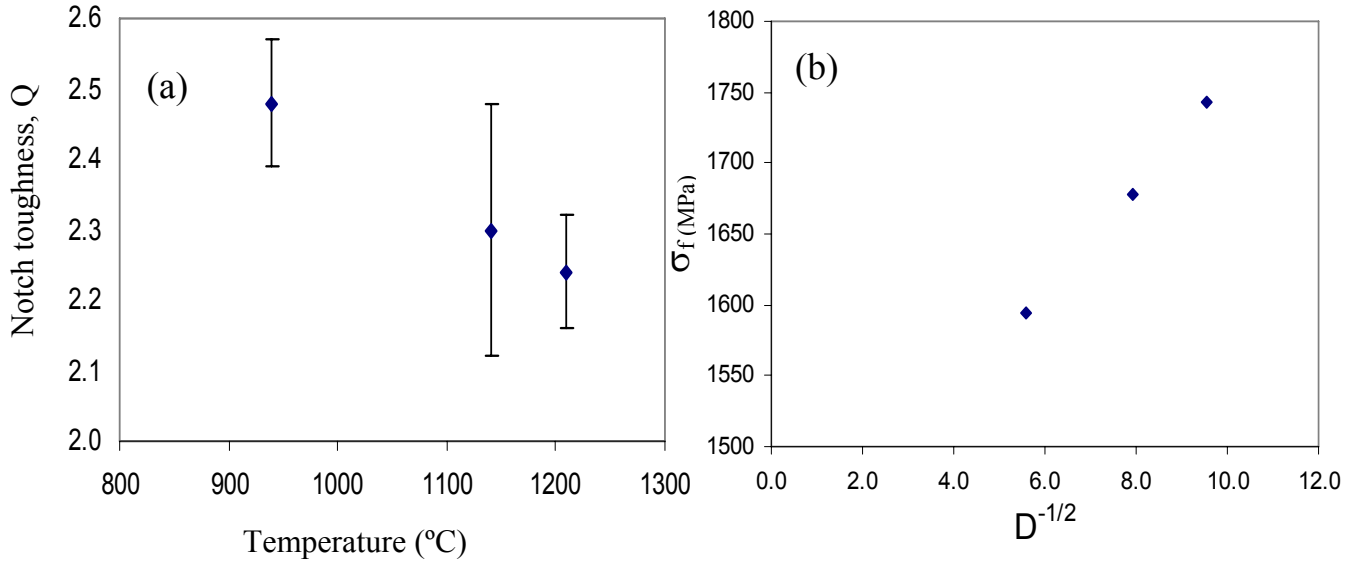

Fig. 6.11: (a) Increase in the notch toughness, $Q=(\sigma_f / \sigma_y)$, for the notch-bend test samples with the decrease in grain size as reheating temperature decreased (940 °C, 1140 °C and 1210 °C). (b) Average σ_f increasing with $D^{-1/2}$ (D is the average ECD grain size).

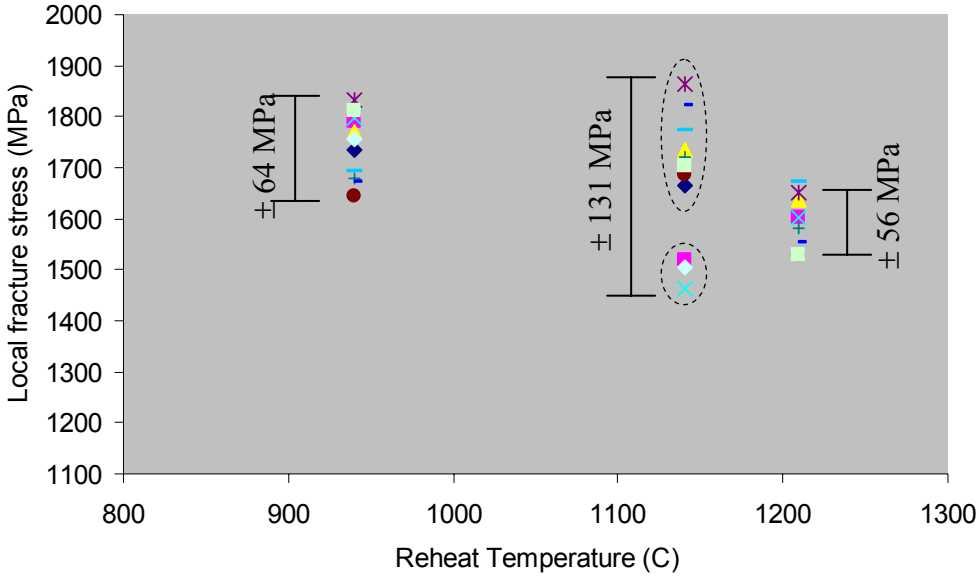

Fig. 6.12: Variation in local fracture stress, σ_f (MPa) for the bend test samples reheated to different temperatures (940 °C, 1140 °C and 1210 °C) (data in **Table 6.5**). For slab 1-1140-700-hold samples σ_f values appear to separate into two groups, which are indicated by dotted ovals.

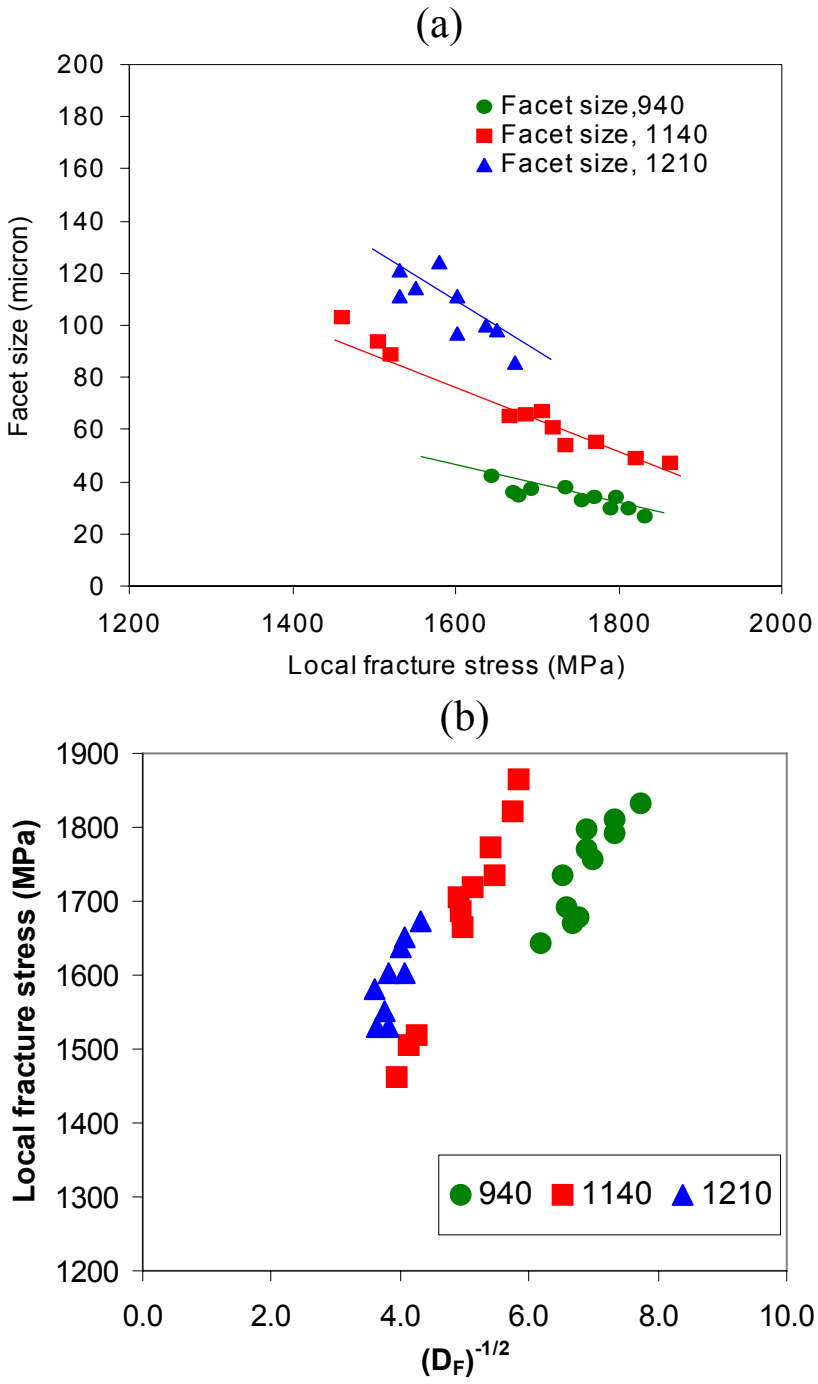

Fig. 6.13: Facet size distribution for the notch-bend test samples showing that (a) the facet size (μm) values (given in **Table 6.5**) increase with the increase in local fracture stress (MPa) values. (b) Local fracture stress values increase with $(D_F)^{-1/2}$ (where, D_F is the cleavage initiating grain size).

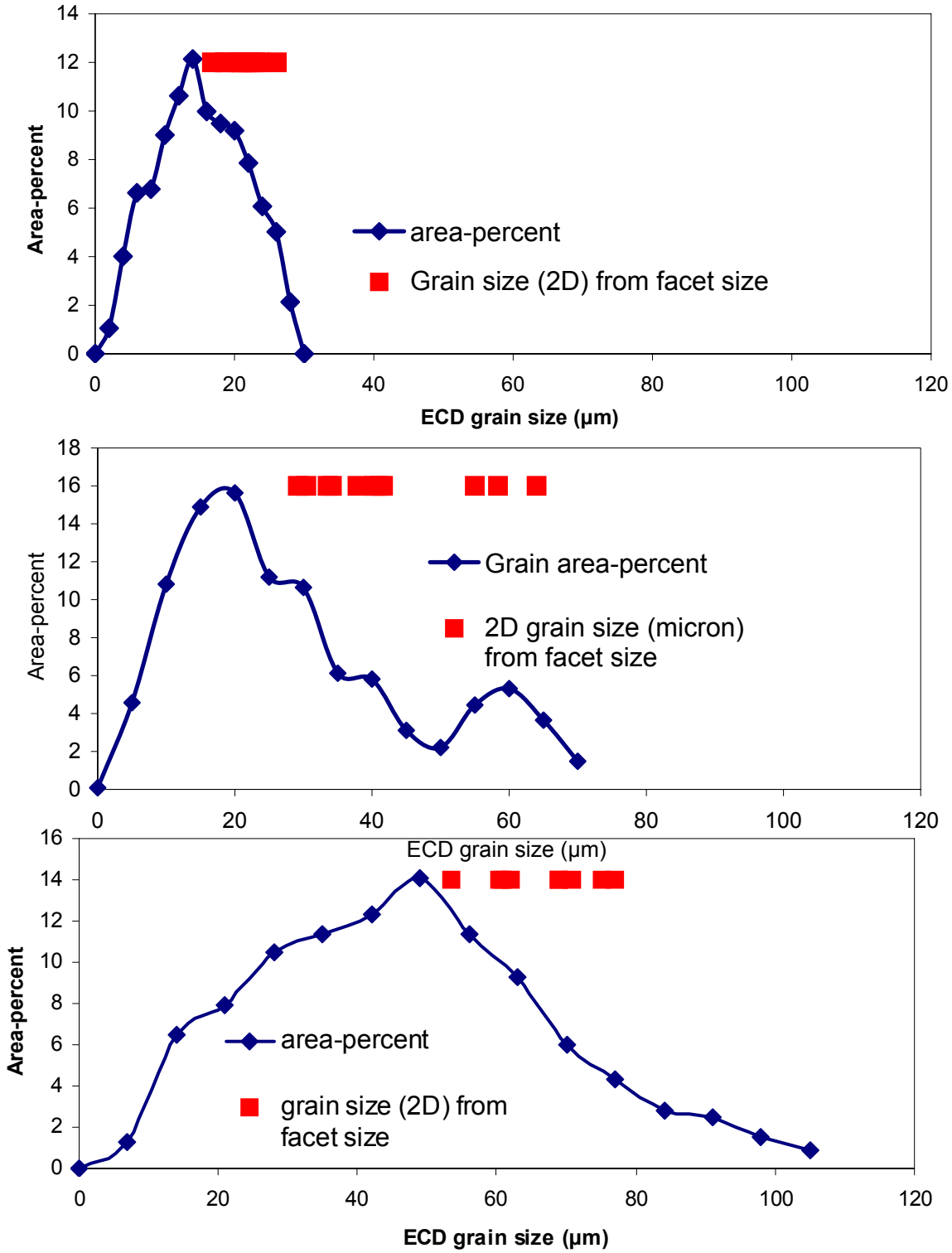

Fig. 6.14: Cleavage originating grain size, D_F (2Dim), values (obtained from facet size using a factor 1.61) superimposed on the corresponding ECD-grain size (2Dim) distributions (area-percent) for (a) slab 1-940-700-hold (b) slab 1-

1140-700-hold and (c) slab 1-1210-700-hold steel, to identify the part of the grain size distribution responsible for the cleavage fracture.

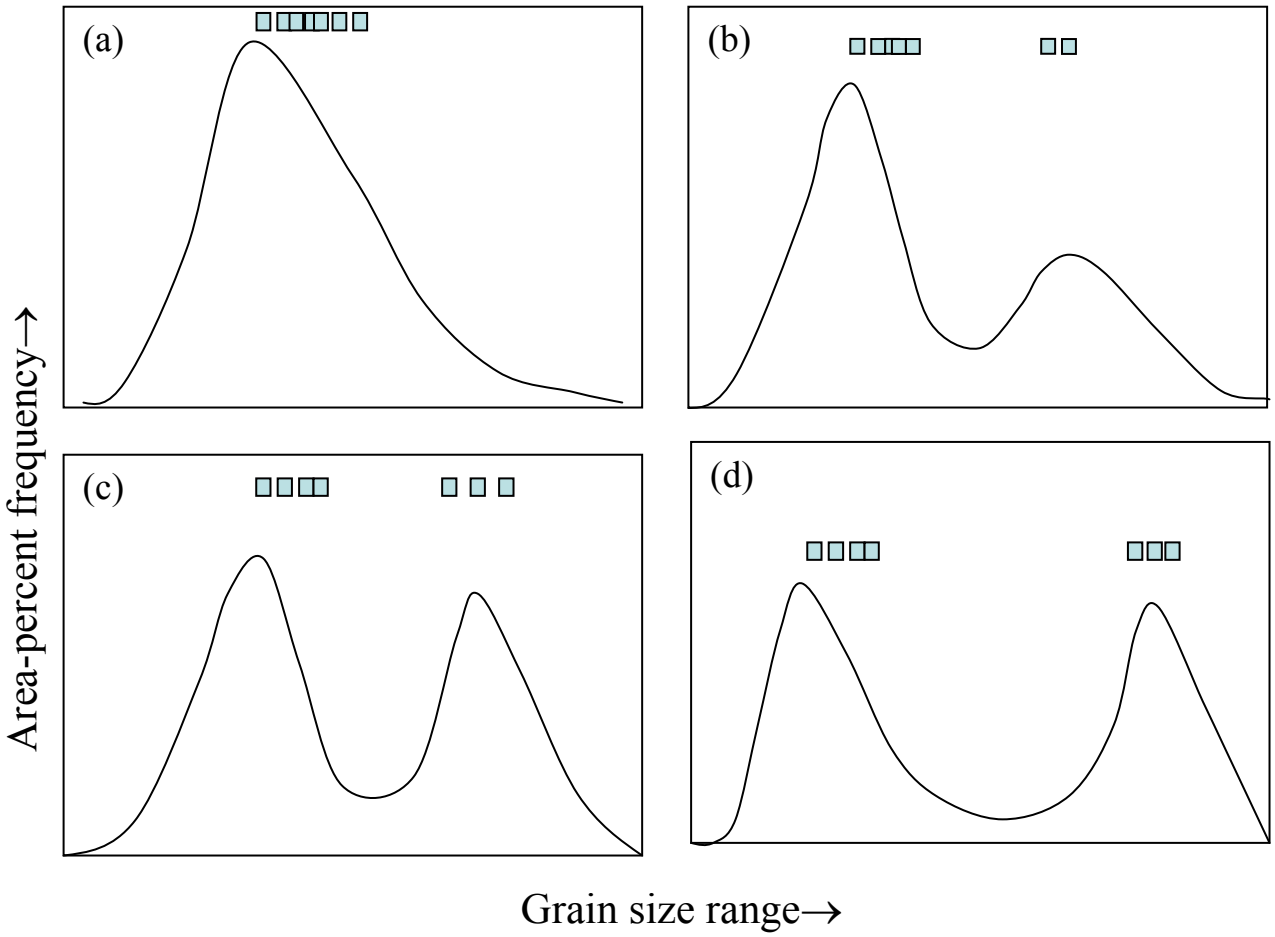

Fig. 6.15: Various theoretical grain size distributions to visualise the cleavage originating grain sizes and the hence, possible scatter in fracture stress.

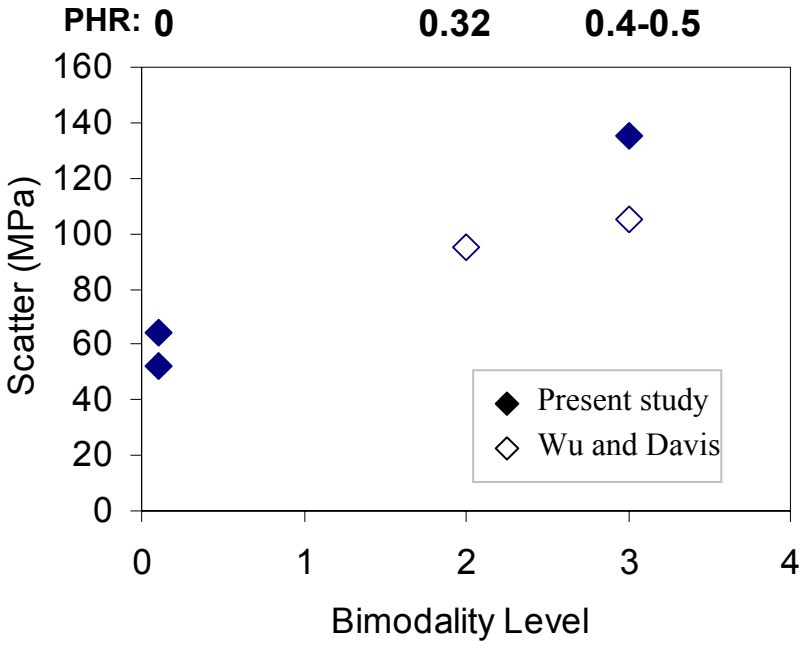

Fig. 6.16: Relation between the scatter (standard deviation value) in local fracture stress (σ_f) and the bimodality level (visual scale or PHR) for various steel samples studied in the present investigation as well as by Wu and Davis [Wu 2004 a].

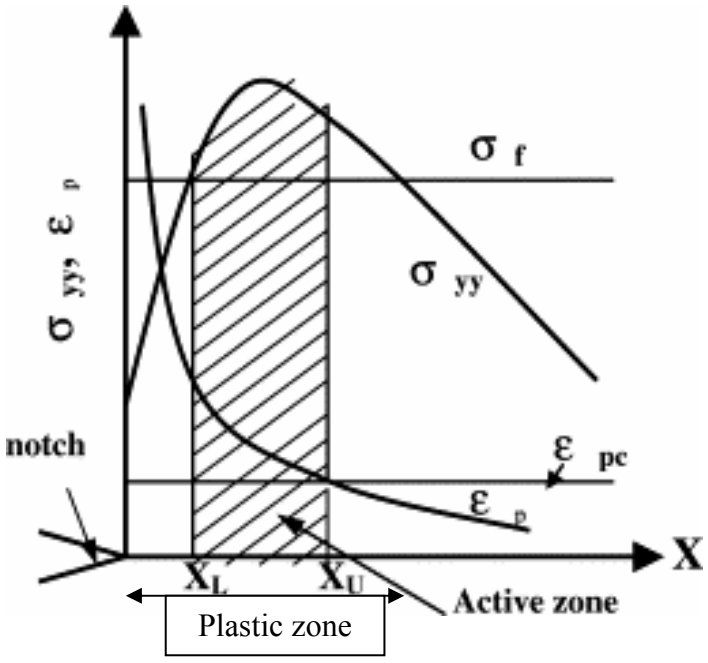

Fig. 6.17: Schematic diagram showing the active zone for the cleavage fracture in notched specimens. σ_f: fracture stress i.e. the critical tensile stress required for the propagation of the crack, σ_{yy}: normal stress ahead of the notch-tip, ε_{pc}: critical plastic strain required to initiate a crack nucleus, ε_p: plastic strain ahead

of the crack tip, X_L: Lower boundary of the active zone, X_U: Upper boundary of the active zone.

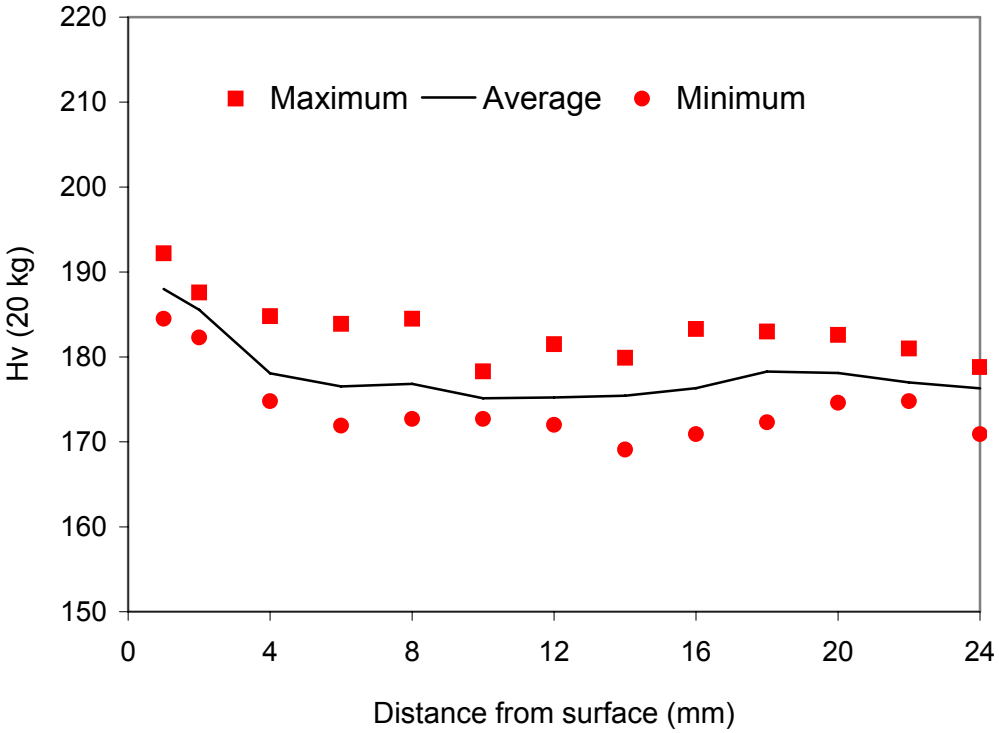

Fig. 6.18: Vickers macrohardness (20 kg) profiles measured along the thickness direction of the TMCR-1 rolled plate

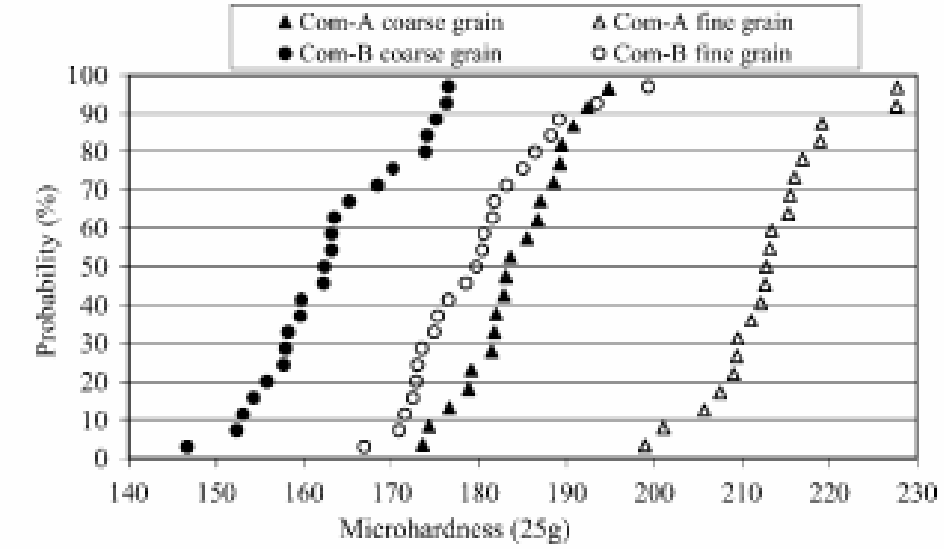

Fig. 6.19: Statistical analysis of the microhardness values (25 g) obtained from both coarse and fine grain bands in two commercial TMCR steels (Com-A and Com-B) [Wu 2004 a]. Microhardness values within fine grain regions are higher than that within coarse grain regions.

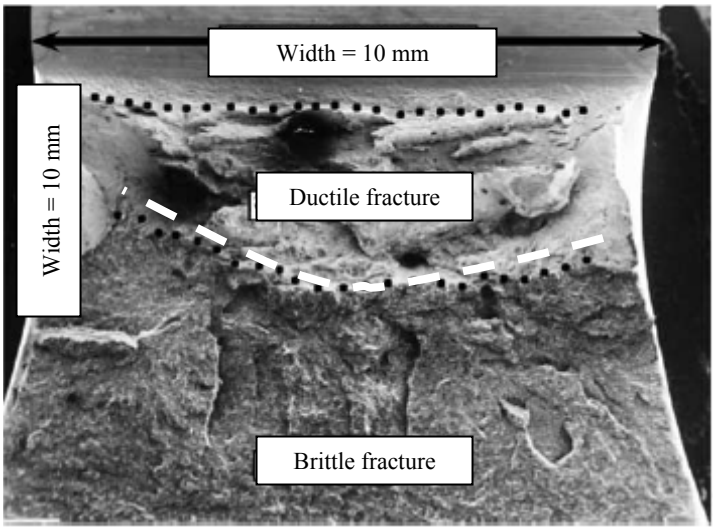

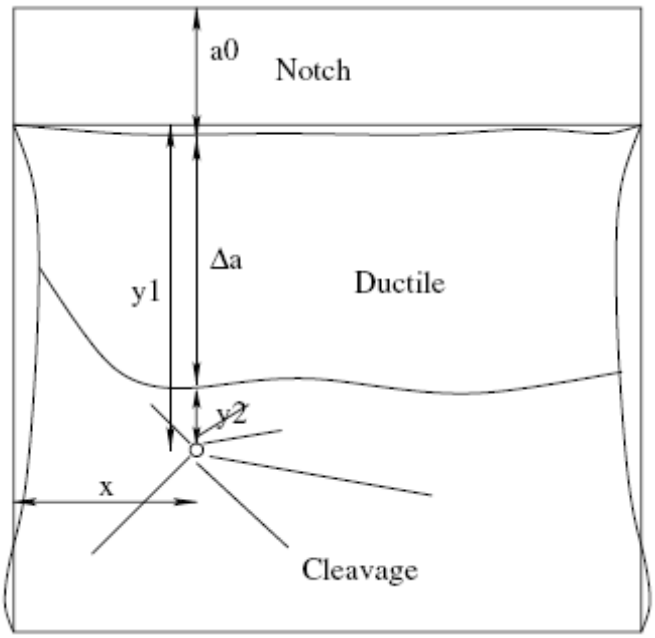

Fig. 6.20: (a) Typical experimental fracture surface of a Charpy specimen failed in impact transition region, (b) schematic showing the ductile and brittle regions and the distances usually measured to locate the cleavage initiation site during fractographic study [Tanguy 2005 a, b].

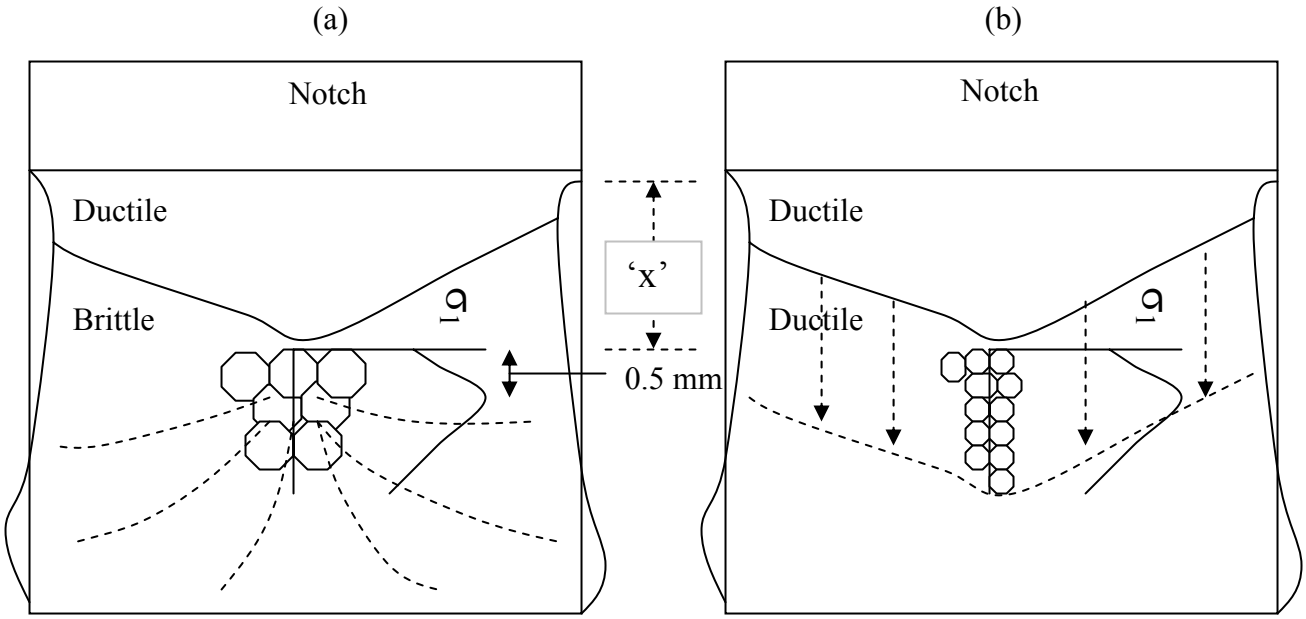

Fig. 6.21: Schematic diagram showing the possible effects of bimodal grain structure on fracture in impact transition region: (a) Presence of coarse grains in the critical volume in front of the ductile crack tip (where principle stress, σ_1, is a maximum) may promote brittle (or cleavage) fracture, whilst, (b) fine grains in the critical volume resist cleavage initiation and the ductile crack front propagates further resulting in a higher impact energy than situation (a).

Dist	Microstructure	Ferrite grain size distribution
22 mm	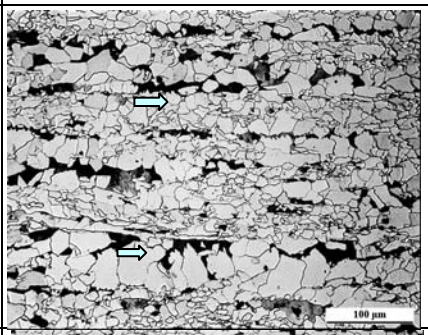	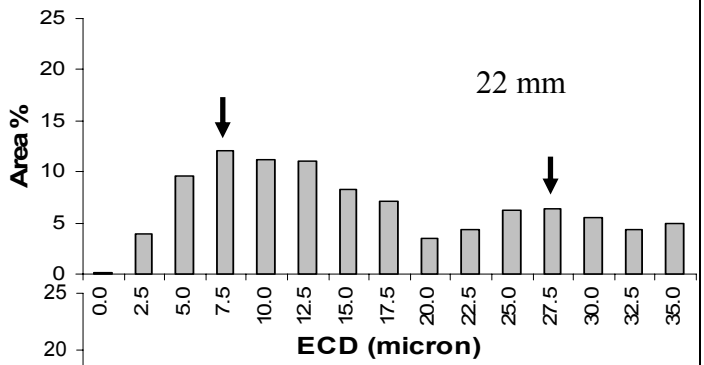
12 mm	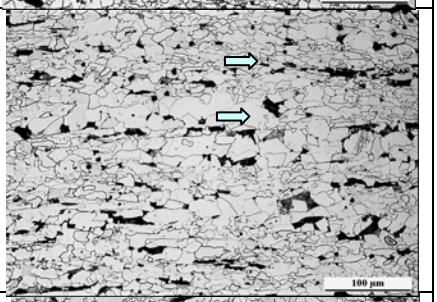	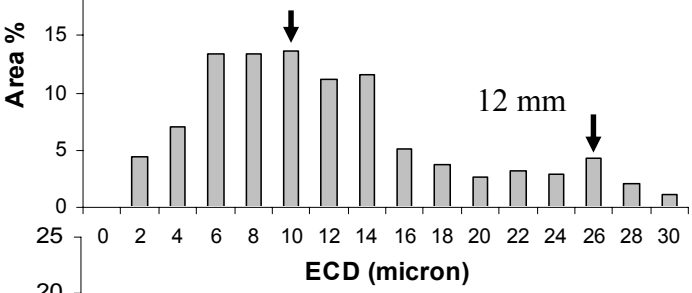
6 mm	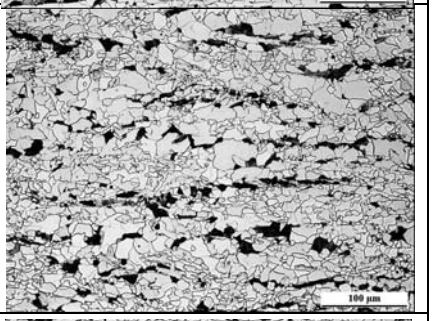	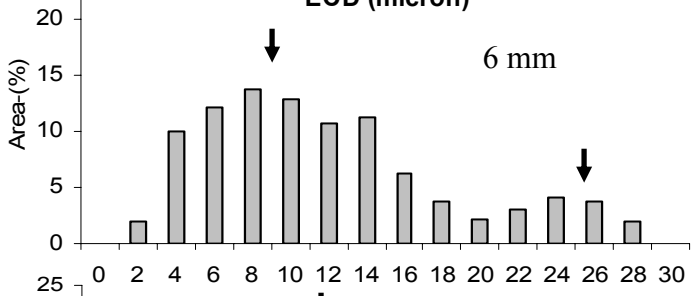
2 mm	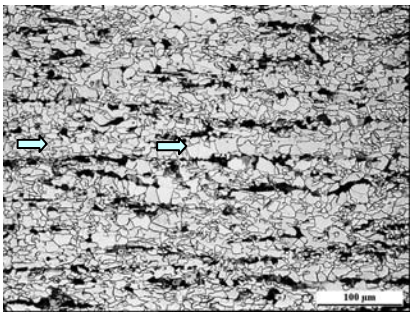	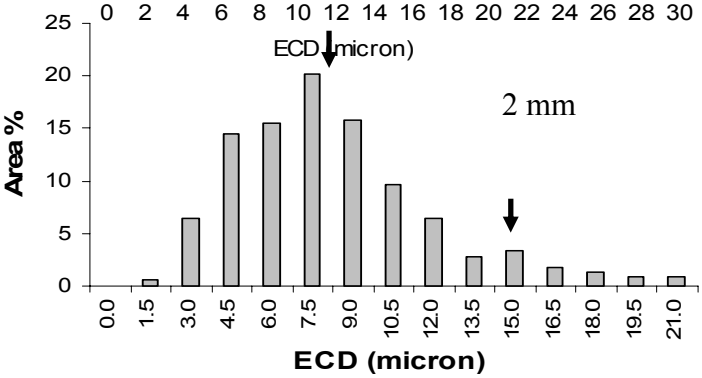
0 mm	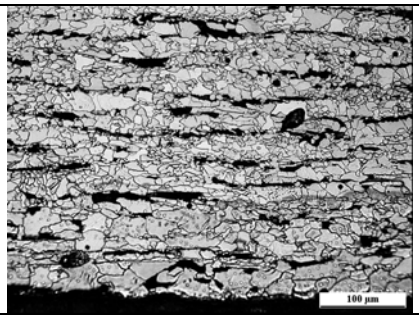	

Fig. 6.22: Microstructure of the commercial TMCR plate along thickness (at different positions from sub-surface towards mid-thickness). Also shown are the ferrite grain size distributions at sub-surface (2 mm), $^{1}/_{8}$ –thickness (6 mm), ¼-thickness (12 mm) and ½-thickness (22 mm) locations plotted in terms of area-percent frequency histograms based on ECD-scale (15 class). Both the peaks (peaks corresponding to coarse and fine grain populations) of the bimodal distributions are arrowed.

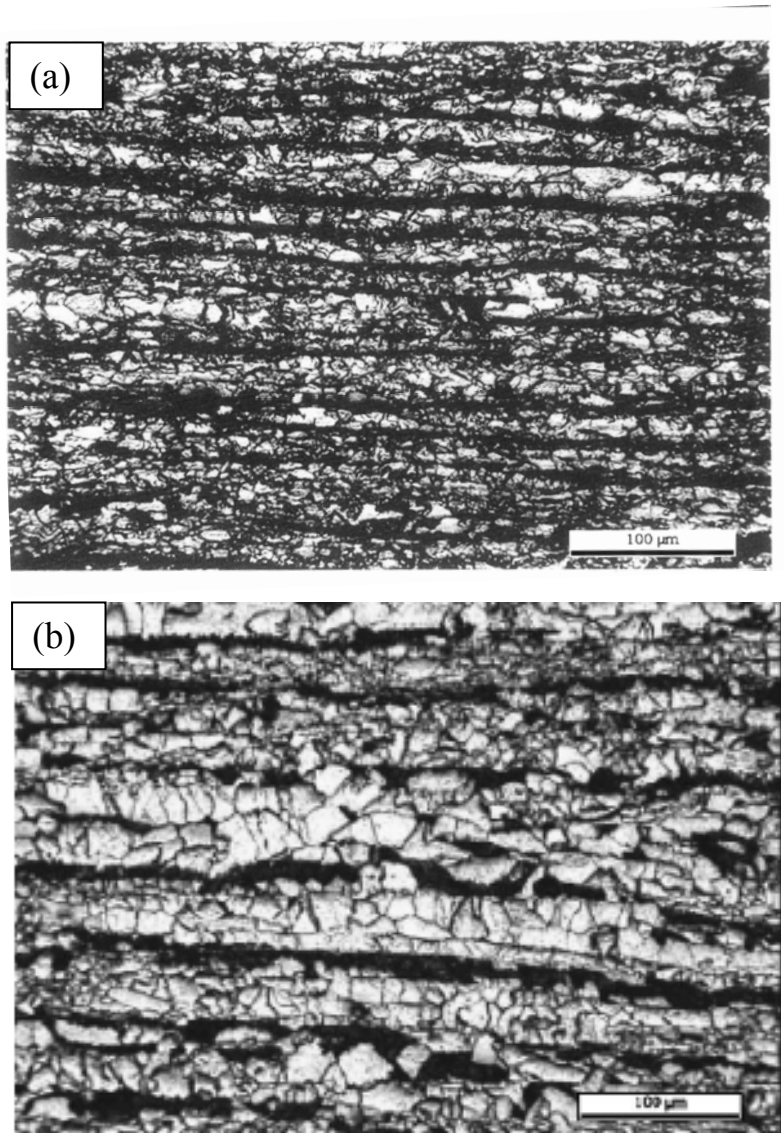

Fig. 6.23: Microstructures of TMCR steel at (a) sub-surface and (b) ½-thickness positions as reported by Wu and Davis [Wu 2004c]. Compared to sub-surface the frequency of coarse-grain patches are higher at mid-thickness.

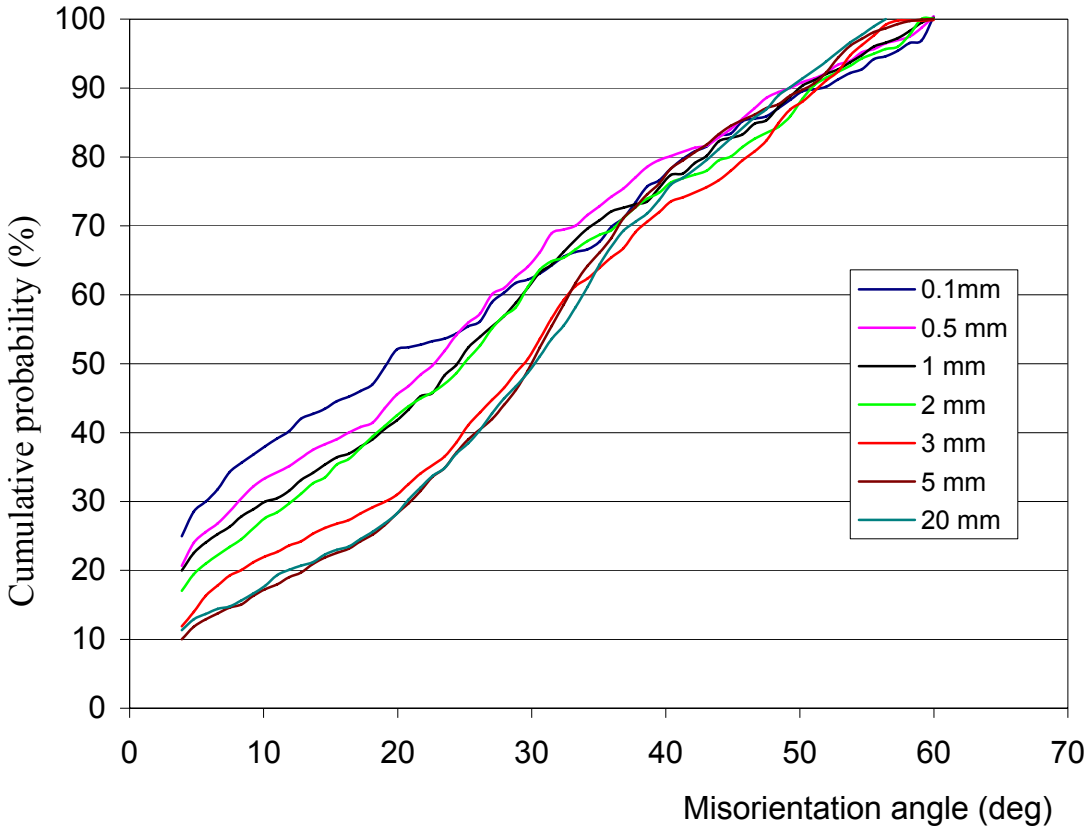

Fig. 6.24: Distribution plots of grain boundary misorientation angles at different locations along the thickness direction of TMCR-1 plate. Measotexture has been reported to be greater at sub-surface (mainly up to a depth of 2 mm) and afterwards reaches a similar level (from 5 mm depth to mid-thickness, 20 mm) [Wu 2004c]. That is the reason why mesotexture have not been measured at 10 mm or 15 mm depth, in the present study.

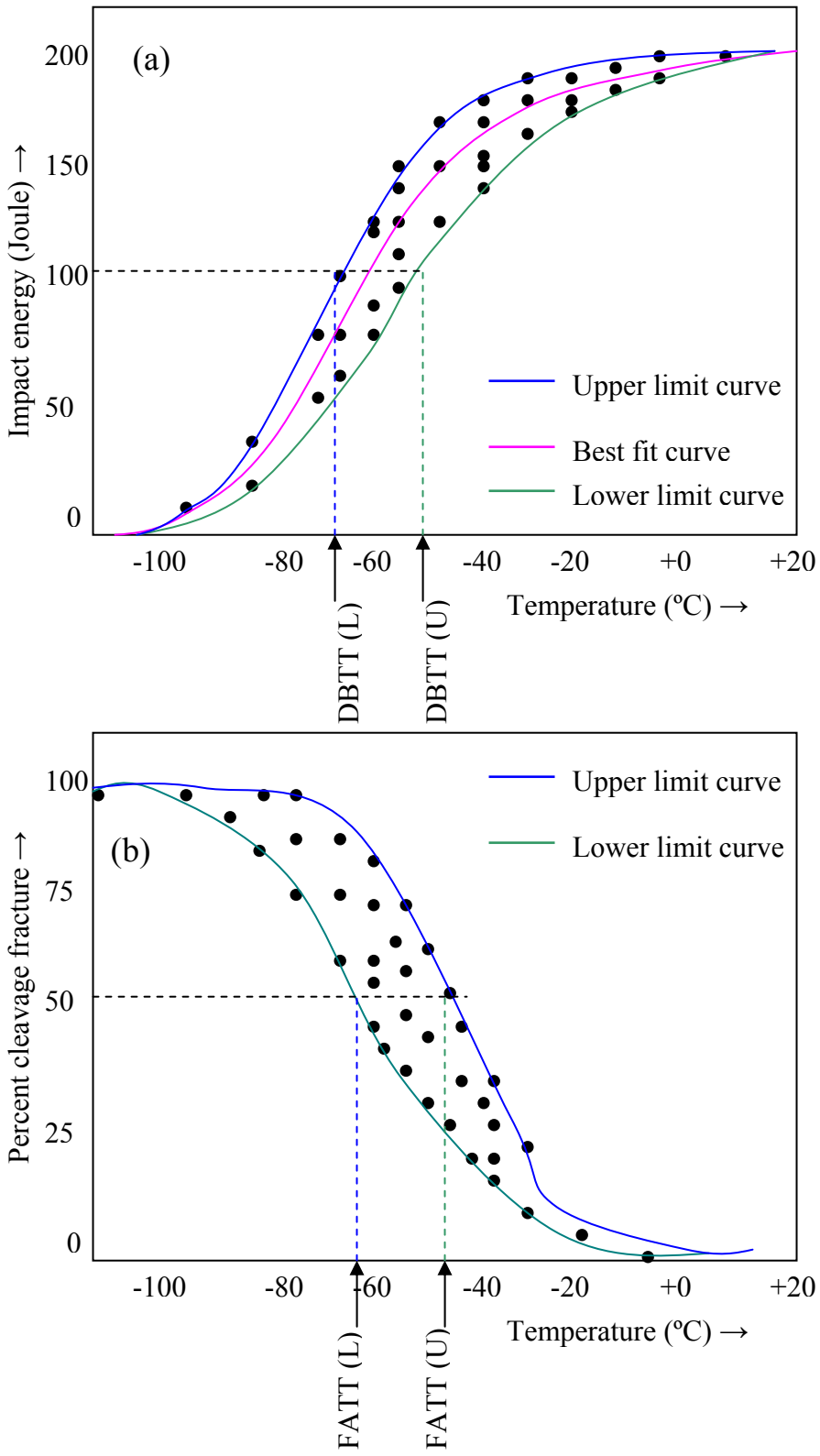

Fig. 6.25: Imaginary scatter in Charpy impact test results typically observed in Nb-microalloyed TMCR steels showing (a) the variation in impact energy (Joule) with temperature and (b) the variation in %-cleavage fracture with

temperature. Upper and lower limit curves are used to represent the scatter in DBTT and FATT values ((U) means the upper bound ITT value, i.e. the worst situation, and (L) the lower bound ITT value, i.e. the best situation).

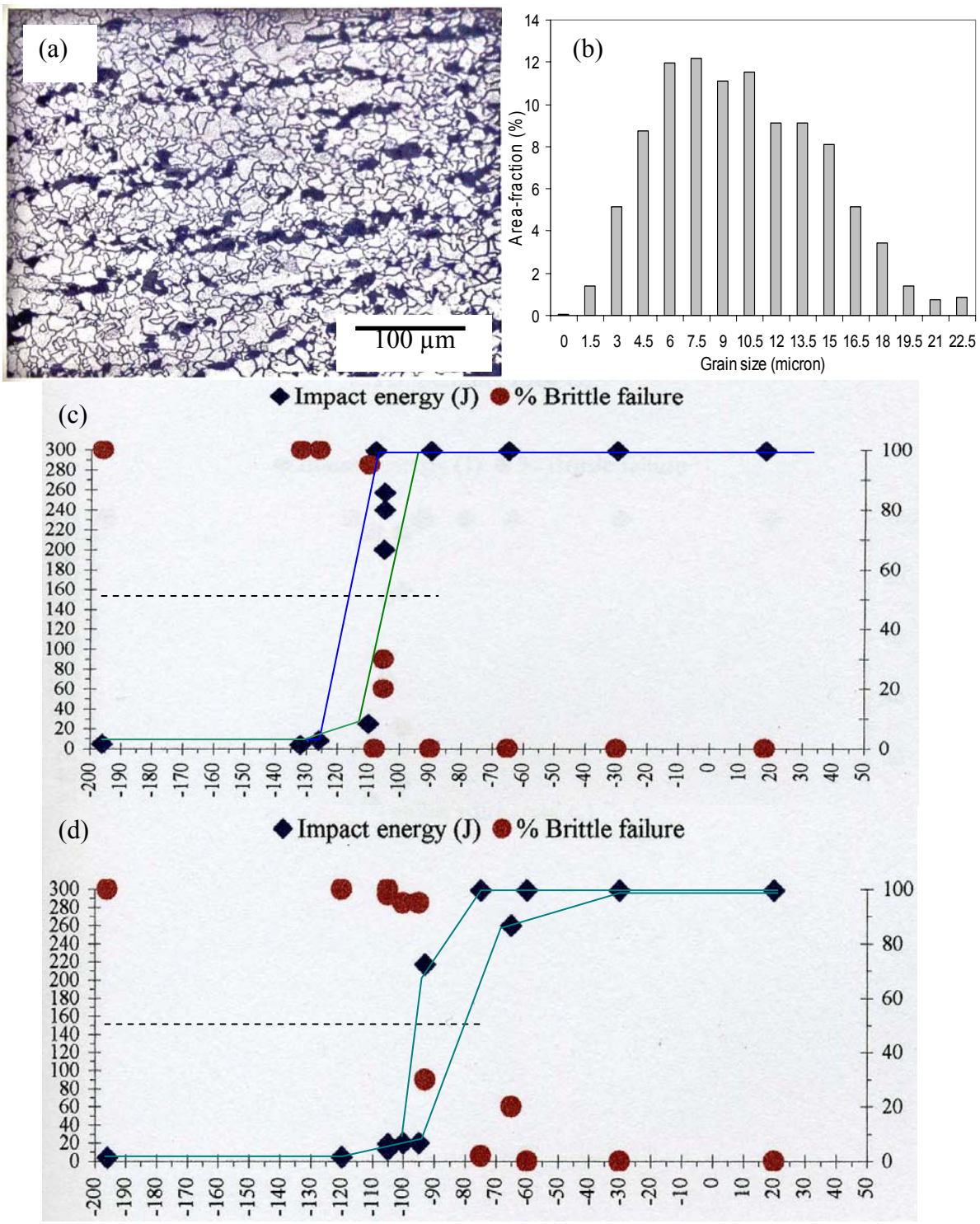

Fig. 6.27: (a) Ferrite + pearlite structure at the mid-thickness position of controlled rolled low Nb (0.023 wt %) steel with (b) unimodal ferrite grain size distribution. (c) and (d) showing the impact energy and fracture appearance transition curves for the same steel rolled in two different commercial controlled rolling schedule. Blue and green lines show the upper and lower limit curves for the impact energy transition, indicating that the range of DBTT is ~ 12 ºC at the most. Same results have been found in high Nb (0.057 wt %) steel.

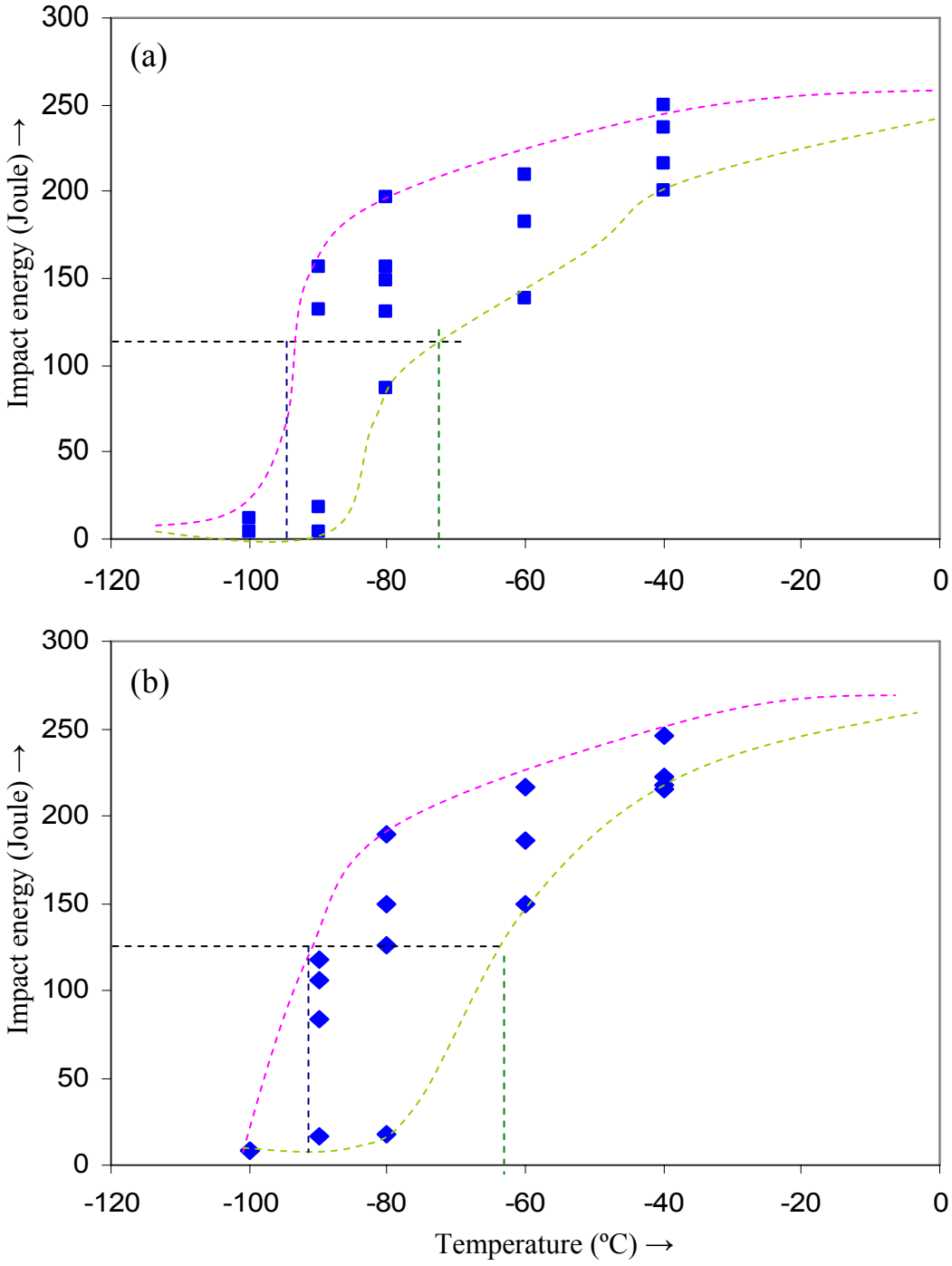

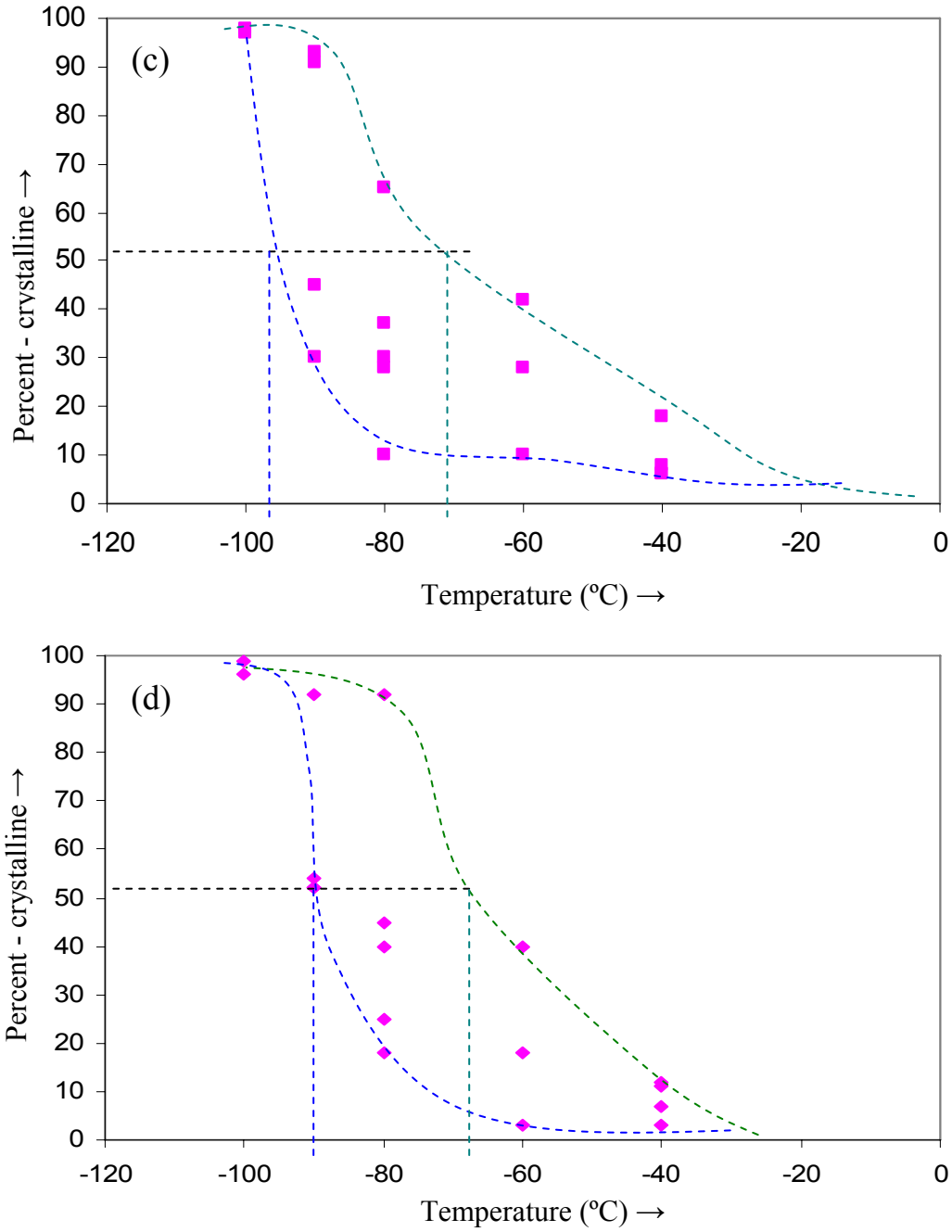

Fig. 6.28: Impact energy transition curves for (a) sub-surface and (b) quarter-thickness positions and fracture appearance transition curves (in terms of the percent crystalline fracture) for (c) sub-surface and (d) quarter-thickness position of TMCR-1 steel. Best and worst BDTT and FATT values are determined using upper limit and lower limit curves (drawn over the scattered data points).

Table 6.1: Average size, number density and constituent of particles on notch-bend test samples

	Average particle size (nm)	Number density of particles ($\times 10^4$-number / mm^2)	Constituent (percentage of precipitates)			Ti/(Ti+Nb) (all wt %) in Nb-Ti-precipitates
			Nb	Nb+Ti (+ V)	Al or Nb+Al	
Slab 1-940-700-hold	82	45	53	27	20	0.15
Slab 1-1140-700-hold	98	30	45	41	15	0.26
Slab 1-1210-700-hold	122	10	32	53	15	0.45

Table 6.2: Hardness values measured at -160 °C for notch-bend test (reheat + hold) samples.

Hardness (H_V) (20 kg) at -160 °C	Slab 1-940-700-hold	Slab 1-1140-700-hold	Slab 1-1210-700-hold
1	220	226	224
2	226	230	230
3	225	234	234
4	222	238	227
5	228	239	223
Average hardness	224.2	233.4	227.6
St. dev	3.2	5.5	4.5
σ_y (MPa) at -160 °C	701.7	730.5	712.4
P_{GY} (kg)	10592.3	11027.0	10753.0

Table 6.3: Calculation of the principal fracture stress (σ_F) from fracture load (L_F) for the bend test samples

Principle fracture stress (σ_F) calculation												
Sample	**Slab 1-940-700-hold**				**Slab 1-1140-700-hold**				**Slab 1-1210-700-hold**			
	L_F (kg)	L_F/L_{GY}	σ_F/σ_y	σ_F (MPa)	L_F (kg)	L_F/L_{GY}	σ_F/σ_y	σ_F (MPa)	L_F (kg)	L_F/L_{GY}	σ_F/σ_y	σ_F (MPa)
1	9915	0.91	2.49	1793	9241	0.85	2.41	1735	10830	1.00	2.59	1865
2	12076	1.11	2.69	1937	6830	0.63	2.14	1541	7991	0.74	2.27	1634
3	11279	1.04	2.63	1894	10376	0.95	2.54	1829	9982	0.92	2.50	1800
4	10683	0.98	2.57	1850	7721	0.71	2.24	1613	10663	0.98	2.57	1850
5	12288	1.13	2.71	1951	11736	1.08	2.67	1922	10663	0.98	2.57	1850
6	9216	0.87	2.43	1750	10218	0.94	2.52	1814	8816	0.81	2.36	1699
7	11231	1.03	2.62	1886	10973	1.01	2.60	1872	9075	0.84	2.40	1728
8	10599	0.98	2.57	1850	11417	1.05	2.64	1901	9826	0.90	2.48	1786
9	10534	0.97	2.56	1843	11001	1.01	2.60	1872	10783	0.99	2.58	1858
10	10614	0.98	2.57	1850	7637	0.70	2.22	1598	7030	0.65	2.15	1548
11	10736	0.99	2.58	1858	9384	0.86	2.42	1742	8786	0.81	2.36	1699
Average	**10834**			**1860**	**9685**			**1767**	**9495**			**1756**
St. Dev	**878**			**58**	**1669**			**132**	**1265**			**104**

Table 6.4: Calculation of local fracture stress (σ_f) using the fracture load (P_F) and the distance of cleavage initiation site from notch-root (I.S) for the notch-bend test samples. Also given are the notch-toughness (Q) values of the tested samples. Underlined σ_f values (also in bold font) of slab 1-1210-700-hold sample have not been considered for the later study, as discussed in section 6.1.3.

	Slab 1-940-700-hold					Slab 1-1140-700-hold					Slab 1-1210-700-hold				
	L_F	L_F/L_{GY}	I.S (μm)	Q $=\sigma_f/\sigma_y$	σ_f	P_F	L_F/L_{GY}	I.S (μm)	Q $=\sigma_f/\sigma_y$	σ_f	P_F	L_F/L_{GY}	I.S (μm)	Q $=\sigma_f/\sigma_y$	σ_f
1	9915	0.94	533	2.47	1734	9241	0.84	333	2.28	1666	10830	1.01	1214	2.00	**1424**
2	12076	1.14	267	2.55	1791	6830	0.62	267	2.08	1520	7991	0.74	478	2.25	1602
3	11279	1.06	454	2.52	1770	10376	0.94	350	2.38	1736	9982	0.93	318	2.30	1638
4	10683	1.01	533	2.56	1798	7721	0.70	200	2.00	1462	10663	0.99	229	2.25	1602
5	12288	1.16	333	2.61	1833	11736	1.06	400	2.55	1864	10663	0.99	267	2.32	1652
6	9216	0.87	350	2.34	1643	10218	0.93	300	2.31	1687	8816	0.82	250	2.10	1511
7	11231	1.06	250	2.39	1678	10973	0.99	297	2.35	1720	9075	0.84	333	2.22	1581
8	10599	1.00	292	2.38	1671	11417	1.03	735	2.49	1822	9826	0.91	867	2.18	1552
9	10534	0.99	833	2.41	1692	11001	1.00	390	2.43	1772	10783	1.00	334	2.35	1673
10	10614	1.00	400	2.50	1756	7637	0.69	229	2.06	1506	7030	0.65	100	1.75	**1246**
11	10736	1.01	686	2.58	1812	9384	0.85	400	2.33	1705	8786	0.82	280	2.15	1531
Avg		1.02		2.48	1743		0.88		2.30	1678		0.88		2.24	1594
Stdev		0.08		0.09	64		0.15		0.18	131		0.09		0.08	56

Table 6.5: Principle fracture stress, local fracture stress and the cleavage facet sizes measured at the cleavage initiation site for the bend test samples

	Slab 1-940-700-hold				Slab 1-1140-700-hold				Slab 1-1210-700-hold			
	σ_F (MPa)	σ_f (MPa)	σ_f/σ_F	Facet size (μm)	σ_F (MPa)	σ_f (MPa)	σ_f/σ_F	Facet size (μm)	σ_F (MPa)	σ_f (MPa)	σ_f/σ_F	Facet size (μm)
1	1793	1734	0.97	38	1735	1666	0.96	65				
2	1937	1791	0.92	30	1541	1520	0.99	89	1634	1602	0.98	111
3	1894	1770	0.93	34	1829	1736	0.95	54	1800	1638	0.91	100
4	1850	1798	0.97	34	1613	1462	0.91	103	1850	1602	0.87	97
5	1951	1833	0.94	27	1922	1864	0.97	47	1850	1652	0.89	98
6	1750	1643	0.94	42	1814	1687	0.93	66	1699	1511	0.90	121
7	1886	1678	0.89	35	1872	1720	0.92	61	1728	1581	0.91	124
8	1850	1671	0.90	36	1901	1822	0.96	49	1786	1552	0.87	114
9	1843	1692	0.92	37	1872	1772	0.95	55	1858	1673	0.90	86
10	1850	1756	0.95	33	1598	1506	0.94	94				
11	1858	1812	0.98	30	1742	1705	0.98	67	1699	1531	0.90	111
Average **Stdev**	**1860** **58**	**1743** **64**	**0.94**	**34** **4**	**1767** **132**	**1678** **131**	**0.95**	**68** **19**	**1767** **81**	**1594** **56**	**0.90**	**107** **12**

Table 6.6: PHR and PGSR values measured from the ferrite-grain size distributions at sub-surface (2 mm depth and 6 mm depth), quarter-thickness (12 mm depth) and mid-thickness (22 mm depth) locations of TMCR 1 steel.

	Bimodality Level	PHR	PGSR (μm)
Sub-surface (2 mm depth)	1	0.17	7.5
Sub-surface (6 mm depth)	3	0.28	16
Quarter-thickness (12 mm depth)	3	0.31	16
Mid-thickness (22 mm depth)	4	0.53	20

Table 6.7: Average ferrite grain size (μm) in equivalent circle diameter (ECD) and the skew of the grain size distribution in TMCR-1 rolled plate

	Average ECD (μm)	Skew
Sub-surface (2 mm from top)	5.6 ± 2.7	1.26
Sub-surface (6 mm from top)	6.1 ± 4.0	1.58
Quarter-thickness (12 mm from top)	6.4 ± 4.5	1.65
Half-thickness (22 mm from top)	8.0 ± 5.6	1.90

Table 6.8: Impact energy (Joule) and percent-crystalline fracture values for the sub-surface and quarter-thickness samples of TMCR 1 plate tested between – 40 ºC to -100 ºC temperatures

TMCR-1 sub-surface samples										
Sample	-40 (Joule)	-40 (%-cryst)	-60 (Joule)	-60 (%-cryst)	-80 (Joule)	-80 (%-cryst)	-90 (Joule)	-90 (%-cryst)	-100 (Joule)	-100 (%-cryst)
1	200	18	138	42	86	65	4	93	11	98
2	216	8	182	28	130	37	18	91	4	97
3	236	6	210	10	149	30	132	45		
4	250	6			156	28	156	30		
5					196	10				
Average	**226**	**10**	**177**	**27**	**143**	**34**	**78**	**65**	**8**	**98**
St. Dev	**22**	**6**	**36**	**16**	**40**	**20**	**78**	**32**	**5**	**1**
(St. Dev/Average) %	**10**	**60**	**21**	**60**	**28**	**59**	**100**	**50**	**66**	**1**
TMCR-1 quarter-thickness samples										
Sample	-40 (Joule)	-40 (%-cryst)	-60 (Joule)	-60 (%-cryst)	-80 (Joule)	-80 (%-cryst)	-90 (Joule)	-90 (%-cryst)	-100 (Joule)	-100 (%-cryst)
1	215	3	150	40	18	92	16	92	8	99
2	218	12	186	18	126	45	84	54	8	96
3	222	7	216	3	150	40	106	52		
4	246	11			190	25	118	52		
5					190	18				
Average	**225**	**8**	**184**	**20**	**135**	**44**	**81**	**63**	**8**	**98**
St. Dev	**14**	**4**	**33**	**19**	**71**	**29**	**46**	**20**	**0**	**2**
(St. Dev/Average) %	**6**	**50**	**18**	**92**	**53**	**66**	**56**	**32**	**0**	**2**

7 Microstructure and precipitates in the as-cast slabs

The grain size of the final product (plate, strip or sections) is influenced by each of the stages of processing (casting, reheat and rolling) and, in order to understand the formation and severity of a duplex structure, as well as the average grain size, each process needs to be considered.

Continuous casting is the first solid metal industrial processing stage (to make plate, strip or sections), where the liquid steel is solidified into slabs / billets. Variation in grain structure [Zhang 2000], segregation of alloying elements [Couch 2001, Presslinger 2006, Mintz 1986]; and non-uniform distributions (or localised distributions) of precipitates [Couch 2001, Zhang 2000, Tian 1996] have been found in continuously cast HSLA steel slabs. Therefore, the microstructures and the precipitate distributions in as-cast slabs need to be characterised to investigate the role of casting on the formation of bimodality.

7.1 Microstructure of the as-cast slabs

The microstructures of sub-surface, quarter-thickness and mid-thickness positions of continuous cast slab 1 consisted of ferrite and pearlite, **Fig. 7.1**, and were similar in slab 2 and slab 3. The mean size, number density and the area fraction of pearlite at those positions for the three as-cast slabs are listed in **Table 7.1**. The mean size (equivalent circle diameter, ECD) of the pearlite colonies increases and the number density decreases with increasing depth below the surface. The area percentage pearlite was found to vary between 10 and 17 %, which is somewhat higher than predicted by the Lever rule (~ 10%

pearlite). The increase in pearlite fraction towards mid-thickness can be associated to the macro-segregation taking place during casting. Similar pearlite fractions have been found in all three slabs, however, pearlite fraction is expected to be higher in slab 3, compared to the other slabs, due to its highest carbon equivalent $\left(CEV = \%C + \frac{\%Mn}{6} + \frac{\%Ni}{15} \right)$ value (0.38 in slab 3; 0.36 in both slab 1 and slab 2), coming from the highest level of Mn and Ni in slab 3, **Table 4.1**.

The number averaged SDAS and ferrite grain size values measured at several through-thickness locations for all three slabs, **Table 7.2**, indicate that the finest SDAS and ferrite grain sizes are near the sub-surface, which experienced the highest cooling rates. Moving towards the slab centre, the cooling rate decreases and there is an increase in both SDAS and ferrite grain size. Slab 1 shows a significant increase in SDAS values at smaller depths from the top surface than in the other slabs. This is probably due to the greater freezing range and lower undercooling for slab 1 in comparison to slabs 2 and 3. For slab 1 full solidification is predicted at 1471 °C rather than 1481-1486 °C for slabs 2 and 3 [Zhang 2000]. At the quarter-thickness position for all three as-cast slabs both the number-percent and the area-percent histograms represented a normal (unimodal) grain size distribution (PHR=0, PGSR=0), **Fig. 7.2**, which were further confirmed by the visual observation of a more uniform grain structure (not bimodal-'0' level) at that region. However, **Fig. 7.1** and **Fig. 7.2** show that a wide range of grain sizes (for example smallest grain size ~ 8 micron to largest grain size ~ 408 micron at the quarter-thickness position of slab 1) exists in the as-cast steel.

Zhang et al. [Zhang 2000] have earlier reported similar SDAS, ferrite grain sizes (**Table 7.2**) and grain size distribution (**Fig. 7.2**) for continuously cast steels with the same compositions. The absence of any ferrite grain size bimodality in the as-cast steel

suggests that reheating and / or the rolling schedule are responsible for the formation of bimodality and therefore, should be studied. However, to be sure about the uniformity in grain sizes in as-cast steel there is a need to reveal the prior austenite grains (hidden behind the ferrite + pearlite structure) and study the austenite grain size distribution in future. Studying the pearlite colony size distribution, along with the ferrite grain size distribution, can also be useful for that purpose as pearlite forms in interdendritic regions and ferrite forms in dedritic regions of as-cast steel.

7.2 Inclusions in the As-Cast Slabs

To maintain high toughness properties large (> 1μm) inclusions are undesirable [Balart 2000]. Finer inclusions (less than 1 μm in size) may take part in pinning the austenite grain boundaries during reheating [Gladman 1997]. Therefore, from the microstructure and mechanical property point of view the nature and the distribution of inclusions in continuously cast slabs need to be studied. Sulphide (MnS and fine CuS) inclusions, **Fig. 7.3**, with a largely equiaxed shape (0.5-11 μm size range) and oxide (Al_2O_3 or SiO_2) inclusions, **Fig. 7.4**, of irregular shape (0.5-3 μm size range) were observed optically and also by SEM in all the three slabs. Sulphide and oxide inclusions coexisted in some cases, **Fig 7.5**, probably due to the formation of the MnS, **Fig. 7.5 d**, on pre-existing Al_2O_3 inclusion, **Fig. 7.5 e**. EDS analysis showed that Mg could also take part in the formation of the inclusions (both sulphide and oxide), **Fig. 7.4, Fig. 7.5**. Mg would have come from the magnesium-oxide (MgO) refractory used in steel making. Mg has a high affinity for both oxygen and sulphur and therefore, very small levels of Mg can be active in forming inclusions. Rarely Zr_2O_3 inclusions have been found and that might have come from refractory particles worn from the submerged entry nozzle, **Fig. 7.5 f**.

The largest and most numerous inclusions observed were MnS-based and the distributions of these with depth have been determined, **Fig. 7.6**. **Fig. 7.6** does show the distributions in all slabs to be skewed to larger sizes. Towards the mid-thickness the MnS inclusions become larger in size (average size at 20-mm from surface: 1.5-1.8 μm and at mid-thickness: 2.2-2.4 μm) compared to the sub-surface, however, the number density drops (number density at 20-mm from surface: 45-75 / mm^2 and at mid-thickness: 25-45 / mm^2). The area-fraction of inclusions also increases from sub-surface (0.013-0.020 %) to quarter-thickness (0.017-0.024 %) and to mid-thickness (0.021-0.030 %). The slower cooling towards mid-thickness therefore, leads to stronger segregation and a larger dendritic arm spacing, which allows the inclusions to grow to a larger size compared to at the sub-surface. The average area percent (including all three locations, sub-surface, ¼-thickness and ½-thickness, studied) of MnS inclusions was highest in slab 3 (~0.025 %) and were similar in slab 1 and in slab 2 (~0.020 %). This suggests that the amount of MnS depends on both the Mn and S levels in the steel, rather than the individual amount of Mn or S. The highest level of Mn and the intermediate level of S in slab 3 explains the highest amount of MnS formed in that slab. However, the similar area fraction of MnS in slab 1 and slab 2 is difficult to explain as slab 1 contains a much higher S level than slab 2, with similar Mn level in both steels, **Table 4.1**. More than sufficient Mn was available both in slab 1 (1.42 wt%) and in slab 2 (1.41 wt%) to combine with all the S present in those steels, as, 0.001 and 0.005 wt% S only requires 0.002 and 0.009 wt% Mn, respectively, to form MnS.

Al_2O_3 inclusions are a liquid de-oxidation product that remains entrapped in the steel, whereas, MnS inclusions form during solidification either within the liquid or within the solid. Thermo-Calc software predicts that the temperature of MnS formation (slab 1: 1465 ºC, slab 2: 1310 ºC, and slab 3: 1385 ºC) decreases with the drop in S

content in the steel. The corresponding Thermo-Calc prediction for the complete solidification temperatures for all three slabs (slab 1: 1469 ºC, slab 2: 1482 ºC and slab 3: 1482 ºC) indicates that MnS formed after complete solidification in all three slabs (however, in slab 1 MnS formation and complete solidification temperatures were quite close).

7.3 Precipitates in the As-Cast Slabs

An inhomogeneous distribution of precipitates was found on the polished surface of all three as-cast slabs, **Fig. 7.7 a**, with the precipitate-rich regions (indicated by A, B & C in **Fig. 7.7 a**) separated by regions of low precipitate density (D). The separation of precipitate-rich regions was consistent with the distances between interdendritic regions as the centre-to-centre distances between regions, such as A, B and C, at the quarter-thickness position of the slabs lie between 200 and 250 μm, i.e. similar to the SDAS at that position (211 μm for slab 1 and 198 μm for slab 2 and slab 3). Energy dispersive spectroscopy, EDS, analysis on the cluster of precipitates in precipitate-rich regions, **Fig. 7.7 (b and d)**, and the isolated precipitates in the precipitate-lean regions, **Fig. 7.7 c**, revealed that the inhomogeneously distributed precipitates were Nb-rich carbonitrides (Nb(C, N) or (Nb, Ti)(C, N)), **Fig. 7.7 e**. Apart from secondary electron imaging (SE), backscattered electron imaging (BSE) has also been used to study the precipitate distribution. **Fig. 7.8** shows the SE and BSE images of a precipitate-rich (**Fig. 7.8 a** and **b**) and a precipitate-poor (**Fig. 7.8 c** and **d**) region. Nb-rich precipitates appear bright against the iron-matrix during backscattered electron imaging (BSE), **Fig. 7.8 b**, as the atomic number of Nb=41 is higher than that of Fe=26 and BSE image in compositional mode creates atomic number contrast, and therefore, BSE clearly distinguishes the precipitate-rich regions from the precipitate-poor regions. Precipitate-rich regions were

found to coincide with the interdendritic regions of the steel (on or around pearlite colonies) and precipitate-poor regions coincided with the dendrite centre regions (ferrite dendrite centre). Thus, interdendrtic segregation or microsegregation is consistent with the inhomogeneous precipitate distribution and may be its cause. This hypothesis can further be supported by the separation of the precipitate-rich regions, which is similar to the SDAS. Apart from the Nb-rich microalloy precipitates, AlN particles can also be seen in **Fig. 7.8** (**b and d)** that appear dark in BSE image (as atomic weight of Al=13 is less than Fe=26). Unlike the Nb-rich precipitates, the irregular AlN particles were distributed uniformly between precipitate-rich and -poor regions. No TiN particles have been observed in the as-cast slabs, but Ti was present along with Nb in the carbo-nitride precipitates.

The shape, size and the number density of the Nb(C, N) and AlN precipitates at the sub-surface, quarter-thickness and mid-thickness positions of the as-cast slabs have been studied. Precipitates in slab 2 were found to be similar in nature to those in slab 1, but fewer in number. That is expected as both the Nb and Ti levels in slab 2 are lower than in slab 1. Slab 3 contained the least amount of Nb and most Ti. Therefore, the precipitates in slab 1 and slab 3 were quantified in detail.

7.3.1 Shape and size of the precipitates in the as-cast slabs

Nb-rich precipitates in the precipitate-rich region were spherical, cubic or star (winged precipitates) shaped, whereas, in the precipitate-poor region spherical and cubic shapes were observed but star shaped precipitates were not seen. **Fig. 7.9** shows the different shapes and the corresponding EDS analyses of the Nb-rich precipitates in the precipitate-rich region of slab 1. EDS analyses of the winged precipitates showed them to be complex (Nb, Ti)(C, N) or (Nb, Ti, V)(C, N), **Fig. 7.9**. **Fig. 7.10** shows that the centre

of winged precipitates were Ti-rich, whilst, the wings were rich in Nb and V. The winged morphology was observed by Mintz et al. [Mintz 1997] and Kejian et al. [Kejian 1997], who suggested that the precipitation of Nb-rich phase on a pre-existing Ti-rich core forms the wings. The presence of such precipitates, specifically in the interdendritic regions, has been attributed to the interdendritic-segregation of microalloying elements [Mintz 1997, Kejian 1997]. The observed cubic precipitates were Nb(C, N), or complex carbonitrides, (Nb, Ti)(C, N), **Fig. 7.9**. The centre of the cubic (Nb, Ti)(C, N) precipitates were richer in Ti compared to the cube edges, **Fig. 7.11**. The spherical precipitates were either Nb(C, N) or (Nb, V)(C, N), **Fig. 7.12**. Spherical, star and cube shapes are commonly observed in as-cast steels with similar compositions (refer **section 1.2.5**) [Couch 2001, Zhang 2000, Kneissi 1992, Jun 2003]. Ti-rich cores within Nb-rich carbonitride precipitates of 200-500 nm size range have also been observed [Kneissi 1992, Jun 2003].

The precipitate size distributions in the precipitate-rich regions at the quarter-thickness position of slab 1 and slab 3, **Fig. 7.13**, show that Nb-rich precipitates were present in the size range ~ 0 - 470 nm in slab 1 and ~ 0 - 580 nm in slab 3. **Fig. 7.14** related the sizes and the fractions of the precipitates in terms of their shapes. Spherical precipitates were the smallest (10 - 150 nm) and most frequently observed (80 % of all precipitates). Cubic (60-300 nm size) and star shaped (150 - 500 nm size) precipitates were larger and less frequent (10 % cubic and 10 % star shaped precipitates). The average size of the Nb-rich precipitates increased from the sub-surface towards the mid-thickness location for all the slabs (average size at sub-surface, quarter-thickness and mid-thickness are 70 nm, 76 nm and 83 nm, respectively, for slab 1 and 78 nm, 83 nm and 87 nm, respectively, for slab 3) possibly due to: (i) the increase in solute level (macro-segregation) towards slab centre and (ii) slower cooling rate allowing more time for the precipitates to grow in size. The larger precipitate size in slab 3 is possibly due to the

higher Ti content in that steel compared to slab 1, which will produce larger Ti-rich nuclei and therefore result in larger sized cubic or winged precipitates of (Nb, Ti)(C, N). In general more Nb-rich carbo-nitride precipitates showed separate Ti-peaks in slab 3 (43 % of total precipitates) compared to slab 1 (15 %). The average Ti level in those (Nb, Ti)(C, N) precipitates was also higher in slab 3 (Ti/Ti+Nb=0.35) than in slab 1 (Ti/Ti+Nb=0.2). Therefore, the higher nominal Ti level in slab 3 (0.009 wt %) resulted in an increase in Ti-level within the carbonitride precipitates compared to slab 1 that contained only 0.002 wt % Ti. The precipitate size range was much smaller at the dendrite centre regions (~ 0 - 260 nm), **Fig. 7.15**, compared to the interdendrtic regions, as the dendrite centre regions were solute-lean due to microsegregation. However, **Fig. 7.15**, shows that the interdendritic regions contained not only more precipitates of large size (> 250 nm) but also more precipitates of small size (< 50 nm) compared to the dendrite centre regions whilst the number average precipitate sizes at both the regions were almost the same. However, the volume fraction of precipitates were higher at the interdendritic regions (**refer section 7.3.2**) due to a higher solute level (micro-segregation).

AlN particles were faceted and irregular in shape, **Fig. 7.16 (a),** appear dark in BSE image **Fig. 7.16 (b),** and could be identified from the presence of Al and N peaks in the EDS spectrum **Fig. 7.16 (c)**. A typical size distribution of AlN particles at the quarter-thickness position of slab 1 (average particle size 114 nm) is shown in **Fig. 7.17**. Shape (irregular or faceted precipitates) and size (average size ~ 110 - 115 nm) of the AlN precipitates were similar everywhere, i.e. no difference between the intredendritic or dendrite core areas.

7.3.2 Number density and distribution of the precipitates in as-cast slab

The extent of inhomogeneity in the distribution of Nb-rich precipitates in slab 1 has been quantified in terms of the average (local) precipitate area density (number / mm^2) at the interdendritic and dendrite centre regions, **Table 7.3, Fig. 7.18**. The overall average area density (number / mm^2) was also measured by considering both interdendritic and dendrite centre regions over continuous fields of view. The equilibrium precipitate number density (shown in **Fig. 7.18 a and b**) can be determined assuming that the precipitates are spherical in shape and using the following parameters: (**i**) average precipitate size (experimentally measured precipitate size, **section 7.3.1**) at the quarter-thickness position, (**ii**) the equilibrium composition of carbo-nitride precipitates at room temperature (predicted from the overall steel composition, **Table 4.1,** using Thermo-Calc software), and (**iii**) the densities of simple microalloy carbides and nitrides (NbN: 8.5 gm / cm^3, NbC: 7.8 gm / cm^3, TiN: 5.4 gm / cm^3, TiC: 4.9 gm / cm^3, VN: 6.1 gm / cm^3, VC: 5.7 gm / cm^3).The area densities of Nb-rich precipitates were higher in slab 1 compared to slab 3 due to the higher average Nb-level in slab 1. At the quarter-thickness position the average precipitate density of interdendritic regions was ~ 3.8-5.0 times higher than that of the dendrite centre regions, **Table 7.4, Fig. 7.18**. The difference in average precipitate density between precipitate-rich and precipitate-poor regions at a particular location represents the inhomogeneity in precipitate distribution at that location. The average precipitate density and the inhomogeneity of the distribution both increase with increasing distance from the slab surface, **Fig. 7.18**.

The increase in average local precipitate density towards the slab centre is probably due to macro-segregation during solidification (liquid gets richer in solute towards the slab centre as solidification proceeds) and / or the sweeping action of the advancing solidification front (sweeping any precipitates towards the slab centre). Mn has a tendency to segregate within the solidifying steel [Ghosh 2001, Krauss 2003,

Presslinger 2006], however, not as strongly as S, P or Nb (refer **section 1.2.2**). Therefore, any evidence of macrosegregation of Mn, which is present in solution, also points to the macrosegregation of Nb, which is present in the form of precipitates. The average Mn levels in the investigated slabs have been determined at the sub-surface, quarter-thickness and mid-thickness locations by EDS point analysis (taken from the matrix), **Fig. 7.18 c**. **Fig. 7.18 c** shows that the local Mn level at the sub-surface location is ~ 0.8 - 0.9 times the overall Mn level in the steel, **Table 4.1**. However, the local Mn level exceeds the overall Mn level and increases towards the quarter-thickness (~1.2 - 1.3 times of overall Mn level) and mid-thickness (~1.44-1.55 times of overall Mn level) locations. The increase in local Mn level (within the matrix) towards the slab centre indicates macro-segregation taking place during solidification**.** The precipitate number density follows a similar trend to the local Mn level, **Fig. 7.18**, as the local precipitate density at the sub-surface location is lower than the equilibrium precipitate density and increases towards mid-thickness exceeding the equilibrium precipitate density. Therefore, macro-segregation would appear to be the dominant factor responsible for the increase in precipitate number density from sub-surface towards slab centre. Moreover, the precipitate number density at the slab centre does not represent fully the total microalloy level at that location, as microalloying elements have also been found in the form of large networks (only at the slab centre), which were several microns in thickness (discussed later). This also indicates macro-segregation of the microalloying elements and is discussed in **section 7.4.2** in detail.

To determine the cause of the inhomogeneous distribution of Nb-rich precipitates, EDS and WDS spectra were taken from the interdendritic and dendrite centre regions at the quarter-thickness positions of the as-cast slabs. The EDS area analysis spectrum from the interdendritic region (spectrum 1) is compared to the spectrum from the dendrite

centre region (spectrum 2) for slab 1 in **Fig. 7.19**. The Nb (L) peak (made of Lα and Lβ peaks) is evident in spectrum 1 (~ 2.2 keV), however, the same peak is absent in spectrum 2, **Fig. 7.19 (b and c)**. That is due to the higher Nb-level (~ 0.1 wt %) within the interdendritic region, compared to the dendrite centre region (~ 0.03 wt %). Considering all the spectra examined the average Nb-level at the interdendritic regions (0.070 % for slab 1 and 0.040 % for slab 3) was 2.5 - 3.0 times higher than that at dendrite centre regions (0.025 % for slab 1 and 0.016% for slab 3). Besides the difference in Nb-levels the comparison of EDS spectrums also indicated a difference in Si levels (spectrum 1: 0.43 %; spectrum 2: 0.26 %), **Fig. 7.19 c**, and Mn levels (spectrum 1: 2.4 %; spectrum 2: 1.3 %), **Fig. 7.19 d**, between the interdendritic and dendrite centre regions. All the above findings indicate that micro-segregation (or interdendritic segregation) was taking place during solidification and that the micro-segregation of Nb (along with C and N) has resulted in an inhomogeneous distribution of Nb-rich precipitates. This hypothesis can also explain why the separation between the precipitate-rich regions is similar to the average SDAS at the same location. The delay in complete solidification with increasing distance from slab surface can give rise to higher interdendritic- or micro-segregation, and hence, a more inhomogeneous precipitate distribution occurred towards mid-thickness.

Besides the random distribution of Nb-rich precipitates, particles were often clustered together in regions of high precipitate number densities, **Fig. 7.20 a** (mainly in slab 1). Nb-rich precipitates have also been found in arrays, **Fig. 7.20 b to d**. Tian et al. [Tian 1996] mentioned that Nb has a high tendency of clustering (or aligning) in steels, especially when the Nb level exceeds ~ 0.04 % Nb, possibly due to the high segregation tendency of Nb. Knessi et al. [Knessi 1992] mentioned that the alignment of Nb precipitates was due to Nb-partitioning at prior δ or γ grain boundaries. In the present

study Nb-precipitates have been found both in cluster (at the interdendritic region) and in aligned fashion (on the pre-existing δ or γ boundaries).

AlN particles were distributed almost uniformly (particle density ~ 5 - 6×10^4 / mm^2) (between the precipitate-rich and precipitate-lean regions) with no obvious spatial inhomogeneity, however, row precipitation (possibly nucleated on dislocations) or aligned precipitation (precipitation along prior δ or γ grain boundaries) was observed, **Fig 7.20 e to g**.

7.4 Segregation of microalloying elements at large (> 1 μm) deposits

7.4.1 Ring around MnS

So far microsegregation has been identified from the inhomogeneous distribution of microalloy precipitates. Further evidence of microsegregation was found in the deposition of Nb-rich constituents (also containing Ti and V in lesser quantity) around the MnS inclusions at the interdendritic regions of the slabs. The BSE image in **Fig. 7.21** shows this segregation in the form of a bright (incomplete) ring of ~ 2 μm in diameter and thickness varying between 60 - 620 nm around the MnS inclusion, which appears dark. The ring appears bright as it contains microalloying elements (mostly Nb), **Fig. 7.21**, that are heavier than Fe. MnS appears dark as the atomic numbers of Mn (25) and S (16) are lower than Fe (26). Such constituents are probably Nb-rich complex (Nb, Ti, V)(C, N) carbonitrides and were observed throughout the slab thickness (sub-surface, quarter-thickness and mid-thickness) only within the interdendritic regions. MnS inclusions at dendrite centre regions were free from such deposits. The formation of such deposits is related to the microsegregation in steel slab, as the excess solute (particularly Nb) from segregated regions was preferentially deposited on the pre-existing MnS inclusions to

form the segregation ring. A precipitate free zone, pfz (~ 1-1.5 μm) has also been found around the deposits (due to depletion of Nb through a collector-plate type action of the interface) with a high density of Nb-rich precipitates beyond that pfz. Solute levels in the dendrite centre region (solute-lean) were insufficient to form such deposits.

7.4.2 Network of (Nb, Ti)(C, N) at slab centre

At the centre location of all three investigated slabs networks of large deposits (up to 10 μm in thickness) have been seen, **Fig. 7.22**. The network deposits were located at the heavily segregated regions, i.e. along pre-existing (δ or γ) grain boundaries, **Fig. 7.22 (a to c)** and closely connected to large MnS inclusions, **Fig. 7.22 (a), (d)**. Previous researchers have suggested that such grain boundary networks are the evidence of macro-segregation in steel and are either phosphides (macrosegregation of P resulting in Fe-phosphide or (Fe, Mn)-phosphide) [Zhang 2002] or microalloy-carbonitrides, (Nb, Ti, V)(C, N) [Li 1998, Mintz 1986, Presslinger 2006]. Li and Priestner [Li 1998] attributed the formation of such microalloy-segregates to the strong segregation of Nb, weaker segregation of Ti and almost negligible segregation of V in the last solidifying liquid. In the present study EDS analysis on the network deposits indicates the presence of Nb (L) peaks in all analyses and Ti (K) (**Fig. 7.22 f** and **Fig. 7.23 c**) and V (K) peaks (**Fig. 7.23 c**) in 93 % and 67 % of analyses, respectively. The deposits were clearly Nb-rich as Ti/(Nb+Ti) ~ 0.15 and V/(V+Nb) ~ 0.01. The presence of Ti and V peaks as well as Nb peaks suggests that the networks are made of microalloy-carbonitride not phosphide.

However Nb (L) peaks (Nb Lα~2.16 keV, Lβ~2.25 keV) and P (K) peaks (P Kα ~2.01 keV, Kβ~2.14 keV) are close to each other. Therefore, a possibility exists that the element identification system of EDS Inca-software might misinterpret P-peaks as Nb-peaks. Moreover, both phosphides and carbonitrides could be present in the network

deposits and there could be a chance of overlapping of Nb (L) and P (K) peaks. However the presence of (i) Nb (L), Ti (K) and V (K) peaks in spectrum 1 (EDS taken from network deposit over 0-20 keV range) and not in spectrum 2 (EDS taken from the matrix over 0-20 keV range), **Fig. 7.23 (b and c)**; and (ii) the presence of Nb (K) peak at ~ 16.6 keV in spectrum 1 and not in spectrum 2, **Fig. 7.23 (b and d)** suggest that Nb must be there in the network (not P) along with Ti and V (**Fig. 7.23**).

To make sure that Nb (L) and P (K) peaks were not superimposed a WDS scan was carried out over the energy level 1.8-2.3 keV. Resolution of WDS is better than EDS and therefore, WDS scans can resolve the peaks separately. The WDS scan, **Fig. 7.23 (e)**, identified sharp Nb (Lα and Lβ) peaks but not the P (K) peaks. Therefore, it can be concluded that microalloying elements, particularly Nb, segregates strongly in commercial continuously cast steels forming large macro-segregated deposits at the slab centre location.

7.5 Solidification sequence in as-cast slabs

The distribution of precipitates will be controlled by the overall alloy composition and amount of micro- and macro-segregation and hence, the solidification sequence in the steel. For typical HSLA steel compositions (e.g. 0.1 C, 1.4 Mn, 0.02 – 0.06 Nb, 0.005 V, 0.001-0.007 Ti, all wt%) the slabs will start to solidify as δ-ferrite and, as cooling rates are not slow enough to be equilibrium, will at some depth change to solidification as both δ-ferrite and austenite. The position of this change in solidification sequence will depend on composition and cooling rate.

The equilibrium solidification sequences of slabs 1, 2 and 3 have been calculated using Thermo-Calc software, **Fig. 7.24**. The solidification starts at around the same temperature (~ 1516-1517 ºC) with the formation of δ-ferrite in all the slabs. Austenite starts to form at around 1485-1488 ºC. Complete solidification is predicted at 1469°C in

slab 1 and at 1482 °C in both slab 2 and slab 3. Therefore, slab 1 shows a greater freezing range in comparison to slabs 2 and 3. Greater freezing range promotes dendrite coarsening and that results in higher SDAS [El-Bealy 1996], which increases the segregation at the interdendritic regions [Krauss 2003] (**section 1.2.3**).

7.6 Partitioning of elements during solidification

The micro-segregation behaviour is known to be different for the various alloying elements seen in HSLA steels. Nb has been shown to be the most effective microalloying element to achieve grain refinement during rolling, but has a greater tendency to partition to interdendritic regions during solidification, along with carbon and nitrogen, than Ti [Tither 1992, Chen 1987]. Partitioning of various alloying elements, usually found in HSLA steels (Nb, Al, Ti, V, C, N, S, and P), between liquid and solid phases during equilibrium solidification of slab 1 have been calculated using Thermo-Calc software, **Fig. 7.25**. **Fig. 7.25** shows that the partitioning ratio for Nb between the liquid and solid at the final stages of solidification can be as high as 7 (composition in the final liquid compared to the average composition). The partitioning ratio shows an abrupt change when solidification changes from δ-ferrite to mixed δ-ferrite and austenite indicating that there is greater partitioning to austenite than to δ-ferrite. Titanium can also be seen to segregate, although less strongly compared to Nb (maximum partition ratio of about 5 between the final liquid to solidify and the austenite solidifying in equilibrium at that temperature). To predict the partitioning of Ti, Thermo-Calc uses a partitioning co-efficient, $k_p \approx 0.2$. However, Li and Priestner [Li 1998, Priestner 1998] observed a weaker segregation tendency of Ti in HSLA steel and suggested a different partitioning coefficient ($k_p \approx 0.61$) for Ti, which gives a maximum partition ratio ~ 2.4. Vanadium shows limited partitioning (partition ratio of approximately 1.8 between the final liquid to

solidify and the solid phase) and aluminium shows a very small tendency to segregate to the solid phase during solidification (either δ-ferrite or austenite) with a partition ratio of approximately 0.9 between the final liquid to solidify and the solid phase. SEM analysis on the as-cast slabs revealed that fine scale Al-rich precipitates (predicted to be AlN) were observed throughout the slabs with no obvious spatial inhomogeneity, as expected from the segregation behaviour predicted by Thermo-Calc. Sulphur shows the strongest segregation tendency with a maximum partition ratio as high as ~ 70. P also segregates (maximum partition ratio ~ 5) but not as strongly as S or even as Nb. As austenite starts to form the enrichment of C (maximum partition ratio ~ 4) and N (maximum partition ratio ~ 2.5) drop in the liquid. This is due to the increased solubility of those elements in austenite compared to ferrite. The maximum partition ratios for all the alloying elements present in the investigated slabs are listed in **Table 7.5**. The maximum partition ratio for all the elements remains within a close range of values (Nb: 6.4-7, Ti: 4.94-5.35, V: 1.69-1.78, C: 3.80-3.84, N: 2.40-2.47, Mn: 1.41-1.42, Ni: 1.1.3-1.22, Al: 0.98, S: 63-71, P: 4.5-5.2) for the compositions of the investigated steels. As an example, **Fig. 7.26** compares Nb partitioning in slab 1 (0.045 wt % Nb), slab 2 (0.027 wt % Nb) and slab 3 (0.020 wt % Nb) with maximum partition ratio of 7.00, 6.47 and 6.44, respectively. The shorter freezing ranges in slab 2 and slab 3 could be responsible for the lower partition ratio of Nb compared to slab 1 (**section 1.2.3**). The ratio between the Mn level at the slab centre to the overall Mn level in steel (~ 1.4 - 1.5) as determined by EDS point analysis from the matrix, **Fig. 7.18**, was similar to the Mn partition ratio predicted by Thermo-Calc (1.41-1.42). **Table 7.5**.

However, the partition ratio of an element does not solely decide the significance of any segregation of that element in steel. The amount of the element that is present is also important. For example, Mn is generally present in much higher concentrations than

P, and plays a more important role in segregation and banding than P despite P having the higher value of k_p [Krauss 2003]. **Fig. 7.27** compares the maximum and minimum compositions of various elements in liquid and in δ-ferrite for slab 1, slab 2 and slab 3 predicted from Thermo-Calc. **Fig. 7.27** shows a clear difference in the intensity of Nb segregation between the steels. The highest Nb level in the last liquid of slab 1 (0.32 wt %) is around 0.2 wt % higher than that in slab 3 (0.12 wt %), however, the maximum partition ratios of Nb in slab 1 and slab 3 are similar. This is due to the difference in Nb levels in both steels as slab 1 (0.045 wt% Nb) contains more than twice the amount of Nb than in slab 3 (0.020 wt% Nb). The highest Nb level in the last liquid of slab 2 is intermediate (0.18 wt %) to both slab 1 and slab 3, **Fig. 7.27 b**, due to the intermediate Nb level (0.027 %) in slab 2. The Ti levels in the steels are much lower than the Nb levels and Ti also segregates to a lesser extent than Nb. The extent of V segregation is also far less than the Nb segregation, **Fig. 7.27**. Therefore, Nb segregation should have a dominant effect on the distribution of Nb-rich microally precipitates and the difference in Nb levels may result in a difference in grain structure between the investigated slabs during the later stages of processing.

7.7 Dependence of micro-segregation on the solidification sequence

During thick slab continuous casting the initial metal to solidify will do so as Nb-depleted δ-ferrite at the interface with the water-cooled copper mould. This region will be associated with the surface and sub-surface regions of the rolled plate. Solidification at the sub-surface region generally will be completed as δ-ferrite, due to the increased cooling rate resulting in non-equilibrium solidification, so that micro-segregation of elements such as Nb to interdendritic or cellular boundary areas will coincide with δ/δ grain boundaries. If full transformation from δ-ferrite to austenite occurs prior to

precipitation of Ti- and Nb-rich phases then the centres of the austenite grains will correspond to the solute-enriched regions whilst γ/γ grain boundaries will be solute-depleted. As cooling proceeds the higher solute content in the austenite grain centres will result in a greater driving force for precipitation and so formation at higher temperatures leading to greater time for growth and a higher volume fraction due to the greater amount of solute. The number density of particles will depend on the nucleation rate and so the precise relationship between the cooling rate and the continuous-cooling-transformation (CCT) curve. Hence, it is expected that there will be a greater Nb(C, N) precipitate size and number density in pearlite, and the ferrite grains close to the pearlite regions for low carbon steels with limited pearlite content, since the γ/γ grain boundaries will tend to transform to α-ferrite and the centre of the austenite grains will form pearlite. The separation between the high precipitate number density regions is therefore expected to be similar to the separation between δ/δ grain boundaries, i.e. the secondary dendrite arm spacing (SDAS). The development of higher resolution scanning electron microscopes (SEM) in recent years has meant that it is possible to view the small (≈ 10nm diameter) precipitates, which would otherwise need the transmission electron microscopy (TEM). Another advantage of SEM is that larger areas of material can be imaged allowing more accurate quantification of precipitate spatial distributions. **Fig. 7.7** shows clustering of precipitates, where the spacing between the precipitate rich regions is approximately equal to the average SDAS, providing a link to the segregation behaviour during solidification.

Moving further into the cast slab the overall Nb and Ti levels increase, due to macro-segregation behaviour, leading to greater volume fractions and larger sizes of precipitates, **section 7.3**. Similar behaviour has also been reported by Davis and Strangwood (for rolled plates) [Davis 2002] and Zhang et al. (for as-cast slabs) [Zhang

2000]. At a certain depth (determined by slab composition and cooling rate) the solidification sequence changes to mixed δ/γ which will result in different segregation behaviour. For example, at the mid-thickness position a more complex spatial distribution of precipitates might be expected; initial segregation occurs during δ-ferrite formation, however, as the solidification product changes to austenite some microalloying solute may be trapped at the δ/γ boundaries (for example due to the solidification front trapping small solute-rich liquid areas), whilst the majority of the solute atoms will be segregated to the remaining interdendritic liquid and hence will be at the γ/γ boundaries after solidification. There is a slight preference for Nb to be in δ-ferrite compared to austenite, **Fig. 7.26**, during the final stages of solidification, however this is likely to have a minimal effect on the segregation levels as the main micro-segregation effect is between the liquid and solid. On continued cooling the δ-ferrite transforms to austenite resulting in solute rich regions at both γ/γ boundaries, from the solute-rich interdendritic liquid that solidifies last, and potentially within the austenite grains from solute trapped at the δ/γ boundaries during solidification. The resultant solute distribution would therefore show clusters of high precipitate density that are not necessarily separated by the secondary dendrite arm spacing. Experimental evidence has shown that Nb-rich precipitates do continue to show strong segregation at the mid-thickness position in HSLA slabs, where this solidification sequence change is expected, **Fig. 7.18**. SEM analysis has also indicated that the precipitate clusters are generally associated with the interdendritic regions, i.e. the pearlite and ferrite areas close to pearlite, suggesting that there is limited solute enrichment at the δ/γ boundaries during solidification. However, it should be noted that, for the steel examined, equilibrium cooling predicts 85% solidification as δ-ferrite with a final pearlite content of 12%, hence any δ/γ boundary segregation would be

difficult to distinguish from the high solute content expected in pearlite, and neighbouring ferrite, from interdendritic segregation.

7.8 Summary on as-cast microstructure and precipitates

The major findings from the characterisation of the as-cast slabs in terms of microstructure and precipitates can be summarised as follows:

- A wide range of grain sizes exists in the as-cast slabs; however, the ferrite grain size distribution did not show any bimodality. A study of prior austenite grain size distribution in as-cast steel, however, is required in future to confirm the unimodal nature of grain sizes in continuously cast structure.
- Largely equiaxed sulphides (MnS or CuS with 0.5 - 11 μm size range) and irregular shaped oxides (Al_2O_3 or SiO_2) are the major inclusions found in the as-cast slabs.
- Star, cubic or spherical shaped Nb-rich microalloy carbonitrides (0 - 600 nm size range) and irregular shaped AlN (0 - 600 nm size range) are present in the slabs.
- Interdendritic segregation during casting can generate an inhomogeneous distribution of Nb-rich microalloy precipitates in the as-cast slabs, with precipitate-rich regions separated by a distance similar to the secondary dendritic arm spacing (SDAS).
- The inhomogeneity in precipitate distribution and the average precipitate density both increase from sub-surface towards the mid-thickness of the slabs, possibly due to micro- and macro-segregation, respectively.
- Large networks (several microns in size) of microalloying element-rich phases (possibly made of Nb-rich complex microalloy carbo-nitrides) can be found at the

segregated regions of the mid-thickness location. Such networks indicate strong segregation taking place during solidification.

- Thermo-Calc software can be used to predict the partitioning of various elements during solidification. The prediction shows that Nb segregates strongly in the as-cast HSLA steels, which has been shown to affect the precipitate distribution.
- Grain size bimodality has not been found in the as-cast slabs, however, an inhomogeneous precipitate distribution was present. The processing stage that comes after continuous casting is the reheating of slabs. Therefore, to follow any changes taking place in the grain structure and in grain size bimodality the microstructure and the precipitates in the reheated steels need to be studied.

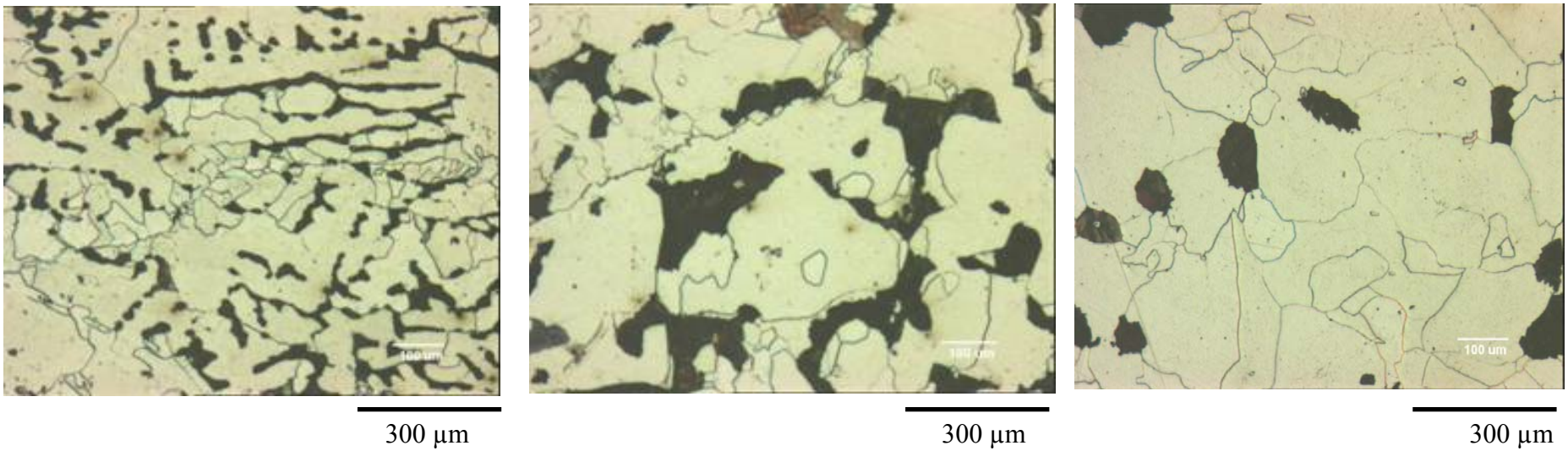

Fig. 7.1: Microstructure at (a) sub-surface (20 mm from top), (b) quarter-thickness and (c) mid-thickness of as-cast slab 1.

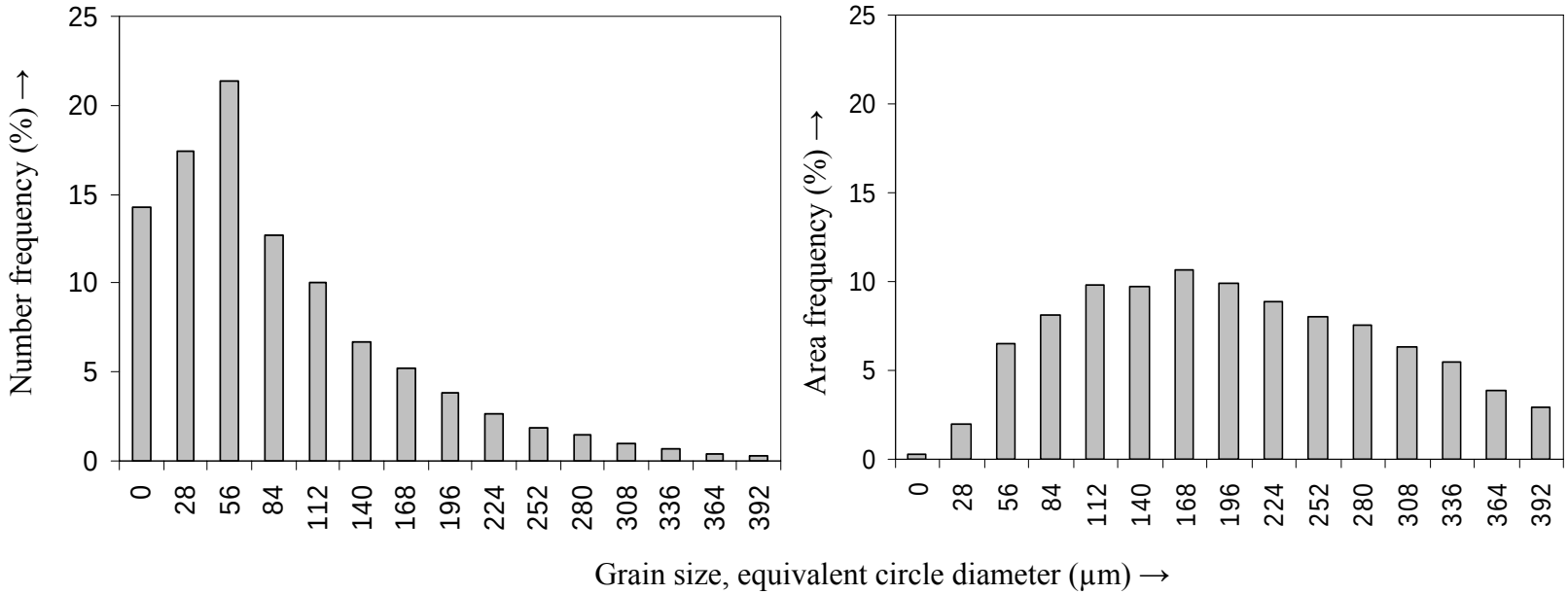

Fig. 7.2: (a) Number fraction (%) and (b) area fraction (%) ferrite grain size distribution of as-cast slab 1 at quarter-thickness position.

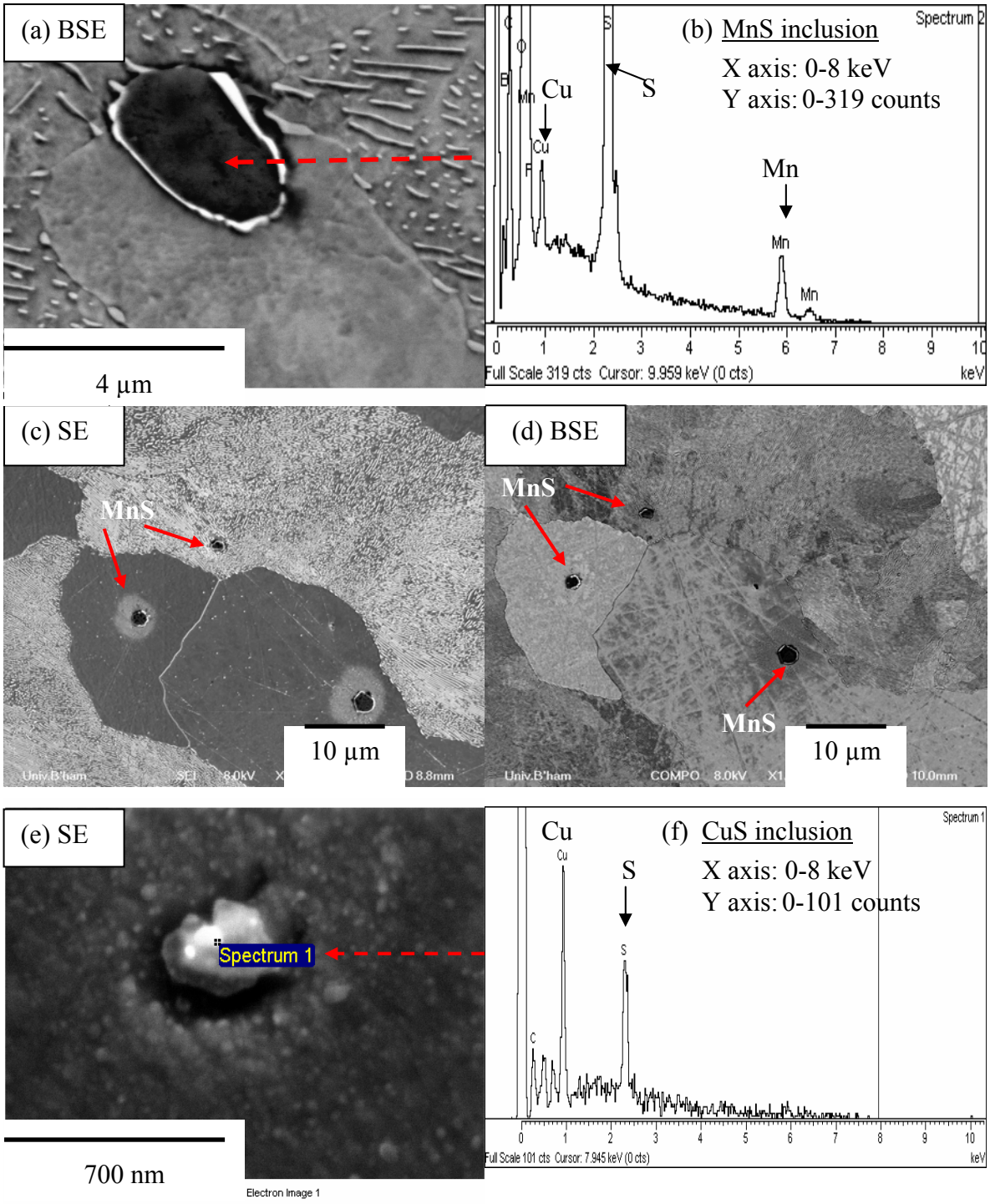

Fig. 7.3: Inclusions in as-cast steel: (a) Backscatter electron (BSE) image and the corresponding (b) EDS analysis of MnS inclusion (also showing the presence of Cu); (c) Secondary electron (SE) image as well as (d) BSE image showing the MnS inclusions in dark contrast on ferrite matrix; (e) SE image and the corresponding (f) EDS analysis of a CuS inclusion.

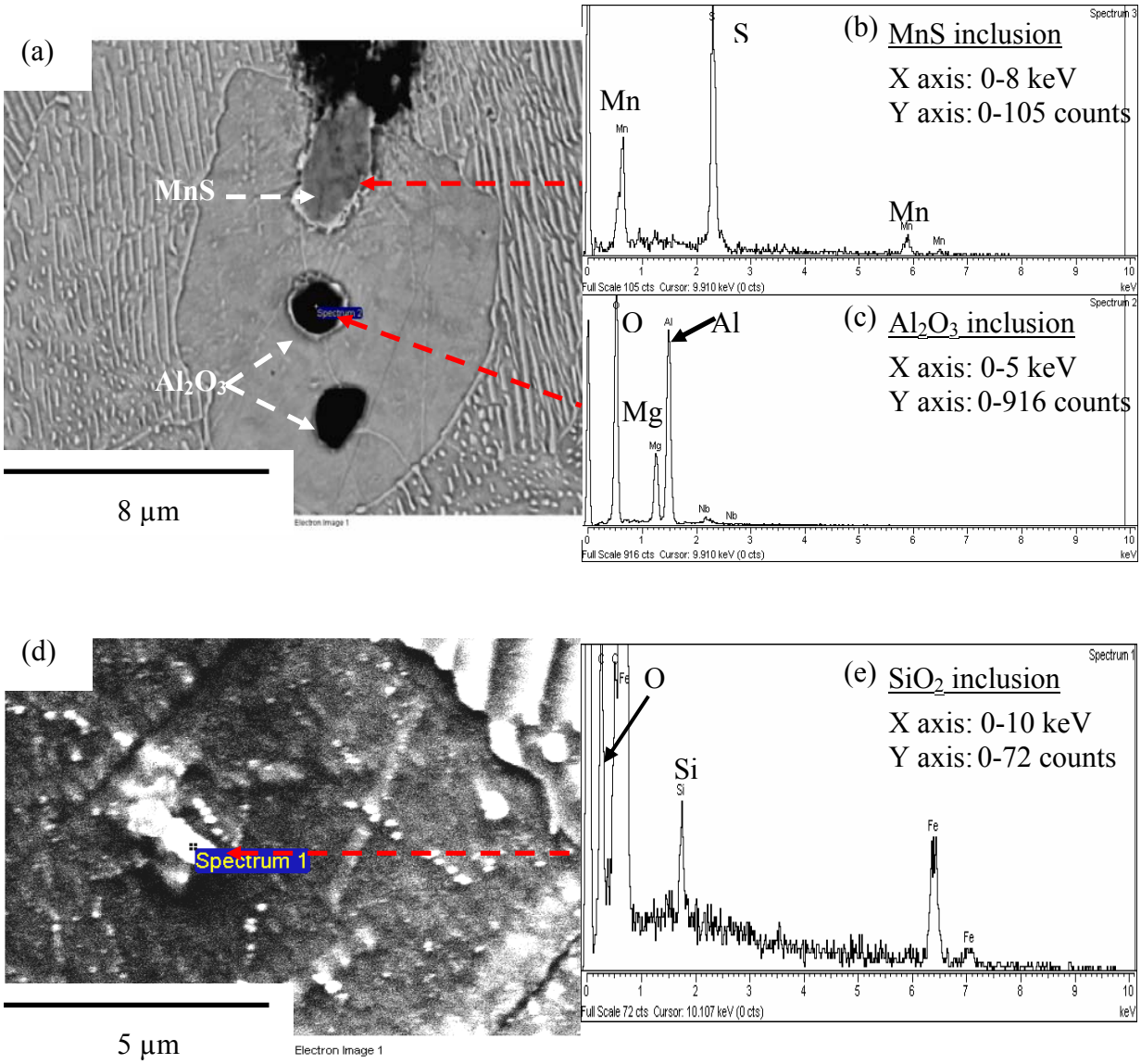

Fig. 7.4: Inclusions in as-cast steel: (a) Backscatter electron (BSE) image and the corresponding EDS analysis showing the presence of both (b) MnS and (c) Al_2O_3 inclusions (Mg is present within oxide inclusion); (d) Secondary electron (SE) image and the corresponding (e) EDS analysis of the SiO_2 inclusion.

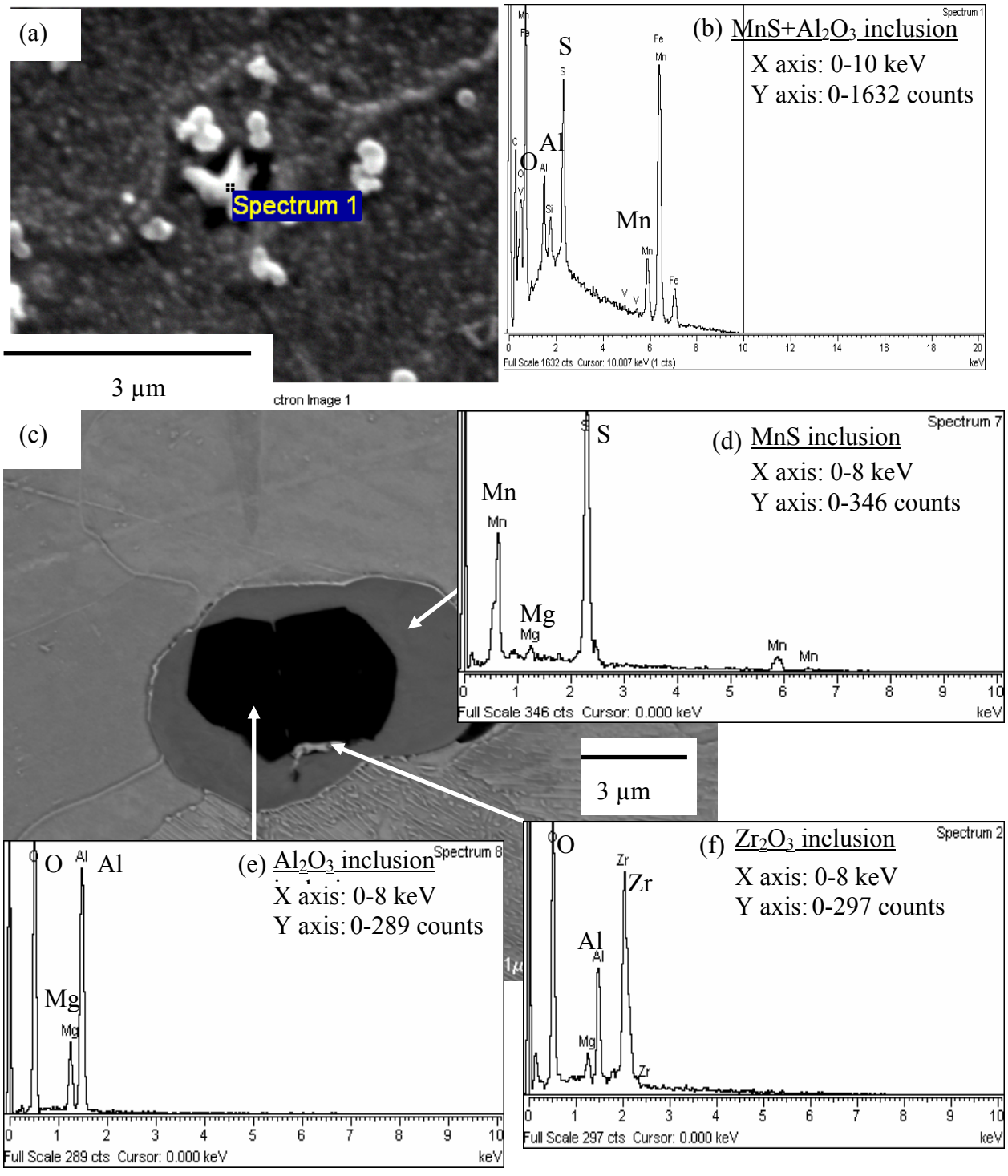

Fig. 7.5: Inclusions in as-cast steel: (a) SE image and the corresponding (b) EDS analysis showing a combined inclusion made of MnS and Al_2O_3 on the ferrite matrix; (c) BSE image and the corresponding EDS analysis showing the formation of (d) MnS on the pre-existing (e) Al_2O_3 inclusion (both MnS and Al_2O_3 inclusions contain Mg); (f) Small bright piece of Zr_2O_3 can also be seen.

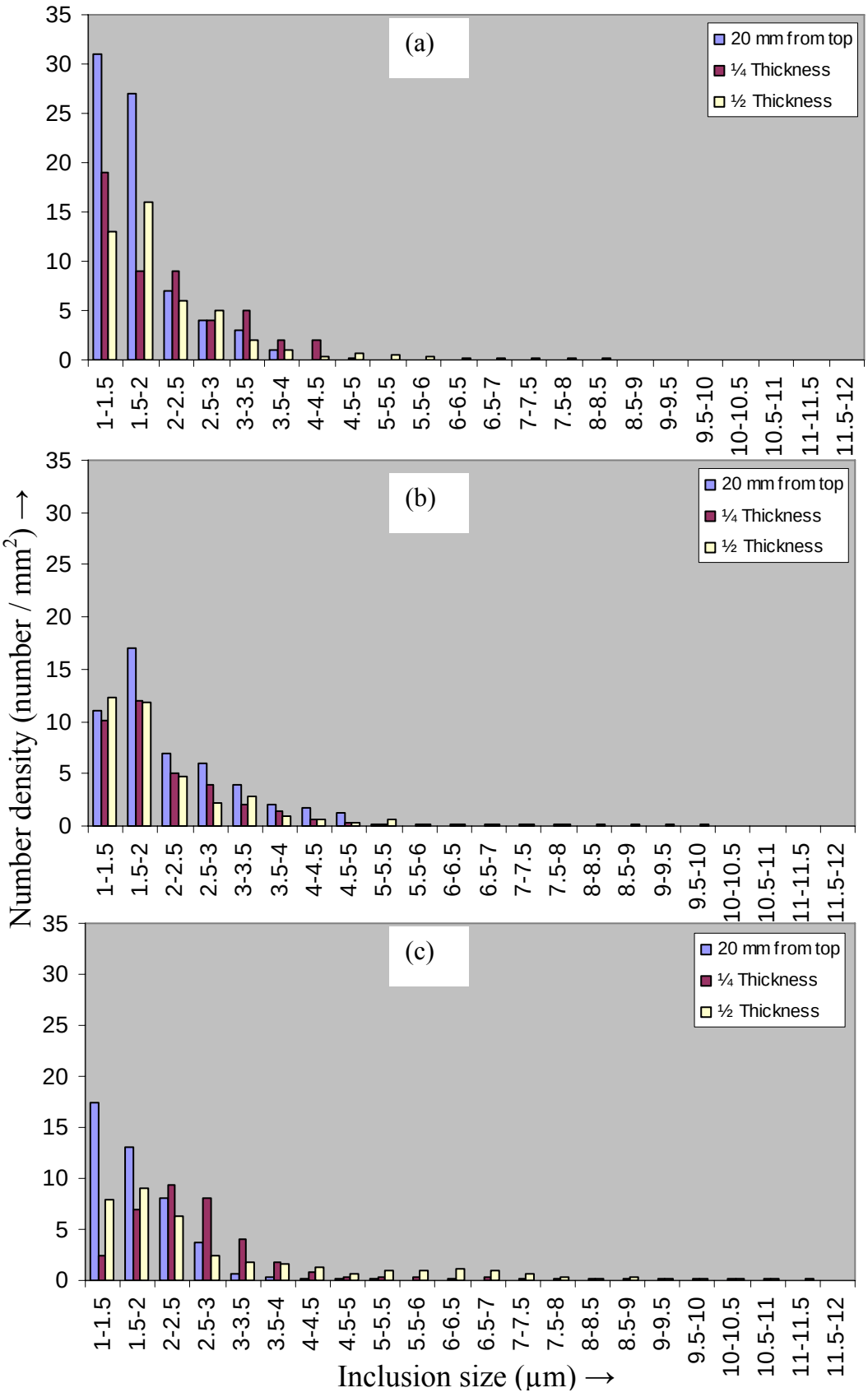

Fig. 7.6: Size distribution of MnS particles at the sub-surface (20 mm from top), quarter-thickness and mid-thickness position of the as-cast slabs (a) slab 1, (b) slab 2 and (c) slab 3.

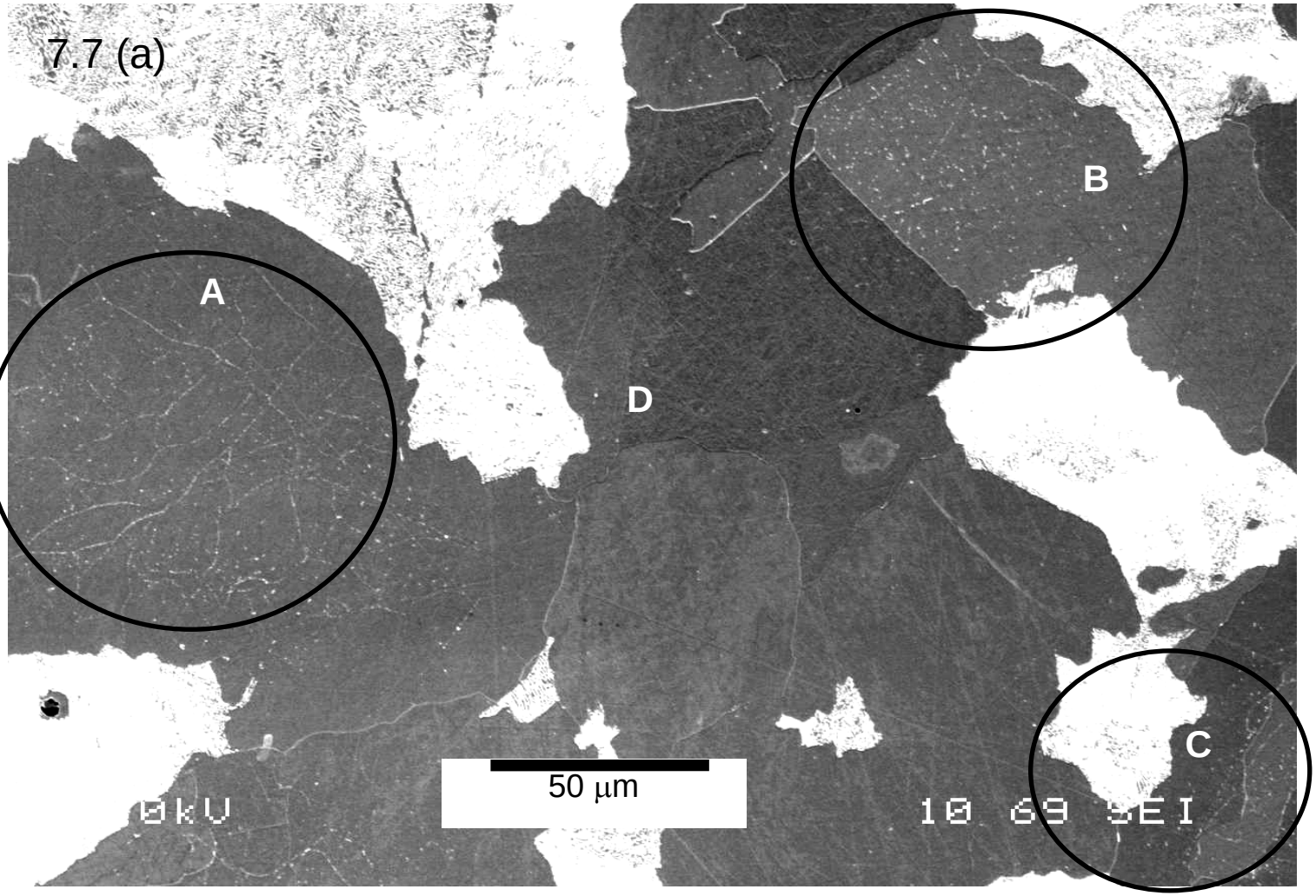

Caption next page

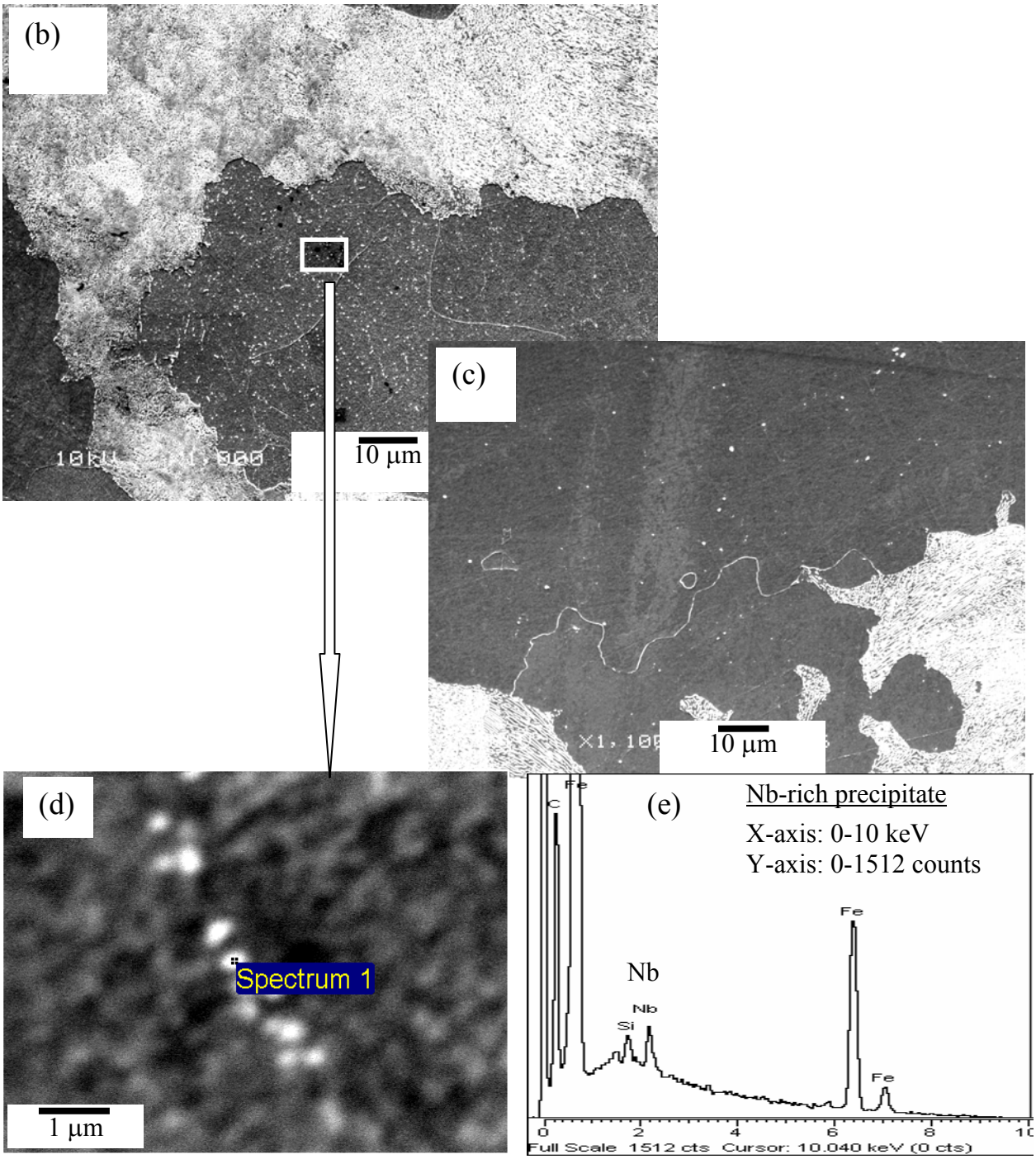

Fig. 7.7: (a) Inhomogeneous precipitate distribution in as-cast slab 1 with precipitate-rich regions, marked A, B and C, separated by the precipitate poor region, marked D; (b) high density of precipitates in a precipitate rich region; (c) lack of precipitates in precipitate poor region; (d) cluster of precipitates from the precipitate rich region and the corresponding (e) EDS analysis showing that the precipitates in the cluster are Nb-rich (possibly Nb(C, N)). Si peak in (e) is coming from the matrix.

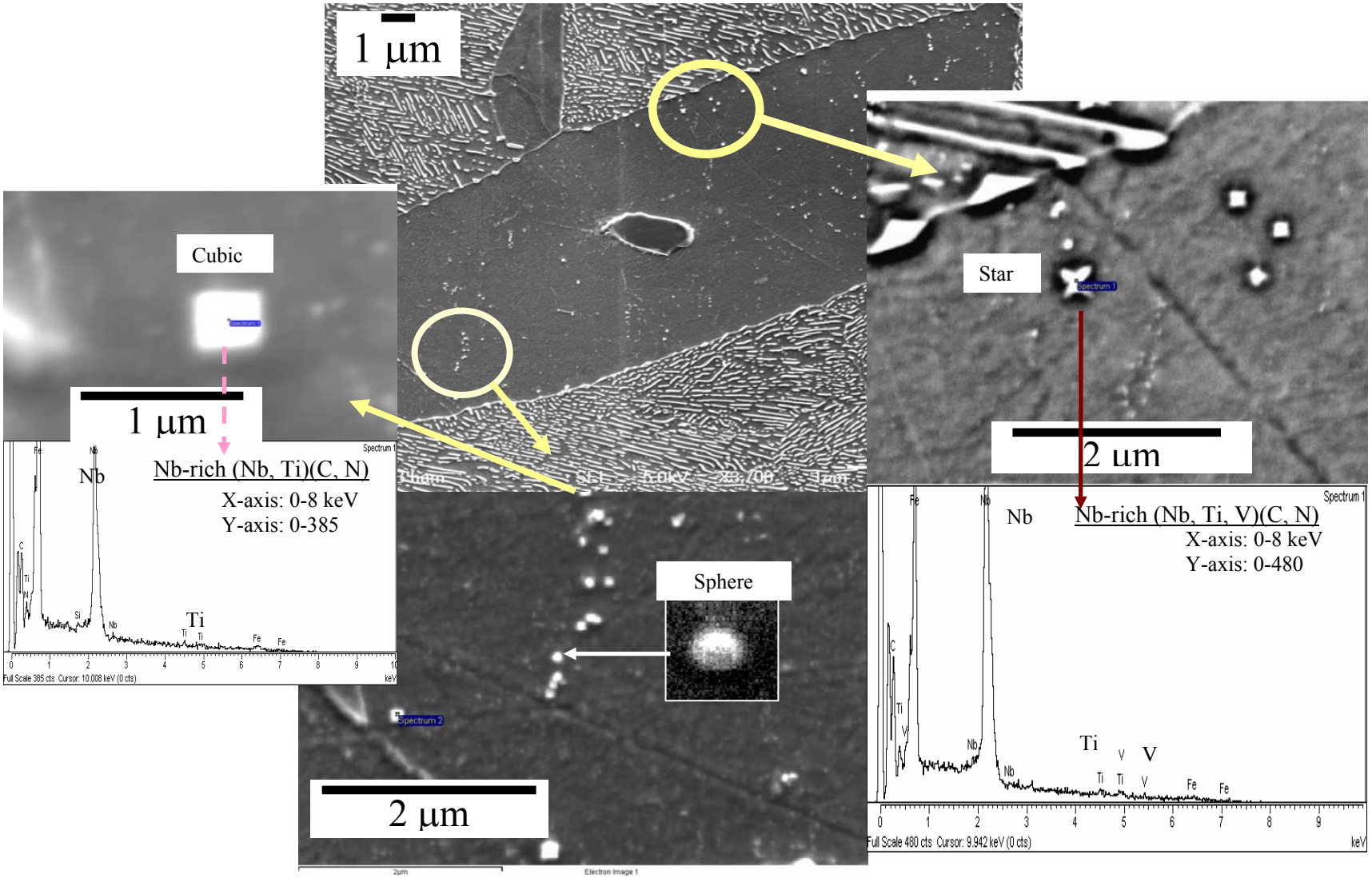

Fig. 7.9: Different shapes (star, cubic and spherical) of Nb-rich precipitates present within the precipitate-rich (interdendritic) regions, and the EDS analysis on star and cubic shaped precipitates.

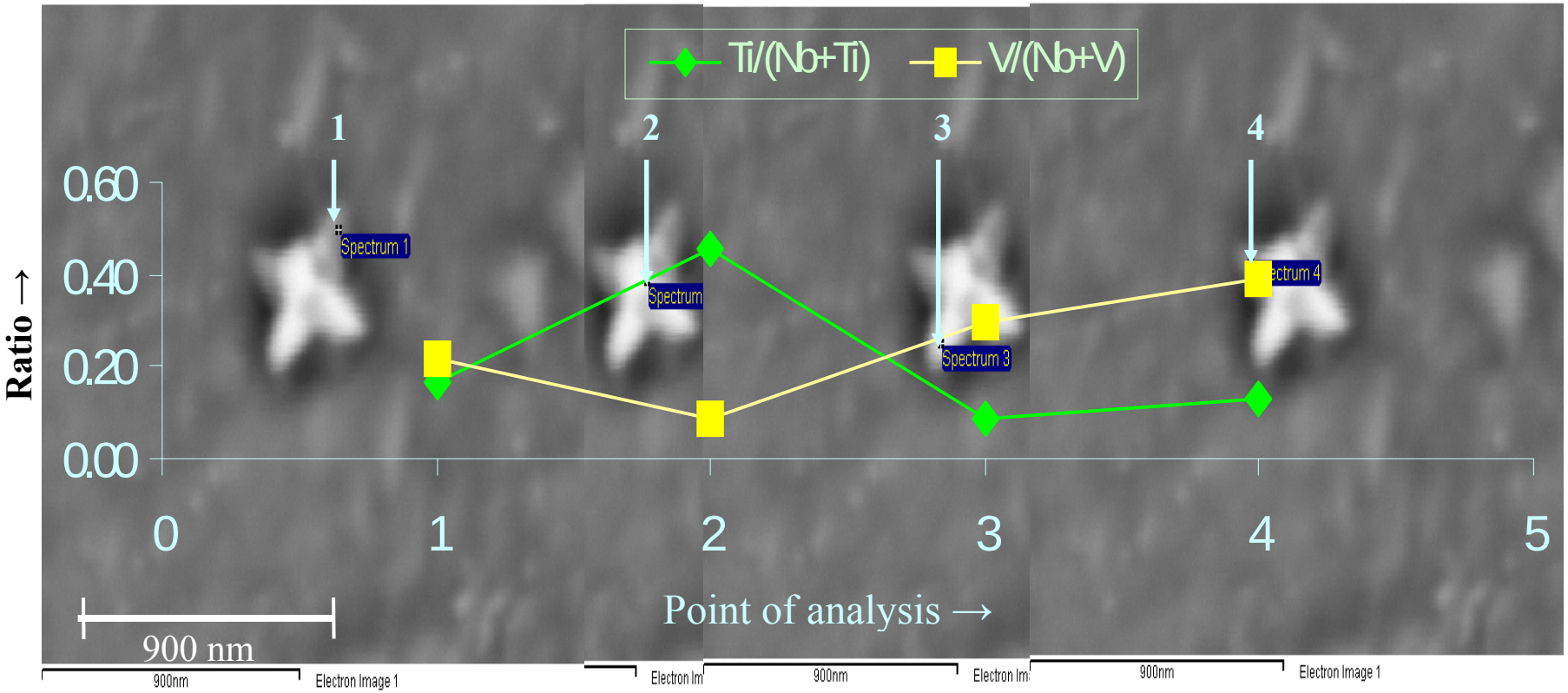

Fig. 7.10: Variation in Ti / (Nb+Ti) and V / (Nb+V) ratios (all elements in wt % composition) with the location of EDS spectra taken from a winged precipitate that is Nb-rich and also contains Ti and V. At the centre of the precipitate Ti content is higher (~40 % Ti, ~7 % V and rest ~53 % Nb, out of all microalloying elements) and towards the wings Nb (~ 60-70 %) and V (~ 20-40 %) levels are higher and Ti (~ 5-20 %) is lower.

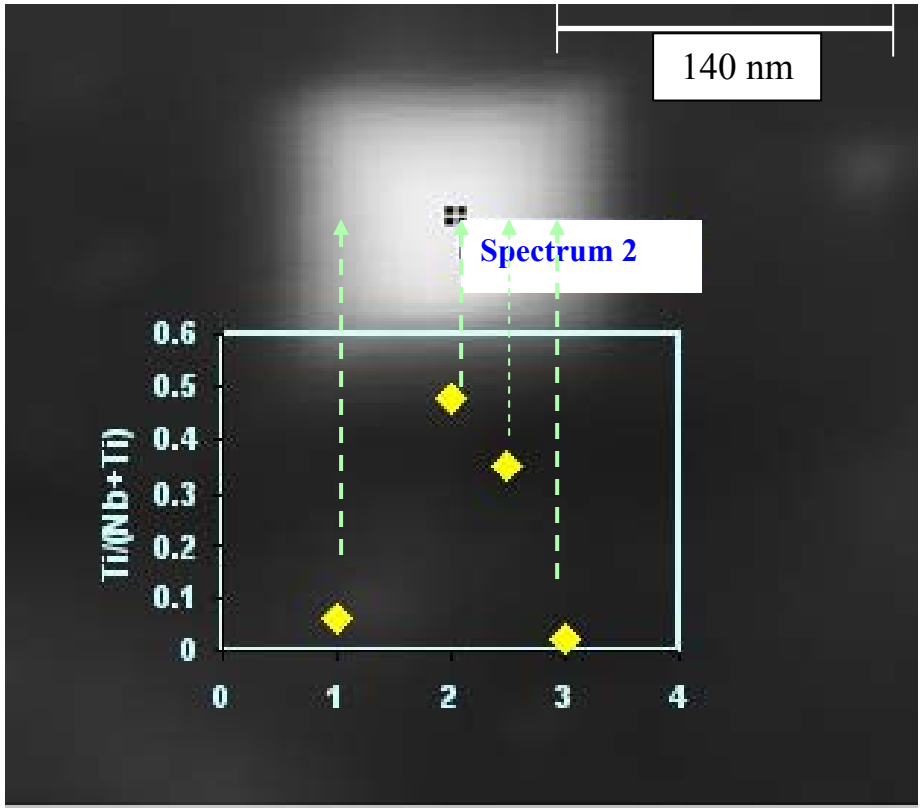

Fig. 7.11: Variation in Ti / (Nb+Ti) ratio (all elements in wt % composition) with the location of EDS spectra taken from a cubic Nb-rich (Nb, Ti)(C, N) precipitate. At the centre of the precipitate Ti content is higher (~50 % Ti and ~50 % Nb, out of total microalloy content) and towards the edges Nb (~ 95 %) levels are much higher than Ti (~ 0-5 %).

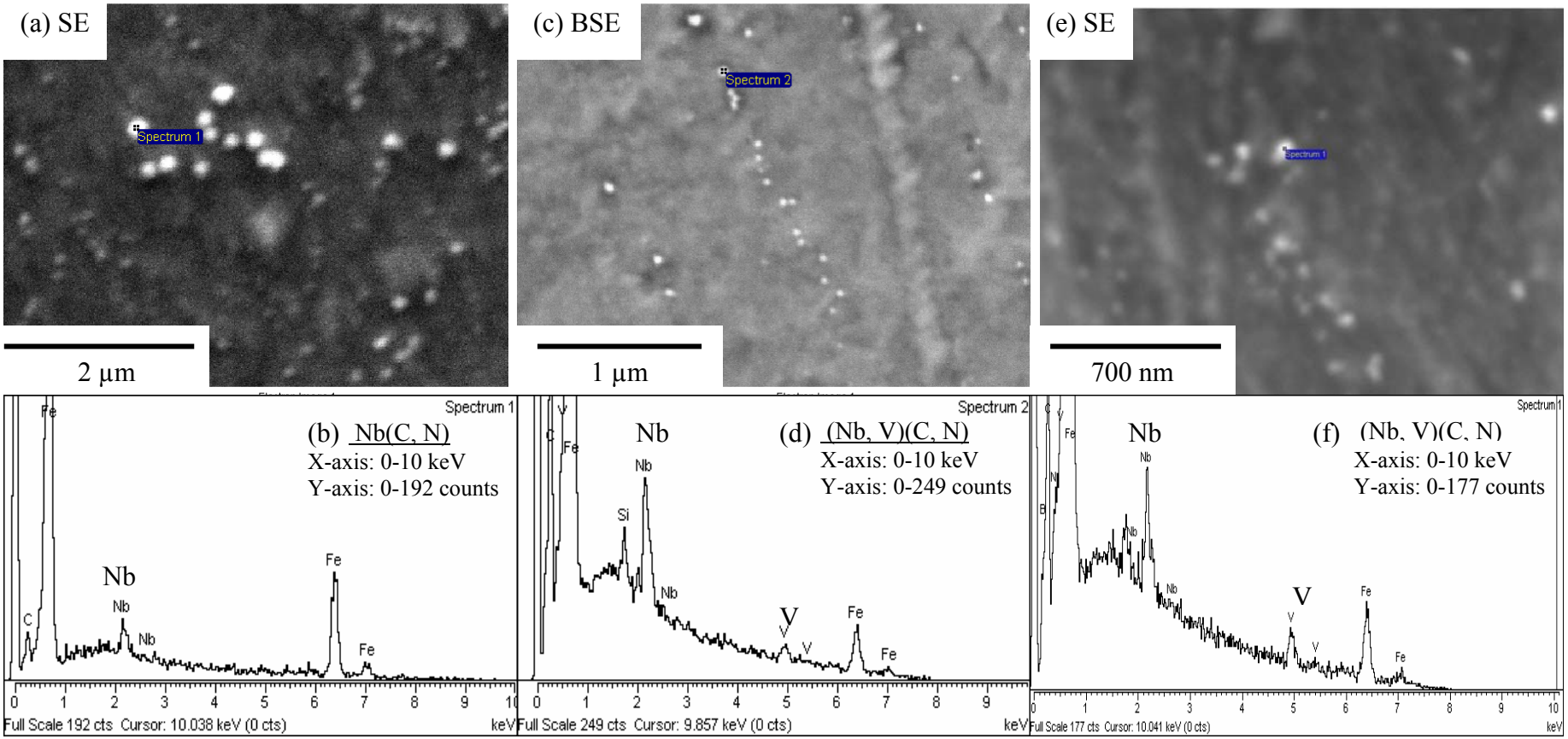

Fig. 7.12: Spherical precipitates in (a), (c) and (e) and the corresponding EDS analyses in (b), (d) and (f), respectively, showing that the spherical precipitates are either Nb(C, N) or (Nb, V)(C, N).

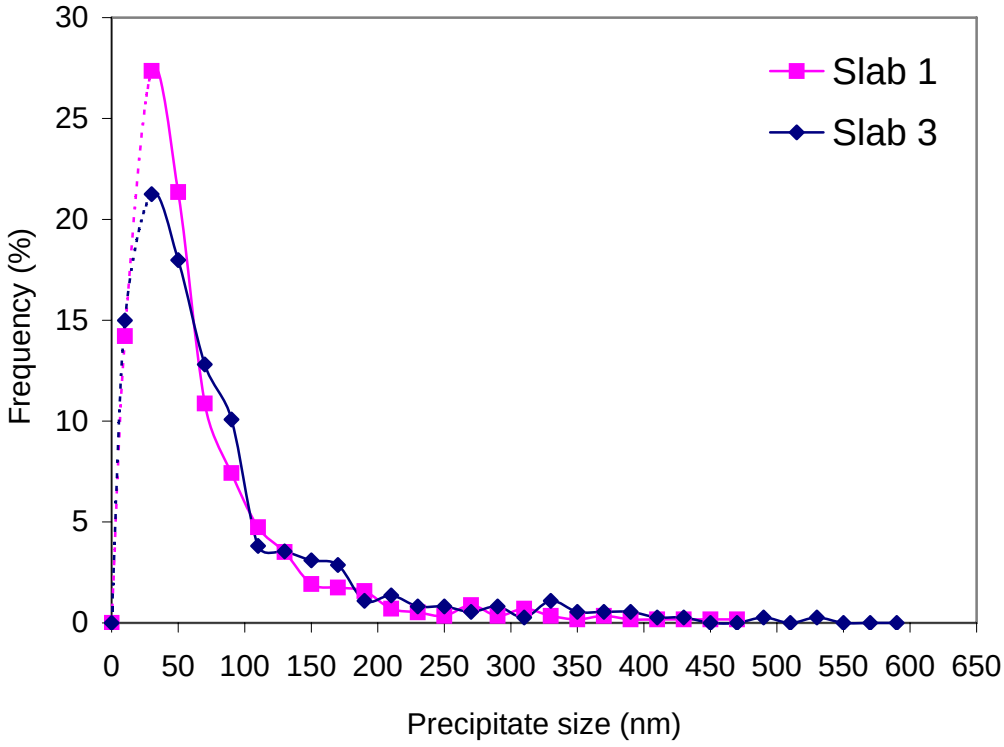

Fig. 7.13: Precipitate size distributions at the precipitate-rich regions of the quarter-thickness positions of slab 1 and slab 3. As the SEM could not pick up the fine precipitates reliably, dashed lines are used for the precipitates sizes, smaller than the size, corresponding to the maximum frequency.

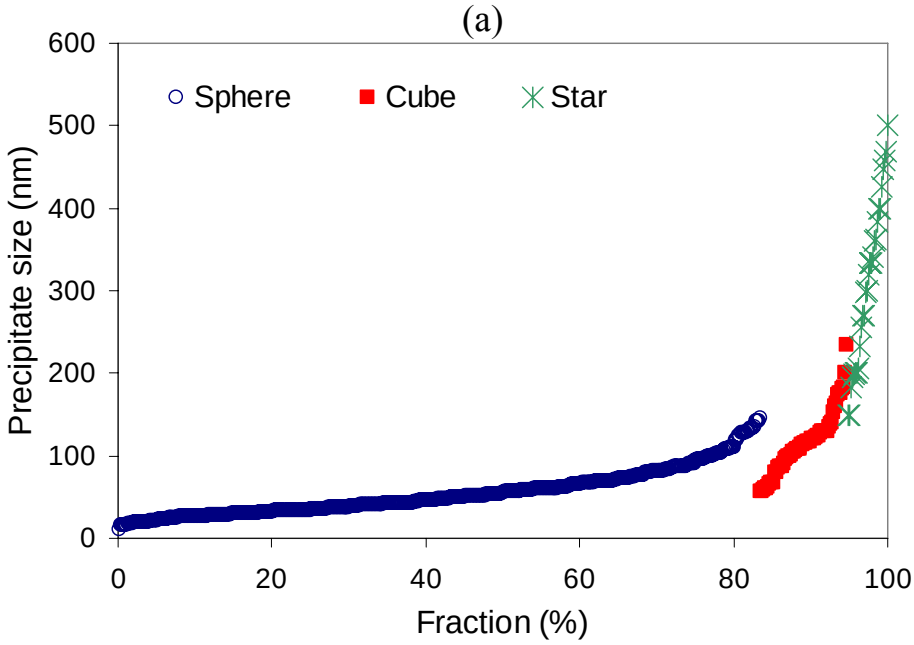

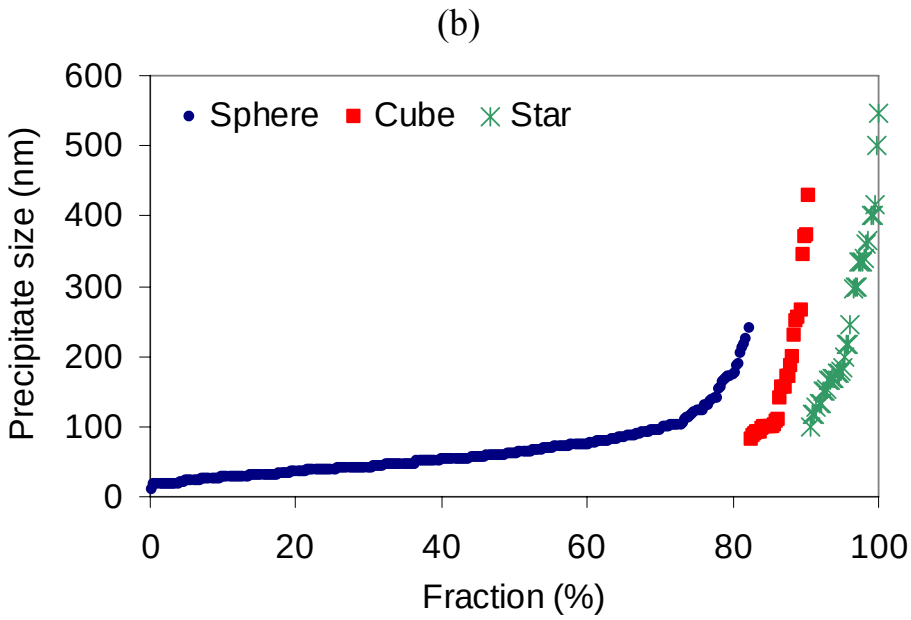

Fig. 7.14: Sizes (nm) (equivalent circle diameter, ECD, for spherical precipitates, edge length for cube precipitates and maximum feret length for star shaped precipitate) and the number fractions (%) of precipitates of different shapes studied at the quarter-thickness position of (a) slab 1 and (b) slab 3.

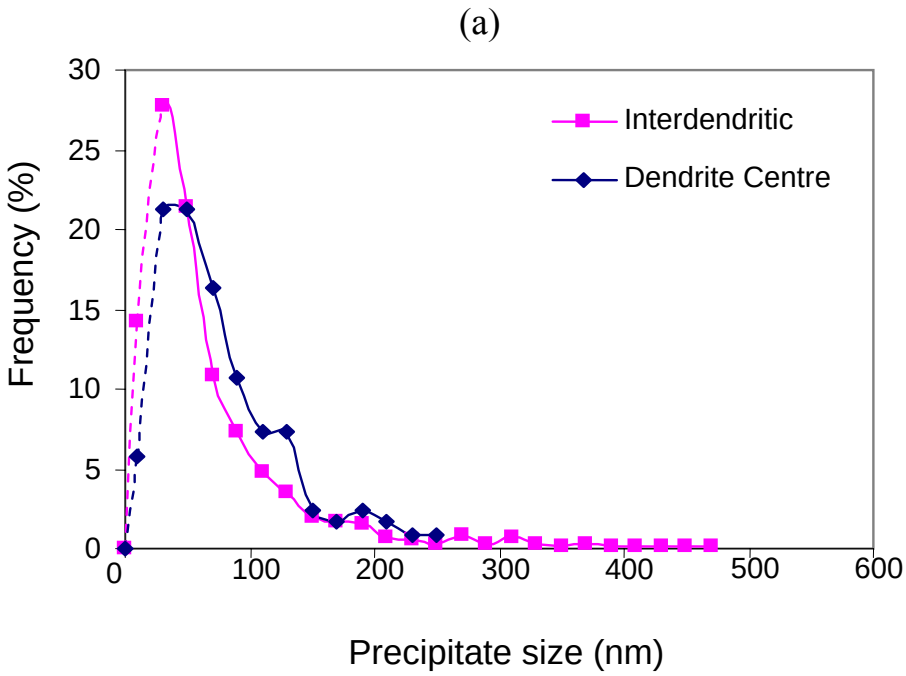

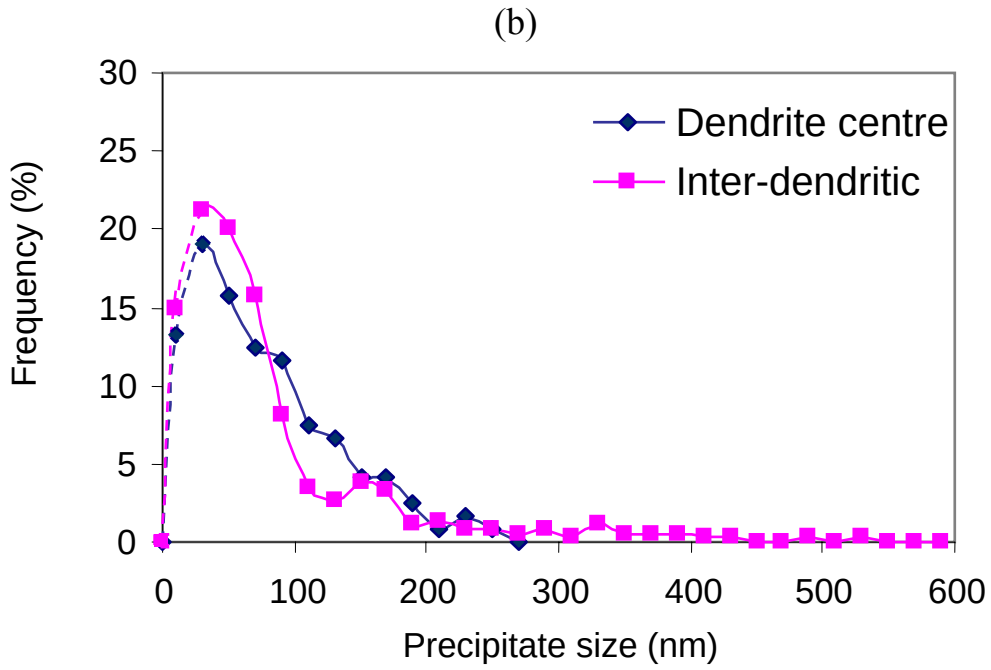

Fig. 7.15: Precipitate size distributions at the dendrite centre and inter-dendritic regions for the quarter-thickness positions of (a) slab 1 and (b) slab 3. Dashed lines are used for the precipitates sizes, smaller than the size, corresponding to the maximum frequency.

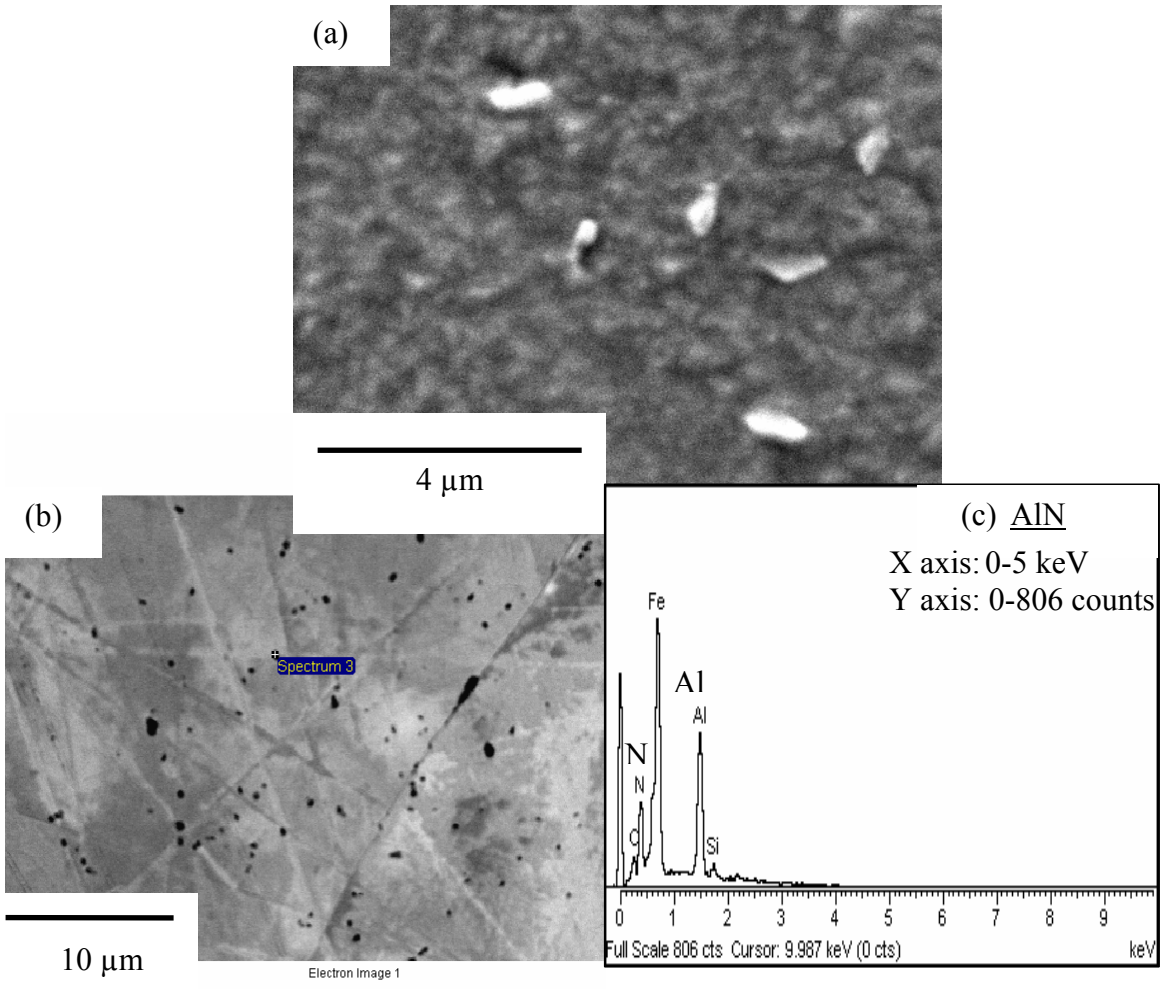

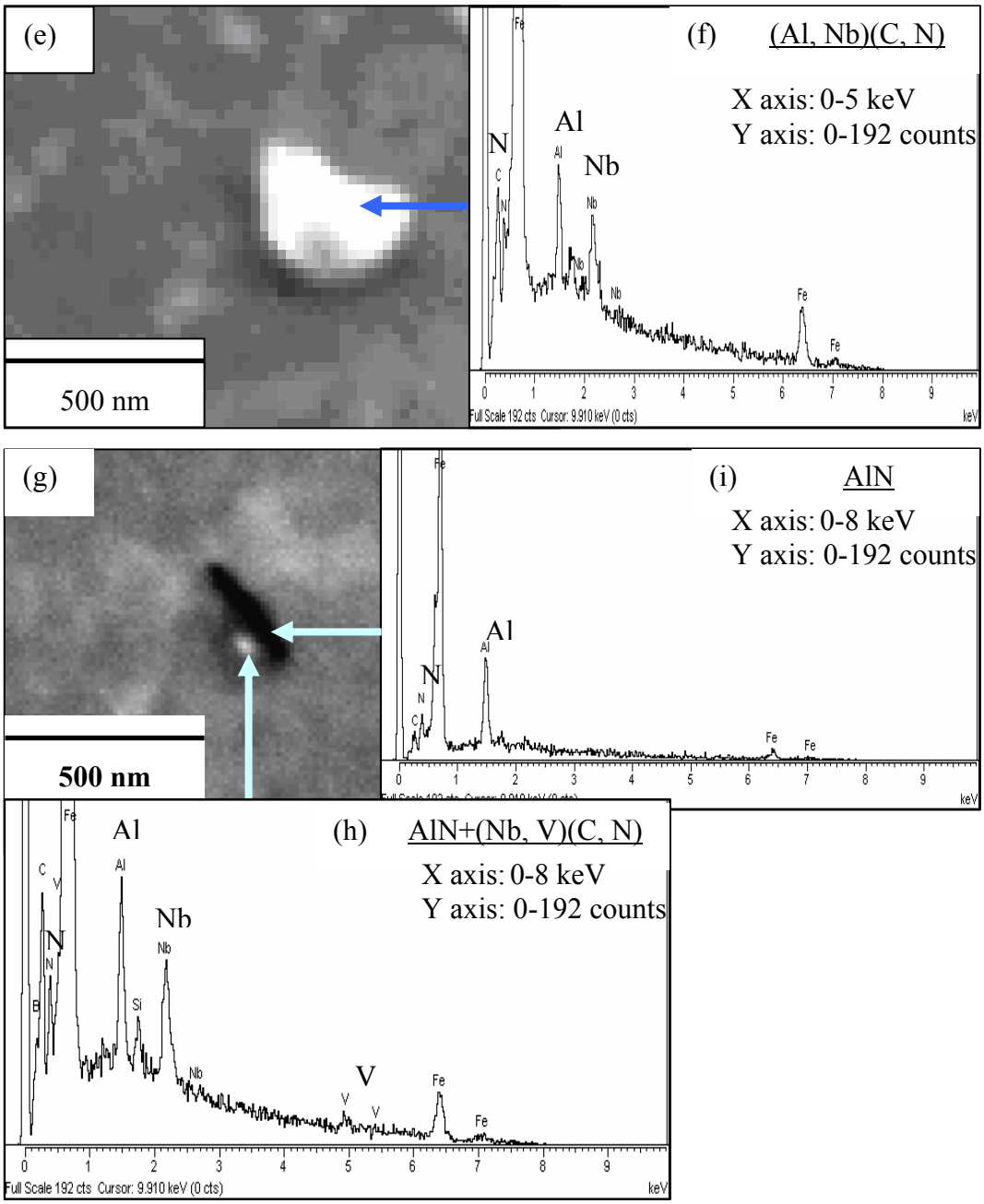

Fig. 7.16: (a) SE image of faceted AlN precipitates (b) BSE image showing AlN particles (dark particles) on ferrite (c) EDS analysis spectrum collected from an AlN particle selected from (b); (d) SE image of a particle and (f) EDS spectrum taken from that particle showing both Al and Nb peaks; (g) detailed study revealed that such particles could form by the precipitation of Nb(C, N) (spectrum in h) on pre-existing AlN (spectrum in i).

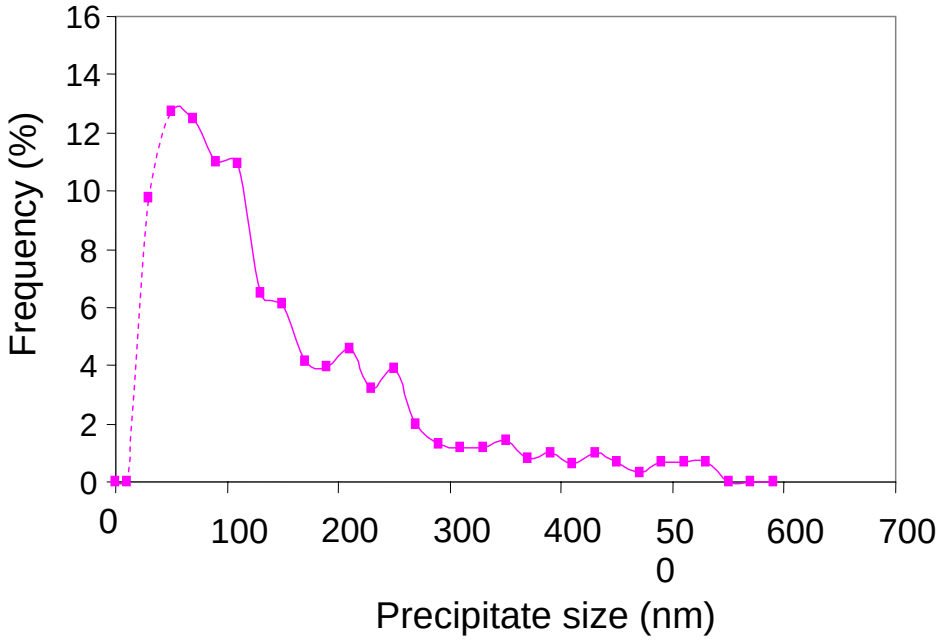

Fig. 7.17: Size distribution of the AlN particles for the quarter-thickness position of slab 1, which is representative of the other locations studied. Dashed lines are used for the precipitates sizes, smaller than the size, corresponding to the maximum frequency.

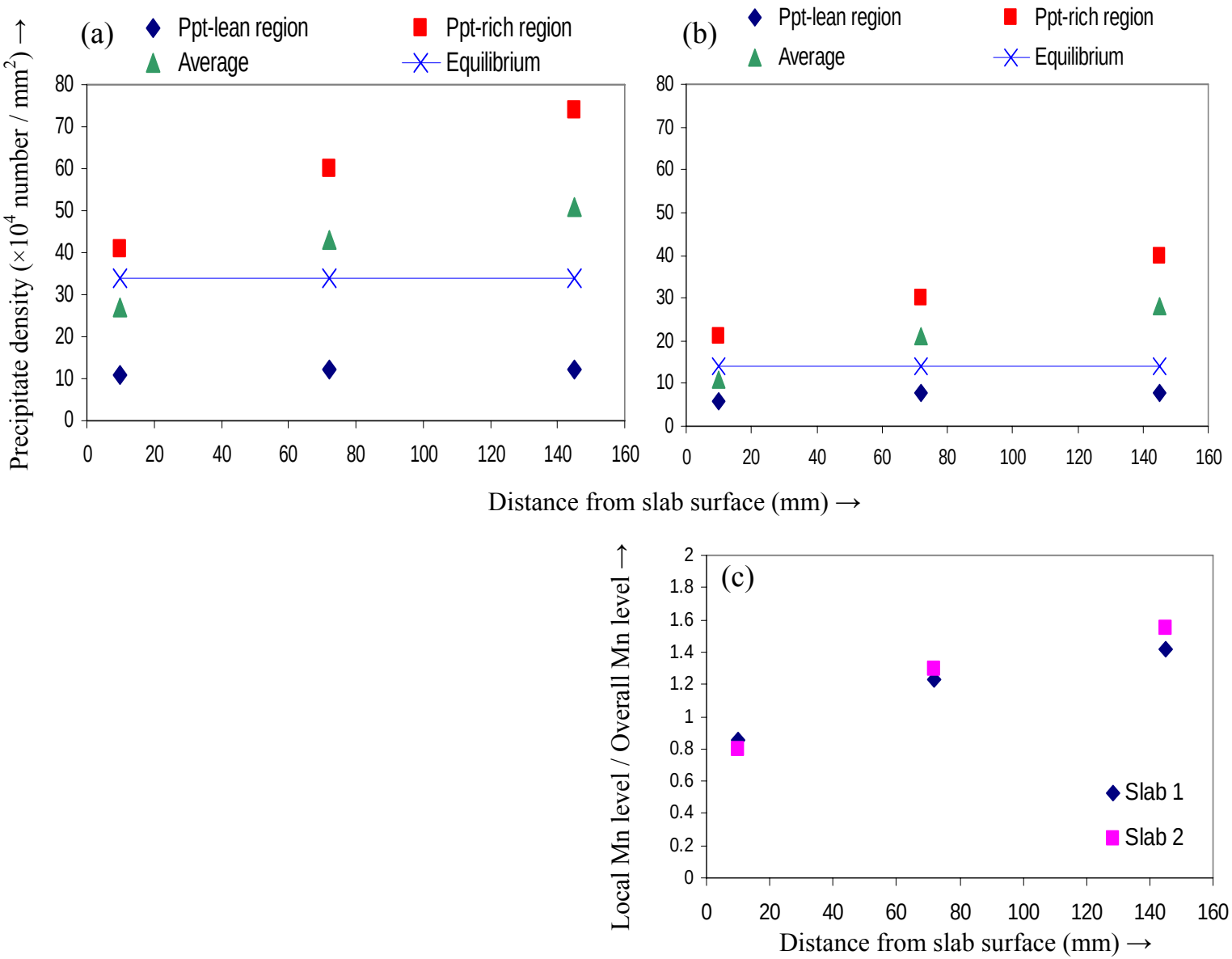
(a)
Ppt-lean region
Ppt-rich region
Average
Equilibrium
Precipitate density (×10^4 number / mm^2) →
(b)
Ppt-lean region
Ppt-rich region
Average
Equilibrium
Distance from slab surface (mm) →
(c)
Local Mn level / Overall Mn level →
Slab 1
Slab 2
Distance from slab surface (mm) →

Fig. 7.18: Precipitate area density at sub-surface, quarter-thickness and mid-thickness locations for (a) slab 1 and (b) slab 3. The average precipitate densities at precipitate-rich and precipitate-lean regions are given. The overall average density (considering both precipitate-rich and -lean regions) and the equilibrium density (calculated using Thermo-Calc from the steel compositions) are also reported; (c) showing the rise in local Mn level (compared to overall Mn level) towards mid-thickness of the slabs.

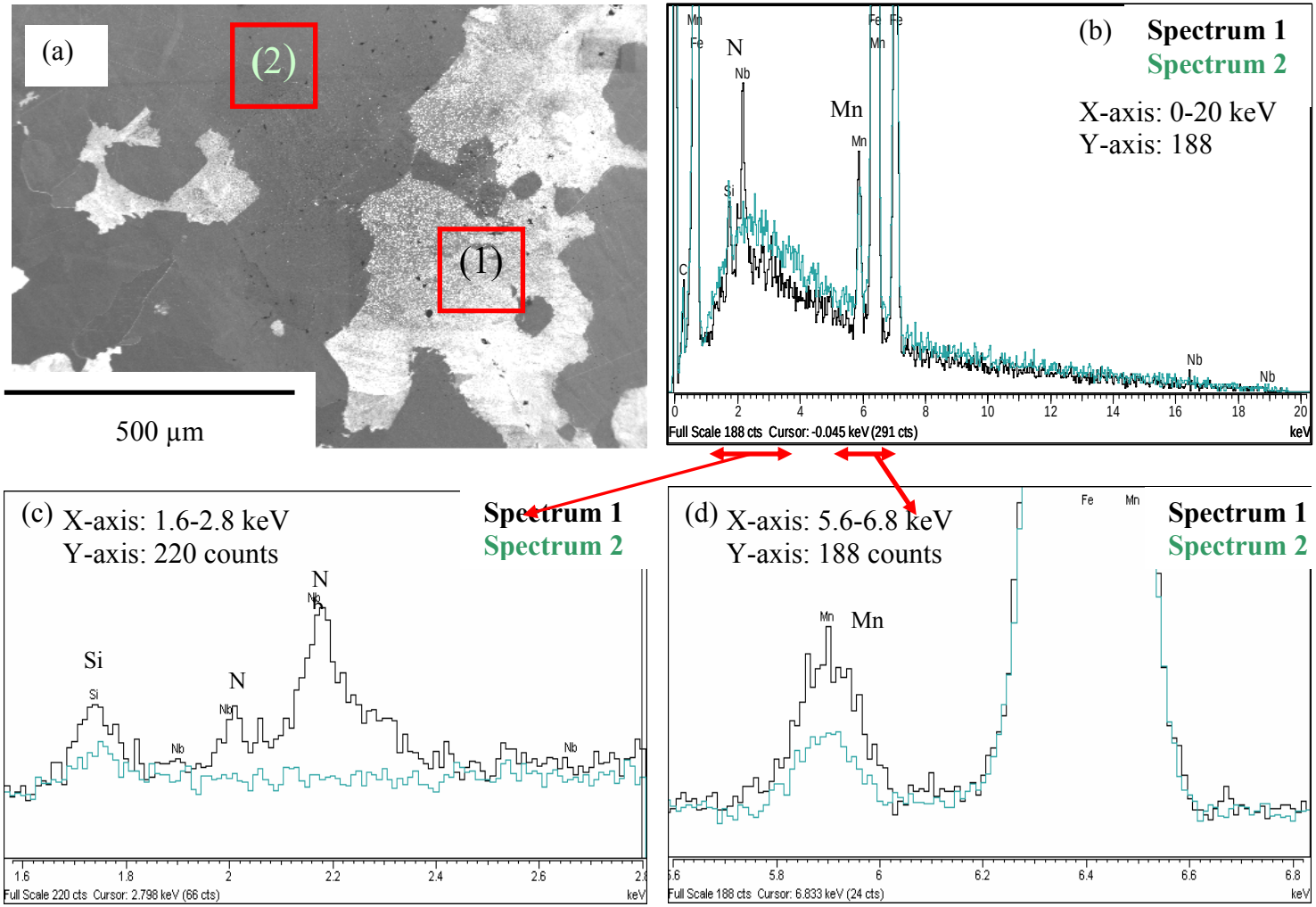

277

260

Fig. 7.19: (a) EDS spectrum 1 and spectrum 2 collected from the selected areas of interdendritic region and the dendrite centre region, respectively; (b) comparison of the EDS spectra 1 and 2 over 20 keV range; (c) enlarging the scale of both spectrums (and background correction) over 1.6-2.8 keV range showing higher Nb and higher Si peak in spectrum 1 compared to the spectrum 2; (c) similar enlarging (and background correction) over 5.6-6.8 keV range showing higher Mn peak in spectrum 1 compared to spectrum 2.

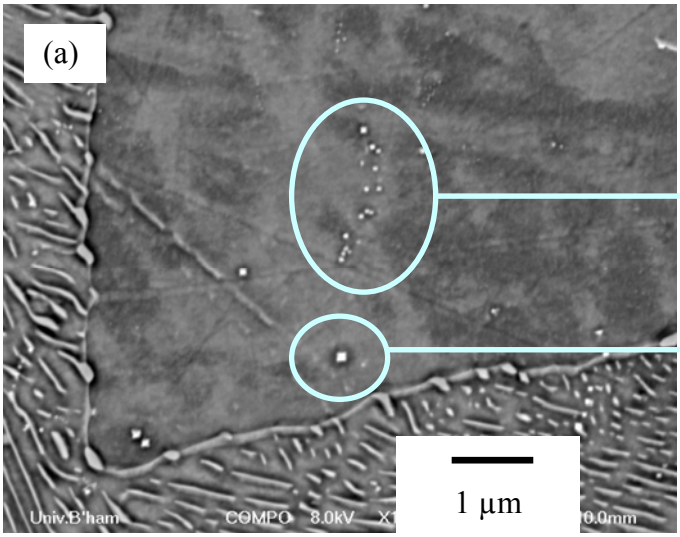

(a) Nb-rich precipitates were distributed either in isolated fashion or in cluster.

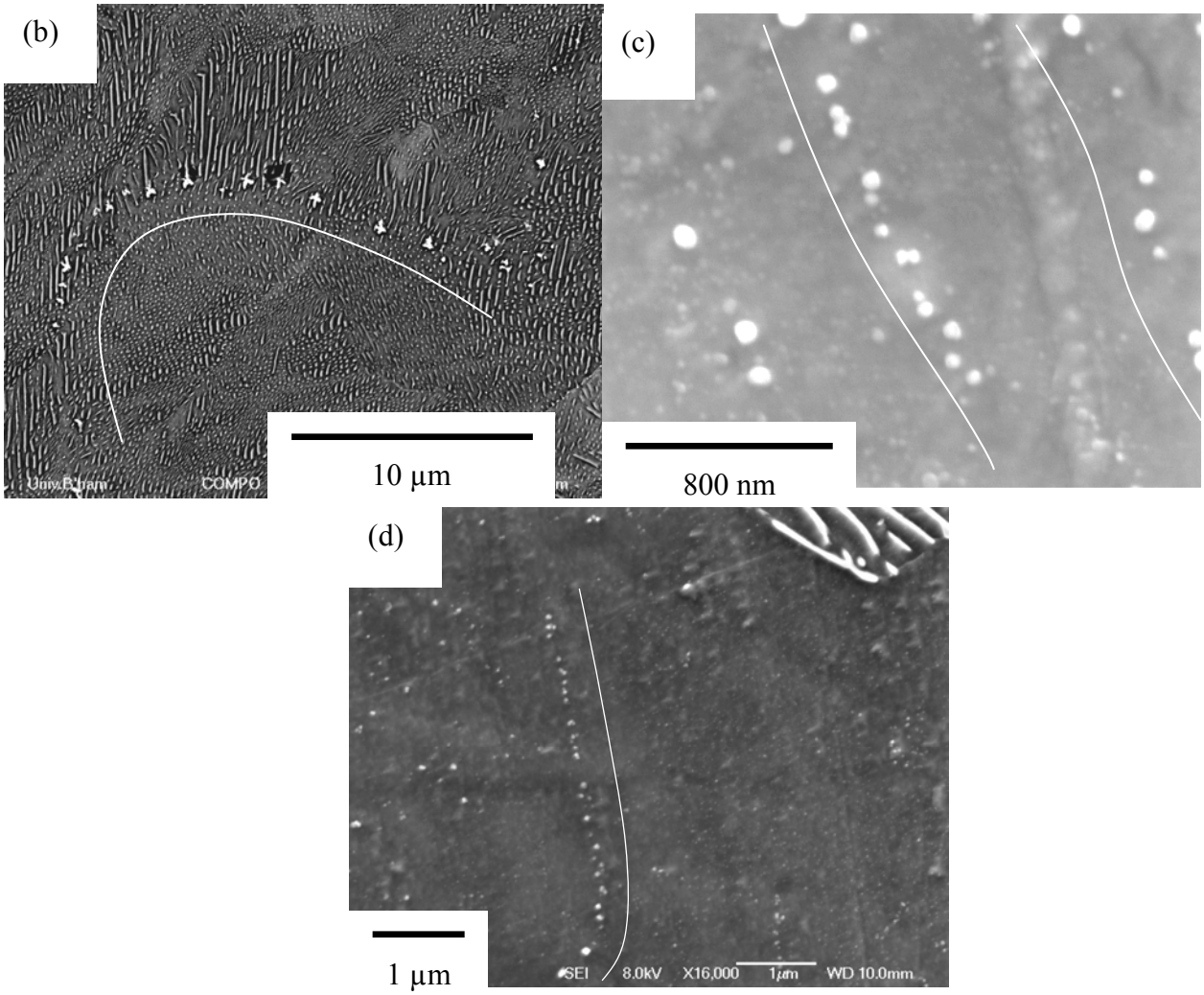

(b to d) SE or BSE images showing the distribution of Nb-rich precipitates in aligned fashion (white lines are following the array of precipitates) on (b) pearlite and on (c and d) ferrite.

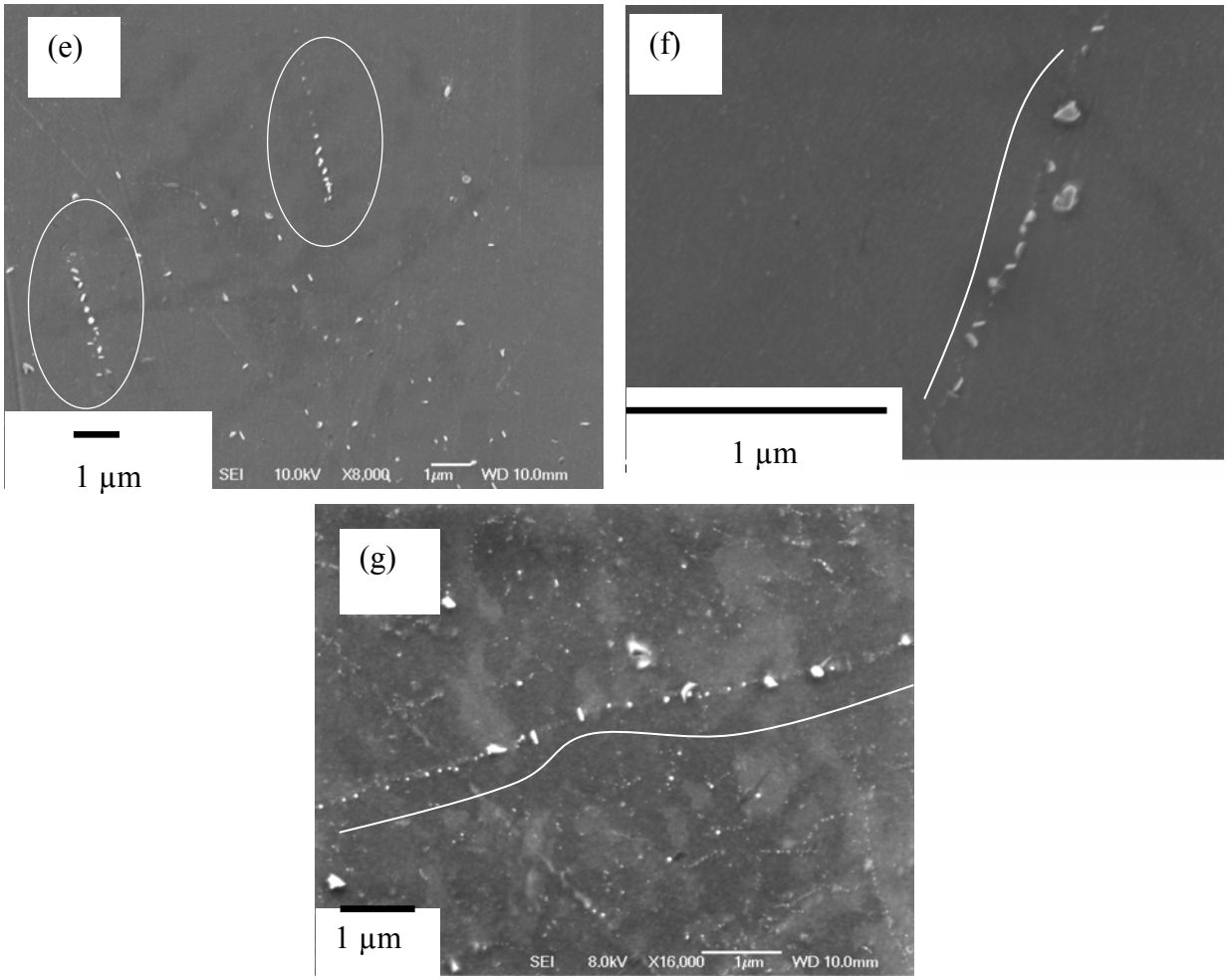

(e and f) AlN particles precipitated in rows or in arrays. The precipitate array in (g) comprised of both AlN and Nb(C, N). White lines are following the array of precipitates.

Fig. 7.20: Various images (both secondary and backscatter images) of the Nb-rich precipitates and AlN particles distributed in different fashion (on ferrite and on pearlite) at the quarter-thickness location of as-cast slabs.

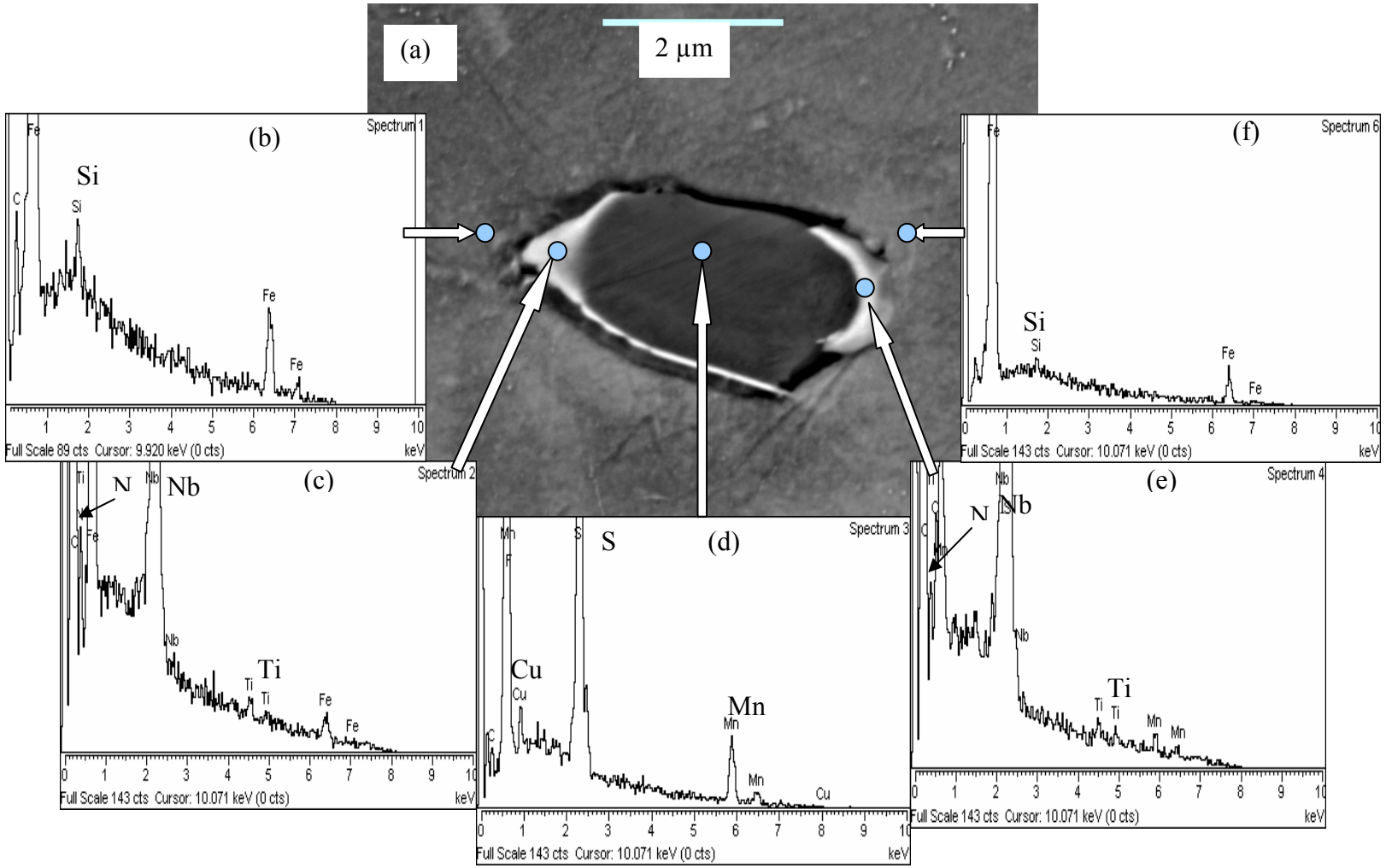

Fig. 7.21: (a) BSE image showing a bright ring around a dark particle. EDS analyses taken from different locations: (b) and (e) show Si (K peak ~ 1.8 keV), C (K peak ~ 0.28) and Fe (Kα ~ 6.40, Kβ ~ 7.05) peaks from the matrix; (c) and (e) indicate that the bright ring is probably (Nb, Ti)(C, N) as Nb (L peaks~2.2 keV), Ti (K peaks~4.5 keV) and N (K peak~0.4 keV) peaks are identified

beside the Fe and C peaks from the bright ring; and (d) showing the dark particle as a MnS inclusion (also containing some Cu).

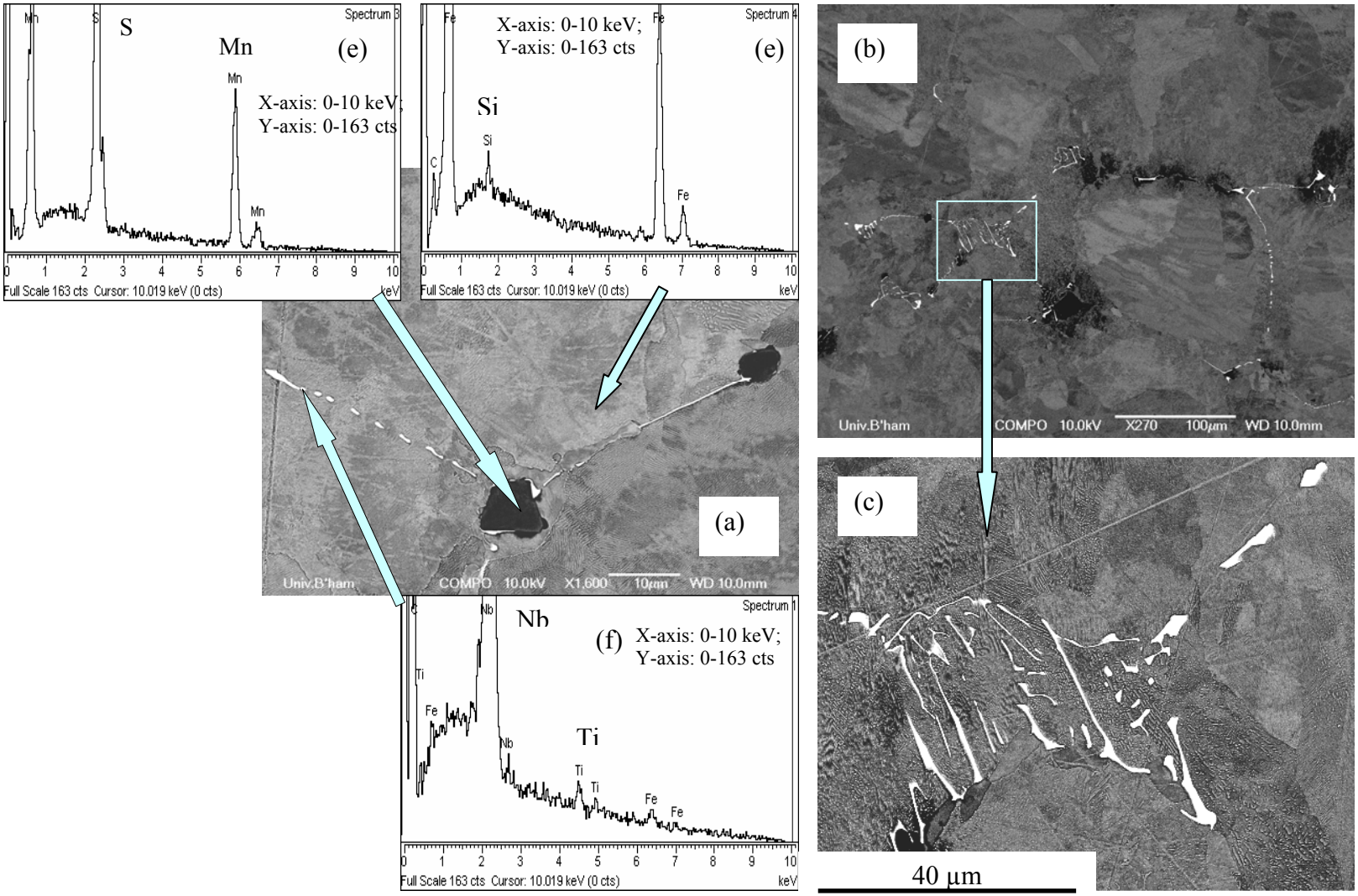

Fig. 7.22: (a), (b) and (c) are BSE images from the mid-thickness position of slab 1 showing bright networks (with up to 5 μm in thickness) at the interdendritic regions following the prior δ or γ boundaries. EDS spectra collected from the (d) dark inclusion, (e) matrix and (f) network show that the network is comprised of (Nb, Ti)(C, N) and is associated to MnS inclusions.

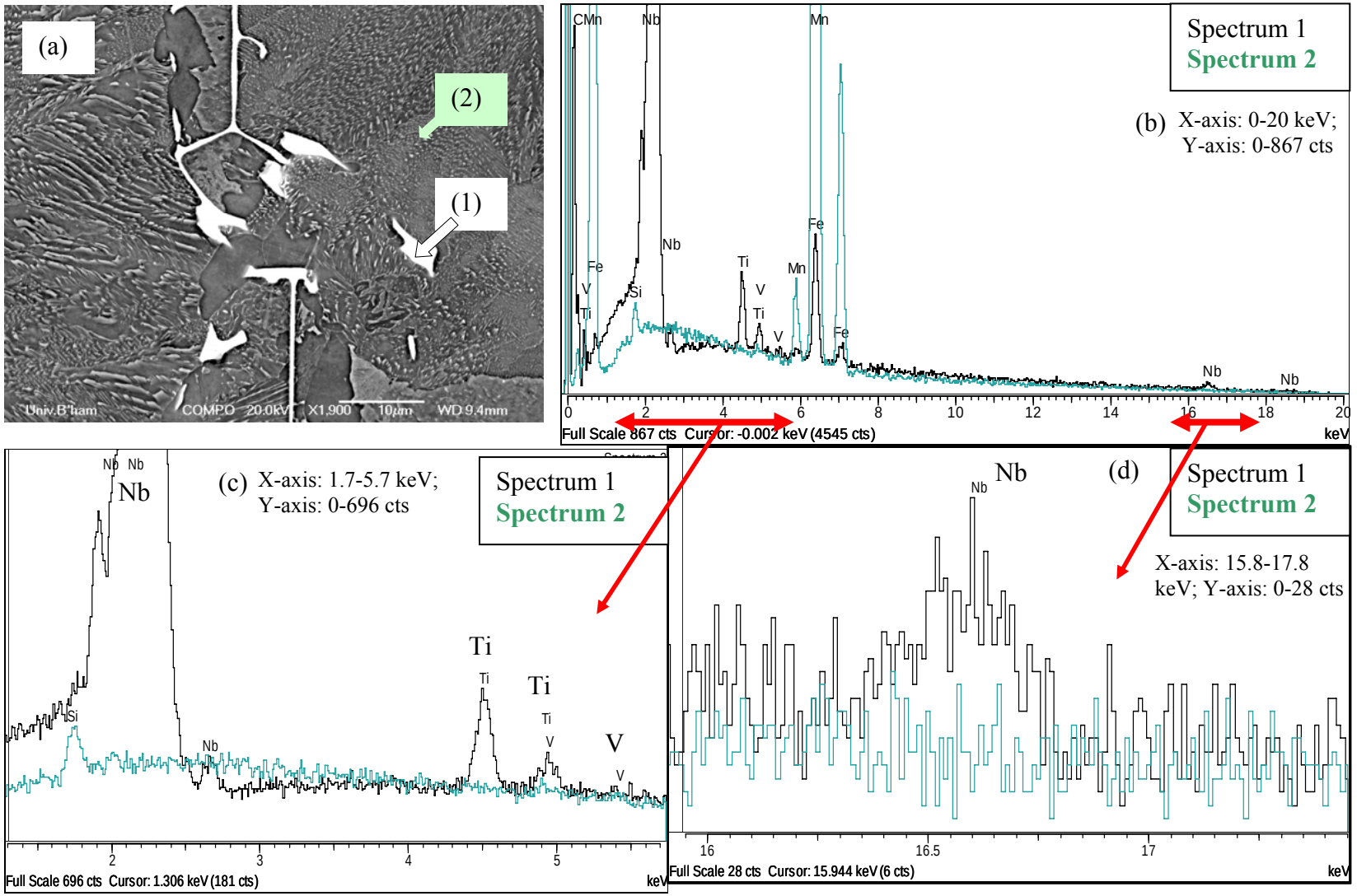

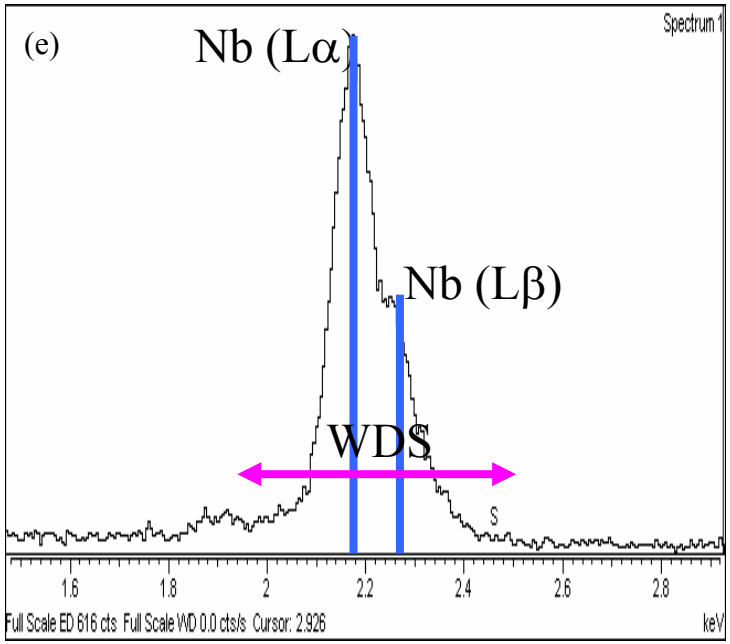

Fig. 7.23: (a) BSE image of the network deposit and the locations of EDS spectrum 1 (collected from the network) and spectrum 2 (collected from the matrix); (b) Comparison of spectra 1 and 2 over 20 keV energy range; (c) Expanding the scale of the spectra between 1.7-5.7 keV shows that Nb (L), Ti (K) and V (K) peaks are present in spectrum 1 and are absent in spectrum 2; (d) Expanding the scale between 15.8-17.8 keV shows that the Nb (K) peak is present in spectrum 1 (network spectrum), however, the same peak is absent in spectrum 2 (matrix spectrum); (e) WDS analysis conducted over 1.8-2.3 keV energy range confirmed that the EDS peaks at ~ 2.2 keV were Nb L-peaks and not the P K-peaks.

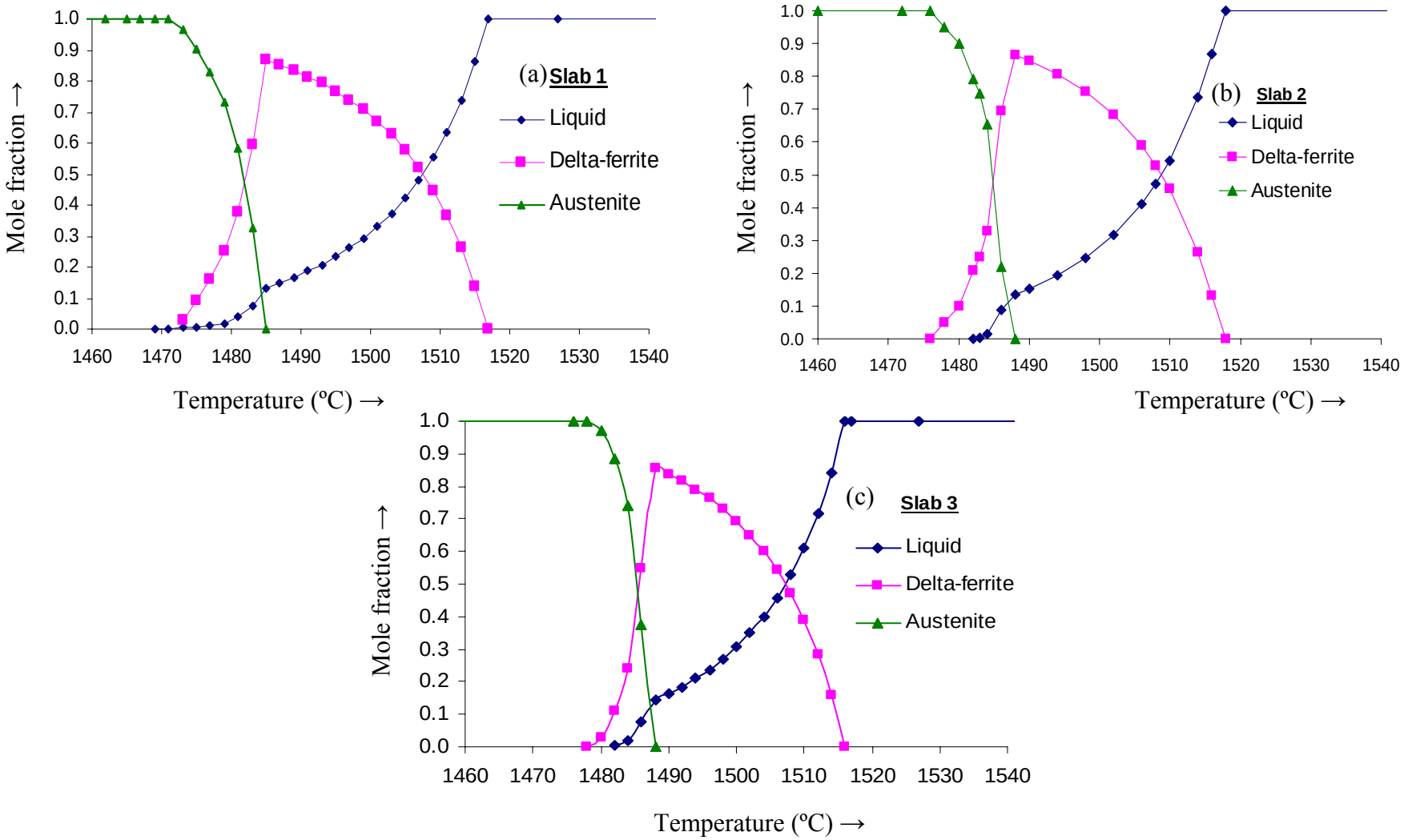

Fig. 7.24: Solidification sequence in the investigated steel slabs predicted by Thermo-Calc software: (a) slab 1, (b) slab 2 and (c) slab 3.

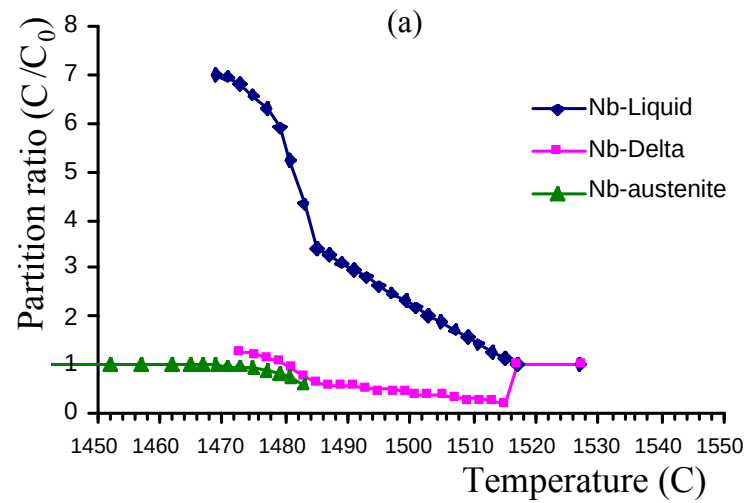
(a)
Partition ratio (C/C0)
Temperature (C)
Nb-Liquid
Nb-Delta
Nb-austenite

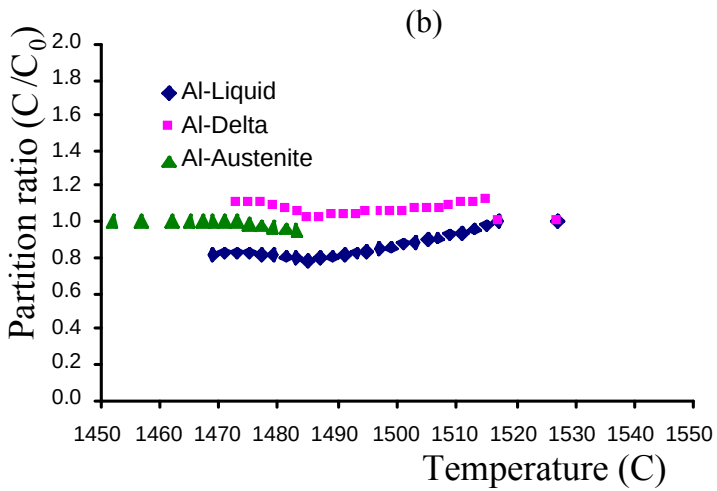
(b)
Partition ratio (C/C0)
Temperature (C)
Al-Liquid
Al-Delta
Al-Austenite

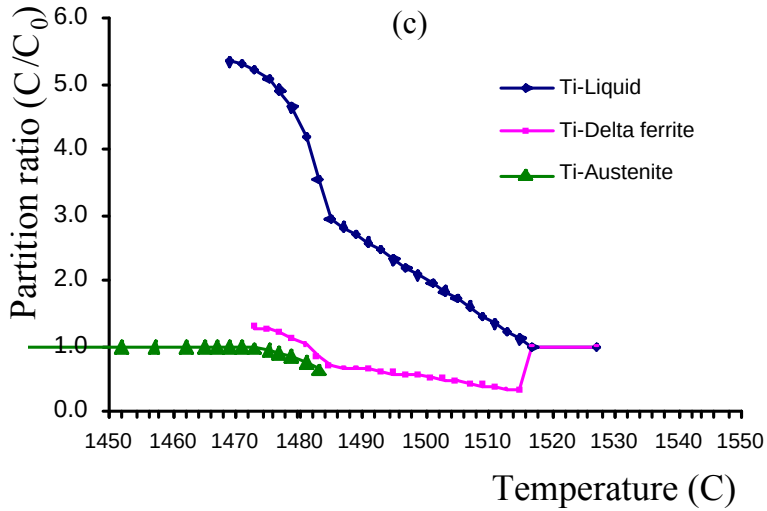
(c)
Partition ratio (C/C0)
Temperature (C)
Ti-Liquid
Ti-Delta ferrite
Ti-Austenite

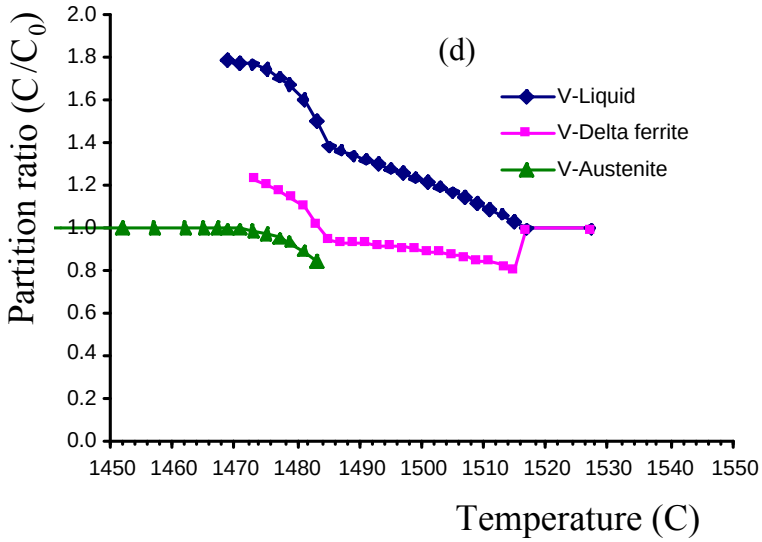
(d)
Partition ratio (C/C0)
Temperature (C)
V-Liquid
V-Delta ferrite
V-Austenite

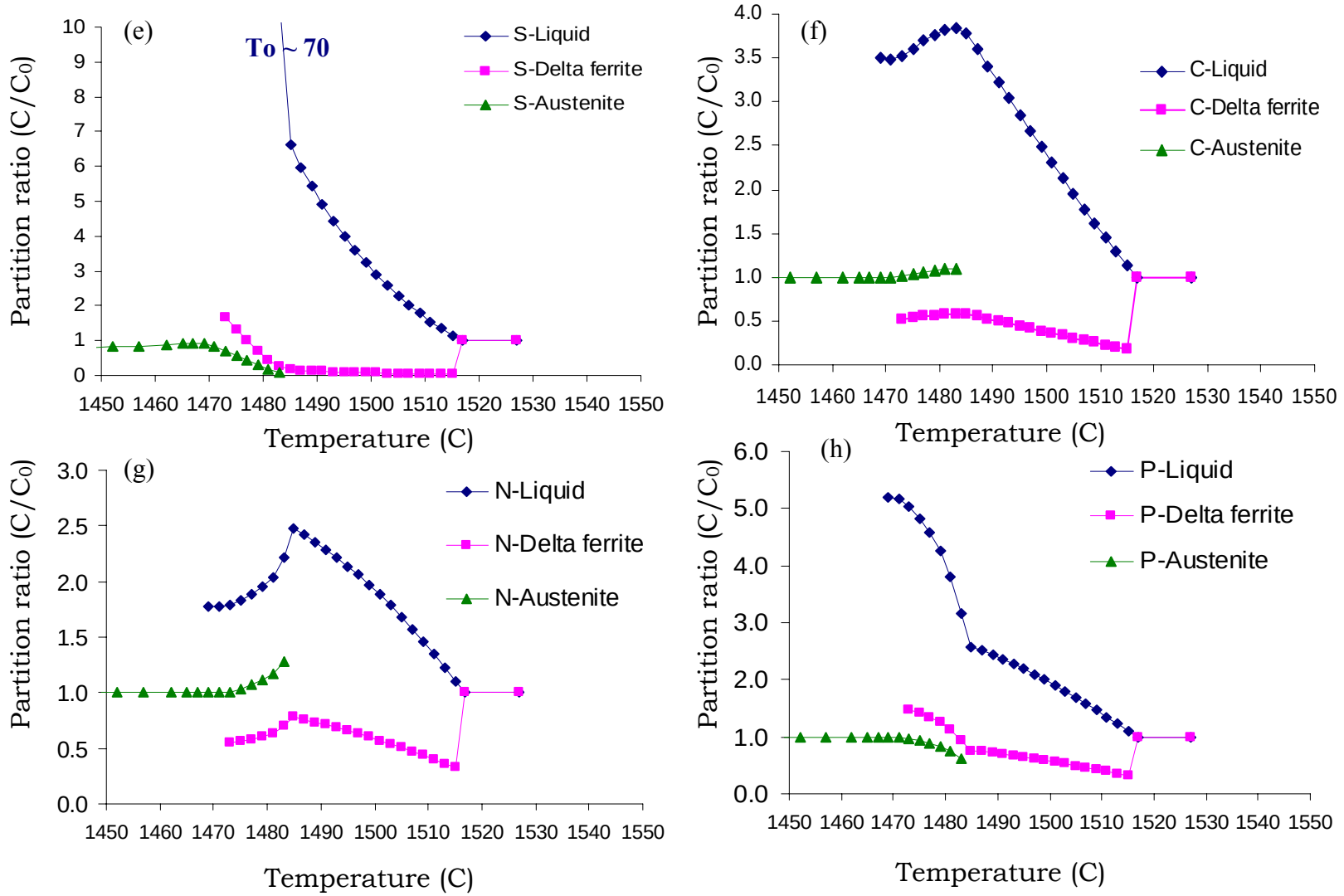

Fig. 7.25: Thermo-Calc predicted elemental partitioning within liquid, delta-ferrite and austenite phases during solidification of slab 1 (similar in slab 2 and slab 3): (a) Nb, (b) Al, (c) Ti, (d) V, (e) S, (f) C, (g) N, (h) P. Partition ratio: C/C_0, where, C is the composition within a phase and C_0 is the average composition).

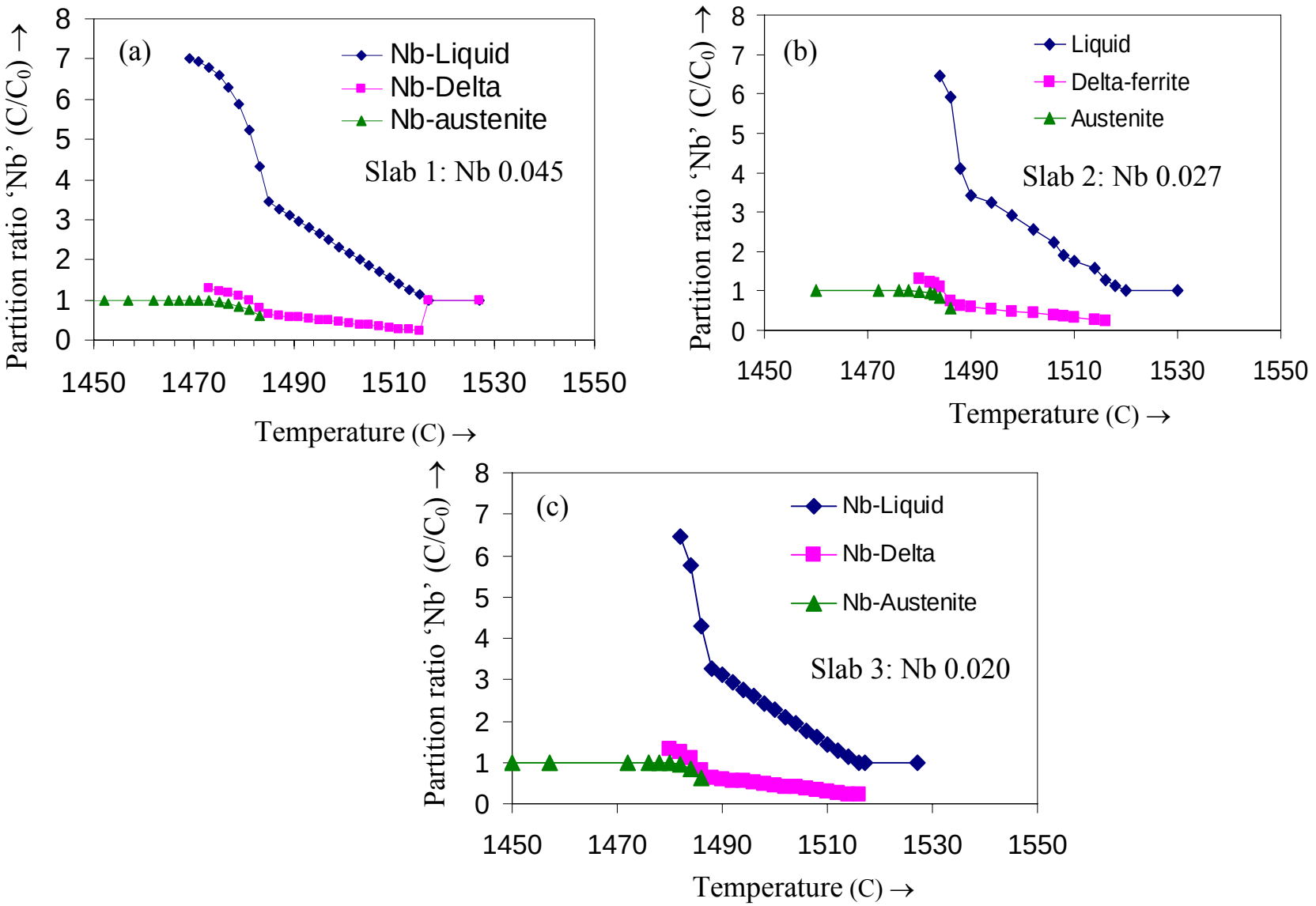

Fig. 7.26: Thermo-Calc prediction of Nb partitioning in (a) slab 1, (b) slab 2 and (c) slab 3.

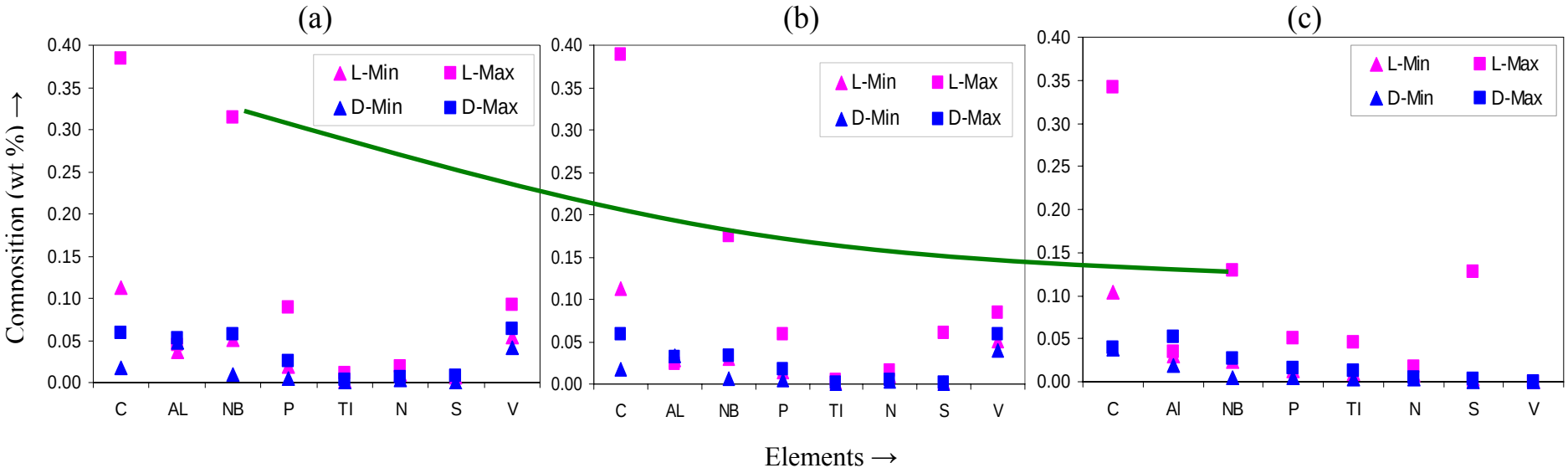

Fig. 7.27: Thermo-Calc predicted maximum and minimum levels of various elements within liquid (L) and δ-ferrite (D) phases during solidification of the investigated steels: (a) slab 1, (b) slab 2 and (c) slab 3. Drop in highest Nb level in liquid steel from slab 1 to slab 3 is shown by the green line.

Table 7.1: Mean size (equivalent diameter in μm), number density (number/mm^2) and area % of pearlite in as-cast slabs

Position	Slab 1			Slab 2			Slab 3		
	Mean Size, μm	No/mm^2	Area fraction (%)	Mean Size, μm	No/mm^2	Area fraction (%)	Mean Size, μm	No/mm^2	Area fraction (%)
10 mm	55±22	45.9 ±5.7	11.7 ±1.5	55±28	47.2 ±4.9	13.0 ±1.9	47±30	55.2 ±5.5	13.0 ±1.4
20 mm	58±31	36.8 ±5.3	11.7 ±2.1	55±30	44.2 ±3.1	12.6 ±2.0	53±31	50.9 ±8.0	15.3 ±1.3
30 mm	64±24	35.7 ±4.5	10.5 ±1.1	59±30	37.3 ±3.3	13.5 ±1.1	68±35	34.2 ±4.5	15.0 ±1.3
¼ Thickness	99±67	14.2 ±4.2	15.8 ±2.6	91±54	27.4 ±4.2	15.0 ±1.7	89±63	14.9 ±2.8	16.1 ±1.4
½ Thickness	113 ±74	12.1 ±2.5	17.0 ±2.4	105±58	17.4 ±4.1	16.5 ±2.3	104 ±77	10.6 ±1.6	15.5 ±1.2

Table 7.2: Average secondary dendrite arm spacing and average ferrite grain size (equivalent circle diameter) of as-cast slabs.

	Secondary dendrite arm spacing (μm)			Average ferrite grain size (μm)		
Position	Slab 1	Slab 2	Slab 3	Slab 1	Slab 2	Slab 3
10 mm from top	92 ± 28	88 ± 14	91 ± 26	50 ± 44	51 ± 47	50 ± 47
20 mm from top	108 ± 27	96 ± 20	97 ± 28	61 ± 54	59 ± 52	58 ± 51
30 mm from top	111 ± 27	112 ± 23	113 ± 27	67 ± 56	65 ± 56	70 ± 59
Quarter thickness	211 ± 36	198 ± 33	198 ± 29	86 ± 62	77 ± 58	89 ± 64
Mid-thickness	230 ± 38	219 ± 38	231 ± 33	113 ± 84	104 ± 87	102 ± 76

Table 7.3: Quantification of Nb-rich precipitates in as-cast slab 1.

	Precipitate Area Density (Number/mm^2)		
	Ppt-lean region	Ppt-rich region	Average
Sub-surface (10 mm)	11×10^4	41×10^4	$(27\pm7)\times10^4$
¼-Thickness	12×10^4	60×10^4	$(43\pm14)\times10^4$
½-Thickness	12×10^4	74×10^4	$(51\pm19)\times10^4$

Table 7.4: Quantification of Nb-rich precipitates in as-cast slab 3.

	Precipitate Area Density (Number/mm^2)		
	Minimum (Ppt-lean region)	Maximum (Ppt-rich region)	Average
Sub-surface (10 mm)	6×10^4	21×10^4	$(11\pm5)\times10^4$
¼-Thickness	8×10^4	30×10^4	$(21\pm14)\times10^4$
½-Thickness	8×10^4	40×10^4	$(28\pm19)\times10^4$

Table 7.5: Maximum partition ratios in liquid as predicted by Thermo-Calc software.

Element	Slab 1	Slab 2	Slab 3
Mn	1.42	1.41	1.42
Ni	1.21	1.13	1.22
Si	1.58	1.61	1.60
C	3.84	3.80	3.80
Al	0.98	0.98	0.98
Nb	7.00	6.45	6.47
P	5.20	4.50	4.58
Ti	5.36	4.94	5.16
N	2.47	2.47	2.40
S	70.99	60.57	63.90
V	1.78	1.69	0.00

8. Bimodality in reheated samples

Previous studies [Palmiere 1994, Cuddy 1983, Couch 2001] have reported austenite grain structures with significant duplex nature, or bimodality, (abnormally large grains present along with finer grains) found upon reheating samples, taken from as-cast HSLA steel slabs (0.06-0.09 C, 0.02-0.09 Nb) to temperatures between 1050-1200 ºC. Couch [Couch 2001] has observed most severe bimodality after reheating the samples taken from the quarter-thickness position of an as-cast slab with a composition very similar to that of slab 1, used in the present study, to 1150°C for 1 hr. The commercial reheating temperatures of as-cast slabs 1, 2 and 3 were also between 1150 and 1200 ºC. Therefore, to investigate the effect of reheating temperature on bimodality three reheating temperatures were selected: 1075 ºC (lower than commercial reheat temperature range), 1150 ºC (reheat temperature where severe bimodality is expected) and 1225 ºC (higher side of commercial reheat temperatures). To explain the effect of reheating on bimodality the present investigation not only studied the austenite grain structures upon reheating, but also measured the grain size distributions, spacing between the grain size bands and the effect of precipitates on the formation of the reheated grain structure. All of these have not been considered by the previous researchers [Palmiere 1994, Cuddy 1983, and Couch 2001].

8.1 Microstructure in the Reheated Samples

The reheated samples showed microstructures with uniformly coarse, uniformly fine or bimodal grain size distributions, **Fig. 8.1**. The extent of bimodality

has been quantified by the peak height ratio (PHR) and peak grain size range (PGSR), as discussed in **chapter 4 and chapter 5**, **Fig. 4.4**, and is shown in **Table 8.1**.

Reheating samples from ¼-thickness position of slab 1, slab 2 and slab 3 for 1 hour at temperatures between 1075 and 1150 °C resulted in a bimodal prior austenite grain structure (shown by water quenching and tempering), **Fig. 8.1 (a to f)**. **Table 8.1** shows that the bimodality (quantified by PHR and PGSR) increased significantly for slab 1 and slab 2 as the reheating temperature increased from 1075 °C to 1150 °C, with the most severe bimodality being found in slab 1-1150 sample. The average distance between two neighbouring fine austenite grain regions, measured normal to the length of the fine grain bands, is 247 μm (± 45 μm) in slab 1-1150 sample (224 μm for slab 2-1150 sample), which is similar to the average SDAS value of 211 μm for the quarter thickness position of as-cast slab 1 (SDAS=198 μm for quarter thickness of slab 2), **Fig. 8.2**. The bimodality disappeared for reheating at 1225 °C when a more homogeneous, but coarse, grain size resulted, **Fig. 8.1** (**g and h**). A more uniform grain size distribution (with slight bimodality) was found in slab 3 structures for reheating at 1075 and 1150°C, **Fig. 8.1 (i and j)**, with much lower bimodality than slab 1 and slab 2 samples, reheated to the same temperatures. Therefore, a clear difference in bimodality exists between the reheated samples of slab 1 (most severely bimodal) and slab 3 (slightly bimodal).

Microalloy precipitates are known to pin the prior austenite grain boundaries and control the austenite grain structure during reheating [Gladman 1997]. Hence, the nature (shape, size and composition) and the distribution of precipitates in the reheated samples of slabs 1 and 3 need to be studied to explain the difference in the severity of bimodality between both slabs.

8.2 Nature of the precipitates in the reheated samples

The precipitates pinning the prior austenite grain boundaries were studied under high-resolution SEM. **Fig. 8.3** shows that Nb-rich precipitates (arrowed) are present at the austenite grain boundaries of slab 1-1150 sample. A few precipitates can also be seen within the austenite grains.

8.2.1 Composition of precipitates

The majority of the particles pinning the prior austenite grain boundaries in samples of all three slabs, reheated to 1075 and 1150°C, were Nb-rich microalloy precipitates (~ 90 % of those present), **Fig. 8.3, Fig. 8.4** (**a and b**), which were distributed inhomogeneously in the as-cast structure. AlN particles (**Fig. 8.4 c and d**) and small sized (~ 500 nm) sulphide inclusions (**Fig. 8.4 e and f**) have also been found at the prior austenite grain boundaries of reheated samples. **Fig. 8.5** (**a and b**) shows that, compared to the as-cast samples, the fraction (among all the precipitates analysed) of Ti-containing precipitates, i.e. (Nb, Ti)(C, N), as well as the Ti-level within those precipitates increased in the reheated samples. As-cast slab 1 contained 0.05 wt % V and 24 % of all the as-cast carbonitride precipitates showed the existence of V during EDS analysis, **Fig. 8.5 (a)**. However, the precipitate V-content was negligible for the slab 1-1150 reheated sample, **Fig. 8.5 (a and b)**. The above findings suggest that Nb dissolved partially and V almost completely upon 1150 ºC reheating and the precipitates become richer in Ti. This can be further supported by the drop in precipitate number density, as finer precipitates dissolve almost completely and the number density of large precipitates decreases (discussed later). **Fig. 8.5** (**c**) indicates that the fraction of Ti-containing microalloy precipitates as well as the Ti-level within

those precipitates were higher in slab 3 compared to slab 1. Therefore, pinning precipitates in slab 3 were richer in Ti compared to the precipitates in slab 1 and that could have resulted from the higher initial Ti level in slab 3 (0.009 wt % in slab 3 and 0.002 wt % in slab 1).

8.2.2 Distribution of precipitates

To study the precipitate distribution in the reheated steel samples an area was selected from the bimodal austenite grain structure of slab 1-1150 sample, as shown in **Fig. 8.6 (a)**. The selected area covers part of a coarse grain band (marked as region C) and part of a fine grain band (marked as region F), **Fig. 8.6 (b)**. **Fig. 8.6 (b)** indicates that there was a higher density of microalloy precipitates (Nb-rich precipitates appearing bright in the BSE image and some precipitates are arrowed) within the fine grain band ('F') compared to the coarse grain band ('C'). The difference in precipitate density becomes more evident by viewing the coarse grained region 'C' (**Fig. 8.6 c and d)**, and the fine grained region 'F' (**Fig. 8.6 e and f)** at higher magnifications. Therefore, the fine grained regions were precipitate-rich compared to the coarse grained regions and the same observation was found to be true for all other coarse and fine grained regions studied for precipitates distributions, in all the reheated samples with bimodal grain structures. Hence, as for the as-cast steel, the precipitate distribution in the reheated samples was inhomogeneous. Within the fine grained region (F) in **Fig. 8.6 f** winged precipitates could be seen (arrowed), but similar precipitates were not found within the coarse grained regions. In addition, large micron-sized areas, containing Nb and Ti (**Fig. 8.6 e**) have also been observed around the MnS inclusions, but only within fine grained regions. Such ring shaped segregates were noticed only in the intertdendritic regions (also the precipitate-rich regions) of

the as-cast steel (**section 7.4.1**). Therefore, in the fine austenite grain regions of the reheated samples, the presence of (i) the higher precipitate density (compared to coarse grain regions) (ii) the winged precipitates and (iii) the ring-shaped microalloy areas around MnS inclusions indicate that fine grained regions were associated with the interdendritic regions of the as-cast steel. The absence of all those features in the coarse grained regions of the reheated steel suggests that such regions corresponding to the dendrite centre regions of the as-cast steel.

The average number densities of pinning precipitates (Nb-rich precipitates + AlN) in the fine and coarse grained regions were quantified on 1075 and 1150 ºC reheated samples of slab 1 and slab 3, **Table 8.2**. The decrease in average precipitate number density, with increased in reheat temperature from 1075 to 1150 ºC indicates that the dissolution of Nb-rich microalloy precipitates (also AlN) occurs within that temperature range. The number density of precipitates becomes almost negligible upon reheating to 1225 ºC and also at the dendrite centre region of the slab 1-1150 sample. SEM-EDS study of the particles present at the austenite grain boundaries in the 1150 °C reheated sample (slab 1-1150) indicated approximately three times as many particles per unit length of boundary (0.15 – 0.16 μm^{-1}) for smaller (<30 μm diameter) grains than for larger (>30 μm diameter) grains (0.05 – 0.06 μm^{-1}). Precipitates have not been found along the boundary of grains with an ECD > ~140 μm, which were usually present towards the centre of the coarse grain bands. The higher the number of precipitates per unit (μm) length of grain boundary (precipitate line density) the higher is the pinning force. Therefore, precipitates exert a higher pinning force in the fine grained regions compared to the coarse grained regions. The number of precipitates per unit length of the grain boundary also decreases with the increase in reheating temperature from 1075 ºC to 1225 ºC, **Fig. 8.7**. The decrease in

the precipitate number density as well as the precipitate line density with the increase in reheating temperature (from 1075 ºC to 1225 ºC), shows that dissolution of precipitates, and simultaneously, a drop in grain boundary pinning force is taking place. As mentioned earlier the number density of precipitates in the 1225 ºC reheated samples was almost negligible, **Table 8.2 and Fig. 8.7**, however, precipitates were still very occasionally seen in those samples. Such precipitates were observed to be present in localised regions within or around the fine austenite grains (< 30 μm in size), **Fig. 8.8**, that fall at the extreme left end of the grain size distribution, **Fig. 8.1 (h)**, and covered less than ~ 1 % area of the microstructure. Almost all precipitates observed contained Ti in a similar level to Nb.

8.2.3 Size of precipitates

The distributions of precipitates sizes measured on reheated samples of slab 1 (slab 1-1075, slab 1-1150), when compared to the distribution in the as-cast slab 1 (interdendritic regions), **Fig. 8.9**, showed a gradual decrease in the frequency of precipitates (particularly the smaller sized precipitates) with increase in reheating temperature, starting from the as-cast condition. The average precipitate sizes also became larger as the reheating temperatures increased, **Table 8.3**. That points to faster dissolution of the smaller precipitates with the increase in reheating temperatures. **Fig. 8.10 (a)** compares the precipitate size distributions of slab 1-1150 and slab 3-1150 samples with the distributions in the as-cast slab 1 and slab 3, respectively. Upon reheating to 1150 ºC the distribution in precipitate size appears to be similar in both steels. However, close observation of the precipitate distributions, **Fig. 8.10 (b)**, indicates that the distribution for slab 1-1150 sample is slightly shifted towards the right hand side (i.e. towards the larger precipitate size) compared to slab 3-1150

distribution. That results in a slightly higher average precipitate size in slab 1-1150 sample (116 nm) than that in slab 3-1150 sample (106 nm). However, the average precipitate size at the quarter-thickness of as-cast slab 1 (76 nm), was less than that of slab 3 (83 μm), **Table 8.3**. That suggests a smaller extent of precipitate dissolution in slab 3-1150 sample in comparison to slab 1-1150 sample. Reduced dissolution of precipitates indicates a higher thermodynamic stability, which may be due to the higher Ti-content within the precipitates in slab 3, compared to the precipitates in slab 1, **section 7.3.1** (as-cast precipitates) and **Fig. 8.5 (c)** (reheated precipitates). TiN is more stable than Nb-carbonitrides [Gladman 1997] and a higher Ti-level can therefore, increase the stability of complex (Nb, Ti)(C, N). The precipitate size distributions for the as-cast steels are not Gaussian (i.e. inverted bell shaped), **Fig. 8.10**, but, being composed of different carbo-nitride phases, is skewed to larger sizes at around 100 nm size. This side-peak does not reduce at the same rate as the main (smaller sized particle) peak (around 30 nm) in reheated samples (both in slab 1-1150 and slab 3-1150 samples) and so its persistence results in an increase in average size even though all sizes are dissolved.

8.3 Role of segregation on the formation of bimodal grain structures during reheating

In the case of continuously cast slabs 1 and 2 inhomogeneous distributions of Nb-rich precipitates have been found, with the precipitate-rich regions being associated with the interdendritic area and separated from each other by a distance similar to the average secondary dendritic arm spacing (SDAS). These precipitates were found to pin the prior austenite grain boundaries during reheating to low (1075 °C) reheat temperatures. During reheating to 1150 °C bimodal grain structures

occurred with more precipitates being observed on prior austenite grain boundaries in the fine-grained regions for slab 1 and slab 2. Uniform coarse grain structures were observed after reheating to 1225 °C and very few precipitates were seen in these samples.

The above findings suggest that the inhomogeneous precipitate distribution could be the result of micro-segregation of, primarily, Nb to the interdendritic regions during solidification (**refer section 7.3.2**) as the steel is continuously cast, **Fig. 8.11 (a)**, as seen by other researchers [Mintz 1986, Chen 1987, Tither 1992, Couch 2001]. The presence of increased levels of C, N and Nb in the interdendritic regions will increase the precipitation of Nb-rich carbo-nitrides. The dissolution temperature of a precipitate is proportional to the local matrix composition of the solutes constituting the precipitate (**refer section 1.3.3**). Hence, in interdendritic regions precipitates are expected to have a relatively high solvus temperature due to the high local solute composition. By comparison, any precipitates formed in the precipitate-lean regions exist in a matrix with low solute levels and so have a relatively low solvus temperature. The high solvus temperature precipitates undergo less dissolution (and / or coarsening) in the precipitate-rich interdendritic regions, whereas low solvus temperature precipitates dissolve and coarsen more easily, **Fig. 8.11 (b)**, during reheating. Measurement of precipitates in reheated samples of slab 1 showed a higher area fraction of precipitates (slab 1-1075 and slab 1-1150 samples) and a slightly lower average precipitate size (slab 1-1075) in the fine grained austenite regions, compared to the coarse grained regions (**refer section 8.2.2 and 8.2.3**). Zener [Zener 1948] originally pointed out that, in the presence of a second phase, grain-boundary migration may be inhibited because the second-phase particles replace part of the grain-boundary, and this part of the grain boundary area must be re-created, which is

energetically unfavourable, if the boundary is to move away from the particles (**refer section 1.4.1**). Gladman [Gladman 1966] refined this idea, and derived a retarding force (Zener drag) that particles exert on the grain boundary. Differences in precipitate size distributions and solubility can create a local variation in the volume fraction and size of precipitates effectively pinning austenite grain boundaries during reheating through Zener drag, which varies as [Zener 1948, Gladman 1966, and Kwon 1991]:

$$F_P \propto \frac{\gamma . f}{r}$$

Where, F_P is the maximum pinning force, f is the volume fraction of precipitate; r is the average precipitate radius and γ is the grain boundary energy per unit area.

As a result the effective pinning force will be higher in the precipitate-rich, interdendritic regions, which retain a higher volume fraction of particles, f (and slightly smaller size of particles) compared to precipitate-lean regions. The limiting condition for grain growth following Zener's model: $D = \xi . \frac{d}{f}$ (where, D is the grain diameter, d is the precipitate diameter, f is the precipitate volume fraction and ξ a constant) therefore, yields a finer grain size (D) during and after reheating in the precipitate-rich region, **Fig. 8.11 (c)**. Grains in the precipitate-lean regions would be expected to grow to a larger size.

As an example, the macroscopic view of a the polished + etched surface of the reheated slab 1-1150 sample shows that the alternate bands of coarse and fine austenite grain regions resemble a dendritic pattern, **Fig. 8.12 (a)**. Therefore, the dendritic structure still remains upon reheating to 1150 °C, with the fine austenite grains in the interdendritic regions and coarse austenite grains in the dendrite centre regions. On reheating to 1225 °C, as most of the precipitates dissolved, the dendritic

structure has been removed and the grain size distribution becomes more uniform, **Fig. 8.12 (b)**.

8.4 Effect of precipitate densities in as-cast steel on bimodality

Experimental observations of the precipitate distributions at the quarter-thickness position showed an inhomogeneous distribution of Nb-rich precipitates in all the as-cast slabs. The approximate ratio of precipitate number density at the interdendritic regions compared to the dendrite core varies within a close range (3.8 : 1 to 5 : 1), **section 7.3.2**, which is probably due to the similar partitioning ratio of Nb in all slabs. However, the slightly higher partition ratio of Nb in slab 1, compared to slab 3, **Table 7.5**, did result in greater inhomogeneity in precipitate distribution in slab 1, **Table 7.4**. The grain boundary pinning force is directly proportional to the precipitate volume fraction $\left(F_P \propto f\right)$, which is dependent (at least partially) on the precipitate number density. Therefore, the ratio of precipitate number densities between interdendritic and dendrite centre regions indicates the ratio of grain boundary pinning forces between the same regions (assuming the precipitate size in both regions are similar). However, the difference in magnitude of the precipitate densities between precipitate-rich and precipitate-poor regions is also important as it determines (in part) the difference in magnitude of the pinning force between both regions. The difference in precipitate number densities not only depends on the partition ratio but also on the actual Nb level in the steel. The increase in the difference in precipitate number densities with the increase in Nb level (difference in slab 1: 60-12$\times 10^4$ / mm^2, in slab 2: 39-9$\times 10^4$ / mm^2, and in slab 3: 30-8$\times 10^4$ / mm^2, at the quarter thickness position), can be related to the extent of segregation in the steels. The extent of Nb segregation can be represented by a Thermo-Calc prediction

showing the increasing difference between maximum and minimum Nb levels in the liquid and solid steel with increasing in overall Nb level (from slab 3 to slab 2 and to slab 1), **Fig. 7.27**. The extent of segregation (or the difference in precipitate density between precipitate-rich and precipitate-lean regions) qualitatively agrees with the severity of the bimodal austenite grain size structure, **Table 8.1**, following reheat to 1150 °C, as slab 1, slab 2 and slab 3 are showing the highest, the intermediate and the least bimodality, respectively.

8.5 Role of thermodynamic stability of precipitates on the formation of bimodality in the presence of segregation

The precipitate number density in the as-cast steel is not entirely retained in the reheated structure. The as-cast precipitates undergo dissolution upon reheating and the extent of precipitate dissolution depends on the thermodynamic stability of the precipitates and their size. Thermo-Calc software can be used to predict the sequence of precipitate dissolution for the different slabs considering the overall compositions, **Fig. 8.13. Fig. 8.13** predicts a decrease in the volume of precipitates with an increase in reheat temperature, as observed experimentally in **Table 8.2** and **Fig. 8.7**. Thermo-Calc predicts, for slab 1, dissolution in the temperature range 1158 – 1165°C and for slab 2, 1105 – 1125 °C. For slab 3 the predicted temperature for complete dissolution of carbo-nitride precipitates is 1180 °C. Dissolution of pinning precipitates is associated with grain growth. Therefore, **Fig. 8.13** suggests that the lowest temperature grain growth occur in slab 2 followed by slab 1 and slab 3.

Fig. 8.13 also indicates that the higher stability of carbo-nitride precipitates in slab 3, compared to slab 1, may be a reason behind the difference between slab 1 (severe bimodality) and slab 3 (slight bimodality) in terms of the grain size bimodality

(upon reheating to 1150 ºC). Thermo-Calc software can also be used to predict the internal composition within the carbo-nitride precipitates in the investigated steels, **Fig. 8.14**. With the increase in reheating temperature the composition within the precipitates is expected to change, as the Nb-, V- and C-levels drop and the precipitates become richer in Ti and N, **Fig. 8.14**. A similar trend (precipitates becoming Ti-rich and lean in Nb and V as reheating temperatures increase) has been found using EDS, collected from the microalloy precipitates in the present investigation, **Fig. 8.5**. EDS analysis also showed higher Ti-levels within the precipitates in slab 3, compared to slab 1, **Fig. 8.5 (c)**, consistent with the Thermo-Calc calculations. Higher Ti-levels within the precipitates in slab 3 are expected from the higher overall Ti-level in that steel (0.009 wt % in slab 3, 0.002 wt % in slab 1 and 0.001 wt % in slab 2) and are responsible for higher stability of carbo-nitride precipitates in slab 3 compared to slab 1 and slab 2.

8.5.1 Difference in precipitate stability between interdendritic and dendrite-centre regions

As mentioned earlier, the stability of precipitates is not the same everywhere in a slab and is proportional to the local solute levels. In the presence of micro-segregation the stability of precipitates, therefore, is expected to be higher within the solute-rich interdendritic regions compared to the solute-lean dendrite core regions. In the present investigation SEM-EDS and -WDS (initially measured by EDS area analysis and also checked by WDS point analysis) was used to measure the local composition at interdendritic (pearlite) and dendrite centre (ferrite) regions over a 1 mm^2 area at the quarter thickness position of the as-cast slabs (also discussed in **section 7.3.2**). At the interdendritic (pearlite) regions the average Nb- levels were

found to be 2.5 - 3 times higher than at the dendrite centre (ferrite) regions (Nb-levels at interdendritic regions 0.075 wt % for slab 1, 0.050 wt % for slab 2 and 0.040 wt % for slab 3 and at dendrite-centre regions 0.027 wt % for slab 1, 0.020 wt % for slab 2 and 0.016 wt % for slab 3). Therefore, the local Nb-levels for slab 1 lies within the range obtained by Couch [Couch 2001] (~ 0.45-0.10 wt % at interdendritic and ~ 0.20-0.45 wt% at dendrite centre regions) using laser ablation spectroscopy (LA-ICP-MS) on the quarter-thickness position of a slab of the same composition steel. Under SEM-EDS and -WDS the distribution of Al (0.48 wt% at interdendritic and 0.41 wt% at dendrite centre for slab 1), Ti (0.0024 wt% at interdendritic and 0.0018 wt% at dendrite centre for slab 1) and V (0.056 wt% at interdendritic and 0.047 wt% at dendrite centre for slab 1) were found to be more homogeneous compared to the Nb-distribution (also supported by LA-ICP-MS) [Couch 2001]. To understand the effect of micro-segregation on the stability of the precipitates, Thermo-Calc predictions were carried out for dendritic (ferrite) and interdendritic (pearlite) Nb-levels and Al-levels determined by SEM-EDS (for all other elements the overall composition was used for the prediction) on all three slabs, **Fig. 8.15**.

The Nb content is high (0.045 wt %) in slab 1 steel and the Ti content is low (0.002 wt %). Therefore, the microalloy carbonitrides, (Nb,Ti,V)(C,N), are Nb- rich (~ 60 - 80 wt % Nb) and lean in Ti (~ 2 - 20 wt %). V-precipitates start to appear ~ 1075 °C and the V content rises from ~ 2 wt % to ~ 12 wt % in (Nb,Ti,V)(C,N) as the temperature drops further, **Fig. 8.14 (a)**. For slab 1, **Fig. 8.15 (a)**, reheating to 1075 °C is predicted to dissolve most of the (Nb,Ti,V)(C,N) precipitates in the dendritic (ferrite) regions (only ~0.00005 molar fraction is expected to remain). This can be supported by the drop in experimentally measured Nb(C, N) precipitate density in the dendrite centre areas from 12×10^4 to 4×10^4 (per mm^2) as the as-cast slab 1 is reheated

to 1075 ºC, **Table 8.2**. Lack of of Nb(C, N) in the dendrite centre decreases the component of Zener drag from grain boundary pinning. However, AlN is not predicted to dissolve as much as Nb(C, N) and after 1075 ºC reheating there is little difference in the amounts of AlN present in the dendritic (~0.00020 molar fraction) and interdendritic (~0.00035 molar fraction) regions. The dissolution of most of the Nb(C, N) in the dendrite centre (~0.00005 molar fraction remaining) compared to much higher level (~0.00060 molar fraction) of Nb(C, N) precipitates remaining in the interdendritic areas is expected to cause bimodality (from the difference in Zener drag) but the presence of AlN at reasonably high levels (more than ~0.00020 molar fraction) throughout the microstructure means that there is some pinning available in dendrite centre areas, not allowing the bimodality to be severe (level 2 bimodality), **Table 8.1**.

In contrast, for slab 3 reheated to 1075 °C, **Fig. 8.15 (b)**, AlN is expected to have fully dissolved from both the dendritic and interdendritic regions. The greater amount of Ti present in slab 3 (0.009 wt %) increases the stability of the (Nb,Ti)(C,N) particles, which contains ~ 30-60 % Nb and ~ 20 - 50 % Ti, **Fig. 8.14 (b)**, so that ~0.00030 molar fractions of carbonitride-particles are present in the dendritic and ~0.00055 molar fraction in interdendritic areas. Therefore, the difference in total molar fractions of pinning precipitates (Nb-rich particles + AlN) between dendrite centre and interdendritic regions is smaller for slab 3 (0.00030 in dendrite centre and 0.00055 in interdendritic) compared to slab 1 (0.00025 in dendrite centre and 0.00095 in interdendritic). A smaller difference in molar fractions leads to smaller difference in Zener drag values resulting in a lower bimodality level in slab 3-1075 sample (level 1) compared to slab 1-1075 sample (level 2).

The major difference between the slabs occurs for reheating to 1150 °C. For slab 1 at this temperature, all AlN and the dendritic (Nb,Ti,V)(C,N) are predicted to have dissolved leaving little Zener drag in the dendritic regions, where large prior austenite grains can develop. The interdendritic regions retain around a third of the (Nb,Ti,V)(C,N) molar fraction (~0.0003) and so grain boundaries here are still pinned to an extent leading to a severe bimodal grain structure (level 4). The (Nb, Ti)(C,N) particles in slab 3 show dissolution over a very narrow temperature range, which in the dendritic region is close to 1150 °C (1210 °C in the interdendritic regions). Due to the steep nature (sharp drop in molar fraction towards the dissolution temperature) of the dissolution curve the (Nb, Ti)(C,N) precipitates are unlikely to have fully dissolved at 1150 °C in the dendritic regions due to kinetic considerations. This can be supported by the experimental observation of precipitates, **Table 8.2**, in the same regions of slab 3-1150 sample. Therefore, it is expected that reasonable levels of Zener drag are present in both areas during reheating to 1150 °C so that significant bimodality does not develop (level 1), **Table 8.1**. For the slab 3 composition, bimodal grain structures would be expected for reheating into the ~ 1160 – 1200 °C temperature range. To verify this prediction a slab 3 quarter-thickness sample was reheated to 1180 °C. The austenite grain structure, **Fig. 8.16**, following water quenching and tempering, revealed a 'quite-bimodal' (level 3) structure and the PHR and PGSR values, **Table 8.1**, confirm the bimodal nature of this structure.

For reheating to 1225 °C complete dissolution of all particles in both regions is expected for all the slabs so that no difference in Zener drag is expected, which is consistent with the absence of bimodality, **Table 8.1**, and large prior austenite grain size, **Fig. 8.1 (g)**.

8.5.2 Calculation of Zener drag values to explain bimodality

The difference between slab 1 and slab 3 in terms of bimodality can be better explained from the predicted mass-fractions of the precipitates. Beside the mole fraction values of the Thermo-Calc software also provided the mass-fractions of the microalloy carbo-nitride and AlN precipitates expected at various temperatures, **Fig. 8.17**.

AlN is a pure compound and therefore, the density of AlN particles can be considered a constant (3.26 gm / cm^3). However, the composition within carbonitride precipitates changes with temperature, **Fig. 8.14**. Considering the internal composition within the complex carbo-nitride precipitate at a particular temperature and using the density of simple microalloy carbides or nitrides (NbN: 8.5 gm / c.c, NbC: 7.8 gm / c.c, TiN: 5.4 gm / c.c, TiC: 4.9 gm / c.c, VN: 6.1 gm / c.c, VC: 5.7 gm / c.c) the approximate densities of complex microalloy carbonitride can be determined at that temperature. **Fig. 8.18** shows the variations in the density of the microalloy precipitates for the as-cast and reheated slab 1 and slab 3 steels. The lower density of carbo-nitride precipitates in slab 3-reheated samples (than slab 1-reheated samples) is due to their higher Ti levels. The density of the steel matrix does not change significantly over temperature and therefore, can also be considered as a constant ~ 7.78 gm / c.c. The densities of AlN, microalloy carbo-nitride and the steel matrix can be used to calculate the approximate volume fractions of the AlN and Nb-rich carbo-nitrides from the mass-fractions of the same precipitates (**Fig. 8.17**) as predicted by Thermo-Calc. The total volume fractions (approximate) of pinning precipitates (microalloy precipitates + AlN) thus obtained for as-cast and reheated samples for the slab 1 and slab 3 are shown in **Fig. 8.19**.

Average precipitate sizes (equivalent circle diameter) were measured in precipitate-rich (interdendritic) and precipitate-lean regions (dendrite-centre) of as-cast and reheated samples of slab 1 and slab 3, **Fig. 8.20**. Using the average precipitate sizes and the precipitate number densities (number / mm^2) measured at interdendritic and dendrite centre regions of as-cast and reheated samples the approximate volume fractions of precipitates can also be calculated at those regions. To calculate the volume fractions all the precipitates were assumed to be perfectly spherical in shape. This assumption is reasonable as (i) the precipitate sizes were measured in ECD and (ii) the precipitates observed in the as-cast and reheated steels (sphere, cube or star shaped) were equiaxed in shape (aspect ratio ~ 0.9-1.0). **Fig. 8.21** compares the precipitates volume fractions obtained from Thermo-Calc prediction (using EDS and WDS compositions at interdendritic and dendrite-centre regions) and measured from the precipitate number density and precipitate size (observed by SEM on the polished + etched samples). **Fig. 8.21** shows that the predicted and calculated volume fractions follow the same trend and lie within a close range of values. The agreement is better for dendrite centres; and for the reheated samples rather than the as-cast steel, which is expected as as-cast is continuously cooled rather than the slow heating and isothermal holding in reheated samples. In addition, using the average particle sizes, r (radius) and volume fractions, f (Thermo-Calc predicted volume fraction was used), the Zener drag, F_p (precipitate pinning force acting on grain boundary in MJ / m^2), can be calculated, **Fig. 8.22**, using the following equation based on the rigid boundary model [Kwon 1991]:

$$F_P = \frac{6.\gamma.f}{\pi.r} \quad \text{……eqn. 8.4.1}$$

where, γ is the grain boundary energy, taken as 0.8 J m^{-2}.

According to **Fig. 8.21** the inhomogeneity in precipitate distribution is higher in slab 1, compared to slab 3. The reason behind this is the higher Nb level in slab 1, as discussed in earlier sections. The difference in precipitate volume fractions between precipitate-rich (interdendritic) and precipitate-poor (dendrite-centre) regions in slab 1-1075 is ~ 0.0007, whereas, for slab 3-1075 sample it is ~ 0.0003. As the precipitate sizes are similar in slab 1-1075 and slab 3-1075 samples, **Fig. 8.21**, the larger difference in volume fractions resulting in a greater difference in Zener drag, **Fig. 8.22**, between interdendritic and dendrite-centre regions, in slab 1 (0.12 MJ/m^2 at interdendritic and 0.04 MJ/m^2 at dendrite-centre) compared to slab 3 (0.064 MJ/m^2 at interdendritic and 0.031 MJ/m^2 at dendrite-centre). This leads to higher bimodality (level 2) in slab 1-1075 sample compared to slight bimodality (level 1) in slab 3-1075 sample. However, ~ 0.0004-0.0005 fraction of precipitates remained undissolved in the dendrite-centre region of slab 1 and therefore, the grains still remained pined at that location (by a Zener drag ~ 0.04 MJ/m^2). Hence, bimodality in slab 1-1075 sample (level 2) was not severe in scale.

On other hand, in slab 1-1150 sample, the precipitates dissolved completely at the dendrite-centre region and therefore, the Zener drag should be negligible there (**Fig. 8.22**), allowing the grains in that regions to grow in an unstable fashion until the grains impinge. At the interdendritic regions precipitates remained with a volume fraction of ~ 0.0004, exerting a Zener drag of ~ 0.033 MJ/m^2 and that restricted grain growth. Hence, severe bimodality (level-4) developed in the slab 1-1150 sample. Due to the steep nature of the dissolution curve the carbo-nitride precipitates are unlikely to fully dissolve at 1150 ºC in the dendritic region of slab 3-1150 sample. Assuming the volume fraction of carbo-nitride precipitates at 1140 ºC is still retained at 1150 ºC, the difference in volume fraction and Zener drag between the interdendritic and

dendrite-centre regions in the slab 3-1150 sample remains similar to slab 3-1075 sample, **Fig. 8.21 and Fig. 8.22**. Therefore, the same level of bimodality (level 1) is expected in slab 3-1150 sample as in the slab 3-1075 sample.

At 1180 ºC, the precipitates are expected to dissolve completely at the dendrite-centre regions of slab 3, however, at the interdendritic regions ~ 0.025 mass-percent of carbo-nitride precipitates of density ~ 5.5 gm / cm^3 and average diameter ~ 120 nm (measured experimentally) remained undissolved. At the interdendritic region that gives a precipitate volume fraction of ~ 0.0003, which will exert a Zener drag of ~ 0.024 MJ/m^2 on the grain boundaries. The absence of any Zener drag at the dendrite-centre region allows the grains in that region to grow freely, and therefore, high bimodality (level 3) was observed in the slab 3-1180 sample. However, the Zener drag at the interdendritic region is higher in slab 1-1150 sample (~ 0.030 MJ/m^2) than slab 3-1180 sample (~ 0.024 MJ/m^2) and that could be the reason behind the slightly lower bimodality observed in the slab 3-1180 sample (level 3) compared to the slab 1-1150 sample (level 4).

Precipitates are expected to dissolve completely upon reheating to 1225 ºC. However, microalloy-precipitates have been seen in those samples. Davis and Strangwood [Davis 2002] and Palmiere et al. [Palmiere 1996] reported that Ti-rich or Nb-rich (Nb, Ti)(C, N) particles could remain undissolved at temperatures as high as 40 - 70 ºC above the equilibrium dissolution temperature. The existence of precipitates at such high temperatures has been attributed to segregation, which increases the local stability of precipitates (in the highly segregated region) to greater than that predicted from the average composition. In 1225 ºC reheated samples precipitates were found in the present study within or around the fine grains (< 30

μm), and the fact that such grains remained with a fine size could be due to Zener drag exerted by those precipitates.

8.5.3 Relation between Zener drag and the variation in average grain size of the reheated samples

Beside the severity in bimodality, the variation in average austenite grain size (not the local average but the overall average) with the reheating temperature, **Fig. 8.23**, can be explained from the local Zener drag values, **Fig. 8.22**, acting in the reheated samples of slab 1 and slab 3. To study the average austenite grain size variation, apart from the high reheating temperatures (1075 ºC and above) two slab 1 samples have also been reheated to lower temperatures, 940 ºC and 1000 ºC, within the austenite phase field, **Fig. 8.23**. **Fig. 8.23** shows that the average austenite grain size increases with increasing reheating temperature and with the dissolution of pinning precipitates. The lower average austenite grain size in slab 1-1075 sample (19 μm) than slab 3-1075 sample (25 μm) can be due to the higher Zener drag values acting in slab 1-1075 sample (interdendritic region: 0.11 MJ/m^2; dendrite-centre region: 0.04 MJ/m^2) compared to slab 3-1075 sample (interdendritic region: 0.06 MJ/m^2; dendrite-centre region: 0.03 MJ/m^2). However, the situation is reversed upon reheating to 1150 ºC and the average grain size becomes larger in slab 1-1150 sample (36 μm) than in the slab 3-1150 sample (36 μm). That could be due to the loss in Zener drag at the dendrite-centre region of slab 1, allowing the grains to grow into very large size, and hence, increasing the average grain size. The Zener drag values in slab 3-1150 sample are close to those in the slab 3-1075 sample (interdendritic region: 0.046 MJ/m^2; dendrite-centre region: 0.022 MJ/m^2) and therefore, the average grain sizes also remain close (25 and 28 μm). In slab 3-1180 sample, the Zener drag

becomes negligible at the dendrite-centre regions and reaches a low value (0.02 MJ/m^2) even in the interdendritic regions resulting in a much higher average grain size (70 μm). In 1225 ºC samples, negligible Zener drag in both interdendritic and dendrite-centre regions allowing the average grain sizes to increase further.

8.5.4 Prediction of limiting grain size

As discussed in **section 1.4** the average grain diameter (D) can be related to the average diameter (d) of the pinning particles and to the volume fraction (f) of particles by the following equation:

$$D = \xi.\frac{d}{f} \qquad \text{……..……...……..……eqn. 8.4.2}$$

where, ξ is a constant and for Zener's model, ξ = 4/3. Gladman [Gladman 1966] pointed out that Zener's model overestimates the driving force for grain growth and therefore, could overestimate the equilibrium grain size. Hillert [Hillert 1965] and Gladman [Gladman 1966] considered the inhomogeneity in grain size distribution and introduced the grain size heterogeneity factor, Z. Gladman [Gladman 1966] suggested, $\xi = \frac{\pi}{6}\left(\frac{3}{2} - \frac{2}{Z}\right)$, and compared his model with the experimental studies on the growth of austenite grains in the presence of NbC and AlN particles [Gladman 1966]. For the normally observed range of Z values (1.41 - 2.00) excellent agreement was reported between Gladman's model and experimental data [Gladman 1966]. In the current investigation the austenite grains grow in the presence of similar particles and at similar temperature range (1050 - 1250 ºC) studied by Gladman [Gladman 1966] and therefore, Gladman's model can be considered as appropriate. Considering Z = 2, for which ξ=0.26, and using the volume fractions (both Thermo-Calc predicted

volume fractions and experimentally observed volume fractions) and average precipitate sizes, the limiting grain sizes can be predicted at the interdendritic and dentrite-centre regions of the reheated samples. Limiting grain size values represent the average grain sizes at which grain growth stops in a particular region. The predicted grain size values, **Table 8.4**, when superimposed on the corresponding (measured) grain size distributions in the reheated samples show the similar trend as the distributions, **Fig. 8.24**. In the absence of pinning particles (as in slab 1-1150 sample at dendrite-centre region, or in 1225 ºC reheated samples) the Zener drag becomes negligible and, therefore, the grains can grow as large as possible until they impinge upon one another.

8.5.5 Application to bimodality in slab 2

The concepts derived from the previous discussion about the difference between slab 1 (severe bimodality) and slab 3 (slight bimodality) in terms of bimodality can be used to explain the bimodality in slab 2. The Ti content (0.001 wt %) in slab 2 steel is even lower than that of slab 1 and therefore, in spite of the intermediate Nb content (0.027 wt %), the (Nb,Ti,V)(C,N) precipitates in slab 2 are rich in Nb (50 - 80 wt %), **Fig. 8.14 (c)**. The low Ti content (3-20 wt %) in the precipitates, therefore, makes them less stable in nature. The Thermo-Calc prediction for slab 2 based on the Nb-levels at the interdendritic and dendrite-centre regions, **Fig. 8.25**, shows that at the dendrite centre regions (Nb,Ti,V)(C,N) particles are expected to dissolve at ~ 1080 °C and therefore reheating at 1075 °C is expected to produce bimodality, similar to slab 1-1075 sample, **Table 8.1**. Both for slab 1 and slab 2 at 1150 °C AlN and (Nb,Ti,V)(C,N) precipitates are expected to dissolve at the dendrite centre regions. However, the molar fraction of the (Nb,Ti,V)(C,N) precipitates present

at the interdendritic regions of slab 2 at 1150 °C (~ 0.00013) is half of that for slab 1 (~ 0.00027) at that temperature. This is due to the lower Nb content in slab 2 compared to slab 1 (hence, the severity of Nb segregation is also expected to be lower in slab 2). That results in a higher effective pinning force at the interdendritic region for slab 1 in comparison to slab 2 and therefore, less severe bimodality in the slab 2, 1150 °C reheated sample (level 3) compared to the slab 1, 1150 °C reheated sample (level 4), **Table 8.1**.

8.6 Summary

The major findings from the above discussion are as follows:

- Bimodal austenite grain structures can develop during the reheating of the as-cast slabs
- Inhomogeneous precipitate distributions, originating during solidification after continuous casting, can create a difference in precipitate pinning force between different regions of the steel, during reheating, and can result in the formation of a bimodal grain structure.
- The reheat temperature has a significant effect on the degree of grain size bimodality with low (1075 °C) and high (1225 °C) reheat temperatures typically showing no or low bimodality but intermediate (1150 or 1180 °C) reheat temperatures showing heavily bimodal microstructures.
- The volume fraction of precipitates can either be obtained from the direct observation and quantification of precipitates (under SEM or TEM) or from thermodynamic predictions based on the steel compositions.

- Thermodynamic software can be used to account for the variation in bimodality by considering the segregated slab compositions and reheating temperatures.

In addition to the above findings the discussion in Chapter 7 and Chapter 8 indicates that among the microalloying elements Nb segregates the most in the as-cast steel and results in bimodality during commercial reheating. Ti also segregates in steel, however, not as strongly as Nb, and can even prevent, or limit bimodality within the temperature range used for commercial reheating by increasing the stability of microalloy precipitates (as in slab 3). V segregates weakly in steel and is mostly ineffective in terms of bimodality as it completely dissolves during commercial reheating. Al, whilst not a common microalloying element is better than Nb in terms of bimodality, as Al only segregates weakly in steel and AlN particles (that can pin the austenite grain boundaries) remain almost uniformly distributed. Therefore, considering just the extent of bimodality point of view, Nb level could be reduced and Ti and Al levels could be increased in steel.

However, Nb plays a vital role in retarding recrystallisation and achieving grain refinement during TMCR and from that aspect, it is difficult to substitute Nb in HSLA steels. Therefore, reheating should be carried out at a temperature (as 1225 ºC in the present study) sufficiently higher than the complete dissolution temperature of Nb(C, N), so that, Nb(C, N) completely dissolves not only at the dendrite-centre regions, but also at the interdendritic regions, and an uniform grain structure can be achieved everywhere. However, a high reheating temperature requires additional energy consumption as it can increase the average grain size, which requires higher deformation during rolling to achieve the required fine grain structure in the final product. Therefore, all the above factors need to be considered at the time of

designing the composition and processing schedule for a steel grade. A lower reheat temperature could be used (along with Ti additions) to limit the amount of bimodality (e.g. slab 3-1150) whilst maintaining fine average grain size (better for final properties).

8.7 Future Work

The present investigation has identified that the direct observation and quantification of microalloy-precipitates (which is laborious and time-consuming) may not be essential to determine the extent of Nb segregation in steel. EDS and / or WDS analysis (with WDS being more sensitive than EDS in picking up local composition), attached to an SEM can be used to determine the local compositions (specifically the Nb-levels) at the solute-rich (interdendritic) and solute-lean (dendrite-core) regions and those compositions can then be used with thermodynamic software to predict the stability of the precipitates (mole-fraction or mass-fraction of precipitates) at those regions. From the local precipitate stabilities at interdendritic and dendrite-centre regions the bimodality level at a particular reheating temperature can be predicted. However, the determination of local compositions requires specimen preparation (polishing + lightly etching) and compositional analysis in SEM. Nb segregation is the key factor behind the formation of bimodality, through the development of an inhomogeneous precipitate distribution and by creating a local difference in precipitate stability. Therefore, it may be more useful industrially to avoid detailed experimental studies and to accurately predict the partitioning of Nb during solidification between interdendritic and dendrite-centre regions, from the overall steel composition.

As a first step for the prediction of segregation levels a simplistic approach can be taken based on the assumption that approximately half of the total solid (f_s=0.5) has already been formed as δ-ferrite phase, during solidification is taking place at the quarter-thickness position of the slab. Therefore, using the following (Scheil) equation (as discussed in **section 1.2.2**) the Nb level within the solidifying liquid (C_L) can be determined based on the equilibrium partition ratio, k_p = 0.23, for Nb.

$$C_L = C_0(1 - f_S)^{k_p - 1} \quad \text{..... eqn. 8.6.1}$$

The Scheil equation can predict the Nb-level within the liquid phase (~ 0.08 wt% for slab 1, 0.046 wt% for slab 2 and 0.034 wt% for slab 3), and within the solid phase (~ 0.02 wt% for slab 1, 0.011 wt% for slab 2 and 0.008 wt% for slab 3) at f_S = 0.5, considering the overall Nb content (C_0) in the steel (0.045 wt% for slab 1, 0.027 wt% for slab 2 and 0.020 wt% for slab 3). The liquid is expected to form the interdendritic regions and the solid the dendrite-centre regions, and the predicted values at those regions, are not very far from the experimentally measured values (at interdendritic regions ~ 0.075 wt% for slab 1, 0.050 wt% for slab 2 and 0.040 wt% for slab 3 and at dendrite-centre regions ~ 0.027 wt% for slab 1, 0.020 wt% for slab 2 and 0.016 wt% for slab 3). Also the predicted values lie within the Nb levels reported by Couch [Couch 2001] at interdendritic and dendrite-centre regions for slab 1 steel.

However, a more sophisticated analysis system (such as EPMA or optical emission spectroscopy), which is more sensitive in picking up the segregation levels (compared to EDS or WDS), could be used for more accurate determination of local compositions. The current prediction is also based on simple assumptions. Therefore, more study and calculations are certainly required to understand (i) the solidification

sequence at various depth within the slabs, (ii) the formation and structure of dendrites, (iii) the volume fraction of solidification and (iv) the corresponding segregation of elements, to finally achieve a more accurate and reliable prediction. Besides Nb, the effect of segregation of other elements, particularly Ti, also needs to be considered in greater detail.

Finally it needs to be remembered that reheating is only an intermediate processing stage and what matters is the bimodality in final rolled product. During commercial rolling the bimodality developed in reheated steel can remain unchanged or can become more or less severe. Therefore, the effect of deformation on grain size bimodality needs to be studied within an originally segregated structure, this is considered in the next chapter.

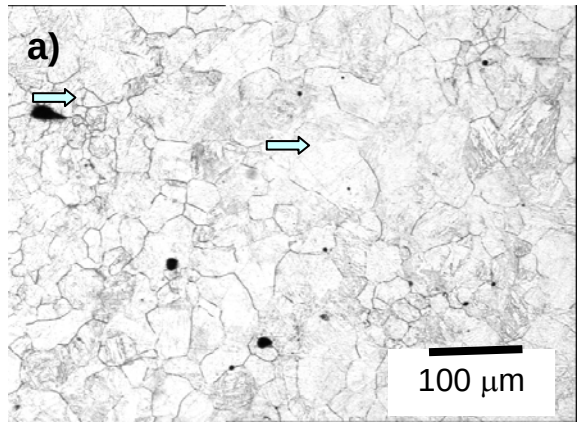

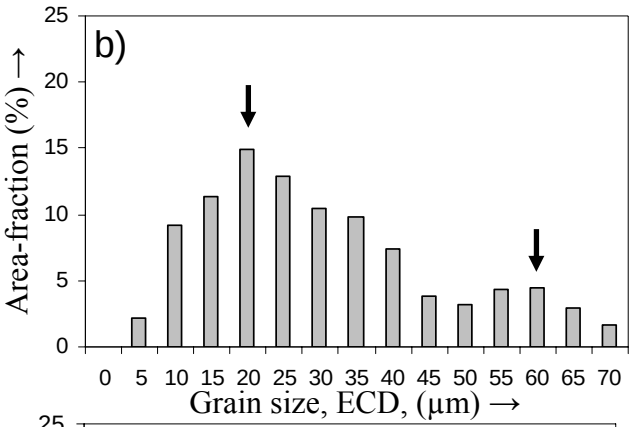

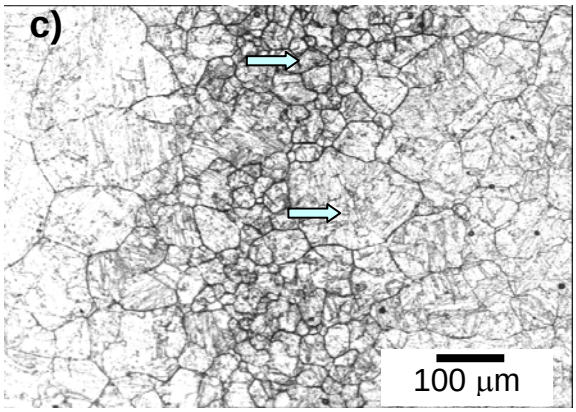

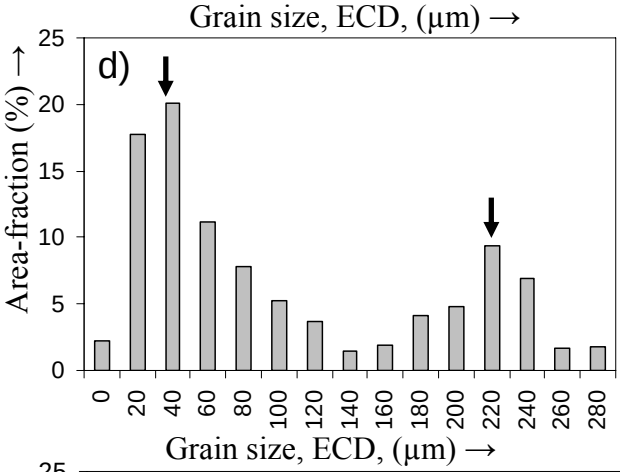

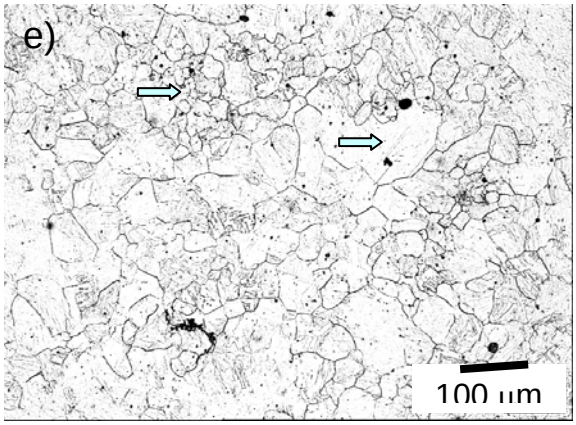

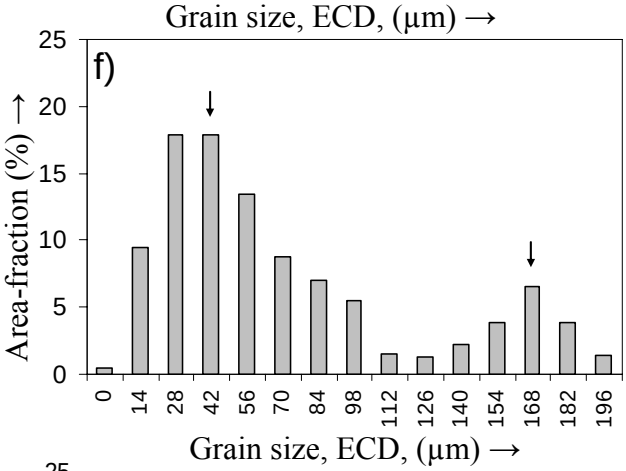

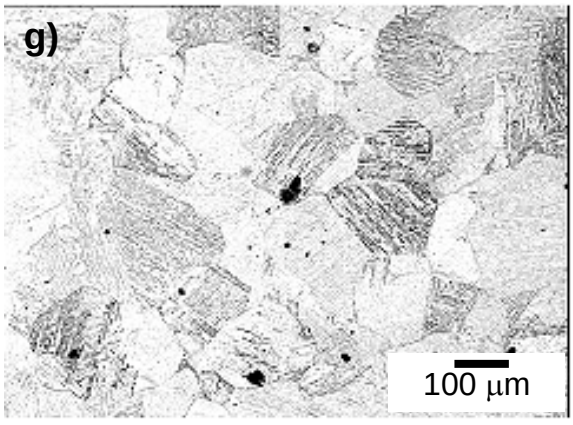

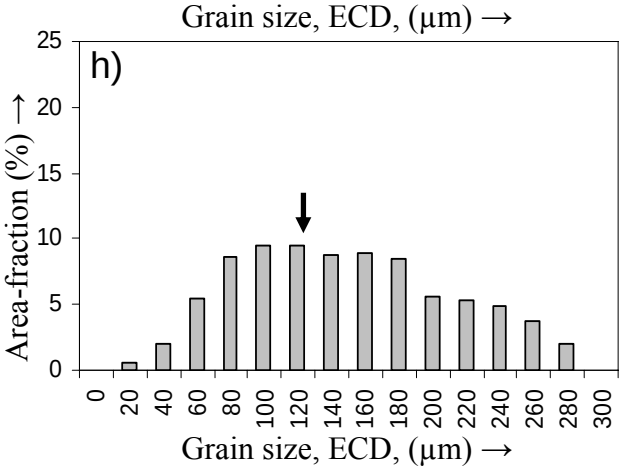

(**caption in next page)

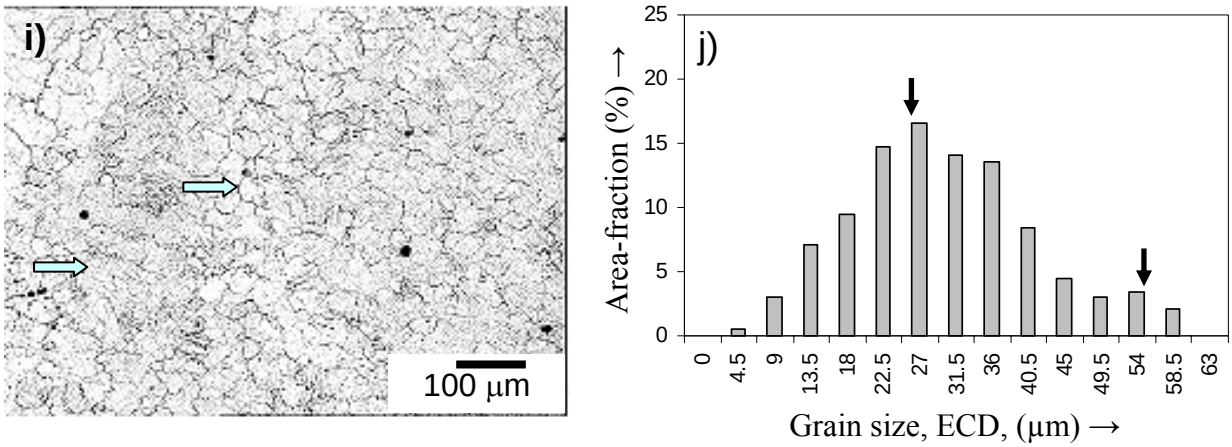

Fig. 8.1: Prior austenite grain structure in (a) slab 1-1075, (c) slab 1-1150 and (e) slab 2-1150 sample showing coarse and fine grain regions (arrowed), (b), (d) and (f) are the grain size distribution plots for (a), (c) and (e), respectively, and showing bimodality (peaks indicated by arrows), (g) uniform coarse grain structure from slab 1-1225 sample, (h) grain size distribution for (g) showing the unimodal nature, (i) grain structure in slab 3-1150 sample and (j) its grain size distribution plot showing slight bimodality (peaks indicated by arrows).

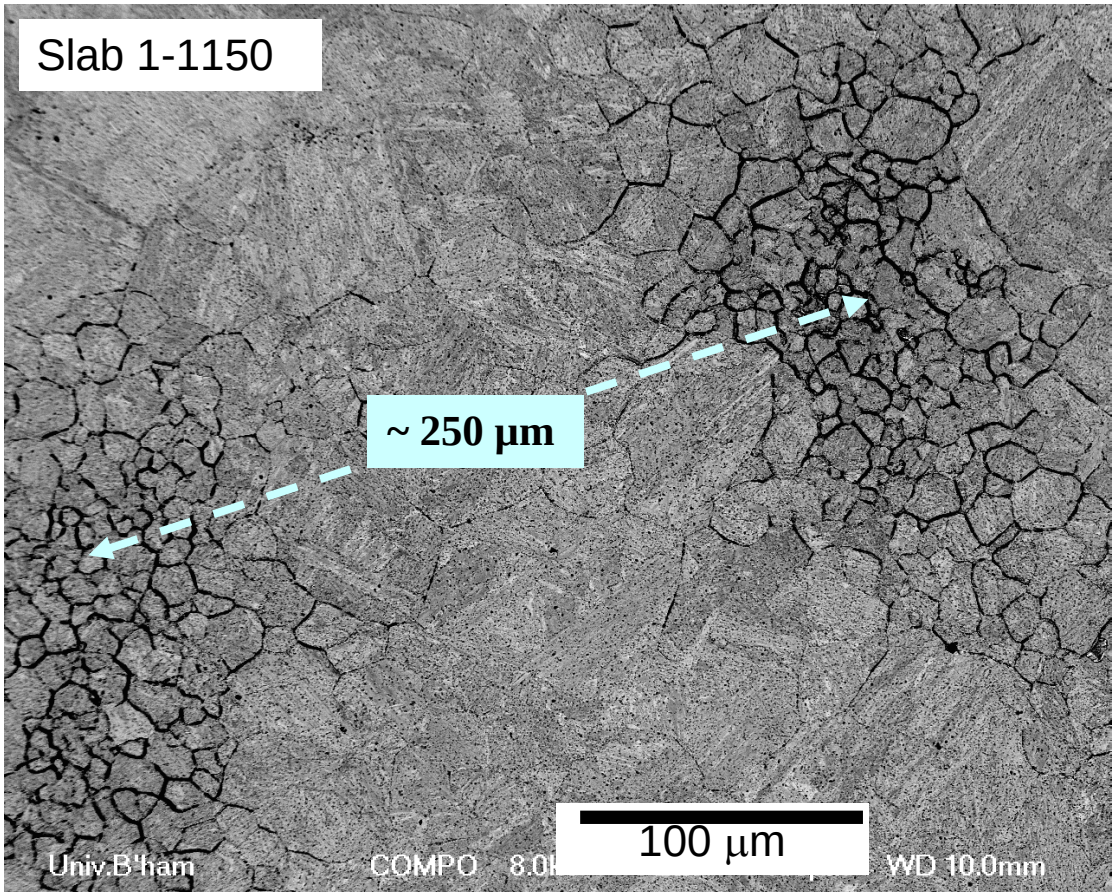

Fig. 8.2: Centre to centre distance between the two neighbouring fine grain regions ~ 250 µm in slab 1-1150 sample with bimodal grain structure.

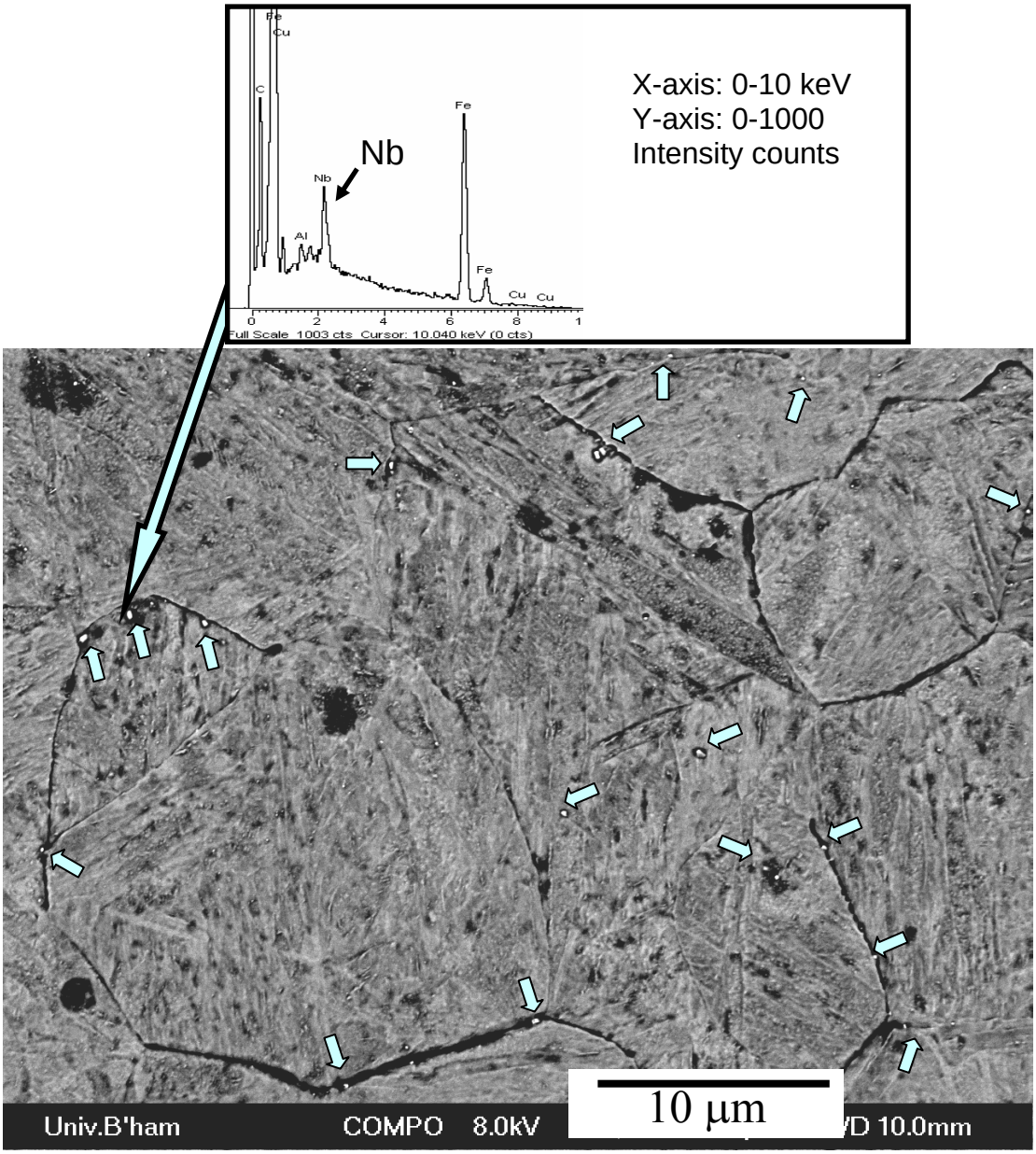

Fig. 8.3: BSE image and the EDS analysis showing Nb-rich precipitates (appearing bright and arrowed) at the austenite grain boundaries (few precipitates were observed within austenite grains).

Table 8.1: PHR and PGSR values for the reheated samples with different levels of bimodality. All samples are from the quarter thickness position.

Bimodality Level	Sample ID	PHR	PGSR (μm)
Reheated samples			
0	slab 1/ 2/ 3-1225	0	0
1	slab 3-1150	0.2	27
1	slab 3-1075	0.16	40
2	slab 1-1075	0.3	50
2	slab 2-1075	0.31	55
3	slab 2-1150	0.36	126
3	slab 3-1180	0.38	210
4	slab 1-1150	0.46	180

* PHR: Peak height ratio; PGSR: Peak grain size range.

Table 8.2: Area density ($\times 10^4$ number / mm^2), of Nb-rich precipitates, AlN particles and the total particle density (density of Nb-rich precipitates + AlN particles) at the precipitate-rich (interdendritic) and precipitate-poor (dendrite-centre) regions of the as-cast and reheated samples (reheating temperatures: 1075 ºC, 1150 ºC, and 1225 ºC) taken from the quarter-thickness position of slab 1 and slab 3.

Sample location	As-cast			Reheated								
				1075 ºC			1150 ºC			1225 ºC		
	Nb(C, N)	AlN	**Total**	Nb(C, N)	AlN	**Total**	Nb(C, N)	AlN	**Total**	Nb(C, N)	AlN	**Total**
Slab 1-precipitate-rich	60	4	**64**	16	2	**18**	5.5	0.5	**6**	0.2	0	**0.2**
Slab 1- precipitate-poor	12	4	**16**	4	2	**6**	0	0	**0**	0	0	**0**
Slab 3- precipitate-rich	30	5	**35**	10	2	**12**	6	0.1	**6.1**	0.3	0	**0.3**
Slab 3- precipitate-poor	8	4	**12**	5	0.5	**5.5**	4	0	**4**	0	0	0

Table 8.3: Average size of microalloy precipitates in as-cast and reheated samples (reheated to 1075 ºC, 1150 ºC and 1225 ºC) of slab 1 and slab 3.

	As-Cast	Reheated		
		1075 ºC	1150 ºC	1225 ºC
Slab 1	76	92	116	149
Slab 3	82	93	106	141

Table 8.4: Average limiting grain size (D) values calculated at interdendritic (D_I) and dendrite centre (D_C) regions for the reheated samples of slab 1 and slab 3.

Slab No.	Reheating temperature	(D_I) Interdendritic region (μm)		(D_C) Dendrite centre region (μm)	
		Predicted volume fraction	Measured volume fraction	Predicted volume fraction	Measured volume fraction
Slab 1	1075 °C	21	20	61	51
Slab 1	1150 °C	72	52	∝	∝
Slab 1	1225 °C	∝	∝	∝	∝
Slab 3	1075 °C	38	29	77	60
Slab 3	1150 °C	49	45	82	65
Slab 3	1180 °C	100	90	∝	∝
Slab 3	1225 °C	∝	∝	∝	∝

**∝: Infinity, i.e. very large size until impingement.

9. Effect of deformation on bimodality

Following reheating HSLA steel slabs are subjected to thermo-mechanical controlled rolling (TMCR), **Fig. 1.1.2**. TMCR not only refines the coarse austenite grains by combined deformation and recrystallisation, but also generates a high density of crystalline defects, which can act as nucleation sites for ferrite grains during austenite to ferrite transformation. The defects can act to increase diffusion rates accelerating any diffusion controlled process. Hence, a fine ferrite grain structure can be achieved in the final rolled plate (**section 1.5**). As discussed in **chapter 6** any bimodality in ferrite grain structure can affect the impact energy and cleavage fracture toughness of the steel by generating a high degree of scatter in toughness levels. In the present study (**chapter 7**), grain size bimodality has not been found within the as-cast slabs. Bimodality appeared upon reheating to certain temperatures (for example, 1150 ºC for slab 1); however, reheating to a higher temperature (~ 1225 ºC) removed the grain size bimodality (**chapter 8**). Commercial reheating is usually carried out within 1150 ºC to 1250 ºC for HSLA steels [Tither 1992]. Therefore, the starting austenite grain structure can either be unimodal or bimodal. The starting grain structure will have an effect on the grain sizes during and after rolling. If the steel composition and the applied deformation strain is uniform everywhere (i.e. completely homogenised steel is uniformly deformed) then the rolling deformation and subsequent recrystallisation will reduce the grain sizes by the same proportion everywhere [Sellars 1979, 1980, 1985]. However, a coarser grain in the reheated slab will remain coarser in the plate than a finer grain, although the sizes of all the grains will be reduced.

The microalloying elements (mainly Nb) were segregated within the as-cast slabs, **chapter 7**, and therefore, the composition was not the same everywhere. The

interdendritic regions (i.e. the solute-rich regions), are separated by ~ 200 - 250 μm distance (i.e. the interdendritic spacing, SDAS), hence, Nb atoms would need to diffuse over a distance of approximately 100 - 150 μm to reach the dendrite centres (solute-poor region) in order to completely remove segregation. Microalloying elements diffuse slowly (**Fig. 1.3.2)** and the diffusion times predicted from the diffusivity of Nb, **Fig. 9.1**, show that for Nb atoms to diffuse 100 μm requires 2-3 days of continuous heating (**Fig. 9.1 b**) at 1225 ºC. Such extended heating is uneconomical commercially. It has been shown, **section 8.2.2**, that reheating a slab 1 sample for 1 hour at 1225 ºC does not completely dissolve all the precipitates in the solute-rich regions, and with a predicted diffusion distance of 12 μm for Nb, the segregated Nb levels are expected to remain. Starting with a uniform grain structure in reheated steel (as in slab 1-1225) the presence of segregation may have an influence on the grain sizes in the rolled steel.

Grain size bimodality has been reported in the commercially rolled HSLA steel plates [Wu 2004a, Bhattacharjee 2003, Bodin 1982] but it is not necessarily clear whether this is solely due to the bimodality that originated during reheating or could be altered by deformation. In the present investigation the ferrite grain structure and the precipitates have been studied on a similar (TMCR-1) plate. It is important to understand the effect of rolling deformation on the grain size bimodality in a segregated structure, and the present investigation aims to do that. To achieve that objective two studies have been carried out: (i) mathematical calculations on the precipitation-recrystallisation interaction in a segregated structure, with initially bimodal or unimodal austenite grain size distributions and (ii) plane-strain compression studies (one-hit test) in Gleeble 3500 to verify some of the theoretical calculations. Within this project it was not possible to simulate commercial rolling deformation, however, the influence of deformation above and below

recrystallisation stop temperatures within the solute-rich and solute-poor regions (in a segregated structure) has been studied.

9.1 Microstructure and precipitates in the TMCR 1 plate

In terms of chemical composition, TMCR 1 steel is similar to slab 1 (particularly similar Nb levels), **Table 4.1**, with the only exception being in Ti levels (twice as much Ti, in TMCR 1, 0.004 wt %, as in slab 1, 0.002 wt %). Slab 1 showed severe bimodality upon reheating to 1150 ºC. Thermo-Calc software prediction of precipitate stability at interdendritic (pearlite) and dendrite centre (ferrite) regions of as-cast slabs slab 1, **Fig. 8.15 a**, indicates that bimodality can be expected upon reheating to 1150-1200 ºC temperatures. Slab 3 steel contained much more Ti (0.009 wt % Ti, beside 0.020 wt % Nb) than slab 1, but still showed bimodality upon reheating to 1180 ºC. Therefore, bimodal austenite grain structures could be expected in the TMCR 1 steel after reheating to temperatures between 1150 to 1200 ºC. The microstructures of TMCR 1 plate (reheating temperature varied between 1150 ºC to 1200 ºC) at different locations have been discussed in **section 6.2.4** in detail. The microstructures are composed, **Fig. 6.22**, of patches of coarse ferrite grains in a banded fine ferrite and pearlite matrix, and as expected with a bimodal ferrite grain size distribution.

On the polished and etched surface of TMCR 1 plate spherical (10 - 130 nm diameter), cubic (100 - 250 nm side length), needle (10 × 100 nm) and rounded (not perfectly spherical but oval, longest side between 100 and 300 nm) shaped Nb-rich carbonitride precipitates (also containing Ti and V in some cases) have been observed (**Fig. 9.2**). These were found to be distributed inhomogeneously, as shown in **Fig. 9.3**, with higher precipitate number densities in pearlitic or in fine ferritic grain bands, compared to the coarse grained ferrite bands. Spherical precipitates with diameters less

than 10 nm have been reported [Gladman 1997, Ubhi 1989, Morales 2003, Gunduz 2005] in TMCR plates, particularly those microalloyed with V (**section 1.5.1**), however, the observation of such fine-precipitates was beyond the resolution limit of the Jeol 7000 SEM used in the present study and would have required TEM. Although more detailed study and quantification of finer precipitates in the fine- and coarse-grained bands in the rolled plate, coupled with the determination of the local composition levels at both regions would be beneficial, the larger nanometre-sized particles indicate that segregation persists in TMCR-1, **Fig. 9.3 (a)**. In addition to the spatial segregation of nanometre-sized microalloy precipitates, micron-sized (up to 50 μm in length and 1-5 μm in thickness) deposits of microalloying elements (Nb-rich complex carbonitrides also containing Ti and V) were also detected at the centre of the TMCR-1 plate, **Fig. 9.4**. These latter, large particles are consistent with remnants of centre-line microalloying element macro-segregation, **section 7.4.2**, from the as-cast slabs, **Fig. 7.22**. The coarseness of the centre-line particles (closer to eutectic than precipitation in the solid-state) meant that the thermo-mechanical exposure experienced by TMCR-1 was insufficient for full dissolution. Re-heating trials on slab 1 at 1150 ºC and 1200 ºC for 1 hr also revealed retention of significant amounts of coarse particles, **Fig. 9.5**. Hence, segregation can prevent microalloying elements dissolving completely even at temperatures higher than the equilibrium dissolution temperature of steel (~ 1155 ºC for slab 1 steel, as predicted by Thermo-Calc, **Fig. 8.13**), as discussed by Palmiere et al. [Palmiere 1994]. Therefore, beside the starting austenite grain structure segregation may also play an important role in deciding the grain size bimodality in the TMCR plate.

9.2 Mathematical calculations based on Dutta-Sellars model

As discussed earlier the initial austenite grain sizes and the local compositions (segregation) can influence the effect of deformation on bimodality and final grain sizes through their role on the kinetics of recrystallisation, kinetics of strain-induced precipitation and hence, on the precipitation-recrystallisation interaction (**section 1.5.2**). **Section 1.5.3** discusses how the Dutta-Sellars model [Dutta 1987] has been widely used to study the interaction between strain-induced Nb(C, N) precipitation and austenite recrystallisation in Nb-microalloyed steels and that most of the other models in the literature are based on the original Dutta-Sellars approach [Rose 1996]. Researchers have proposed three-stages of recrystallisation-precipitation interaction in Nb-containing HSLA steels using a RPTT (recrystallisation – precipitation – time - temperature) diagram, **Fig. 9.6** and **Fig. 1.5.9 (a)**, where both recrystallisation and precipitation kinetic curves are superimposed [Hansen 1980, Speer 1987, Kwon 1991, Palmiere 1996]. The RPTT-diagram, **Fig. 9.6**, shows that, above the precipitate dissolution temperature, T_{SOL}, precipitation is thermodynamically impossible and therefore, recrystallisation kinetics are unaffected by precipitation. After austenitisation above T_{SOL}, when specimens are deformed and held isothermally between T_{SOL} and T' temperatures (region-I in **Fig. 9.6**), recrystallisation kinetics remain unaffected by precipitation, as recrystallisation is completed before precipitation starts (no interaction). In regime-II (between T' to T_R) recrystallisation precedes precipitation, but precipitation sets in before recrystallisation is complete. As a result, after a certain fraction of recrystallisation, further recrystallisation gets delayed due to the retardation from the strain-induced Nb(C, N) precipitation. Region-II can be termed as the partial recrystallisation region [Palmiere 1996]. In region-III (below T_R) precipitation starts before the onset of recrystallisation and that retards both the start and the finish of recrystallisation. Therefore, in **Fig. 9.6**, T_R can be considered as the recrystallisation stop temperature, RST (although, a sharp RST at one

temperature is a theoretical concept, **section 1.5.1**). Dutta and Sellars [Dutta 1987] suggested equations to predict recrystallisation and precipitation times (**eqn. 1.5.2** and **eqn. 1.5.5**) after deformation and isothermal holding of Nb-microalloyed steels at different temperatures (**section 1.5.3**). Superimposition of those recrystallisation and precipitation kinetic curves in time-temperature space can indicate the RST, **Fig. 1.5.9 (a)**.

In the present study the composition, precipitation and segregation levels for slab 1 steel have been used in the Dutta-Sellars equations (**eqn. 1.5.2** and **eqn. 1.5.5**) to predict the precipitation and recrystallisation kinetics after reheating to 1225 ºC and 1150 ºC (for 1 hr). 1225 ºC and 1150 ºC have been selected as reheating temperatures are close to the industrial reheating temperatures and offer two extremes of bimodality in the starting microstructure (with similar levels of segregation), unimodal austenite grains at 1225 ºC and severely bimodal grains at 1150 ºC. A true strain, $\varepsilon = 0.3$ and strain rate, $\dot{\varepsilon} = 10 / s$ have been used for the calculations as those values are usual in commercial practice and have been used in several previous studies regarding precipitation-recrystallisation interaction [Kwon 1991, Palmiere 1996, Dutta 2001]. Thay also satisfy the range where the Dutta-Sellars equations [Dutta 1987] were verified (**section 1.5.3**).

9.2.1 Precipitation-recystallisation interaction after 1225 ºC reheating

A 1 hr reheating time is insufficient to remove segregation even at 1225 ºC, which implies that the initial segregation levels for Nb, calculated at the interdendritic (0.070 wt % Nb) and dendrite-centre regions (0.025 wt %) of as-cast slab 1, can remain (almost) unchanged even after reheating to 1225 ºC (for 1 hr). However, the precipitates dissolved (almost) completely and a uniform grain structure was achieved after 1225 ºC reheating. As the dissolved [Nb] level in austenite controls the recystallisation and precipitation

kinetics (**section 1.5.3**), the time for 5 % precipitation and 5 % and 85 % recrystallisation will be different in the different regions (dendrite-centre and interdendritic). As the austenite grain size distribution was unimodal after 1225 ºC reheating, the average grain size (D_0~120 μm) in slab 1-1225 sample is appropriate to quantify the initial grain structure, and hence was used in **eqn. 1.5.5** for both the solute-rich and solute-poor regions. Therefore, the difference in Nb levels is the only factor that can create a difference in grain size between the different regions (dendritic and interdendritic) after deformation.

Fig. 9.7 shows the time required for 5 % precipitation (P_S) and 5 % and 85 % recrystallisation (R_S and R_f, respectively) to take place in the solute-rich and solute-poor regions after reheating to 1225 ºC, followed by deformation and isothermal holding at different temperatures. According to **Fig. 9.7**, above ~ 1100 ºC, precipitation is not predicted to start in either region within the commercial inter-pass delay times (~ 10 s [Dutta 2001]) and recrystallisation is predicted to be complete everywhere at a much shorter time (within 1 s), without any interaction with precipitation. Therefore, an initial unimodal grain structure is expected to remain unimodal after deformation in this region. Even below 1100 ºC, down to ~ 1050 ºC recrystallisation will reach completion everywhere within 2 sec, however, precipitation can start within the solute-rich region after holding for 2 to 10 s. The slightly slower recrystallisation kinetics in the solute-rich region, compared to the solute-poor region, are due to higher solute drag, coming from the higher dissolved [Nb] level at the solute-rich region. Interaction between strain-induced Nb(C,N) precipitation and austenite recrystallisation will start below ~ 1050 ºC initially in the solute-rich region and afterwards in the solute-poor region.

Using the same concept as discussed earlier (**Fig. 9.6** and **Fig. 1.5.9 a**) the recrystallisation stop temperature (RST) can be determined separately for the solute-rich

(as 1010 ºC) and solute-poor (930 ºC) regions from **Fig. 9.7**. Therefore, in the temperature range 930 ºC to 1010 ºC, the onset of recrystallisation will be retarded in the solute-rich region due to strain-induced precipitation, whilst, in the solute-poor region recrystallisation can proceed uninterruptedly (no interaction with precipitation) and can reach completion. This indicates that successive deformation in that temperature range may create a grain size difference between the originally solute-rich regions (coarse-unrecrystallised grains) and solute-poor regions (fine-recrystallised grains). Palmiere et al. [Palmiere 1996] previously reported that the partial recrystallisation regions in Nb microalloyed steels (0.02-0.09 wt % Nb) spread over a 30 - 70 ºC range between 900-1030 ºC, depending on the actual Nb level in steel, **section 1.5.2**. They recommended avoiding deformation within that temperature range, as partial recrystallisation can result in 'duplex' grain sizes (i.e. mixed coarse-unrecrystallised and fine-recrystallised grains), however, the effect of microalloying element segregation on the partial recrystallisation region, banding and the size distribution of grain sizes were not been discussed. The RPTT diagram shown in **Fig. 9.8** is calculated using the same conditions as used in **Fig. 9.7**, but with a uniform average Nb level (0.046 wt %) everywhere (i.e. no segregation). Comparison between **Fig. 9.7** and **Fig. 9.8** indicates that, in the presence of segregation, the range of partial recrystallisation (930 ºC to 1050 ºC) is much higher than that in the absence of segregation (990 - 1030 ºC) as in the segregated structure separate partial recrystallisation bands exist for the solute-rich region and for the solute-poor region. The RST, in absence of segregation (990 ºC), **Fig. 9.8**, is in between the RST in the solute-rich region (1010 ºC) and in the solute-poor region (930 ºC), **Fig. 9.7**.

In summary **Fig. 9.7** suggests that even starting with a uniform grain structure (after reheating) bimodality may appear during deformation within a certain temperature range (approximately ~ 900 - 1050 ºC), with fine recrystallised grains forming in the

solute-poor regions and coarse-non-recrystallised grains remaining in the solute-rich regions. The nature of the bimodal structure would be bands of fine grains and coarse grains reflecting the interdendritic segregation bands seen in the as-cast slab. During the commercial double hold TMCR schedule, as used for processing of TMCR-1 plate, deformation in that partial recrystallisation region is avoided, as far as possible, by applying the second hold time (during which temperature drops from about 1000 ºC to below 800 ºC), however, the larger temperature range for partial recrystallisation in a segregated structure may mean that this region is not always avoided, as predictions of this region may be inaccurate using average composition.

9.2.2 Precipitation-recystallisation interaction after 1150 ºC reheating

After reheating slab 1 to 1150 ºC undissolved precipitates, especially in the interdendritic (segregated) regions, are ineffective in retarding recrystallisation during deformation as those precipitates are randomly distributed on the matrix and not precipitated on the defects generated due to deformation [Hansen 1980]. However, recrystallisation will be retarded by the fresh (strain-induced) precipitates (preferentially precipitated on dislocations and retarding their mobility), which will come from the dissolved [Nb] in austenite, **section 1.5.3**. Thermo-Calc predictions based on the segregated initial Nb levels measured in the as-cast slab 1 (0.070 wt % Nb in the interdendritic and 0.025 wt % Nb in the dendrite-centre regions, **section 7.3.2**) can be used to obtain (approximately) the dissolved [Nb] content in austenite (0.063 wt % in interdendritic region and 0.025 wt % in dendrite-centre region) at 1150 ºC. This approach is reasonable as the volume fraction of Nb-rich precipitates predicted by Thermo-Calc in the interdendritic (0.042 %) and dendrite-centre regions (negligible) of slab 1-1150 sample were similar to the experimentally observed values (interdendritic: 0.050 %,

dendrite-centre: negligible) in the same regions (refer **section 8.5**). The average grain sizes (ECD) for the fine-grained (~ 40 μm) and for the coarse-grained (~ 220 μm) populations in the bimodal austenite-grain size distribution for slab 1-1150 sample (level-4 bimodality) were used as D_0 (initial grain sizes) along with the Thermo-Calc predicted [Nb] levels in **eqn. 1.5.2** and **eqn. 1.5.5** to calculate the RPTT diagram for the 1150 ºC reheated, deformed (strain, ε = 0.3 and strain rate, $\dot{\varepsilon}$ = 10 / s) and isothermally held sample, **Fig. 9.9**.

Fig. 9.9 shows that the recrystallisation kinetics in the solute-poor (dendrite-centre) region are slower compared to those the solute-rich (interdendritic) region, in spite of the higher solute-drag in the solute-rich region due to the higher [Nb] level. This is because of the abnormally large grain sizes in the solute-poor region, which provide far less grain boundary area for the recrystallised strain-free grains to nucleate on, compared to the solute-rich region, where the grain sizes were much smaller. Above 1100 ºC, strain-induced precipitation is not predicted to start and recrystallisation is completed very quickly (within 1 s) everywhere, and therefore, the bimodal starting grain structure should remain bimodal (although, the grain sizes will become smaller) after the standard inter-pass delay time (~ 10 s). The interaction between precipitation and recrystallisation starts at ~ 990 ºC in the solute-rich region after holding for ~ 1 s. In solute-poor regions, however, interaction does not commence until 20 s at ~ 980 ºC. Therefore, **Fig. 9.9** suggests that, if deformation occurs between 980 ºC to 1005 ºC with a 10 s delay after the deformation pass, then recrystallisation would not be complete in the solute-poor regions, although it would be in the solute-rich regions. However, below 990 ºC interaction starts in the solute-rich region and recrystallisation is not predicted to be complete within 10 s. Hence, the interaction is more complicated in the 1150 ºC reheated sample, however, the delay in recrystallisation kinetics in the solute-poor region can enhance grain size

bimodality in a narrow temperature range (~ 990 ºC - 1000 ºC) by preventing the abnormally large and deformed austenite grains in the solute-poor region to recrystallise quickly.

The recrystallisation stop temperature (RST) for the solute-rich region (~ 960 ºC) is close to that for the solute-poor region (~ 952 ºC). Also the partial recrystallisation temperature band for the solute-rich region (~ 960 ºC to 1000 ºC) is similar to that for the solute-poor region (~ 950 ºC to 980 ºC). Therefore, not much difference is expected in the recrystallisation behaviour between the solute-rich and solute-poor regions and overall, the initial bimodal-microstructure is likely to remain bimodal after deformation, without much change.

At temperatures below the complete recrystallisation stop temperatures (i.e. below 930 ºC for the 1225 ºC reheated sample and 950 ºC for the 1150 ºC reheated sample) recrystallisation will be retarded everywhere (both in the solute-rich and solute-poor regions) in the deformed samples, and further deformation should not significantly change the level of bimodality. If the deformation occurs when all the Nb is present in precipitate form (deformation in completely precipitated structure) then the level of bimodality is also not expected to change, as pre-existing precipitates are ineffective in retarding recrystallisation [Hansen 1980] and the final grain sizes will be proportional to the applied strain (ε) and the initial grain size (D_0), **eqn. 1.5.4** [Sellars 1980]. The various possibilities discussed in this section are summarised in **Table 9.1**.

9.3 Plane-strain compression studies using a Gleeble 3500

As discussed in **section 9.2** and **Table 9.1**, deformation in the different temperature regions is predicted to have different effects on grain size bimodality. To

verify some of the predictions experimentally, plane-strain compression tests have been carried out following the schedule shown in **Fig. 9.10**.

9.3.1 Deformation at temperatures higher than the precipitation start temperature (within the interpass time)

After reheating the slab 1 steel to 1225 ºC (unimodal structure) and 1150 ºC (bimodal structure), deformation above ~ 1100 ºC and 10 s hold (similar to the interpass delay time) is predicted not to change the bimodality level, as recrystallisation will be completed throughout the deformed sample within 1-2 s, i.e. before any strain-induced precipitation can occur (**Fig. 9.7** and **Fig. 9.9**).

Prolonged heating (for 1 hour) of the samples within the chamber of Gleeble 3500 can be problematic due to thermocouple failure and to avoid that the reheating schedule of the tested samples has been divided into two stages. Before the compression tests samples from the quarter-thickness position of slab 1 were reheated in a furnace (first stage of reheating) at 1225 ºC or 1150 ºC temperatures for 55 minutes, and water-quenched, **Fig. 9.10**. In the Gleeble, the samples were again reheated (at 20 ºC / sec heating rate) to the same temperature used during the first stage of reheating (second stage of reheating), and held for a further 5 minutes. Therefore, Gleeble specimens were reheated for 1 hr in total but in two stages. The austenite grain structures after the double reheating stage (and water-quenching) were found to be almost the same as for single stage reheating. For both slab 1-1225, and slab 1-1150 samples the difference in average grain sizes and largest grain sizes between single stage reheat and two-stage reheat were within ± 5 μm. The bimodality parameters for slab 1-1150 samples (single reheat) were PHR=0.43, PGSR=180 μm compared to PHR=0.46, PGSR=180 μm for two-stage reheat. Therefore, the starting austenite grain structures (1225 ºC and 1150 ºC reheated

structures) before Gleeble deformation were almost the same as those considered earlier (**section 9.2.1** and **9.2.2**). The same level of dissolution of precipitates is expected for both single stage and two stage reheating as the total time for reheating is the same. Water quenching in between two stage reheating schedule prevents any re-precipitation, and heating at a rate 20 ºC / sec for second stage reheating is unlikely to cause any re-precipitation as precipitation kinetics in un-deformed austenite is extremely sluggish (after complete dissolution of Nb-precipitates, precipitation start time is ~ 30 minutes at 900 ºC for 0.07 wt % C, 0.04 wt % Nb, 0.010 wt % N steel) [DeArdo 2003].

As shown in **Fig. 9.10** following reheating the plane-strain samples were cooled down (at a rate of 10 ºC / s) to 1110 ºC or 980 ºC, deformed immediately to a strain, ε = 0.3 and a strain rate, $\dot{\varepsilon}$, of 10 / s (as used for the theoretical calculation), held at the same temperature for 10 s before quenching under forced water (water sprayed on the samples from the nozzles). The heating rate, cooling rate, strain, strain rate and delay time values used in the present study are similar to those in commercial rolling and have been used in a number of previous deformation studies [Kwon 1991, Palmiere 1996, Dutta 2001]. As mentioned earlier, precipitation in deformed austenite is extremely sluggish [DeArdo 2003] and therefore, cooling at a rate of 10 ºC / sec to the deformation temperature is unlikely to cause any precipitation.

Fig. 9.11 (**a** and **b**) compares the cross sections of the 1225 ºC and 1150 ºC reheated and 1110 ºC deformed samples (termed as 1225-1110 and 1150-1110, respectively). The larger grain sizes after 1225 ºC reheating, compared to 1150 ºC reheating (shown in the undeformed regions of the samples), resulted in larger grain sizes in the deformed region of the 1225-1110 sample, compared to the 1150-1110 sample. Higher magnification inspection at the centre of the deformed region showed that the

grains are completely recrystallised after deformation and 10 s holding in both the 1225-1110 and 1150-1110 samples.

It can be seen from **Fig. 9.12** and **9.13** that the nature of the grain structure (unimodal or bimodal) remains unchanged by the deformation cycle for both the 1225-1110 and 1150-1110 samples. However, the grains become smaller in size (average grain size 49 μm in 1225-1110, and 22 μm in 1150-1110) compared to the reheated grains (average grain size 120 μm in slab 1-1225, and 38 μm in slab 1-1150) due to recrystallisation. The amount of grain refinement is similar to that predicted from **eqn. 1.5.4** (predicted values for the average grain sizes are 52 μm in 1225-1110, and 24 μm in 1150-1110 samples) considering complete recrystallisation in 1225-1110 and 1150-1110 samples. PHR (=0.41) in the deformed region of 1150-1110 sample, is also similar to the PHR (=0.43) in slab 1-1150 sample (originally reheated structure). Therefore, as expected from the theoretical calculations, deformation at temperatures above 1100 ºC resulted in no change in bimodality (initially bimodal structure remained bimodal and initially unimodal structure remained unimodal).

9.3.2 Deformation at temperatures where precipitation occurs within the interpass time (~ 10 s)

From **Fig. 9.7** and **Fig. 9.9** partially recrystallised microstructures are expected upon deformation and isothermal holding (10 s) of 1225 ºC reheated (slab 1) steel between 930 to 1040 ºC and 1150 ºC reheated (slab 1) steel between 960 ºC to 990 ºC. As partial recrystallisation can give rise to grain size 'duplexity' [Palmiere 1996], 980 ºC was selected as the deformation + hold temperature in the Gleeble experiments following reheating to 1225 ºC and 1150 ºC (samples termed as 1225-980 and 1150-980, respectively). As expected, both the samples show partially recrystallised austenite grain

structures, **Fig. 9.14 (a)** and **Fig. 9.15 (a)**, with fine-recrystallised grains lying between coarse-unrecrystallised (deformed) grains. The corresponding grain size distributions, **Fig. 9.14 (b)** and **Fig. 9.15 (b),** show severe bimodality (PHR=0.46 for 1225-980 and PHR=0.53 for 1150-980 sample).

Therefore, partial recrystallisation after deformation can turn an initially unimodal distribution of grain sizes in the reheated steel (PHR=0 after 1225 ºC reheating) into a severely bimodal distribution (PHR=0.46 for 1225-980 sample). Almost complete recrystallisation in the solute-poor region and retardation of recrystallisation in the solute-rich region (following 980 ºC deformation and 10 sec holding) are expected from **Fig. 9.7** and therefore, in the 1225-980 sample fine-recrystallised grains and coarse-unrecrystallised grains are expected to be present preferentially in the solute-poor and solute-rich region, respectively. To confirm the link between the coarse un-recrystallised grains and the solute-rich regions TEM investigation is required as the strain-induced precipitates are expected to be less than 10 nm in size and not resolvable using SEM. Austenite grain sizes in the 1150-980 sample showed a slightly higher bimodality (PHR=0.53) compared to the 1150 ºC reheated sample (0.46). Deformation at 980 ºC and isothermal holding for 10 s reduced the average grain sizes (62 μm in 1225-980 and 33 μm in 1150-980) compared to the as-reheated samples (120 μm in slab 1-1225, and 38 μm in slab 1-1150), however, not as much as observed upon complete recrystallisation (49 μm in 1225-1110, and 22 μm in 1150-1110).

9.4 Significance of deformation simulation for commercial rolling practice

Theoretical calculations and deformation simulation results indicate that bimodality can appear upon commercial rolling of HSLA steel in the temperature range between 930 - 1040 ºC (approximately), and that temperature range can depend on the

steel composition, reheating temperature, and the extent of segregation. The hold period used for commercial thermo-mechanical controlled rolling (TMCR) typically takes place between about 1050 °C and 800 °C to avoid any deformation in the partial recrystallisation region, which should mean that little bimodality is introduced during rolling for the steel composition studied in this work. Therefore, it is unlikely that the rolling deformation will have much effect on the grain size bimodality.

At the quarter-thickness position (12 mm depth) of TMCR-1 steel the average centre-to-centre distance between two neighbouring fine ferrite grain bands, in a direction normal to the bands, was found to be 46 μm (± 9 μm), which is approximately one fifth of the SDAS value for the slab 1 at this position, 211 μm (± 36 μm). The separation between fine-to-fine and coarse-to-coarse grain regions in the slab 1-1150 sample was similar to the SDAS. As discussed in **section 4.1** the total rolling reduction given in TMCR-1 steel was ~ 5 : 1. The above details indicate that the rolling deformation compressed the coarse and fine grain regions into parallel and alternate arrays to the same extent as the reduction ratio and therefore, the influence of cast structure and segregation has (almost) persisted through rolling deformation. Differences in grain size upon reheating, therefore, can be carried forward through the rolling stages and finally result in a bimodal distribution of ferrite grains in the final rolled plate. Hence, to avoid bimodality in rolled structures there is a need to control / eliminate bimodality in the reheated structure.

TMCR schedules involve rolling in different temperature regimes to different deformations (light or heavy). Rolling in the majority of TMCR schedules finishes within the single (austenite) phase region [Gladman 1997, Tither 1992]. In that situation any deformation within the partial recrystallisation temperature range (discussed in **section 9.3**), or even a non-uniform distribution of rolling stain may result in bimodality. Higher strength requirement steels are sometimes finish-rolled within the intercritical or two-

phase (austenite + ferrite) region [Gladman 1997, Tither 1992]. Intercritical rolling during austenite to ferrite transformation can generate bimodality in the resulting ferrite grain structure, as discussed in **section 1.5.5** [Bodin 2001, Hong 2002b]. In addition, rolling texture can allow some favourably oriented ferrite grains to grow and restrict the growth of the other ferrite grains and that can also generate bimodality [Petrov 2004]. However, these factors are mainly influenced by the rolling schedules followed and are not likely to be affected by the cast structure or the grain sizes after reheating. Hence, these are not included in the present study.

9.5 Future studies on the effect of rolling deformation on bimodality

The previous discussion indicates a need for a more detailed study on the strain-induced precipitates and precipitation-recrystallisation interaction (including observation of strain-induced precipitates using TEM), separately in the solute-rich and solute-poor regions to relate the effect of initial segregation and deformation on the development of bimodality. This will allow quantification of the precipitation rates and resulting precipitate structure effects on grain boundary movement. Deformation can provide additional fast-diffusion paths, as well as providing an increased number density of nucleation sites. The significance of this effect needs to be checked over a range of rolling temperatures and times. If all those factors are linked together, the effect of segregation can be incorporated in the precipitation-recrystallisation interaction models, such as the Dutta-Sellars model.

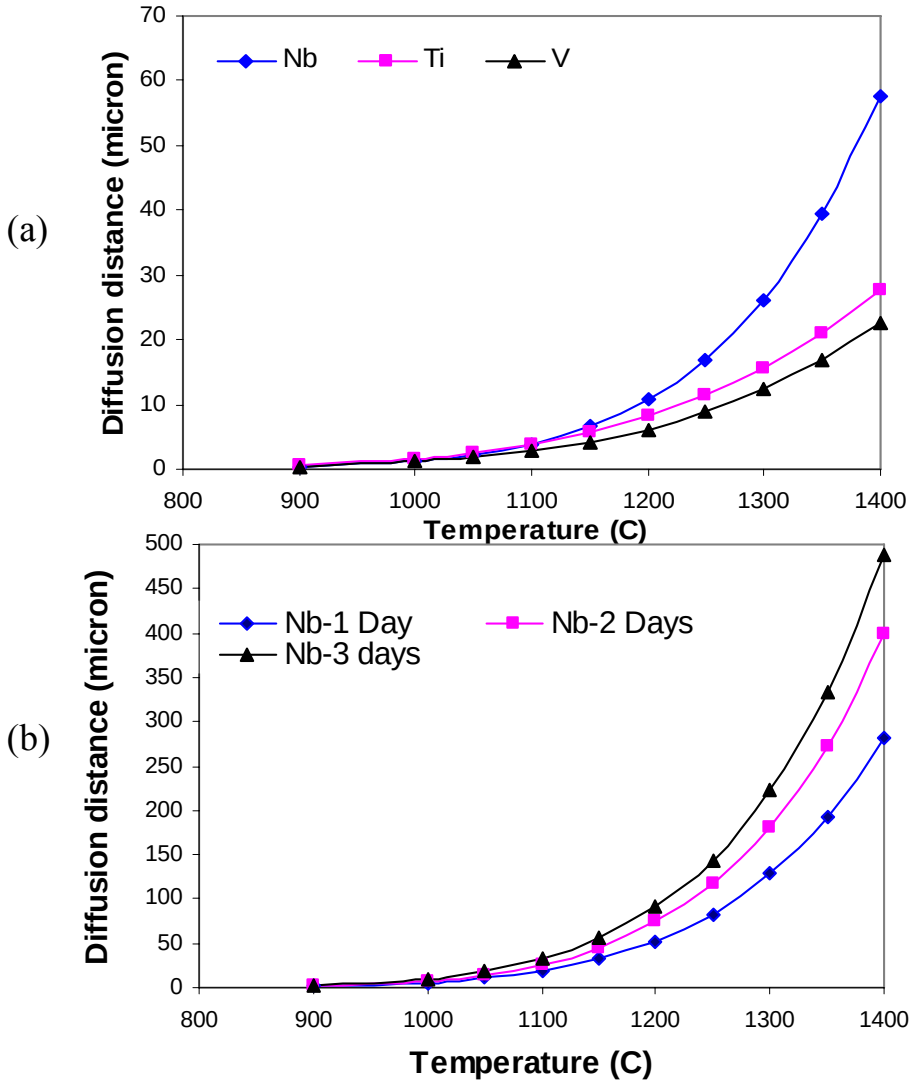

Fig. 9.1: (a) Diffusion distances of the microalloying elements at various reheating temperatures for 1 hr. time. (b) Diffusion distances of Nb at various reheating temperatures for 1 to 3 days time.

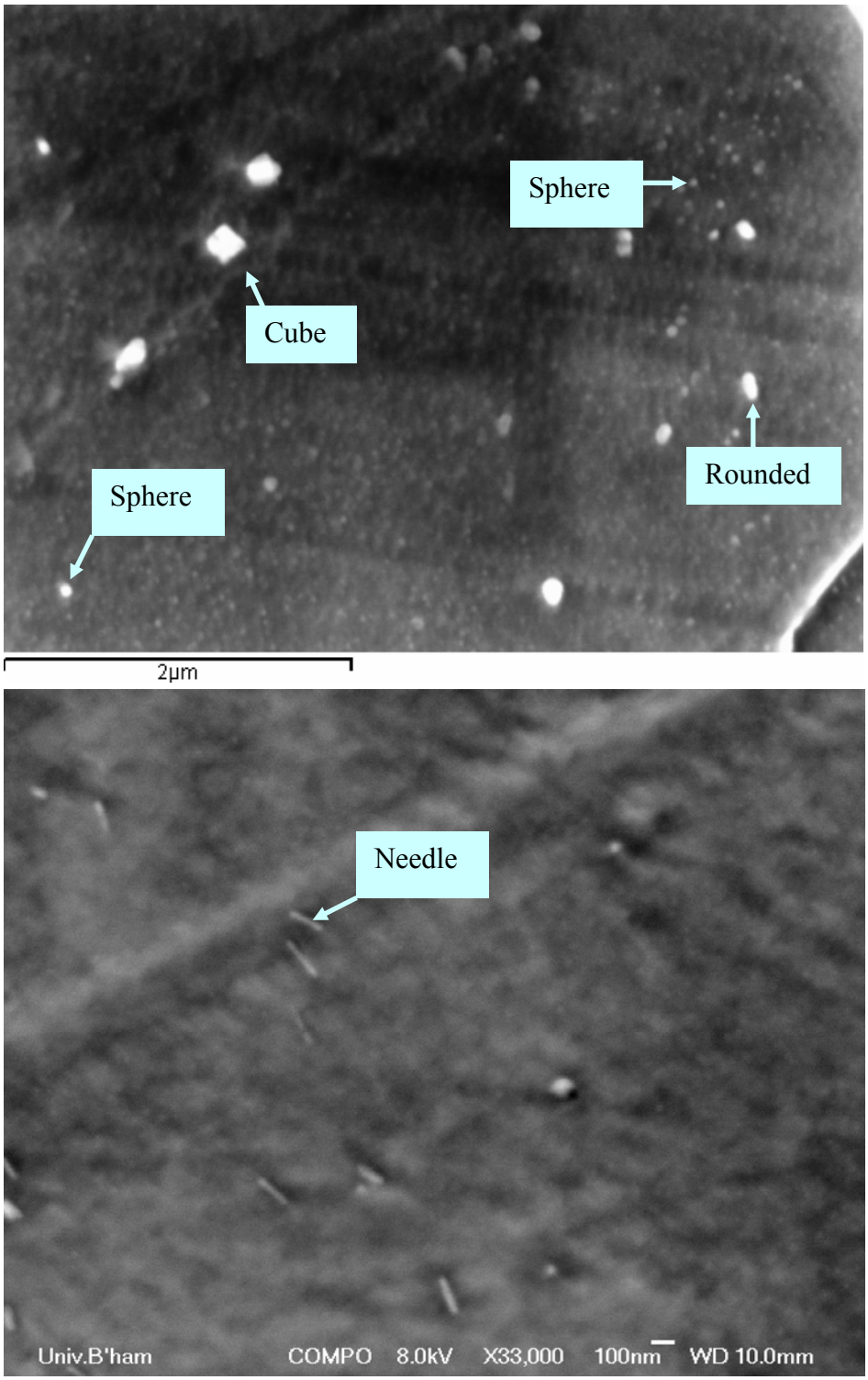

Fig. 9.2: (a and b) Different shapes of precipitates in TMCR-1 steel; (a) showing cubic, spherical and rounded shaped and (b) showing needle shaped precipitates.

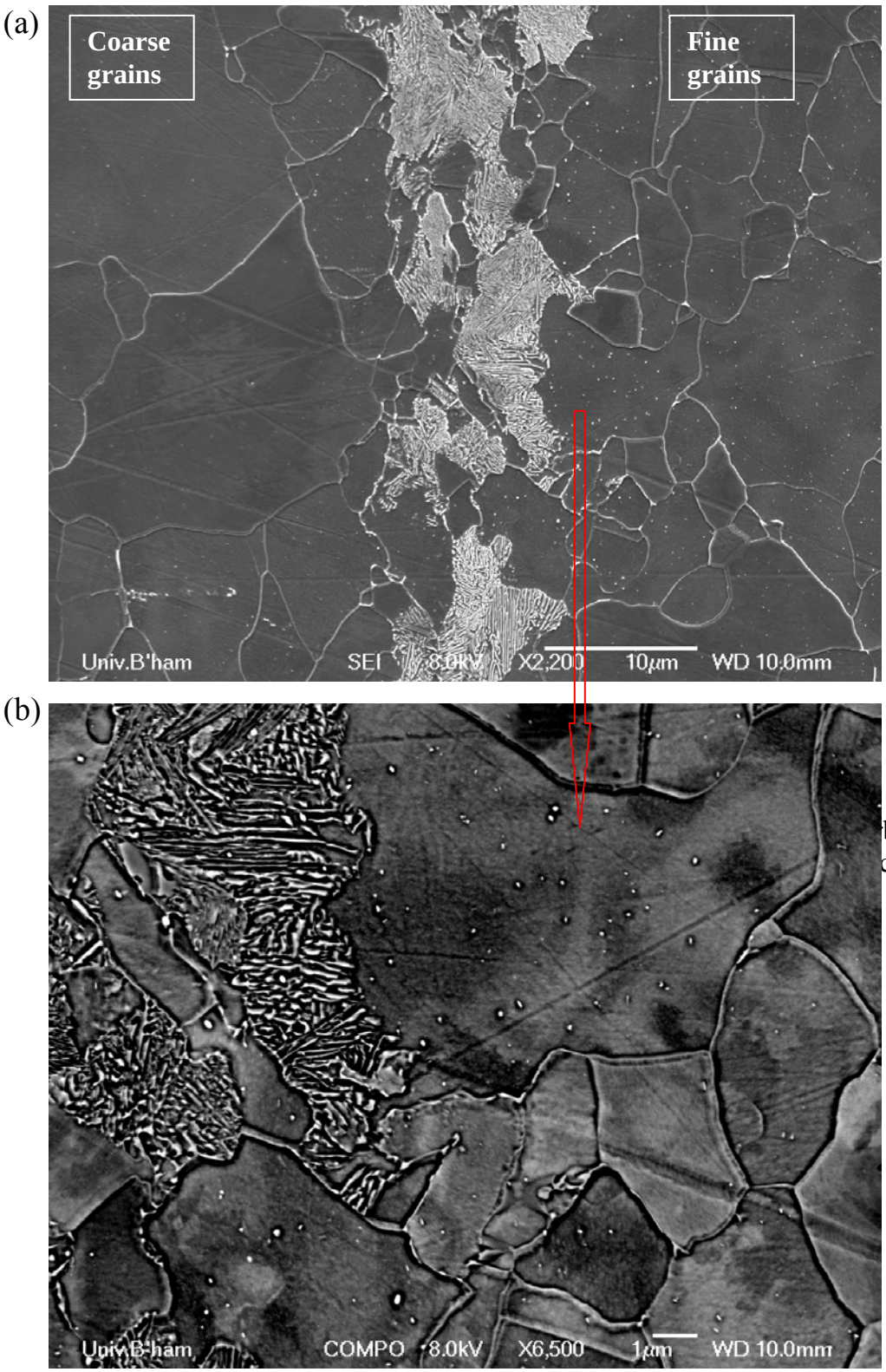

bonitride
can be

Fig. 9.3: (a) SE and (b) BSE image showing the distribution of Nb-rich microalloy precipitates in TMCR-1 steel. Higher volume fraction of precipitate can also be seen within the finer grains, compared to the coarser grains in (a).

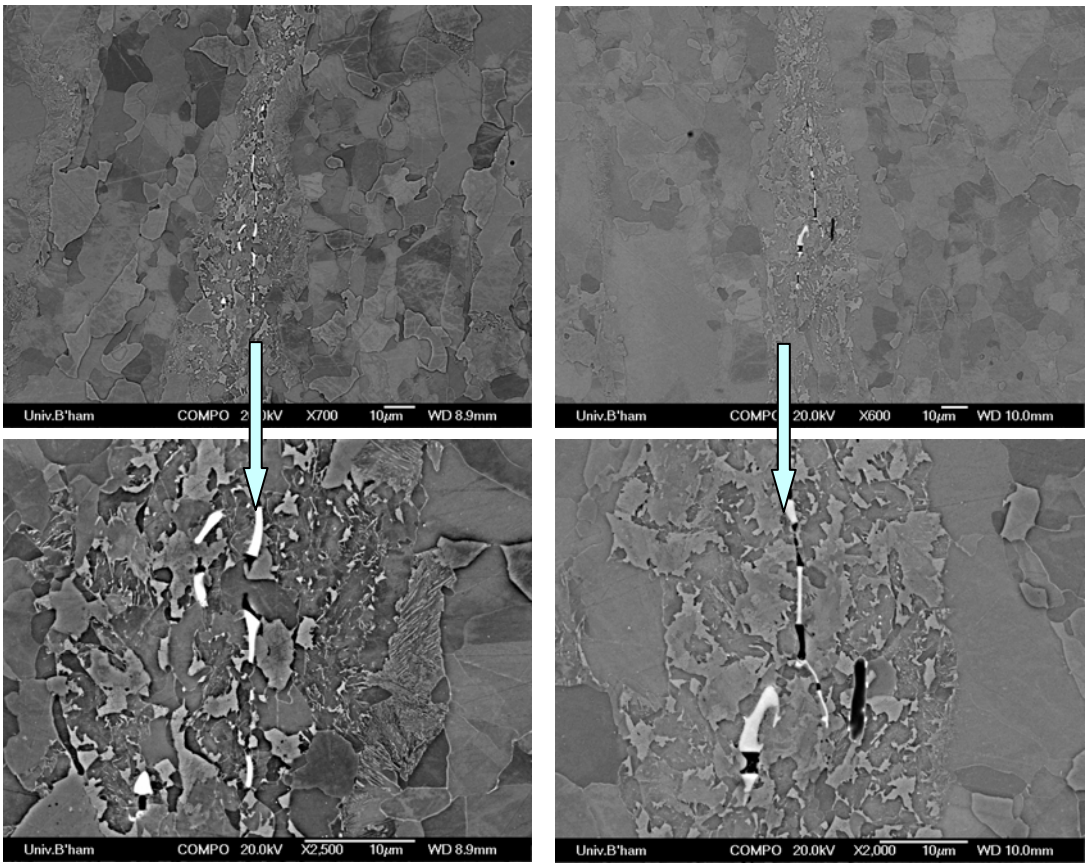

Fig. 9.4: BSE images showing the deposit of microalloy carbonitrides (Nb-rich) at the centre of the TMCR-1 plate, within the segregated (bainitic) region. Similar deposits have been found at the centre of the as-cast slabs.

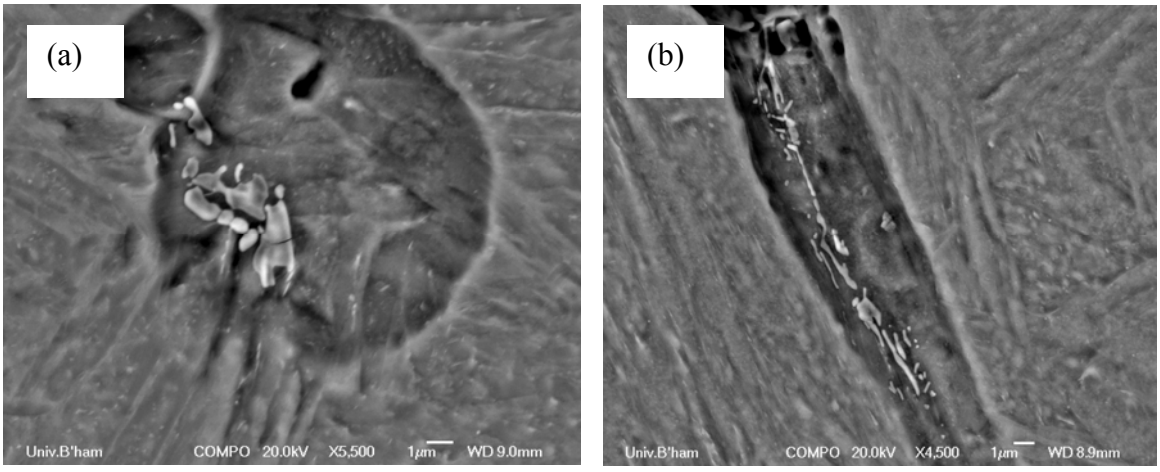

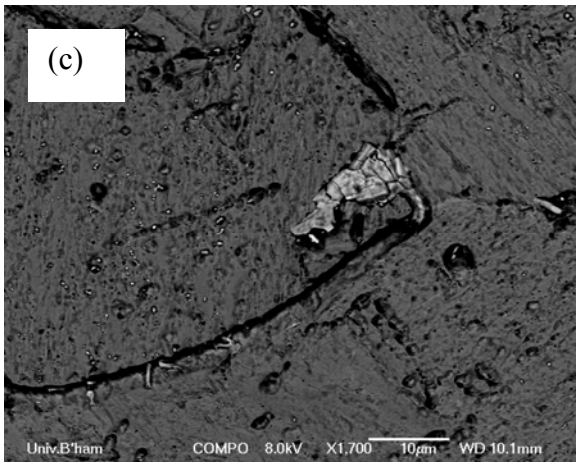

Fig. 9.5: BSE images showing the deposit of microalloy carbonitrides (Nb-rich) in the slab 1 mid-thickness samples reheated to (a and b) 1150 ºC and (c) 1200 ºC and water quenched.

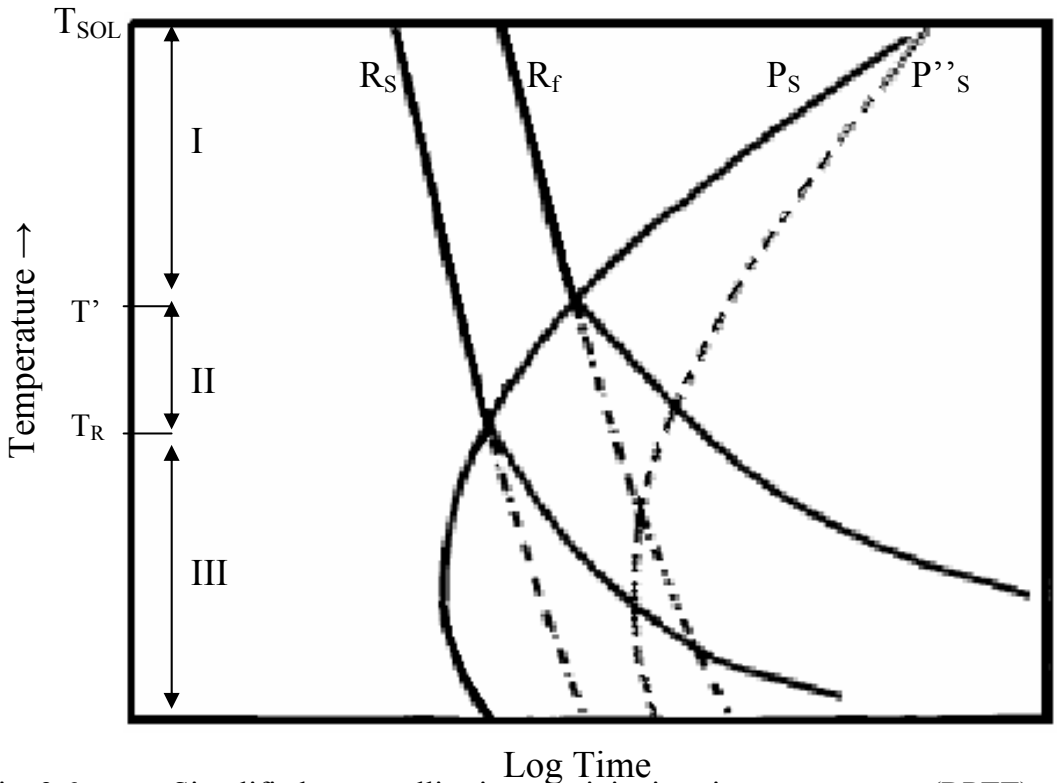

Fig. 9.6: Simplified recrystallisation-precipitation-time-temperature (RPTT) diagram [Kwon 1991] showing three stages (stage I, stage II and stage III) of recrystallisation-precipitation interaction (in austenite region) after reheating the steel at temperatures above T_{SOL}, followed by single pass deformation and isothermal holding at various temperatures for different times. T' and T_R temperatures are at the intersection between stage I and stage II and between stage II and stage III, respectively. R_S: Recrystallisation start, R_f: Recrystallisation finish, P_s: Precipitation start in deformed structure, P''_s: Precipitation start in undeformed structure.

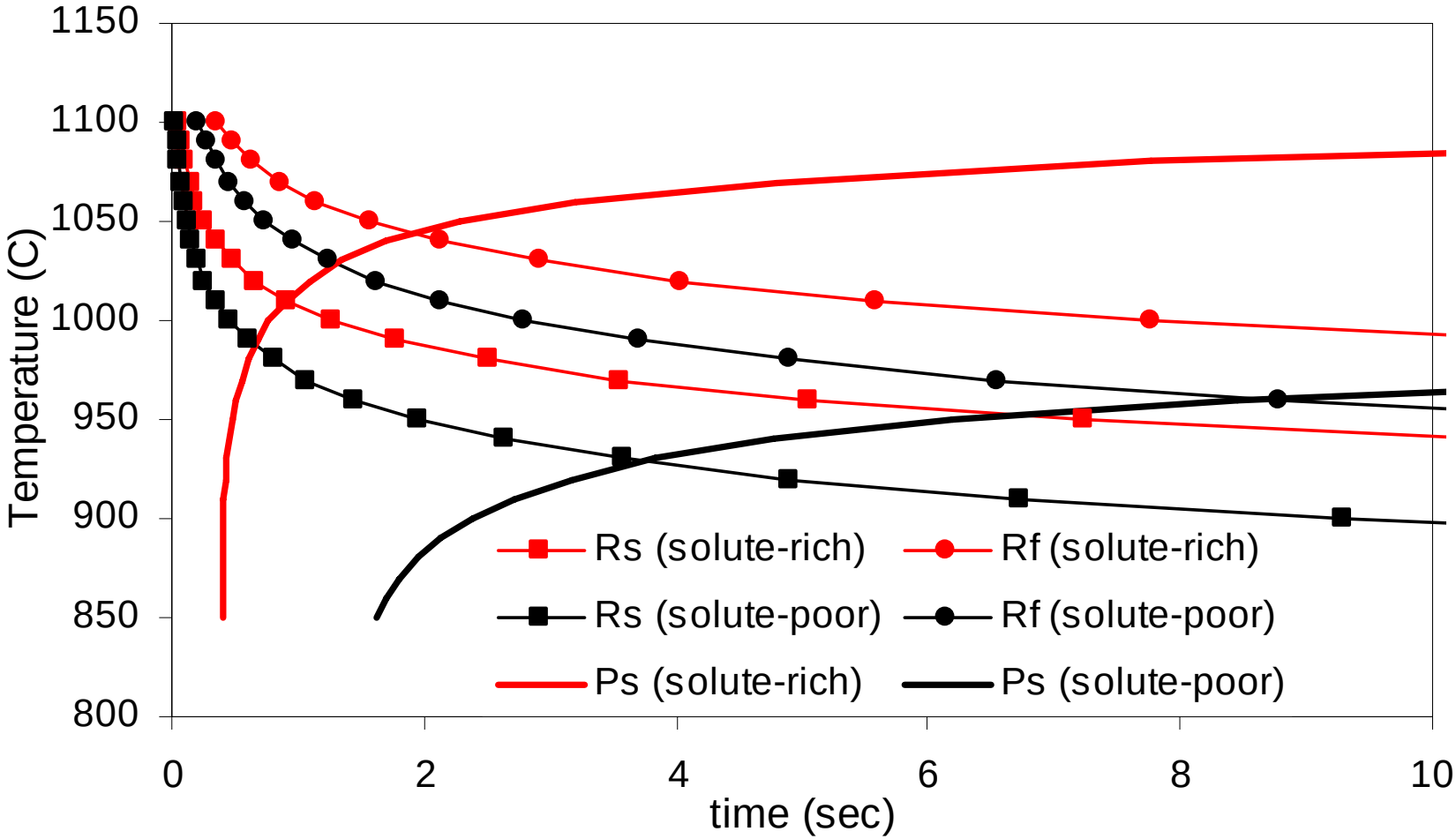

Fig. 9.7: Recrystallisation start (Rs) and finish (Rf) times and precipitation start (Ps) times for the solute-rich (interdendritic) and solute-poor (dendritic) non-segregated regions (calculated using eqn. 1.5.2 and eqn. 1.5.5) for slab 1 steel upon 1225 ºC reheating (1 hr.), deforming ($\varepsilon = 0.3$, $\dot{\varepsilon} = 10$ / sec) and isothermal holding.

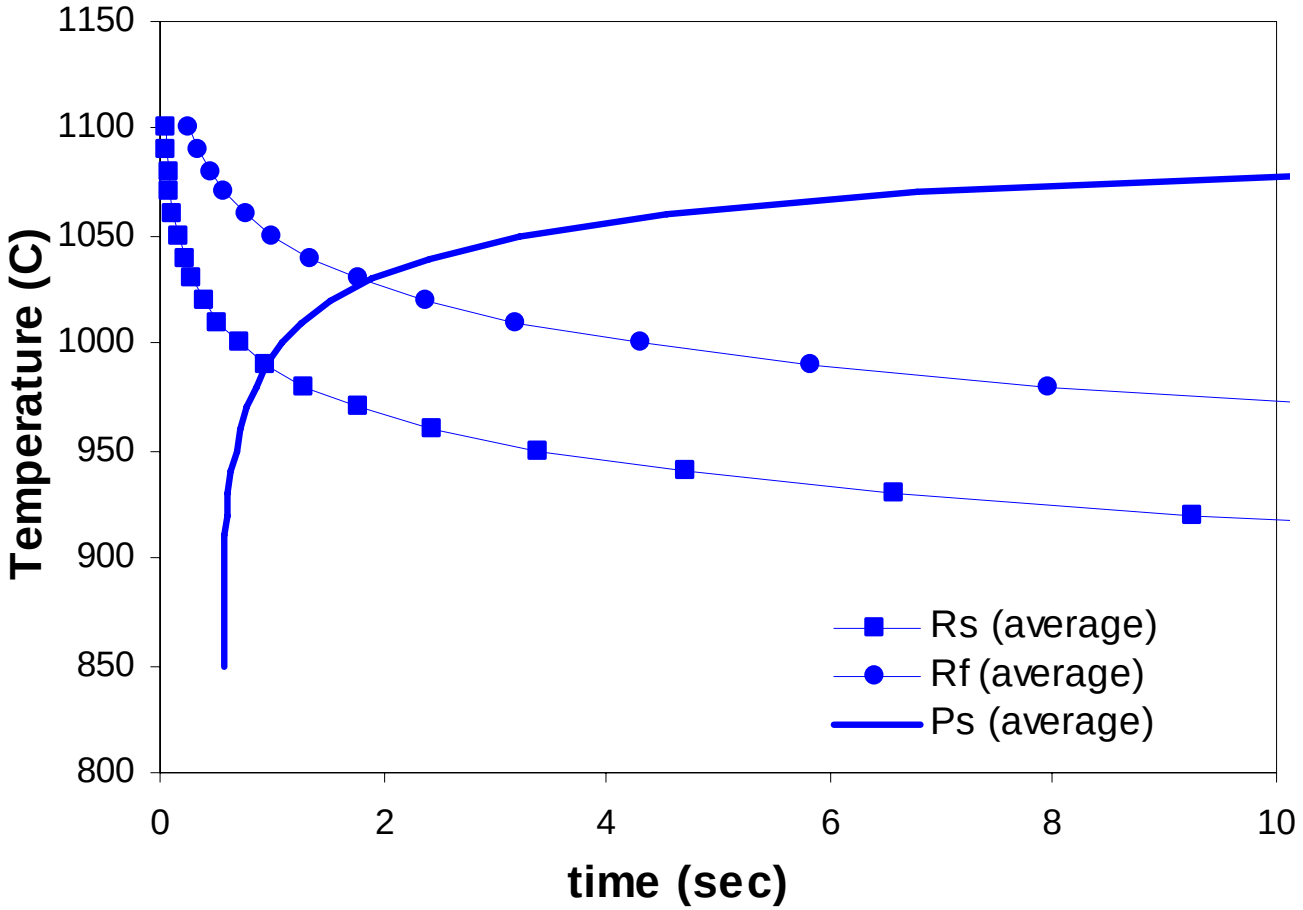

Fig. 9.8: Recrystallisation start (Rs) and finish (Rf) time and precipitation start (Ps) time for the same initial condition as used in Fig. 9.8 (i.e. 1225 ºC reheating), only considering a uniform average Nb level (0.046 % Nb) throughout the steel.

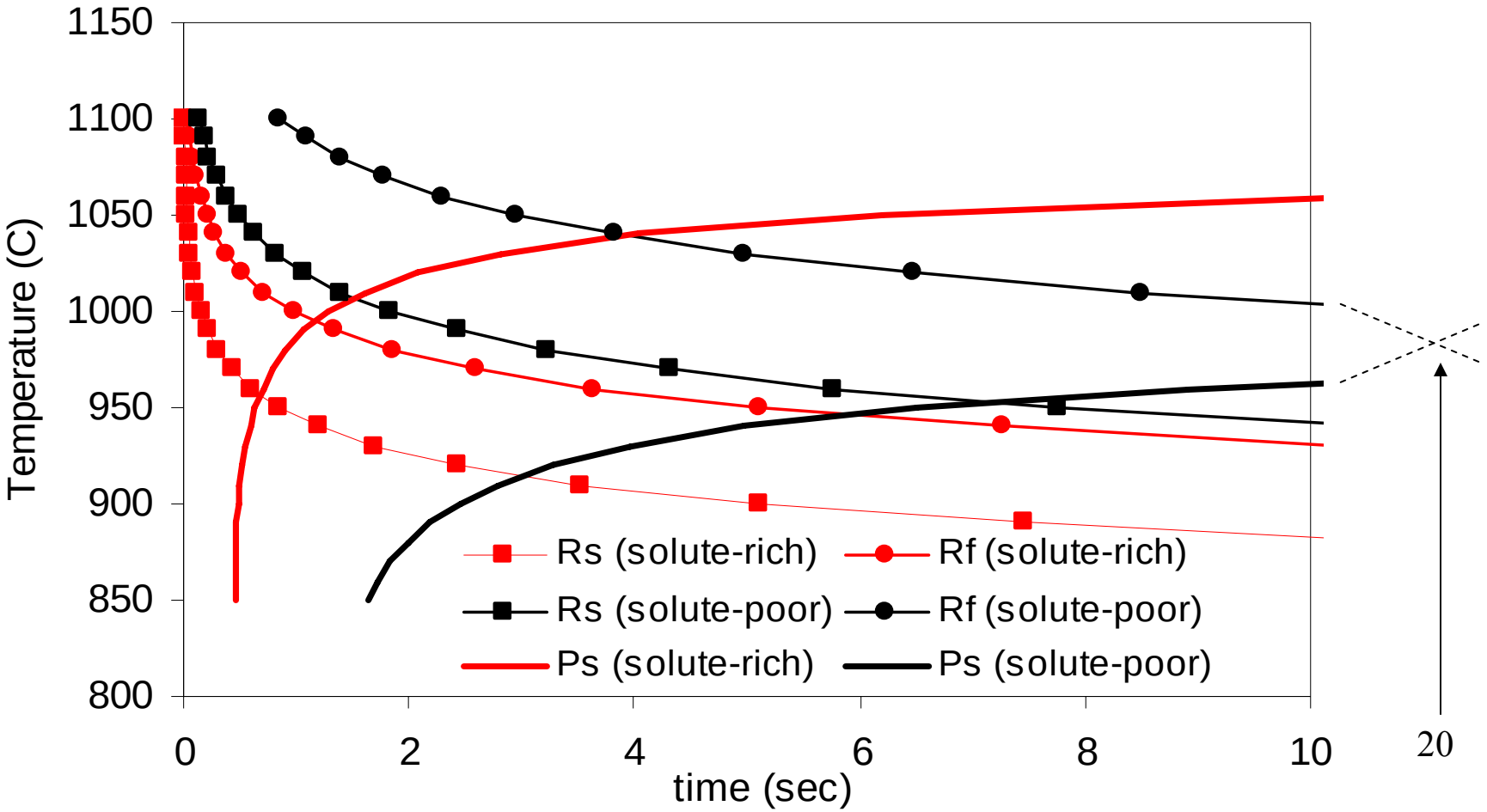

Fig. 9.9: Recrystallisation start (Rs) and finish (Rf) times and precipitation start (Ps) times for the solute-rich and solute-poor regions (calculated using eqn. 1.5.2 and eqn. 1.5.5) of slab 1 steel upon 1150 ºC reheating (1 hr.), deforming ($\varepsilon = 0.3$, $\dot{\varepsilon} = 10$ / sec) and isothermal holding.

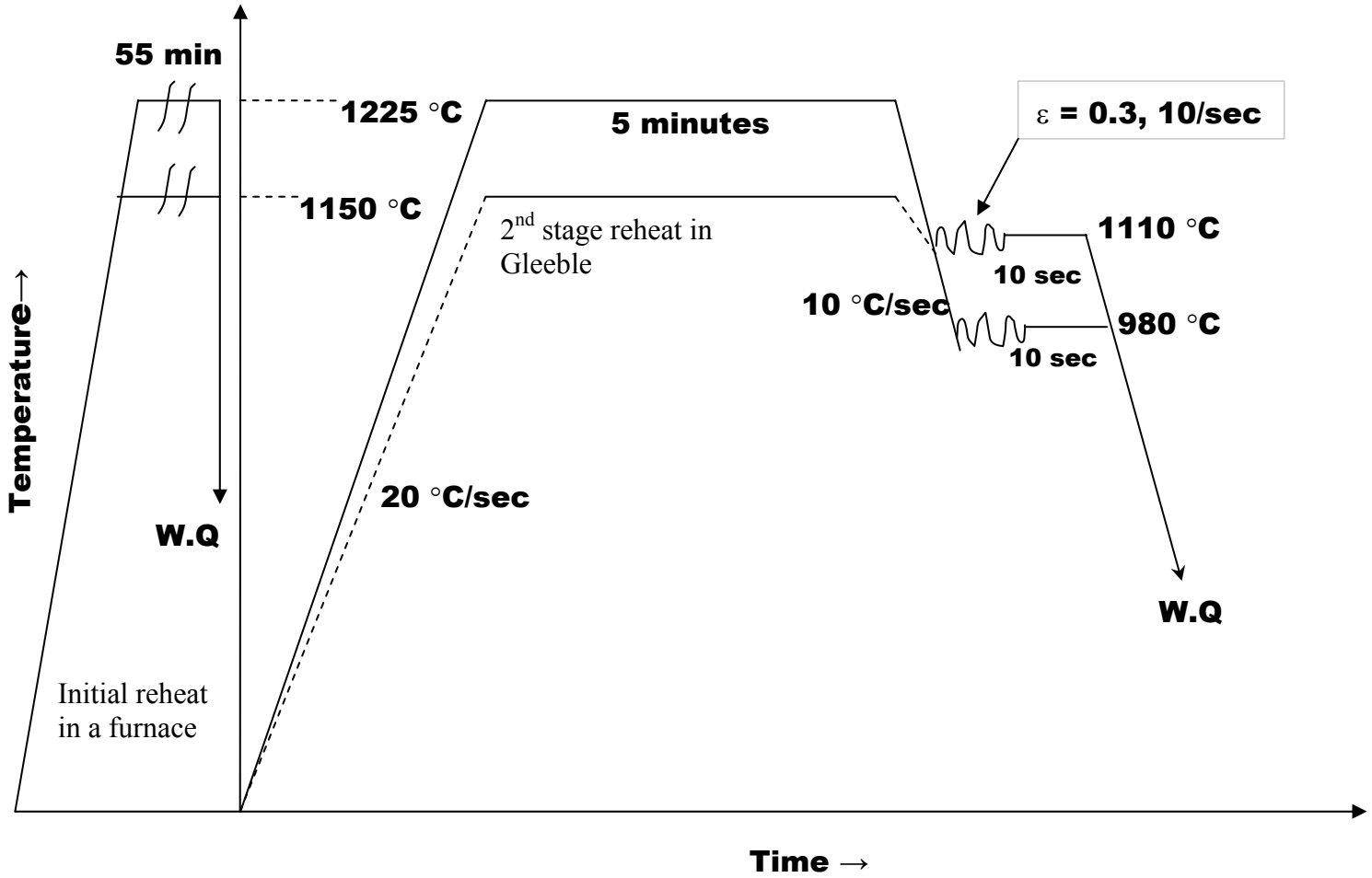

Fig. 9.10: Thermo-mechanical schedule used in the Gleeble 3500 comprising of reheating to 1225 ºC or 1150 ºC for 5 minutes (after initial reheating of the sample in a furnace for 55 minutes and water-quenching) followed by deformation either at 1110 ºC or at 980 ºC, isothermal holding (10 sec) and water-quenching. Two stage reheating schedule is used to avoid prolonged reheating inside Gleeble as that may cause hazard.

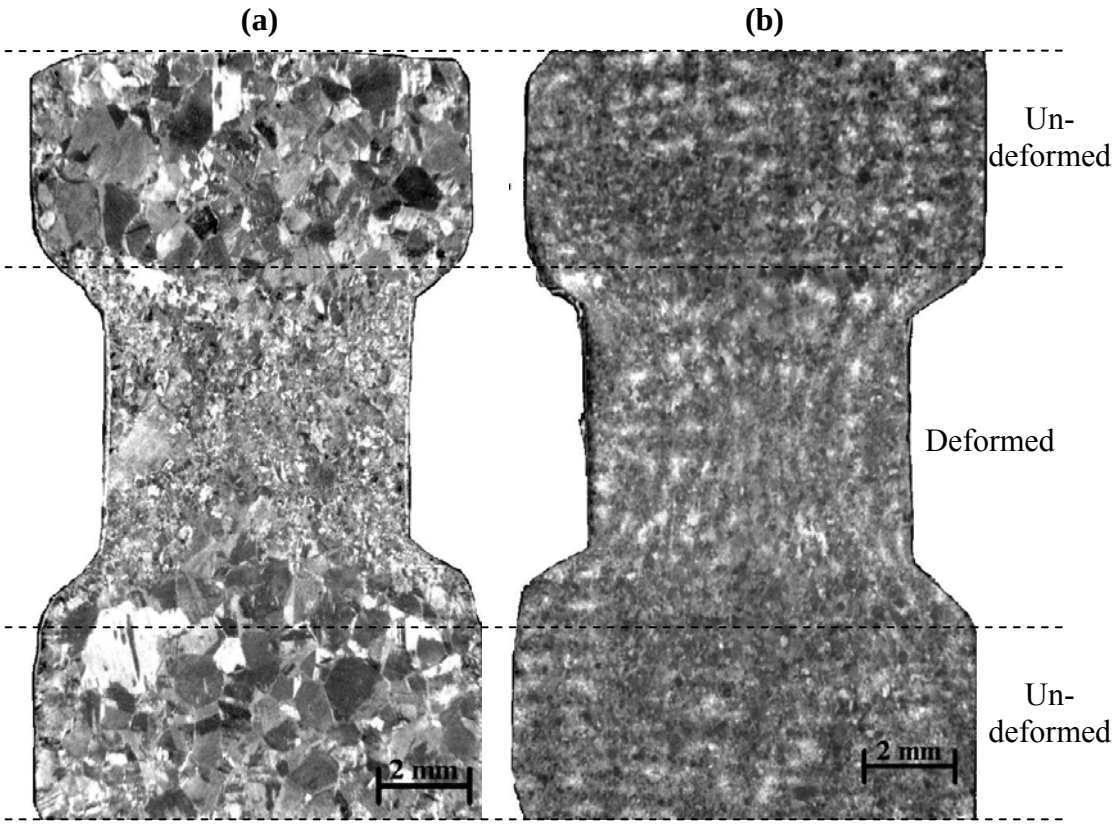

Fig. 9.11: Macro-view of (a) 1225-1110, and (b) 1150-1110 Gleeble tested samples, showing the un-deformed and deformed regions.

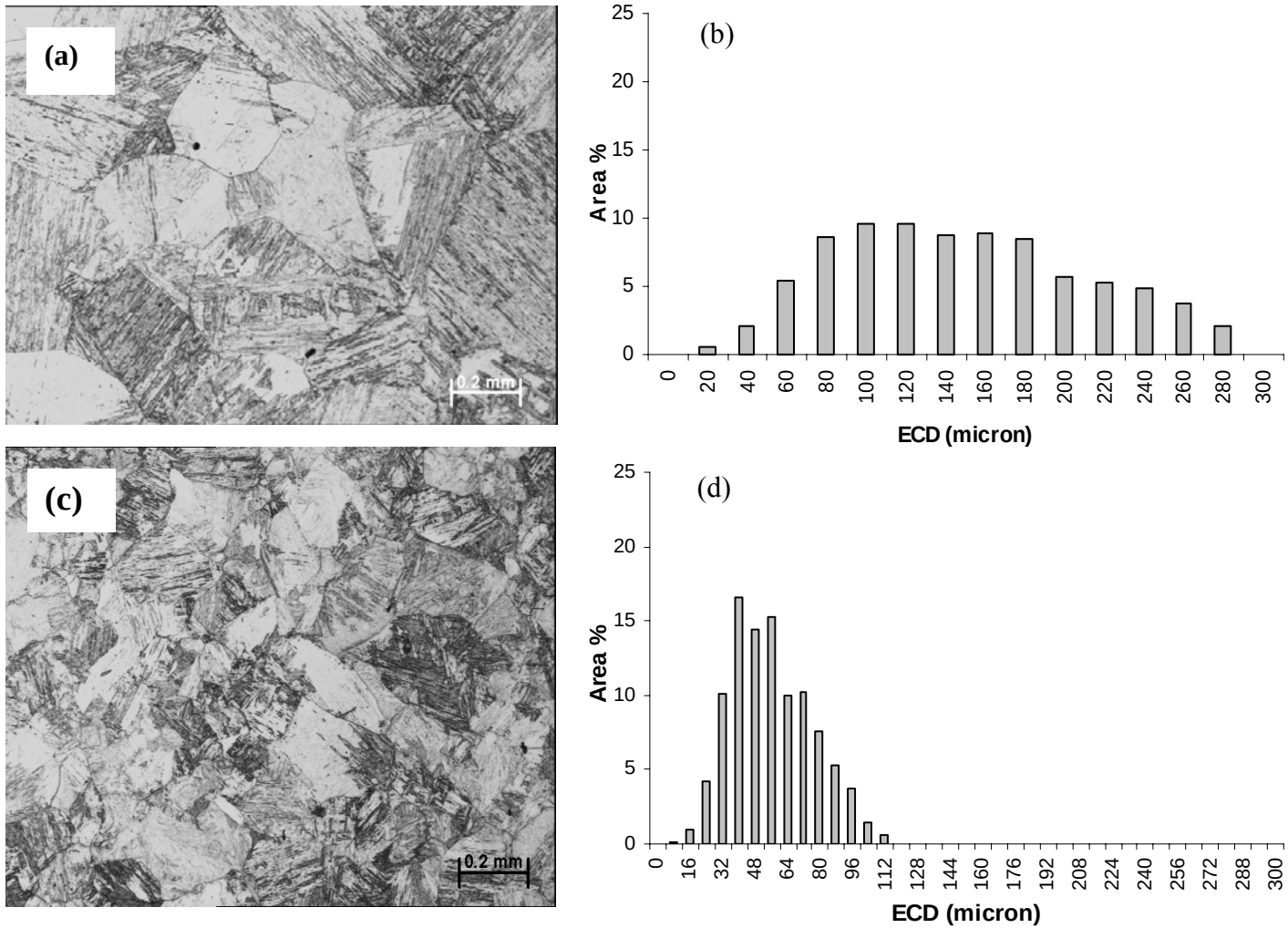

Fig. 9.12: (a) Uniform grain structure at the un-deformed region of 1225-1150 sample and (b) the corresponding 'unimodal' grain size distribution. (c) The completely recrystallised and unimodal grain structure at the deformed region of 1225-1110 sample, and (d) the corresponding grain size distribution.

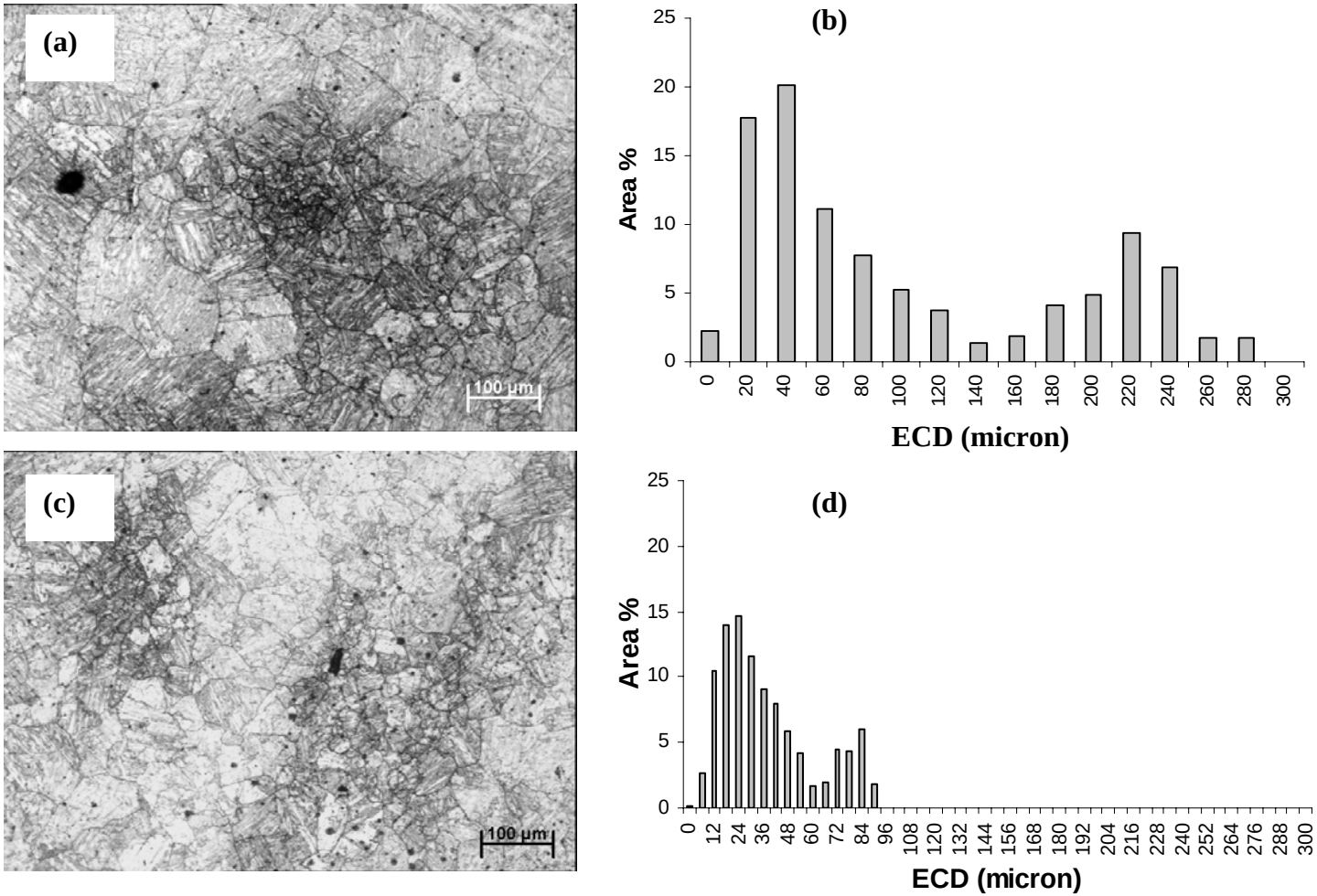

Fig. 9.13: (a) Duplex (coarse + fine) grain structure at the un-deformed region of 1150-1110 sample and (b) the corresponding 'bimodal' grain size distribution. (c) The 'duplex' recrystallised grain structure at the deformed region of 1150-1110 sample, and (d) the corresponding 'bimodal' grain size distribution.

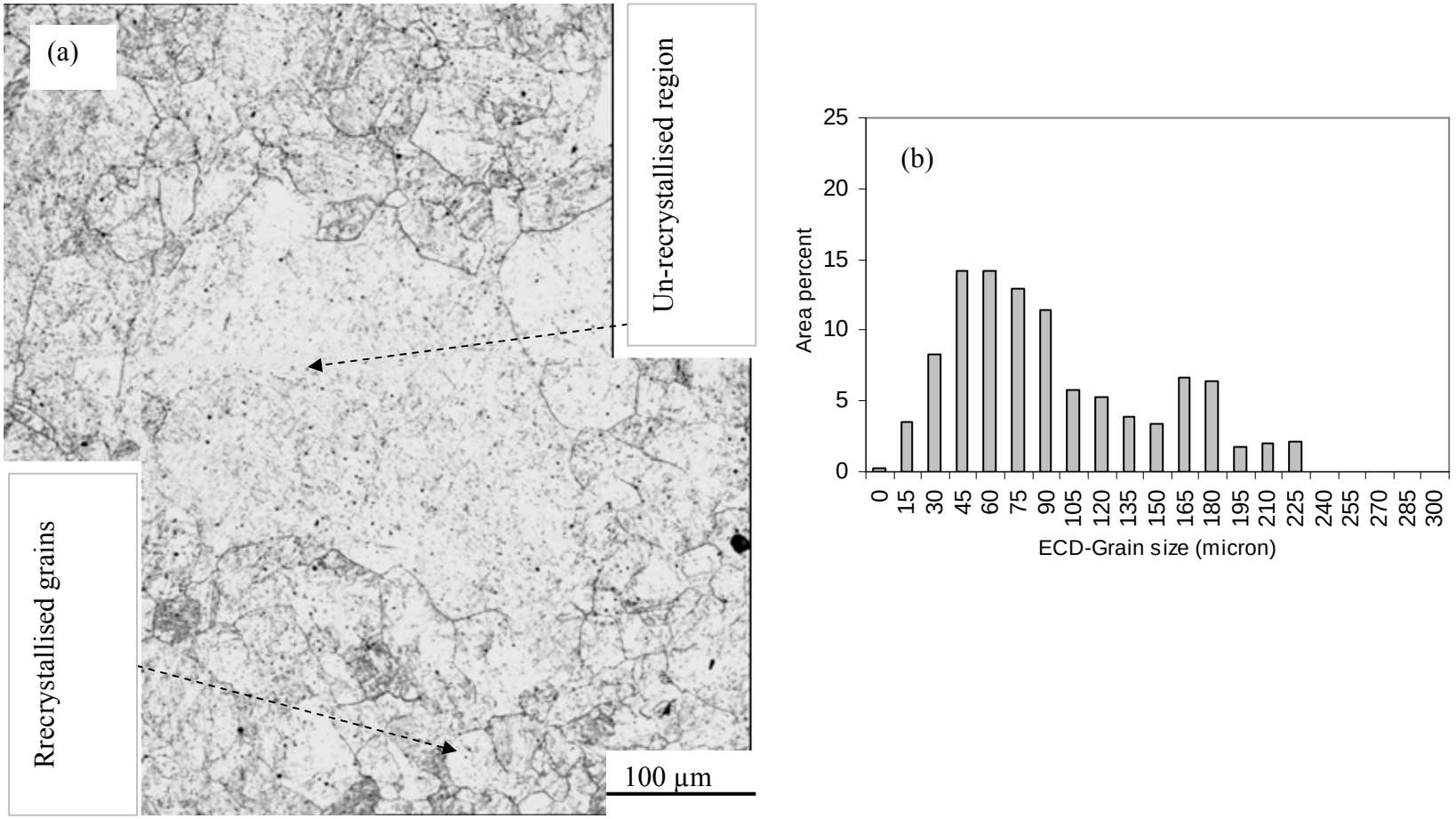

Fig. 9.14: Partially recrystallised (duplex) austenite grain structure at the deformed region of 1225-980 sample, comprising of coarse-unrecrystallised region and fine-recrystallised grains, and (b) the corresponding grain size distribution shows bimodality.

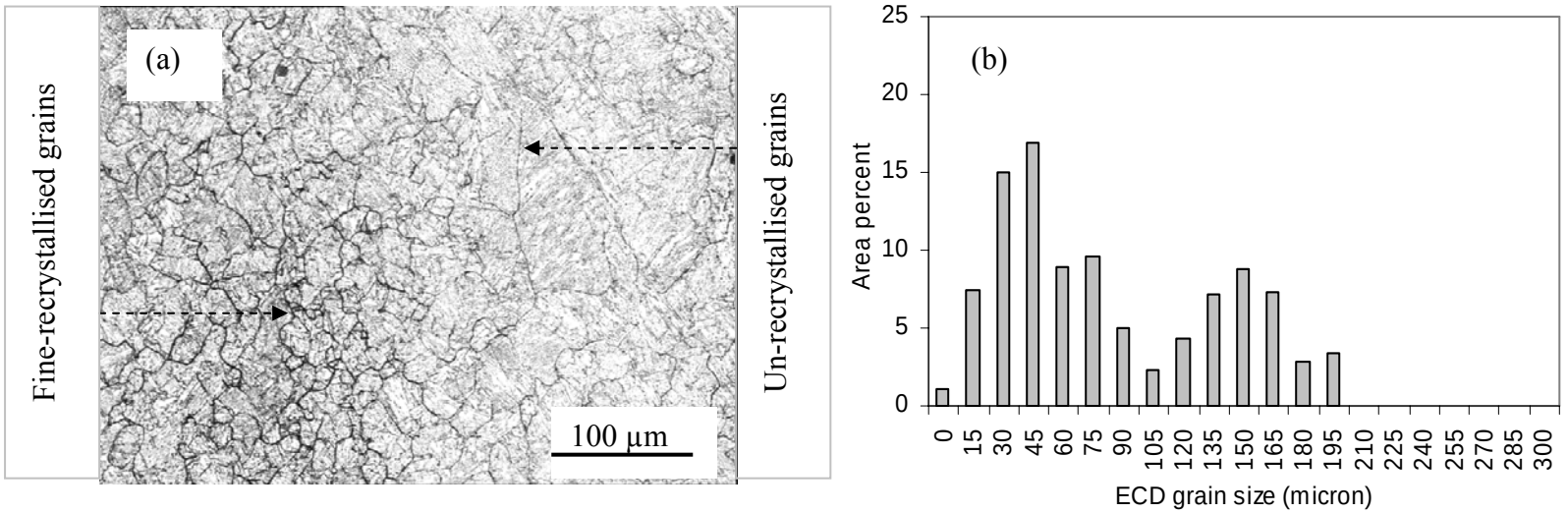

Fig. 9.15: (a) Partially recrystallised (duplex) austenite grain structure at the deformed region of 1150-980 sample, comprising of coarse-unrecrystallised and fine-recrystallised grains, and (b) the corresponding grain size distribution shows bimodality.

10 Conclusions and further work

10.1 Conclusion

In this thesis studies have been carried out in three major areas (i: formation of bimodality, ii: measurement of bimodality and iii: the effect of bimodality on toughness) and the findings from these areas are summarised below:

Formation of bimodality

- A wide range of grain sizes was found to exist in the as-cast slabs; however, the ferrite grain size distribution did not show any bimodality.
- Interdendritic segregation during casting can generate an inhomogeneous distribution of Nb-rich microalloy precipitates in the as-cast slabs, with precipitate-rich regions separated by a distance similar to the secondary dendritic arm spacing (SDAS).
- The inhomogeneity in precipitate distribution and the average precipitate density both increased from sub-surface towards mid-thickness locations of the slabs, possibly due to micro- and macro-segregation, respectively.
- Large deposits (several microns in size) of microalloying elements (comprised of Nb-rich complex microalloy carbo-nitrides) were found in the solute-rich regions at the mid-thickness location of the as-cast slabs, reheated slabs and rolled plate in the form of continuous networks. Such deposits indicate that severe macro-segregation took place during solidification.
- Thermo-Calc software was used to predict the partitioning of various elements during solidification. The prediction showed that Nb segregates strongly in as-cast

HSLA steels, whereas Al does not segregate significantly. The segregation of the different microalloying elements was verified experimentally.

- The reheat temperature has a significant effect on the degree of grain size bimodality. Unimodal and less bimodal distributions have been found at high (1225 °C) reheat temperatures (as most of the precipitates dissolve and are unavailable to pin the austenite grain boundaries) and low (1075 °C) reheat temperatures (as enough precipitates remain everywhere to provide pinning), respectively. In between those temperatures exists a critical temperature range (around 1150 or 1180 °C), which shows heavily bimodal austenite grain structures. Inhomogeneous precipitate distributions due to segregation in as-cast slab can create a difference in precipitate pinning force between different regions of the steel during reheating and can result in the formation of a bimodal grain structure. Almost complete dissolution of precipitates in the solute-poor region during reheating within the critical temperature range makes the bimodality severe.

- Thermodynamic software can be used to give an indication of the variation in bimodality by considering the segregated slab compositions and reheating temperatures.

- If the as-cast steel is segregated, bimodality may appear during (rolling) deformation within a certain temperature range (approximately ~ 900 - 1050 °C), even if the starting grain structure is uniform (after reheating), with fine recrystallised grains forming at solute-poor regions and coarse-unrecrystallised grains remaining at the solute-rich regions.

Measurement of bimodality

- Grain size distributions (plotted as number percent or area percent) based on ASTM grain size number (G) scale were unable to distinguish the steel microstructures in this work with less severe bimodality.
- A new distribution, based on an ECD-scale, 15 classes, and area percent was proposed in this work. The distributions differentiated the bimodal structures seen in this work (where the minimum-area percent class in between both the modes was considered as the 'breakpoint') for the steel microstructures studied here.
- Standard parameters used in the literature to quantify bimodal grain structures (area-percent and average-size corresponding to 'coarse' and 'fine' populations) provide useful microstructural details but are subjective in nature. The parameters, suggested in this work, of PHR and PGSR are easy to measure and less subjective (as they are independent of 'breakpoint' selection) and therefore, can be used to quantify and classify different microstructures in terms of bimodality.

Effect of bimodality on toughness

- It was found that for a bimodal grain structure the large grains of the 'fine population' and the grains belonging to the 'coarse population' take part in low-temperature cleavage fracture. That resulted in a separation of local fracture stress (σ_f) values into two groups, leading to higher scatter in σ_f values compared to the uniform grain structures.
- The grain sizes that initiate cleavage fracture were found to be large in size and also covering sufficient area-percent ($\geq$ 5 %) in the microstructure, so that they can be frequently sampled at the 'active zone'.
- Grain size bimodality does not create significant scatter in the upper shelf energy, USE, and lower shelf energy, LSE, regions of Charpy impact transition curves. However, it can generate higher scatter (in impact energy or fracture appearance)

within the impact transition region depending on whether a coarse- or fine-grain size band is predominantly sampled at the notch root.

10.2 Further work

From the investigation the following work plan can be considered for the future.

(i) It is discussed in **section 8.7** that there is a need for accurate prediction of the level of segregation of microalloying elements (particularly Nb) in the as-cast steel (compositional distribution in various regions) using the average steel composition (initial input). The current study has shown that Thermo-Calc can provide an indication of the critical temperature range where bimodality may result, however, it over predicts the Nb-levels in the interdendritic and dendritic regions of the as-cast slab when compared to measured values. Parameters used during continuous casting may be required, as different casting conditions may result in different levels of segregation and different separations between solute-rich and solute-poor regions. To establish such a model accurate measurement of the segregation levels is also needed for different steel compositions.

(ii) If compositional distribution (or variation) can be predicted then the variation in the stability of the precipitates can also be obtained using thermodynamic and kinetic predictions. Variation in precipitate stability can then be used to predict the grain size distribution after reheating [Andersen 1995a, b, Couch 2001], using Zener's or Gladman's concept. The heating rate during reheating has also been found to be an important parameter [Couch 2001] in determining the extent of bimodality and that effect should also be studied in detail. The

effect of reheating time and temperature on the initial segregation should also be considered to find out the compositional variation in reheated steel.

(iii) If the variation in (initial) grain structure and composition in the reheated steel is known, then those values can be used to predict the kinetics of strain-induced Nb-precipitation, austenite recrystallisation and the interaction between them (**Chapter 9**). During a single pass deformation process the interaction between precipitation and recrystallisation can be used to identify the fraction of recrystallised and un-recrystallised grains. The same concept can be used over the entire commercial rolling schedule (as in the models developed by Sellars [Sellars 1980]) to predict final grain size variation after deformation in the austenite region. Austenite grain sizes can be related to ferrite grain sizes and that can provide the ferrite grain size distribution in the final rolled product. However, predicting the variation in final ferrite grain sizes (using the composition and grain size variation in the reheated steel) will be the most difficult step (as different factors such as, rolling parameters, texture effects may become important). The problem can become further complicated if intercritical deformation is carried out, as intercritical deformation can itself generate variation in ferrite grain size and even bimodality (**section 1.5.5**).

(iv) At present the average ferrite grain sizes after rolling can be predicted [Sellars 1980], however, prediction of the entire grain size distribution would be more useful (as the variation in some properties depends on the variation in grain sizes). If the final ferrite grain size distribution can be determined then that can

be used to predict the variation in properties. The final ferrite grain size distribution (in the rolled plate) may be unimodal or bimodal. If unimodal, the distribution can be characterised by the average grain size and skew of the distribution. The average grain size is useful in predicting the average strength and toughness of steel (**chapter 2**). The skew in the grain size distribution can have an effect on the scatter in properties. If that is identified then the variation in properties can also be predicted.

(v) As well as the average-grain sizes and area-fractions corresponding to coarse- and fine-grain populations [ASTM] bimodal grain size distribution can also be quantified using the parameters (PHR and PGSR) proposed in **chapter 5**. These parameters have been related to the scatter in fracture toughness (as shown in **Fig. 6.16**) however, further work is required to verify this relationship to all prediction of scatter from the grain size distribution. For a full prediction of scatter in the toughness the role of other factors, such as phase balance and inclusions would need to be accounted for.

Therefore, using the starting average steel composition and processing parameters as input, predicting the final grain size distribution in rolled product (using thorough process model) and the scatter in properties can be a difficult journey, however, it is achievable.

References

(Arranged alphabetically)

A

Adrian 1995	Adrian H, "Thermodynamic calculations of carbonitride precipitation as a guide for alloy design of microalloyed steels";Proc. Conf. 'Microalloying 95', Iron and Steel Society, Pittsburgh, (1995), pp. 285-305.
Akamatsu 1993	Akamatsu S, Senuma T, Hasebe M; "mathematical modelling of nb(C, N) precipitation applicable to extra low carbon steels";Proc. Int. Symp. on 'Low C-steels for the 90's', (ed. R. Asgahami and G. Tither) The Minerals, Metals & Materials Society, Pittsburgh, (1993), pp. 187-194.
Anand 1975	Anand L, Gurland J; "Relationship between the size of cementite particles and the subgrain size in quenched-and-tempered steels".Metallurgical Transactions A, v 6A, n 4, (1975), pp. 928-931.
Andersen 1995a and b	Andersen I, Grong O; "Analytical modelling of grain growth in metals and alloys in the presence of growing and dissolving precipitates - I. Normal grain growth and -II. Abnormal grain growth"; Acta Metallurgica et Materialia, v 43, n 7, (1995), (a) pp. 2673-2688, (b) pp. 2689-2700.
Ardell 1972	Ardell A J; "On the coarsening of grain boundary precipitates";Acta Metallurgica, v 20, (1972), pp. 601-609.
Arieta 1993	Arieta F G, Sellars C M; "Precipitation kinetics of Nb (C, N) in austenite for the low C high Nb HSLA steels";Proc. International Symposium on Low-Carbon Steels for the 90's, (eds. R. Asfahani and G. Tither), pub. TMS, Pittsburg, PA, USA, (1993), pp. 101-112.
Asahi 1998	Asahi H, Yagi A, Ueno M; "Effect of ferrite formation on abnormal austenite grain coarsening in low-alloy steels during the hot rolling process"; Metallurgical and materials Transactions A, v 29 A, (1998), pp. (1375-1381).
Ashby 1958	Ashby M F: "Oxide dispersion strengthening", (ed. GS. Ansell et al.), Gordon and Breach, New York, (1958), pp. 143-205.
ASTM A 20	ASTM A 20: "Standard specifications for general requirements for steel plates for pressure vessels"; ASTM International, 1990; Annual Book of ASTM Standards, ASTM International, (2006).
ASTM E 112	ASTM E 112; "Test method for determining average grain size"; Annual Book of ASTM Standards, ASTM International, (2005).
ASTM E 1382	ASTM E 1382; "Test methods for determining average grain size using semiautomatic and automatic image analysis"; Annual Book of ASTM Standards, ASTM International, (2005).

Bai 1992	Bai D Q, Yue S, Sun W P, Jonas J J; “Effect of test variables on the critical temperatures Tnr and Ar3 of high Nb - low C plate steel Ar3 of high Nb - low C plate steel”;Proc. of the Int. Conference on Processing, Microstructure and Properties of Microalloyed and Other Modern High Strength Low Alloy Steels, published by Iron & Steel Soc of AIME, Pittsburgh, PA, USA, (1992), pp. 165-173.
Baker 1969	Baker R G and Nutting J; “The Tempering of a Cr-Mo-VW and a Mo-V Steel, Precipitation Processes in Steels”;ISI Report No 64, London, (1969), pp.1-22.
Baker 1972	Baker T J, Charles J A; “Morphology of manganese sulphide (MnS) in steel”;Journal of the Iron and Steel Institute, v 210, n Part 10, London, (1972), pp. 702-706.
Bakkaloglu 2002	Bakkaloglu A; “Effect of processing parameters on the microstructure and properties of an Nb microalloyed steel”;Materials letters, v 56, n 3, (2002), pp. 200-209.
Balart 2000	Balart M J, Davis C L, Strangwood M; “Cleavage initiation in Ti-V-N and V-N microalloyed ferritic-pearlitic forging steels”;Materials Science and Engineering A, v 284, n 1-2, (2000), pp. 1-13.
Bhattacharjee 2003	Bhattacharjee D, Davis C L and Knott J F; “Predictability of Charpy impact toughness in thermomechanically control rolled (TMCR) microalloyed steels”; v 30, n 3, (2003), pp. 249-255.
Bhattacharjee 2004	Bhattacharjee D, Knott J F, Davis C L; “Charpy-Impact-Toughness Prediction using an "Effective" Grain Size for Thermomechanically Controlled Rolled Microalloyed Steels”;Metallurgical and Materials Transactions A, v 35 A, n 1, (2004), pp. 121-130.
Bleck 2005	Bleck W, Phiu-On K; “Microalloying of clod-formable multi phase steel grades”; Conf. Proc. on ‘Microalloying for new steel processes and applications’, San Sebastian, Spain, (2005), published inMaterilas Science Forum, v 500-501, (2005), pp. 97-112.
Bodin 2001	Bodin A, Sietsma J, van der Zwaag S; On the nature of the bimodal grain size distribution after intercritical deformation of a carbon-manganese steel;Materials Characterization, v 47, (2001), pp. 187-193.
Bowen 1986	Bowen P, Druce S G, Knott J F; “Effects of microstructure on cleavage fracture in pressure vessel steel”;Acta Metallurgica, v 34, n 6, (1986), pp. 1121-1131.
Bowen 1987	Bowen P, Druce S G, Knott J F; “Micromechanical modelling of fracture toughness”;Acta Metallurgica, v 35, n 7, (1987), pp. 1735-1746.
Bower 1967	Bower T F, Flemings M C; “Formation of chill zone in ingot solidification”Transactions Metallurgical Society of American Institute of Mining, Metallurgical and Petroleum Engineers, v 239, n 2, (1967), pp. 216-219.

Bramfitt 1973	Bramfitt B L, Marder A R; “Processing and properties of low carbon steels”;American Institute of mining Metallurgical and Petroleum Engineers, New York, (1973), pp. 191-224.
Bramfitt 1997	Bramfitt, B L; “Effects of composition, processing, and structure on properties of irons and steels”; Materials Park, OH: ASM International, (1997). pp. 357-382.
BSEN 10045	BSEN 10045; “Charpy impact test on metallic materials”; Europian Standard, (1990).

C

Cabrera 1996	Cabrera J M, Flores E, Al Omar A, Prado J M; “Abnormal grain growth in medium carbon V-Ti-Al microalloyed steels”;Proc 1996 Symp Fundam Appl Microalloying Forging Steels, Golden, CO, USA, Minerals, Metals & Materials Soc (TMS), (1996), pp. 173-186.
Cai 2005	Cai S, Boyd J D; “Mechanism of microstructural banding in hot rolled microalloyed steels”; Materials Science Forum, v 500-501, (2005), pp. 171-178.
Chen 1987	Chen Z, Loretto M H, Cochrane R C; “Nature of large precipitates in titanium-containing HSLA steels”.Materials Science and Technology, v 3, n 10, (1987), pp. 836-844.
Chen 1990	Chen J H, Zhu L, Ma H; “On the scattering of the local fracture stress, sf*”;Acta Metallurgica et Materialia, v 38, n 12, (1990), pp. 2527-2535.
Chen 1992	Chen J H, Yan C; “Comparison of toughness of C-Mn steel with different grain sizes”;Metallurgical Transactions A, v 23A, n 9, (1992), pp. 2549-2556.
Chen 1997	Chen J H, Wang G Z, Yan C, Ma H, Zhu L; “Advances in the mechanism of cleavage fracture of low alloy steel at low temperature”;Internatioal Journal of Fracture, v 83, (1997), pp. 139-157.
Chen 1998	Chen J H, Wang G Z; “On scattering of measured values of fracture toughness parameters”;International Journal of fracture, v 94, (1998), pp. 33-49.
Cheng 2000	Cheng L M, Hawbolt E B, Meadowcroft T R; “Dissolution and coarsening of aluminium nitride precipitates in low carbon steel-distribution, size, morphology”;Canadian Metallurgical Quarterly, v 39, (2000), pp. 73-86.
Chen 2004	Chen J H, Wang G Z, Wang Q, Liu Y G; “Effects of sizes of ferrite grains and carbide particles on toughness of notched and precracked specimens of low-alloy steels”; International Journal of Fracture, v 126, n 3, (2004), pp. 223-241.
Cochrane 1978	Cochrane R C; “The effect of phosphorous ob the precipitation hardening by niobium carbide in C-Mn-nb steels”;British steel Internal report number T / PDM / Tn / 838 / 1 / 78 / D, (1978).
Coladas 1977	Coladas R, Masounave J, Guerin G, bailon J P; “Austenite grain growth in

medium and high carbon steels microalloyed with niobium";Metal Science, v 11, (1977), pp. 509-516.

Coladas 1977 — Coladas R, Masounave J, Guerin G, Bailon J P; "Austenite grain growth in medium- and high-carbon steels microalloyed with niobium".Metal Science, v 11, n 11, (1977), pp. 509-516.

Cottrell 1958 — Cottrell A H; Theory of brittle fracture in steel and similar metals;Transactions AIME, v 212, n 2, (1958), pp. 192-203.

Couch 2001 — Couch A J; "Grain growth and dissolution kinetics in high strength low alloy (HSLA) steels";Ph.D Thesis, The University of Leeds, (2001).

Craven 2000a — Craven A J, He K, Garvie L A J, Baker T N; "Complex heterogeneous precipitation in titanium-niobium microalloyed Al-killed HSLA steels - II. Non-titanium based particles";Acta Materialia, v 48, n 15, (2000), pp. 3869-3878.

Craven 2000b — Craven A J, He K, Garvie L A J, Baker T N; "Complex heterogeneous precipitation in titanium-niobium microalloyed Al-killed HSLA steels - I. (Ti,Nb)(C,N) particles";Acta Materialia, v 48, n 15, (2000), pp. 3857-3868.

Crowther 1997 — Crowther D N, Morrison W B; "The influence of hypo-stoichiometric additions of titanium on the properties of microalloyed structural steels";'Titanium technology in microalloyed steels', (Proc. of Conf. in Sheffield, 1994), edited by T. N. Baker, Book 662, The Institute of materials, London, (1997), pp. 44-64.

Cuddy 1981 — Cuddy L J; "Microstructures developed during thermomechanical treatment of HSLA steels";Metallurgical Transactions A, v 12A, n 7, (1981), pp. 1313-1320.

Cuddy 1982 — Cuddy L J; "Effects of microalloy concentration on the recrystallization of austenite during hot deformation";Proc. Conf. on 'Thermomechanical Processing of Microalloyed Austenite', Metallurgical Soc of AIME, Warrendale, Pa, USA, (1982), pp. 129-140.

Cuddy 1983 — Cuddy L J, Raley J C; "Austenite grain coarsening in microalloyed steels";Metallurgical Transactions A, v 14A, n 10, (1983), pp. 1989-1995.

Cuddy 1984 — Cuddy L J; "Grain refinement of Nb steels by control of recrystallisation during hot-rolling";Metallurgical and Materials Transactions A, v 15A, n 1, (1984), pp. 87-98.

Curry 1976 — Curry D A, Knott J E; "Relationship Between Fracture Toughness and Microstructure in the Cleavage Fracture of Mild Steel";
Met.al Science, v 10, n 1, (1976), pp. 1-6.

Curry 1978 — Curry D A, Knott J E; "Effects of microstructure on cleavage fracture stress in steel";Metal Science, v 12, (1978), pp. 511-514.

Curry 1980 — Curry D A; "Cleavage micromechanisms of crack extension in steels". Metal Science, v 14, n 8-9, (1980), pp. 319-326.

D

Davenport 1977 — Davenport A T, Miner R E and Kot R A;Proc. of Int. Conf. on 'The Hot Deformation of Austenite', The Metallurgical Society of AIME, New York, (1977), pp. 186-203.

Davis 2002 — Davis C L, Strangwood M; "Preliminary study of the inhomogeneous precipitate distributions in Nb-microalloyed plate steels; Journal of materials Science, v 37, (2002), pp. 1083-1090.

DeArdo 2003 — DeArdo A J; "Niobium in modern steels";International Materials Reviews, v 48, n 6, (2003), pp. 371-402.

Dieter 1988 — Dieter G E, 'Mechanical Metallurgy', McGraw-Hill, London, (1988).

Dogan 1992 — Dogan O N, Michal G M, Kwon H W; "Pinning of austenite grain boundaries by AIN precipitates and abnormal grain growth";Metallurgical Transactions A, v 23A, n 8, (1992), pp. 2121-2129.

Doherty 1987 — Doherty R D, Srolovitz D J, Rollett A D, Anderson M P; "On the volume fraction dependence of particle limited grain growth".Scripta Metallurgica, v 21, n 5, (1987), pp. 675-679.

Dutta 1987 — Dutta B, Sellars C M; "Effect of composition and process variables on nb(c, n) precipitation in niobium microalloyed austenite";Materials Science and Technology, v 3, n 3, (1987), pp. 197-206.

Dutta 1992 — Dutta B, Valdes E, Sellars C M; "Mechanism and kinetics of strain induced precipitation of Nb(C, N) in austenite";Acta Metallurgica et Materialia, v 40, n 4, (1992), pp. 653-662.

Dutta 2001 — Dutta B, Palmiere E J, Sellars C M; "Modelling the kinetics of strain induced precipitation in Nb microalloyed steels";Acta Materialia, v 49, n 5, (2001), pp. 785-794.

Dutta 2003 — Dutta B, Palmiere E J; "Effect of prestrain and deformation temperature on the recrystallization behavior of steels microalloyed with niobium";Metallurgical and Materials Transactions A, v 34 A, n 6, (2003), pp. 1237-1247.

E

Echeverria 2003 — Echeverria A, Rodriguez-Ibabe J M; "The role of grain size in brittle particle induced fracture of steels";Materials Science and Engineering A, v 346, n 1-2, (2003), pp. 149-158.

Eckstein 1993 — Eckstein H J, Fennert M, Osker J; "Application of the thermodynamic computation to the solution behaviour of niobium and vanadium carbonitrides";Steel Research, v 64, (1993), pp. 143-147.

El-Bealy 1996 — El-Bealy M, Thomas B G; "Production of dendritic arm spacing for low alloy steel casting processes;Metallurgical and Materials Transactions B, v 27B, (1996), pp. 689-693.

F

Fairchild 2000a — Fairchild D P; "Mechanism of brittle fracture in a microalloyed steel: Part I. Inclusion-induced cleavage"; Metallurgical and Materials Transactions A, v 31A, n 3, (2000), pp. 641-652.

Fairchild 2000b — Fairchild D P; "Mechanism of brittle fracture in a microalloyed steel: Part II. Mechanistic modelling"; Metallurgical and Materials Transactions A, v 31A, n 3, (2000), pp. 653-667.

Faulkner 1996 — Faulkner R G, Song S H, Flewitt P E J; "Combined quenching and tempering induced phosphorus segregation to grain boundaries in 2.25Cr-1Mo steel"Materials Science and Technology, v 12, n 10, (1996), pp. 818-822.

Fernandez 2003 — Fernendez A L, Uranga P, Lopez B, Rodriguez-Ibabe J M; "Dynamic recrystallization behaviour covering a wide austenite grain size in Nb and Nb-Ti microalloyed steels"; Materials Science and Engg. A; v 361, (2003), pp. 367-376.

Flemings 1967 — Flemings M C, Nereo G E; "Macrosegregation—1"; Transactions AIME, v 239, n 9, (1967), pp. 1449-1461.

Flemings 1974 — Flemings M C; "Solidification Processing";McGraw-Hill, New York, (1974).

Flores 1997 — Flores O, Martinez L; "Abnormal grain growth of austenite in a V-Nb microalloyed steel";Journal of Materials Science, v 32, n 22, 1997, pp. 5985-5991.

Fredrickson 1972 — Fredrickson H; "Solidification sequence in an 18-8 stainless steel, investigated by directional solidification";Metallurgical and Materials Transactions, v 3A, n 11, (1972), pp. 2989-2997.

From 1999 — From A, Sandstrom R; "Influence of mixed grain size distributions on the toughness in high and extra high strength steels"; Materials Characterization, v 42, n 2-3, (1999), pp. 111-122.

G

Gerberich 1985 — Gerberich W W, Kurman E; "New contributions to the effective surface energy of cleavage";Scripta Materialia, v 19, n 3, (1985), pp. 295-298.

Ghosh 2001 — Ghosh A; "Segregation in cast products"; Sadhana, v 26, n 1 and 2, (2001), pp. 5-24.

Gladman 1966 — T Gladman; "On the theory of the effect of precipitate particles on grain growth in metals";Proceedings of Royal Society of London; v 294, (1966), pp. 298-309.

Gladman 1967 — Gladman T, Pickering F B; "Grain coarsening of austenite";Journal of Iron and Steel Institute, v 205, (1967), pp. 653-664.

Gladman 1992 — Gladman, T; "Second phase particle distribution and secondary

recrystallisation"; Scripta Metallurgica et Materialia, v 27, n 11, (1992), pp. 1569-1573.

Gladman 1997 — Gladman T; "The Physical Metallurgy of Microalloyed Steels"; Book 615, The Institute of Materials, London, (1997)

Gray 1983 — Gray R J, Irving W R, Baker R; "Steel making, casting, and rolling of pipeline steels in BSC";Ironmaking and Steelmaking, v 10, n 4, (1983), pp. 185-192.

Griffith 1921 — Griffith A A; "The Phenomena of Rupture and Flow in Solids";Philosophical Transactions of the Royal Society of London, Series A, v 221, (1921), pp. 163-198.

Griffith 1971 — Griffith J R, Owen D R J; "An eleastic-plastic stress analysis for a notched bar in plane strain bending"; Journal of Mech. Phys. Solids, v 19, (1971), pp. 419-431.

Groom 1975 — Groom J DG, Knott J F; "Cleavage fracture in prestrained mild steel";Metal Science Journal, v 9, n 8, (1975), pp. 390-400.

Gunduz 2005 — Gunduz S, Cochrane R C; "Influence of cooling rate and tempering on precipitation and hardness of Vanadium microalloyed steels", Materials and Design, v 26, (2005), pp. 486-492.

H

Haggart 1990 — Haggart J E, Hardie A W, Bruce D W; "Control of segregation in continuously cast slabs for high quality plate applications at British Steel, Ravenscraig Works";Ironmaking and Steelmaking, v 17, n 2, (1990), pp. 130-134.

Hahn 1984 — Hahn G T; "Influence of microstructure on brittle fracture toughness";Metallurgical Transactions A; v 15 A, n 6, (1984), pp. 947-959.

Hall 1951 — Hall E O; "Deformation and ageing of mil steel";Proceedings Physical Society, v 64, n 381B, (1951), pp. 742-747.

Hansen 1980 — Hansen S S, Vander Sande J B, Cohen M; "Niobium carbonitride precipitation and austenite recrystallization in hot-rolled microalloyed steels";Metallurgical Transactions A, v 11A, n 3, (1980), pp. 387-402.

Hausild 2005 — Hausild P, Berdin C, Bompard P; "Prediction of cleavage fracture for a low-alloy steel in the ductile-brittle transition temperature range"; Materials Science and Engg. A, v 391, (2005), pp. 188-197.

He 2005 — He J Z, Liu Y Z, Shi B H, Liu Q Y, Wang X L, Li D G; "Effect of microstructure of continuous cast slab on formation of mixed grain in rolled producer";Kang T'ian / Iron and Steel (Peking), v 40, n 2, (2005), pp. 69-71.

Hertzberg 1995 — Hertzberg RW; "Deformation and Fracture Mechanics of Engineering Materials"; J. Wiley & Sons, New York, (1995).

Heisterkamp 1971	Heisterkamp F, Meyer L; “Mechanical properties of pearlite reduced steels”;Thyssen Forsch, v 3, n 1-2, (1971), pp. 44-65.
Hellman 1975	Hellman P, Hillert M; “On the effect of second-phase particles on grain growth”;Scandinavian journal of metals, v 4, (1975), pp. 211-219.
Hendrickson 1958	Hendrickson J A, Wood D S, Clarke D S; “The cleavage fracture of mild steel”; Transactions ASM, (1958), v 50, pp. 656-676.
Hillert 1965	Hillart M; “on the theory of normal and abnormal grain growth”;Acta Metallurgica, v 13, (1965), pp. 227-238.
Hillert 1970	Hillert M, Staffanson L I; “The regular solution model for stoichiometric phases and ionic melts”;Acta Chem. Scand., v 24, (1970), pp. 3618-3626.
Hodgson 1992	Hodgson P D, Gibbs R K; “A mathematical model to predict the mechanical properties of hot rolled C-Mn and microalloyed steels”;ISIJ international, v 32, n 12, (1992), pp. 1329-1338.
Hong 2002a	Hong S G, Kang K B, Park C G; “Strain-induced precipitation of NbC in Nb and Nb-Ti microalloyed HSLA steels”;Scripta Materialia, v 46, n 2, (2002), pp. 163-168.
Hong 2002b	Hong S C, Lim S H, Lee K J, Shin D H, Lee K S; “Inhibition of abnormal grain growth during isothermal holding after heavy deformation in Nb steel”;ISIJ international, v 42, (2002), pp. 1461-1467.
Hong 2003	Hong S G, Jun H J, Kang K B, Park C G; “Evolution of precipitates in the Nb-Ti-V microalloyed HSLA steels during reheating”;Scripta Materialia, v 48, (2003), pp. 1201-1206.
Houghton 1993	Houghton D C; “Equilibrium solubility and composition of mixed carbonitrides in microalloyed austenite”;Acta Metallurgica et Materialia, v 41, n 10, (1993), pp. 2993-3006
Houghton 1993	Houghton D C; “Equilibrium solubility and composition of mixed carbonitrides in microalloyed austenite”;Acta Met. Mater., v 41, (1993), pp. 2993-3006.
Hull 1960	Hull D; “Twining and fracture of single crystals of 3 % silicon iron”;Acta Metallurgica, v 8, n 1, (1960), pp. 11-18.

I

Irvine 1967	Irvine K J, Pickering F B, Gladman T; “Grain-refined C-Mn steels”;Iron and Steel Institute -- Journal, v 205, n 2, (1967), pp. 161-182.
Irving 1993	Inving W R; “Continuous casting of steel”;Book 584, The Institute of materials, London, (1993).

J

Janampa 1982	Janampa C S; “The role of nitrogen in the hot working of niobium microalloyed steels”;Ph.D. Theis, The University of Sheffield, (1982).

Jansson 1993	Jansson B, Schalin M, Selleby M, Sundman B; "The Thermo-Calc database system";Proc. of 2nd Int. Symp. on 'Computer software in chemical and extractive metallurgy', (ed. C. W. Bale, G. A. Irons) Quebec City, Montreal, (1993), pp. 57-71.
Jian 1990	Jian Li, Sun F, Xu W C; "On the evaluation of yield strength for microalloyed steels";Scripta Metallurgica et Materialia, v 24, n 7, (1990), pp. 1393-1398.
Jun 2003	Jun H J, Kang K B, Park C G; "Effects of cooling rate and isothermal holding on the precipitation behaviour during continuous casting of Nb-Ti bearing HSLA steels;Scripta Materialia, v 49, (2003), pp 1081-1086.

K

Kejian 1997	Kejian H, Baker T N; "Complex carbonitrides in multi-microalloyed Ti-containing HSLA steels and their influence on the mechanical properties";'Titenium technology in microalloyed steels', (Proc. of Conf. in Sheffield, 1994), edited by T. N. Baker, Book 662, The Institute of materials, London, (1997), pp. 115-132.
Kelly 1971	Kelly A, "Introduction"; in 'Strengthening methods in crystals', (ed. Kelly A, Nicholson R B), Elsevier, Amsterdam, Netherlands, (1971), pp. 1-8.
Kneissi 1992	Kneissi A C, Garcia C I, DeArdo A J; "Characterisation of precipitates in HSLA steels"; Proc. 2nd Int. Conf. On 'HSLA steels: processing, properties and applications', (ed. G. Tither et al.), Baijing, China, TMS, Warrendale, (1992), pp. 99-105.
Knott 1963b	Knott J F, Cottrell A H; "Notch brittleness in mild steel"; Journal of Iron and Steel Institute, v 201, (1963), pp. 249-260.
Knott 1966	Knott J F; "Some aspects of hydrostatic tension on fracture behaviour of mild steel"; Journal of Iron and Steel Institute, v 204, (1966), pp. 104-111.
Knott 1973	Knott J F, 'Fundamentals of fracture mechanics', Butterworths, London, (1973).
Knott 1981	Knott J F; "The relationship between microstructure and fracture toughness"; Conf. Proc. Steels for line pipe and pipeline fittings; London, October (1981); pp. 79-89.
Knott 1982	Knott J F, 'Strength and Toughness of Steels'; The Metals Society, (1982), pp. 181-198.
Knott 2007	Knott J F; "Microstructural heterogeneity in high-strength structural steels and effects on scatter in toughness values"; Proceedings of the International Conference on Microalloyed Steels - Emerging Technologies And Applications, March 2007, Kolkata, India, (2007), pp. 10-23.
Korchynsky 2005	Korchynsky M; "Advanced Metallic Structural Materials and a New Role for Microalloyed Steels";Materials Science Forum, v 500-501, (2005), pp. 471-480.

Krauss 2003	Krauss G; “Solidification, segregation and banding in carbon and alloy steels”;Metallurgical and Materials Transactions B, v 34B, (2003), pp. 781-792.
Kwon 1991	Kwon O, DeArdo A J; “Interactions between recrystallization and precipitation in hot-deformed microalloyed steels”;Acta Metallurgica et Materialia, v 39, n 4, (1991), pp. 529-538.

L

le Bon (1975)	le Bon A, Rofes-Vernis J, Rossard C; “Recrystallization and precipitation during hot working of a Nb-bearing HSLA steel”.Metal Science Journal, v 9, n 1, (1975), pp. 36-40.
Leap 2002	Leap M J, Brown E L; “Crystallography of duplex AlN-Nb(C, N) precipitates in 0.2 % C steel”;Scripta Materialia, v 47, (2002), pp 793-797.
Lesoult 2005	Lasoult G; “Macrosegregation in steel strands and ingots”, Characterisation formation and consequences”;Materials Science and Engineering A, v 413-414, (2005), pp. 19-29.
Li 1998	Li P H, Ibraheem A K, Pristner R; “Eutectic precipitation of (Ti, Nb, V)(C, N) in cast, microalloyed low-C austenite and effects of reheating; Materials Science Forum, v 284-286, (1998), pp. 517-524.
Lifshitz 1961	Lifshitz I M, Slyozov V V; “The kinetics of precipitation from supersaturated solid solutions”;Journal of Phys. Chem. Solids, v 19, (1961), pp. 35-50.
Linaza 1995	Linaza M A, Romero J L, Rodriguez-Ibabe J M, Urcola J J; “Cleavage fracture of microalloyed forging steels”.Scripta Metallurgica et Materialia, v 32, n 3, (1995), pp. 395-400.
Lincoln 1993	Lincoln E; The Procedure Handbook of Arc Welding. Cleveland: Lincoln Electric; (1993), ISBN 99949-25-82-2,
Lindley 1970	Lindley T C, Oates G, Richards C E; “A critical of carbide cracking mechanisms in ferride/carbide aggregates”;Acta Metallurgica, v 18, n 11, (1970), pp. 1127-1136.
Liu 1982	Liu Z; “Cleavage fracture initiated by pearlite packets”; ‘Iron Steel Sinica’, v 17, (1982), pp. 12-20.
Low 1954	Low J R jr.; “The relation of microstructure to brittle fracture”;Symposium on relation of properties to microstructure, Transactions ASM, Metals Park, Ohio, USA, v 46A, (1954); p.163-174.
Luton 1980	Luton M J, Dorvel R, Petkovic R; “Interaction between deformation, recrystallization and precipitation in niobium steels”;Metallurgical Transactions A, v 11A, n 3, (1980), pp. 411-420.

M

McMahon 1965	McMahon C J, Cohan M; Initiation of cleavage in polycrystalline iron; Acta Metall., v13, (1965), pp. 591-604.

Medina 1991	Medina S F, Fabregue P; “Activation energy in the static recrystallisation of austenite”;Journal of materials Science, v 26, (1991), pp. 5427-5432.
Medina 1994	Medina S F, Mancilla J E; “Static recrystallization of austenite and strain induced precipitation kinetics in titanium microalloyed steels”;Acta Metallurgica et Materialia, v 42, n 12, (1994), pp. 3945-3951.
Medina 1995	Medina S F; “Influence of niobium on the static recrystallization of hot deformed austenite and on strain induced precipitation kinetics”; Scripta Metallurgica et Materialia, v 32, n 1, (1995), pp. 43-48.
Medina 1996	Medina S F, Quispe A; “Influence of microalloy type and content on induced precipitation kinetics in microalloyed steels”;Steel research, v 67, (1996), pp. 257-262.
Mendiratta 1996	Mendiratta M G, Goetz R L, Dimiduk D M; “Notch fracture in gamma - titanium aluminides”; Metallurgical and Materials Transactions A, v 27A, n 12, (1996), pp. 3903-3912.
Mintz 1982	Mintz B, Morrison W B, Cochrane R C; “Influence of grain boundary carbide thickness and grain size on the impact properties of steels”.Proc. Conf. on ‘Advances in the Physical Metallurgy and Applications of Steels’, Liverpool, Metals Soc (Book 284), London, (1982), pp. 222-228.
Mintz 1986	Mintz B, Wilcox J R, Crowther D N; “Hot ductility of directly cast C-Mn-Nb-Al steel”;Materials Science and Technology, v 2, (1986), pp. 589-594.
Mintz 1997	Mintz B, Crowther D N; “The influence of small additions of Ti on the hot ductility of steel”;‘Titanium technology in microalloyed steels’, (Proc. of Conf. in Sheffield, 1994), edited by T. N. Baker, Book 662, The Institute of materials, London, (1997), pp. 98-114.
Moore 1984	Moore J J; “Review of axial segregation in continuous cast steel”; Continuous casting, Iron and Steel Society, v 3, (1984), pp. 11-20.
Morales 2003	Morales E V, Gallego J, Kestenbach H J; “On coherent carbonitride precipitation in commercial microalloyed steels”;Philosophical Magazine Letters, v 83, n 2, (2003), pp. 79-87.
Morrison 1966	Morrison W B; “Effect of grain size on stress-strain relationship in low-carbon steel”;ASM Transactions Quarterly, v 59, n 4, (1966), pp. 824-846.

N

Nes 1985	Nes E, Ryum N, Hunder O; “On the Zener drag”;Acta Metallurgica, v 33, (1985), n 1, pp. 11-22
Novikov 1997	Novikov V Yu; “Grain Growth and Control of Microstructure and Texture of Polycrystalline Materials”; CRC Press, Boca Raton, FL, USA,(1997).

O

Okaguchi 1987	Okaguchi S, Hashimoto T; “Characterisation of precipitates and mechanical properties in Ti-bearing HSLA steels”;Transactions of Iron and Steel Institute of Japan (Trans. ISIJ), v 27, (1987), pp. 467-473.

Orowan 1946	Orowan, E; “Notch brittleness and strength of metals”;Transactions of Inst. of Engineers and Shipbuilders in Scotland, v 80, (1946), pp. 165-196.
Orowan 1948	Orowan E;“Proc. Symp. ‘Internal stress in metals and alloys”; The Institute of Metals, London (1948), pp. 451 – 460.
Ouchi 1982	Ouchi C, Sampei T, Okita T;Proc. of Int. Conf. on ‘The Hot Deformation of Austenite’, (ed. J B Balance), The Metallurgical Society of AIME, New York, (1977), pp. 316-340.

P

Palmiere 1994	Palmiere E J, Garcia C I, DeArdo A J; “Compositional and microstructural changes which attend reheating and grain coarsening in steels containing niobium”; Metallurgical and Materials Transactions A, v 25A, n 2, (1994), pp. 277-286.
Palmiere 1996	Palmiere E J, Garcia C I, DeArdo A J; “Influence of niobium supersaturation in austenite on the static recrystallization behavior of low carbon microalloyed steels”;Metallurgical and Materials Transactions A, v 27A, n 4, (1996), pp. 951-960.
Petch 1986	Petch N J; “Influence of grain boundary carbide and grain size on the cleavage strength and impact transition temperature of steel”;Acta Metallurgica, v 34, n 7, (1986), pp. 1387-1393.
Pickering 1963	Pickering F B, Gladman T; “Investigation into some factors which control strength of carbon steels”;Iron and Steel Institute -- Special Report No. 81, (1963), pp. 10-25.
Porter 1992	Porter D A, Easterling K E; “Phase transformations in metals and alloys”;2nd edition, Chapman and Hall, London, (1992).
Presslinger 2006	Presslinger H, Mayr M, Tragl E, Bernhard C; “Assessment of the primary structure of slabs and the influence on hot- and cold-rolled strip structures”; Steel Research Int., v 77, n 2, (2006), pp. 107-115.
Priestner 1998	Priestler R, Li P H, Zhou C, Ibraheem A K; “Microally precipitation in HSLA steel austenite”; Microstructural Science, v 26, (1998) Ottawa, Canada, pp. 447-454.

Q

Qiu 2006	Qiu H, Ito R, Hiraoka K; “Role of grain size on the strength and ductile-brittle transition temperature in the dual-sized ferrite region of the heat-affected zone of ultra-fine grained steel”; Materials Science and Engineering A, v 435-436, (2006), pp. 648-652.

R

Rainforth 2002	Rainforth W M, Black M P, Higginson R L, Palmiere E J, Sellars C M, Prabst I, Warbichler P, Hofer F; “Precipitation of NbC in a model

austenitic steel";Acta Materialia, v 50, n 4, (2002), pp. 735-747.

Reed-Hill 1973 — Reed-Hill R E; "Physical Metallurgy principles"; 2nd edition, D Van Nostrand Company, New York, (1973).

Rios 1987 — Rios P R; "A theory for grain boundary pinning by particles";Acta Metallurgica, v 35, n 12, (1987), pp. 2805-2814.

Ritchie 1973 — Ritchie R O, Knott J F, Rice J R; "On the relationship between critical tensile stress and fracture toughness in mild steel".Journal of the Mechanics and Physics of Solids, v 21, n 6, (1973), pp. 395-410.

Ritchie 1974 — Ritchie R O, Knott J F; "Micro cleavage cracking during fatigue crack propagation in low strength steel"; Materials Science and Engineering, v 14, n 1, (1974), pp. 7-14.

Rose 1996 — Rose A J, Howe A A; "Precipitation in niobium treated HSLA steels";Report number SL / PM / R / S 2924 / 5 / 96 / A, British Steel Internal Report, Swinden, UK, (1996).

Rose 1997 — Rose A J, Gladman T, 'referred in "The Physical Metallurgy of Microalloyed Steels" by T. Gladman; Book 615, The Institute of Materials, London, (1997).

Rosenfield 1986 — Rosenfield A R, Shetty D K; "Particle-induced cleavage crack initiation in steel";Scripta Metallurgica, v 20, n 3, (1986), pp. 439-440.

S

Saito 1997 — Saito Y; "Modelling of microstructural evolution in thermomechanical processing of structural steels";Materials Science and Engineering A, v 223A, (1997), pp. 134-145.

San 2005 — San Martin D, Caballero F G, Capdevila C, Garcia de Anders C; "Discussion of the rate controlling process of coarsening of niobium corbonitride in a niobium microalloyed steel";Materials Science Forum, v 500-501, (2005), pp. 703-710.

San Martin 1999 — San Martin J I, Rodriguez-Ibabe J M; "Determination of energetic parameters controlling cleavage fracture in a Ti-V microalloyed ferrite-pearlite steel";Scripta Materialia, v 40, n 4, (1999), pp. 459-464.

Sarian 1969 — Sarian S J; "Diffusion of Ti in TiCx";Journal of Applied Physics, v 40, (1969), pp. 3515-3520.

Schrewe 1987 — Schrewe H; "Continuous casting of steel – Fundamental principles and practice"; Verleg Stahleisen mbH, Dusseldorf, (1989).

Sellars 1979 — Sellars C M, Whiteman J A; "Recrystallisation and grain growth in hot working";Metal Science, v 13, n 3-4, (1979), pp. 187-193.

Sellars 1980 — Sellars C M; "The physical metallurgy of hot working";Proc. Conf. on 'Hot working and forming processes', (eds. C. M. Sellars, G. L. Davies), Book 264, The Metals Society, London, (1980), pp. 3-15.

Sellars 1985	Sellars C M; 'HSLA steels, metallurgy and applications', Proc. Int. Conf. 'HSLA steels 85', Chinese Society of Metals, baijing, China, (1985), (ed. by JM Gray et al.), published by American Society of Metals, Metals Park, Ohio, USA (1986) pp. 73-82.
Shanmugam 1996	Shanmugam P, Pathak S D; "Some studies on the impact behavior of banded microalloyed steel"; Engineering Fracture Mechanics. v 53, n 6, (1996), pp. 991-1005.
Shanmugam 2005	Shanmugam S, Tanniru M, Misra R D K, Panda D, Jansto S; "Precipitation in v bearing microalloyed steel containing low concentrations of Ti and Nb";Materials Science and Technology, v 21, n 8, (2005), pp. 883-892.
Shehata 1982	Shehata M T, Boyd J D; "Quantitative correlations between toughness and microstructure for commercial line pipe steel";Proc. Conf. On 'Advances in the Physical Metallurgy and Applications of Steels', Liverpool, Metals Soc (Book 284), London, (1982), pp. 229-236.
Shewmon 1963	Shewmon P G; "Diffusion in solids", McGraw-Hill, New York, (1963).
Smith 1966	Smith E; "The nucleation and growth of cleavage microcracks in mild steel";Proc. Conf. Physical Basis of Yield and Fracture, Inst. Of Physics and Physical Society, Oxford, (1966), pp. 36-45.
Smith 1981	Smith W F; "Structure and properties of engineering alloys";McGraw-Hill, New York, (1981).
Smithells 1983	Smithells Metal Refernce book, 6th edition, (edited by E. A. Brandes), Butterworths, London, (1983).
Speer 1987	Speer J G, Michael J R, Hansen S S; "Carbonitride precipitation in niobium / vanadium microalloyed steels";Metallurgical and Materials Transactions A, v 18A, n 2, (1987), pp. 211-222.
Speer 1989	Speer J G, Hansen S S; "Austenite recrystallization and carbonitride precipitation in niobium microalloyed steels";Metallurgical Transactions A, v 20A, n 1, (1989), pp. 25-38.
Srolovitz 1984	Srolovitz D J, Anderson M P, Grest G S, Sahni P S; "Computer simulation of grain growth: iii. Influence of a particle dispersion";Acta Metallurgica, v 32, n 9, (1984), pp. 1429-1438.
Sterjovski 2004	Sterjovski Z, Dunne D P, Carr D G, Ambrose S; "The effect of cold work and fracture surface splitting on the Charpy impact toughness of quenched and tempered steels"; ISIJ International, v 44, n 6, (2004), pp. 1114-1120.
Strid 1985	Strid J, Easterling K; "On the chemistry and stability of complex carbides and nitrides in microalloyed steels";Acta Metallurgica, v 33, n 11, (1985), pp. 2057-2074.
Stroh 1954	Stroh A N; "The formation of cracks as a result of plastic flow";Proceedings of Royal Society of London; v 223 A, (1954), pp. 404-414.
Sun 1993	Sun W P, Militzer M, Bai D Q, Jonas J J; "Measurement and modelling of

the effects of precipitation on recrystallization under multipass deformation conditions";Acta Metallurgica et Materialia, v 41, n 12, (1993), pp. 3595-3604.

Sun 2000 — Sun J, Boyd JD; "Effect of thermomechanical processing on anisotropy of cleavage fracture stress in microalloyed linepipe steel";International Journal of Pressure Vessels and Piping, v 77, n 7, (2000), pp. 369-377.

T

Talbot 2000a — Talbot D, Davis C L, Strangwood M; "The effects of different plate rolling processes on microstructure and mechanical properties in a Nb-containing HSLA steel"; Proc. of 32nd Annual IMS Convention on 'Understanding Processing / Structure / Property / Behaviour Correlations', Pub ASM Intl ISBN 0-87170-687-3 (2000), in Microstructural Science, v 27, n 4, pp. 56-65.

Talbot 2000b — Talbot D, Davis C L and Strangwood M; Proc 'Thermomechanical Processing of Steels', London, pub. IoM Communications ISBN I-86125-122-X, (2000), pp. 681-691

Talbot 2002 — Talbot D; "The effects of plate processing parameters on the microstructure, mechanical properties and precipitation characteristics of niobium containing high strength low alloy steels"; Thesis submitted to University of Birmingham, (2002).

Tanguy 2005 — Tanguy B, Besson J, Piques R, Pineau A; "Ductile to brittle transition of an A508 steel Characterised by Charpy impact test Part 1: Experimental results"; v 72, (2005), pp. 49-72.

Tanaka 1981 — Tanaka T; Controlled rolling of steel plate and strip";International Metals Reviews, v 26, n 4, (1981), pp. 185-212.

Teoh 1995 — Teoh L L; "Thermomechnalical processing and microstrcuture of microalloyed steel bar and wire rod products";Journal of Materials Processing Technology, v 48, n 1, (1995), pp. 475-481.

Tian 1996 — Tian D W, Karjalianen L P, Qian B, Chen X; "Non uniform distribution of carbonitride particles and its effect on prior austenite grain size in the simulated coarse grained heat-effected zone of thermomechanical control processed steels";Metallurgical and Materials Transactions A, v 27A, n 12, (1996), pp. 4031-4038.

Tither 1992 — Tither G; "The development and applications of niobium-containing HSLA steels"; Proc. 2nd Int. Conf. On 'HSLA steels: processing, properties and applications', (ed. G. Tither et al.), Baijing, China, TMS, Warrendale, (1992), pp. 61-80.

Todinov 2001 — Todinov M T, "An efficient method for estimating from sparse data the parameters of the impact energy variation in the ductile-brittle transition region"; International Journal of Fracture (Netherlands). v 111, n 2, (2001), pp. 131-150.

Tsai 1997 — Tsai W C; "Factors affecting the evolution of ferrite grain size in controlled rolled steels"; Masters Thesis, The University of Leeds, (1997).

Tweed 1984	Tweed C J, Ralph B, Hansan N; "The pinning by particles by low and high angle grain boundaries during grain growth";Acta Metallurgica, v 32, n 9, (1984), pp. 1407-1414.
Tweed 1987	Tweed J H' Knott J F; "Micromechanisms of failure in c-mn weld metals";Acta Metallurgica, v 35, n 7, (1987), pp. 1401-1414.

U

Ubhi 1989	Ubhi H S, Baker T N; "The influence of Manganese and Silicon on the precipitation of Vanadium Carbide in Steel"; Materials Science and Engineering A, v 111, (1989), pp. 189-199.
ULSAB 1998	Ultra Light Steel Auto Body; Electronic Report; 1.0, AISI, Washington, (1998).
Underwood 1968	Underwood E E; "Quantitative microscopy";(ed. R.T. DeHoff and F.N. Rhines), McGraw-Hill, New York, (1968), pp. 77-127.

V

Verger 1985	Verger-Gaugry J L, Ocampo G E, Embury J D; "Microanalysis of TiNb carbonitrides in HSLA steels";Metallography, v 18, (1985), pp. 381-393.
Vodopivec 2001	Vodopivec F, Breskvar B, Arzensek B, Kmetic D, Vojovodic-Tuma J; "Change of fracture mode in Charpy toughness transition temperature range"; Materials Science and Technology, v 18, (2002), pp. 61-67.
Vodopivec 2003	Vodopivec F, Arzensek B, Kmetic D, Vojvodic-Tuma J; "On The Charpy Fracturing Process"; Materials and Technology, v 37, n 6, (2003), pp. 317-326.

W

Wagner 1952	Wagner C: "Thermodynamics of Alloys";Addison-Wesley Press, Reading, (1952).
Wallin 1991	Wallin K; "Statistical modelling in the brittle to ductile region", in 'Defect assessment in components – Fundamental and applications, Mechanical engineering publications, London, (1991).
Wang 1998	Wang G Z, Chen J H; "Cleavage fracture criterion of low alloy steel and weld metal in notched specimens"; International Journal of Fracture, v 89, n 3, (1998), pp. 269-284.
Wang 2002	Wang C Z, Chen j H, Wang J G; "on the measurement and physical meaning of cleavage fracture stress in steel";International Journal of Fracture, v 118, (2002), pp. 211-227.
Watanabe 1977	Watanabe H, Smith Y, Pehlke R D: "Precipitation kinetics of niobium varbonitride in austenite in high-strength low-alloy steels";Proc. Int. Conf. on 'The Hot Deformation of Austenite', (ed. J B Balance), The Metallurgical Society of AIME, New York, (1977), pp. 140-168.
Weiss 1981	Weiss T, Fitzsimons G L, Mielityinen-Tiitoo K, DeArdo A J; "Influence of

niobium, vanadium and nitrogen on the response of austenite to reheating and hot deformation in microalloyed steels";Proc. Int. Conf. on 'Thermomechanical Processing of Microalloyed Austenite', (ed. A J DeArdo et al.): Warrendale, USA, Metallurgical Soc of AIME, (1982), pp. 33-57.

Wolf 1987 — Wolf M;in Proc. of the 3rd International Conference on 'Solidification Processing', 21-24 Sept. Sheffield (1987), pub. Inst. of Metals, London, (1988), pp. 163-182.

Wu 2004a — Wu S J, Davis C L; "Effect of duplex ferrite grain size distribution on local fracture stresses of Nb-microalloyed steels";Materials Science and Engineering A, v 387-389, n 1-2, (2004), pp. 456-460.

Wu 2004b — Wu S J, Knott J F; "On the statistical analysis of local fracture stresses in notched bars";Journal of the Mechanics and Physics of Solids, v 52, n 4, (2004), pp. 907-924.

Wu 2004c — Wu S J, Davis C L; "Investigation of the microstructure and mesotexture formed during TMCR in microalloyed steels;Journal of Microscopy, v 213, (2004), pp. 262-272.

Wu 2005 — Wu S J, Davis C L, Shterenlikht A and Howard I C; Modelling the ductile-brittle transition behaviour in thermomechanically controlled rolled steels"; Metallurgical and Materials Transactions, 36A, (2005), pp. 989-997.

Y

Yan 1993 — Yan C, Chen J H, Sun J, Wang Z; "Critical assessment of local cleavage stress in notched specimens of C-Mn steel";Metallurgical Transactions, 24A, (1993), pp. 1381–1389.

Z

Zajac 2005 — Zajac S; "Precipitation of microalloy carbo-nitrides prior, during and after g / a transformation";Materials Science Forum, v 500-501, (2005), pp. 75-86.

Zener 1948a — Zener C; quoted by Smith C S; "Grains, phases and interphases, an interpretation of microstructure";Transactions of Metallurgical Society of AIME; v 175, (1948), pp. 15-51.

Zener 1948b — Zener C; "The micromechanism of fracture";Transactions ASM, v 40 A, (1948), pp. 3-31.

Zener 1950 — Zener C, Wert C; "Interface of growing spherical precipitate particles";Journal of Applied Physics, v 21, (1950), pp. 5-8.

Zhang 1999 — Zhang L P, Davis C L, Strangwood M; "Effect of TiN [titanium nitride] particles and microstructure on fracture toughness in simulated heat-affected zones of a structural steel"; Metallurgical and Materials Transactions A, v 30A, n 8, (1999), pp. 2089-2096.

Zhang 2000a — Zhang L P, Davis C L, Strangwood M; “Assessment of microstructural development during continuous casting of microalloyed bars”;Proc. Conf. On ‘Thermomechanical processing of steels’, published by IoM Communications, ISBN I-86125-122-X, London, (2000), pp. 764-775.

Zhang 2000b — Zhang X Z, Knott J F; “The statistical modelling of brittle fracture of homogeneous and heterogeneous steel microstructures”;Acta Materialia, v 48, n 9, (2000), pp. 2135-3146.

Zhang 2001 — Zhang L P, Davis C L, Strangwood M; “Dependency of fracture toughness on the inhomogeneity of coarse TiN particle distribution in a low alloy steel”; Metallurgical and Materials Transactions A, v 32A, n 5, (2001), pp. 1147-1155.

Zhen 1992 — Zhen L, Hongtao Z, Baorong W; “Effect of Nb on hot ductility of low carbon low alloy steel and its mechanism”;Proc. 2nd Int. Conf. On ‘HSLA steels: processing, properties and applications’, (ed. G. Tither et al.), Baijing, China, TMS, Warrendale, (1992), pp. 239-244.

Zou 1991 — Zou H, Kirkaldy J S; “Carbonitride precipitate growth in Ti / Nb microalloyed steels”;Metallurgical and Materials Transactions A, v 22A, (1991), pp. 1511-1524.